



## Multimetallic organometallic complexes

in pursuit of novel dinuclear complexes bearing N-heterocyclic carbene ligands

Nielsen, Mathias Thor

*Publication date:*  
2022

*Document Version*  
Publisher's PDF, also known as Version of record

[Link back to DTU Orbit](#)

*Citation (APA):*  
Nielsen, M. T. (2022). *Multimetallic organometallic complexes: in pursuit of novel dinuclear complexes bearing N-heterocyclic carbene ligands*. DTU Chemistry.

---

### General rights

Copyright and moral rights for the publications made accessible in the public portal are retained by the authors and/or other copyright owners and it is a condition of accessing publications that users recognise and abide by the legal requirements associated with these rights.

- Users may download and print one copy of any publication from the public portal for the purpose of private study or research.
- You may not further distribute the material or use it for any profit-making activity or commercial gain
- You may freely distribute the URL identifying the publication in the public portal

If you believe that this document breaches copyright please contact us providing details, and we will remove access to the work immediately and investigate your claim.

**Multimetallic organometallic complexes: in pursuit of novel  
dinuclear complexes bearing *N*-heterocyclic carbene ligands**

a dissertation presented

by

Mathias Thor Nielsen

to

The Department of Chemistry

in partial fulfilment of the requirements

for the degree of

PhD

in the subject of

Chemistry

The Technical University of Denmark

Kongens Lyngby, Denmark

July 2022



## Abstract

Pursuant to the exploration of dinuclear complexes, two naphthalene-based macrocyclic tetra imidazolium proligands were developed and characterized by a variety of different techniques. Both were envisioned to ditopically coordinate *via* the chelating *N*-heterocyclic carbenes, NHCs, and the naphthalene moieties serving to separate the metal centers and induce a discriminating binding pocket. To support that two palladium(II) ions spatially fit a ligand architecture comprising two fused benzene rings, the homoleptic paddlewheel complex resulting from 1,8-naphthyridine was studied. Indeed, support for such an arrangement and proximity-induced redox properties were found.

Encouraged by this result, the connectivity of the metal complexes resulting from the naphthalene-proligands was sought through three different strategies focusing on palladium(II) following its predictable coordination chemistry: the metalation adducts are all telling of single complex architecture, wherein the metal bears a macrocyclic NHC ligand. Additionally, a subtle intraligand difference concerning the NHC spacing results in the separation of either a square-planar complex, demonstrating accessible axial coordination sites, or a complex demonstrating a would-be unsymmetric binding pocket.

Of the former type, the chemistry concerning nickel(II) and palladium(II) complexes was explored from which surprisingly stable high-valent adducts were isolated; the *bona fide* Ni(III) and Pd(IV) complexes demonstrate surprising stability in air. Furthermore, I found data suggesting that a dichlorido Pd(IV) complex acts as an apt catalyst precursor for water-oxidation, specifically the oxygen-evolving reaction.

In closing, a chapter on my research exchange with Professor Theodore Betley at Harvard University, where I account for the synthesis of a triruthenium cluster, the cluster framework supported by a weak-field ligand, and each Ru bound by a phosphine.

## Resumé

Det har været målsætningen med mit ph.d.-studium, at syntetisere naphthalen-baserede makrocycliske tetra imidazolium prolignander og undersøge disses koordinationskemi med henblik på tilblivelsen af ditopiske koordinationsforbindelser gennem *N*-heterocycliske carbener. Naphthalen var valgt, for sikre at to palladium(II) ioner blev tvunget tilstrækkelig tæt på hinanden, så synergi mellem to de metaller blev opnået. I denne sammenhæng studerede jeg det homoleptiske møllehjuls kompleks mellem 1,8-naphthyridin og palladium(II); delvist for at understøtte, at to palladium(II) ioner fysisk ville kunne tvinges så tæt på hinanden, og delvist for at forstå en eventuel synergi som følge af ændringer i kompleksets elektrokemiske egenskaber.

Med udgangspunkt i disse resultater forsøgte jeg at tilvejebringe de ønskede bimetalliske komplekser gennem tre forskellige strategier, med udgangspunkt i palladium (II)s forudsigelige koordinationskemi som desværre vidner om én enkelt struktur, hvor et metal koordineres af en makrocyclisk ligand gennem fire NHC'er. Yderligere fandt jeg, at en subtil forskel i den rummelige adskillelse af de chelaterende NHC'er ledte til henholdsvis et plankvadratisk kompleks med tilgængelige aksiale koordinationsflader, og et kompleks, der demonstrerer en usymmetrisk bindingslomme.

Af den førstnævnte type udforskede jeg kemien af nikkel(II) og palladium(II) komplekser, hvor Ni(III) og Pd(IV) komplekser, som udviser en overraskende stabilitet i luft, blev isoleret og karakteriseret. Desuden argumenteres der med udgangspunkt i substantiel empirisk evidens, at et af Pd(IV) kompleksene fungerer som præ-katalysator for den oxygenudviklende vand-oxidationsreaktion.

Afslutningsvis præsenteres i Kapitel 6 de resultater fra mit udvekslingsophold ved Harvard University i professor Theodore Betleys forskningsgruppe vedrørende ruthenium.

# Tables of Content

<b>Chapter. 1. Polymetallic clusters and dinuclear complexes</b>	<b>1</b>
1.1 Introduction to cluster and dinuclear compounds	1
1.2 The interaction between two metals	6
1.3 Two metals: reactivity of the metal-metal bond	9
1.4 Dinuclear complexes as biomimetic compounds	16
1.5 References	18
<b>Chapter. 2. The paddlewheel complex of 1,8-naphthyridine and palladium(II)</b>	<b>23</b>
2.1 Introduction	23
2.2 Complex synthesis and characterization	26
2.3 The paddlewheel complex as a synthon for Pd-Pd bonded complexes	39
2.4 Conclusion	42
2.5 References	43
<b>Chapter. 3. Synthesis of tetra imidazolium proligands</b>	<b>46</b>
3.1 Introduction	46
3.2 Tethering imidazole to naphthalene	47
3.3 Synthesis of naphthalene-based, methylene-linked macrocycle tetra imidazolium salt	50
3.3.1 Structural characterization of <b>3.1</b>	55
3.3.2 Anion metathesis	58
3.4 Synthesis of naphthalene-based, ethylene-linked macrocycle tetra imidazolium salt	60
3.4.1 Structural characterization of <b>3.4</b>	63
3.5 Synthesis of anthracene-based, methylene-linked macrocycle tetra imidazolium salt	65

3.6	Macrocycles <b>3.1</b> and <b>3.4</b> as anion receptor: binding of phosphate.....	70
3.7	Conclusion.....	73
3.8	References .....	74
<b>Chapter. 4. In pursuit of ditopic NHC-complexes .....</b>		<b>76</b>
4.1	Introduction .....	76
4.1.1	Dipalladium and dinickel complexes bearing NHC ligands .....	85
4.2	Monopalladium complex syntheses .....	87
4.2.1	Concurrent deprotonation-metalation.....	87
4.2.2	Carbene-transfer reagents in transmetalation reactions.....	88
4.3	Seeking dipalladium complexes via the “acetate route” .....	97
4.3.1	Structural characterization of complexes <b>4.13</b> and <b>4.14</b> .....	102
4.4	Seeking dipalladium complexes via transmetalation .....	109
4.4.1	Exploration of silver-intermediates: synthesis and characterization .....	109
4.4.2	Exploring transmetalation as means of synthesizing dinuclear complexes.....	120
4.5	Seeking dinuclear complexes by metalation of free-carbenes .....	124
4.5.1	The-not-so-encouraging metalation-results.....	128
4.6	Conclusion.....	132
4.7	References .....	135
<b>Chapter. 5. High-valent Ni and Pd complexes bearing a macrocyclic tetra NHC ligand .....</b>		<b>137</b>
5.1	Introduction .....	138
5.1.1	Complexes bearing N-porphyrin and macrocyclic tetra NHC ligands.....	138
5.2	Pd (IV) dihalido complexes bearing a macrocyclic tetra NHC ligand.....	149
5.2.1	Structural characterization of complexes <b>5.1</b> and <b>5.2</b> .....	158
5.3	Water: a peculiar reductant.....	162

5.4	A Ni (III) complex bearing a macrocyclic tetra NHC ligand.....	168
5.4.1	Characterization of complex 5.4.....	169
5.4.2	Towards Ni (IV) .....	178
5.5	Conclusion.....	180
5.6	References .....	182
<b>Chapter 6. In pursuit of ruthenium clusters .....</b>		<b>186</b>
6.1	Introduction .....	188
6.2	Synthesis of Ru (II) complexes bearing internal bases .....	188
6.3	Transmetalation reactions.....	191
6.4	Conclusion.....	196
6.5	References .....	197

## Acknowledgements

The foregoing four years of PhD studies have been nothing but fantastic. To my supervisor, Martin Nielsen, my sincerest thank you. Thank you for the opportunity that you presented, enabling me to pursue research, learn, and broaden my perspective on organometallic chemistry. But mostly, thank you for being a mentor in the truest sense, through ups and downs. Thank you to my co-supervisors Kasper and Susanne, for their insights and interest and for providing further grounds for fruitful discussions on spectroscopy and fundamental studies. To Ted, I am grateful to you for hosting me in Boston, allowing me to pursue cluster chemistry, further broadening my appreciation of inorganic chemistry, our many insightful discussions, and your interest in my projects.

To my friend Mike, it has been a pleasure sharing the highs, the lows, and everything in-between through four years. With Alexander and Danielle, the many hours spent in the laboratory around the three of you were a daily highlight of mine. Luca and Brenda thank you for your friendship. I would like to express my gratitude to my collaborators at DTU Chemistry, whose expertise has helped the different projects tremendously.

To the entirety of the Betley lab, thank you for welcoming me to Boston. Thank you, Nick, Trevor, Ivan, Yifan, and Jeewhan for your friendship, the many hours of fun, the introduction to the CCB facilities (especially the X-ray lab), and the countless discussion on chemistry.

Lastly, my deepest gratitude to my closest family, especially my parents, Flemming and Solveig, and my brother Martin, for their unconditional support and encouragement, without you, I would not be where I am today. To my closest friends, thank you for all your support, your overbearingness, and your genuine interest in my research. To Carlota, your love, support, and company enrichen my every day.

## List of Figures

<b>Figure 1.1.</b> Complexes capable of facilitating N <sub>2</sub> fixation.....	1
<b>Figure 1.2.</b> Compounds representative of molecular cluster compounds. ....	2
<b>Figure 1.3.</b> Murray's trimetallic platform. ....	5
<b>Figure 1.4.</b> Simplified molecular orbital diagram accounting Re-Re quadruple bond in Re <sub>2</sub> Cl <sub>8</sub> <sup>2-</sup> . 6	
<b>Figure 1.5.</b> Naphthyridine-tetrapyridine explored by Tilley.....	8
<b>Figure 1.6.</b> Dinuclear complexes stabilized by arene interactions explored by Agapie. ....	8
<b>Figure 1.7.</b> Dinuclear complexes relevant as biomimetic compounds.....	16
<b>Figure 2.1.</b> Stacked <sup>1</sup> H NMR spectra comparing <b>2.1</b> (top), napy (middle), and [Pt(napy) <sub>4</sub> ] 2PF <sub>6</sub> (lower) to one-another. ....	28
<b>Figure 2.2.</b> Single-crystal X-ray structure of the paddlewheel complex <b>2.1</b> .....	29
<b>Figure 2.3.</b> Optical absorption spectra of <b>2.1</b> and napy in DMF.....	30
<b>Figure 2.4.</b> DFT-calculated frontier molecular orbitals. ....	32
<b>Figure 2.5.</b> Mid-infrared and far-infrared spectral regions pertaining to <b>2.1</b> .....	33
<b>Figure 2.6.</b> The animation of the large-amplitude concerted out-of-plane N--Pd--N bending mode of <b>2.1</b> . ....	35
<b>Figure 2.7.</b> The experimental far-infrared attenuated-total-reflectance spectrum of <b>2.1</b> (blue trace) together with a simulation of the spectrum at the TPSS-D4/def2-TZVP level of theory (red trace). ....	35
<b>Figure 2.8.</b> Stacked cyclic voltammograms of napy (blue trace) and <b>2.2</b> (black and red traces)..	37
<b>Figure 2.9.</b> Voltammogram of <b>2.2</b> over various scan rates. Increasing the scan-rate results in a species that demonstrate electrochemical reversibility with respect to oxidation/reduction. ....	37
<b>Figure 2.10.</b> Single-crystal X-ray structure of isolable material following Ce (IV) oxidation of <b>2.2</b> , complex <b>2.3</b> .....	39
<b>Figure 2.11.</b> Single-crystal X-ray structure of a phosphine-napy-Pd (II) complex, complex <b>2.4</b> .	41
<b>Figure 3.1.</b> Different dinuclear complexes are known to facilitate multi-electron transformations. ....	46
<b>Figure 3.2.</b> Envisioned dinuclear complex of interest to this PhD-study.....	47

<b>Figure 3.3.</b> 2D $^1\text{H}$ NMR of $^{\text{Me,Naph}}\text{LH}_4\text{-4Br}$ crude. A selected range of the $\{^1\text{H}\text{-}^1\text{H}\}$ COSY spectrum (in $\text{DMSO-}d_6$ ) of the recovered material from initial self-assembly.....	51
<b>Figure 3.4.</b> Stacked 1D $^1\text{H}$ NMR of solids obtained from macrocycle self-assembly at various conditions.....	53
<b>Figure 3.5.</b> HSQC of compound <b>3.1</b> . ....	56
<b>Figure 3.6.</b> Solid-state structure of compound <b>3.1</b> obtained in DMSO.....	57
<b>Figure 3.7.</b> Stacked 1D $^1\text{H}$ NMR spectra demonstrating counterion influence on macrocycle $^1\text{H}$ resonances.....	59
<b>Figure 3.8.</b> Stacked 1D $^1\text{H}$ NMR spectra ( $\text{DMSO-}d_6$ ) of <b>3.4</b> comparing crude material to its single crystals. ....	61
<b>Figure 3.9.</b> Changes occurring to the $^1\text{H}$ NMR spectra ( $\text{DMSO-}d_6$ ) shifts following salt metathesis of compound <b>3.4</b> .....	64
<b>Figure 3.10.</b> Changes occurring to the $^{13}\text{C}$ NMR ( $\text{DMSO-}d_6$ ) shifts following salt metathesis of compound <b>3.4</b> . ....	64
<b>Figure 3.11.</b> Comparing $^1\text{H}$ NMR ( $\text{DMSO-}d_6$ ) spectra of isolated materials pertinent to compound <b>3.6</b> , crude isolate (top), and isolated $\text{PF}_6$ salt (lower) .....	67
<b>Figure 3.12.</b> $\{^1\text{H}\text{-}^{13}\text{C}\}$ HSQC of crude <b>3.6</b> .....	69
<b>Figure 3.13.</b> Compounds <b>3.1</b> and <b>3.4</b> binding with iP and Glc-1-P.. ....	71
<b>Figure 3.14.</b> <b>3.1</b> binding isotherm to iP and Glc-1-P .....	71
<b>Figure 3.15.</b> <b>3.4</b> binding isotherm to iP and Glc-1-P. ....	71
<b>Figure 4.1.</b> Prototypical carbene motif observed in organometallic chemistry.. ....	76
<b>Figure 4.2.</b> Qualitative molecular orbital diagram demonstrating electronic ground state differences in NHCS, following the electronic nature of the vicinal substituent and depiction of the mesomeric effect.....	77
<b>Figure 4.3.</b> Bonding modes pertaining to NHC-metal complexes. The figure depicts the interaction between a ground state singlet NHC to that of an arbitrary metal center.. ....	79
<b>Figure 4.4.</b> The two first reported NHC-metal complexes.....	79
<b>Figure 4.5.</b> Representative architectures of macrocyclic poly NHC-Ag intermediates .....	82
<b>Figure 4.6.</b> HEP scale with selected mono dentate NHC ligands .....	84



<b>Figure 4.7.</b> Comparison between $^1\text{H}$ NMR spectra ( $\text{DMSO}-d_6$ ) of compound <b>4.2</b> with complex <b>4.6</b> .....	90
<b>Figure 4.8.</b> Comparison between $^{13}\text{C}$ NMR spectra ( $\text{DMSO}-d_6$ ) of compound <b>4.2</b> with complex <b>4.6</b> . .....	90
<b>Figure 4.9.</b> Single-crystal X-ray structures of monopalladium bis-NHC complex <b>4.9</b> .....	92
<b>Figure 4.10.</b> Single-crystal X-ray structures of monopalladium bis-NHC complex <b>4.10</b> .....	92
<b>Figure 4.11.</b> Consideration of each NHC's twist-angle to Pd and bonding metrics of <b>4.9</b> and <b>4.10</b> .....	93
<b>Figure 4.12.</b> Comparison between $^1\text{H}$ NMR spectra (in $\text{CD}_3\text{CN}$ ) of <b>4.9</b> (top) and <b>4.10</b> (bottom) .....	95
<b>Figure 4.13.</b> Comparison between $^{13}\text{C}$ NMR spectra (in $\text{CD}_3\text{CN}$ ) of <b>4.9</b> (top) and <b>4.10</b> (bottom).....	95
<b>Figure 4.14.</b> Metalation of <b>3.1</b> with $\text{Pd}(\text{OAc})_2$ .....	98
<b>Figure 4.15.</b> The solid-state structure of complex <b>4.13</b> .....	98
<b>Figure 4.16.</b> Metalation of <b>3.4</b> with 1.0 equiv. $\text{Pd}(\text{OAc})_2$ .....	100
<b>Figure 4.17.</b> The solid-state structure of complex <b>4.14</b> . .....	100
<b>Figure 4.18.</b> Illustration of bonding metrics pertaining to the core of <b>4.13</b> .....	103
<b>Figure 4.19.</b> Comparison between $^1\text{H}$ NMR spectra (in $\text{CD}_3\text{CN}$ ) of <b>4.13</b> (top) and <b>4.14</b> (bottom). .....	103
<b>Figure 4.20.</b> FT-IR spectrum of complex <b>4.13</b> .....	104
<b>Figure 4.21.</b> Illustration of bonding metrics pertaining to the core of <b>4.14</b> .....	105
<b>Figure 4.22.</b> Selected regions of the $^{13}\text{C}$ NMR spectrum ( $\text{CD}_3\text{CN}$ ) of <b>4.14</b> . .....	106
<b>Figure 4.23.</b> Suggested fluxional behavior of complex <b>4.14</b> .....	107
<b>Figure 4.24.</b> Stacked $^1\text{H}$ NMR spectra (in $\text{CD}_3\text{CN}$ ) of complex <b>4.14</b> at selected temperatures..	107
<b>Figure 4.25:</b> Transmetalation of <b>3.1</b> in DMSO .....	110
<b>Figure 4.26.</b> Transmetalation of <b>3.1</b> in MeOH.....	112
<b>Figure 4.27.</b> Transmetalation of <b>3.1</b> in MeOH.....	112
<b>Figure 4.28.</b> Transmetalation of compound <b>3.2</b> in MeCN .....	113
<b>Figure 4.29.</b> Tetrasilver dimer, complex <b>4.15</b> .....	114

<b>Figure 4.30.</b> Reacting compound <b>3.4</b> with Ag <sub>2</sub> O in MeOH, isolated material dissolved in MeOH- <i>d</i> <sub>4</sub> .....	116
<b>Figure 4.31.</b> Hexasilver trimer, complex <b>4.16</b> .....	117
<b>Figure 4.32.</b> <sup>1</sup> H NMR spectral properties (in CD <sub>3</sub> CN) of the silver-adduct following Ag-metalation of compound <b>3.6</b> .....	119
<b>Figure 4.33.</b> Synthesis and solid-state of complex <b>4.18</b> .....	121
<b>Figure 4.34.</b> <sup>1</sup> H and <sup>13</sup> C NMR (CD <sub>3</sub> CN) spectral properties of complex <b>4.18</b> .....	122
<b>Figure 4.35.</b> Bonding metrics pertaining to the core of <b>4.18</b> .....	122
<b>Figure 4.36.</b> Metalation of the free-carbene <b>3.1</b> with excess Pd(OAc) <sub>2</sub> .....	126
<b>Figure 4.37.</b> <sup>31</sup> P NMR spectra of reaction adducts following ligand substitution of Pd <sub>2</sub> (μ-dppm)Cl <sub>2</sub> with free carbenes.....	128
<b>Figure 4.38.</b> <sup>31</sup> P NMR spectra of reaction adducts following ligand substitution of Pd <sub>2</sub> (μ-dppm)Cl <sub>2</sub> with the free carbene of compound <b>3.4</b> .....	129
<b>Figure 4.39.</b> <sup>1</sup> H NMR spectra of reaction adducts following ligand substitution of [Pd <sub>2</sub> (MeCN) <sub>6</sub> ] 2BF <sub>4</sub> with the free carbene of <b>3.1</b> .....	130
<b>Figure 5.1.</b> Electronic differences between complexes bearing <i>N</i> -porphyrins and macrocyclic tetra NHC ligands. ....	139
<b>Figure 5.2.</b> Half-cell potential of the Fe <sup>2+/3+</sup> redox-couple changes with the number of NHC ligands.....	140
<b>Figure 5.3.</b> First lanthanide and actinide complexes bearing macrocyclic tetra NHC ligands ...	144
<b>Figure 5.4.</b> Cyclic voltammograms of complexes <b>4.13</b> at different scan-rates and redox-events relationship with scan-rate.....	149
<b>Figure 5.5.</b> Cyclic voltammograms of complexes <b>4.9</b> at different scan-rates and redox-events relationship with scan-rate.....	150
<b>Figure 5.6.</b> Solid-state structure of <b>5.1</b> .....	152
<b>Figure 5.7.</b> Solid-state structure of <b>5.2</b> .....	152
<b>Figure 5.8.</b> <sup>19</sup> F NMR spectrum (CD <sub>3</sub> CN) of XeF <sub>2</sub> oxidation of <b>4.13</b> .....	153
<b>Figure 5.9.</b> <sup>1</sup> H NMR (CD <sub>3</sub> CN, ambient atmosphere) spectra comparison of <b>4.13</b> to its high-valent Pd (IV) congeners.....	154

<b>Figure 5.10.</b> Combined $^1\text{H}$ NMR spectrum ( $\text{CD}_3\text{CN}$ ) and $\{^1\text{H}-^1\text{H}\}$ COSY of <b>5.3</b> (putative).....	155
<b>Figure 5.11.</b> Halide-NHC bridge interaction was reported by the Kraft group .....	157
<b>Figure 5.12.</b> Bonding metrics of the Pd(IV) core of <b>5.1</b> and <b>5.2</b> .....	159
<b>Figure 5.13.</b> HOMO/LUMO of Pd (IV) complexes .....	161
<b>Figure 5.14.</b> Progressive reduction of Pd (IV) dichlorido.....	163
<b>Figure 5.15.</b> Water-oxidation under catalytic conditions .....	164
<b>Figure 5.16.</b> $^1\text{H}$ NMR spectra of an aliquot following water oxidation .....	165
<b>Figure 5.17.</b> Cyclic voltammogram of complex <b>4.18</b> .....	168
<b>Figure 5.18.</b> $^1\text{H}$ NMR spectra ( $\text{CD}_3\text{CN}$ ) of complex <b>4.18</b> and its adduct following $\text{Br}_2$ addition .....	169
<b>Figure 5.19.</b> Synthesis and solid-state structure of complex <b>5.4</b> .....	170
<b>Figure 5.20.</b> Bonding metrics pertaining to complexes <b>4.18</b> and <b>5.4</b> .....	171
<b>Figure 5.21.</b> EPR spectrum following $\text{Br}_2$ addition to complex <b>4.18</b> .....	172
<b>Figure 5.22.</b> Complex <b>5.4</b> and substitution reactions with various nucleophiles.....	172
<b>Figure 5.23.</b> DFT-calculated metal-centered SOMO and LUMO .....	173
<b>Figure 5.24.</b> Spin-density plot of complex <b>5.4</b> .....	176
<b>Figure 5.25.</b> $^1\text{H}$ NMR spectra ( $\text{CD}_3\text{CN}$ ) of complex <b>4.18</b> reacting with increasing equivalents of $\text{PhICl}_2$ .....	178
<b>Figure 6.1.</b> Single-crystal structure following attempted ligand substitution of $[\text{RuCl}_2(\text{cod})]_n$ , <b>6.1</b> .....	190
<b>Figure 6.2.</b> $^1\text{H}$ NMR spectra ( $\text{C}_6\text{D}_6$ ) comparing $^{\text{Me,F}}\text{LH}_6$ (top) to its Mg-adduct (lower) .....	192
<b>Figure 6.3.</b> $^{19}\text{F}$ NMR spectra ( $\text{C}_6\text{D}_6$ ) comparing $^{\text{Me,F}}\text{LH}_6$ (top) to its Mg-adduct (lower) .....	192
<b>Figure 6.4.</b> $^1\text{H}$ NMR spectra ( $\text{C}_6\text{D}_6$ ) of isolated transmetalation adduct .....	194
<b>Figure 6.5.</b> $^{19}\text{F}$ (top) and $^{31}\text{P}$ (lower) NMR spectra ( $\text{C}_6\text{D}_6$ ) of isolated transmetalation adduct ..	195
<b>Figure 6.6.</b> HR-MS (Maldi-TOF) of isolated transmetalation adduct .....	195

## List of Schemes

<b>Scheme 1.1.</b> A triruthenium cluster apt at catalyzing the hydrogenation of hydrazine and diazene. ....	3
<b>Scheme 1.2.</b> Dick Holm's seminal work. ....	3
<b>Scheme 1.3.</b> Metalation of a sterically encumbered tritopic ligand. ....	4
<b>Scheme 1.4.</b> Multiple-electron transfer reactions by a molecular triiron cluster. ....	4
<b>Scheme 1.5.</b> "Double decker" ligand platform explored by Lu and Thomas ....	6
<b>Scheme 1.6.</b> Exposure to carbonyl ferrate and cobaltate facilitate core expansion.....	9
<b>Scheme 1.7.</b> Oxidative addition across a Pd-Pd bond .....	10
<b>Scheme 1.8.</b> Oxidative addition leading to loss of M-M bond .....	10
<b>Scheme 1.9.</b> Suggested elementary steps involved in the transformation of PhI, mediated by a dipalladium (I) complex. ....	11
<b>Scheme 1.10.</b> A related dinickel(I) fragment dissociates into monometallic complexes .....	11
<b>Scheme 1.11.</b> Oxidative addition across a polarized M-M bond .....	12
<b>Scheme 1.12.</b> Substrate activation mediated by an intermediary metal-metal bonded dipalladium complex.....	12
<b>Scheme 1.13.</b> Stoichiometric studies of heterobimetallic complexes .....	13
<b>Scheme 1.14.</b> Silane binding of a dinickel (0) complex .....	14
<b>Scheme 1.15.</b> Different oxidation states available to Uyeda's dinickel complex.....	14
<b>Scheme 1.16.</b> Metal-meta interaction suggested key to high activity of a dirhodium complex ....	15
<b>Scheme 1.17.</b> Substrate activation facilitated by a dinickel complex .....	15
<b>Scheme 1.18.</b> Dinickel (II) bearing terminal hydrides react as masked low-valent $\text{Ni}_2^{2+}$ .....	17
<b>Scheme 1.19.</b> Biomimetic dicopper complex demonstrating oxygen activation relevant to metalloenzymes .....	17
<b>Scheme 2.1.</b> Two-center oxidative addition of $\text{I}_2$ by a dirhodium(I) complex .....	24
<b>Scheme 2.2.</b> Shortest Pd-Pd separation and Pd-Pd bond length .....	26
<b>Scheme 2.3.</b> Synthetic outline for chemical oxidation of the paddlewheel complex .....	40

<b>Scheme 2.4.</b> Synthetic outline for comproportionation reactions .....	41
<b>Scheme 3.1.</b> Synthesis and solid-state structure of <b>3.1</b> . ....	50
<b>Scheme 3.2.</b> Synthetic approach for functionalization of 1,8-naphthalene.....	52
<b>Scheme 3.3.</b> Synthetic approach for triflation, tosylation, nosylation .....	53
<b>Scheme 3.4.</b> Salt metathesis of <b>3.1</b> .....	58
<b>Scheme 3.5.</b> Synthesis and solid-state structure of compound <b>3.4</b> . ....	60
<b>Scheme 3.6.</b> Different synthetic approach targeting the ethylene-linked macrocycle.....	62
<b>Scheme 3.7.</b> Synthesis of anthracene congener.....	65
<b>Scheme 3.8.</b> Phosphate-receptor-dependent phosphorylase-catalyzed formation of $\alpha$ -1,4-glucans.....	70
<b>Scheme 4.1.</b> Wanzlick equilibrium .....	78
<b>Scheme 4.2.</b> Chelate complex preparation through the “acetate route” .....	88
<b>Scheme 4.3.</b> Preparation of NHC-Ag intermediates through two routes.....	89
<b>Scheme 4.4.</b> Transmetalation route using silver-carbene transfer-reagents. ....	91
<b>Scheme 4.5.</b> Transmetalation differences. ....	92
<b>Scheme 4.6.</b> Conceptual approach targeting dipalladium complexes.....	98
<b>Scheme 4.7.</b> The conceptual framework for Ag-metalation.....	110
<b>Scheme 4.8.</b> Ag-metalation of compound <b>3.2</b> .....	114
<b>Scheme 4.9.</b> Metalation of compound <b>3.6</b> . ....	119
<b>Scheme 4.10.</b> The conceptual framework for transmetalation towards dinuclear complexes.....	121
<b>Scheme 4.11.</b> Synthetic approaches investigated in this PhD study, toward dinuclear complexes. ....	125
<b>Scheme 4.12.</b> The conceptual approach to synthesize dinickel (I) complex .....	132
<b>Scheme 5.1.</b> Hydroxylation of inactive C-H bonds .....	138
<b>Scheme 5.2.</b> Metal-templated synthesis of the first macrocyclic tetradentate.....	142
<b>Scheme 5.3.</b> High-dilution synthesis of a propyl linked macrocyclic tetra NHC Pd (II) complex.....	142

<b>Scheme 5.4.</b> First catalytic aziridination reaction with macrocyclic tetra NHC complex.....	143
<b>Scheme 5.5.</b> Reactivity of all ferrous complex bearing macrocyclic tetra NHC.....	145
<b>Scheme 5.6.</b> Macrocyclic tetra NHC Fe-complexes in epoxidation catalysis .....	146
<b>Scheme 5.7.</b> The reactivity of an Fe (II) macrocyclic tetra NHC complex with O <sub>2</sub> . ....	147
<b>Scheme 5.8.</b> Elucidation on the reactivity of a Co (II) macrocyclic tetra NHC complex with O <sub>2</sub> . .....	148
<b>Scheme 5.9.</b> Initial oxidation reactions targeting Pd (IV) complexes.....	151
<b>Scheme 5.10.</b> Oxidation of <b>4.13</b> with halide (surrogates) .....	152
<b>Scheme 5.11.</b> Experiments to verify that <b>4.13</b> does not form multiple ligand-metal bonds. ....	161
<b>Scheme 5.12.</b> A strategy targeting dihydroxy Pd (IV) complex .....	166
<b>Scheme 5.13.</b> Suggested catalytic cycle pertaining to oxygen-evolving reaction .....	167
<b>Scheme 5.14.</b> Oxidation of Ni (II) bearing an inverted N-porphyrin .....	177
<b>Scheme 6.1.</b> The synthetic strategy targets either organoruthenium (II) complexes .....	188
<b>Scheme 6.2.</b> The synthetic approach targets the Ru (II)-NTMS base .....	190
<b>Scheme 6.3.</b> Synthesis of trismagnesium cluster synthon .....	191
<b>Scheme 6.4.</b> Synthetic strategy concerning transmetalation .....	193

## List of Charts

<b>Chart 2.1.</b> Mixing of <i>d</i> -orbitals in paddlewheel complexes. ....	24
<b>Chart 2.2.</b> Representative paddlewheel complex ligands.....	25
<b>Chart 3.1.</b> Various synthetic approaches explored towards the direct tether of imidazole to naphthalene .....	48
<b>Chart 4.1.</b> Different successful preparation of NHC metal complexes. ....	81
<b>Chart 4.2.</b> Prototypical coordination geometries of low-valent dipalladium(I) complexes.....	86
<b>Chart 4.3.</b> Complexes found following the “acetate route”. ....	102
<b>Chart 4.4.</b> CCDC structures of Ni (II) complexes bearing macrocyclic tetra NHC ligands.....	124
<b>Chart 4.5.</b> Dinuclear complexes were investigated in this study .....	128
<b>Chart 5.1.</b> All the different macrocyclic tetradentate NHC complexes .....	141
<b>Chart 5.2.</b> Oxidation of Ni (II) complexes bearing inverted <i>N</i> -porphyrin ligands .....	177
<b>Chart 6.1.</b> The tritopic ligand <sup>tbs</sup> LH <sub>6</sub> provides the basis for versatile transformations .....	187

## List of Tables

<b>Table 3.1.</b> Binding parameters for the interaction of compounds <b>3.1</b> and <b>3.4</b> with iP and Glc-1-P in HEPES buffer (D <sub>2</sub> O, 50 mM, pH 6.8) at 298 K. ....	72
<b>Table 5.1.</b> DFT reproduced bond-length of complex <b>5.4</b> .....	173
<b>Table 5.2.</b> DFT calculated EPR parameters .....	175

## List of Acronyms, symbols, and units

$^{13}\text{C}$	carbon-13
$^1\text{H}$	proton
Ar	Aryl
$\text{cm}^{-1}$	Wavenumbers, inverse centimetres
$\text{C}_n$	Carbon atom at the $n$ th position of a moiety, ylidine or naphthalene
$\text{C}_n\text{-H}$	Proton associated a carbon atom at the $n$ th position of a moiety, ylidine or naphthalene
CV	Cyclic voltammetry
d	doublet in NMR
DCM	Dichloromethane
DFT	Density-functional theory
DMF	<i>N, N'</i> -Dimethylformamide
DMSO	Dimethyl sulfoxide
$d_n$	deuterated, $n$ indicates the number of H replaced by D
EPR	Electron Paramagnetic Resonance
Equiv.	Equivalents of component X
Et	Ethyl
$\text{Et}_2\text{O}$	Diethyl ether
$\text{Fc}/\text{Fc}^+$	Ferrocene/Ferrocenium redox couple
HOMO	Highest Occupied Molecular Orbital
LUMO	Lowest Unoccupied Molecular Orbital
Me	Methyl
MeCN	Acetonitrile
Mes	Mesityl, 2,4,6-trimethylphenyl
MHz	Megahertz, $10^6 \text{ s}^{-1}$
mmol	Millimole, $10^{-3}$ mole
Napy	1,8-naphthyridine
NHC	<i>N</i> -heterocyclic carbene
NMR	Nuclear Magnetic Resonance
$^n\text{J}(\text{X-Y})$	$n$ th bond coupling constants between nuclei X and Y
o.n.	Overnight
Pd	Palladium
Ph	Phenyl
RT	Room temperature
s	singlet in NMR
$S$	Total spin-multiplicity, $2ns + 1$ , $s$ = number of unpaired electrons
SOMO	Singly occupied Molecular Orbital
t	Triplet in NMR
TBAX	$n$ -tetrabutyl ammonium bearing anion X, <i>e.g.</i> X = Br, I, $\text{PF}_6$
THF or thf	Tetrahydrofuran
UV-Vis	Ultraviolet-visible absorption spectroscopy
$\delta$	The chemical shift in NMR
$\varphi$	Twist angle of ylidine $\pi$ -system relative to the plane of coordination



## List of publications, dissemination activities, and awards

### *Published publications*

1. **Nielsen, M.T.**; Padilla, R.; and Nielsen, M. *J. Clust. Sci.*, **2020**, *31*, 11 – 61.

### *Manuscripts in preparation – included as appendices*

1. **Nielsen, M. T.**; Mihrin, D.; Jørgensen, S. B. M.; Yan, X.; Xiao, X.; Berg, R. W.; Larsen, R. W.; and Nielsen, M. “The paddlewheel complex of 1,8-naphthyridine and palladium(II). Synthesis, characterization, and reactivity studies”
2. **Nielsen, M. T.**; and Nielsen, M. “Exploration of unsymmetric coordination environment in a Pd (II) complex bearing a macrocyclic tetra NHC ligand”.
3. **Nielsen, M. T.**; Jørgensen, S. B. M.; Litak, N.; Zheng, S.-L.; Mossin, S. L.; and Nielsen, M. “A surprisingly stable organometallic Ni (III) complex bearing a macrocyclic tetra *N*-heterocyclic ligand”.

### *Poster contributions*

1. “Chemistry of high-valent macrocyclic Ni and Pd NHC-complexes” **Nielsen, M.T.**, Jørgensen, M. S. B., Yan, X., Piccirilli, L., Xiao, X., Mossin, S. L., and Nielsen, M. 2022 Inorganic Chemistry Gordon Research Seminar and Conference, New Port, Rhode Island, United States, 2022.
2. “Can polynuclear metal clusters behave as “extended” organometallic complexes? *En route* to understanding cluster reactivity” **Nielsen, M. T.**; Nielsen, M. Inorganic Graduate Student Seminar 3 (IGSS 3), DK, 5000-Odense, 2019
3. “Can polynuclear metal clusters behave as “extended” organometallic complexes?” **Nielsen, M. T.**; and Nielsen, M. DTU Chemistry PhD Symposium, DK, 3070-Snekkersten, 2018.

### *Presentations*

1. “Fra gymnasie til en forskningskarriere i kemi”, KVUC, DK, 1120-Copenhagen, 2019

### *Honors and awards*

1. Foundation Taumoses instrumentation award 2020, towards the acquisition of a state-of-the-art electrochemical workstation.
2. Ministry of Higher Education and Science Denmark - Elite Research Travel grant 2020
3. Kaj and Hermilla Ostenfeld's Travel grant
4. Reinholdt W. Jorck and Wife's Travel grant
5. Christian and Otilia Brorson Travel grant
6. Idella Foundation Travel grant
7. Danmark Amerika Foundation Travel grant

## Chapter. 1. Polymetallic clusters and dinuclear complexes

### 1.1 Cluster compounds

Sequestration of  $N_2$  as  $NH_3$  and transformation of other small molecules *viz.*  $CO_2$  and  $H_2O$  all require catalysts apt at mediating multi-electron transfer processes. Industrially,  $N_2$  fixation is realized through the Haber-Bosch process, which employs metal surfaces that through poorly understood synergistic Fe-Fe interactions facilitate the six-electron, proton-coupled transformation of  $N_2$  into  $NH_3$  at elevated pressure and temperatures<sup>1,2</sup>. A molecular complex, shown on the left-hand side of **Figure 1.1**, as demonstrated by Schrock effects the same transformation at an isolated site, however, the transformation is difficult to achieve as the reaction requires meticulous control of the order in which reagents are added<sup>3,4</sup>.

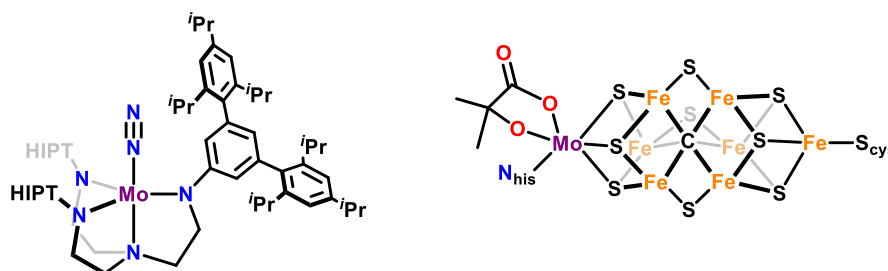


**Figure 1.1.** Complexes capable of facilitating  $N_2$  fixation. A molybdenum (III) complex and the nitrogenase FeMo-cofactor.

In contrast, Nature achieves the same transformation under benign conditions, by instead engaging polynuclear cluster ensembles in multi-electron transfer processes; nitrogenase fixates  $N_2$  into  $NH_3$  through the enzyme's FeMo-cofactor, right-hand side of **Figure 1.1**, which in part acts as the site of transformation, and in part as an electron reservoir, rendering the enzyme able to accumulate charge to effect multi-electron processes whilst circumventing high-energy intermediates, as would otherwise result from multiple consecutive electron transfers<sup>5,6</sup>.

The term *cluster*, was coined by Cotton in 1964 as a finite number of metal atoms joined together, either through metal-metal interactions or metal-nonmetal bonds, and *cluster nuclearity* is defined as the number of metals comprising a given cluster<sup>7-9</sup>. A bimetallic, trinuclear cluster thus defines a cluster core comprising three metals, of which two are distinctive, such as (dppe)M( $\mu_3$ -S){Ru(N)Me<sub>2</sub>}<sub>2</sub>, [MRu<sub>2</sub>], M = Ni, Pd, and Pt<sup>10</sup>.

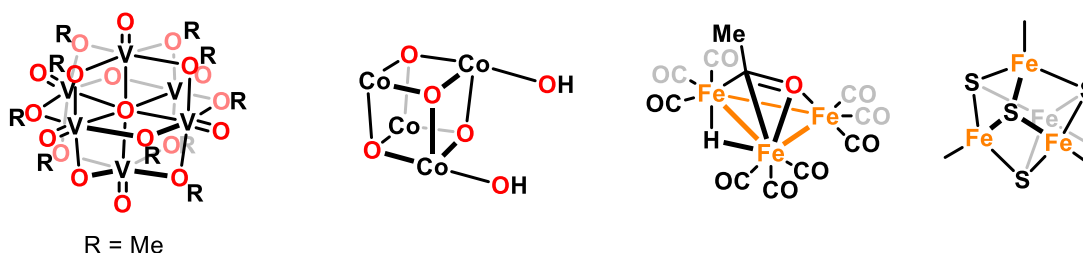
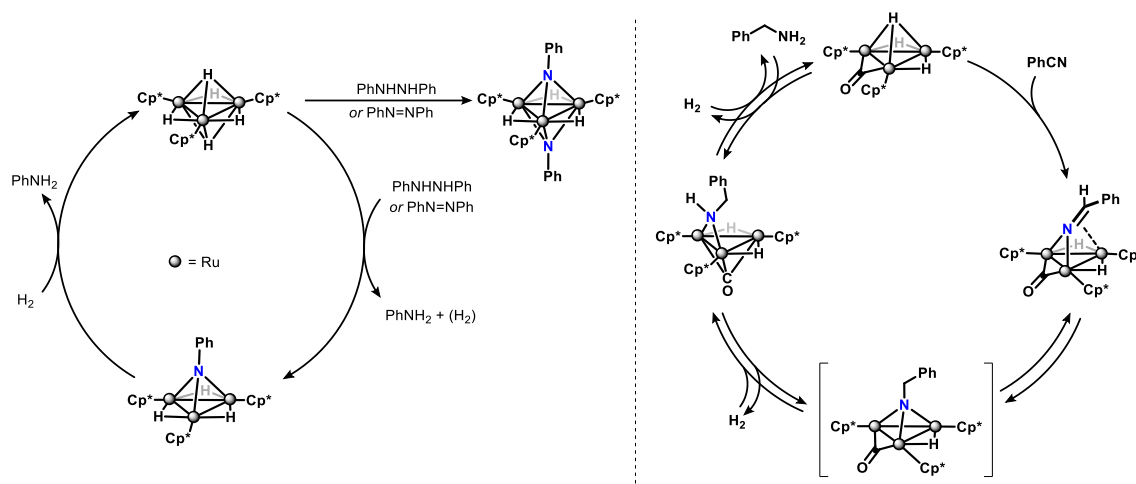


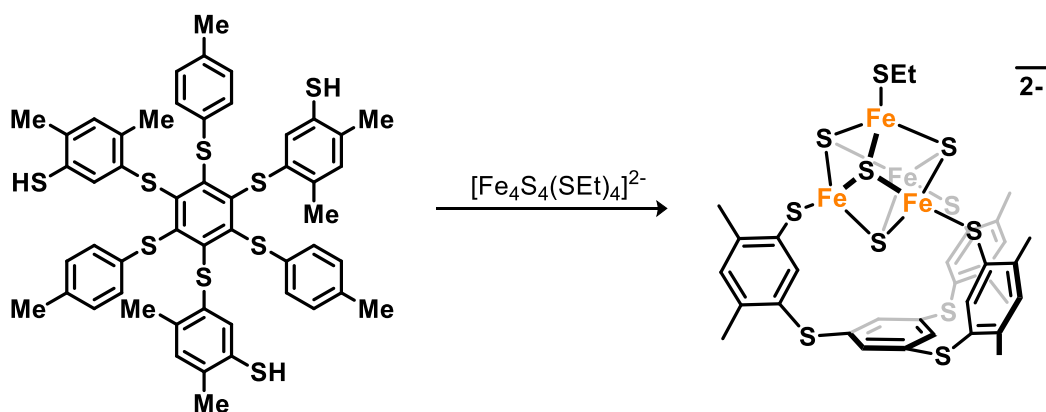
**Figure 1.2.** *Compounds representative of molecular cluster compounds.* Cluster compounds resulting from self-assembly processes, present little to no synthetic control of resulting nuclearity.

Many cluster compounds, such as polyoxymetalates<sup>11,12</sup>, metal oxo cubane clusters<sup>13</sup>, carbonyl clusters<sup>14,15</sup>, and iron-sulfide clusters<sup>16,17</sup>, representative structures are shown in **Figure 1.2**, form from serendipitous self-assembly processes, leaving little control in terms of the resulting cluster's nuclearity and electronic properties in the context of redox chemistry and magnetic properties. In particular carbonyl clusters, and derivatives bearing other fluxional ligands *e.g.* ( $\mu$ -) H, find wide use in homogeneous catalysis<sup>18</sup>, however, few clusters demonstrate transformations mediated by genuine “synergistic” interactions between multiple metal-centers, as suggested by Suzuki in the catalytic hydrogenation of benzonitrile, shown in **Scheme 1.1**<sup>19,20</sup>. Rather, many transformations occur at an isolated site, the remaining metals acting instead as an electron reservoir, and ligands confer spatial preclusion<sup>18</sup>. Moreover, the lability of these fluxional ligands often results in metal extrusion producing (unsaturated) monometallic species, which can engage in side-reactions or aggregate into nanoparticles responsible for any observed phenomena<sup>21</sup>.



**Scheme 1.1.** A triruthenium cluster apt at catalyzing the hydrogenation of hydrazine and diazene. Deactivation pathways result from a full saturation at the apical sites by imido ligands.

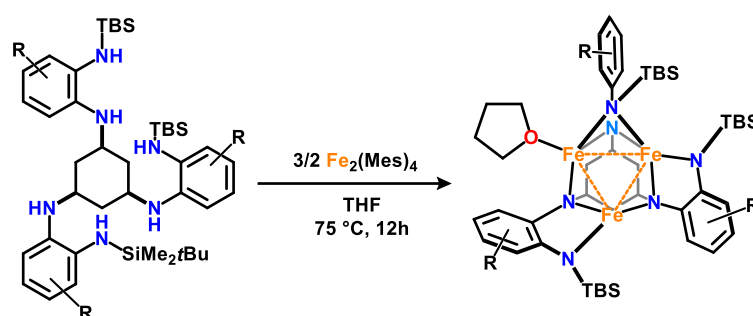
Holm, however, proved that tailor-made ligands may induce a discriminating coordination environment, furnishing cluster aggregation in a controllable and predictable manner<sup>22</sup>, as shown in **Scheme 1.2**; such molecular entities possess distinctive properties reminiscent of metal-surfaces, however, presents other more straightforward analyses for understanding the nature of any metal-metal interactions *e.g.* single-crystal X-ray diffraction, NMR, IR, and EPR.



**Scheme 1.2.** Holm's seminal work. The ligand's ability to coordinate the Fe-sulfide cubane demonstrated that purposefully made ligands may facilitate cluster formation. The resulting structure features only the coordinating arms for simplicity.

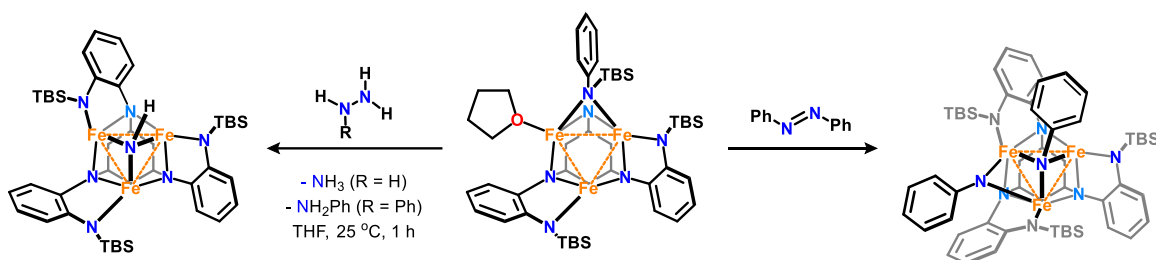
In contrast to their heavier congeners, cluster cores composed of first-row transition metals bearing polynucleating, polytopic ligands imparting a distinctive coordination environment, yield complexes demonstrating extensive metal-metal exchange apt at facilitating substrate transformation through multielectron transfer processes. The Betley

lab has demonstrated that the tritopic ligandplatform  $R_{\text{tbs}}\text{LH}_6 = 1,3,5\text{-C}_6\text{H}_9(\text{NH-C}_6\text{H}_4\text{-nR}_n\text{-}o\text{-NHSiMe}_2\text{tBu})_3$ , effects well-defined trinuclear clusters in a predictable manner, **Scheme 1.3**, whose electronic environment is tunable through substitution of H atom(s) of the diaza-catechole for heteroatoms such as F or functional groups as MeO or Me<sub>2</sub>N. Functionalization of the primary anilines with sterically encumbering groups, prevents the dimerization into the analogous hexairon clusters<sup>23</sup>, however, may also be effected by the addition of exogenous ligands such as pyridine or tertiary phosphines, *cf.* Chapter 6.



**Scheme 1.3.** Metalation of a sterically encumbered tritopic ligand. The resulting triiron cluster demonstrates an open-shell configuration capable of mediating multiple electrons towards the reduction of substrates.

As a result of the high delocalization within the triangular [Fe<sub>3</sub>]-core<sup>24</sup>, the cluster mediate multiple electron transfers: upon exposure to hydrazines, the all-ferrous cluster (center structure) mediates a two-electron reduction, expelling primary amines, concurrently decorating the cluster by an  $\mu^3$ -imido, left-hand side of **Scheme 1.4**, whereas diazenes reacts with the same all-ferrous cluster through a four-electron reduction, resulting instead in the formation of a bis- $\mu$ -nitrido decorated cluster, as shown on the right-hand side of **Scheme 1.4**<sup>25</sup>.



**Scheme 1.4.** Multiple-electron transfer reactions by a molecular triiron cluster. The cluster demonstrates up to four equivalents of electrons transferred from the cluster core, in line with biological systems.

The Murray lab has developed a tritopic, cyclophane ligand, shown in **Figure 1.3**, which upon installation of mid to late transition metals ( $M = \text{Mn, Fe, Co, and Cu}$ ) readily encapsulates  $\text{N}_2$  into the center pocket; this platform serves as a prudent model to understand multimetallic assemblies and in relation to biological systems from small molecule activation such as  $\text{O}_2$ <sup>26</sup>.

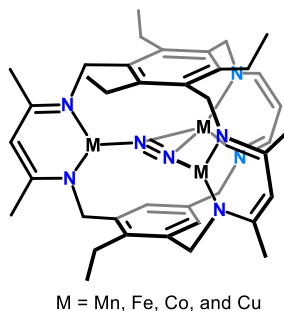


**Figure 1.3.** Murray's tritopic platform. The center pocket binds a variety of different small molecules.

Despite these successes, complexes bearing multiple metal centers featuring distinctive redox properties are synthetically challenging to realize; dinuclear, or bimetallic complexes, offer a similar entry into the study of metal-metal interactions in the context of facilitating multiple electron transfer processes towards the realization of hitherto unexplored chemical space, however, prove synthetically more straightforward.

The proximity of two transition metal ions, and interactions between the  $d$ -orbitals, lead to favorable metalophilic interactions, which can ultimately furnish the formation of metal-metal bond(s), best exemplified by Cotton. In his seminal study of  $[\text{Re}_2\text{Cl}_8]^{2-}$ , Cotton accounts for the extremely short Re-Re distance, unsupported by the ligands, and that the two  $[\text{Re}^{\text{III}}\text{Cl}_4]^-$ -units found in an eclipsed conformation, by invoking a molecular orbital description as outlined in **Figure 1.4**; the eclipsed configuration engenders the maximum possible bond order of 4, consistent with the complex' diamagnetic nature<sup>27,28</sup>.

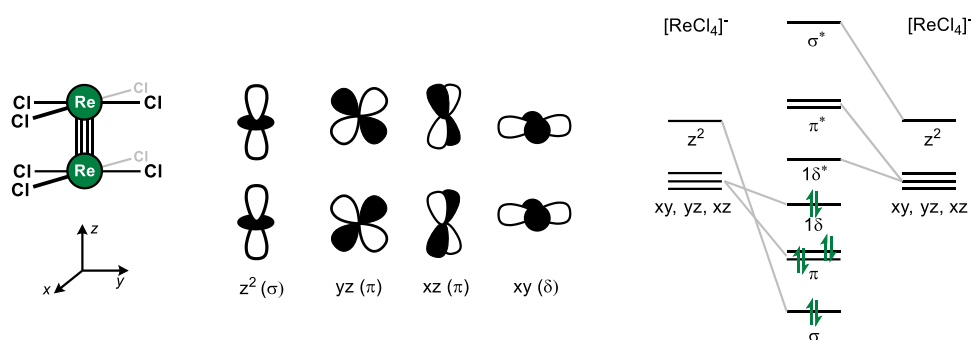
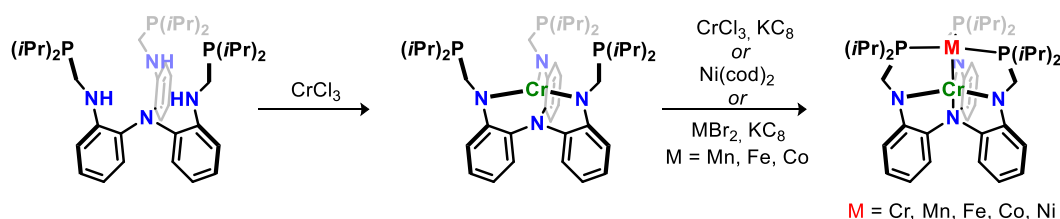


**Figure 1.4.** Simplified molecular orbital diagram accounting Re-Re quadruple bond in  $\text{Re}_2\text{Cl}_8^{2-}$ . The interpretation considers only the orbitals involved in the  $d$ -manifold, the relative position of  $\sigma$ ,  $\pi$ , and  $\delta$  vary between complexes.

## 1.2 The interaction between two metals

Cotton's seminal work, ignited a lasting interest in multimetallic complexes; further the understanding of molecular architectures resulting in metal-metal bond formation, to obtain beneficial properties such as magnetism<sup>29</sup>, their non-benign role in homogeneous catalysis otherwise explained by mechanisms invoking monometallic complexes<sup>30</sup>, and how to exploit these bonds to facilitate substrate transformations<sup>31</sup>.

The molecular orbital treatment invoked by Cotton, is quite simplistic and does not account for the easily perturbed  $\delta$  bonds, as any  $\delta$  orbitals are affected by ligand charge, metal identity, and valence  $d$ -electron count, rendering the metal-metal interaction difficult to assess based on crystallographic data alone<sup>32,33</sup>. To find better descriptors, and provide a fundamental understanding of the nature of the metal-metal bond, the Lu lab has realized a series of heterobimetallic complexes bearing so-called “double decker” ligands, a representative structure is shown in **Scheme 1.5**<sup>34</sup>, to rationalize the metal-metal interaction in the context of understanding unique magnetic, redox, and catalytic properties<sup>35</sup>.





**Scheme 1.5.** “Double decker” ligand platform explored by Lu and Thomas. The discriminating binding sites enable the rapid realization of various heterodinuclear complexes.

The ligand features two distinctive binding pockets discriminating between metals following hard-soft acid-base (HSAB) guidelines; the modularity enables the rapid preparation of multiple metal-combinations. Moreover, the three-fold geometry further engages all *d*-orbitals in bonding interactions to engender a maximum of  $[1\sigma + 2\pi + 2\delta]$  orbitals. From their studies, Lu instead suggests that one considers the total valence of *d*-electrons and the polarity as a difference between the metal’s group number in terms of understanding the resulting complex’ properties. A greater delocalization of valence electrons limits redox properties observed in multiple bounded species, as observed in the quintuple bonded Cr<sub>2</sub> complex, M = Cr in **Scheme 1.5**, which features few redox events. In contrast, the analogous heterobimetallic CrNi complex, M = Ni in **Scheme 1.5**, whose metal interaction was established as a dative Ni-Cr interaction, and the complex shows wealthy redox chemistry different from the constituents: the heterobimetallic complex shows three reversible redox events, whereas the individual metals only demonstrate irreversible reduction waves<sup>36</sup>.

Tilley has demonstrated that the neutral, redox-innocent naphthyridine-tetrapyridine ligand platform shown in **Figure 1.5**, similarly binds two transition metal ions; the proximity renders the ligand suitable for studying metal-metal interactions pertinent to active dinuclear sites in, for instance, heterogeneous surfaces such as the dinuclear site attributed as the active site in cobalt-oxide (CoO<sub>x</sub>) water-oxidation catalysts. The ligand coordinates two octahedrally coordinated Co centers, sharing two bridging hydroxide ions. The authors suggest that, this particular coordination environment mimics that of CoO<sub>x</sub>, and find that this complex, however sluggish, functions as a competent catalyst in water-oxidation catalysis; more importantly, it illustrated that phosphate, from buffers

commonly employed under  $\text{CoO}_x$ -mediated water-oxidation catalysis, deactivates the complex from isolated dicobalt complexes bearing bridging phosphate ligands<sup>37</sup>.

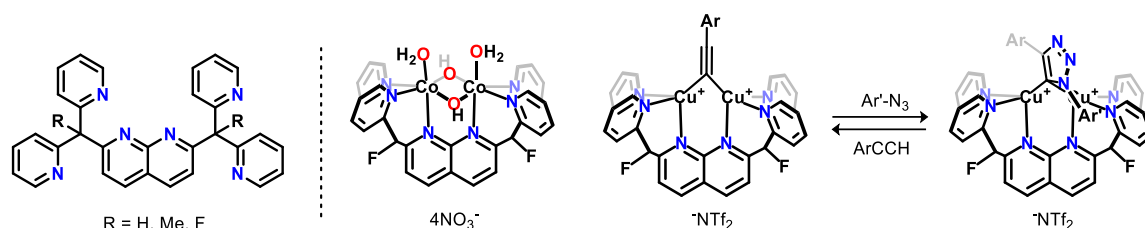


**Figure 1.5.** *Naphthyridine-tetrapyridine* was explored by Tilley. Two late 3d metals are readily accommodated by binding substrate through a metalophilic, synergistic interaction.

The dicopper (I) complex binds alkynyls (alkanes and aryls<sup>38</sup>) through both copper centers; exposure of the alkynyl complex to organoazides furnishes the regioselective 1,3-dipolar cycloaddition to the alkynyl, forming an isolable  $\mu$ -triazolide<sup>39</sup>. The addition of excess alkyne regenerates the parent alkynyl complex, suggesting that this complex is active in the so-called copper-catalyzed “click reaction” (CuAAC). Moreover, this transformation strongly supports CuAAC mechanisms invoking cooperation between two copper ions.

Agapie has demonstrated that a terphenyl platform, in addition to binding isolated metals<sup>40,41</sup>, binds a variety of mid to late transition metals, including diiron (0)<sup>42</sup>, dicobalt (0)<sup>42</sup>, dinickel (I)<sup>43</sup>, and dipalladium (I)<sup>44</sup>, representative structures are shown in **Figure 1.6**. The latter complex, binds a variety of substrates such as arenes, heterocycles, and aromatics across the two metals, and this binding to the dipalladium (I) complex was used as a proxy to better understand binding to metal surfaces<sup>44</sup>.

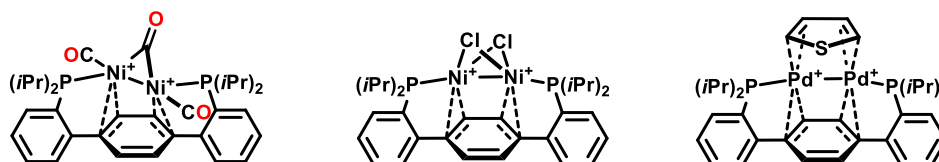
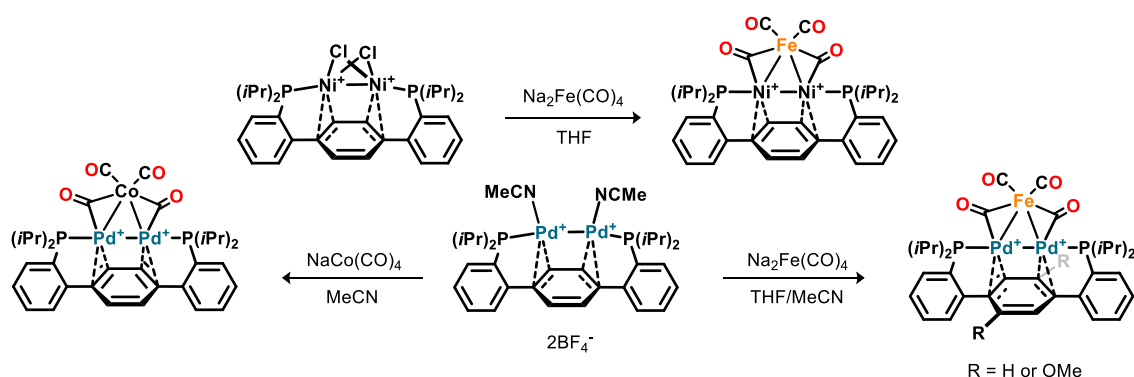


**Figure 1.6.** *Dinuclear complexes stabilized by arene interactions* explored by Agapie. The two metal centers bind various substrates also through a synergistic interaction between the two metal centers.

More interestingly, the authors found that the dinickel (I) and dipalladium (I) complexes react with ferrate and cobaltate carbonyl salts resulting in expansion of the metal core, as shown in **Scheme 1.6**. This reactivity was leveraged by the authors to better understand how cluster properties form, and understand how the change in metal identity and ligand-centered electronic perturbations affect the resulting cluster's properties<sup>45</sup>. To this end, the central arene was functionalized with bis-*p*-methoxy moieties, to probe electronic effects owing to close and distant coordinating ligands/moieties. From their study, the authors conclude that both ligand and metal affect cluster properties, however, the closer moiety infers a larger perturbation; whereas the methoxy-bearing ligand cathodically shifts oxidation events by  $\sim 200\text{mV}$ , and redshifts CO-stretching frequencies by  $\sim 7\text{ cm}^{-1}$ , the substitution of Fe for Co interestingly, anodically shifts the redox events by  $\sim 1\text{V}$ , and redshifts CO-stretching frequencies by  $\sim 20\text{ cm}^{-1}$ .

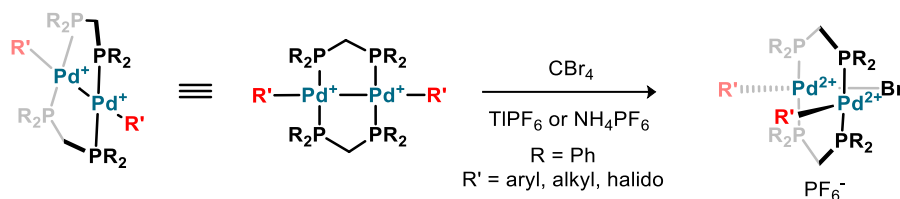


**Scheme 1.6.** Exposure to carbonyl ferrate and cobaltate facilitates core expansion. The seemingly straightforward core expansion enabled the authors to investigate properties differentiating bimetallic complexes from clusters.

### 1.3 Two metals: reactivity of the metal-metal bond

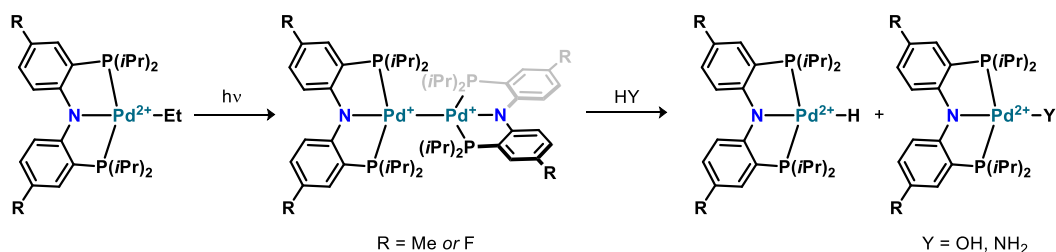
Homobimetallic and heterobimetallic complexes featuring metal-metal bond(s), can facilitate oxidative addition across different substrates, the bond reacting as a two-electron reductant. Retention of the complex' nuclearity throughout any reactions relate to the ligand's architecture, where polytopic ligands often render the complex able to regain the metal-metal bond resulting from metal-metal proximity. For instance, Kubiak

found that a bridged dipalladium (I) complex forms under reductive conditions in presence of the ditopic phosphine ligand dppm (diphenylphosphinomethane),  $\text{Pd}_2\text{Cl}_2(\mu\text{-dppm})_2$ <sup>46</sup> or directly from comproportionation reactions between  $\text{Pd}^0$  and  $\text{Pd}^{\text{II}}$ <sup>47</sup>. This complex adds across a variety of substrates such as CO,  $\text{SO}_2$ ,  $\text{CH}_2\text{N}_2$ , S, and HCl adopting an “A-frame” geometry, shown in **Scheme 1.7**<sup>46</sup>.



**Scheme 1.7.** Oxidative addition across a Pd-Pd bond. The complex adopts an “A-frame” geometry following oxidative addition.

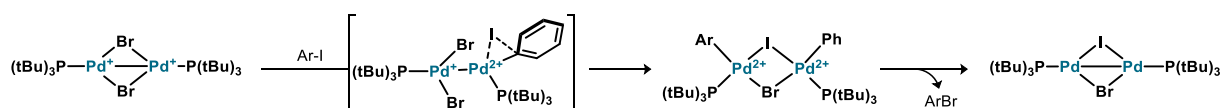
Ozerov, found that irradiation of a parent Pd (II) PNP-complex, shown on the most left-hand side of **Scheme 1.8**, facilitates photolysis, expelling an alkyl radical and generates a Pd (I) center, which rapidly dimerizes into two Pd(I) PNP-complexes adjoined by an unsupported Pd-Pd bond<sup>48</sup>. Exposure to water and ammonia, respectively, effects the formation of two new Pd (II) complexes, isolated as a Pd (II) hydride complex alongside the corresponding hydroxide and amido Pd (II) complex.



**Scheme 1.8.** Oxidative addition leads to loss of the M-M bond. The unsupported bond results in two monometallic Pd (II) complexes.

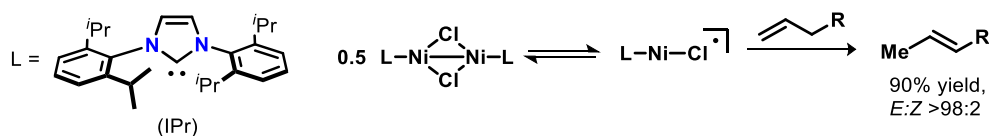
Mingos reported that a mixture of  $\text{Pd}_2\text{dba}_3$  and  $\text{P}(t\text{Bu})_3$  oxidatively adds to  $\text{CH}_3\text{X}$  ( $\text{X} = \text{Br}, \text{I}$ ), furnishing the formation of an edge-sharing complex,  $\text{Pd}_2(\mu\text{-X})_2\text{P}(t\text{Bu})_3$ <sup>49</sup>. A later study by Fenske revealed that the two Pd (I) ions form a bonding interaction from through-spacer interactions different to the motif of Kubiak and Ozerov<sup>50</sup>. Hartwig has suggested that this complex acts as a source of the highly reactive unsaturated 12 valence-

electron Pd(0) complex, PdP'Bu<sub>3</sub>, following a disproportionation reaction; this Pd (0) complex showed a high efficacy as (pre)catalyst for Pd-catalyzed amination reactions of arylchlorides<sup>51,52</sup>. In contrast, Schoenebeck has reported that Mingos' dipalladium (I) complex mediates novel catalytical C-X bond formations, as shown in **Scheme 1.9**; the halido atoms may facilitate transmetalation with different nucleophiles (Nu) and tether the intermediary Pd<sup>II</sup>Pd<sup>I</sup> redox pair following oxidative addition at an isolated Pd (I) site, which in turn can reductively eliminate the desired C-Nu<sup>53–58</sup>. Curiously, whereas the bromido compound is highly air sensitive, reactions involving the iodo-congener need no actions taken toward the exclusion of air, and the complex is bench-top stable.



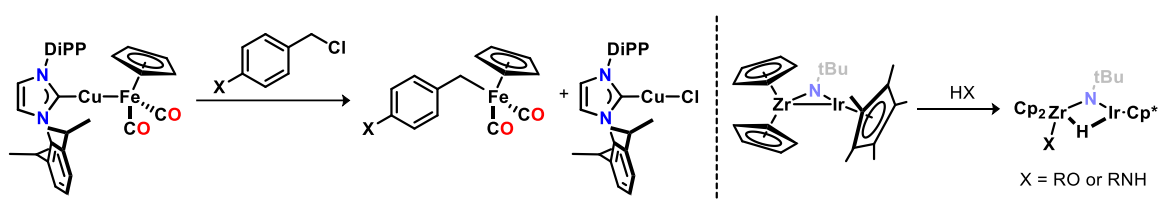
**Scheme 1.9.** Suggested elementary steps involved in the transformation of ArI to ArBr, mediated by a dipalladium (I) complex. The authors found an interesting reactivity, which later has been leveraged in multiple functionalization reactions of aryl halides.

Two analogous dinickel (I) complexes, the so-called “Sigman’s dimers”<sup>59</sup>, effected from a comproportionation reaction between Ni(cod) (cod = 1,5-cyclooctadiene), NiCl<sub>2</sub>(dme) (dme = 1,2-dimethoxy ethane) and the free (S)IPr N-Heterocyclic Carbene, NHC, of imidazolidine (SIPr = 1,3-bis(2,6-diisopropylphenyl)-imidazolidine-2-ylidene) and imidazole (IPr = 1,3-bis(2,6-diisopropylphenyl)-imidazole-2-ylidene), found similar use by the Schoenebeck group: although sharing a similar coordination motif to Mingos’ dipalladium (I) complex, the imidazole-based dinickel (I) complex readily undergoes dissociation, and the monomeric complexes are in turn responsible for the observed transformation, as shown in **Scheme 1.10**<sup>60</sup>.



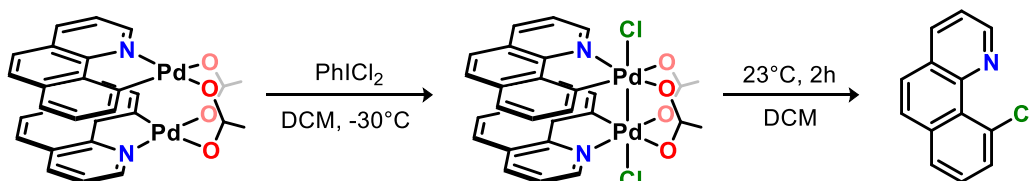
**Scheme 1.10.** A related dinickel(I) fragment dissociates into monometallic complexes. Dinickel (I) complexes in the same geometry readily dissociate, which are responsible for the observed transformations.

Heterobimetallic complexes demonstrate bond polarity owing to electronegativity differences between the metals, leading to regioselectivity upon oxidative addition as demonstrated by Mankad, shown on the left-hand side of **Scheme 1.11**. The heterobimetallic complex IPrCuFp, Fp = FeCp(CO)<sub>2</sub>, bearing an unsupported Cu-Fe bond, was found to react with benzylic chlorides analogous to an S<sub>N</sub>2-reaction through a two-electron transfer process<sup>61</sup>. The complex' observed regioselectivity was attributed to the Cu-Fe bond as comprising of a cationic Cu(I) unit bound by an anionic Fe(-I) unit.



**Scheme 1.11.** Oxidative addition across a polarized M-M bond. Any regioselectivity may be understood by a difference in electronegativity between the involved metals to locate formal charges.

Bergman's study of a Zr-Ir bridging imido complex, Cp<sub>2</sub>Zr(μ-N<sup>t</sup>Bu)IrCp\*, further suggests that regioselectivity of oxidative addition reactions may be rationalized from electronegativity differences and HSAB<sup>62</sup>; this complex oxidatively adds across anilines (and alcohols), resulting in a complex featuring a bridging hydride, whereas the anilide (alkoxide) exclusively binds the Zr-site, whilst the parent imido moiety works towards retaining the complex' nuclearity, right-hand side of **Scheme 1.11**.



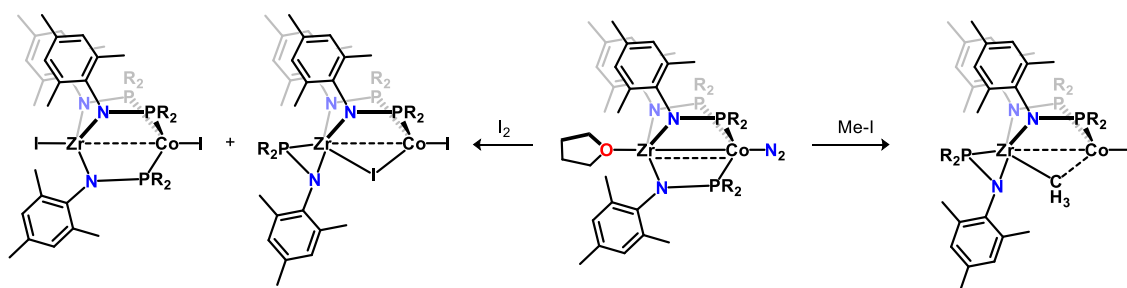
**Scheme 1.12.** Substrate activation is mediated by an intermediary metal-metal bonded dipalladium complex. The transformation was suggested by the authors to work following palladophilic interactions lowering energy barriers associated with the initial oxidation.

Dinuclear complexes in paddlewheel geometries, may engage in oxidative addition reactions; upon oxidation, the complex' metal core may form M-M bonds. Ritter isolated a dipalladium (III) species, following oxidation using PhICl<sub>2</sub>, which undergoes a bimetallic reductive elimination of the intermediary dipallada(III) cycle<sup>63</sup>, as shown in

**Scheme 1.12**, amounting to a regioselective C-H bond activation of 2-phenylpyridyl. This study provide an alternative description to the same transformation earlier reported by Sanford, wherein a mechanism involving a Pd(II/IV) cycle was invoked<sup>64</sup>. The proximal Pd (II) centers facilitate substrate transformation under milder reaction conditions following the metalophilic interaction supporting charge delocalization *i.e.* lowering the initial Pd (II) oxidation potential.

Beyond reactivity through the loss (and gain) of a  $\sigma$ -type bond, bimetallic complexes may facilitate transformations through multiple bonds *e.g.* of  $\pi$  and  $\delta$  symmetry, or mediate electron transfers through redox-non innocent ligands.

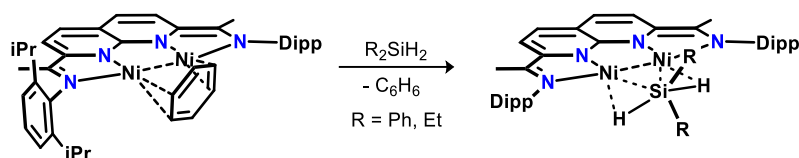
Thomas' reactivity studies on heterobimetallic complexes comprising early and late transition metals, demonstrate that the metal-metal bond contains a significant  $\pi$ -contribution<sup>65,66</sup>. Upon exposure to various electrophiles bearing (a)polar bonds, the complex oxidatively adds, in an analogous manner to the preceding heterobimetallic examples, resulting in an expansion of the metal-metal distance as suggested in **Scheme 1.6**.



**Scheme 1.13.** *Stoichiometric studies of heterobimetallic complexes.* Thomas has studied substrate activation across heterobimetallic complexes comprising early and late transition metals.

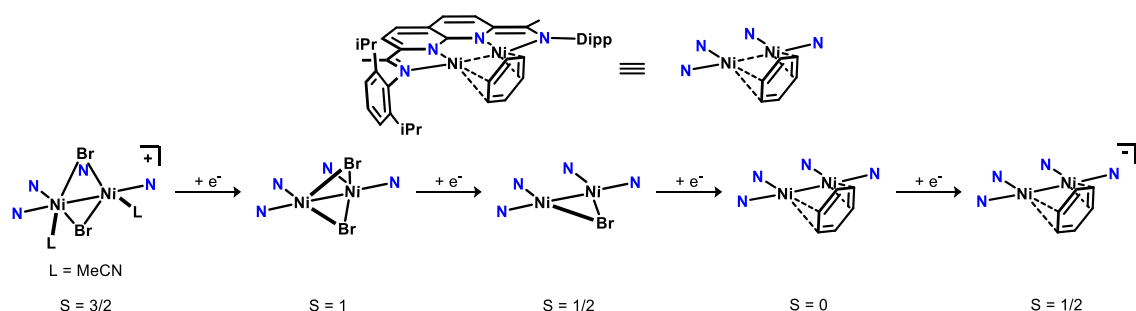
Uyeda has shown that a dinickel complex bearing a naphthyridine-diimine ligand demonstrates a unique reactivity and catalyzes a variety of different transformations *viz.* hydrosilylation of alkenes and alkynes, mediated by activation of silane delocalized over

both Ni sites, as shown in **Scheme 1.14**<sup>67</sup>, cyclotrimerization of alkynes<sup>68</sup>, and regioselective cyclopropanation group transfer to unsymmetrical 1,3-dienes<sup>69</sup>.



**Scheme 1.14.** Silane binding of a dinickel (0) complex. The authors account, that the agostic bonding is complimentary to monometallic congeners.

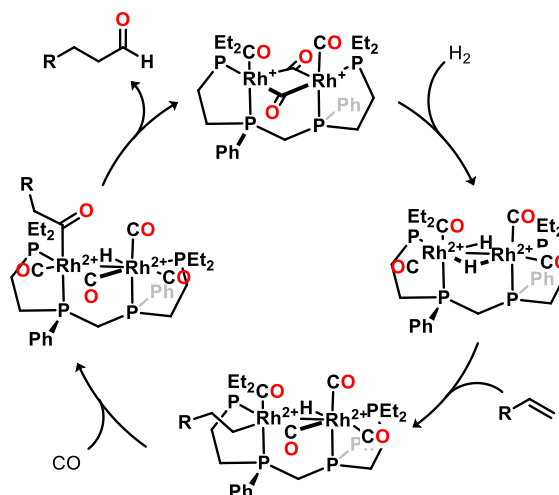
The complex' distinctive properties are attributed to the ligand's redox non-innocence, and each isolated Ni-site may individually bind substrate or stabilize substrates through a bridging interaction, as shown in **Scheme 1.15**<sup>70</sup>. These properties combined, play a key role in stabilizing intermediates different from the relevant mononickel complexes, and emphasize how metal-metal interactions obtain further beneficiary properties combined with metal-ligand interactions.



**Scheme 1.15.** Different oxidation states are available to Uyeda's dinickel complex. The redox-non-innocence of the ligand renders the complex able to undergo multiple successive reversible redox events.

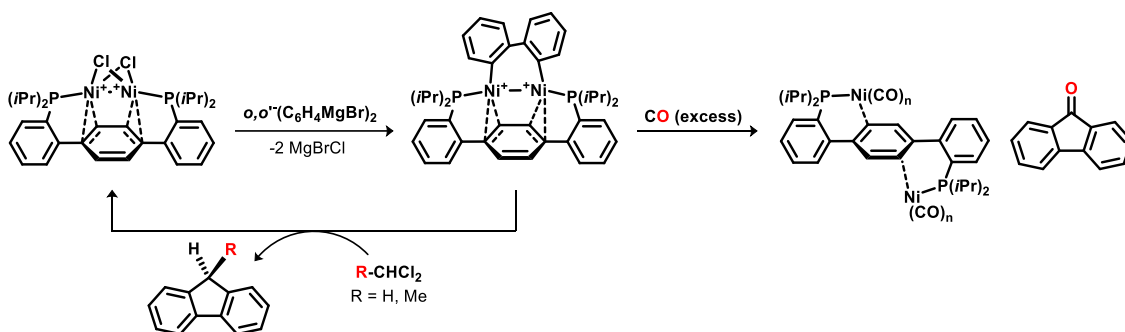
Stanley's study on a tetraphosphine ligand, capable of supporting two rhodium atoms, relevant to hydroformylation<sup>71</sup>, further adds to examples of dinuclear complexes demonstrating metal cooperativity. Close association of the two Rh(I) centers facilitates facile oxidative addition of H<sub>2</sub> resulting in a complex Rh<sub>2</sub><sup>4+</sup> complex bearing two bridging hydrido ligands, shown in **Scheme 1.16**; DFT calculations suggest that insertion of these hydrides into any terminally bound acyl groups readily happens as this process demonstrate a low energy-barrier.





**Scheme 1.16.** Metal-metal interaction is suggested key to high activity of a dirhodium complex. The authors argue the initial  $[\text{Rh}_2]^{2+}$  charge enables ready CO ligand substitution.

Agapie additionally found, that both nickel centers of the dinickel (I) complex bearing the terphenyl ligand engage in cooperative substrate activation<sup>43</sup>, as shown in **Scheme 1.17**. Whereas the dichlorido bridged bisnickel (I) species reacts with the diaryl Grignard reagent (*o,o'*- $\text{C}_6\text{H}_4\text{MgBr}$ )<sub>2</sub>, forming an isolable biphenyldiyl dinickel (I) product, center most structure, similar exposure of the dichlorido bisnickel (I) complex to  $\text{PhMgBr}$  led to the isolation of biphenyl products, suggested by the authors to form through an intermediate like the bridging biphenyldiyl complex.



**Scheme 1.17.** Substrate activation is facilitated by a dinickel complex. Agapie's continued work on the terphenyl framework showed that the dinickel complex may activate relevant to the formation of new C-C bonds.

Exposure of the biphenyldiyl dinickel (I) complex, center structure, to geminal chloroalkanes, furnish C-C bond formation from the detection of fluorene derivatives alongside isolation of the parent bridged dichlorido bisnickel (I) complex. The authors comment that both a radical and a non-radical-based mechanism may account for the

observed reactivity. Reacting the biphenyl dinickel (I) complex with CO liberates fluorenone and a dinickel (0) complex, which despite having lost the metal-metal bond retains the complex' nuclearity, stabilized by metal-arene interactions. Other late, low-valent dipalladium complexes have been reported demonstrating that the arene-palladium stabilizing interaction is critical to the structure<sup>72,73</sup>.

#### 1.4 Dinuclear complexes as biomimetic compounds

The Meyer group, has studied two pyrazolate-based ligands in the context of biomimetic complexes; one bearing  $\beta$ -diketiminato<sup>74</sup>, the other 1,4,7-triazacyclononane (tacn)<sup>75</sup>, to furnish binding of two transition metal ions featuring distinctive coordination environments; representative metal complexes of both shown in **Figure 1.7**. The pyrazolate-ligand scaffold is well-known to bind two metals *viz.* Fe, Co, Ni, Cu, and Zn, to serve as a model for the active sites in metalloenzymes, *e.g.* ribonucleotide reductase and urease<sup>76</sup>.

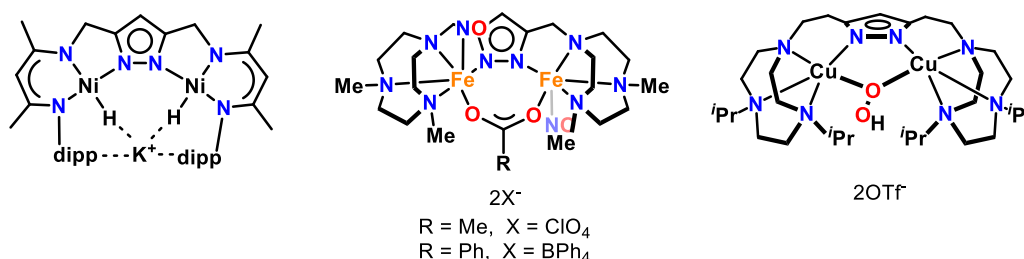
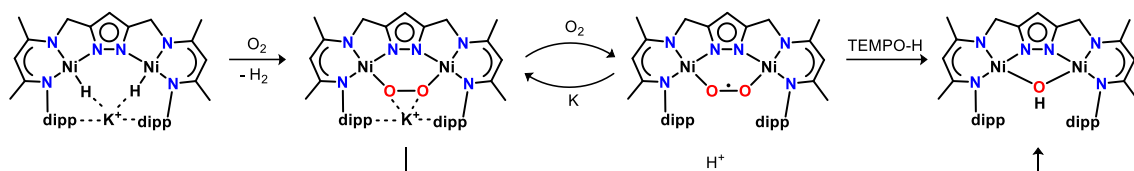


**Figure 1.7.** Dinuclear complexes are relevant as biomimetic compounds. Ready modifications were made to the pyrazolate ligand, which was leveraged in the context of introducing different coordination environments to various metals.

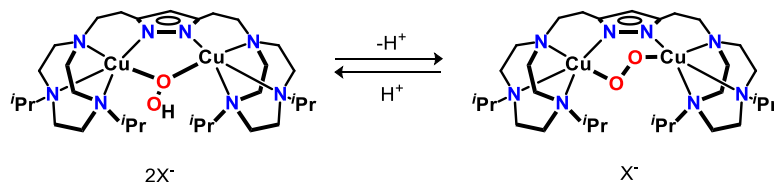
Wanting to study processes involving hydride transfers and low-valent dinickel complexes, the  $\beta$ -diketiminato-functionalized pyrazolate ligand was reported to readily install two Ni(II)-ions into the center “pocket”, each capped by a terminal hydride ligand; the intramolecular reductive elimination of H<sub>2</sub> reveals a reactive, “masked” dinickel (I) complex rendering substrate activation through a two-electron reduction process, the intermediary complex stabilized by nickel-nickel interactions<sup>74</sup>.



**Scheme 1.18.** Dinickel (II) bearing terminal hydrides react as masked low-valent  $\text{Ni}_2^{2+}$ . Loss of  $\text{H}_2$  gas is a low barrier, leading to a dinickel (I) intermediate, which readily reduces various small molecules, such as  $\text{O}_2$ .

Upon exposure of the parent bishydrido dinickel (II) complex to  $\text{O}_2$ , the complex extrudes  $\text{H}_2$  gas, and forms an isolable  $\mu$ -1,2-peroxo dinickel (I) complex<sup>77</sup>. Further exposure forms the corresponding  $\mu$ -1,2-superoxo complex, as shown in **Scheme 1.18**; protonation of both complexes led to the formation of  $\mu$ -hydroxide species, suggesting the parent hydride complex may serve as a potent activator of challenging substrates, relevant to proton-coupled electron transfer reactions, including also  $\text{NO}$ <sup>78</sup>.

The tacn-functionalized pyroazolate ligand, binds Fe (II) and Cu (I) ions; acetate serves as a fluxional secondary bridge between the two iron centers of the former complex, resulting in a pentadentate coordination environment and a single vacant site available to bind  $\text{NO}$ ; single-electron reduction furnish ligand scrambling over  $\text{N}_2\text{O}$  release<sup>75</sup>. The dicopper (I) complex, as its ethyl congener, was used to study  $\text{O}_2$  activation: upon exposure, both complexes furnish the formation of an isolable *cis*- $\mu$ -1,1-peroxo complex, as shown in **Scheme 1.19**<sup>79,80</sup>. The ethyl complex demonstrates a triplet term ground state ( $S = 1$ ), displaying ferromagnetic coupling following a short Cu-Cu distance enforced by the ligand resulting in a Cu-O-O-Cu torsion close to  $90^\circ$ . This peroxide configuration is suggested as the initial stages of  $\text{O}_2$  binding in biological type III dicopper sites, such as in catechol oxidase<sup>81–83</sup>.



**Scheme 1.19.** Biomimetic dicopper complex demonstrating oxygen activation relevant to metalloenzymes. The isolation of a peroxo dicopper (II) complex was used to obtain a further understanding on  $\text{O}_2$  activation in dicopper sites pertinent to metalloenzymes.

Some generalities can be extracted from the preceding examples, such as oxidative addition reactions across metal-metal bonds appear more frequently to happen at an isolated site in complexes comprising 4 and 5d metals, contrasting a “synergistic” interaction stabilized by bridging bonding more widely found in base-metal containing complexes. Moreover, dinuclear complexes, bearing non-fluxional, polytopic ligands provide necessary complex/cluster stability to accommodate structural changes, *e.g.* M-M bond rupture or ligand dissociation, whilst retaining overall nuclearity and cluster integrity.

This consequence is perhaps unsurprising, as dinuclear complexes featuring unsupported metal-metal bonds often survive just a few turn-over numbers; the “odd” oxidation state, frequently required to retain the complex’ nuclearity, is seldomly regained, resulting instead in fragments engaging in transformation following well-documented pathways, *e.g.* Pd(0/II) cycles. In contrast, complexes bearing bridging ligands, which have been demonstrated as apt at facilitating chemical transformations in a catalytic capacity; some complexes mediate transformations possible through monometallic complexes, however, under much more desirable conditions, some complexes demonstrate a completely novel reactivity.

In this project, we seek to explore the development of a non-fluxional polynucleating ligand that provides the necessary stability to the bimetallic complex, by accommodating structural changes, *e.g.* M-M bond rupture or ligand dissociation, whilst retaining overall nuclearity and complex integrity.

## 1.5 References

- (1) Qian, J.; An, Q.; Fortunelli, A.; Nielsen, R. J.; Goddard, W. A. *J. Am. Chem. Soc.* **2018**, *140*, 6288–6297.
- (2) Smith, C.; Hill, A. K.; Torrente-Murciano, L. *Energy Environ. Sci.* **2020**, *13*, 331–344.

- (3) V., Y. D.; R., S. R. *Science* **2003**, *301*, 76–78.
- (4) Weare, W. W.; Dai, X.; Byrnes, M. J.; Chin, J. M.; Schrock, R. R.; Müller, P. *Proc. Natl. Acad. Sci. U. S. A.* **2006**, *103*, 17099–17106.
- (5) Liu, T.; Gau, M. R.; Tomson, N. C. *J. Am. Chem. Soc.* **2020**, *142*, 8142–8146.
- (6) McSkimming, A.; Suess, D. L. M. *Nat. Chem.* **2021**, *13*, 666–670.
- (7) Cotton, F. A. *Inorg. Chem.* **1964**, *3*, 1217–1220.
- (8) Cotton, F. A. *Q. Rev. Chem. Soc.* **1966**, *20*, 389.
- (9) Rosenberg, E. R. and Laine, M. in *Catalysis by Di- and Polynuclear Metal Cluster Complexes*; Adams, R. D.; Cotton, F. A. (eds.), (Wiley-VCH, Weinheim), **1998**.
- (10) Kuiper, J. L.; Shapley, P. A.; Rayner, C. M. *Organometallics* **2004**, *23*, 3814–3818.
- (11) Song, Y.-F.; Tsunashima, R. *Chem. Soc. Rev.* **2012**, *41*, 7384–7402.
- (12) VanGelder, L. E.; Kosswattaarachchi, A. M.; Forrestel, P. L.; Cook, T. R.; Matson, E. M. *Chem. Sci.* **2018**, *9*, 1692–1699.
- (13) Amtawong, J.; Nguyen, A. I.; Tilley, T. D. *J. Am. Chem. Soc.* **2022**, *144*, 1475–1492.
- (14) Seyferth, D.; Williams, G. H.; Eschbach, C. S.; Nestle, M. O.; Merola, J. S.; Hallgren, J. E. *J. Am. Chem. Soc.* **1979**, *101*, 4867–4878.
- (15) Wong, W.-K.; Chiu, K. W.; Wilkinson, G.; Galas, A. M. R.; Thornton-Pett, M.; Hursthouse, M. B. *J. Chem. Soc., Dalt. Trans.* **1983**, *8*, 1557–1563.
- (16) Brown, A. C.; Suess, D. L. M. in *Comprehensive Coordination Chemistry III: Synthetic Iron-Sulfur Clusters*; Constable, E. C., Parkin, G., Que Jr, L. (eds.); (Elsevier: Amsterdam), **2021**, *8*, 134–156.
- (17) Brown, A. C.; Thompson, N. B.; Suess, D. L. M. *J. Am. Chem. Soc.* **2022**, *144*, 9066–9073.
- (18) Nielsen, M. T.; Padilla, R.; Nielsen, M. *J. Clust. Sci.* **2020**, *31*, 11–61.
- (19) Nakajima, Y.; Suzuki, H. *Organometallics* **2005**, *24*, 1860–1866.
- (20) Takao, T.; Horikoshi, S.; Kawashima, T.; Asano, S.; Takahashi, Y.; Sawano, A.; Suzuki, H. *Organometallics* **2018**, *37*, 1598–1614.
- (21) Hagen, C. M.; Vieille-Petit, L.; Laurenczy, G.; Süss-Fink, G.; Finke, R. G. *Organometallics* **2005**, *24*, 1819–1831.
- (22) Stack, T. D. P.; Holm, R. H. *J. Am. Chem. Soc.* **1988**, *110*, 2484–2494.
- (23) Harris, T. D.; Zhao, Q.; Sánchez, R. H.; Betley, T. A. *Chem. Commun.* **2011**, *47*, 6344.
- (24) Hernández Sánchez, R.; Bartholomew, A. K.; Powers, T. M.; Ménard, G.; Betley, T. A. *J. Am. Chem. Soc.* **2016**, *138*, 2235–2243.
- (25) Powers, T. M.; Betley, T. A. *J. Am. Chem. Soc.* **2013**, *135*, 12289–12296.

- (26) Ferreira, R. B.; Murray, L. J. *Acc. Chem. Res.* **2019**, *52*, 447–455.
- (27) Cotton, F. A.; Curtis, N. F.; Harris, C. B.; Johnson, B. F. G.; Lippard, S. J.; Mague, J. T.; Robinson, W. R.; Wood, J. S. *Science* **1964**, *145*, 1305–1307.
- (28) Cotton, F. A. *Inorg. Chem.* **1965**, *4*, 334–336.
- (29) Gould, C. A.; McClain, K. R.; Reta, D.; Kragoskow, J. G. C.; Marchiori, D. A.; Lachman, E.; Choi, E.-S.; Analytis, J. G.; Britt, R. D.; Chilton, N. F.; Harvey, B. G.; Long, J. R. *Science* **2022**, *375*, 198–202.
- (30) Day, C. S.; Somerville, R. J.; Martin, R. *Nat. Catal.* **2021**, *4*, 124–133.
- (31) Ackerman, L. K. G.; Lovell, M. M.; Weix, D. J. *Nature* **2015**, *524*, 454–457.
- (32) Tereniak, S. J.; Carlson, R. K.; Clouston, L. J.; Young, V. G.; Bill, E.; Maurice, R.; Chen, Y.-S.; Kim, H. J.; Gagliardi, L.; Lu, C. C. *J. Am. Chem. Soc.* **2013**, *136*, 1842.
- (33) Tereniak, S. J.; Carlson, R. K.; Clouston, L. J.; Young, V. G.; Bill, E.; Maurice, R.; Chen, Y.-S.; Kim, H. J.; Gagliardi, L.; Lu, C. C. *J. Am. Chem. Soc.* **2014**, *136*, 1842–1855.
- (34) Eisenhart, R. J.; Clouston, L. J.; Lu, C. C. *Acc. Chem. Res.* **2015**, *48*, 2885–2894.
- (35) Moore, J. T.; Lu, C. C. *J. Am. Chem. Soc.* **2020**, *142*, 11641–11646.
- (36) Clouston, L. J.; Siedschlag, R. B.; Rudd, P. A.; Planas, N.; Hu, S.; Miller, A. D.; Gagliardi, L.; Lu, C. C. *J. Am. Chem. Soc.* **2013**, *135*, 13142–13148.
- (37) Davenport, T. C.; Ahn, H. S.; Ziegler, M. S.; Tilley, T. D. *Chem. Commun.* **2014**, *50*, 6326–6329.
- (38) Ziegler, M. S.; Torquato, N. A.; Levine, D. S.; Nicolay, A.; Celik, H.; Tilley, T. D. *Organometallics* **2018**, *37*, 2807–2823.
- (39) Ziegler, M. S.; Lakshmi, K. V.; Tilley, T. D. *J. Am. Chem. Soc.* **2017**, *139*, 5378–5386.
- (40) Lin, S.; Day, M. W.; Agapie, T. *J. Am. Chem. Soc.* **2011**, *133*, 3828–3831.
- (41) Buss, J. A.; Cheng, C.; Agapie, T. *Angew. Chem. Int. Ed.* **2018**, *57*, 9670–9674.
- (42) Horak, K. T.; Velian, A.; Day, M. W.; Agapie, T. *Chem. Commun.* **2014**, *50*, 4427–4429.
- (43) Velian, A.; Lin, S.; Miller, A. J. M.; Day, M. W.; Agapie, T. *J. Am. Chem. Soc.* **2010**, *132*, 6296–6297.
- (44) Lin, S.; Herbert, D. E.; Velian, A.; Day, M. W.; Agapie, T. *J. Am. Chem. Soc.* **2013**, *135*, 15830–15840.
- (45) Horak, K. T.; Lin, S.; Rittle, J.; Agapie, T. *Organometallics* **2015**, *34*, 4429–4432.
- (46) Kullberg, M. L.; Kubiak, C. P. *Organometallics* **1984**, *3*, 632–634.
- (47) Lin, W.; Wilson, S. R.; Girolami, G. S. *Inorg. Chem.* **1994**, *33*, 2265–2272.

- (48) Fafard, C. M.; Adhikari, D.; Foxman, B. M.; Mindiola, D. J.; Ozerov, O. V. *J. Am. Chem. Soc.* **2007**, *129*, 10318–10319.
- (49) Vilar, R.; Mingos, D. M. P.; Cardin, C. J. *J. Chem. Soc. Dalt. Trans.* **1996**, No. 23, 4313–4314.
- (50) Kostic, N. M.; Fenske, R. F. *Inorg. Chem.* **1983**, *22*, 666–671.
- (51) Stambuli, J. P.; Kuwano, R.; Hartwig, J. F. *Angew. Chem. Int. Ed.* **2002**, *41*, 4746–4748.
- (52) Sperger, T.; Stirner, C. K.; Schoenebeck, F. *Synthesis (Stuttg.)* **2017**, *49*, 115–120.
- (53) Bonney, K. J.; Proutiere, F.; Schoenebeck, F. *Chem. Sci.* **2013**, *4*, 4434.
- (54) Kalvet, I.; Bonney, K. J.; Schoenebeck, F. *J. Org. Chem.* **2014**, *79*, 12041–12046.
- (55) Yin, G.; Kalvet, I.; Schoenebeck, F. *Angew. Chem. Int. Ed.* **2015**, *54*, 6809–6813.
- (56) Kalvet, I.; Deckers, K.; Funes-Ardoiz, I.; Magnin, G.; Sperger, T.; Kremer, M.; Schoenebeck, F. *Angew. Chem. Int. Ed.* **2020**, *59*, 7721–7725.
- (57) Kreisel, T.; Mendel, M.; Queen, A. E.; Deckers, K.; Hupperich, D.; Riegger, J.; Fricke, C.; Schoenebeck, F. *Angew. Chem. Int. Ed.* **2022**, *134*, e202201475.
- (58) Kundu, G.; Opincal, F.; Sperger, T.; Schoenebeck, F. *Angew. Chem. Int. Ed.* **2022**, *61*, e202113667.
- (59) Dible, B. R.; Sigman, M. S.; Arif, A. M. *Inorg. Chem.* **2005**, *44*, 3774–3776.
- (60) Kapat, A.; Sperger, T.; Guven, S.; Schoenebeck, F. *Science* **2019**, *363*, 391–396.
- (61) Karunananda, M. K.; Parmelee, S. R.; Waldhart, G. W.; Mankad, N. P. *Organometallics* **2015**, *34*, 3857–3864.
- (62) Baranger, A. M.; Bergman, R. G. *J. Am. Chem. Soc.* **1994**, *116*, 3822–3835.
- (63) Powers, D. C.; Ritter, T. *Nat. Chem.* **2009**, *1*, 302–309.
- (64) Dick, A. R.; Hull, K. L.; Sanford, M. S. *J. Am. Chem. Soc.* **2004**, *126*, 2300–2301.
- (65) Greenwood, B. P.; Rowe, G. T.; Chen, C.-H.; Foxman, B. M.; Thomas, C. M. *J. Am. Chem. Soc.* **2010**, *132*, 44–45.
- (66) Wu, B.; Gramigna, K. M.; Bezpalko, M. W.; Foxman, B. M.; Thomas, C. M. *Inorg. Chem.* **2015**, *54*, 10909–10917.
- (67) Steiman, T. J.; Uyeda, C. *J. Am. Chem. Soc.* **2015**, *137*, 6104–6110.
- (68) Kwon, D.-H.; Proctor, M.; Mendoza, S.; Uyeda, C.; Ess, D. H. *ACS Catal.* **2017**, *7*, 4796–4804.
- (69) Maity, A. K.; Kalb, A. E.; Zeller, M.; Uyeda, C. *Angew. Chem. Int. Ed.* **2021**, *60*, 1897–1902.
- (70) Zhou, Y.-Y.; Hartline, D. R.; Steiman, T. J.; Fanwick, P. E.; Uyeda, C. *Inorg. Chem.* **2014**, *53*, 11770–11777.

- (71) Broussard, M. E.; Juma, B.; Train, S. G.; Peng, W.-J.; Laneman, S. A.; Stanley, G. G. *Science* **1993**, *260*, 1784–1788.
- (72) Christmann, U.; Vilar, R.; White, A. J. P.; Williams, D. J. *Chem. Commun.* **2004**, No. 11, 1294–1295.
- (73) Christmann, U.; Pantazis, D. A.; Benet-Buchholz, J.; McGrady, J. E.; Maseras, F.; Vilar, R. *J. Am. Chem. Soc.* **2006**, *128*, 6376.
- (74) Manz, D.-H.; Duan, P.-C.; Dechert, S.; Demeshko, S.; Oswald, R.; John, M.; Mata, R. A.; Meyer, F. *J. Am. Chem. Soc.* **2017**, *139*, 16720–16731.
- (75) Kindermann, N.; Schober, A.; Demeshko, S.; Lehnert, N.; Meyer, F. *Inorg. Chem.* **2016**, *55*, 11538–11550.
- (76) Dalle, K. E.; Meyer, F. *Eur. J. Inorg. Chem.* **2015**, *2015*, 3391–3405.
- (77) Duan, P.-C.; Manz, D.-H.; Dechert, S.; Demeshko, S.; Meyer, F. *J. Am. Chem. Soc.* **2018**, *140*, 4929–4939.
- (78) Ferretti, E.; Dechert, S.; Demeshko, S.; Holthausen, M. C.; Meyer, F. *Angew. Chem. Int. Ed.* **2019**, *58*, 1705–1709.
- (79) Dalle, K. E.; Gruene, T.; Dechert, S.; Demeshko, S.; Meyer, F. *J. Am. Chem. Soc.* **2014**, *136*, 7428–7434.
- (80) Kindermann, N.; Bill, E.; Dechert, S.; Demeshko, S.; Reijerse, E. J.; Meyer, F. *Angew. Chem. Int. Ed.* **2015**, *54*, 1738–1743.
- (81) Brinkmeier, A.; Schulz, R. A.; Buchhorn, M.; Spyra, C.-J.; Dechert, S.; Demeshko, S.; Krewald, V.; Meyer, F. *J. Am. Chem. Soc.* **2021**, *143*, 10361–10366.
- (82) Brinkmeier, A.; Dalle, K. E.; D’Amore, L.; Schulz, R. A.; Dechert, S.; Demeshko, S.; Swart, M.; Meyer, F. *J. Am. Chem. Soc.* **2021**, *143*, 17751–17760.
- (83) Lohmiller, T.; Spyra, C.-J.; Dechert, S.; Demeshko, S.; Bill, E.; Schnegg, A.; Meyer, F. *JACS Au* **2022**, *2*, 1134–1143.



## Chapter. 2. The paddlewheel complex of 1,8-naphthyridine and palladium (II)

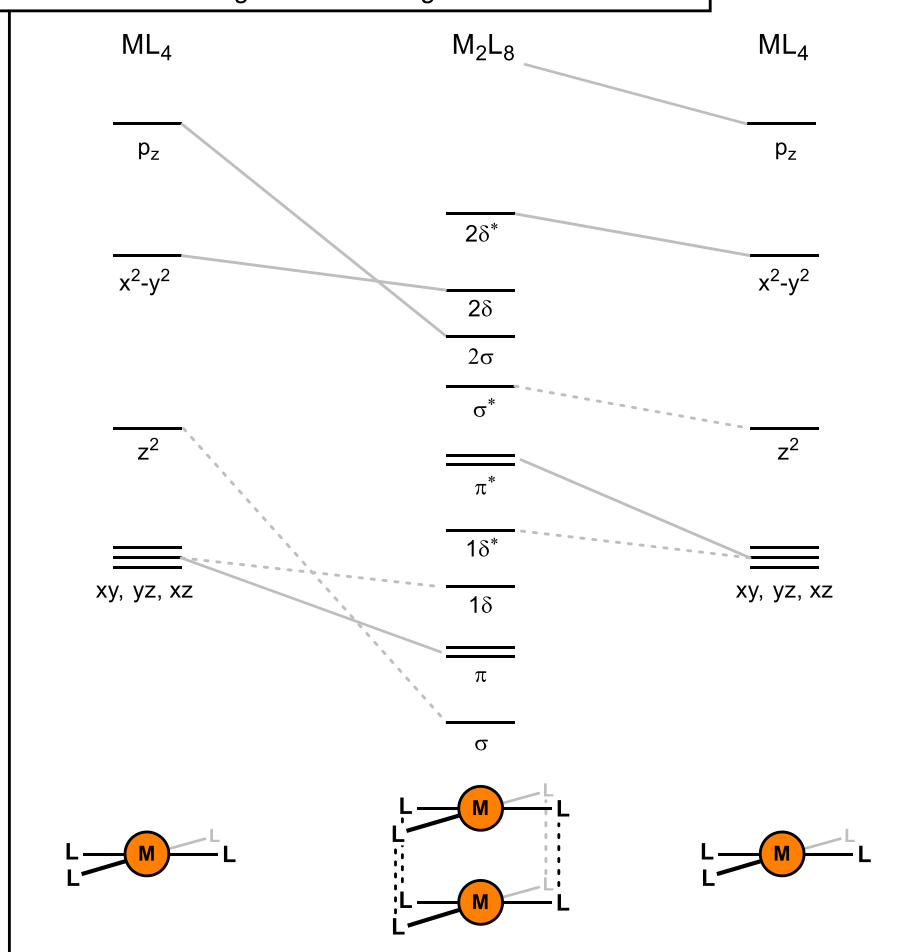
### 2.1 Introduction

Transition-metal paddlewheel complexes are well-known bimetallic entities with a distinct electronic configuration leading to interesting proximity-induced properties, such as expanded redox profiles and an opportunity for the formation of multiple metal-metal bonds<sup>1</sup>. We may rationalize such properties arising from metal-metal bonding and (partial) population of metal-based orbitals. To this end, we can consider the symmetry-allowed interactions between the *d*-orbitals owing to two idealized square-planar ( $D_{4h}$ ) homo metal ions dispositioned in an eclipsed configuration, as shown in **Chart 2.1**.

The eclipsed disposition facilitates maximum orbital mixing, which manifests in three distinctive interactions (decreasing in strength)  $\sigma$ ,  $\pi$ , and  $\delta$ . Thus, **Chart 2.1** provides a (qualitative) understanding of a “bimetallic core” in terms of bonding, to the effect that two  $d^8$  ions (16 electrons) lead to a net-zero M-M bond order ( $\sigma^2\pi^4\delta^2\delta^*2\pi^*4\sigma^*2$ ), whereas two  $d^4$  ions result in a quadruple bonding, *viz.*  $\text{Cr}_2(\mu\text{-OAc})_4^2$  ( $\sigma^2\pi^4\delta^2$ ). Additionally, given that the energy disparity between the *np* and (*n*-1)*d* orbitals is not too large, two *p<sub>z</sub>* orbitals may form another  $\sigma$ -type orbital, which is sufficiently low in energy, rendering excitations feasible leading to complexes demonstrating useful optical properties, as known from discrete Rh(I) polymetallic entities<sup>3</sup>, and in Pt-pop,  $[\text{Pt}_2(\mu\text{-P}_2\text{O}_5\text{H}_2)_4]^{4+}$ <sup>4</sup>. However, the large energy difference between the 4*d* and 5*s*/5*p* valence orbitals in Pd disfavors such orbital mixing<sup>5</sup>.

This particular arrangement of two metal centers, renders the complex able at mediating unique transformations different from monometallic analogues, as perhaps best exemplified by Gray’s study of oxidative addition of a dicationic Rh(I)-dimer,  $[\text{Rh}_2(\mu\text{-1,3-diisocyanopropane})_4] 2\text{BPh}_4^6$ , to  $\text{I}_2$  (and MeI), as shown in **Scheme 2.1**.

Qualitative M.O. diagram describing the "bimetallic core"



Bonding interactions resulting from mixing of d-orbitals

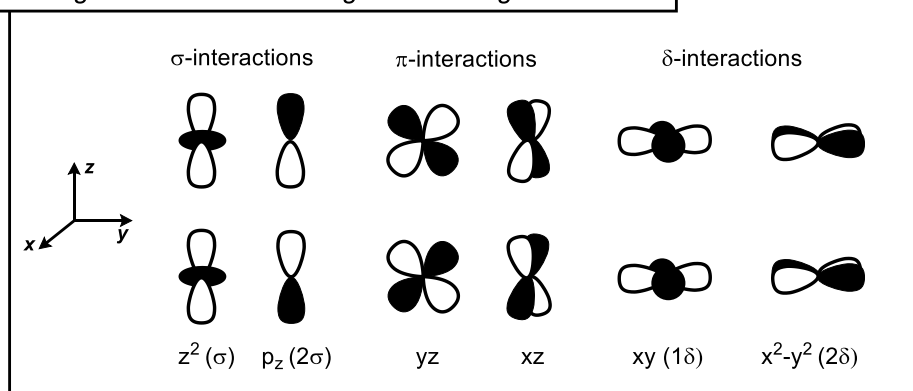
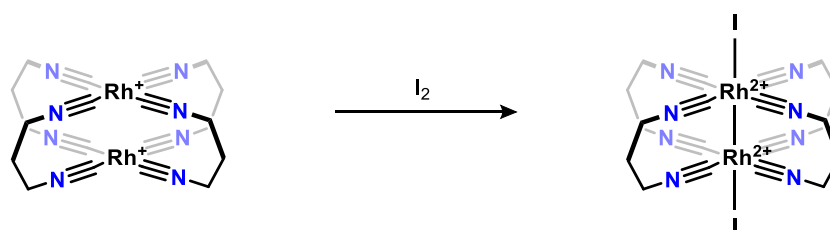


**Chart 2.1.** Mixing of *d*-orbitals in paddlewheel complexes. The relative orbital ordering is qualitative, under the assumption that the strength of the interactions follows  $\sigma > \pi > \delta$ .



**Scheme 2.1.** Two-center oxidative addition of  $I_2$  by a dirhodium(I) complex. The two-electron oxidation rapidly forms a new species demonstrating spectroscopically distinctive properties.

The complex is a 16-valence electron complex, which according to **Chart 2.1**, has a net Rh-Rh bonding order of 0. Upon exposure to I<sub>2</sub>, the complex undergoes oxidative addition, forming a symmetrically substituted product, as evident by IR stretches and <sup>1</sup>H NMR resonance consistent with a single [RhL<sub>4</sub>I]<sup>+</sup> unit, as shown in **Scheme 2.1**. The isolable product features intense UV-Vis absorption bands, one of which (397 nm) the authors attribute as a Laporte allowed σ to σ\* transition, from the just-formed Rh-Rh bond.

The Rh<sub>2</sub><sup>2+</sup> complex reacts in a similar manner with MeI, leading to the rapid formation of a symmetrical *trans*-substitution, from the emergence of a new resonance in the <sup>1</sup>H NMR around 1.3 ppm demonstrating a splitting of 1-2Hz (<sup>2</sup>J(<sup>1</sup>H-<sup>103</sup>Rh)) is consistent with the Rh-bound Me-group. The mechanistic insights are still ambiguous, however, the authors argue for both a stepwise process through the formation of a methyl radical following an initial Rh(I) attack at the heavy atom.

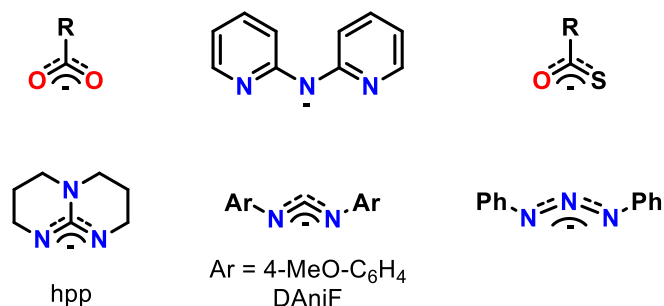
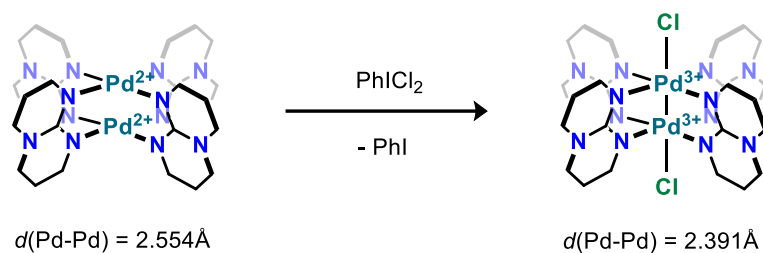


**Chart 2.2.** Representative paddlewheel complex ligands. DAniF and hpp find extensive use.

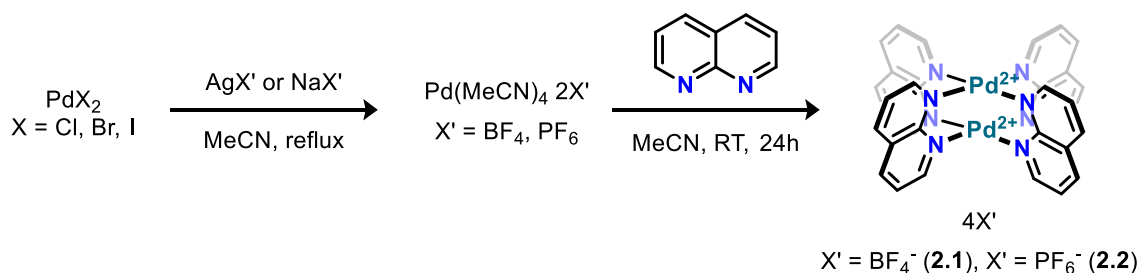
Paddllewheel complexes often employ rigid anionic ligands, such as guanadinate derivatives, carboxylates, and formamidinate, some shown in **Chart 2.2**, as these ligands impart directionally during complex synthesis as well as stabilization of metals in higher oxidation states<sup>7</sup>. Triazabicyclodecene (hpp) in particular, has seen wide application by Cotton in the preparation of homodimetallic complexes, including the first dipalladium (III) complex, shown in **Scheme 2.2**<sup>8</sup>.



**Scheme 2.2.** Shortest Pd-Pd separation and Pd-Pd bond length. The hpp ligand is central in many of Cotton's studies on paddlewheel complexes, as in addition to imparting rigidity, electronically stabilizes high-valent metal centers e.g. Pd(III).

While it fundamentally is of interest to investigate whether formally neutral ligands facilitate a similar synthesis of paddlewheel complexes, we primarily sought to use 1,8-naphthyridine (abbreviated napy) as a proxy for our naphthalene-based ligand-manifold, *cf.* Chapter 3. Based on Tilley's work, *cf.* Chapter 1, one would expect napy to bind two metals, however, the Pd ion is larger than Co and Cu, and napy may not spatially accommodate two proximal Pd ions. Especially because, despite the close disposition of the two parallel *N*-centered lone pairs, napy appear able to coordinate metal ions in dinuclear homoleptic<sup>9–14</sup> and heteroleptic complexes<sup>15–22</sup>, as well as coordinating bidentate<sup>23</sup>, and in a monodentate<sup>10</sup> fashion.

## 2.2 Complex synthesis and characterization



**Scheme 2.1.** Synthetic route for the preparation of complex **2.1** and **2.2**. Different counterions than BF<sub>4</sub> are readily prepared demonstrated by a halide abstraction of PdX<sub>2</sub>, X = Cl, Br, I.

I found that sequential coordination between tetraacetonitrilepalladium(II) tetrafluoroborate, [Pd(MeCN)<sub>4</sub>] 2BF<sub>4</sub>, and napy in acetonitrile over 30 hours precipitates out the tetracationic paddlewheel-dipalladium complex of tetra-μ-napy-dipalladium(II) tetrafluoroborate, [Pd<sub>2</sub>(μ-napy)<sub>4</sub>] 4BF<sub>4</sub>, abbreviated **2.1**, as a lightly-pink colored powder, as in **Scheme 2.1**. Alternatively, the same sequential addition of napy may be realized

following halide abstraction of  $\text{PdX}_2$  ( $\text{X} = \text{Cl}, \text{Br}, \text{I}$ ) using two equivalents of  $\text{AgX}'$  or  $\text{NaX}'$  ( $\text{X}' = \text{BF}_4, \text{PF}_6$ ) to furnish the same paddlewheel compound, however, featuring a different counterion, *e.g.* the hexafluorophosphate, compound **2.2**. The salts of complexes **2.1** and **2.2** are stable toward the air, moisture, and light. Leaving reaction mixtures of either **2.1** or **2.2** to stir for an additional 16 hours appears to consume any precipitates, likely from the transformation of **2.1** into a mixture of monopalladium MeCN adducts. This suggestion is based on the isolated complexes of **2.1** and **2.2** slowly undergo ligand substitution in strongly coordinating solvents, *e.g.*, DMSO, MeCN, and DMF (over several hours, RT).

The  $^1\text{H}$  NMR resonances of complex **2.1**, shown in the top insert of **Figure 2.1**, show three well-resolved and diamagnetic resonances, which are downfield shifted relative to that of free napy (middle spectrum). The three resonances, upon ligand substitution or extrusion of a Pd center from complexes **2.1** and **2.2** split into six; our attempts to prepare the diplatinum (II) congener under the same conditions, yields instead the dicationic salt of tetra-( $\kappa$ -*N*-napy) platinum(II) hexafluorophosphate,  $[\text{Pt}(\text{napy})_4] 2\text{PF}_6$ . This complex, shows six resonances (lower insert of **Figure 2.1**), comprising four individual and two overlapping peaks, one for each of the  $\text{C}_2$  through  $\text{C}_7$  positions of the napy-backbone, in agreement with findings reported by Biffis<sup>14</sup>.

Finally, the  $^1\text{H}$  NMR spectral properties of complexes **2.1** and **2.2** are identical in chemical shift values and splitting patterns; the weakly coordinating nature of the counterions infer that any distinctive properties thus result from the complex' metal-core.

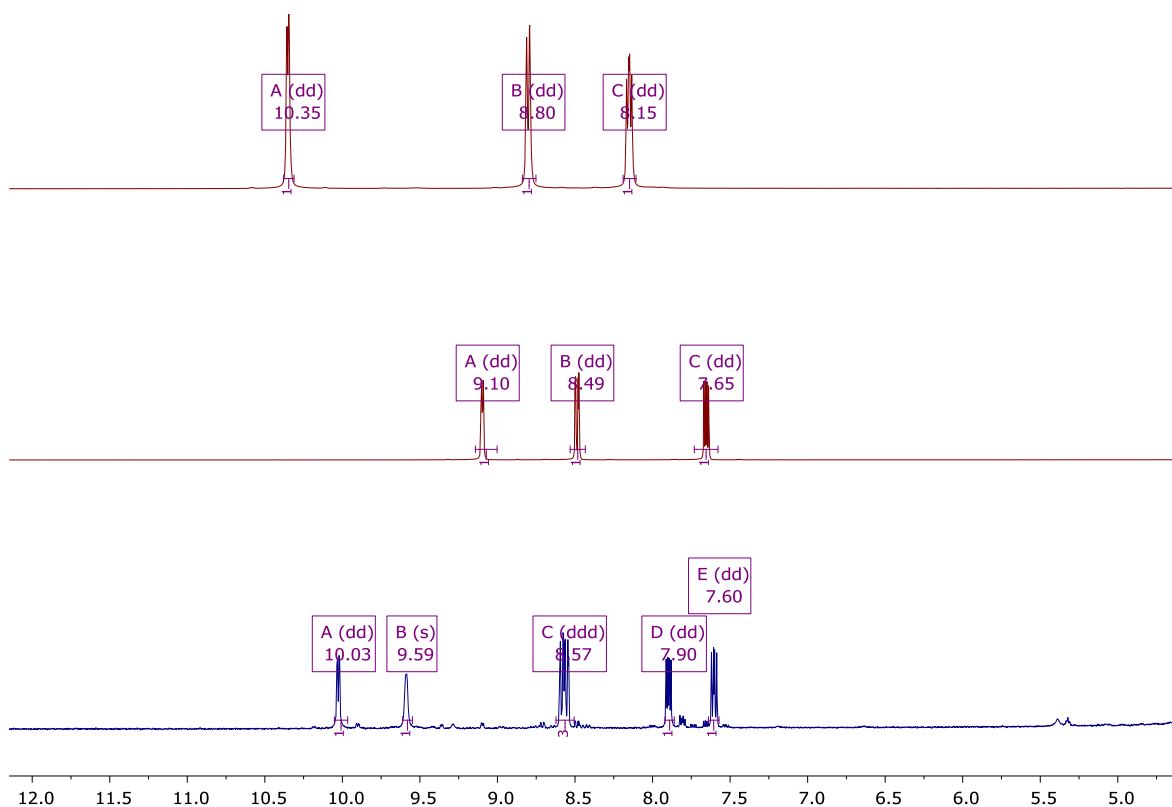


**Figure 2.1.** Stacked  $^1\text{H}$  NMR spectra comparing **2.1** (top), napy (middle), and  $[\text{Pt}(\text{napy})_4] 2\text{PF}_6$  (lower) to one-another. Upon complexation, napy experience quite a significant downfield-shift, and monometallic complexes show additional resonances following a lower symmetry. All spectra are recorded in  $\text{DMSO-d}_6$ , at  $20^\circ\text{C}$

**Figure 2.2** shows that each palladium (II) center of **2.1** is coordinated in a square planar fashion by four symmetry-related napy ligands in a paddlewheel geometry. The average Pd-N bond length is  $2.043 \text{ \AA}$  and the Pd-Pd separation is  $2.5639(5) \text{ \AA}$ , significantly shorter than Pd's van der Waals radius of  $3.26 \text{ \AA}$ . While these distances compare well to the platinum congener,  $[\text{Pt}_2(\mu\text{-napy})_4] 4\text{OTf}^{14}$ , they are on average shorter.  $[\text{Pt}_2(\mu\text{-napy})_4] 4\text{OTf}$  feature average bond distances of Pt-N (napy)  $2.050(4) \text{ \AA}$  and a Pt-Pt' separation of  $2.5841(4) \text{ \AA}$ , respectively. The napy ligands in **2.1** bridge the two metal centers planarly, as in the molybdenum<sup>19</sup>, rhodium<sup>13</sup>, and platinum<sup>14</sup> analogues. Finally, comparing the same distances of **2.1** to that of the neutral dipalladium(II)-hpp complex,  $\text{Pd}_2(\text{hpp})_4$ , reported by Cotton and co-workers<sup>8</sup>, reveals bond distances more comparable, from average Pd-N (hpp) bond lengths of  $2.038 \text{ \AA}$  and Pd-Pd' separation of  $2.554 \text{ \AA}$ .

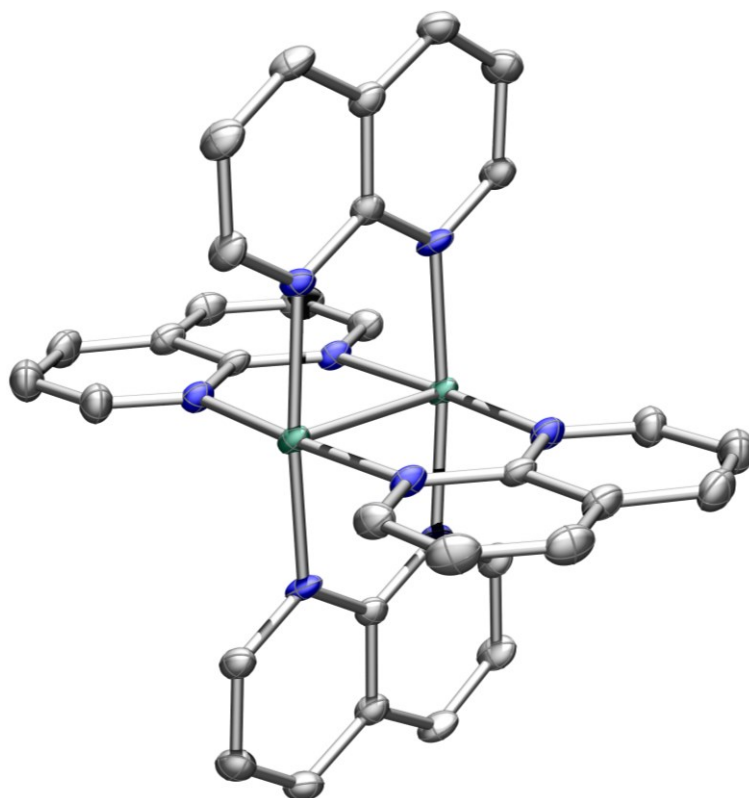


**Figure 2.2.** *Single-crystal X-ray structure of the paddlewheel complex.* The solid-state structure of **2.1** with thermal ellipsoids at 50% probability level.  $\text{BF}_4^-$ -counterions, co-crystallized MeCN, and H-atoms are omitted for clarity. Color coding: C grey, N blue, Pd sea green.

We sought to explore the electronic structure of **2.1** (and by extension **2.2**) with respect to the nature of the Pd-Pd interaction given the short metal-metal distance and the complex' high symmetry. Optical absorption spectroscopy, **Figure 2.3**, features an absorption in the visible region,  $\epsilon(543.8 \text{ nm } (\lambda_{\text{max}})) = 36.6 \text{ M}^{-1} \text{ cm}^{-1}$ , and further absorptions are present in the UV-region, likely relating to metal-to-ligand charge-transfer (MLCT). In this context, various dinuclear napy-complexes feature strong MLCT in the region from 450 to 330 nm<sup>9,11</sup>. Interestingly, the dimolybdenum(II) napy complex,  $[\text{Mo}_2(\mu\text{-napy})_4(\text{MeCN})_2]^{4+}$ , feature an additional low-energy transition ( $\lambda = 699 \text{ nm}$ ,  $\epsilon = 717 \text{ M}^{-1} \text{ cm}^{-1}$ ), which the authors assign to a  $\delta \rightarrow \delta^*$  transition<sup>19</sup>. Differently, in the dipalladium formamidinate complex,  $\text{Pd}_2(\text{DAni})_4$  (DAni = di-*p*-anisylformamidinate)<sup>24,25</sup>, a low-energy transition is observed in the visible region ( $\lambda \sim 500 \text{ nm}$ ), which disappears upon oxidation to the corresponding  $\text{Pd}_2^{5+}$ -core.

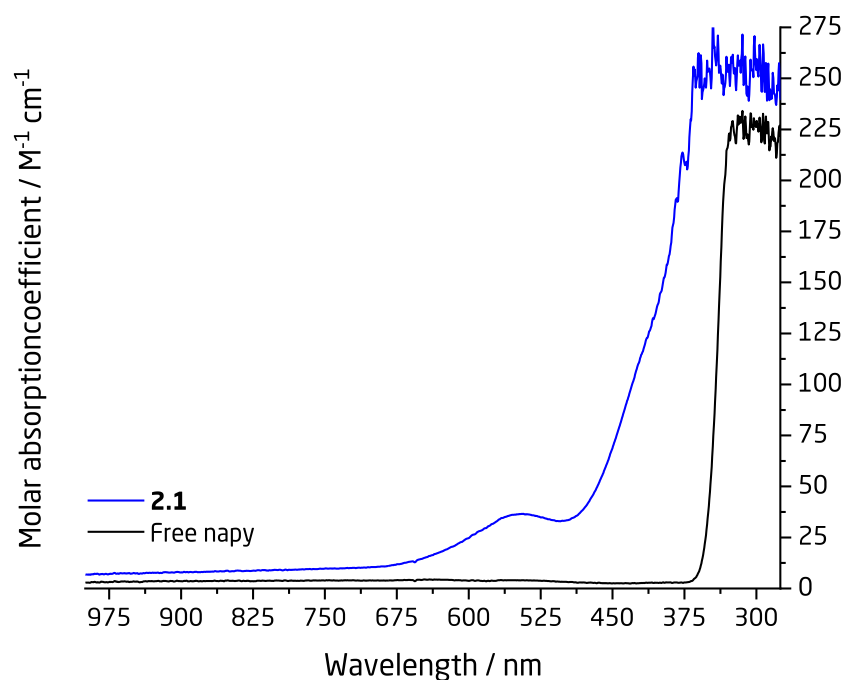


**Figure 2.3.** Optical absorption spectra of **2.1** and napy in DMF. The stacked UV-Vis spectra of the paddlewheel complex and free napy demonstrate a small absorption coefficient ( $\epsilon(543.8 \text{ nm } (\lambda_{\text{max}})) = 36.6 \text{ M}^{-1} \text{ cm}^{-1}$ ). DMF solutions (in mM) of **2.1** (10.0, blue) and napy (10.0, black).

These examples, combined with the magnitude of the absorption coefficient of the low-energy transition found in **Figure 2.2**, suggests that this transition may originate from a spin-allowed, Laporte-forbidden transition between the HOMO (highest-occupied molecular orbital) and the LUMO (lowest-unoccupied molecular orbital), where the orbital symmetries as expected from **Chart 2.1**.

To further explore this transition, I sought to apply Density-Functional Theory (DFT) calculations to gain further insight into the electronic properties of **2.1**. **Figure 2.4** shows that the frontier-molecular orbitals of the ground-state follows the expected metal-centered disposition in a paddlewheel complex: The HOMO comprises an antibonding interaction ( $\sigma^*$ ) between the two Pd atomic  $d(z^2)$  orbitals. However, the LUMO comprises an antibonding interaction between the two atomic  $d(x^2-y^2)$  orbitals and the ligands ( $\sigma^*(\text{M-L}), d(x^2-y^2)\text{-L}(\sigma^*)$ ), thus deviating from an expected stabilizing  $\delta$  interactions between the two  $d(x^2-y^2)$  orbitals, rendering any transitions Laporte forbidden following that both orbitals feature an *ungerade* parity.



In collaboration with PhD Dmytro Mihrin and Associate Professor René W. Larsen, DTU Chemistry, we were able to obtain further understanding of the orbitals involved in the excitations observed in **Figure 2.3**, through time-dependent DFT (TD-DFT), as well as on the mid and far infrared spectra, *vide infra*. The quantum chemical calculations (in a vacuum) predict two transitions; a low-energy, low-intensity transition, at 484 nm, followed by a high-energy transition at 338 nm, in line with commonly observed MLCT for napy-complexes, both relating to an MLCT transition. The former comprises a transition from the HOMO to the LUMO+2 and the LUMO+3, whereas the higher-energy transition is between HOMO-1 to LUMO+2, and HOMO-2 to LUMO+3, respectively.

To account for the polar solvation shell present in **Figure 2.3**, and a resulting stabilization of an excited charge-distribution centered on the ligand, two implicit DMF models were investigated: conductor-like polarizable continuum model (CPCM), and cavity-dispersion-solvent structure (CDS) term, respectively. These calculations suggest the UV transition redshifts to 590 nm, which, despite a somewhat crude model, from the lacking hydrogen bonds, provides some insight into how solvent polarity affects the spectrum. Based on these findings, we suggest that the absorption spectrum of **2.1** displays a transition from the HOMO(-1,-2) to the ligand's  $\pi^*$ -system, although the magnitude of the observed MLCT are lower than usually encountered. Moreover, TD-DFT corroborates that no  $\sigma$ -orbitals originating from mixing of two 5pz orbitals are involved in transitions, precluding the complex' application in photolytic reactions.

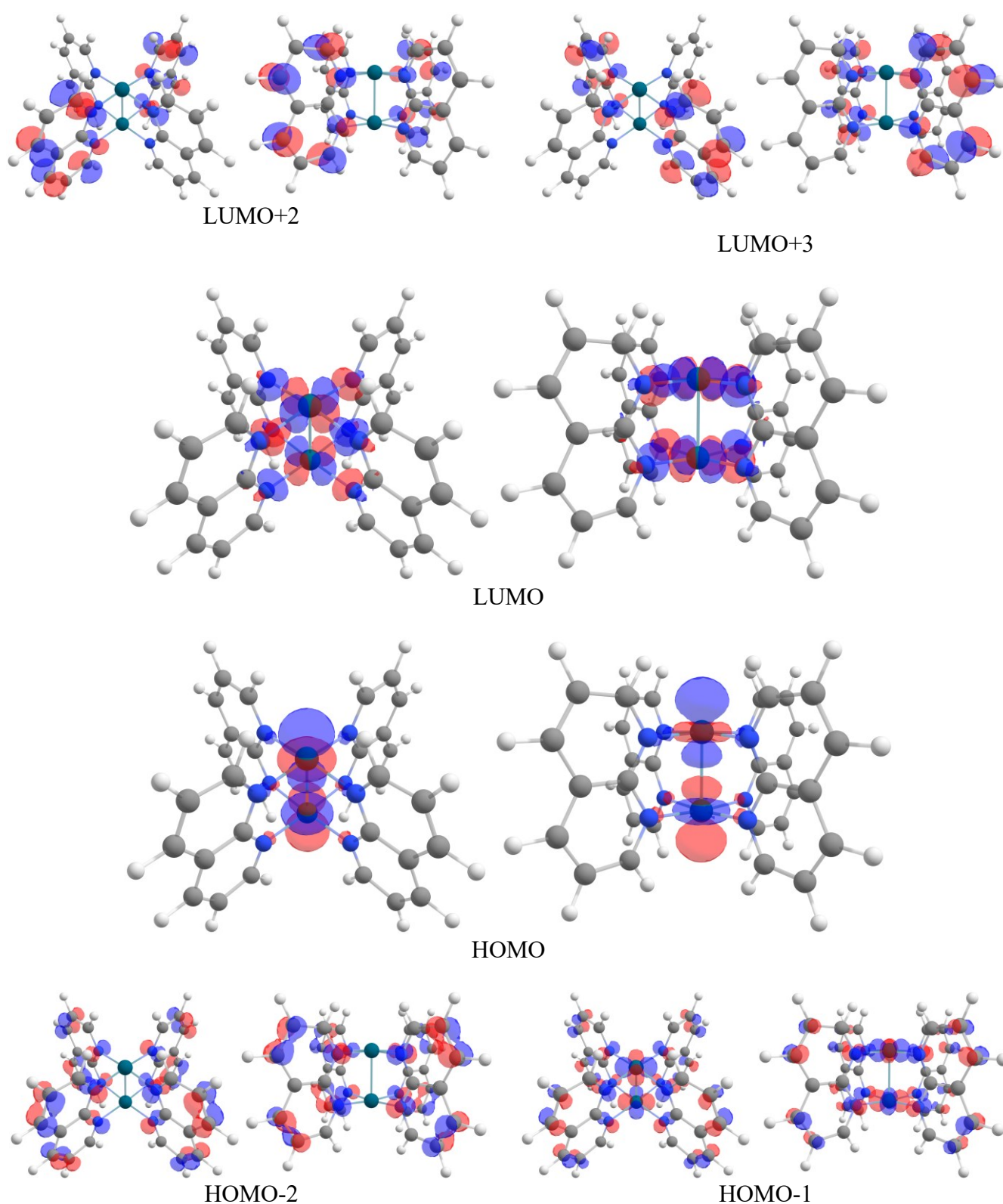


**Figure 2.4.** *DFT-calculated frontier molecular orbitals.* Depicting orbitals involved in electronic transitions calculated by TD-DFT for UV-Vis spectra: HOMO  $\rightarrow$  LUMO+2,+3 and HOMO-1,-2  $\rightarrow$  LUMO+2,3 for transition in the visible and UV spectral range, respectively. Isodensity plot ( $0.040 \text{ e}/\text{\AA}^2$ ).

The reported vibrational assignments of monomeric napy were inspired by the assignments for the structurally similar naphthalene molecule. The complete vibrational spectrum of free napy ligand has previously been reported in a combined Raman/infrared investigation of napy embedded in a Nujol mull<sup>26</sup>, and later in a surface-enhanced Raman spectroscopic (SERS) investigation of napy adsorbed on silver colloids<sup>27</sup>.

The attenuated-total-reflectance (ATR) spectra of **2.1** collected in the mid-infrared (MIR) fingerprint (600-1700  $\text{cm}^{-1}$ ) and the far-infrared (150-600  $\text{cm}^{-1}$ ) (FIR) spectral regions are shown in **Figure 2.5**. The mid-infrared part of the spectrum features the infrared-active vibrational fundamental transitions of  $A_{2u}$  and  $E_u$  symmetry associated with the slightly perturbed intramolecular normal modes of the napy ligands, whereas the far-infrared part of the spectrum additionally features several fundamental transitions associated with large-amplitude vibrational motion involving the metal-ligand bonds.

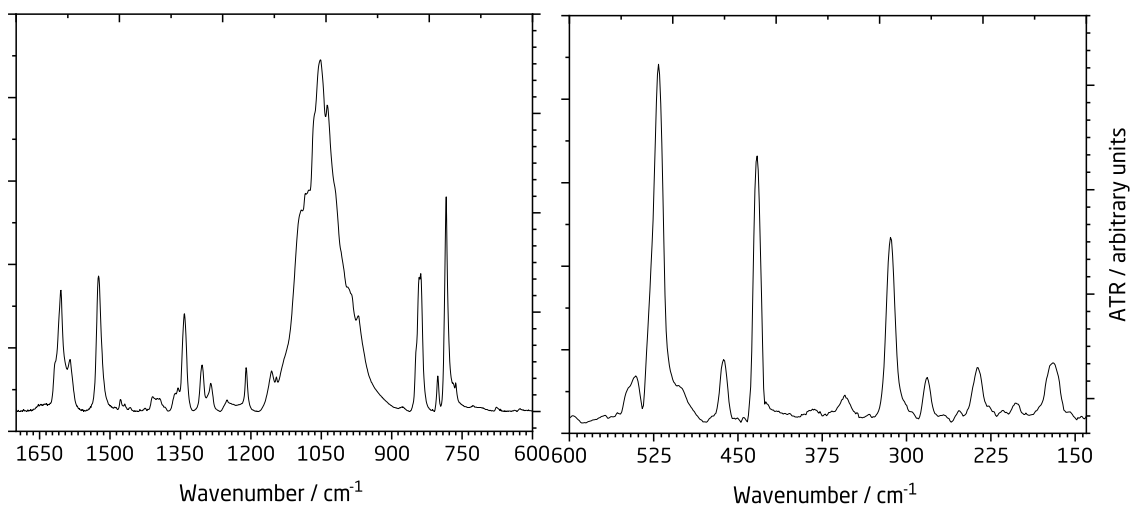


**Figure 2.5.** Mid-infrared and far-infrared spectral regions pertaining to **2.1**. B-F stretching modes obscures the MIR region between 1200-900  $\text{cm}^{-1}$ ; FIR contain N-Pd-N bending modes.

Our spectroscopic observations for **2.1** agree rather well with the literature, although the mid-infrared part of the spectrum is significantly blurred in the 900–1175  $\text{cm}^{-1}$  range due to the very strong and broad absorption feature resulting from the B-F stretching modes of the  $\text{BF}_4$  counter-ion.

The far-infrared spectrum reveals several absorption bands, which have previously been assigned to different modes involving the torsional and bending motion of the aromatic rings of the napy monomer. Three bands observed at 169, 433, and 463  $\text{cm}^{-1}$ , respectively, relates directly to the torsional motions of the ring, and gain intensity in napy due to the asymmetry introduced by the *N*-heteroatoms.

Additionally, the two bands observed at 521 and 543  $\text{cm}^{-1}$ , respectively, have both previously been assigned to bending motions of the aromatic rings<sup>26,27</sup>. More interestingly, the observation of three distinctive vibrational transitions, not previously observed in monomeric napy, at, 236, 281 and 314  $\text{cm}^{-1}$ , respectively, are indicative of the complexation between napy and Pd (II).

Although some ambiguity exists on the particular far-infrared assignments of the N··Pd··N bending and Pd··N stretching modes for palladium (II) complexes, as a variety of studies has assigned vibrational transitions associated with large-amplitude Pd··N stretching modes in the 400-550  $\text{cm}^{-1}$  range and other investigations have assigned these stretching transitions in the 200-300  $\text{cm}^{-1}$  range<sup>28,29</sup>.

However, a normal mode analysis of the present harmonic vibrational predictions provides further insight into the observed transitions, from an association with the large amplitude N··Pd··N bending motion involving the metal-ligand bonds. Two of the three transitions, 236 and 314  $\text{cm}^{-1}$ , respectively, are associated with two different concerted out-of-plane N··Pd··N bending modes involving all four napy subunits. The last transition at 281  $\text{cm}^{-1}$  is associated with a concerted in-plane N··Pd··N bending mode.

**Figure 2.6** illustrates a normal mode animation of the highest-energy out-of-plane N··Pd··N bending mode, and **Figure 2.7** compares the theoretical simulation of the far-

infrared spectrum with the experimental spectrum. The absolute wavenumber scale of the simulated spectrum has been scaled slightly (scaling factor of 0.98) to match the observed band origins of the intramolecular vibrational bands from experiments. The agreement between the simulation and experiment is surprisingly good although the undertaken harmonic vibrational predictions clearly are more challenging for the N··Pd··N bending modes due to the more anharmonic character for this class of large-amplitude vibrational motion.

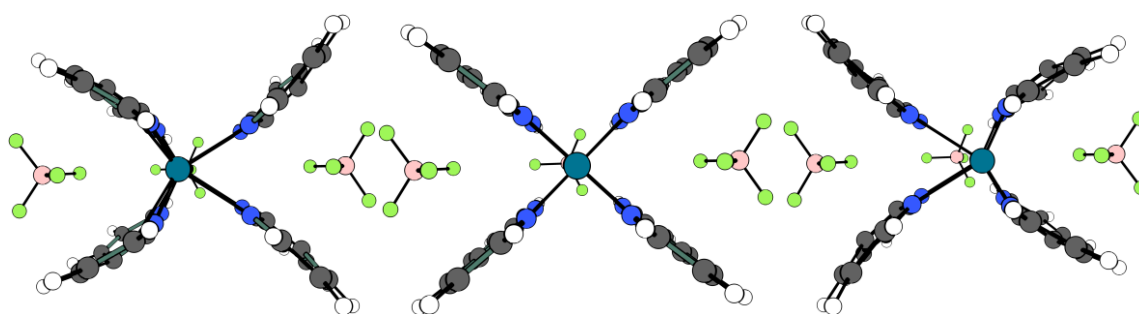


**Figure 2.6.** The animation of the large-amplitude concerted out-of-plane N··Pd··N bending mode of **2.1** predicted by the TPSS-D4/def2-TZVP level of the theory. The equilibrium configuration of **2.1** is shown (center) together with the configurations at the two outer vibrational turning points of the normal mode (left and right). Front counter-ion omitted for clarity.

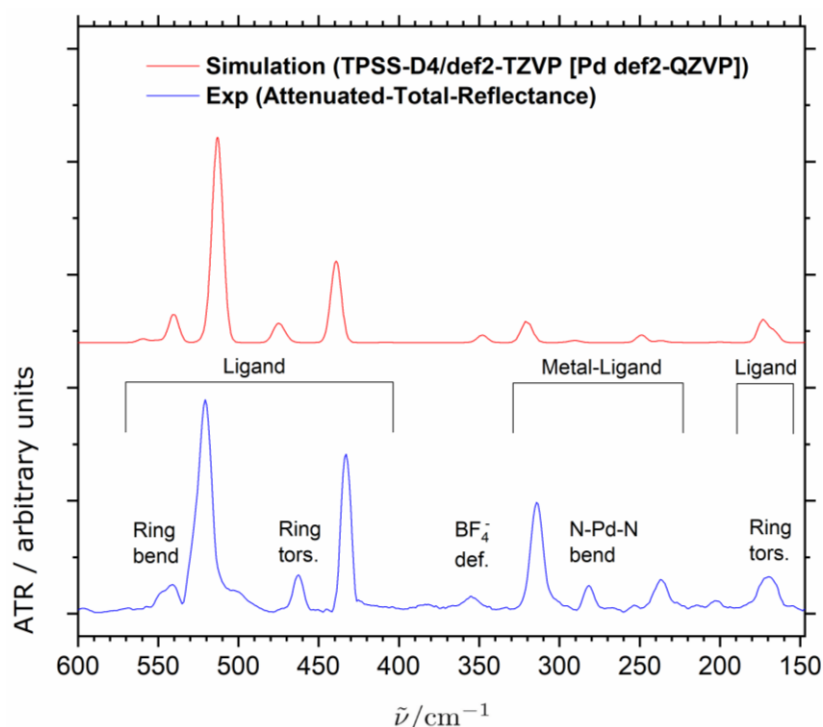


**Figure 2.7.** The experimental far-infrared attenuated-total-reflectance spectrum of **2.1** (blue trace) together with a simulation of the spectrum at the TPSS-D4/def2-TZVP level of theory (red trace). The present vibrational assignments of the intramolecular ring modes from the napy ligands, the deformation of the counter-ions  $\text{BF}_4$  and the large-amplitude concerted N··Pd··N bending modes of **2.1** are indicated.

Motivated by the spectroscopic and computational results, we sought to gain insight into the electrochemical properties of the complex in collaboration with PhD Xiaomei Yan and Researcher Xinxin Xiao, specifically concerning any distinctive oxidation events owing to the formation of a  $\text{Pd}_2^{6+}$ -core. Concerning paddlewheel complexes, the ligand's electronic properties play a pivotal role in the stabilization of dipalladium(III).

In this context, Cotton demonstrated that *N,N'*-tolylamidinato ligands enable the electrochemical preparation of such a  $\text{Pd}_2^{6+}$ -core<sup>30</sup>, while Bear instead found that the phenyl-congener only gave rise to the mixed-valent  $\text{Pd}^{\text{II}}\text{Pd}^{\text{III}}$ -complex<sup>31</sup>. From a systematic comparison of the oxidation potentials of monopalladium, clamshell dipalladium, and paddlewheel palladium complexes, Budnikova reports a linear decrease in oxidation potential following the Pd-Pd distance<sup>32</sup>, of which paddlewheel complexes demonstrate lower oxidation potentials, typically in the range of ~0.4 to 0.6 V vs.  $\text{Fc}^+/\text{Fc}$ , with electron-rich bridging units at the lower end. Accordingly, should **2.1** (or **2.2**) thus facilitate multiple oxidation events towards dipalladium (III), these events would be expected within this range, perhaps with an onset of oxidation at ~0.8 V.

**Figure 2.8** show our initial voltammograms of napy (blue trace) and **2.2** (black and red traces), which clearly demonstrate that any redox events are a consequence of the complex. Unfortunately, no reversible oxidations events are measurable within the expected range attributable to the Pd(II/III) redox couple. Instead, we find several reduction events.

However, the associated oxidation peaks are difficult to fully discern at the given scan rate ( $20 \text{ mVs}^{-1}$ ), and as such, we repeated the measurement at a higher concentration with varying scan rates to probe the stability of any formed species, shown in **Figure 2.9**, to probe the reversibility.

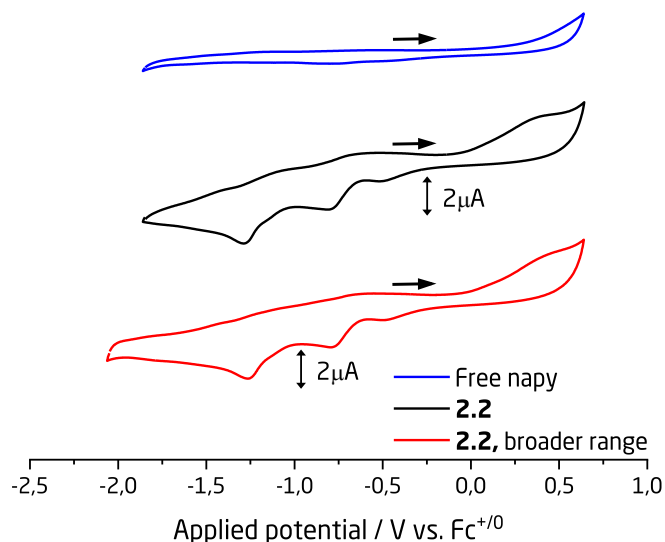


**Figure 2.8.** Stacked cyclic voltammograms of napy (blue trace) and **2.2** (black and red traces). Under the low scan rate ( $20 \text{ mV s}^{-1}$ ), **2.2** appear to undergo two distinctive irreversible electrochemical reductions. The arrow indicates starting potential and proceeds in the anodic direction.

The voltammogram shown in **Figure 2.9**, better demonstrates the redox events owing to **2.2**. The broad oxidation wave onset of  $\sim 0.4 \text{ V vs. Fc}^{+/0}$ , is consistent with a quasi-reversible ligand-based oxidation. In Biffis' analysis of  $[\text{Pt}_2(\text{napy})_4] 4\text{OTf}$ , the authors account for two ligand-centered oxidation events: a quasi-reversible oxidation at  $1.12 \text{ V vs SCE (MeCN)}$ , and an irreversible oxidation at  $1.5 \text{ V vs SCE}$ , respectively<sup>14</sup>. In this context, we did characterize napy-oxidation products, while we were unable to isolate a mixed-valent  $\text{Pd}^{\text{II}}\text{Pd}^{\text{III}}$  compound. These findings suggest that oxidation to the  $\text{Pd}_2^{6+}$ -core is highly unlikely, and napy is a poorly suited ligand to support strongly oxidizing metal-centres<sup>7</sup>.

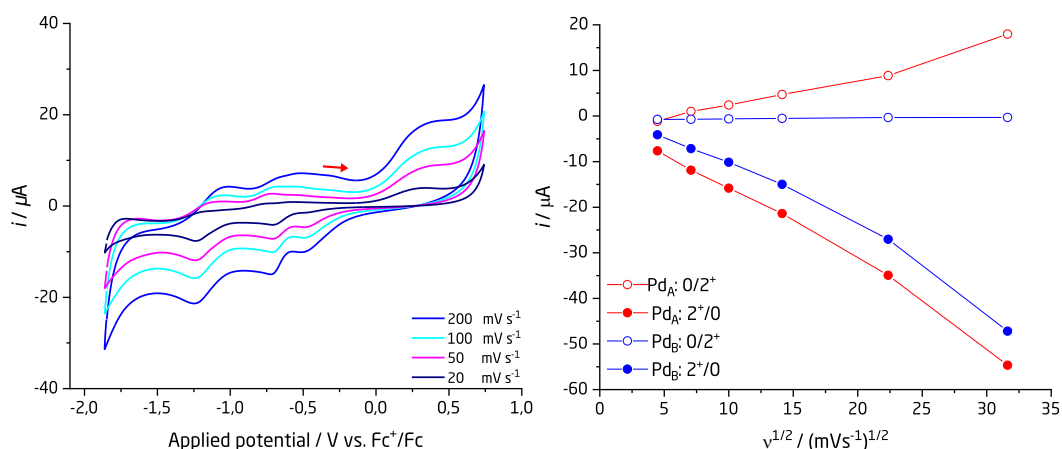


**Figure 2.9.** Voltammogram of **2.2** over various scan rates. Increasing the scan-rate results in a species that demonstrate electrochemical reversibility with respect to oxidation/reduction. The left-hand graph depicts the average of three scans. The scan starts at  $-0.36 \text{ V}$  and proceeds in the cathodic direction.

Two pronounced reduction events follow, at approximately -0.7V and -1.25V, with accompanying oxidation events. Both pairs follow a linear relationship between the peak current ( $i_p$ ) and square-root of the scan-rate ( $v^{1/2}$ ), right-hand of **Figure 2.9**, with peak separations of 67 mV, and 65 mV, respectively. The oxidation events appear frequency dependent, appear to anodically shift and broaden following increasing scan-frequency, and at 20 mVs<sup>-1</sup> they are gone, as found in **Figure 2.8**.

Both redox events also appear to relate to a two-electron transfer, estimated from the relationship between the half-peak potential ( $E_{p/2}$ ) and midpoint redox potential ( $E_{1/2}$ ),  $E_{p/2} = E_{1/2} \pm \frac{28 \text{ mV}}{n}$ . These redox events significantly differ from the other complexes presented by Budnikova, as those predominantly demonstrate irreversible reductions. However, while the presence of two reduction waves additionally differ from monopalladium complexes, the observed potentials do fall within the range of reduction potentials (DMF) of monopalladium complexes, varying between >-2.03 to -0.88V vs. Fc<sup>+/0</sup>.<sup>33</sup> We therefore suggest that this distinctive electrochemical profile is a consequence of a combination of the napy ligand and metal proximity, contrasting redox properties affected solely by metal proximity.

Our interpretation of the redox events can be understood from two different redox processes, either adequately accounting for the observed events in **Figure 2.9**: 1) a stepwise heterolytic reduction of each Pd (II) center ( $\text{Pd}^0\text{Pd}^{\text{II}}$ ,  $\text{Pd}^0\text{Pd}^0$ ), or 2) a stepwise homolytic reduction  $\text{Pd}^{\text{I}}\text{Pd}^{\text{I}}$ ,  $\text{Pd}^0\text{Pd}^0$ . However, we cannot discern between the two based on the presented electrochemical data alone, and we therefore sought to investigate the fate of this species following reactivity studies, and most likely relate to reduction of two isolated Pd (II) ions.



### 2.3 The paddlewheel complex as a synthon for Pd-Pd bonded complexes

To corroborate our electrochemical findings, we initially sought to oxidize **2.2** with various outer and inner-sphere oxidants, as outlined in **Scheme 2.3**. Compound **2.2** was chosen, as  $\text{BF}_4$ -counterions are more susceptible to engage in reactivity, than  $\text{PF}_6$ , with highly electrophilic metal centers or decompose into  $\text{BF}_3$ . While the reaction between **2.2** and Ce (IV) ( $\text{Ce}(\text{SO}_4)_2$  with and without  $\text{BaCl}_2$ ) in MeCN or (water and MeCN) yields a bright yellow powder, the isolated compound, rather than a  $\text{Pd}_2^{6+}$ -core, instead comprises what was isolated as a dithiocarbamate, shown in **Figure 2.10**. The mechanism behind the formation of this decomposition product is unknown; CAN ( $(\text{NH}_4)_2\text{Ce}(\text{NO}_3)_6$ ) oxidations similarly lead to unproductive decomposition reactions.

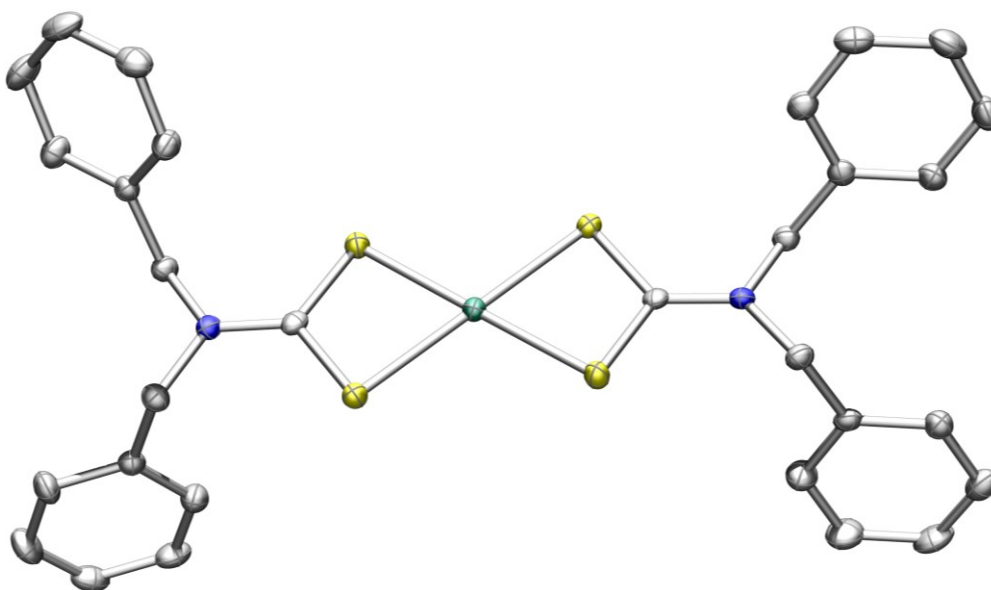
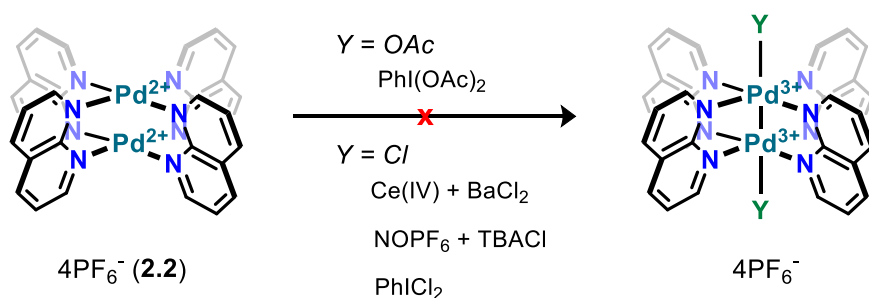


**Figure 2.10.** Single-crystal X-ray structure of isolable material following Ce (IV) oxidation of **2.2**, complex **2.3**. Thermal ellipsoids at a 50% probability level and H-atoms are omitted for clarity. Color coding: C grey, N blue, S yellow, Pd sea green.

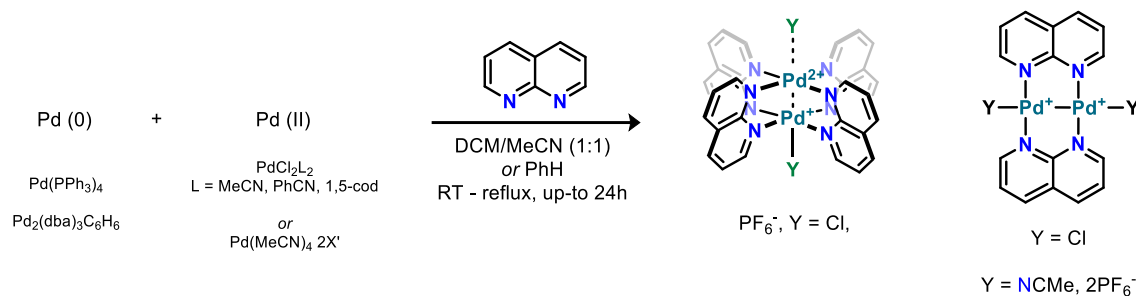
Exposure of **2.2/2.1** to  $\text{NOPF}_6/\text{BF}_4$  also failed to furnish any metal-based oxidation. Finally, we sought to employ hypervalent iodane sources, analogous to Cotton's preparation of  $\text{Pd}_2^{6+}$ -complex<sup>8</sup>, and in preparation of diplatinum(III) lantern complexes<sup>34</sup>. Discouragingly, we were able to recover >90% of **2.2/2.1** from the reaction mixture along with other Pd (II) salts.



**Scheme 2.3.** Synthetic outline for chemical oxidation of the paddlewheel complex. A range of single- and two-electron oxidants were attempted for the preparation of a  $\text{Pd}_2^{6+}$ -core.  $\text{X}' = \text{BF}_4, \text{PF}_6$ ;  $\text{Y} = \text{OAc}, \text{Cl}$ , or solvent molecules. All attempts failed in our hands.

Following these results, we then sought to obtain structural insight on any low-valent Pd entity consistent with reduction waves observed in the CV of **2.2**. We tested two different single-electron reductants ( $\text{Cp}^*_2\text{Fe}$ ,  $\text{Cp}^*_2\text{Co}$ ) and a two-electron reductant (Zn); we were unable to isolate any  $\text{Pd}^{\text{I}}\text{Pd}^{\text{I}}$  or mixed-valent ( $\text{Pd}^{\text{I}}\text{Pd}^{\text{II}}$  or  $\text{Pd}^0\text{Pd}^{\text{II}}$ ) compounds, instead, recovering materials predominantly consisting of unreacted **2.2** (>85%),  $[\text{Pd}(\text{MeCN})_4] 2\text{X}'$ , or ill-defined mixtures, with a noticeable deposition of a Pd-mirror when reducing with  $\text{Cp}^*_2\text{Co}$ .

We then sought to explore comproportionation between different Pd(0) and Pd(II) sources in presence of napy, as outlined in **Scheme 2.4**. The coordination geometry of Pd in such dipalladium(I) complexes is different from Pd (II), in that the Pd-Pd bond is oriented along one of the coordinate axes; a consequence manifesting in the variety of complexes bearing (un)supported Pd-Pd bonds, such as  $[\text{Pd}_2(\text{MeCN})_6] 2\text{BF}_4$ <sup>35</sup>,  $[(^i\text{Bu}_3\text{P})\text{Pd}(\mu\text{-X})]_2$  ( $\text{X} = \text{Br}, \text{I}$ )<sup>36</sup>, and  $\text{Pd}_2\text{Cl}_2(\mu\text{-dppm})_2$ <sup>37</sup>, respectively. However, the mixed-valent  $[\text{Ni}^{\text{I}}\text{Ni}^{\text{II}}(\mu\text{-napy})_4\text{Br}_2] \text{BPh}_4$  complex instead shares two square-pyramidal  $\text{Ni}^{1.5}$ -centers, coordinated in the basal plane by the napy. As such, if possible, we may isolate a similar complex, or a dipalladium (I) complex bearing napy in varying numbers *e.g.*  $[\text{Pd}_2((\mu\text{-})\text{napy})_n] 2\text{X}'$  ( $n = 2, 4, 6$ ).



**Scheme 2.4.** Synthetic outline for comproportionation reactions. Suggested outcome owing to the formation of either a mixed-valent or dipalladium(I) both having bridging napy ligands.

Various combinations of Pd-precursors, solvents, reaction time, order of addition, as well as the rate of addition, were all unfruitful. These reactions either led to the deposition of a significant amount of Pd in form of a Pd-mirror or precipitation of Pd-black or showed no reactivity at all. Moreover, a yellow/orange filtrate was collected from the reaction utilizing exogenous or Pd-precursors bearing  $\text{PPh}_3$ , from which we were able to crystallize small amounts of  $\text{PdCl}_2\text{PPh}_3(\kappa\text{-N-napy})$ , shown in **Figure 2.11**, demonstrating napy in a monodentate coordination mode to Pd.

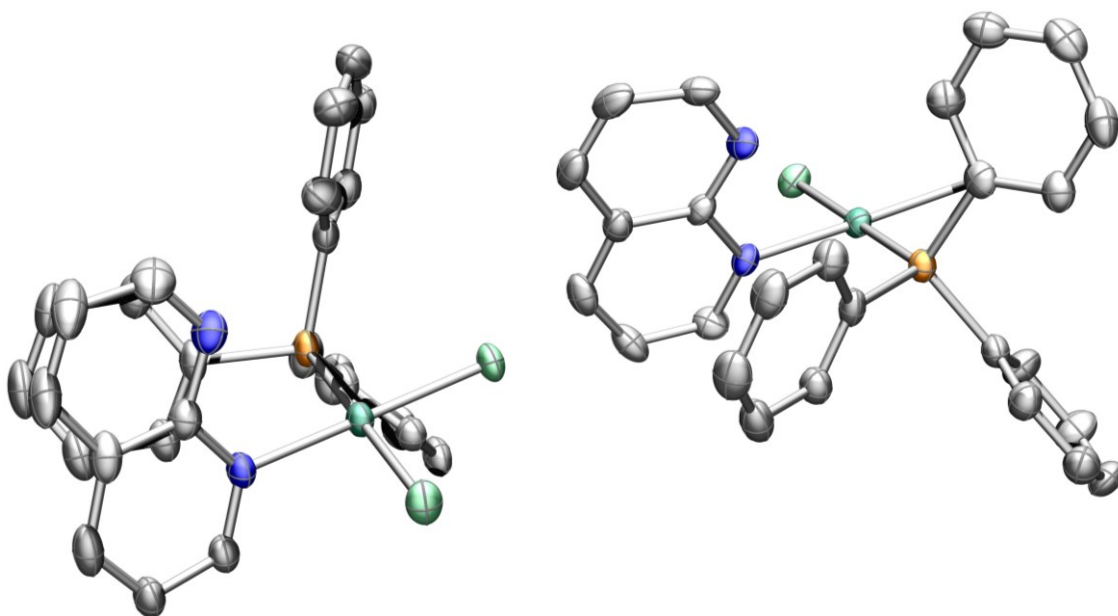


**Figure 2.11.** Single-crystal X-ray structure of a phosphine-napy-Pd (II) complex, complex 2.4. The solid-state structure of crystals is found from comproportionation reactions, with thermal ellipsoids at 50% probability level. H-atoms and co-crystallized DCM molecules are omitted for clarity. Color coding: C grey, N blue, Cl green, P yellow, Pd sea green.

To corroborate these findings, we sought to understand napy's interaction with the "naked" dipalladium(I) source  $[\text{Pd}_2(\text{MeCN})_6] \cdot 2\text{BF}_4$ ; starting from  $[\text{Pd}_2(\text{MeCN})_6] \cdot 2\text{BF}_4$  and adding in (increasing equivalents of) napy (one to six equivalents) in different

solvents (DMF, MeCN, DCM/MeCN (1:1)) quickly led to the precipitation of Pd-black (or deposition of Pd-mirror). The addition of the  $\text{Pd}_2^{2+}$ -precursor to varying equivalents of napy similarly resulted in a rapid formation of Pd-black.

The (electronic) nature of the coordinating ligand seems to greatly affect the stability of the dipalladium(I) complex. Although  $[\text{Pd}_2(\text{MeCN})_6] 2\text{BF}_4$  is an isolatable species, we observed slow decomposition in the solution. In their study of this complex, Murahashi and Kurosawa were able to coordinate various ligands with retention of the Pd-Pd bond<sup>35</sup>; two equivalents of 1,10-phenanthroline (phen) and an *N,N*-ethylenebis(benzaldimine), whereas, the addition of >2 equivalents of  $\text{PPh}_3$  resulted in unidentified species. Related, Walther reported the synthesis and structure of a low-valent  $[\text{Pd}_2(1,5\text{-cod})_2\text{Cl}_2]$ , that is thermally unstable at temperatures  $T > -20\text{ }^\circ\text{C}$ <sup>38</sup>.

A tentative explanation for the observed decomposition products relates to how napy inadequately stabilizes the electron-rich Pd(I)-centers, which is different from aromatic phosphines, *e.g.*  $\text{dppm}$ , and  $\text{PPh}_3$ , and even from heteroaromatics *viz.* phen.

While a putative  $[\text{Pd}_2(\text{napy})_n] 2\text{X}'$  ( $n = 2, 4, 6$ ) may form, it is likely subject to quick thermal decomposition; thus rendering  $[\text{Pd}_2(\text{MeCN})_6] 2\text{BF}_4$  the better option in the context of exploring ligand substitution of a synthon bearing an unsupported Pd-Pd bond and labile ligands.

## 2.4 Conclusion

We present evidence that supports the notion that napy tethers two metals closely together giving rise to distinctive electrochemical redox properties. The formation of complexes **2.1** and **2.2** was achieved differently from its Group 10 congeners; the nickel-analogue forms under reductive conditions supported by half a Ni-Ni bond, and the platinum-congener starts from a complex already featuring a Pt-Pt bond.

Spectroscopic and computational analysis suggests that the close Pd-Pd distance is metalphilic in nature, however, does not constitute a formal bond, following the full population of bonding and antibonding metal-metal molecular orbitals. Optical absorption spectroscopy combined with TD-DFT provides insight into the observed excitations.

Electrochemical analysis indicates two reversible metal-centered redox events, a consequence of the ligand and the Pd-Pd proximity; our reactivity studies, strongly suggest, that neither complexes **2.1** nor **2.2** supports the formation of neither a Pd<sub>2</sub><sup>6+</sup> nor a Pd<sub>2</sub><sup>2+</sup>-core, despite complex **2.2** demonstrating distinctive redox properties from other paddlewheel complexes. Rather, the reduction of **2.2** seems to center on two distinctive Pd (II) centers that each undergo two-electron reduction (Pd<sup>II/0</sup>), contrasting the formation of a Pd-Pd bond (Pd<sub>2</sub><sup>2+</sup>-core).

Moreover, we also demonstrate that napy does bind Pd (II) by isolation of a mixed phosphine-napy adduct, despite a poor match considering the hard and soft (Lewis) acid and base (HSAB). Independent preparation of this complex has thus far been unsuccessful.

## 2.5 References

- (1) *Multiple Bonds Between Metal Atoms*; Cotton, F. A., Murillo, C. A., Walton, R. A., (eds.); (Springer-Verlag: New York), **2005**.
- (2) Cotton, F. A.; Hillard, E. A.; Murillo, C. A.; Zhou, H.-C. *J. Am. Chem. Soc.* **2000**, *122*, 416–417.
- (3) Mann, K. R.; Gordon, J. G.; Gray, H. B. *J. Am. Chem. Soc.* **1975**, *97*, 3553–3555.
- (4) Roundhill, D. M.; Gray, H. B.; Che, C. M. *Acc. Chem. Res.* **1989**, *22*, 55–61.
- (5) Bercaw, J. E.; Durrell, A. C.; Gray, H. B.; Green, J. C.; Hazari, N.; Labinger, J. A.; Winkler, J. R. *Inorg. Chem.* **2010**, *49*, 1801–1810.
- (6) Lewis, N. S.; Mann, K. R.; Gordon, J. G.; Gray, H. B. *J. Am. Chem. Soc.* **1976**, *98*, 7461–7463.
- (7) Cotton, F. A.; Daniels, L. M.; Murillo, C. A.; Timmons, D. J.; Wilkinson, C. C. *J. Am. Chem. Soc.* **2002**, *124*, 9249–9256.

- (8) Cotton, F. A.; Gu, J.; Murillo, C. A.; Timmons, D. J. *J. Am. Chem. Soc.* **1998**, *120*, 13280–13281.
- (9) Munakata, M.; Maekawa, M.; Kitagawa, S.; Adachi, M.; Masuda, H. *Inorganica Chim. Acta* **1990**, *167*, 181–188.
- (10) Griffith, W. P.; Tse Yuen Koh; White, A. J. P.; Williams, D. J. *Polyhedron* **1995**, *14*, 2019–2025.
- (11) Maekawa, M.; Munakata, M.; Kitagawa, S.; Kuroda-Sowa, T.; Suenaga, Y.; Yamamoto, M. *Inorganica Chim. Acta* **1998**, *271*, 129–136.
- (12) Koizumi, T.; Tanaka, K. *Inorganica Chim. Acta* **2004**, *357*, 3666–3672.
- (13) Basato, M.; Biffis, A.; Martinati, G.; Tubaro, C.; Graiff, C.; Tiripicchio, A.; Aronica, L. A.; Caporusso, A. M. *J. Organomet. Chem.* **2006**, *691*, 3464–3471.
- (14) Tubaro, C.; Greggio, G.; Antonello, S.; Graiff, C.; Biffis, A. *Inorganica Chim. Acta* **2017**, *466*, 578–583.
- (15) Gatteschi, D.; Mealli, C.; Sacconi, L. *J. Am. Chem. Soc.* **1973**, *95*, 2736–2738.
- (16) Mealli, C.; Zanolini, F. *J. Chem. Soc., Chem. Commun.* **1982**, No. 2, 97–98.
- (17) Tiripicchio, A.; Camellini, M. T.; Usón, R.; Oro, L. A.; Ciriano, M. A.; Viguri, F. *J. Chem. Soc., Dalt. Trans.* **1984**, No. 2, 125–131.
- (18) Boelrijk, A. E. M.; van Velzen, M. M.; Neenan, T. X.; Reedijk, J.; Kooijman, H.; Spek, A. L. *J. Chem. Soc. Chem. Commun.* **1995**, No. 23, 2465.
- (19) Døssing, A.; Larsen, S.; Van Lelieveld, A.; Bruun, R. M. *Acta Chem. Scand.* **1999**, *53*, 230–234.
- (20) Bencini, A.; Berti, E.; Caneschi, A.; Gatteschi, D.; Giannasi, E.; Invernizzi, I. *Chem. Eur. J.* **2002**, *8*, 3660.
- (21) Aguirre, J. D.; Lutterman, D. A.; Angeles-Boza, A. M.; Dunbar, K. R.; Turro, C. *Inorg. Chem.* **2007**, *46*, 7494–7502.
- (22) Casas, J. M.; Diosdado, B. E.; Forniés, J.; Martín, A.; Rueda, A. J.; Orpen, A. G. *Inorg. Chem.* **2008**, *47*, 8767–8775.
- (23) Singh, P.; Clearfield, A.; Bernal, I. *J. Coord. Chem.* **1971**, *1*, 29–37.
- (24) Cotton, F. A.; Matusz, M.; Poli, R.; Feng, X. *J. Am. Chem. Soc.* **1988**, *110*, 1144–1154.
- (25) Berry, J. F.; Bill, E.; Bothe, E.; Cotton, F. A.; Dalal, N. S.; Ibragimov, S. A.; Kaur, N.; Liu, C. Y.; Murillo, C. A.; Nellutla, S.; North, J. M.; Villagrán, D. *J. Am. Chem. Soc.* **2007**, *129*, 1393–1401.
- (26) Carrano, J. T.; Wait, S. C. *J. Mol. Spectrosc.* **1973**, *46*, 401–418.
- (27) Griffith, W. P.; Koh, T. Y. *J. Raman Spectrosc.* **1995**, *26*, 1067–1070.
- (28) Durig, J. R.; Mitchell, B. R.; Sink, D. W.; Willis, J. N.; Wilson, A. S. *Spectrochim. Acta Part A Mol. Spectrosc.* **1967**, *23*, 1121–1135.
- (29) Morzyk-Ociepa, B.; Dysz, K.; Turowska-Tyrk, I.; Michalska, D. *J. Mol. Struct.*

**2016**, 1103, 202–211.

- (30) Cotton, F. A.; Matusz, M.; Poli, R. *Inorg. Chem.* **1987**, 26, 1472–1474.
- (31) Yao, C. L.; He, L. P.; Korp, J. D.; Bear, J. L. *Inorg. Chem.* **1988**, 27, 4389–4395.
- (32) Dudkina, Y. B.; Kholin, K. V.; Gryaznova, T. V.; Islamov, D. R.; Kataeva, O. N.; Rizvanov, I. K.; Levitskaya, A. I.; Fominykh, O. D.; Balakina, M. Y.; Sinyashin, O. G.; Budnikova, Y. H. *Dalt. Trans.* **2017**, 46, 165–177.
- (33) Budnikova, Y.; Dudkina, Y.; Khrizanforov, M. *Inorganics* **2017**, 5, 70.
- (34) Wilson, J. J.; Lippard, S. J. *Inorg. Chem.* **2012**, 51, 9852–9864.
- (35) Murahashi, T.; Nagai, T.; Okuno, T.; Matsutani, T.; Kurosawa, H. *Chem. Commun.* **2000**, No. 17, 1689–1690.
- (36) Vilar, R.; Mingos, D. M. P.; Cardin, C. J. *J. Chem. Soc. Dalt. Trans.* **1996**, No. 23, 4313–4314.
- (37) Pringle, P. G.; Shaw, B. L. *J. Chem. Soc., Chem. Commun.* **1982**, No. 1, 81–82.
- (38) Schwalbe, M.; Walther, D.; Schreer, H.; Langer, J.; Görls, H. *J. Organomet. Chem.* **2006**, 691, 4868–4873.

## Chapter. 3. Synthesis of tetra imidazolium proligands

### 3.1 Introduction

Another class of dinuclear complexes, capable of engaging in multi-electron reactions, are colloquially known as “Pacman” complexes. Many such complexes tether weak-field ligands co-facial to a rigid aromatic backbone, where binding-pocket owing to for instance dipyrrens<sup>1</sup> and *N*-porphyrins<sup>2</sup>, engender open-shell complexes, suitable at stabilizing two bridged transition metals<sup>3–5</sup> as shown below in **Figure 3.1**. Despite such ligand motifs can accommodate two metal ions proximal for multielectron transfer processes, the same electronic environment lacks prolonged stability, from noticeable metal extrusion as well as deactivation following the formation of thermodynamical “sinks” such as the oxo complex demonstrated on the left-hand side of **Figure 3.1**<sup>1</sup>.

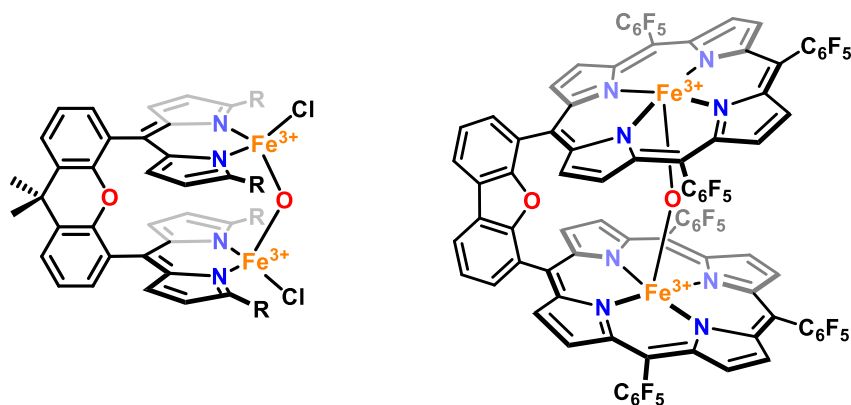


**Figure 3.1.** Different dinuclear complexes are known to facilitate multi-electron transformations. The dipyrrenato framework tethers two metal centers, a diporphyrin “Pacman” complex, and a di-Schiffbase framework.

Relevant to this PhD study, we sought to realize complexes as shown below in **Figure 3.2**, which similarly utilize a rigid aromatic backbone as a “metal spacer”, however, we instead opted to employ strongly binding *N*-heterocyclic carbene ligands as anchor points over dipyrren to circumvent metal-extrusion experienced by Pacman complexes.



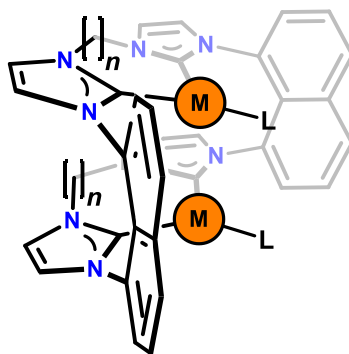


**Figure 3.2.** *Envisioned dinuclear complex of interest to this PhD-study.* We sought to synthesize a complex bearing a macrocyclic tetra NHC ligand, coordinating in a ditopic manner.

Further encouraged by our paddlewheel structure, complex **2.1**, which proved that two fused benzene molecules spatially can hold two Pd (II) ions, we envisioned naphthalene serving as a rigid metal-spacer; the extended  $\pi$ -system further imparting a discriminating binding pocket owing to size exclusion and electrostatic interactions. However, should the naphthalene distance prove too short, anthracene and its derivatives, as seen above, can instead accommodate the two metal centers, and thus serves as a direct handle to change the metal-metal distance.

When taken together, we sought to establish a synthetic protocol targeting the macrocyclic tetra imidazolium salts owing the proligand of the envisioned complexes of **Figure 3.2**. In this context, macrocyclic poly imidazolium salts are a versatile class of compounds used in different aspects of chemistry from fluorescent chemosensors in supramolecular assemblies following their high affinities toward discrete anions<sup>6</sup>, to proligands relevant to organometallic porphyrin-analogues, *cf.* Chapter 5.

### 3.2 Tethering imidazole to naphthalene

To realize the envisioned complex shown in **Figure 3.2**, some synthetic approaches were undertaken in collaboration with a former group member, targeting the direct tether of imidazole to naphthalene, as outlined in **Chart 3.1**. However, the two fused benzene rings render the 1,8 positions spatially close, and we were unsuccessful in this endeavor.

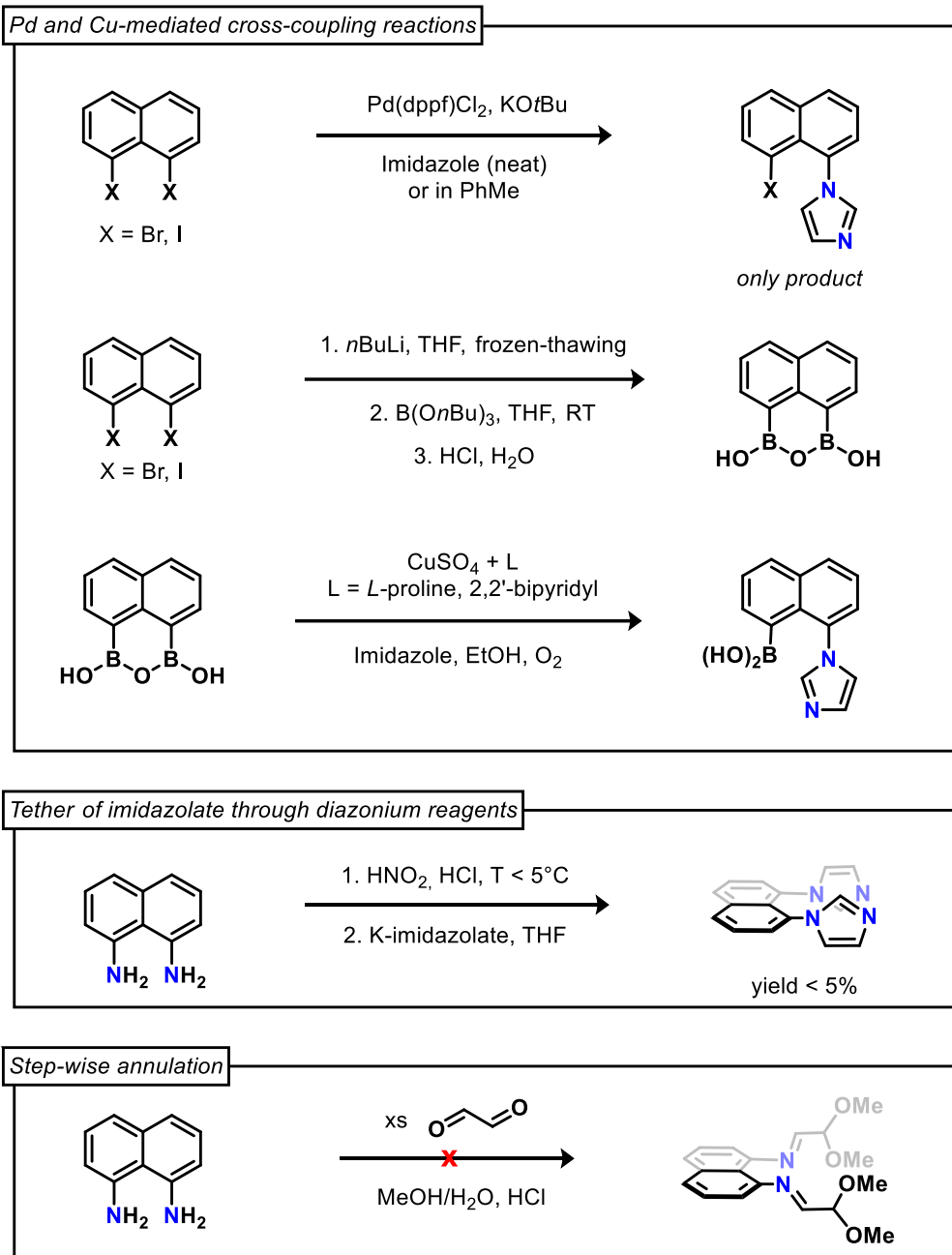


**Chart 3.1.** Various synthetic approaches explored towards the direct tether of imidazole to naphthalene. The only approach leading to poor yields of the desired precursor was through an unstable diazonium intermediate.

While the commercially available 1,8-dihalo naphthalene ( $\text{X} = \text{Br}, \text{I}$ ) reacts with dry imidazole under Pd-mediated cross-coupling reaction conditions, the reaction, seem to furnish the tether of a single imidazole, leaving an asymmetrical substrate in low yields. The chelating ligand dppf, 1,1'-bis(diphenylphosphino)ferrocene, was found necessary

to mediate this transformation; it is likely that the second oxidative addition leads to the formation of a metallacycle, resulting in off-cycle complexes.

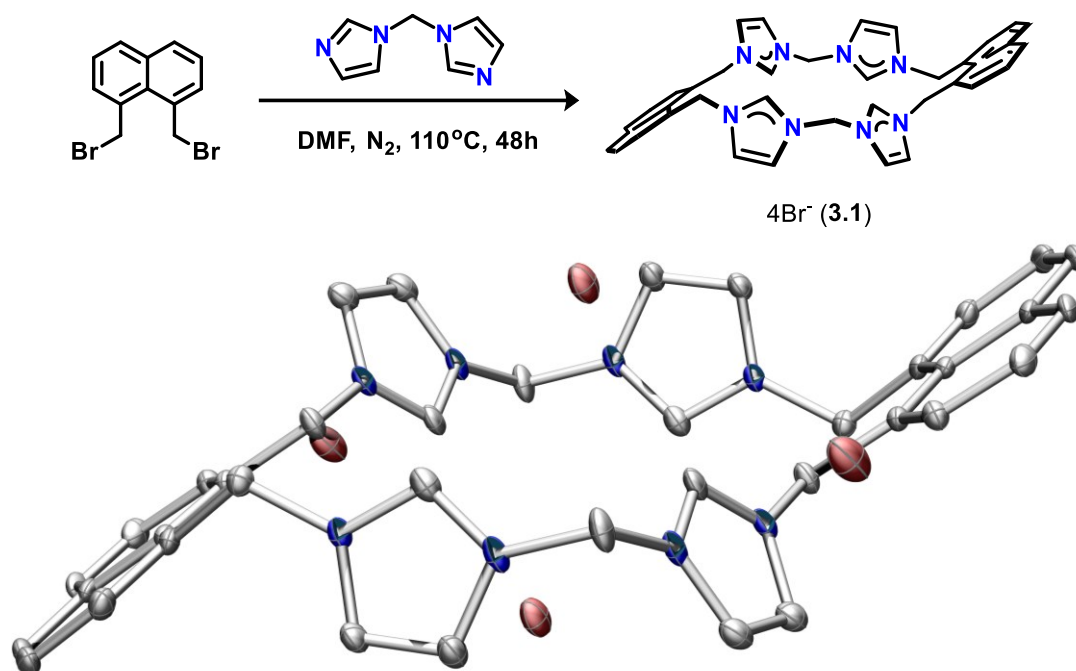
Reacting the same dihalido naphthalene with *n*BuLi furnish metal-halogen exchange, and the carbanion readily reacts with a plethora of electrophiles<sup>7</sup>. Adding in B(O<sup>*n*</sup>Bu)<sub>3</sub>, followed by hydrolysis of borane-ether leaves a boronic anhydride; we thought to use this compound in Chan-Evans-Lam type coupling with imidazole or imidazoles, following the successful application in a Suzuki-Miyaura coupling with aryl halides<sup>8</sup>. However, the anhydride suffers the same fate as the direct amination product; only one imidazole seems to tether, in low yields.

Instead, we sought to explore diazonium chemistry in line with the Sandmeyer transformation. Mass spectrometry successfully identifies an ion consistent with the diimidazole substrate, from the reaction between the crude isolate of the dichloride salt and K-imidazolate. However, this transformation proceeds in poor yield, most likely from a partial hesitation to fully dry the chloride intermediate, as it is a potential explosive, thus limiting the scalability of this approach. The BF<sub>4</sub> congener was not prepared.

Finally, we sought to explore whether the imidazolium salt was accessible through a stepwise annulation through an octamine following a modified Debus-Radziszewski imidazole synthesis; unfortunately, the initial condensation reaction with glyoxal seems to produce a mixture of poorly defined products, rather than an expected imino-acetal that is critical to further annulation.

Based on these findings, we instead turned our attention to the methylene congener, as the benzylic *sp*<sup>3</sup>-methyl group may undergo various transformations, such as S<sub>N</sub>2-substitution and bromination, increasing the possibility of preparing our desired macrocyclic tetra imidazolium precursor.

### 3.3 Synthesis of naphthalene-based, methylene-linked macrocycle tetraimidazolium salt



**Scheme 3.1.** *Synthesis and solid-state structure of 3.1.* Hydrogen atoms are omitted for clarity. Thermal ellipsoids are set at a 50% probability level. Atom color-coding: N blue, C grey, and Br red/brown.

The target methylene-linked macrocycle, <sup>Me,Naph</sup>LH<sub>4</sub>-4Br, **3.1**, was prepared following an S<sub>N</sub>2-substitution reaction between 1,8-bis(bromomethyl)naphthalene and 1,1'-bisimidazole-methane<sup>9</sup> in a 1:1 mixture in DMF, shown in **Scheme 3.1**, in a poor yield of around 3-5%.

The white precipitate that forms under these conditions, turns into a semi-liquid upon solvent removal, which at first was attributed to the compound's inherent property as an ionic liquid. While <sup>1</sup>H NMR of the material reveals a complex mixture, {<sup>1</sup>H-<sup>1</sup>H}-COSY of the aromatic region, shown in **Figure 3.3**, corroborates a characteristic coupling pattern found in imidazolium salts, specifically between the protons at the C<sub>2</sub> (most downfield shifted), C<sub>4</sub>, and C<sub>5</sub> position of the imidazolium moiety. This coupling is found twice, as indicated by (●) and (■), which may suggest that either two compounds

are formed, or that a single compound forms, which at RT interconverts between two conformers.

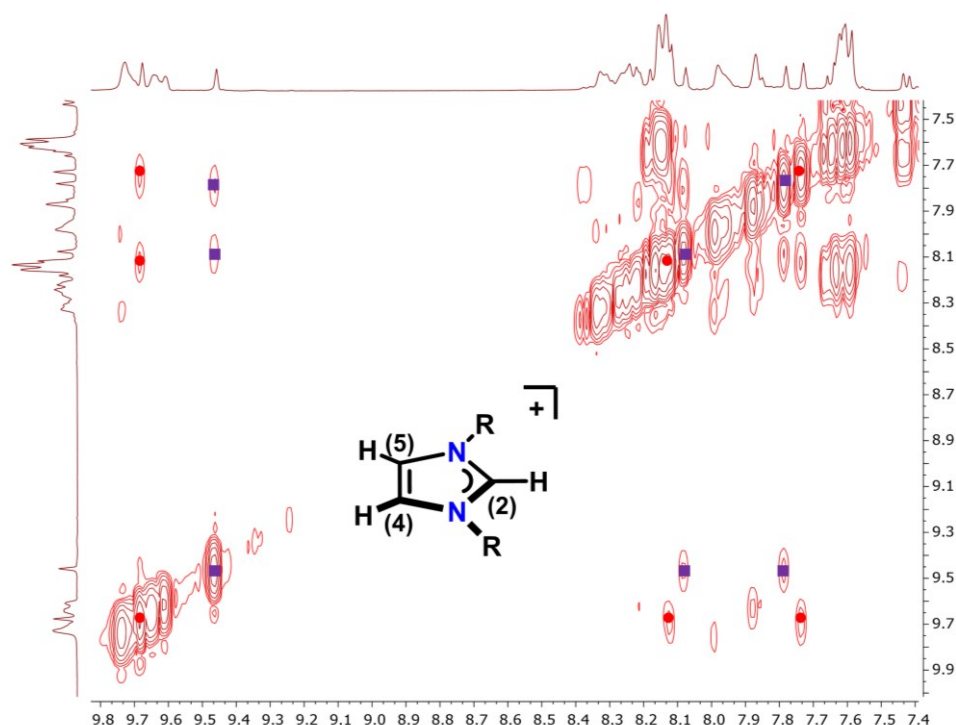
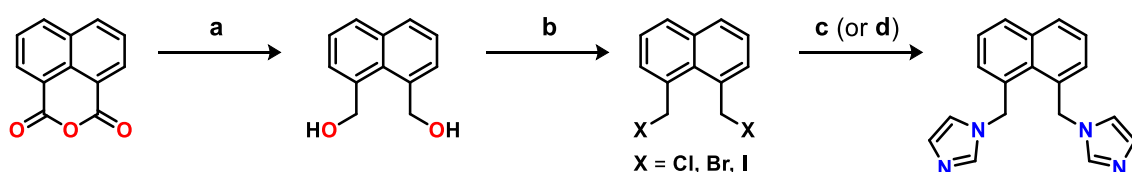


**Figure 3.3.** 2D  $^1\text{H}$  NMR of  $^{\text{Me}}\text{LH}_4\text{-4Br}$  crude. A selected range of the  $\{^1\text{H}\text{-}^1\text{H}\}$ -COSY spectrum (in  $\text{DMSO-}d_6$ ) of the recovered material from initial self-assembly. The structure highlights protons giving rise to the characteristic spin-system of the imidazolium moiety of which two are present (●) and (■), respectively. The numbering refers to the specific position of a C atom.

Nevertheless, the desired macrocycle is isolable following multiple recrystallizations from MeOH; we were able to isolate crystals suitable for single-crystal X-ray diffraction, shown in the lower part of **Scheme 3.1**, corroborating the desired connectivity. More importantly, this powder has a distinctive, symmetrical  $^1\text{H}$  NMR spectrum, shown in **Figure 3.4**, lower spectrum, which does not change over multiple months, precluding the possibility of two interconverting conformers giving rise to the distinctive COSY relationships observed in **Figure 3.3**.

To increase the yield of compound **3.1**, different approaches were undertaken, targeting stronger electrophiles, changing the nucleophile and electrophile-bearing substrates, employing different solvents at various concentrations, and the utilization and variation in additives. To this end, 1,8-bis(hydroxymethyl)naphthalene was used as a

starting point for the preparation of (pseudo) halido-functionalized naphthalene, as shown in **Scheme 3.2**:  $\text{LiAlH}_4$  reduction of naphthalic anhydride<sup>10</sup> (step **a**) yields this compound in moderate to good yield (50 – 70%) as an off-white powder. This diol, reacts with  $\text{PX}_3$  ( $\text{X} = \text{Cl}, \text{Br}, \text{I}$ ) in dioxane (or glyme), and readily transforms the diol into the corresponding 1,8-bis(halidomethyl)naphthalene, (step **b**), which, in water, precipitates out as an off-white powder in near-quantitative yield.



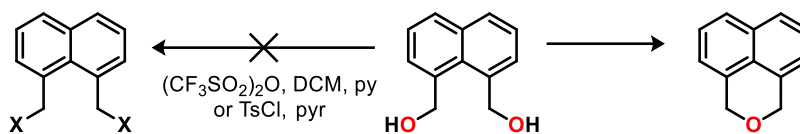
**Scheme 3.2.** *Synthetic approach for functionalization of 1,8-naphthalene.* Reagents and conditions: (**a**) 1.55 equiv.  $\text{LiAlH}_4$  (1M in THF), reflux o.n.; (**b**) 1.5 equiv.  $\text{PX}_3$ , ( $\text{X} = \text{Cl}, \text{Br}, \text{I}$ ), dioxane or glyme, rt, 2 – 4 hours, water. (**c**) 2.05 equiv. of  $\text{C}_3\text{H}_3\text{N}_2\text{Na/K}$ , THF, 1 – 2h, 0 °C to rt, ( $\text{C}_3\text{H}_3\text{N}_2\text{Na/K}$  from 1 equiv.  $\text{C}_3\text{H}_4\text{N}_2$ , 1.05 equiv.  $\text{Na/KH}$ , THF, rt, 2 hr); (**d**) 2.1 equiv.  $\text{Et}_3\text{N}$  (or DMAP), 2.1 equiv.  $\text{C}_3\text{H}_4\text{N}_2$ , THF (or  $\text{Et}_2\text{O}$ ), 40 °C, 2 - 3h, (or RT, o.n.).

Either of these naphtha-halidomethylene compounds serve as a starting point for tethering imidazole to the naphthalene-moiety; through an  $\text{S}_{\text{N}}2$ -substitution reaction with a potassium/sodium imidazolate salt under inert conditions (step **c**), or with the addition of a nucleophilic catalyst *e.g.*  $\text{Et}_3\text{N}$  or 4-dimethylamino pyridine (DMAP) (step **d**) in ethereal solvents.

The latter transformation was done, as we sought to explore the reactivity resulting from changing the substrate bearing the electro- and nucleophile; by reacting imidazole-functionalized naphthalene with any of the halidomethanes,  $\text{CH}_2\text{X}_2$ ,  $\text{X} = \text{Cl}, \text{Br}, \text{I}$ . However, as only limited consumption of the imidazole starting material was observed, this route was not pursued any further.

Pursuant of reactivity different from 1,8-bis(bromomethyl)naphthalene, we then sought to probe various stronger electrophiles through triflation, tosylation, and nosylation of the parent diol, respectively. Instead, the diol proximity, unfortunately, facilitates a rapid intramolecular annulation to 1*H*,3*H*-benzo[de]isochromene, as shown

in **Scheme 3.3**, suggesting these electrophiles would have proven as prudent candidates for macrocyclization, but ultimately renders this approach invalid.



**Scheme 3.3.** *Synthetic approach for triflation, tosylation, nosylation.* The diol rapidly annulates towards isochromene even starting frozen/thawing conditions.

While unsuccessful in preparing a starting material with stronger electrophiles, our attention instead turned to the other organohalides of naphthalene, where unexpected differences became apparent during macrocycle formation. Rather than forming a precipitate, 1,8-bis(chloromethyl) naphthalene resulted in a red liquid with some spectral properties resembling that in **Figure 3.3**. On the other hand, when using the iodo-analog, the reaction formed an insoluble gooey substance. Further separation of the macrocycle from these mixtures were laborious and difficult to achieve. These findings, albeit superficial, indicate the formation of an ionic liquid and a polymeric compound, respectively.

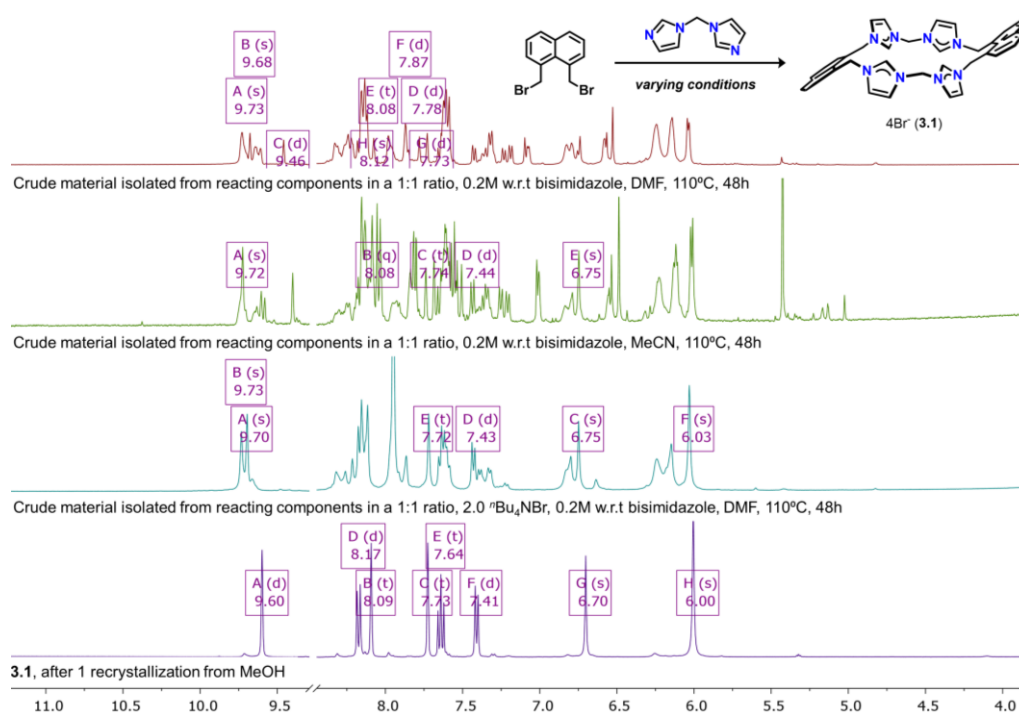


**Figure 3.4.** *Stacked 1D  $^1\text{H}$  NMR of solids obtained from macrocycle self-assembly at various conditions.* The increasingly more resolved was encouraging to us. All spectra in  $\text{DMSO-}d_6$ .

From these findings, we chose to continue with the bromido compound, varying next solvent, concentrations, and further involved additives, specifically *n*Bu<sub>4</sub>NX (TBAX), X = Cl, Br, I, to probe their impact on the macrocycle synthesis, as shown in **Figure 3.4**

Starting from the top of **Figure 3.4**, the first and second entries compare the different powders obtained from the self-assembly reaction performed in DMF and MeCN, respectively, at 110 °C over the duration of 48 hours. The same features are present, and still, two different imidazolium salts appear to form. However, significantly more precipitate was accumulating when performing the reaction in MeCN.

Following these observations, we then sought to vary the concentration from the initially employed 200 mM concentration. A range of different concentrations, 10, 20, 50, 100, 500, and 1000 mM, respectively, each spanning from 24 to 96 hours gave similar purified yields, of around 2 – 6%, irrespective of the order of which substrates were added. Moreover, whereas the desired macrocycle is sparingly soluble in MeCN, in DMF, the product becomes insoluble already below 100 mM. Acknowledging that the synthesis proceeds in a low yield, using DMF will minimize the amount of needed solvent when scaling up.

Finally, we sought to employ ammonium salts as templating agents during the synthesis. To avoid counterion scrambling, TBAX was paired with the appropriate organohalide, *i.e.* TBACl was used with 1,8-bis(chloromethyl) naphthalene. As previously described, when employing X = Cl and I, the resulting products turned out as a liquid and an insoluble material, respectively. The crude material recovered from the addition of two 2 equivalents of TBABr is shown in the third entry from the top in **Figure 3.4**. The spectrum, considering a crude material, is already more well-resolved, consistent with salt **3.1**. However, more importantly, after recrystallization in MeOH compound **3.1**



is isolated as a single entity in yields of around 10%. Additionally, the workup proved much easier, as the two distinct imidazolium compounds readily separate in MeOH; the byproduct, reminiscent in its consistency resembling a caramel, separated from the MeOH-soluble product through decantation. Further screening of different ammonium salts followed this positive result, such as  $^t\text{Et}_4\text{NBr}$ ,  $^t\text{Bu}_3^t\text{EtNBr}$ , and their quantities varying from 0.5 to 20 equivalents, reaction times, and concentrations.

In conclusion, the best setup was found when employing a minimum of four equivalents of TBABr additive, all components dissolved together in DMF (200 mM w.r.t bisimidazole), sparged with  $\text{N}_2$  prior to heating to at 100 °C for 2 days, leading to an optimized yield of around 15%.

### 3.3.1 Structural characterization of **3.1**

As evident from the simplicity of the  $^1\text{H}$  NMR spectrum owing to **3.1**, lower spectrum of **Figure 3.4**, the compound in solution is symmetrical and features two groups of distinctive signals in the aromatic region. As outlined in **Figure 3.3**, *vide supra*, the first set of characteristic signals owing to the imidazolium moiety, namely signals labelled A, B, and C in **Figure 3.4**, respectively. We found that, whereas the multiplicity in 1D  $^1\text{H}$  NMR of the latter two signals greatly varies, often barely reflecting the  $^3J(\text{H-H})$  coupling constant of 1 - 2Hz between the protons at the  $\text{C}_4$  and  $\text{C}_5$  positions,  $\{^1\text{H}-^1\text{H}\}$  COSY consistently reveal this characteristic coupling pattern.

The second pair of signals, owing to the naphthalene moiety, further reflects a symmetrical di-substitution as only a single set of three signals with multiplicities doublet ( $\text{C}_2\text{-H}$ , label F), triplet ( $\text{C}_3\text{-H}$ , label E), and a doublet ( $\text{C}_4\text{-H}$ , label D), respectively, are found. Finally, two singlets, integrate in a ratio of 2:1, owing to protons at the benzylic position (H) and the methylene (G), respectively.

Another characteristic NMR feature of imidazolium compounds relates to  $^{13}\text{C}$  NMR, specifically the  $\text{C}_2\text{-C}$  shift, as it is more downfield-shifted than the other aromatic carbons.  $\{^1\text{H}\text{-}^{13}\text{C}\}$  HSQC provides a one-bond correlation between a proton to its associated carbon, which unambiguously connects the most downfield-shifted proton to the most downfield-shifted carbon, as shown for compound **3.1** in **Figure 3.5**, *i.e.* the imidazolium  $\text{C}_2\text{-H}$  proton. The number, multiplicity, and relative integrals of these signals are consistent with this compound belonging to the  $\text{C}_i$  point group.

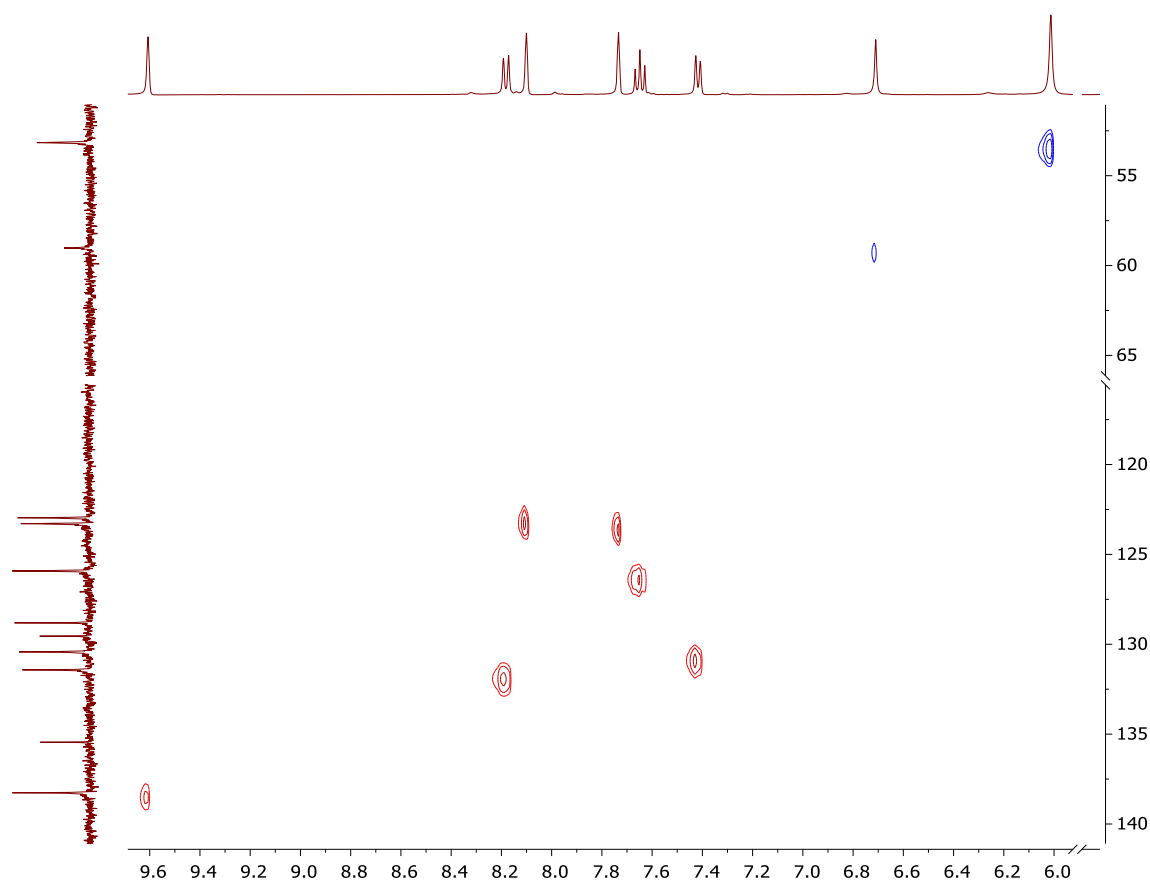


**Figure 3.5.** HSQC of compound **3.1**. The spectrum provides insight into each proton's associated carbon, specifically that the most downfield-shifted carbon and proton are tied together.

Two solid-state structures of compound **3.1** were obtained at RT, from slow solvent evaporation from a saturated methanol solution, **Scheme 3.1**, as well as precipitation from a saturated DMSO solution, shown in **Figure 3.6**, respectively. In either solvent, **3.1**, crystallizes in the triclinic  $P\bar{1}$  space group alongside a substantial amount of co-crystallized solvent,  $\text{H}_2\text{O}$  and DMSO, respectively.

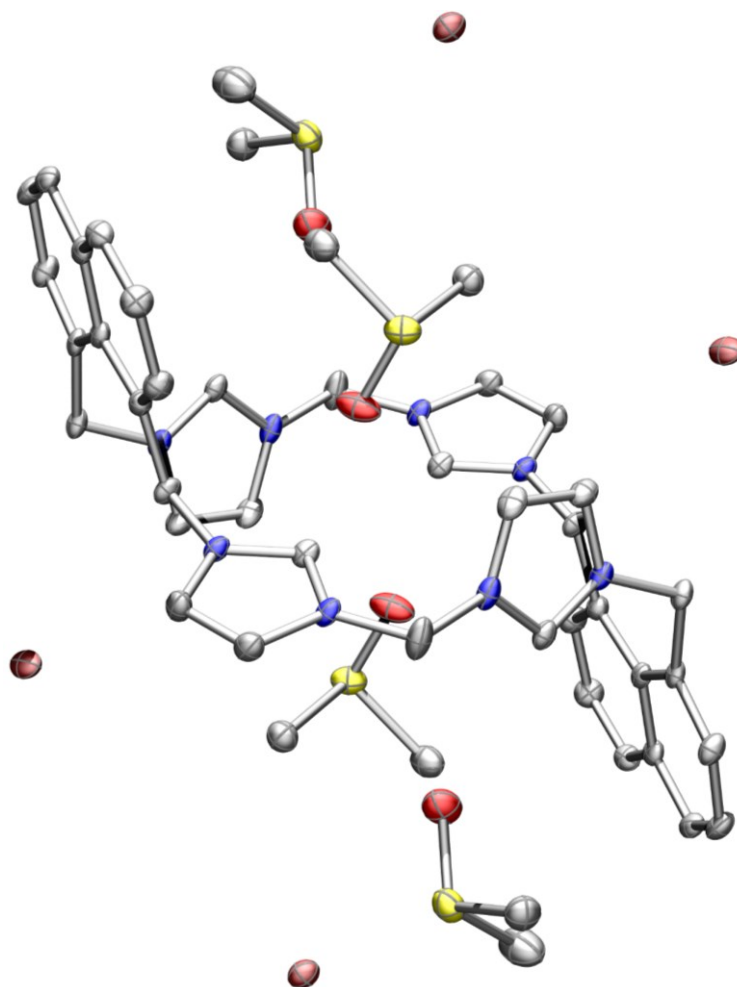


**Figure 3.6.** *Solid-state structure of compound 3.1 obtained in DMSO.* Hydrogen atoms along some DMSO molecules are omitted for clarity. Thermal ellipsoids are set at a 50% probability level. Atom color-coding: N blue, C grey, S yellow, and Br brown.

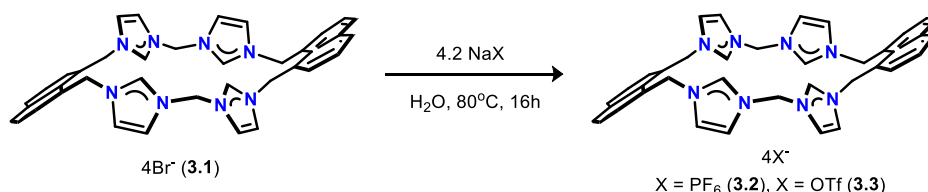
Consistent with the NMR data, the compound has symmetry elements owing to the  $C_i$  point group. The disorder of the co-crystallized  $H_2O$  is readily modeled by applying a solvent mask, specifically PLATON Squeeze<sup>11</sup>: 110 electrons in a volume of  $331\text{\AA}^3$  were found in 2 voids per unit cell, which is consistent with the presence of 11 molecules of water per unit cell. This solvent mask improves the overall model converging to  $R_1 = 3.14\%$  and  $wR_2 = 7.54\%$  (all data).

Differently, the structure obtained from DMSO, shown in **Figure 3.6**, demonstrates little solvent disorder amongst the co-crystallized DMSO, and the model converges to  $R_1 = 3.54\%$  and  $wR_2 = 8.75\%$  (all data). Differences between the two structures relate to the orientation of the imidazolium moieties and the entity residing above the plane spanned

by these. In MeOH, the four imidazolium moieties can be regarded in pairs of two, which demonstrates a syn disposition, similar to a chelating interaction found in metal-complexes; two pairs are oriented anti-parallel to one another, and the structure is relatively flat. Moreover, the bromide-ions are centered above and below the imidazolium plane, showing favorable H $\cdots$ Br interactions of 2.768 Å. Finally, the macrocycle is surrounded by the remaining bromide ions.

In contrast, the structure obtained from DMSO may be regarded as a “crown”, featuring two imidazolium moieties, *trans* to one another, interacting with DMSO residing above and below the plane of imidazolium, reflecting a favorable H $\cdots$ O interaction of 3.001Å. The adjacent imidazolium orients outward at an angle close to 90°, interacting with a DMSO molecule at the periphery, H $\cdots$ O interaction of 3.0027Å. The naphthalene bends at an angle >90° vertical to both imidazolium moieties, which all combined results in a structure resembling a porphyrin more than a chelate. This difference in preorganization, is particularly of interest concerning metalation reactions, as the preorganization found in solvents with a polarity like DMSO likely form tetradentate complexes, whereas different solvents are preferred in accessing the dinuclear bis-chelate complexes.

### 3.3.2 Anion metathesis



**Scheme 3.4.** Salt metathesis of **3.1**. The resulting macrocyclic tetra imidazolium salt precipitates out as these are water insoluble.

Compound **3.1** is largely insoluble in organic solvents but in DMF, DMSO, MeOH, and H<sub>2</sub>O, and for metalation purposes, non-protic solvents are required. Moreover, related to the synthesis of the ethylene-congener, *vide infra*, we sought to have some insights into

how wide the chemical shift of the imidazolium C<sub>2</sub>-H spans with various counterions, as the magnitude of change may prove useful in discerning between multiple imidazolium C<sub>2</sub>-H peaks in a complex mixture. To this end, dissolving compound **3.1** in H<sub>2</sub>O, adding a slight excess of the desired counterion as a simple Na/K-salt, stirring at an elevated temperature overnight, precipitates out the macrocyclic imidazolium salt bearing the desired counterion in quantitative yield, shown in **Scheme 3.4**. Upon exchange, the <sup>1</sup>H NMR spectrum experiences changes centered around the imidazolium C<sub>2</sub>-H shift, as evident in **Figure 3.7**; whereas the naphthalene protons (labels B, E, and F) mostly remain unchanged, the imidazolium experience an upfield shift for C<sub>2</sub>-H (label A) and both C<sub>4/5</sub>-H (label C and D). Furthermore, both protons of the methylene (label G) and the benzylic position (label H) experience a slight upfield shift. Accordingly, changes to these signals work, may work as handles indicative of metalation, changes in metal oxidation states, and ligand-field perturbations in diamagnetic complexes such as exchange processes of fluxional ligands, *e.g.* acetate. Importantly, the PF<sub>6</sub> and OTf-counterions both render the imidazolium salt soluble in MeCN and THF.

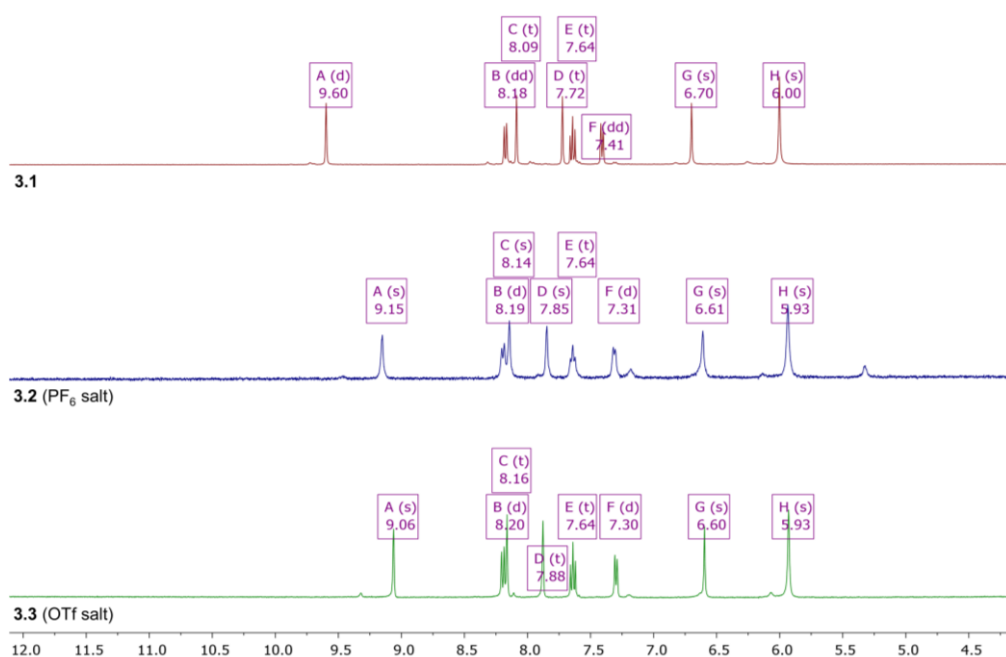
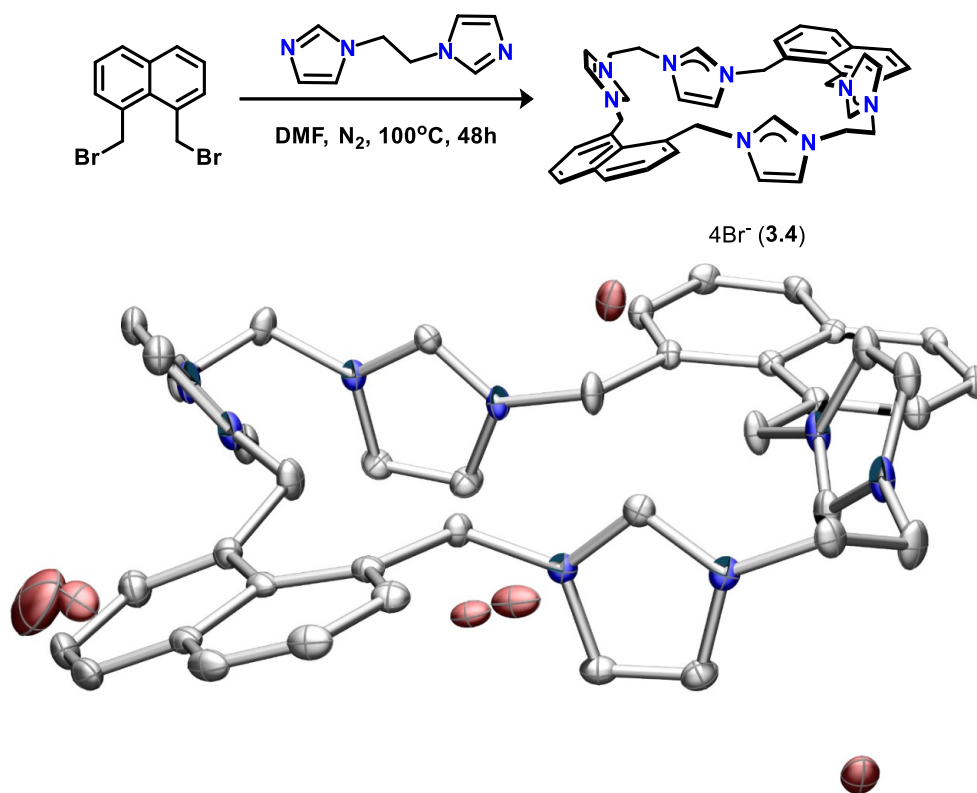


**Figure 3.7.** Stacked 1D <sup>1</sup>H NMR spectra demonstrating counterion influence on macrocycle <sup>1</sup>H resonances. From the top, the tetrabromide salt (**3.1**), the tetrakis hexafluorophosphate salt (**3.2**), and the tetra triflate salt (**3.3**). All spectra are recorded at 20 °C in DMSO-*d*<sub>6</sub>.

### 3.4 Synthesis of naphthalene-based, ethylene-linked macrocycle tetraimidazolium salt



**Scheme 3.5.** Synthesis and solid-state structure of compound **3.4**. Hydrogen atoms have been omitted for clarity. Thermal ellipsoids are set at a 50% probability level. Atom color-coding: N blue, C grey, and Br brown.

The ethylene-linked congener, <sup>Et,Naph</sup>LH<sub>4</sub>-4Br, **3.4**, was approached similarly following an S<sub>N</sub>2-substitution reaction between 1,8-bis(bromomethyl)naphthalene in a 1:1 mixture with 1,2-bisimidazoleethane<sup>12</sup> in DMF, outlined in **Scheme 3.5**. As in the preparation of compound **3.1**, a precipitate slowly starts to form, however, to a much less extent. Nevertheless, concentrating the solution and adding in enough acetone works to precipitate out an orange crystalline material, which upon filtering, similarly demonstrates the properties of a semi-liquid. Differently to **3.1**, the <sup>1</sup>H NMR spectrum of the crude material depicts a much cleaner material, shown in **Figure 3.8**, top spectrum.

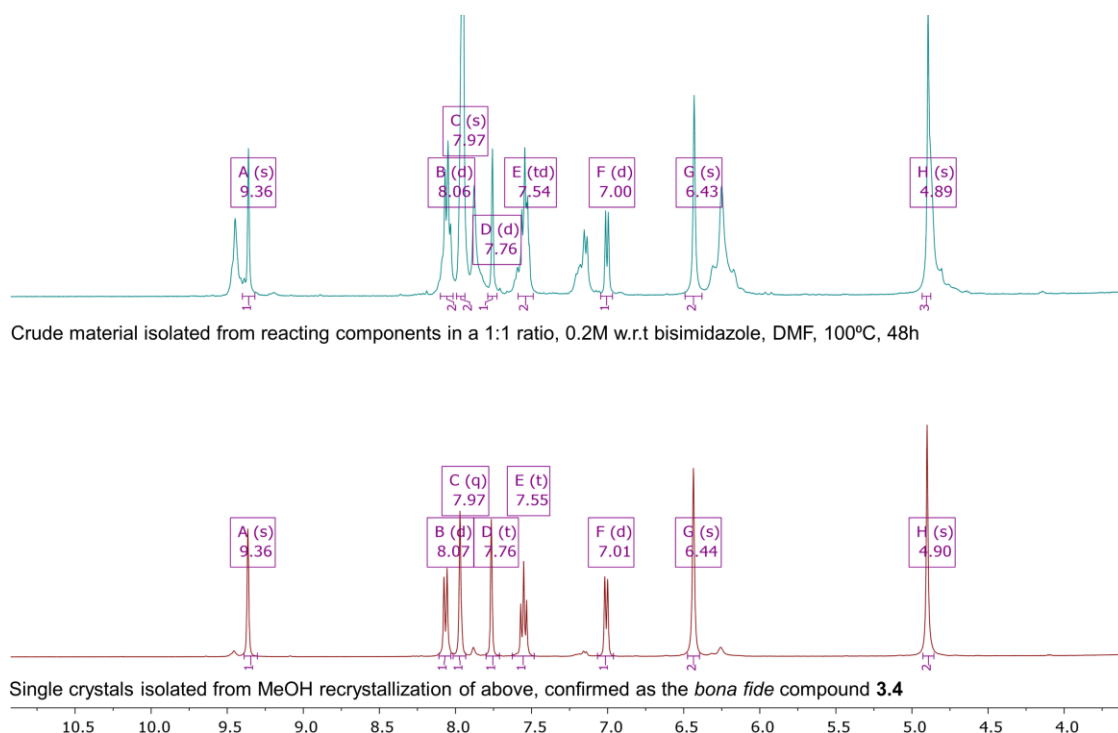
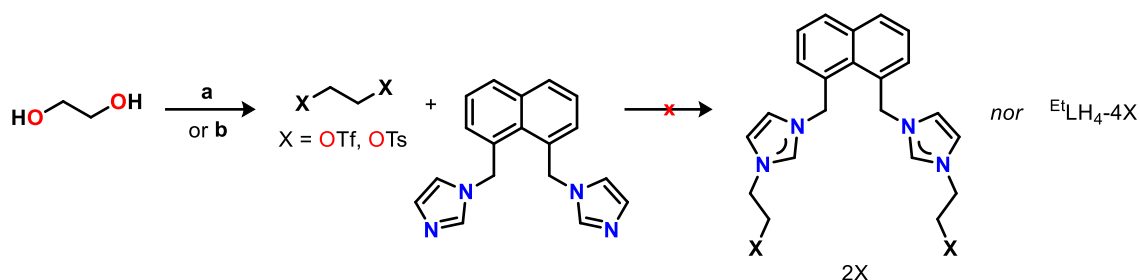


**Figure 3.8.** Stacked 1D  $^1\text{H}$  NMR spectra ( $\text{DMSO}-d_6$ ) of **3.4** comparing crude material to its single crystals. The figure shows the spectra relevant to the isolated crude material following self-assembly (top), and single-crystals (lower) following recrystallization from MeOH.

This material, as a concentrated solution in MeOH, left for slow evaporation, yields colorless single-crystals suitable for single-crystal X-ray diffraction, corroborating the desired connectivity, shown in **Scheme 3.5**. A couple of these crystals were submitted for NMR spectroscopy, and the associated  $^1\text{H}$  NMR spectrum is remarkably close to that of the crude material, **Figure 3.8**, lower spectrum. Moreover, the spectral properties in the  $^1\text{H}$  and  $^{13}\text{C}$  NMR spectra feature the same characteristic properties outlined in the structural analysis of compound **3.1**, *vide supra*.

Despite this positive result, the isolated yield was surprisingly low, also around 2 – 5%, and efforts were put into finding reaction conditions leading to an increased yield, including many of the same approaches described for **3.1**, *vide supra*. In addition to these approaches, we also sought to change the substrate bearing the electrophile and nucleophile; Jenkins showed that 1,2-bis(triflate)ethane reacts with 1,1'-diimidazolemethane to furnish the formation of macrocyclic tetra imidazolium salt in

good yields<sup>13</sup>. Consequently, ethylene glycol was transformed into the stronger electrophiles 1,2-bis(triflate/tosylato) ethane as outlined in **Scheme 3.6**.



**Scheme 3.6.** *Different synthetic approach targeting the ethylene-linked macrocycle.* Reagents and conditions: **(a)**  $\text{X} = \text{OTf}$ , 2.05 equiv.  $(\text{CF}_3\text{SO}_2)_2\text{O}$ ,  $\text{C}_5\text{H}_5\text{N}$  6.0 equiv., DCM (0.2M),  $\text{N}_2$ , 0 °C to rt, 12h; **(b)**  $\text{X} = \text{OTs}$ ,  $\text{TsCl}$  7.0 equiv.,  $\text{C}_5\text{H}_5\text{N}$  (0.1M), 0°C to rt, 18h.

Discouragingly, reacting imidazole-functionalized naphthalene to either electrophile led to the isolation of several viscous orange oils and insoluble (polymeric) materials, even when trying to recover the partially annulated entity. Preparation of 1,2-bisimidazole ethane forms significant amounts of *N*-vinyl imidazole polymerization products following E2-elimination from the intermediary 1-chloro-2-imidazole-ethane. No efforts were made to understand the nature of the unwanted decomposition products from reactions pertaining to **Scheme 3.6**.

Whereas additive TBABr significantly improved the isolated yield and simplified purification of compound **3.1**, no significant improvement was observed in the synthesis of compound **3.4**. Most of the variations made to the synthesis, different from those employed as listed in **Scheme 3.5** proved insignificant; instead, the recrystallization process was done with more care, owing to an increased solubility in MeOH.

The best product isolation was achieved on a decagram scale (minimum 10 g of bisimidazole), under the conditions initially shown in **Scheme 3.5**, limiting the volume of MeOH to just a couple of milliliters (<5 mL) during the recrystallization, affords the imidazolium salts in yields of up to 10%. However, the preparation is severely hampered by the low yield of the 1,2-bisimidazole ethane reagent, being quite inconsistent



(anywhere from 5 – 40%), as it must be made over several large-scale reactions to get an appreciable quantity. Consequently, a different synthetic approach altogether is desirable.

#### 3.4.1 Structural characterization of **3.4**

Compound **3.4**, as **3.1**, has a simplistic  $^1\text{H}$  NMR spectrum, as shown in the lower spectrum of **Figure 3.8**, owing to its symmetrical nature. Signals labelled A, B, and C reflects the characteristic imidazolium moiety; signals B, E, and F reflective of a symmetrical 1,8-disubstitution of naphthalene. The remaining two singlets now integrate in a ratio of 1:1, consistent with the ethylene-bridge.

Reacting compound **3.4** in water with Na/K-salts, *e.g.*  $\text{NaPF}_6$ , in an analogous manner to that described in **Scheme 3.4**, precipitates out the desired tetrakis hexafluorophosphate imidazolium salt in quantitative yield. As evident from **Figure 3.9**, the same protons of compound **3.4** experience an upfield shift in their chemical shifts; the  $\text{C}_2\text{-H}$  experience a  $\sim 0.45$  ppm upfield shift as also seen between compounds **3.1** and **3.2**.

This phenomenon is isolated to the  $^1\text{H}$  NMR spectrum, as evident from **Figure 3.10**, showing that the associated C (the only highlighted resonance) experiences no significant change upon counterion change.

A single solid-state structure of compound **3.4** was obtained at RT, from a slow evaporation of MeOH from a saturated methanol solution, its structure is shown in **Scheme 3.5**. Compound **3.4** crystallizes in the triclinic P-1 space group alongside a substantial amount of co-crystallized  $\text{H}_2\text{O}$  demonstrating disorder. Like compound **3.1**, the symmetry of the molecule is consistent with the  $\text{C}_i$  point-group, which is further reflected in both  $^1\text{H}$  and  $^{13}\text{C}$  NMR spectra. Co-crystallized  $\text{H}_2\text{O}$  was successfully modeled using PLATON Squeeze<sup>11</sup> resulting in just two bromide ions experiencing disorder over two positions; the overall model converges to  $R_1 = 2.87\%$  and  $wR_2 = 6.84\%$  (all data). A

bromide ion resides above and below the imidazolium plane interacting with the C<sub>2</sub>-H position, as well as the benzylic position. The structure is rather flat, featuring a relative orientation of each imidazolium moiety in an anti-parallel fashion with respect to one another and at an angle close to 90° relative to the naphthalene moiety.

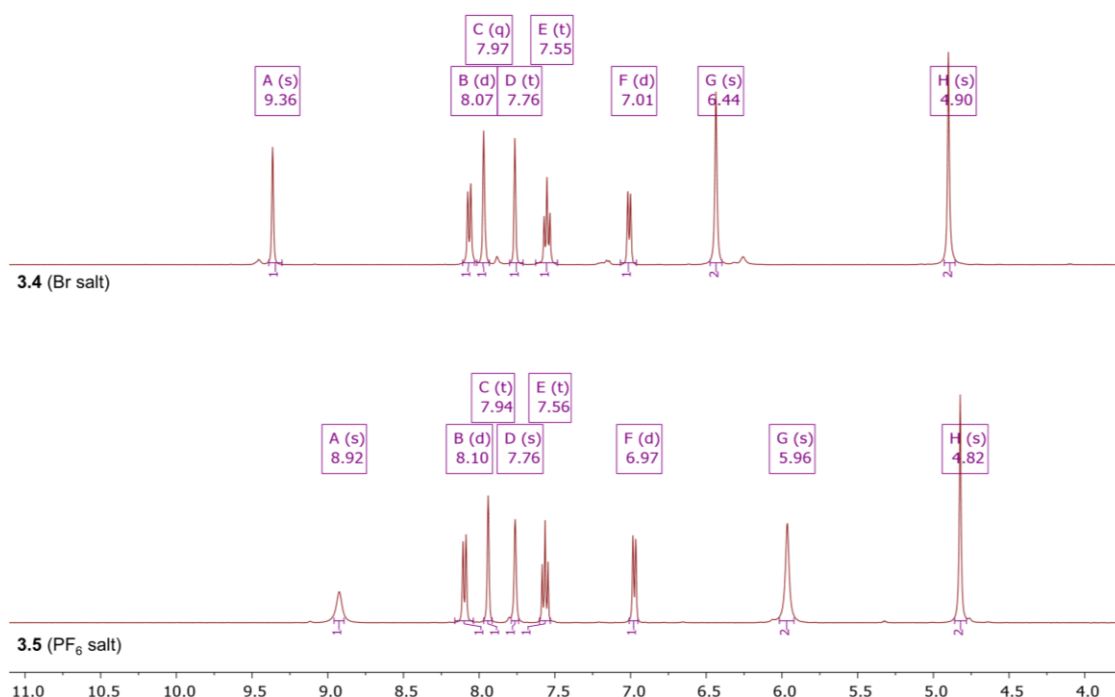


**Figure 3.9.** Changes occurring to the <sup>1</sup>H NMR (DMSO-*d*<sub>6</sub>) shifts following salt metathesis of compound 3.4. The top insert shows resonances owing compound 3.4 and the lower, owing to 3.5

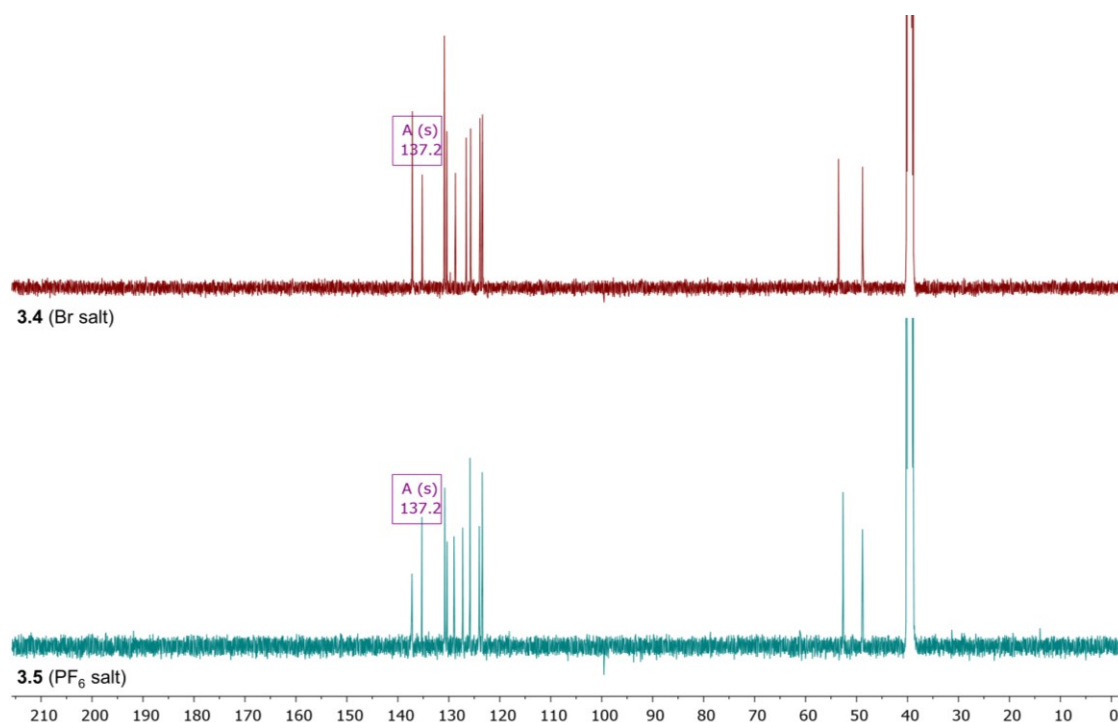
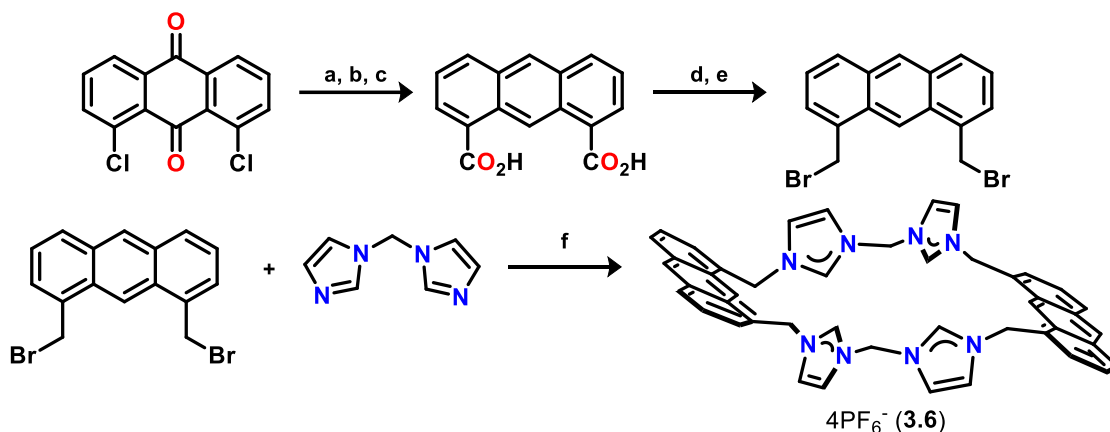


**Figure 3.10.** Changes occurring to the <sup>13</sup>C NMR (DMSO-*d*<sub>6</sub>) shifts following salt metathesis of compound 3.4. The top insert shows resonances owing compound 3.4 and the lower, owing to 3.5.

Compound **3.1** evidently demonstrates a pre-organization towards a macrocyclic complex bearing a tetra NHC ligand, at least in DMSO; whether the same holds true for compound **3.4** remains to be seen, however, is worth having in mind.

### 3.5 Synthesis of anthracene-based, methylene-linked macrocycle tetra imidazolium salt



**Scheme 3.7.** *Synthesis of anthracene congener.* Reagents and conditions: (a) NaBH<sub>4</sub>, MeOH, then *n*BuOH, 24h; (b) 8.8 CuCN, DMAc, reflux, 72h, then NH<sub>4</sub>OH, 96h; (c) KOH, ethylene glycol, 150 °C, min. 30h, or H<sub>2</sub>SO<sub>4</sub> 6M, reflux, min 30h; (d) 2.0 LiAlH<sub>4</sub> (2M in THF) in thawing THF, 4h; (e) 1.55 PBr<sub>3</sub> in glyme, 2h, rt; (f) 1:1 in 200 mM w.r.t bisimidazole, 4.0 equiv. of TBABr, 100 °C, 48h, then added 8.1 KPF<sub>6</sub>, in MeCN.

Relevant to compound **3.1**, the anthracene analogue, in this dissertation compound **3.6**) was reported by the group of Kim in 2012; in their study, the authors account for the macrocycle's ability to bind GTP and ATP in water, under physiologically relevant conditions<sup>14</sup>. The synthesis, analogous to that of **3.1**, was effected by an S<sub>N</sub>2-substitution reaction between 1,8-bis(bromomethyl)anthracene and 1,1'-bisimidazole methane, precipitating out the desired macrocycle in excellent yields.

Unfortunately, despite exhaustive attempts, from a myriad of different combinations that possibly could match their given procedure, we were unable to reproduce their data, instead we isolated insoluble polymeric materials. This insolubility mirrors, instead, the materials we found during the synthesis of the other macrocycles, and we were also unsuccessful in breaking any clusters comprising individual

macrocycles stabilizing through Br-H-C<sub>2</sub> interactions by salt metathesis. As such, we approached the synthesis in a similar fashion to compound **3.1**. As outlined in **Scheme 3.7**, 4.0 equivalents of TBABr were added to the reaction mixture, step **f**, resulting in a crystalline material soluble in MeOH. Moreover, the powder's spectral properties show two distinct imidazolium spin systems, emphasized in the top spectrum of **Figure 3.11**, A1, A2, and A3, and B1, B2, and B3, respectively. This spectrum is surprisingly different from the one reported by the Kim group. What accounts for this difference, still remains unclear.

A yellow-tinted filtrate was recovered from refluxing overnight the recovered material in MeCN with a slight excess of KPF<sub>6</sub> overnight. From this filtrate, a powder is isolable with spectral properties shown in lower spectrum of **Figure 3.11**, albeit in low yields and not completely pure (less than 50 mg was recovered, corresponding to ~5%), consistent with the target macrocycle. While we unfortunately were unable to corroborate the connectivity through single-crystal X-ray diffraction, 1D and 2D NMR techniques prove powerful for a structural assignment by inferring trends found for the previous two macrocyclic compounds.

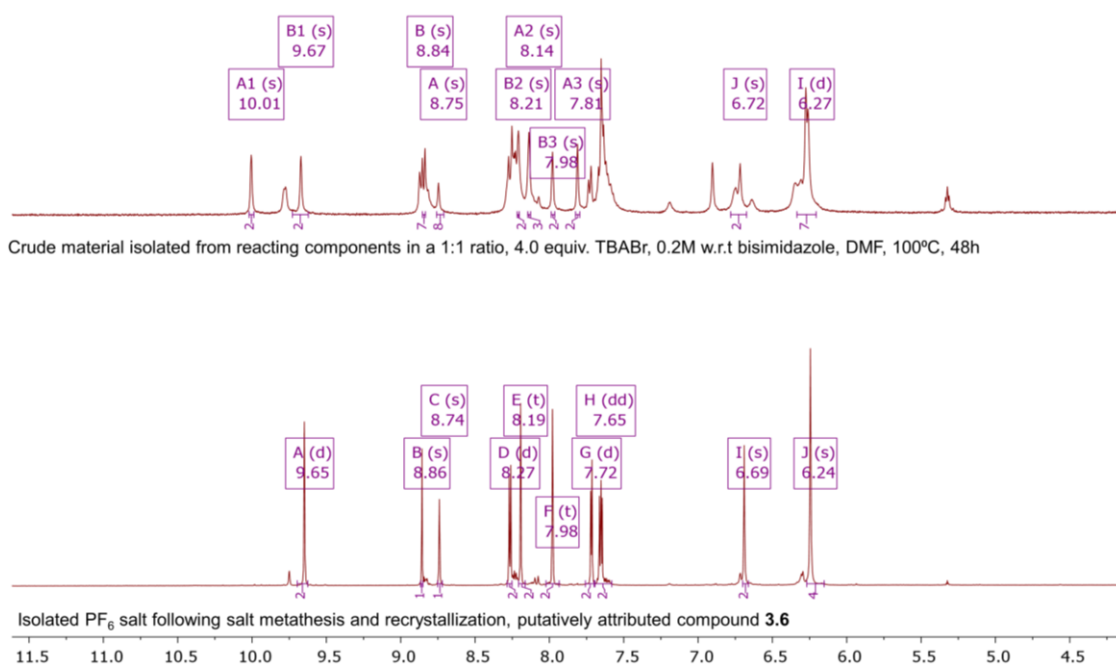


**Figure 3.11.** Comparing  $^1\text{H}$  NMR ( $\text{DMSO-}d_6$ ) spectra of isolated materials pertinent to compound **3.6**, crude isolate (top), and isolated  $\text{PF}_6$  salt (lower). The top spectrum shows the recovered material from self-assembly, emphasizing the two distinct imidazolium spin-systems A(1,2, and 3) and B(1,2, and 3). The bottom spectrum depicts a material consistent with a symmetrical macrocyclic compound.

Firstly, to discern between the three most downfield-shifted signals and assign these owing to the imidazolium and anthracene moiety,  $\{^1\text{H-}^1\text{H}\}$ -COSY establishes a characteristic coupling between signals A, E, and F, consistent with what is outlined in **Figure 3.3**. These three signals often as occur as singlets in the  $^1\text{H}$  NMR spectrum; the  $\text{C}_4/\text{C}_5\text{-H}$  protons can occur as doublets with a small coupling constant ( $^3J(\text{H-H})$ ) of 1 - 2Hz, and occasionally as poorly resolved triplets. Moreover, compound **3.6** likely possesses the same symmetry elements as **3.1** and **3.4**, meaning half of the macrocycle yields distinctive  $^1\text{H}$  signals; integration between the resonances owing to the imidazolium and the  $\text{C}_{9/10}$  positions should therefore result in 2:1:1 ratio, which is observed. Additionally, the associated C atom demonstrates a characteristic downfield shift, distinctive from the other aromatics carbons, as evident from **Figure 3.12**;  $\{^1\text{H-}^{13}\text{C}\}$  HSQC establishes connectivity between signal A and the most downfield-shifted carbon (137.7ppm), suggestive of the imidazolium  $\text{C}_2$ -position, whereas signals B and C feature connectivity to aromatic carbons, consistent with the  $\text{C}_{9/10}$ -positions of the anthracene.

The remaining aromatic peaks reflect a symmetrical 1,8-disubstitution of anthracene from the splitting of the C<sub>2</sub> (signal D), C<sub>3</sub> (signal H), and C<sub>4</sub> (signal G) positions, respectively. Signals I and J are singlets, integrating in a ratio of 1:2, consistent with the protons at the methylene-linker and benzylic position, respectively.

Finally, following salt metathesis from bromide to hexafluorophosphate, the C<sub>2</sub>-H position of the imidazolium moiety is expected to experience a large upfield shift. Comparing the difference found between compounds **3.1** and **3.2**, shown in **Figure 3.7**, and compounds **3.4** and **3.5**, shown in **Figure 3.9**, leave an expected upfield shift of approximately 0.45 ppm.

Indeed, such an upfield shift is observed in **Figure 3.11** between the signals labeled A1 (top spectrum) and the signal labeled A (lower spectrum). The similarities continue, as the associated C<sub>4/5</sub>-H signals (labeled E and F), experience a slight downfield shift, whilst the protons owing to anthracene at the C<sub>2-4</sub>, C<sub>5-7</sub>, and C<sub>9,10</sub> positions, the benzylic, and the methylene signals are less perturbed.

The combined results suggest to us, that the material indeed comprises the macrocyclic tetra imidazolium hexafluorophosphate salt of **3.6**. The material was successfully prepared rather late during the PhD study, and subsequent metalation reactions may appear lacking compared to the analogous studies of compounds **3.1** and **3.4**.

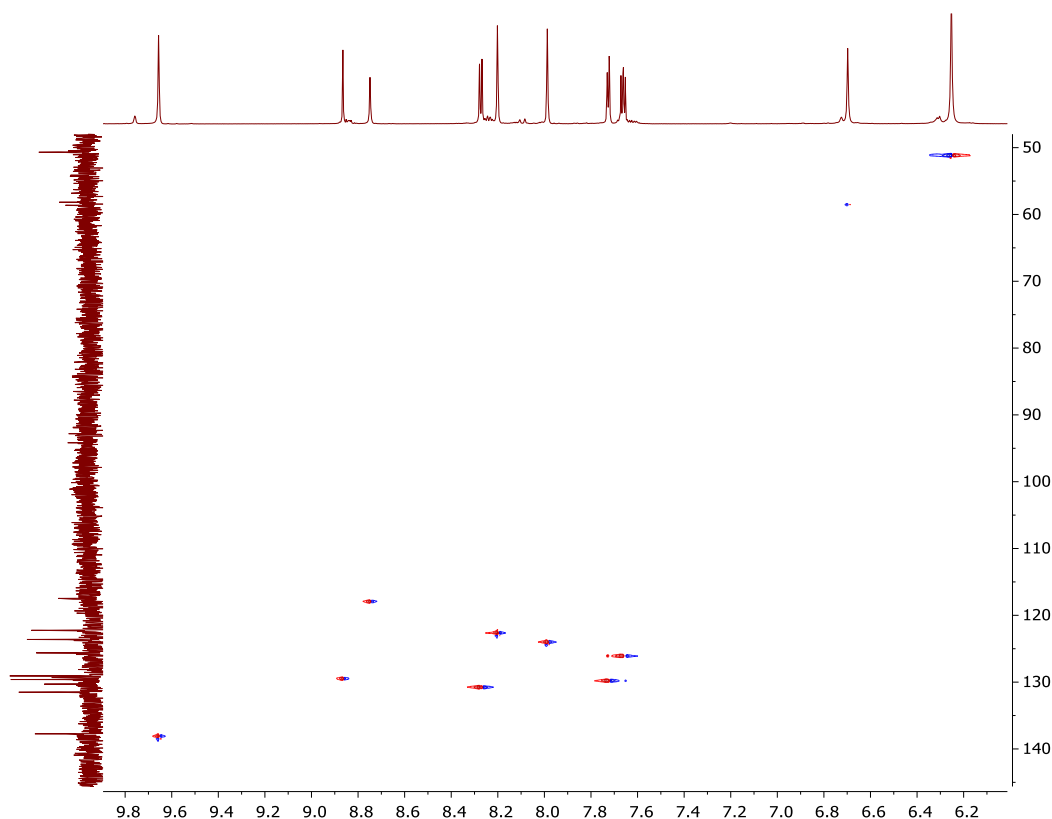


**Figure 3.12.**  $\{^1\text{H}-^{13}\text{C}\}$  HSQC of crude **3.6**. The association between the most downfield shifted proton and carbon is consistent with preceding macrocyclic compounds, meaning the subsequent downfield singlets owes to the anthracene C<sub>9/10</sub> positions, respectively.

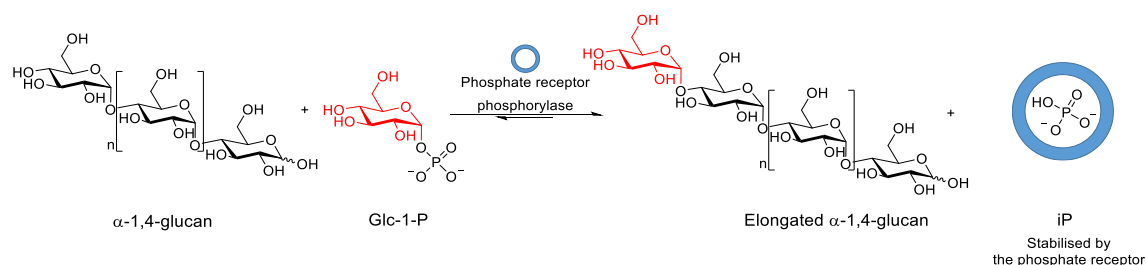
As with compound **3.4**, a different synthesis is preferable to the one presented here, as the preparation of the bromomethyl anthracene is quite time intensive, lengthy, and poorly scales. The central diol is commercially available, however, quite expensive ranging anywhere from 150 to 300 USD pr. gram as of June 29, 2022, combined with the extremely poor macrocycle yield, renders this synthesis an expensive endeavor.

An alternative approach could center on a convergent synthesis, following the partial bromination, by reacting the diol with HBr, as in the preparation of (2-(bromomethyl)phenyl)methanol<sup>15</sup>, which curiously does not annulate. The proximity issue encountered in naphthalene should no longer pose as an issue, and limiting the possibilities of polymerization is likely beneficial; the diimidazolium bromide salts remain quite soluble in polar, aprotic solvents such as MeCN, *cf.* Chapter 4.

### 3.6 Macrocycles **3.1** and **3.4** as anion receptor: binding of phosphate

Intrigued by Kim's study<sup>14</sup>, and poly imidazolium cyclophanes inherent ability to discriminate between specific anions in aqueous media<sup>6</sup>, we sought to leverage the water solubility of compounds **3.1** and **3.4** towards aqueous anion recognition.

To this end, in collaboration with PhD Charlotte Nybro Dansholm, DTU Chemistry, we studied these as phosphate receptors, relevant in the selective binding of inorganic phosphate (iP,  $\text{PO}_4^{3-}$ ) over  $\alpha$ -D-glucose-1-phosphate (Glc-1-P), to effect the phosphorylase-mediated equilibrium towards longer  $\alpha$ -1,4-glucans, schematized in **Scheme 3.8**. Water soluble anion receptors are few, thus making compounds **3.1** and **3.4** quite interesting compounds. However, as many related macrocyclic tetra imidazolium compounds show a high binding affinity for halides<sup>16,17</sup>, we sought to explore phosphate binding using **3.1** and **3.4** bearing weakly coordinating counterions ( $\text{X} = ^-\text{OTf}$ ,  $^-\text{N}(\text{OTf})_2$ ,  $^-\text{PF}_6$ ,  $^-\text{BF}_4$ ,  $^-\text{B}(\text{Ph})_4$ ,  $^-\text{OTs}$ ), to avoid competition between bromide. Unfortunately, none of these salts are water-soluble, leaving us with the bromide salts.



**Scheme 3.8.** *Phosphate-receptor-dependent phosphorylase-catalyzed formation of  $\alpha$ -1,4-glucans.* The blue circle suggests any interaction with phosphate receptor, *e.g.* encapsulation. Scheme reproduced with permission from Charlotte Nybro Dansholm.

$^1\text{H}$  NMR titration renders us able to follow changes in chemical shift with an increasing substrate concentration, as shown in **Figure 3.13**. From this gradual change relevant binding constants pertaining to iP and Glc-1-P, as shown in **Figures 3.14** and **3.15**, respectively, can be extracted. The titrations were performed in HEPES buffer (50 mM,  $\text{D}_2\text{O}$ ,  $\text{pH}(\text{D}) = 6.8$ ), with the addition of  $\text{NaH}_2\text{PO}_4 \cdot 2\text{H}_2\text{O}$  as the source of iP, and  $\alpha$ -D-glucose-1-phosphate disodium salt tetrahydrate as the source of Glc-1-P. **3.1** and **3.4**



were dissolved in D<sub>2</sub>O (1 mM) and sequentially added increasing the equivalents of substrate from 1.0 to 15.0 equivalents.

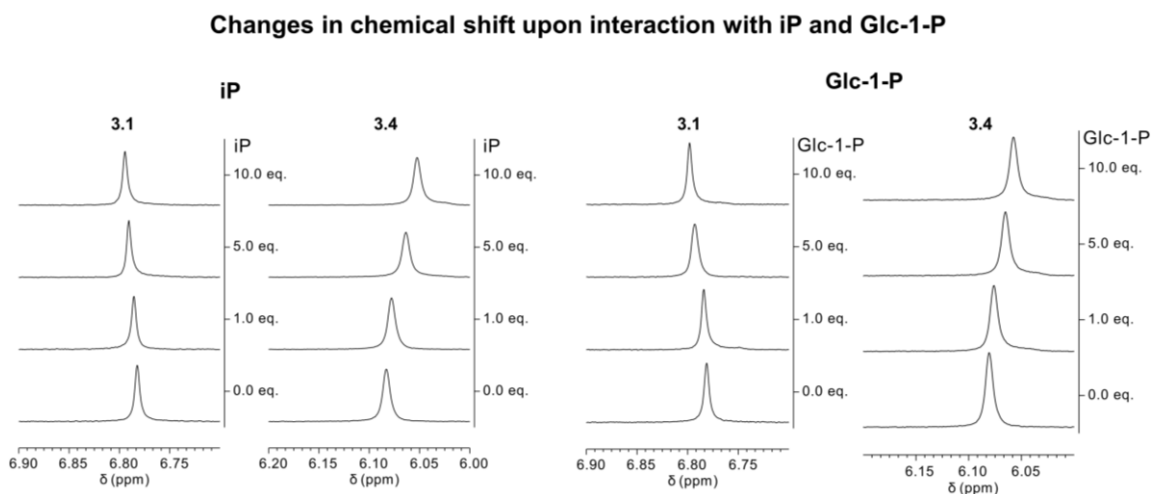


**Figure 3.13.** Compounds **3.1** and **3.4** binding with *iP* and *Glc-1-P*. Selected range of the <sup>1</sup>H NMR spectra shows chemical shift changes following addition of varying amounts of *iP* (left-hand side) and *Glc-1-P* (right-hand side), respectively. **3.1** and **3.4** (1 mM) in HEPES buffer (D<sub>2</sub>O, 50 mM, pH 6.8) at 298 K in the presence of *iP* or *Glc-1-P* (0–10 mM).

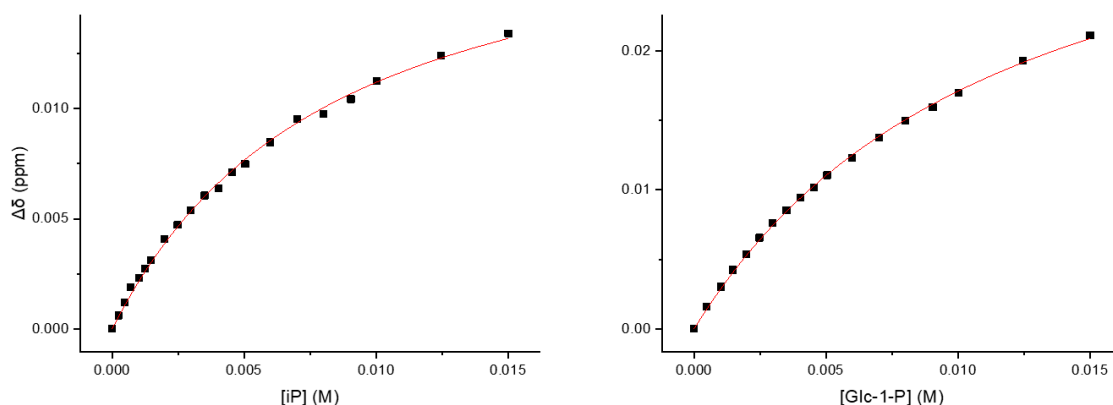


**Figure 3.14.** **3.1** binding isotherm to *iP* and *Glc-1-P*. Fitted isotherms, based of chemical shift changes of the methylene-proton, assuming a 1:1 binding between host and guest.

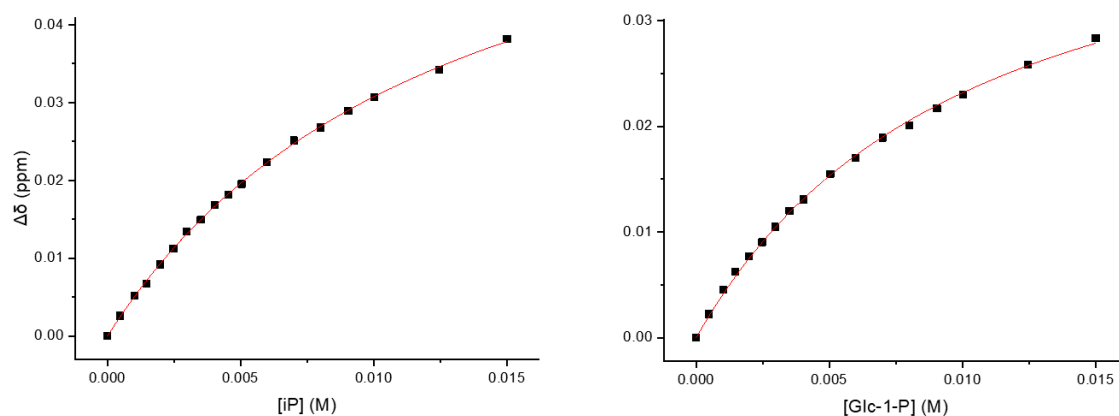


**Figure 3.15.** **3.4** binding isotherm to *iP* and *Glc-1-P*. Fitted isotherms, based of chemical shift changes of the ethylene-proton, assuming a 1:1 binding between host and guest.

While the imidazolium C<sub>2</sub>-H undergoes H/D exchange in D<sub>2</sub>O, rendering it unavailable as an NMR handle, changes in the proton signal of the (m)ethylene linker may instead be leveraged to probe any chemical shift occurring to **3.1** and **3.4**. The changes in chemical shift following the addition of 1, 5, and 10 equivalents to **3.1** and **3.4** are shown in **Figure 3.13**. Curiously, whereas compound **3.1** experiences a downfield shift, the accompanying change in **3.4** results in an upfield shift.

A likely explanation for this opposing change relates to conformational change upon interaction with a guest molecule. These changes in chemical shift were used to model a binding isotherm of **3.1** and **3.4** towards iP and Glc-1-P following a 1:1 binding model, shown in **Figure 3.14** and **Figure 3.15**, respectively.

From these isotherms, fitted bindings constants are determined, which along with fitted  $\Delta\delta_{\max}$  values are reported in **Table 3.1**. As evident from **Figure 3.14** and **Figure 3.15**, **3.1** and **3.4** demonstrate similar affinities for iP and Glc-1-P. Moreover, while **3.1** has a larger affinity towards iP ( $133.6 \text{ M}^{-1}$ ) than Glc-1-P ( $91.5 \text{ M}^{-1}$ ), these magnitudes are too alike and are unlikely to yield any significant shift in the equilibrium. The strong interactions between the anthracene analogue to ATP and GTP, respectively, likely relate to stabilizing  $\pi$ - $\pi$  stacking<sup>14</sup>. A likely explanation for the poor affinity towards iP, is the absence of any favorable  $\pi$ -interactions.

**Table 3.1.** Binding parameters for the interaction of compounds **3.1** and **3.4** with iP and Glc-1-P in HEPES buffer (D<sub>2</sub>O, 50 mM, pH 6.8) at 298 K.

Guest	Host	Receptor <b>3.1</b>		Receptor <b>3.4</b>	
		K <sub>a</sub> (M <sup>-1</sup> )	$\Delta\delta_{\max}$ (ppm)	K <sub>a</sub> (M <sup>-1</sup> )	$\Delta\delta_{\max}$ (ppm)
iP		133.6±6.1	0.020±0.001	84.3±2.1	0.069±0.001
Glc-1-P		91.5±2.7	0.037±0.001	107.2±4.0	0.046±0.001

### 3.7 Conclusion

In closing, seeking to study dinuclear NHC complexes a novel bis-chelating macrocyclic tetra imidazolium salt was envisioned. Unfortunately, this compound was ultimately not synthesized as initial studies pertaining to the direct tether of imidazole to naphthalene, suggested to us that tethering of imidazole via a C-N bond to naphthalene at the 1 and 8 positions is challenging. It was only by reacting K/Na imidazolate salts with a bis-diazonium intermediate we were able to corroborate trace amounts of the diimidazole. However, the yield was extremely poor, and potential explosion hazard associated the diazonium intermediate rendered this synthetic approach unsuitable for large-scale preparation, due to the ratio of C to N being lower than the generally accepted safe C to N ratio of 3.

Instead, by introducing an  $sp^3$ -C center at the benzylic position, we were able to synthesize two proligands, **3.1** and **3.4** to probe whether two metals can be tethered proximal to one another, and proligand **3.4** further intending to probe subtle changes resulting from a wider bite-angle and its consequences in reactivity. Additionally, a synthesis of macrocyclic tetra imidazolium anthracene salt is also presented and was realized to probe whether the ligand-manifold would require a greater metal separation to accommodate multiple metals.

The solid-state structures of compounds **3.1** and **3.4** depict subtle variations resulting from the solvent of crystallization, in addition to differences in the NHC-linker length. The orientation and proximity of the imidazolium moieties seem quite flexible, which may affect metalation, as **3.1** demonstrates a greater extent of preorganization towards a “porphyrin analogue” in highly polar, aprotic media.

$^1\text{H}$  NMR is a proficient tool, to gauge the nature as well as discern the number of different imidazolium compounds forming during self-assembly. While 1D  $^1\text{H}$  NMR reflects the (a)symmetric nature of the compound forming,  $^1\text{H}$ - $^1\text{H}$  correlation spectroscopy (COSY) provides evidence of the number of different imidazolium species present from a distinctive spin-system owing to the characteristic imidazolium moiety.

The nature of the counterion appear to affect self-assembly as the product seem to vary from an ionic liquid, the desired macrocycle, to insoluble polymeric materials. While no general trend accounting for the formation of the desired macrocycle vs. ill-defined side product, based on the nature of the counterion, could be established based on the presented data, bromide (with TBABr as additive) seems to present itself as a good starting point for the preparation of imidazolium-based macrocycles.

Finally, as **3.1** and **3.4** are water soluble and bear a high charge, we investigated these compounds' affinity toward inorganic phosphate. However, their greater affinity towards bromide renders these compounds poor candidates towards the selective binding of phosphate; consequently, different counterions e.g.  $\text{NO}_3$  and  $\text{ClO}_4$  are potentially of interest for other applications.

### 3.8 References

- (1) Johnson, E. J.; Kleinlein, C.; Musgrave, R. A.; Betley, T. A. *Chem. Sci.* **2019**, *10*, 6304–6310.
- (2) Rosenthal, J.; Luckett, T. D.; Hodgkiss, J. M.; Nocera, D. G. *J. Am. Chem. Soc.* **2006**, *128*, 6546–6547.
- (3) Love, J. B. *Chem. Commun.* **2009**, No. 22, 3154–3165.
- (4) Devoille, A. M. J.; Love, J. B. *Dalt. Trans.* **2012**, *41*, 65–72.
- (5) Carsch, K. M.; Lukens, J. T.; DiMucci, I. M.; Iovan, D. A.; Zheng, S.-L.; Lancaster, K. M.; Betley, T. A. *J. Am. Chem. Soc.* **2020**, *142*, 2264–2276.
- (6) Riduan, S. N.; Zhang, Y. *Chem. Soc. Rev.* **2013**, *42*, 9055–9070.
- (7) Prabhakaran, P.; Puranik, V. G.; Chandran, J. N.; Rajamohanan, P. R.; Hofmann, H.-J.; Sanjayan, G. J. *Chem. Commun.* **2009**, No. 23, 3446.

- (8) Watkinson, M.; Whiting, A.; McAuliffe, C. A. *J. Chem. Soc., Chem. Commun.* **1994**, No. 18, 2141–2142.
- (9) Claramunt, R. M.; Elguero, J.; Meco, T. *J. Heterocycl. Chem.* **1983**, 20, 1245–1249.
- (10) Chesnokov, G. A.; Topchiy, M. A.; Dzhevakov, P. B.; Griбанov, P. S.; Tukov, A. A.; Khrustalev, V. N.; Asachenko, A. F.; Nechaev, M. S. *Dalt. Trans.* **2017**, 46, 4331–4345.
- (11) Spek, A. L. *Acta Crystallogr. Sect. C Struct. Chem.* **2015**, 71, 9–18.
- (12) Ortiz, A.; Gómez-Sal, P.; Flores, J. C.; de Jesús, E. *Organometallics* **2018**, 37, 3598–3610.
- (13) Cramer, S. A.; Jenkins, D. M. *J. Am. Chem. Soc.* **2011**, 133, 19342–19345.
- (14) Ahmed, N.; Shirinfar, B.; Youn, I. S.; Bist, A.; Suresh, V.; Kim, K. S. *Chem. Commun.* **2012**, 48, 2662–2664.
- (15) Cao, R.; Müller, P.; Lippard, S. J. *J. Am. Chem. Soc.* **2010**, 132, 17366–17369.
- (16) Serpell, C. J.; Cookson, J.; Thompson, A. L.; Beer, P. D. *Chem. Sci.* **2011**, 2, 494–500.
- (17) Li, Z.; Wiratpruk, N.; Barnard, P. J. *Front. Chem.* **2019**, 7, 1 - 13.

## Chapter. 4. In pursuit of ditopic NHC-complexes

### 4.1 Introduction

The quest for stable carbenes was completed by Bertrand's isolation of a phosphino-carbene in 1988<sup>1</sup> and Arduengo's isolation of an imidazole-2-ylidene in 1991<sup>2</sup>. Since then, NHCs have become a well-established class of ligands in coordination chemistry and homogenous catalysis, with complexes represented by most of the transition metals, including the base metals<sup>3</sup>. **Figure 4.1** shows prototypical carbene ligands, derivatives of divalent C-atoms<sup>4</sup>, often encountered throughout organometallic chemistry, and some characteristic features, such as spin multiplicity and the type of complexes they occur in<sup>5</sup>. Schrock alkylidenes, or Schrock carbenes, and Fischer carbenes belong to so-called reactive carbenes, contrasting the persisting Wanzlick-Arduengo carbenes, formally Fischer carbenes, depicted on the right-hand side.

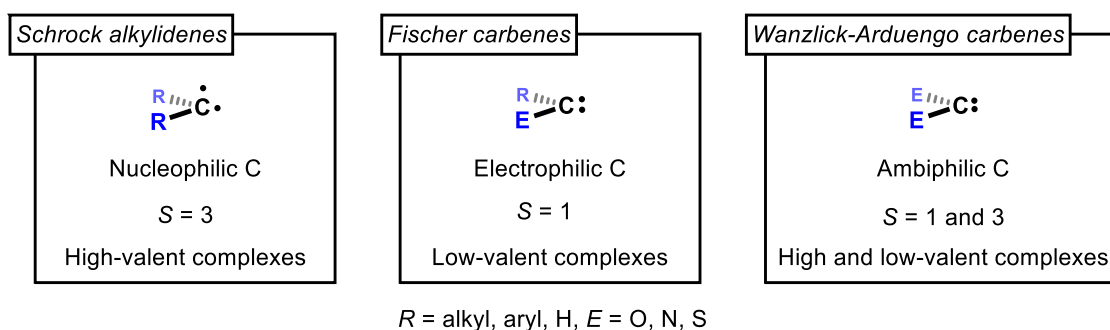


**Figure 4.1.** Prototypical carbene motif observed in organometallic chemistry. Schrock and Fischer carbenes are much more reactive than the NHC congeners.

We may understand this reactivity difference between the former two and NHCs, by considering the *N*-atoms vicinal to the center C-atom, and how these *N* atoms electronically perturbates the resulting carbene, as illustrated in **Figure 4.2**.

First, most aromatic cyclic NHCs adopt a geometry featuring an  $sp^2$ -hybridization of the central carbene C atom, the deviation from linearity breaks the degeneracy of the  $p_x$  and  $p_y$  orbitals found in linear carbenes<sup>6</sup>. The  $sp^2$ -geometry results in the  $p_x$  orbital experiencing some mixing with an *s* orbital, leading to a filled, non-bonding  $sp^2$ -orbital, referred to as a  $\sigma$ -orbital, and a vacant orbital, essentially of pure  $p_y$ -character, often

referred to as a  $p_\pi$ -orbital, shown in the top of **Figure 4.2**; the energy difference between these two orbitals determines the ground state electronic configuration and in turn the carbene's reactivity, and an energy difference of approximately 2 eV is required to impose a singlet state.

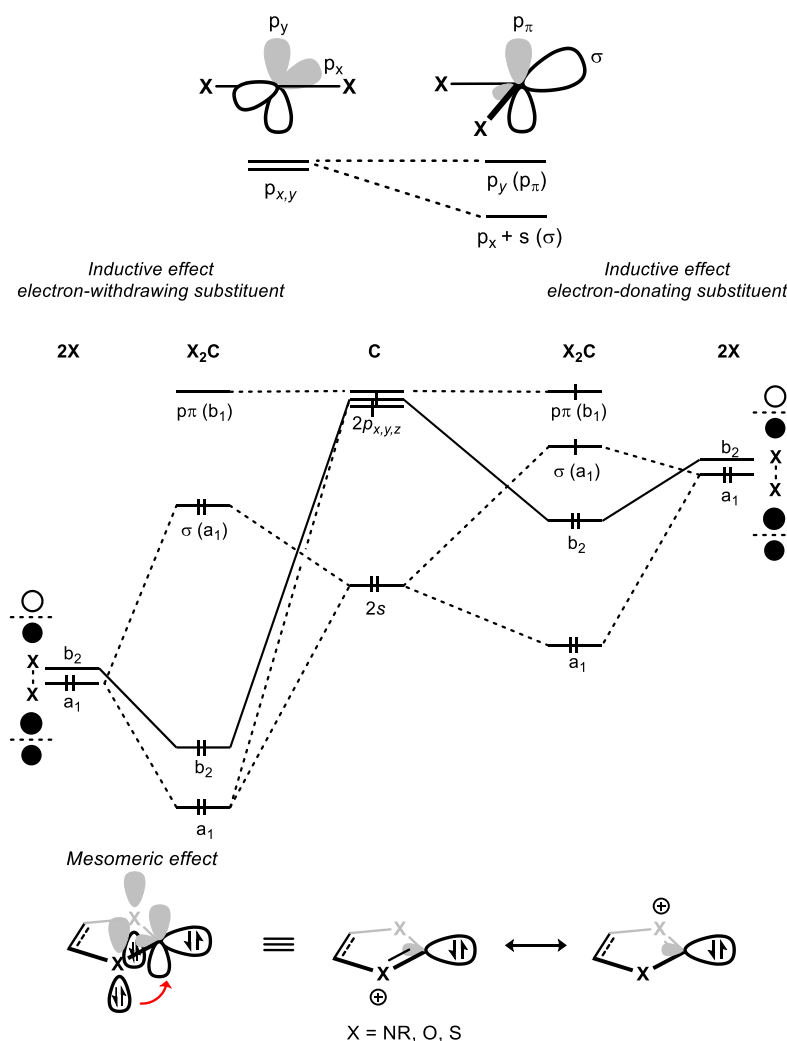
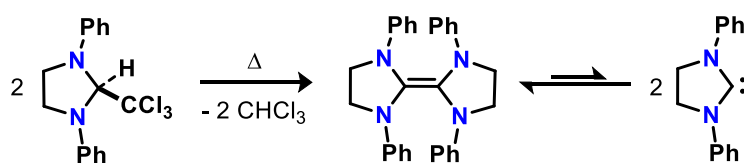


**Figure 4.2.** Qualitative molecular orbital diagram demonstrating electronic ground state differences in NHCS, following the electronic nature of the vicinal substituent and depiction of the mesomeric effect. The initial deviation from a linear carbene breaks the orbital degeneracy; electronegative substituents (X) in the X-C-X fragment further induce a ground state singlet term, whereas electron-donating substituents induces a triplet state<sup>6</sup>.

The left-hand side of the center molecular orbital diagram of **Figure 4.2** demonstrates the electronic perturbation of the central X-C-X fragment by electronegative X-substituents; an increased  $s$ -character of just the  $\sigma$ -orbital<sup>6</sup> inductively stabilizes this orbital, leading to a sufficiently large energy gap between the  $\sigma$  and  $p_\pi$ -orbital that a singlet electronic configuration is preferred. In contrast, as depicted on the

right-hand side of this molecular orbital diagram, electron-rich X-substituents instead lowers this gap; an energy gap that effectively can induce both ground-state singlet and triplet electronic configurations<sup>6</sup>.

Second, this energy gap is further affected by  $\pi$ -electronic-interactions to the vacant  $p_{\pi}$ -orbital, *e.g.* through lone-pairs, known as the mesomeric effect<sup>6</sup>. Whereas  $\pi$  electron-donating groups, *e.g.* -F, -Cl, -NR<sub>2</sub>, and -OR, further stabilize a ground state singlet electronic configuration,  $\pi$  electron-withdrawing moieties *e.g.* -COR, -CN, -BR<sub>2</sub>, -CF<sub>3</sub> stabilize a triplet ground state. This effect thus results in a 4-electron-3-bond interaction in the X-C-X fragment, whose electronic structure may be represented by the superposition of two Zwitter-ionic fragments, the negative charge centered on the C-atom as shown in the lower insert of **Figure 4.2**. From the ground state multiplicity, one can qualitatively gauge the stability of the free carbene; indeed, the propensity of a carbene to dimerize is predominantly observed in triplet carbenes, however, may be influenced by steric encumbrance<sup>7</sup>. Wanzlick, attempting to exploit the  $\alpha$ -elimination of CHCl<sub>3</sub> from 1,3-diphenyl-2-trichloromethylimidazolidine, isolated instead the enetetraamine product; this dimerization is known as the Wanzlick equilibrium, **Scheme 4.1**<sup>8,9</sup>.



**Scheme 4.1.** Wanzlick equilibrium. Ground state triplet NHCs quickly dimerize to the more stable adduct.

Given the symmetry of the frontier molecular orbitals pertaining to NHCs, the interactions to metal-ions are shown in **Figure 4.3**. Perhaps unsurprising, the NHC-metal bond strength was for a long time regarded by its  $\sigma$  contribution alone, however, later investigations by Meyer, Cavallo, Comas-Vives, and Harvey, suggest that these ligands accommodate a significant amount of  $\pi$ -interaction, up to 30% of the total orbital interaction; metal identity, coordination geometry, and ancillary ligands all affect the



extent of backdonation, which is quite pronounced in electron-rich metals, *viz.* late transition and low valent metals<sup>10–12</sup>. Accordingly, extensive back bonding manifest from changes to the angle of the central N-C-N moiety with small perturbations to the N-C bond length.

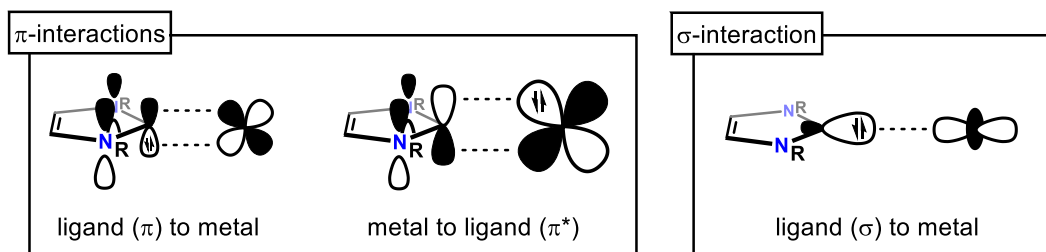


**Figure 4.3.** Bonding modes pertaining to NHC-metal complexes. The figure depicts the interaction between a ground state singlet NHC to that of an arbitrary metal center. The arrows denote the origin of electron density in each interaction.

Considering these elements together, the Lewis structure better representative of bonding in NHC-metal complexes, as shown in **Figure 4.4**, and the one used throughout this dissertation, depicts a single-bond between the central C<sub>2</sub>-atom and the metal ion, in addition to a half-circle between the N-C-N unit; the metal-C bond is predominantly single-bond in nature, and the imidazole-moiety experience delocalization of electron density around the N-C-N fragment.

In 1968, both Wanzlick<sup>13</sup> and Öfele<sup>14</sup> independently prepared NHC-metal complexes by reacting an imidazolium salt with a metal-precursor of Hg (II) and Cr (0), respectively, containing an internal base as shown in **Figure 4.4**.

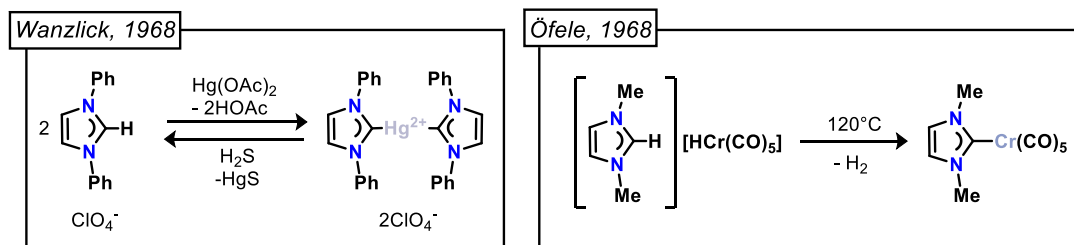


**Figure 4.4.** The two first reported NHC-metal complexes. Despite quite different conditions, metalation was achieved by reacting metal-precursors containing an internal base with an imidazolium salt.

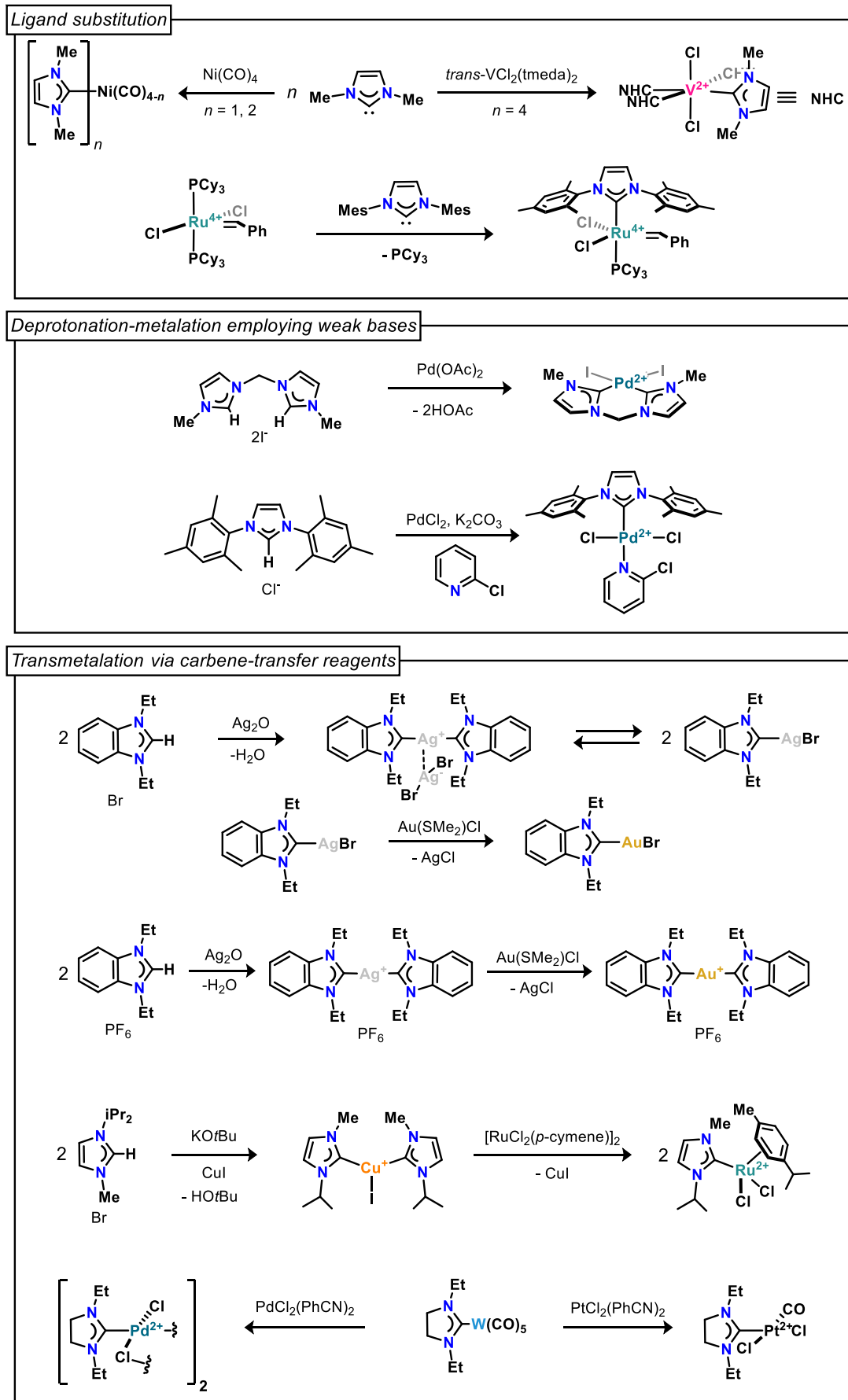


**Chart 4.1.** Different successful preparation of NHC metal complexes. NHC complex preparation shows a wealth of different chemical transformations.

**Chart 4.1** shows three of the more commonly encountered ways of preparing NHC complexes, of which the more straightforward preparation of complexes bearing *N,N'*-disubstituted imidazole-2-ylidene, follows the metalation of the free-carbene achieved by ligand substitution reactions. The strength of the resulting metal-NHC bond is reflected in several reports on ligand-substitution of coordinately saturated complexes bearing strongly coordinating ligands, *e.g.* CO, PCy<sub>3</sub>, *N, N, N', N'*-tetramethyl ethylenediamine (tmeda) with such free carbenes, as shown in the top insert<sup>15–18</sup>. This approach works for carbenes that are sufficiently stable *viz.* imidazole, whereas NHCs bearing benzimidazole and imidazoline architectures dimerize.

Second, by employing weak bases: Herrmann prepared a bishalido chelating NHC Pd(II) complexes by mixing Pd(OAc)<sub>2</sub> with an imidazolium salts<sup>19</sup>, which added an additional amount of acetate, mitigates the formation of abnormal carbenes<sup>20</sup>. This approach relies on an equilibrium reaction, wherein a mild base deprotonates small amounts of the imidazolium salt, following the lowering of imidazolium pK<sub>a</sub> from the Lewis acidic metal center. The free carbene readily coordinates to the Pd center, which further shifts the equilibrium towards the complex<sup>21</sup>.

Third, and perhaps more explored, is a synthetic route exploiting transmetalation of carbene-transfer reagents. In this context, the predominant way of complex preparation follows transmetalation of a Ag-NHC complex, prepared by reacting the imidazolium salt with base and a Ag (I)-source, as first reported by Lin<sup>22</sup>. Other metals also find application, such as Cu (I) or early, low-valent metal carbonyl complexes, as reported by Albrecht<sup>23</sup>, and Liu<sup>24</sup>, respectively. Lin's approach generates (relatively) stable Ag-NHC precursors, which react with metal-halide sources to precipitate insoluble silver-halides that ultimately drives the reaction towards completion. This transmetalation reaction further relies on electronegativity differences and tends to work better with more

electronegative atoms, *viz.* mid to late transition metals<sup>25</sup>. The nature of the NHC-Ag intermediate greatly varies, dependent not only on the complexity of the imidazolium starting material, but also on the nature of the counterion; whereas NHC-halide complexes seem to exist in equilibrium with themselves, between a linear heteroleptic NHC-Ag-X complex and the Ag-NHC<sub>2</sub> dimer (or oligomer<sup>26</sup>), complexes featuring weakly-coordinating counterions *e.g.* <sup>-</sup>PF<sub>6</sub>, <sup>-</sup>OTf, <sup>-</sup>OTs, <sup>-</sup>BF<sub>4</sub>, <sup>-</sup>BPh<sub>4</sub>, tend to adopt predictable connectivity wherein Ag exclusively bridges two NHCs. This structure-counterion dependency leads to differences in transmetalation adducts, as demonstrated in the lower insert of **Chart 4.1**, where weakly coordinating counterions results in transfer of two NHC fragments, opposing transmetalation of intermediary heteroleptic NHC-Ag-X complexes.

Furthermore, intermediary Ag-NHC complexes of macrocyclic poly imidazolium salts seem to fall into either of the three structures shown in **Figure 4.5**: 1) monomeric, Ag-tethering the macrocycle to itself<sup>27,28</sup>; 2) dimeric (polymeric), Ag-bridging the involved macrocycles<sup>29,30</sup>; and 3) dimeric (polymeric), featuring a Ag-tether across each macrocycle<sup>25,28</sup>. The coordination of Ag follows that expected of a d<sup>10</sup> configuration; a linear geometry, further stabilized by argentophilic interactions.

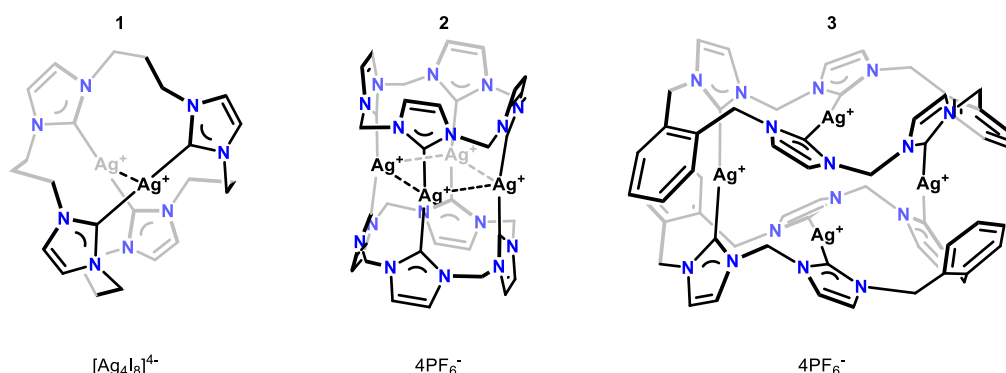


**Figure 4.5.** Representative architectures of macrocyclic poly NHC-Ag intermediates. These intermediates readily facilitate transmetalation reaction into the corresponding complex bearing a macrocyclic poly NHC ligand in high yields.

The efficacy of NHC-Ag precursors in transmetalation is often described in terms of lability of the NHC-Ag bond. A property readily assessed through <sup>13</sup>C NMR, as an

absence of downfield-shifted signals ( $\delta > 150$  ppm) suggests that the Ag-complex may readily undergoes ligand exchange<sup>26,31,32</sup>. As such, while well-resolved signals in a  $^{13}\text{C}$  NMR spectrum provide strong evidence in support of metalation, an absence of any such signals need not imply a given material is absent silver-ions. Rather, this observation may suggest that these synthons readily facilitate transmetalation following from rapid exchange processes.

Different measurements exists to assess the electron properties, emphasizing the strength of donation of NHC, including Tolman's electronic parameter (TEP)<sup>33</sup>, Huyhn's electronic parameter (HEP)<sup>34</sup>, and HEP for chelating NHCs (HEP2)<sup>35</sup>. TEP was originally developed to study the donor strengths of phosphine ligands, by measuring the red (or blue) shift in the carbonyl stretching frequency,  $\bar{\nu}_{\text{CO}}$ , of  $\text{LNi(CO)}_3$  relative to  $\text{Ni(CO)}_4$  ( $\bar{\nu}_{\text{CO}} = 2125 \text{ cm}^{-1}$ )<sup>36</sup> upon ligand substitution with a strongly donating phosphine. As CO is a strong  $\pi$ -acceptor, an increase in electron density at the metal centers from the phosphine leads to further  $\pi^*$ -back donation, which red shifts CO stretching frequencies, reflecting the further weakened C-O bond. The fundamentals of this analysis, similarly apply to NHCs; subsequent studies by Nolan, indeed, corroborate that NHCs are strongly donating, many more so than  $\text{P}(t\text{Bu})_3$ <sup>37</sup>. Crabtree later modified this analysis, such that handling of  $\text{Ni(CO)}_4$  was omitted all together<sup>38</sup>.

Huyhn later developed a unified  $^{13}\text{C}$  scale to probe subtle electronic variations in NHCs, HEP, as the donor strength of an NHC intimately is tied to the different electronic contribution terms to the inductive and mesomeric effects<sup>34</sup>. This method gauges the relative donation strength of a given ligand *trans* to a  $^{13}\text{C}$ -enriched benzimidazole-2-ylidene probe, by measuring changes occurring to the  $^{13}\text{C}$  chemical shift of a probe, as shown in **Figure 4.6**. Generally, free NHCs typically show  $^{13}\text{C}$  chemical shift values of  $>200$  ppm. Accordingly, the larger downfield shifts experienced by the probe should

therefore correlate with a stronger donation exerted by the ligand. This method has since been developed to also encompass chelating ligands, HEP2<sup>35</sup>. As seen by the representative structures in **Figure 4.6**, this method importantly establishes that both the backbone and *N*-substituents greatly affects the resulting NHC donor ability, following term contributions to the inductive and mesomeric effects; electron rich substituents greatly enhance donor properties.

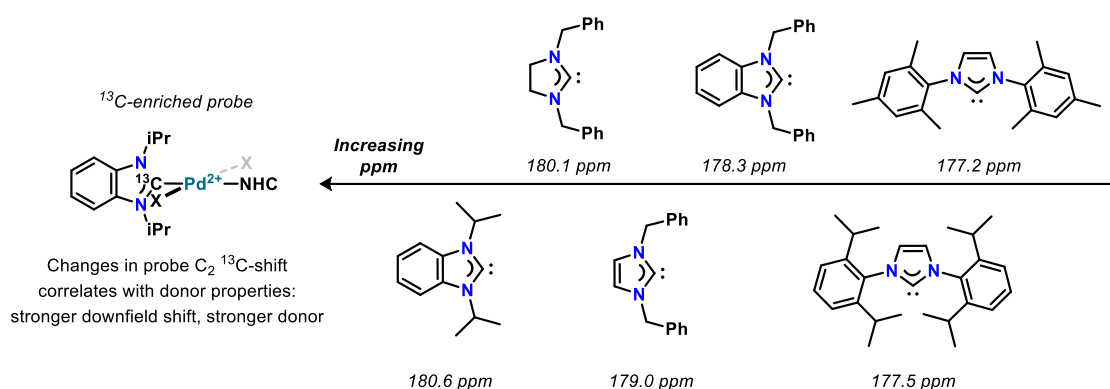


**Figure 4.6.** HEP scale with selected mono dentate NHC ligands. The listed chemical shift values are for the C2-position of the probe upon *trans* NHC ligation. Adapted from Huyhn and co-workers<sup>35</sup>.

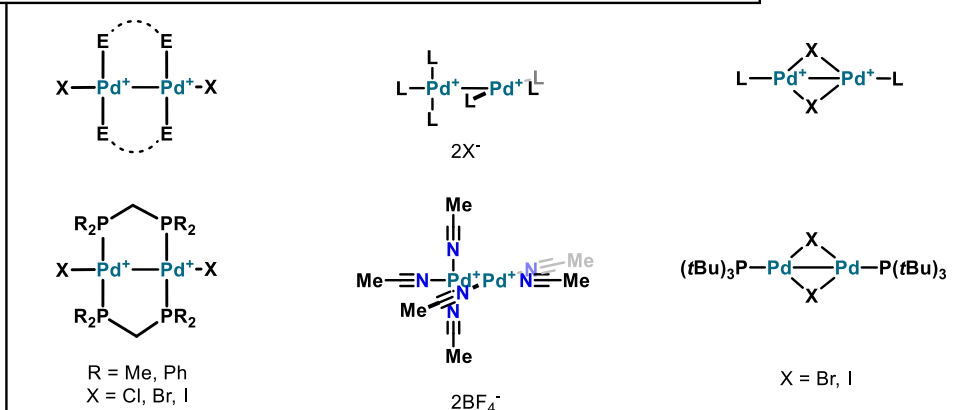
In 1995, Herrmann and co-workers reported the first catalytic application of NHC complexes; a Mizoroki-Heck cross coupling reaction mediated by a highly active bis-NHC Pd complex<sup>19</sup>, shown in **Chart 4.1**. The authors comment on key properties that make NHC appropriate in homogeneous catalysis: strong two-electron donating ligands, on par with electron rich phosphines, complexes remarkably stable towards aerobic oxidation and moisture, which feature highly stable M-C bonds that disfavor ligand dissociation. The latter has some beneficial consequences, as this property mitigates aggregation of low valent metal particles into nanoparticles, aids to create vacant coordination sites at the metal center that in turn can partake in the catalytic cycle, and lowers the required amount of ligand to facilitate transformation. A large excess of phosphine, for instance, is necessary in hydroformylation reaction to prevent deactivation<sup>39,40</sup>. Since this work, a wealth of different catalytical transformation mediated by NHC complexes have been reported including olefin metathesis, and

extensive Pd-facilitated cross-coupling reactions *viz.* amination, silylation, Sonogashira, Stille, Suzuki-Miyaura, Mizoroki-Heck, reductive Heck, and Kumada<sup>41</sup>.

#### 4.1.1 *Dipalladium and dinickel complexes bearing NHC ligands*

The coordination chemistry of dipalladium (I) complexes is wealthy<sup>42</sup> and three reoccurring bonding geometries are apt at facilitating a plethora of different reactions, these are shown in the top insert of **Chart 4.2**. Complexes adhere to either of these bonding architectures, and often sterically encumbering and electron rich ligands, such as tertiary phosphines and NHCs. Specifically, complexes bearing the latter type of ligand is of interest to this project, and some dinickel and dipalladium complexes are found in the literature, shown in the lower insert of **Chart 4.2**. In addition, other bimetallic complexes bearing alkyl bridging NHC ligands are known, including Cr<sup>50</sup>, Cu<sup>51</sup>, Rh<sup>52,53</sup>, Ir<sup>53,54</sup>, and Au<sup>55</sup>.

Prototypical and select examples of low-valent dipalladium (I) complexes



Examples of dinickel (I), dipalladium (I), and dipalladium (II) NHC complexes

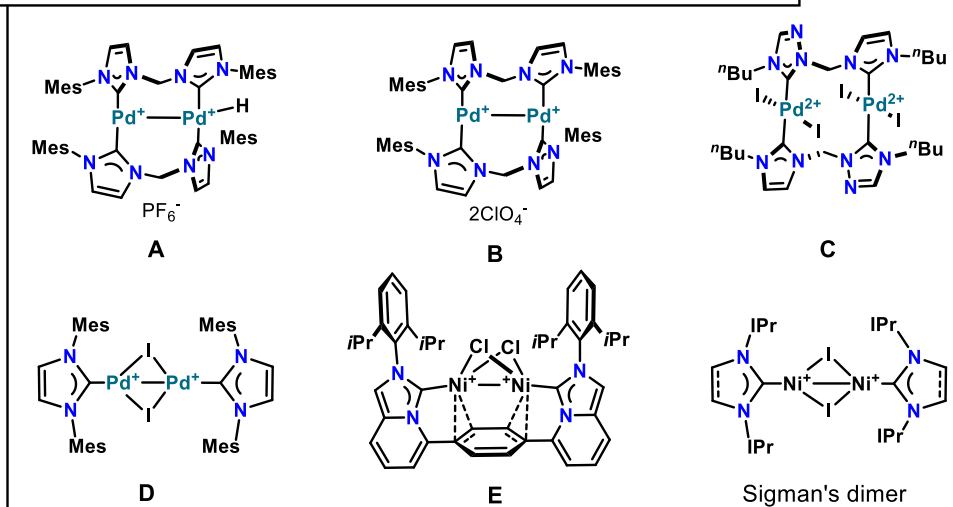


**Chart 4.2.** Prototypical coordination geometries of low-valent dipalladium(I) complexes. Selected examples of both dinickel (I) and dipalladium (I/II) complexes are shown in the lower insert.

Complex **A** was reported by Gardiner as the first well-defined and characterized dipalladium (I) NHC complex featuring a terminal hydride ligand<sup>43</sup>. This complex was prepared under reductive conditions appropriate for C-C/N cross-coupling reactions, by reacting the parent dicationic chelating NHC-Pd-acetonitrile adduct to K<sub>2</sub>CO<sub>3</sub> and MeOH. The authors speculate on what causes the observe ligand rearrangement from a chelate to monodentate and suggests that this rearrangement is a consequence of the chelate being unable to stabilize the low-valent Pd(I) species.

In contrast, complex **B**, reported by Rizzolio and Visentin, differs from complex **A** in its preparation and its stability towards air<sup>44</sup>: whereas complex **A** readily reacts with O<sub>2</sub>, even in the solid-state, complex **B** demonstrate prolonged stability towards air, both



in solution and in the solid-state. Complex **B** was isolated as one of two species from a transmetalation reaction between  $[\text{Pd}(\eta^3\text{-1,1-dimethylallyl})\text{Cl}]$ -dimer,  $\text{AgClO}_4$ , and the bis( $\text{Ag-Br}$ )-NHC adduct, whereas complex **A** cleanly forms as a single product.

Complex **C** was reported by Shreeve in 2006, and was prepared by reacting the parent divalent triazolium salt with  $\text{Pd}(\text{OAc})_2$  in  $\text{DMSO}$ <sup>45</sup>. This complex was used as precatalyst in a Mizoroki-Heck cross coupling reaction with a variety of ionic liquids, however, demonstrated a similar reactivity to  $\text{PdCl}_2$ .

Complex **D**, was synthesized by Gooßen under reductive conditions of a divalent Pd-dimer,  $[\text{PdI}(\mu\text{-I})\text{IMes}]_2$ , ( $\text{IMes}$  = 1,3-bis(2,4,6-trimethylphenyl)-imidazole-2-ylidene) which works as a highly reactive precatalyst for Suzuki–Miyaura, Buchwald–Hartwig, and Sonogashira cross-coupling reactions, suggested from a disproportionation reaction into highly reactive 12-electron  $\text{IPrPd}$  complex<sup>46</sup>, analogous to that proposed by Hartwig of Mingos' dimer. Other variations of the bridging ligands have been reported by Hazari, including allyls and chlorides, and these complexes similarly serve as high-reactive precatalysts for unsaturated NHC-Pd(0) complexes<sup>47</sup>.

Complex **E** was reported by Agapie to cleave reductively cleave  $\text{CO}_2$  with retention of the dinickel framework<sup>48</sup>. The dinickel structure was prepared by a comproportionation reaction between  $\text{Ni}(\text{cod})$ ,  $\text{NiCl}_2(\text{dme})$  and the preformed NHC, or by an oxidation of two  $\text{Ni}(0)$  centers. The ligand platform similarly coordinates two  $\text{Cu}(\text{I})$  or two  $\text{Co}(\text{II})$  ions, which neither demonstrate metal-metal bonding, instead leading to a metal above and below the plane of the central benzene ring.

These examples mean to demonstrate, that dipalladium (and nickel) (I) complexes may be realized through different means, such as comproportionation reactions, under

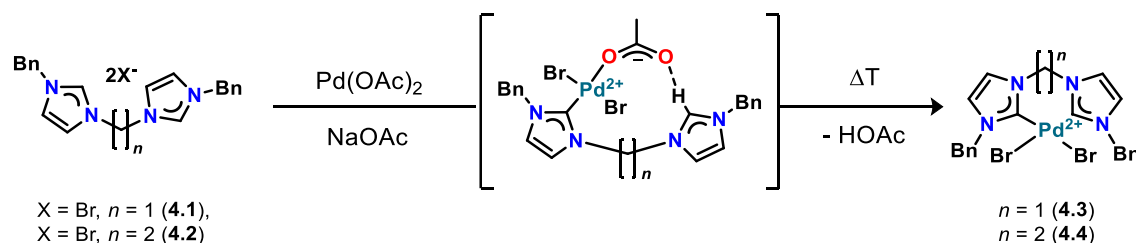
reductive conditions, and from transmetalation reactions where heteroleptic NHC-Ag-X complexes are synthetically isolable.

## 4.2 Monopalladium complex syntheses

Concurrent with synthesizing the macrocyclic proligands, we sought to discern between metal complexes resulting from different metalation protocols by using two mononuclear congeners shown below in **Scheme 4.1**. More importantly, these monometallic congeners serve to make a straightforward and direct comparison between different properties, such as redox events, bonding metrics, and stability.

### 4.2.1 Concurrent deprotonation-metalation

As outlined in **Scheme 4.1**, we first explored concurrent deprotonation-metalation of imidazolium salts using mild (in)organic bases. Specifically, reacting an imidazolium salt with palladium (II) acetate, Pd(OAc)<sub>2</sub>, in an aprotic polar solvent, results in a neutral complex and liberation of acetic acid, an approach often referred to as the “acetate route”. Moreover, relevant to the metalation of chelating imidazolium salts with protons available at the C<sub>2</sub>, C<sub>4</sub>, and C<sub>5</sub> positions, respectively, Herrmann and Gardiner disclosed that additional acetate (NaOAc or NH<sub>4</sub>OAc), beneficially stabilizes a metal-chelate intermediate towards the C<sub>2</sub>-position<sup>20</sup>, thereby mitigating the competitive formation of abnormal carbenes<sup>49</sup>.

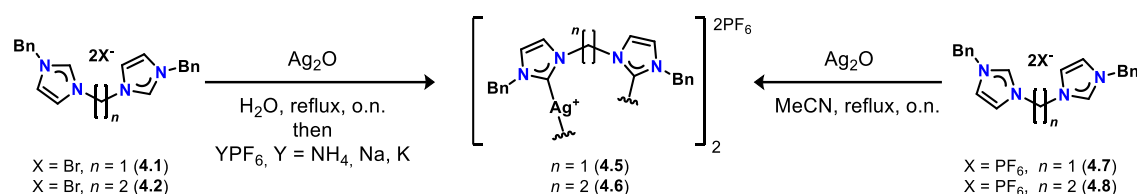


**Scheme 4.2.** Chelate complex preparation through the “acetate route”. Additional acetate stabilizes a putative chelate towards the C<sub>2</sub>-position and further acts as a base.

The wanted complexes have already been prepared by Lee<sup>50</sup>. Analogous to their preparation, reacting the white imidazolium bromide salts **4.1** (MeLH<sub>2</sub>-2Br) and **4.2** (EtLH<sub>2</sub>-2Br), respectively, with Pd(OAc)<sub>2</sub> and NaOAc in DMSO, at incremental

temperature intervals afford yellow powders of  $[(\kappa^2\text{-C},\text{C}^{\text{Me}}\text{L}^{\text{Et}}\text{L})_2\text{Pd(II)bromido}]$ -complexes **4.3** ( $^{\text{Me}}\text{LPdBr}_2$ ), and **4.4** ( $^{\text{Et}}\text{LPdBr}_2$ ), respectively, in good to excellent yield (80 – 90%). Furthermore, in accordance with their reported  $^1\text{H}$  NMR spectra, metalation was corroborated by an absence of downfield-shifted protons in the region around 10 – 9.5 ppm in the  $^1\text{H}$  NMR spectrum of **4.3** and **4.4**, alongside the emergence of a more downfield-shifted signal in  $^{13}\text{C}$  NMR spectrum ( $>160\text{ppm}$ ). However, in agreement with Lee's findings, this resonance was only observed for complex **4.4**.

#### 4.2.2 Carbene-transfer reagents in transmetalation reactions



**Scheme 4.3.** Preparation of NHC-Ag intermediates through two routes. The Ag-NHC intermediate of interest is readily prepared for transmetalation purposes.

We then sought to explore NHC-complex formation following a transmetalation of a silver-carbene-synthon. Mindful of the different intermediates resulting from halide-containing imidazolium starting materials, we sought to work with the  $\text{PF}_6$ -counterion. A light-sensitive colorless powder consistent with  $[\text{NHC-Ag}]_2 2\text{PF}_6$  was recovered from the addition of an excess of  $\text{YPF}_6$  ( $\text{Y} = \text{Na}, \text{K}, \text{NH}_4$ ) to the filtrate following the reaction between compounds **4.1** and **4.2** with an excess of  $\text{Ag}_2\text{O}$  in  $\text{H}_2\text{O}$ , outlined in on the left-hand side of **Scheme 4.3**, as complexes **4.5** ( $[\text{MeLAg}]_2 2\text{PF}_6$ ) and **4.6** ( $[\text{EtLAg}]_2 2\text{PF}_6$ ), respectively. 1D  $^1\text{H}$  and 1D  $^{13}\text{C}$  NMR spectroscopy provide insight into the nature of the powders of **4.5** and **4.6** concerning changes upon metalation, and the following analysis elucidates common characteristic features of such Ag-complexes.

**Figure 4.7** compares a select region of the 1D  $^1\text{H}$  NMR spectra between **4.2** (top spectrum) and **4.6** (lower spectrum) in  $\text{DMSO-}d_6$ . Similarly, **Figure 4.8** compares the associated  $^{13}\text{C}$  NMR spectra. The most striking difference in **Figure 4.7** is an absence of

the characteristic imidazolium C<sub>2</sub>-H (9.24 ppm), a substantial upfield shift of all peaks, and changes in multiplicities of the C<sub>4/5</sub>-H from triplets (poorly resolved) to doublets. **Figure 4.8** further substantiates metalation, following changes to the C<sub>2</sub>-C signal; a significant downfield shift paired with two distinct one-bond couplings between <sup>13</sup>C to the two NMR spin-active isotopes of Ag, <sup>107</sup>Ag and <sup>109</sup>Ag, both I = ½, respectively. The four downfield-shifted signals seen in the lower insert of **Figure 4.8** (labels A, B, C, and D), thus constitute two doublets with coupling constants of <sup>1</sup>J(<sup>13</sup>C-<sup>107</sup>Ag) = 181.7 Hz (B and C), and <sup>1</sup>J(<sup>13</sup>C-<sup>109</sup>Ag) = 209.2 Hz (A and D), respectively. The difference in magnitude between the two coupling constants is consistent with the ratio between the gyromagnetic ratio of the two Ag-isotopes being roughly 1.15.

While we did not obtain solid-state information through X-ray, elemental analysis supports a composition consistent with an NHC-Ag dimer. Finally, powders with identical spectroscopical properties were isolated from metalation of imidazolium PF<sub>6</sub>-salts **4.7** and **4.8** with Ag<sub>2</sub>O in MeCN, outlined in on the left-hand side of **Scheme 4.3**.

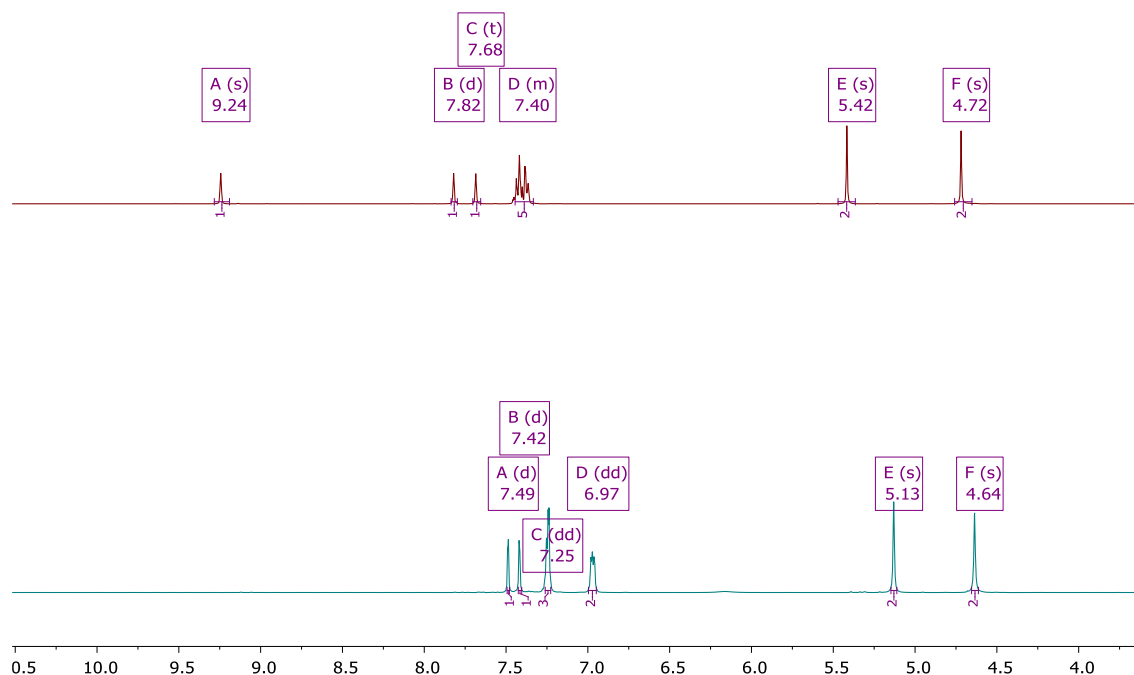


**Figure 4.7.** Comparison between <sup>1</sup>H NMR spectra (DMSO-*d*<sub>6</sub>) of compound **4.2** with complex **4.6**. The top insert shows the imidazolium salt with its characteristic downfield-shifted singlet, which is absent in the bottom insert.

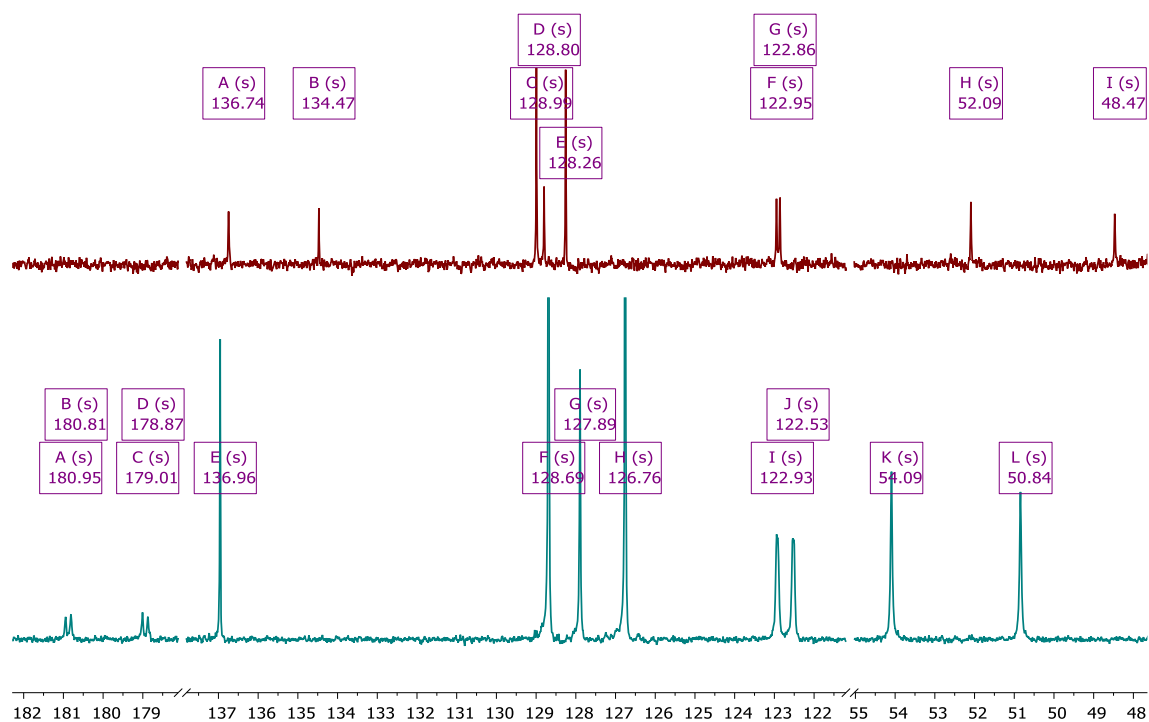
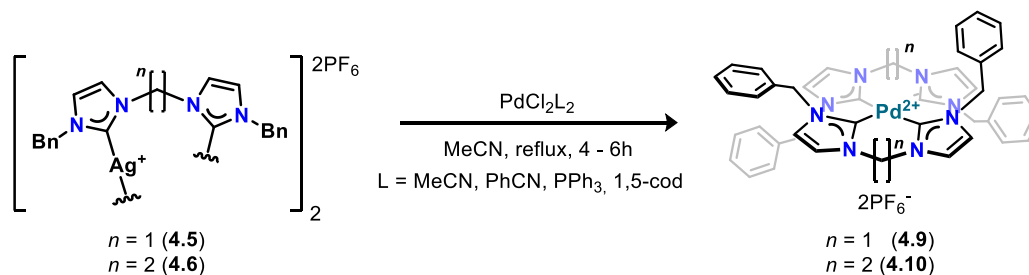


**Figure 4.8.** Comparison between  $^{13}\text{C}$  NMR spectra (DMSO- $d_6$ ) of compound **4.2** with complex **4.6**. The top insert shows the imidazolium salt, and the bottom insert shows two doublets resulting from the coupling between  $^{107/109}\text{Ag}$  and  $^{13}\text{C}$ .

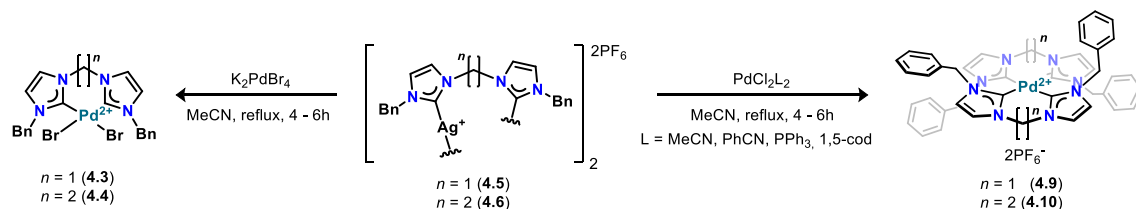
#### Exploration of transmetalation reaction products



**Scheme 4.4.** Transmetalation route using silver-carbene transfer-reagents. Depicted are different Pd(II)-sources and their resulting complex.

With complexes **4.5** and **4.6** in hand, we sought to demonstrate whether different complexes were isolable from differences in the ligand strength from various Pd(II)-salts, or whether such a difference is stoichiometry dependent. **Scheme 4.4** outlines the transmetalation products resulting from reacting **4.5** and **4.6** with various  $\text{PdCl}_2\text{L}_2$  ( $\text{L} = \text{MeCN}, \text{PhCN}, \text{PPh}_3, 1,5\text{-cod}$ ) sources, which when filtered from  $\text{AgCl}$ , leaves a colorless solution, from which crystals suitable for single-crystal X-ray diffraction can be obtained from, revealing bischelating complexes: complexes **4.9** and **4.10** are shown in **Figures 4.9** and **4.10**, respectively.

Whereas an increase in equivalents results in the same complexes, substituting  $\text{K}_2\text{PdBr}_4$  in place of  $\text{PdCl}_2\text{L}_2$  effects yellow powders with spectral properties like complex **4.3** and **4.4**, thus demonstrating synthetic control of the ligators in the resulting complexes from an appropriate combination of precursors, as outlined in **Scheme 4.5**.



**Scheme 4.5.** *Transmetalation differences.* We found changing Pd-precursors to  $\text{K}_2\text{PdBr}_4$  yields the same complexes found following the “acetate” route.

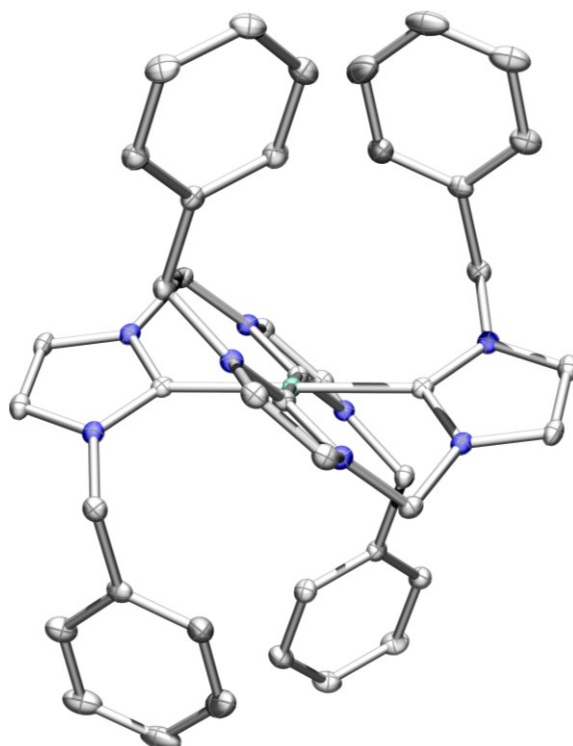


**Figure 4.9.** *Single-crystal X-ray structures of monopalladium bis-NHC complex 4.9.* The solid-state structure of **4.9** with thermal ellipsoids at a 50% probability level. Co-crystallized MeCN, H-atoms, and PF<sub>6</sub>-counterions are omitted for clarity.

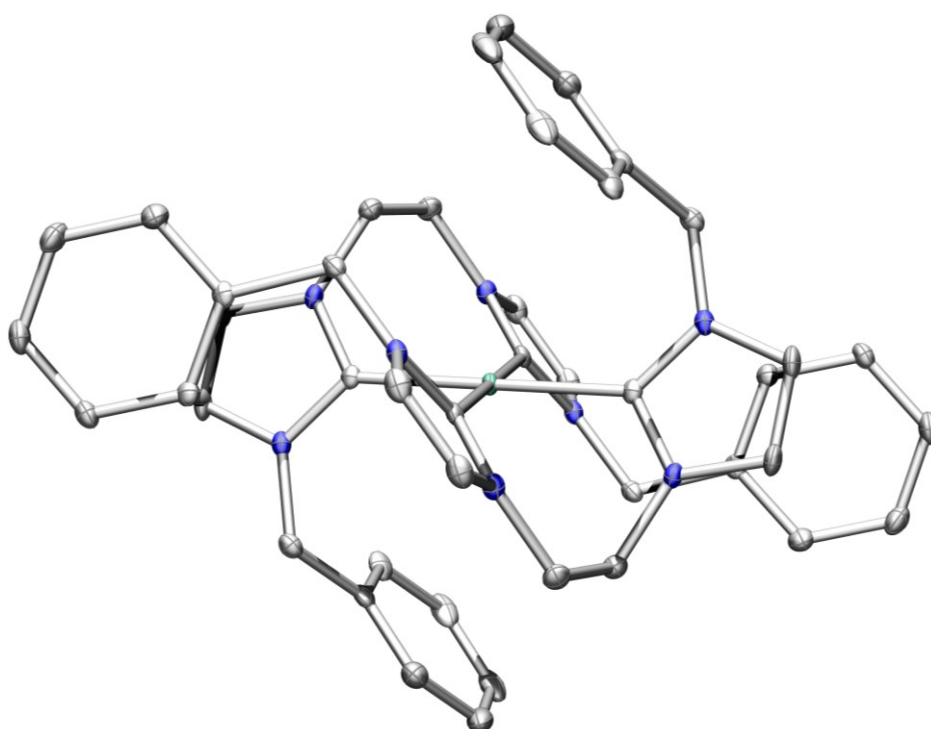


**Figure 4.10.** *Single-crystal X-ray structures of monopalladium bis-NHC complex 4.10.* The solid-state structure of **4.10** with thermal ellipsoids at a 50% probability level. Co-crystallized MeCN, H-atoms, and PF<sub>6</sub>-counterions are omitted for clarity.

### Structural characterization of complexes **4.9** and **4.10**

Both complex **4.9** and **4.10** crystallize in the C2/c space group, and as evident from **Figure 4.8** and **Figure 4.9**, feature a palladium (II) center coordinated square-planar by two symmetry-related chelating-NHC ligands, consistent with a  $d^8$  metal complex.

Crystallographically, the two complexes are similar, however, feature different amounts of co-crystallized MeCN in the asymmetric unit cell, 2 (**4.9**) vs. 1 (**4.10**), as well as the extent of disorder the counterion demonstrates (only in **4.10**). While the complexes look similar, they demonstrate some differences, emphasized in **Figure 4.11**, relating to Pd-C bond lengths between the ylidene C<sub>2</sub>-C and Pd, denoted by  $d$ , and the twist angle each NHC demonstrates relative to the plane of coordination, denoted by  $\phi$ .

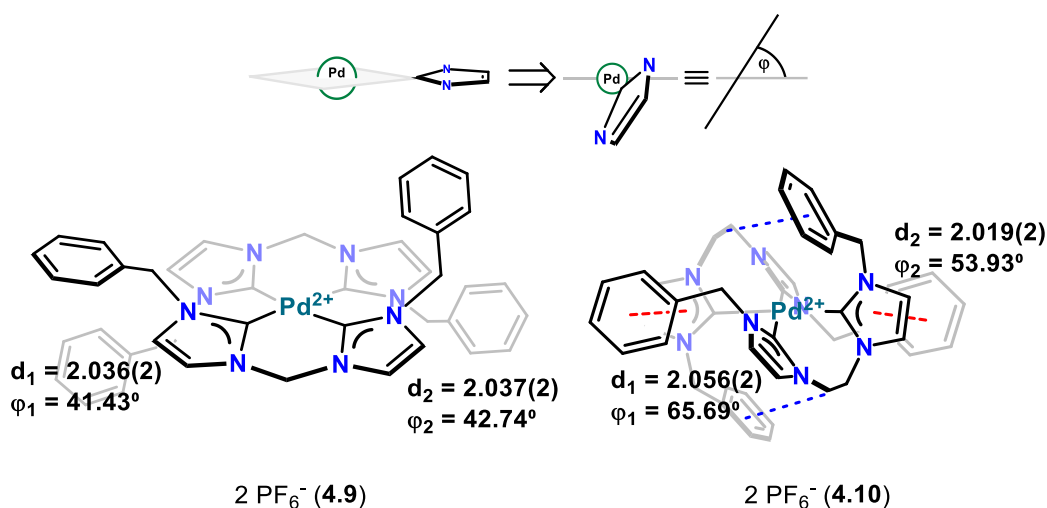


**Figure 4.11.** Consideration of each NHC's twist-angle to Pd and bonding metrics of **4.9** and **4.10**. A general measure of each NHC's twist angle ( $\phi$ ) to Pd from the mean plane spanned by four imidazole-2-ylidenes is shown on the left-hand side of the figure, and the bonding pertaining to **4.9** and **4.10** show a similar bonding.

Whereas complex **4.9** features Pd-C bond lengths of 2.037 and 2.036 Å, **4.10** features Pd-C bond lengths of 2.018 Å and 2.058 Å, respectively. Similarly, whereas complex **4.9** demonstrates  $\phi$  angles of 41.43 and 42.74°, respectively, **4.10** displays angles of 53.93° and 65.69° respectively. In complexes **4.9** and **4.10**, the orientation of the aliphatic linker in each chelate is opposite the ancillary benzylic moiety; in each of the chelates of **4.10**, one pendant phenyl seems to interact with the opposing ylidene-moiety through  $\pi$ - $\pi$  stacking (centroid distance of 3.643 Å), as illustrated by the dotted red line in



**Figure 4.11.** The other phenyl seems to position itself such that it can interact with the benzylic position and the aliphatic linker, illustrated by the dotted blue line. Finally, each of the chelating ligands in **4.9** and **4.10** is related to itself by an inversion through the Pd-center.

**Figures 4.12** compares the room temperature (RT) 1D  $^1\text{H}$  NMR spectra ( $\text{CD}_3\text{CN}$ ) of complex **4.9** (top spectrum) to **4.10** (lower spectrum), which both reflect the symmetrical nature of the complexes. The spectrum of complex **4.9** displays a diastereotopic splitting (AX) of protons owing to the benzylic (signals G and H) and the methylene linker (signals E and F), thus suggesting that the geometry is rigid (at least at RT). Finally, signals A and D, owing the imidazoline-2-ylidine moiety appear as well-resolved doublets ( $^3J(\text{H-H}) \sim 2\text{Hz}$ ), consistent with coupling constants found between cis-oriented protons in  $\text{sp}^2$  fragments.

The spectrum of complex **4.10** is different to **4.9**. First, the ylidine protons (signals labelled B and C) appear to be upfield shifted and feature a smaller chemical shift difference close to 0.1 ppm, quite different from the  $\sim 0.4$  ppm observed between the equivalent protons in complex **4.9**. Second, only the protons owing to the ethylene linker demonstrate diastereotopic splitting, reminiscent of AA'BB' (signals E and G), whereas the benzylic protons appear as a singlet. Moreover, the chemical shift of the former appears to have been upfield shifted, compared to the methylene protons of **4.9**.

Established by HEP, the  $^{13}\text{C}$  chemical shift value of the coordinating C atoms in NHC-complexes provide insights into subtle electronic differences of the ligands<sup>34</sup>. In this context, the ligands in complexes **4.9** and **4.10**, according to the HEP scale for chelating ligands, HEP2, are essentially equal in donor strength<sup>35</sup>.

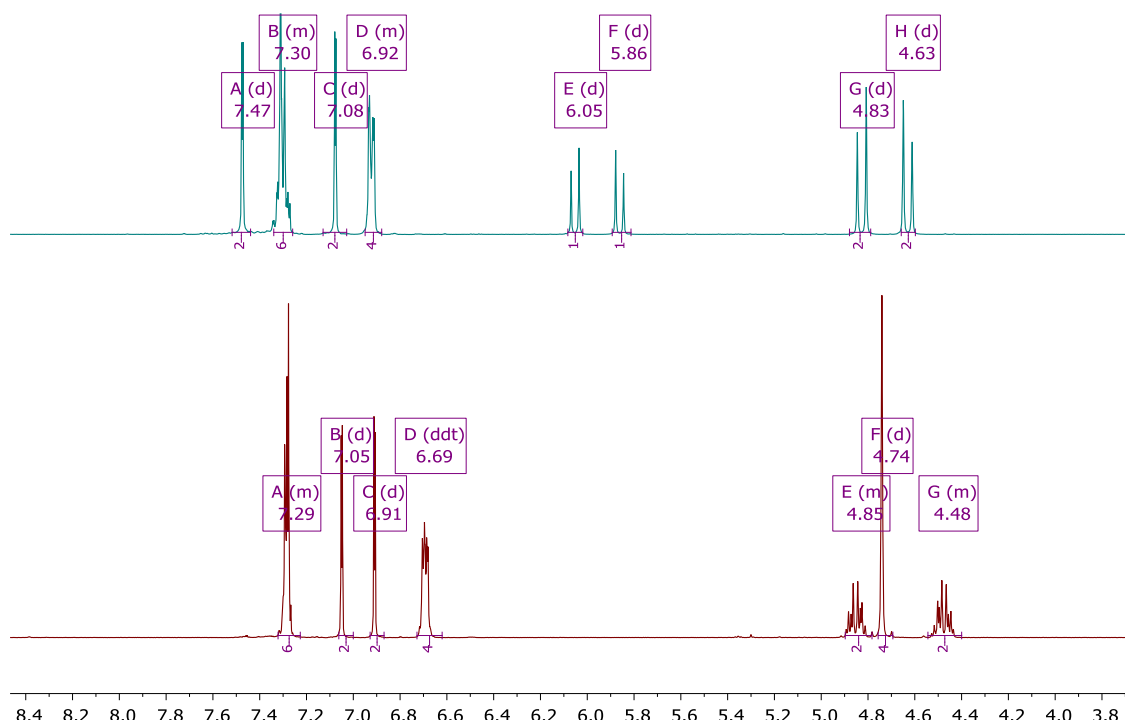


**Figure 4.12.** Comparison between  $^1\text{H}$  NMR spectra (in  $\text{CD}_3\text{CN}$ ) of **4.9** (top) and **4.10** (bottom). The apparent differences relate to an absence of a diastereotopic environment at the benzylic position, suggesting that **4.9** is more rigid.

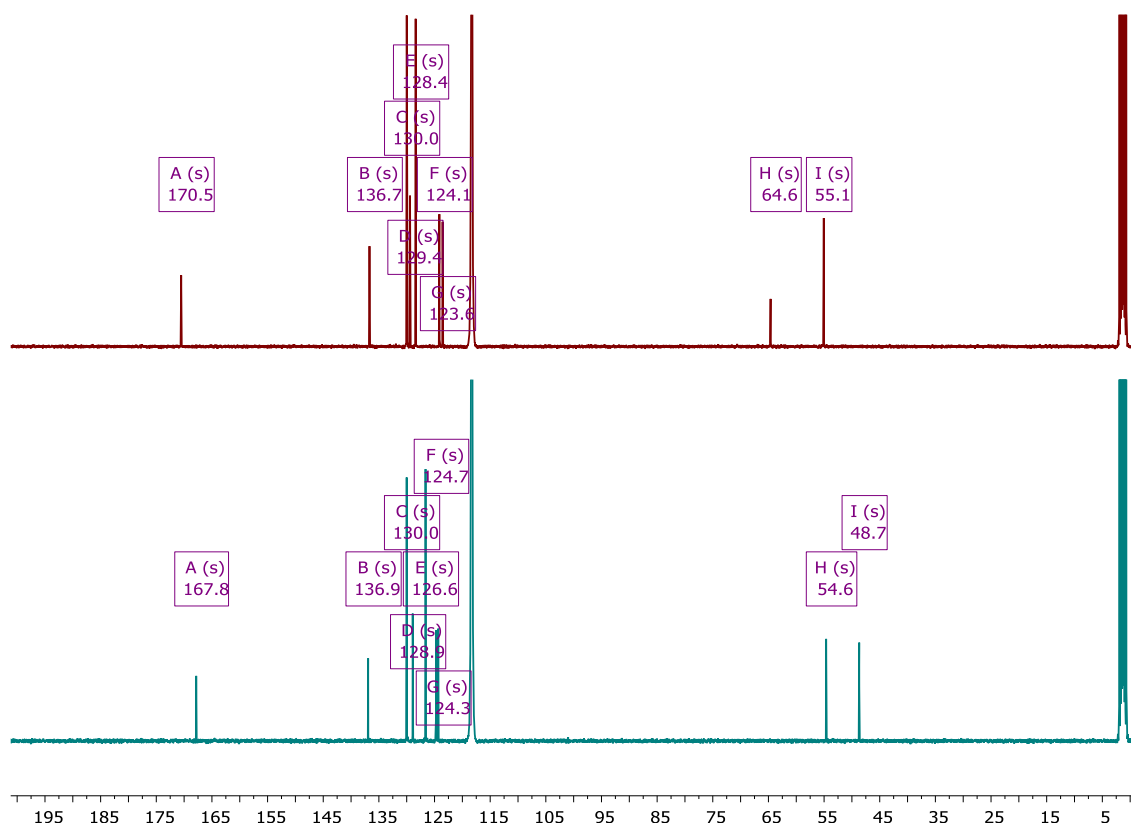
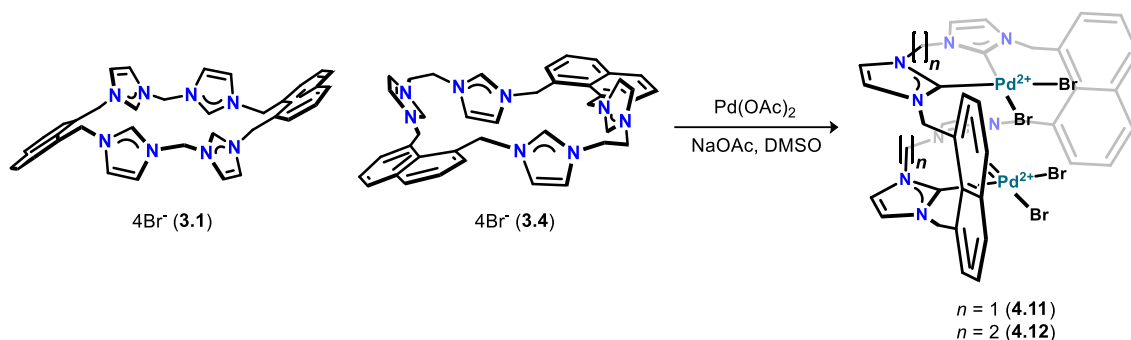


**Figure 4.13.** Comparison between  $^{13}\text{C}$  NMR spectra (in  $\text{CD}_3\text{CN}$ ) of **4.9** (top) and **4.10** (bottom). The associated  $^{13}\text{C}$  NMR spectra reveal differences between **4.9** and **4.10** related to a difference in the chemical shift value of the coordinating C atom, signal A.

As such, from the structural similarities between **4.9** and **4.10**, we may expect close to a nearly identical  $^{13}\text{C}$  chemical shift of the resulting complexes. However, as evident from **Figure 4.13**, complex **4.9** demonstrates an approximately 3 ppm further downfield shift in its chemical shift value relative to **4.10**

This difference may be understood from the structural differences following the complexes' relative flexibility and  $\pi$ - $\pi$ -interaction, suggested in the solid state, persisting in solution between a phenyl ring and an ylidene-moiety in **4.10**. This interactions positively contributes to the inductive effect experienced by the  $\text{C}_2$ -C atom, which overall lowers the electronic "pull" this C-atoms experience, hence a lower chemical shift. This  $\pi$ - $\pi$  interaction, would further help to explain the noticeable upfield-shifted observed in the  $^1\text{H}$  NMR spectrum of complex **4.10**.

### 4.3 Seeking dipalladium complexes via the “acetate route”



**Scheme 4.6.** *Conceptual approach targeting dipalladium complexes.* Initially following the acetate route, we sought to provide dipalladium (II) with the suggested configuration shown above.

With some insight into imidazolium-metalation established, we then sought to metalate compounds **3.1** and **3.4**, targeting two dinuclear complexes, with putative connectivity shown in **Scheme 4.6**. While the moiety separating the chelate, in the suggested structures of **4.11** and **4.12**, is shown as the aliphatic (m)ethylene-linker, it is reasonable to envision a naphthalene-based chelate.

Accordingly, to discern between these two, and whether a mixture forms, metalation was undertaken with a single equivalent of Pd(OAc)<sub>2</sub>. Moreover, a step-wise metalation may yield a different product distribution from adding an excess of metal-sources. Irrespective of the chelate, such a step-wise metalation process, if successful, presents a straightforward path to further explore the chemistry of heterodinuclear complexes, such as synthetic analogues to [NiFe]-hydrogenase.

**Figure 4.14** compares the  $^1\text{H}$  NMR spectra (in  $\text{DMSO-}d_6$ ) between compound **3.1**, an aliquot of the reaction mixture between **3.1** with 1 equiv.  $\text{Pd}(\text{OAc})_2$ , 5 equiv.  $\text{NaOAc}$ , in  $\text{DMSO}$  at  $80\text{ }^\circ\text{C}$  after 5 hours, and the resulting crude  $\text{Pd}(\text{II})$ -complex. The middle spectrum of **Figure 4.14** corroborates the formation of  $\text{HOAc}$ , evident from the broad and downfield-shifted peak at  $\sim 12\text{ ppm}$ , unreacted **3.1**, and more interestingly, the emergence of a new sets of diastereotopic protons: around  $5.40$  and  $5.24\text{ ppm}$ , respectively.

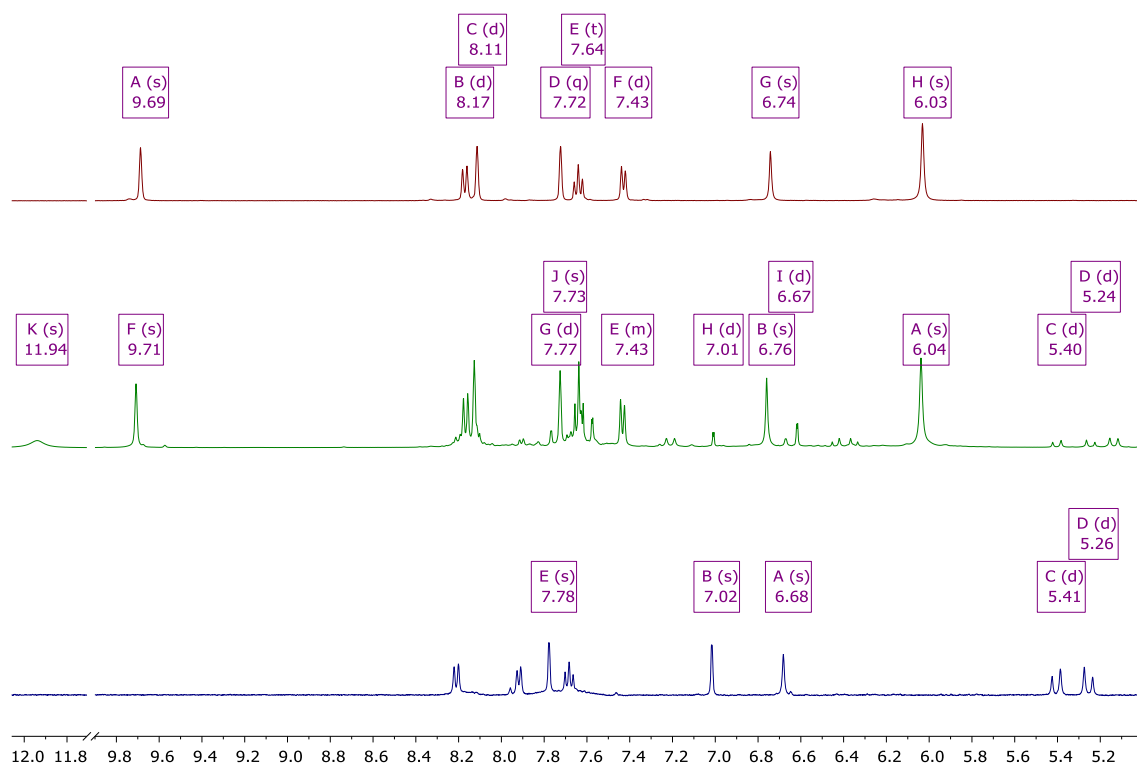


**Figure 4.14.** Metalation of **3.1** with  $\text{Pd}(\text{OAc})_2$ . The top insert shows compound **3.1**, the middle insert shows an aliquot of the reaction of **3.1** with  $\text{Pd}(\text{OAc})_2$  and NaOAc after 5 hours at 80 °C, and the lower insert shows the spectral properties of the isolable product.

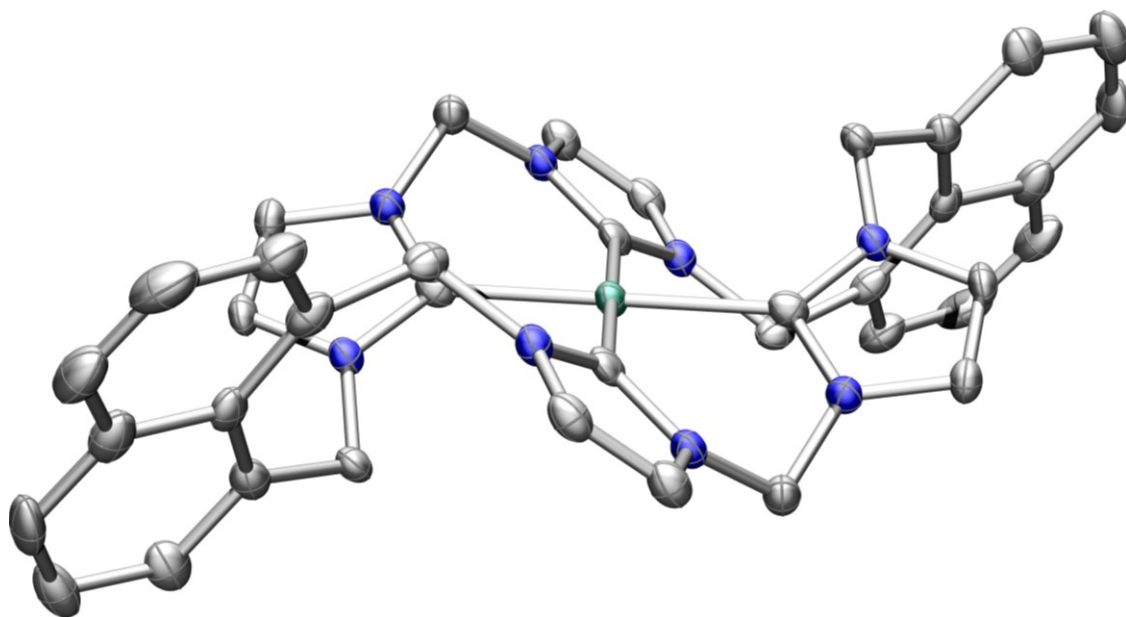


**Figure 4.15.** The solid-state structure of complex **4.13**. Hydrogen atoms and  $\text{PF}_6^-$  counterions have been omitted for clarity. Thermal ellipsoids are set at a 50% probability level. Atom color-coding: Pd Seagreen, N blue, and C grey.

An off-white powder was recovered from this mixture, which spectral properties are shown in the lower insert of the **Figure 4.14**, and by comparing the characteristic signals of the top and lower spectra to the center, it becomes evident that just this entity

forms. Critically, this entity lacks signals owing to residual imidazolium. Single-crystal X-ray diffraction of this complex as the PF<sub>6</sub>-salt, corroborates a Pd(II) ion bearing a macrocyclic tetradentate ligand, shown in **Figure 4.15**. This structure is perhaps not so surprising, bearing in mind the structure of **3.1** that was found in DMSO, **Figure 3.6**, and the excess acetate would work to fully deprotonate. Analyzing the reacting mixture without any additional base, reveals identical spectral properties to the middle insert of **Figure 4.14**, and from the isolation of unreacted **3.1** and complex **4.13**. These findings preclude any step-wise metalation approaches to heterobimetallic complexes bearing **3.1** as the ligand manifold.

Similarly, **Figure 4.16** compares the <sup>1</sup>H NMR spectra between compound **3.4** and an aliquot of **3.4** reacting with Pd(OAc)<sub>2</sub> at 80 °C after 6 hours. At first glance, the spectrum appears to contain a mixture of different products. However, the spectrum contains characteristic splitting patterns, similar to those accounted for in **Figure 4.12**. Aliquots acquired any time before, shows unreacted **3.4** and this new species. Again, the compound lack any signals consistent with unreacted imidazolium, thus again suggesting another Pd(II) ion bearing a macrocyclic tetra NHC ligand. The four sharp doublets, signals 7.93, 7.62, and 7.36, 7.01 ppm, respectively, are consistent with the C<sub>4/5</sub> protons of the ylidene-moiety, further supporting metalation.

The remaining aromatic signals are difficult to fully discern and preclude meaningful analysis. Secondly, the signals at 6.07, 5.78, and 4.36, 4.01 ppm, respectively, adopt a diastereotopic splitting (AX), which is consistent with the observations made in complex **4.9**. However, the chemical shift disparity suggests that one pair is interacting with an electron-rich moiety, *e.g.* a  $\pi$ -system. Finally, the signals at 5.17, 4.97, and 4.56 ppm, respectively, are consistent with protons owing to the ethylene-linker, experiencing geminal and vicinal coupling to explain the observed multiplicity.

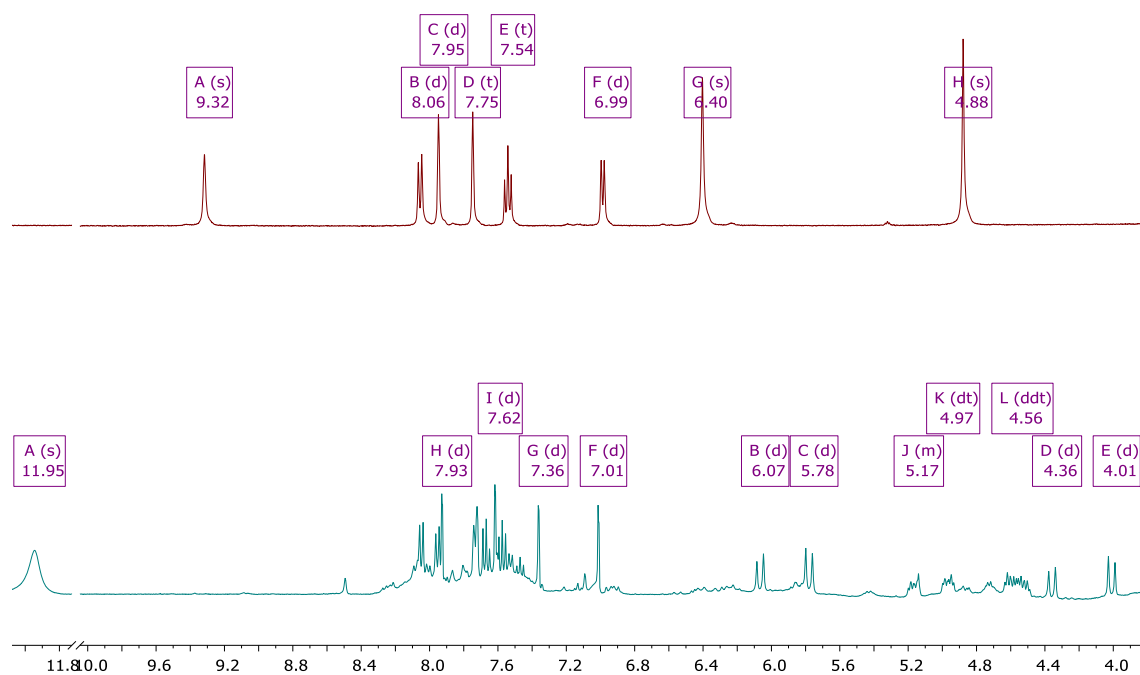


**Figure 4.16.** Metalation of **3.4** with 1.0 equiv.  $\text{Pd}(\text{OAc})_2$ . The top insert shows **3.4**, and the lower insert shows an aliquot of its reaction with  $\text{Pd}(\text{OAc})_2$  and NaOAc after 6 hours at 80 °C.

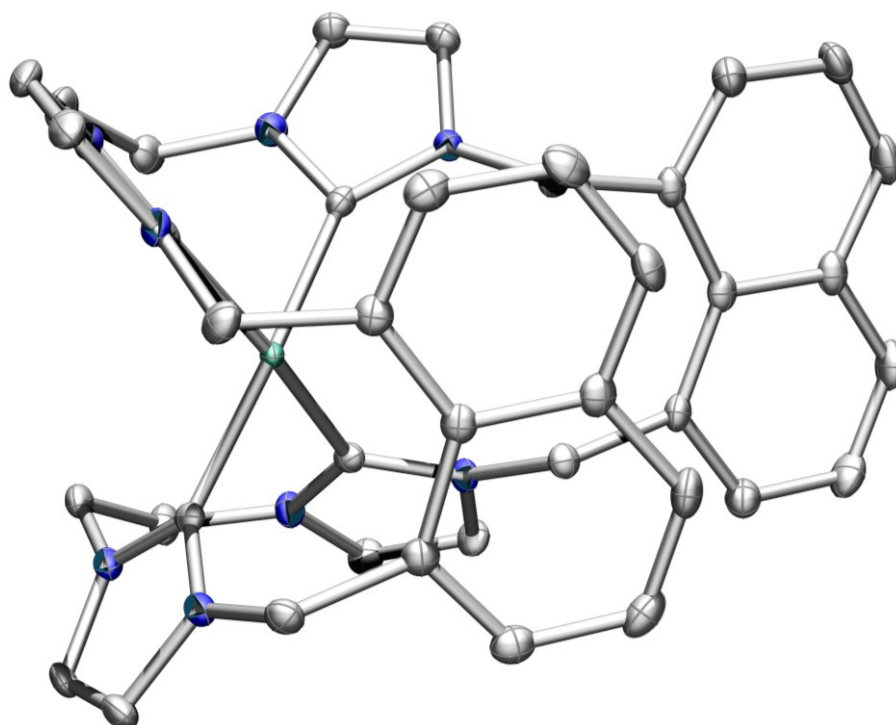


**Figure 4.17.** The solid-state structure of complex **4.14**. Hydrogen atoms, co-crystallized MeCN and bromide counterions have been omitted for clarity. Thermal ellipsoids are set at a 50% probability level. Atom color-coding: Pd Seagreen, N blue, and C grey.

These observations suggest that the entity is symmetrical, and the mirroring of signals into two sets, of which one set demonstrates a substantial upfield shift, likely is a consequence of the orientation of one of the ancillary naphthalenes. Indeed, such an interaction is present in the complex's solid-state, confirmed by single-crystal X-ray diffraction, which structure is shown in **Figure 4.17**.

The structure of complex **4.14** is quite promising, as it demonstrates the desired connectivity drawn for complexes **4.11** and **4.12** in **Scheme 4.6**, in that, the aliphatic linker constitutes the chelate rather than the naphthalene. Moreover, the bond metrics demonstrated by complex **2.1**, *cf.* **Chapter. 2**, further suggest that two proximal palladium centers tethered to the macrocyclic ligand-manifold are within reason.

Consequently, we sought to finalize the exploration of the acetate route, by reacting proligands **3.1** and **3.4** with increasing equivalents (2, 3, 4, ..., 15) of  $\text{Pd}(\text{OAc})_2$  in DMSO and DMF. Discouragingly, these reactions each resulted in the deposition of Pd-black, and any precipitates following filtration displayed spectral properties identical to the porphyrin motifs. Accordingly, metalation of **3.1** and **3.4** *via* the acetate route is summarized in **Chart 4.3** below.

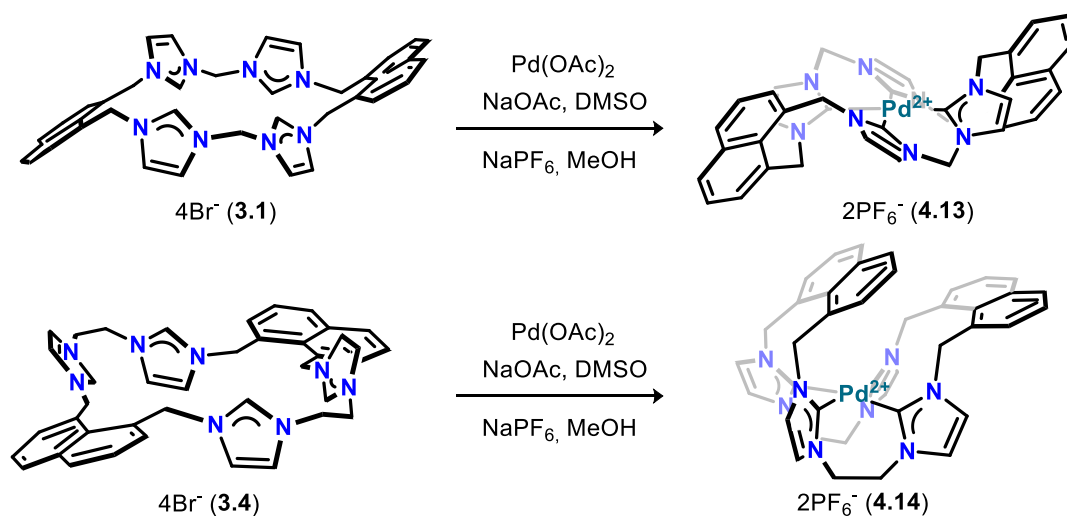


**Chart 4.3.** Complexes found following the “acetate route”. Salts **3.1** and **3.4** both yields monopalladium complexes bearing macrocyclic tetra NHC ligands.



#### 4.3.1 Structural characterization of complexes **4.13** and **4.14**

**Figure 4.15** and **Figure 4.17** demonstrate quite different coordination of Pd(II), the latter deviating from square planar. Whereas complex **4.13** crystallizes in the orthorhombic  $Pnma$  spacegroup, complex **4.14** crystallizes in the monoclinic  $P2_1/c$  spacegroup. In general, obtaining crystals of **4.13** of an appropriate quality was difficult. Regardless of counterion ( $BF_4$ ,  $PF_6$ , Br,  $BPh_4$ , OTf, OTs), the compound often crystallizes as thin plates prone to the varying extent of twinning. Additionally, suitable crystals quickly lost co-crystallized solvents leading to changes in morphology, even during data acquisition. The mediocre quality manifests in disorder displayed by multiple F-atoms of the  $PF_6$ -counterions as well as in the co-crystallized MeCN. However, applying PLATON Squeeze<sup>51</sup> successfully models the solvent disorder: 151 electrons in a volume of  $579\text{\AA}^3$  were found in 3 voids per unit cell, which is consistent with the presence of 1.81 molecules of MeCN per unit cell, accounting for 160 electrons. This solvent mask improves the overall model converging to  $R_1 = 4.79\%$  and  $wR_2 = 11.2\%$  (all data). Differently, better quality crystals of **4.14** were more readily obtained, reflected in limited disorder, and the associated model converges at  $R_1 = 3.54\%$  and  $wR_2 = 9.4\%$  (all data).

**Figure 4.18** illustrates bond metrics concerning complex **4.13**, showing palladium coordinated square-planarly by two crystallographically different C-atoms, featuring similar Pd-C bond lengths of 2.050(4) and 2.053(4) Å, respectively. The complex features symmetry operations that are consistent with the  $S_2$  ( $C_i$ ) point group, with the  $C_2$ -principal axis of rotation perpendicular to the coordination plane spanned by the NHC C atoms, and a horizontal mirror plane parallel to this plane, equivalent to an inversion center through Pd. The two distinctive imidazole-2-ylidenes are twisted at an angle ( $\phi$ ) to this plane of 34.82 and 36.63°, respectively, meaning that an orbital overlap between the  $\pi$ -symmetrical orbitals to the NHC is poor, and we may regard the coordination comprising solely of a  $\sigma$ -interaction.

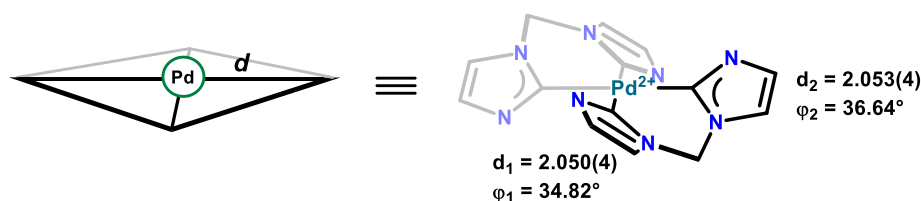


**Figure 4.18.** Illustration of bonding metrics pertaining to the core of **4.13**. The symmetry-related macrocyclic coordination comprises two distinct C atoms coordinating Pd by  $d$  Å. This coordination spans a mean plane, which the NHCs twist ( $\phi$ ) relative to.

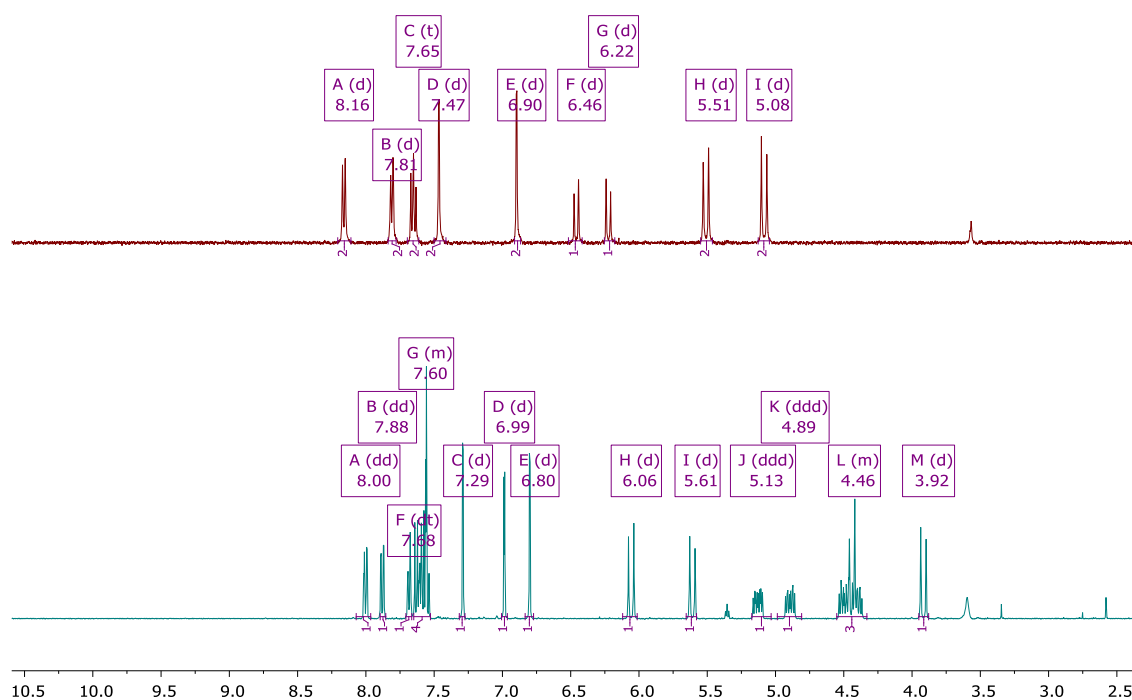


**Figure 4.19.** Comparison between  $^1\text{H}$  NMR spectra (in  $\text{CD}_3\text{CN}$ ) of **4.13** (top) and **4.14** (bottom). Both spectra reconsolidate their solid-state structure, most evidently in **4.14** by two sets of signals, one upfield-shifted.

While the solid-state structure of complex **4.13** presents a constrained structure, one can envision the protons of the methylene linker flipping between an “endo” and “exo” orientation. In this context, the Baker group demonstrates, that related imidazolium cyclophanes demonstrating fluxional behavior from a low-energy barrier between two conformations, feature broad peaks at RT<sup>52</sup>. However, the  $^1\text{H}$  NMR spectrum of complex **4.13** in  $\text{CD}_3\text{CN}$ , shown in the top-insert of **Figure 4.19**, feature well-resolved, well-defined resonances consistent with half of the molecule and lack any broad signals; protons owing to the methylene and benzylic position demonstrate a characteristic

diastereotopic splitting (AX). This observation suggests that any conformational changes between an endo and exo orientation of these protons, either occur too rapidly or not at all on the NMR scale at RT.

Generally, the IR spectrum of these complexes provide little useful information as the complexes lack characteristic groups beyond signals consistent with stretches owing to  $sp^2$  and  $sp^3$  C-H ( $>3000\text{ cm}^{-1}$ ), the imidazole-2-ylidine ( $1500 - 1200\text{ cm}^{-1}$ ) C-N stretches, and P-F counterion ( $750\text{ cm}^{-1}$ ), as seen in **Figure 4.20**, which. This observation renders NMR and solid-state by far the strongest means of characterization.

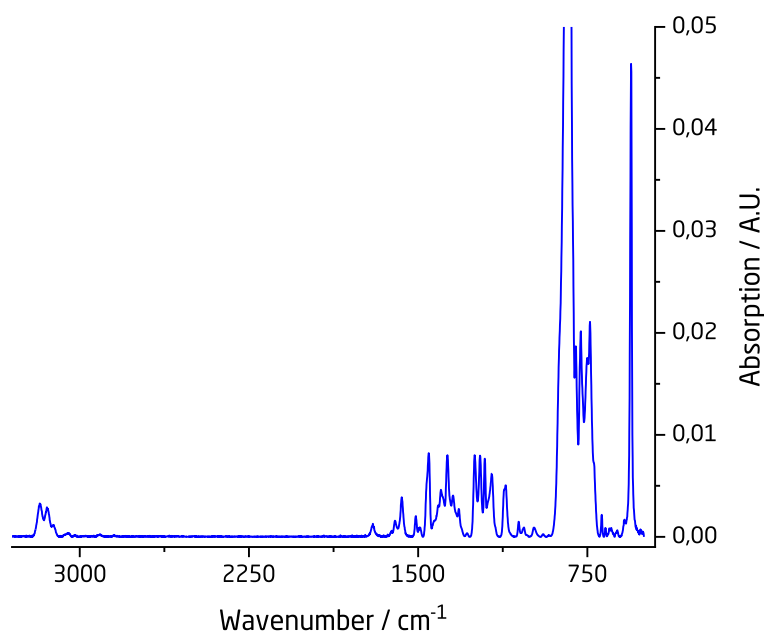


**Figure 4.20.** FT-IR spectrum of complex **4.13**. Other than confirming the high symmetry of the complex, no characteristic signals are found; a multitude of C-H, C-N, and P-F stretches.

Complex **4.14** features a Pd(II) ion, that despite a  $d^8$  electronic configuration, differs in its coordination from an expected square-planar. **Figure 4.21** illustrates bonding metrics pertaining to complex **4.14**, which feature palladium distanced  $0.141\text{Å}$  above a mean plane spanned by the imidazole-2-ylidenes. Moreover, each C atom is crystallographic different, varying in their Pd-C bond length between,  $2.037(3)$ ,  $2.026(3)$ ,  $2.051(3)$ , and  $2.055(3)\text{Å}$ , respectively. Each of these bonds, angle  $\theta^\circ$  out of this plane by  $4.00$ ,  $4.04$ ,  $3.99$ , and  $3.95^\circ$ , respectively. Finally, each of the imidazole-2-ylidenes

demonstrates a twist angle ( $\varphi$ ) to the mean coordination plane of 66.07, 72.80, 58.22, and 75.33°, respectively.

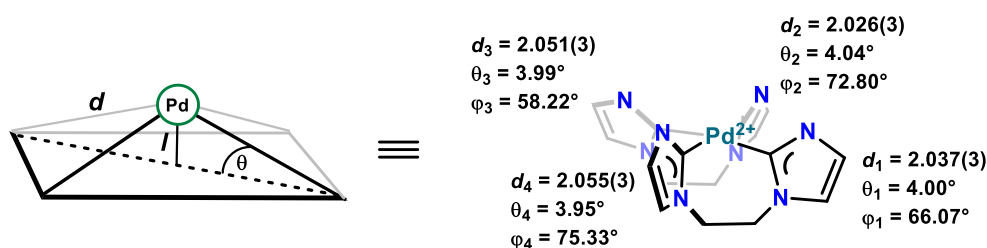


**Figure 4.21.** Illustration of bonding metrics pertaining to the core of **4.14**. The four coordinating C atoms span a mean plane, wherein each C atom binds to Pd at  $d$  Å, at an angle of  $\theta$  degrees, concerning this plane, which Pd is distanced  $l$  Å above.

Considering **Figure 4.17**, the relative orientation of aliphatic linker and ancillary naphthalene is different from that in complex **4.10** (**Figure 4.10**). Instead, complex **4.14** features a parallel orientation of the ethylene-linker, below the plane of coordination. This geometrical feature ultimately results in an assembly wherein a palladium center sits within a “pocket”, like a tetra NHC Ni(II)-**complex** reported by Murphy and Spicer<sup>53</sup>, and Hahn, *vide infra*. The lower spectrum of **Figure 4.19** shows a well-resolved  $^1\text{H}$  NMR spectrum of complex **4.14** in  $\text{CD}_3\text{CN}$ , which, like **4.13**, also reflects the solid-state structure. The signals outlined in the description of the metalation-intermediate from  $\text{Pd}(\text{OAc})_2$  hold; two pairs of the same signals are present, of which one is set upfield-shifted resulting from interacting with a proximal  $\pi$ -system.

Protons in the aromatic region owing to naphthalene are consistent with a symmetrical 1,8-disubstitution of naphthalene, while those owing to the ylidene-moiety reflects two distinctive NHCs. The benzylic position reflects two different chemical environments consistent with a set at the periphery (6.06, 5.61 ppm) and a set at the center of the “pocket” (4.46, 3.92 ppm), which both demonstrate a characteristic geminal coupling (AX).

Similarly, the signals owing to the ethylene-linker demonstrate both geminal and vicinal coupling patterns manifesting in a doublet of doublets of doublets (dd). Similarly,

the associated  $^{13}\text{C}$  NMR spectrum demonstrates signals in pairs of two, of which one set is upfield-shifted, as shown in **Figure 4.22**. This effect is more pronounced at the ethylene (54.9 vs. 54.1 ppm) and benzylic (49.7 vs. 48.4 ppm) positions than at the imidazole-2-ylidene  $\text{C}_2\text{-Pd}$  position (168.0 vs. 167.9 ppm). These observations combined, are consistent with a mirror plane bisecting the complex perpendicularly through the naphthalenes, and the compound's solid-state mirroring its solution structure, and *vice versa*.

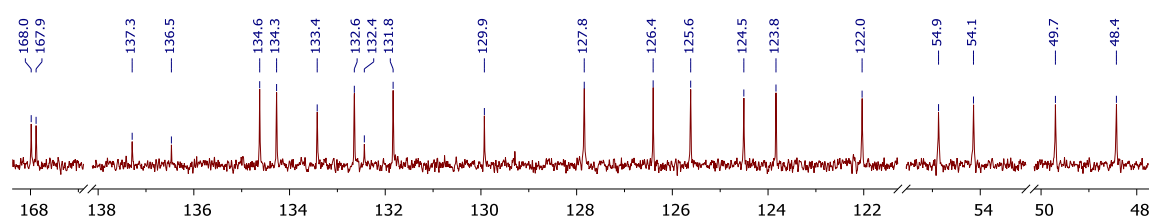


**Figure 4.22.** Selected regions of the  $^{13}\text{C}$  NMR spectrum ( $\text{CD}_3\text{CN}$ ) of **4.14**. In solution, the only two different coordinating C atoms are found, different from the four crystallographically inequivalent C atoms.

This difference in Pd-C binding is like that found in the structures of **4.9** and **4.10**, in that the methylene-linked chelate yields similar bond lengths, whereas the ethylene-linked chelate results in bond lengths with a significant disparity. This difference, however, may just be a consequence of crystal packing.

The coordination of Pd in complex **4.14** is curious, and we sought to explore whether, and how easily conformational changes are thermally induced, conceptually illustrated in **Figure 4.23**; are the ancillary naphthalenes locked in place, or do the benzylic positions readily twists between an endo and exo orientation (1)? does the structure twist into a configuration like complex **4.13** (2)?

To this end, we obtained  $^1\text{H}$  NMR spectra of complex **4.14** over a temperature range, varying from  $-30\text{ }^\circ\text{C}$  to  $70\text{ }^\circ\text{C}$ , at  $20\text{ }^\circ\text{C}$  interval, the individual spectra stacked and presented in **Figure 4.24**. Due to instrumentation limitations, the temperatures  $-30\text{ }^\circ\text{C}$  and  $70\text{ }^\circ\text{C}$  constitute the possible extrema.

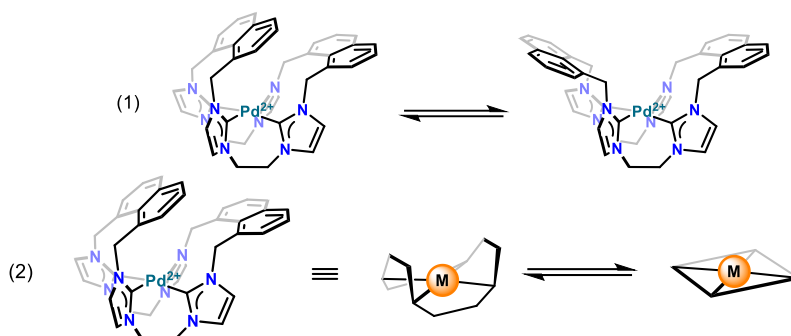


**Figure 4.23.** Suggested fluxional behavior of complex **4.14**. Suggested processes observable employing variable-temperature NMR.

Fluxional properties of macrocyclic poly imidazolium salts have been studied by the Baker group, demonstrating interconversion between different conformers<sup>52</sup>. Characteristic to these systems, is multiple conformations are discernable from resonances featuring well-defined multiplicities giving relative integration ratios consistent with multiple entities. Upon heating, these signals coalesce into broad peaks, however, no secondary set of distinctive signals occur.

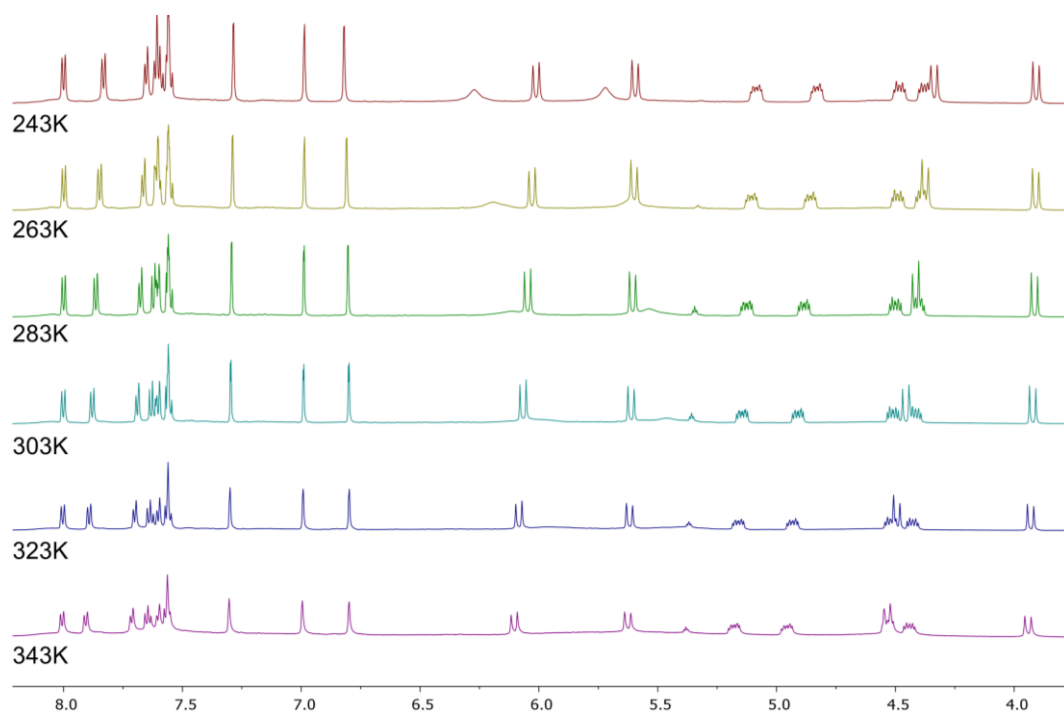


**Figure 4.24.** Stacked  $^1\text{H}$  NMR spectra (in  $\text{CD}_3\text{CN}$ ) of complex **4.14** at selected temperatures. The current temperature range does not appear to unequivocally demonstrate whether a “breathing” motion is possible.

The trend that may be extracted from the spectra shown in **Figure 4.24**, is that a structure consistent with the solid-state is present throughout. However, as complex **4.14** is heated, minor changes appear to take place, consistent with loss of favorable  $\pi$ -

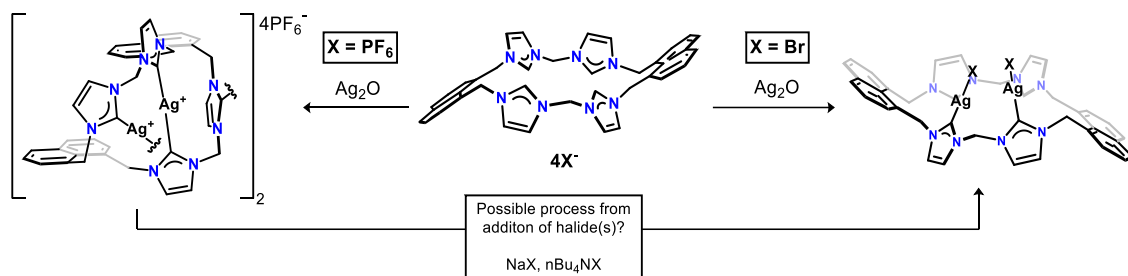
interactions, from an observable downfield-shift in three moieties. Of the most upfield-shifted aromatic protons, these appear to split into three discernable signals; the ethylene-back signals similarly, albeit slightly, similarly downfield shifts, and the second-most upfield-shifted doublet appear to downfield-shift significantly.

Concerning the first process presented in **Figure 4.23**, the current data may be interpreted in two different ways: 1) the benzylic- $\pi$  interaction is quite strong, suggesting that a structure like the solid-state persist in solution, or 2) the interchange between endo-exo position at the periphery naphthalene may be quite fluxional, and to block the motion, even colder temperatures are required. As such, the complex needs further evaluation at even lower operating temperatures. Concerning the second process suggested, it is unrealistic to realize such a process, from the retention of splitting patterns and chemical shift values throughout.

While Pd(II) may adequately serve to elucidate connectivity, its bonding inferred to different metals, to leverage a would-be asymmetric bonding pocket and realize catalysis, early to mid-transition metals are of interest, as these tend to form more stable (intermediary) compounds demonstrating a square-based pyramidal coordination geometry, relative to a putative Pd(IV) complex originating from oxidation of complex **4.14**. For instance, the chemistry between Ru or Fe are ideal candidate, however, due to time constraints, and it being outside of the scope, neither complexes were pursued.

## 4.4 Seeking dipalladium complexes via transmetalation

### 4.4.1 Exploration of silver-intermediates: synthesis and characterization



**Scheme 4.7.** The conceptual framework for Ag-metalation. Two suggested structures, in their preparation, are counterion dependent, and a suggested transformation of one to the other.

In parallel with our concurrent deprotonation-metalation experiments, we sought to investigate the nature of the complexes following metalation of **3.1** and **3.4** with Ag(I) under various conditions, as illustrated with **3.1** (**3.2** or **3.3**) in **Scheme 4.7**.

Specifically, we sought to understand the intermediary silver complexes' connectivity, and establish a relationship between the nature of the counterions and the complex' connectivity, and these Ag-compounds' transmetalation product(s), because transmetalation of NHC-precursors where Ag tethers the macrocycle to itself, demonstrate a predisposition to macrocyclic metal-complexes, *vide supra*.

Additionally, we wanted to answer whether any [NHC-Ag-NHC]<sup>+</sup>-dimers, as on the left-hand side of **Scheme 4.7**, in presence of halide(s), rupture into the fully heteroleptic NHC-AgX (X = Cl, Br, or I) congeners, depicted on the right-hand side of **Scheme 4.7**, to ultimately furnish the formation of the envisioned complexes **4.11** and **4.12**.

For brevity, only reactions with Ag<sub>2</sub>O are described in the following section, because other Ag(I)-sources, *e.g.* Ag<sub>2</sub>CO<sub>3</sub>, AgOAc, yield the same results. Metalation of **3.1** (and **3.4**) was investigated in DMSO and MeOH following our previous results, suggesting that **3.1** may undergo solvent-dependent selective metalation, which further seems supported by the isolation of complex **4.13** from DMSO and DMF.



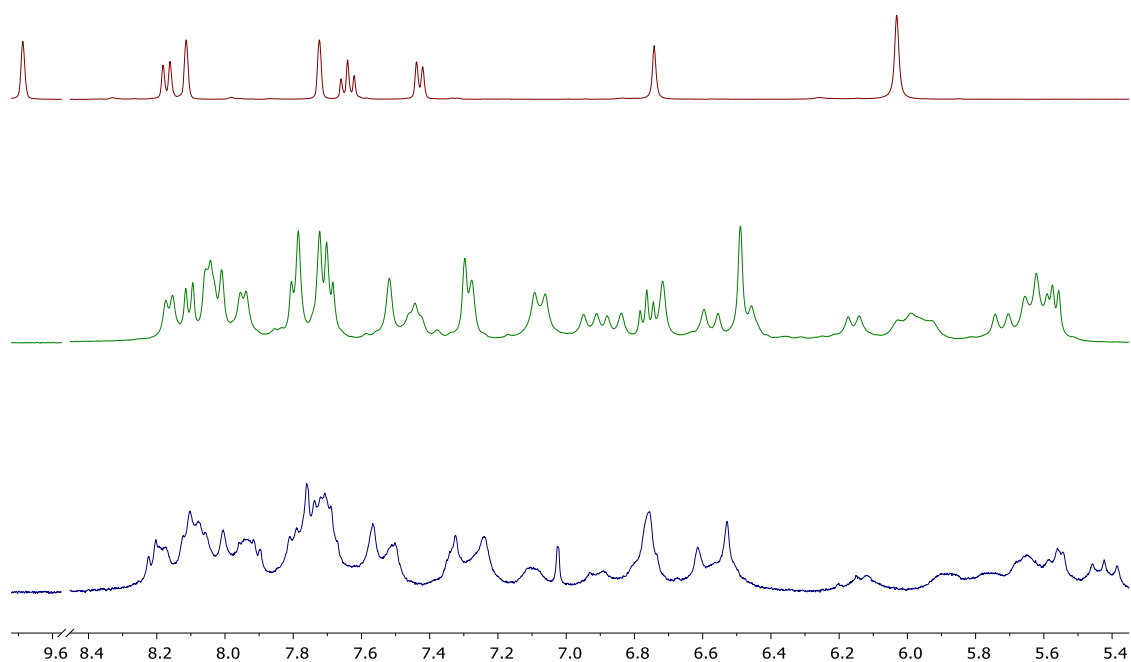


**Figure 4.25:** *Transmetalation of 3.1 in DMSO.* Spectral comparison between  $^1\text{H}$  NMR spectra (in  $\text{DMSO}-d_6$ ) of compound **3.1** (top), **3.1** equiv.  $\text{Ag}_2\text{O}$  in  $\text{DMSO}$  (middle), and **3.1** + 5.2  $\text{Ag}_2\text{O}$  (lower insert).

**Figure 4.25** compare the  $^1\text{H}$  NMR spectra of compound **3.1**, to materials following metalation of compound **3.1** with varying equivalents of  $\text{Ag}_2\text{O}$ : the middle spectrum accounts for 2.1 equivalents, and in the lower spectrum 5.2 equivalents were used; both reveal a full consumption of **3.1**, transformed into an entity less symmetrical than what was found from  $\text{Pd}(\text{OAc})_2$  metalation. A similar species is found from metalation in DMF. This spectrum, despite difficult to fully discern, seems to produce the same signals in pairs of two, such as doublets owing to the induced diastereotopicity at the benzylic positions, as well as the imidazole-2-ylidene  $\text{C}_{4/5}$  positions. The corresponding 1D  $^{13}\text{C}$  NMR spectrum does not provide meaningful information for analysis.

The flasks, despite being covered in foil and the reaction conducted under the preclusion of light, were consistently covered by a pleasingly looking Ag-mirror; excess  $\text{Ag}_2\text{O}$  (>3.0 equiv.), covers the whole flask, suggestive of extensive decomposition. When recovered filtrate was passed through a celite pad eluting in MeOH, a white, particularly light-sensitive powder was found in low yields (<10%, assuming monomeric product), which we were unable to obtain X-ray quality single-crystals of. Moreover, this material

demonstrates properties consistent with a (water-soluble) salt, rather than a neutral species, and therefore connectivity, more appropriately in line with the structure depicted on the left-hand side of **Scheme 4.7**. In other words, a macrocycle is linked to itself by at least one bridging Ag atom, consistent with the right-most architecture illustrated in **Figure 4.5**.

Additionally, metalation in DMSO and DMF, in addition to decomposition products, yields ill-defined materials. **3.4** reacts similarly under these reaction conditions; isolable products include decomposition products and light-sensitive water-soluble salts.

Pursuant to heteroleptic NHC-Ag-Br complexes, we then sought to explore the metalation of **3.1** in MeOH and DCM; the latter does not furnish any reaction owing to insolubility of the starting material. **Figure 4.26** shows the isolated material from transmetalation in MeOH (spectrum recorded in MeOH-*d*<sub>4</sub>), corroborating that **3.1** readily transform into a compound that possess similar spectral properties to that of **4.14**.

The aromatic signals reflect two sets, owing to the C<sub>2</sub>-C<sub>4</sub> of the naphthalene-backbone (signals A, B, C, D, F, and J). The benzylic and methylene <sup>1</sup>H signals both demonstrate a diastereotopic splitting (AX). Curiously, the signals owing to the C<sub>4/5</sub> positions of the ylidene (signals J, F) only reflect a single environment.

This material is isolated as a quite light-sensitive white water-soluble salt (<sup>1</sup>H NMR spectrum in D<sub>2</sub>O, shown in **Figure 4.27**) at an improved yield (>60%, assuming a dimeric product).

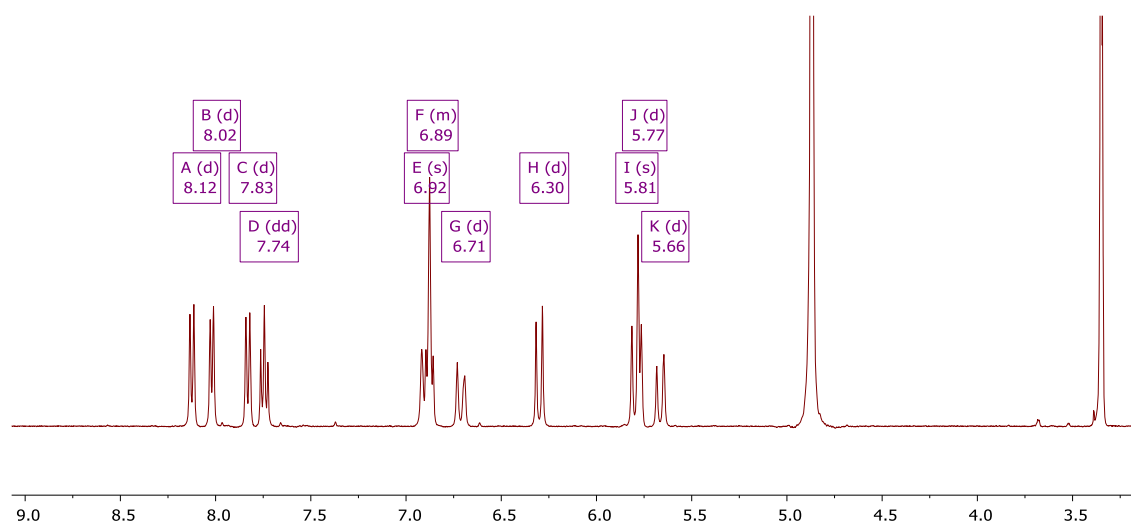


**Figure 4.26.** Transmetalation of **3.1** in MeOH.  $^1\text{H}$  NMR spectrum of isolated material in MeOH- $d_4$ .

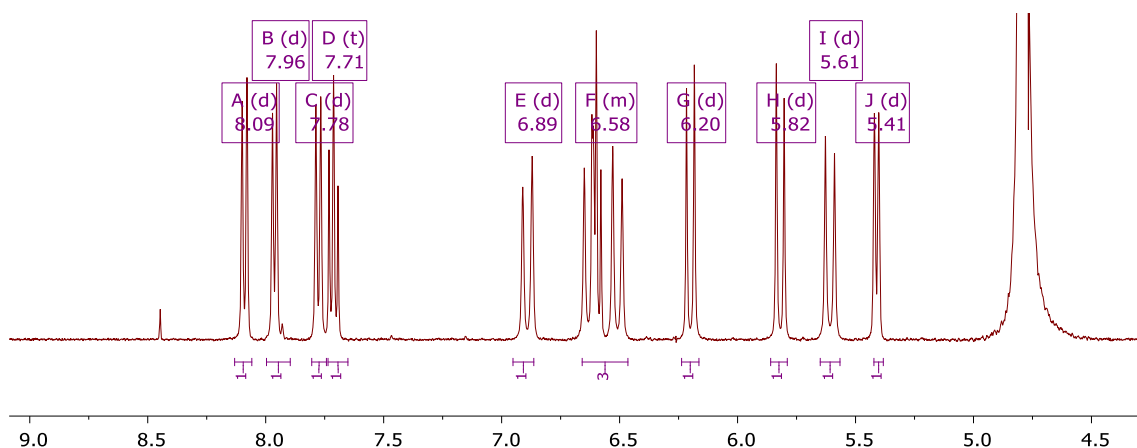
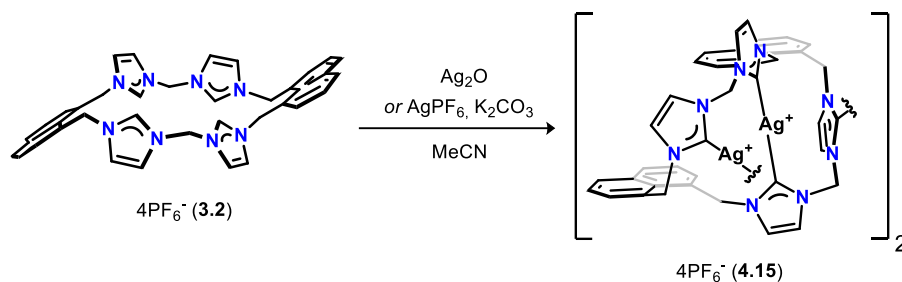


**Figure 4.27.** Transmetalation of **3.1** in MeOH.  $^1\text{H}$  NMR spectrum of isolated material in  $\text{D}_2\text{O}$ .

The connectivity of the salt remains unclear, and structural elucidation concerning the NHC-Ag-NHC linkage is key to understand whether these silver-intermediates are competent precursors for the desired complexes **4.11** and **4.12**. Specifically, is the compound a dimer, wherein a silver-atom tethers each of the macrocycles to itself, which predisposition transmetalation towards macrocyclic products, opposing that of four (a)symmetrical NHC-Ag-NHC linkages. As a result of spectral and chemical properties being consistent with a salt, we instead sought to obtain structural insights *via* the Ag complexes following metalation of the  $\text{PF}_6$ -salt, **3.2**, as schematized in **Scheme 4.8**.



**Scheme 4.8.** *Ag-metalation of compound 3.2.* Synthetic strategy to prepare a dimeric, tetrasilver(I) complex.

The  $^1\text{H}$  and  $^{13}\text{C}$  NMR spectra of the isolated material are shown in **Figure 4.28**, featuring a similar symmetry to the bromide-adduct, and two distinctive C atoms that each couple to  $^{107/109}\text{Ag}$ . This complex, when isolated, appears much less prone to decomposition than the bromide adduct, however, still decomposes in presence of light: transitioning from a white to grey powder, forming insoluble grey/black particles. This complex is isolable in even greater yield (assuming a dimeric nature, >90%), and we were able to obtain a solid-state structure, albeit as the triflate-salt, which is shown in **Figure 4.29**.

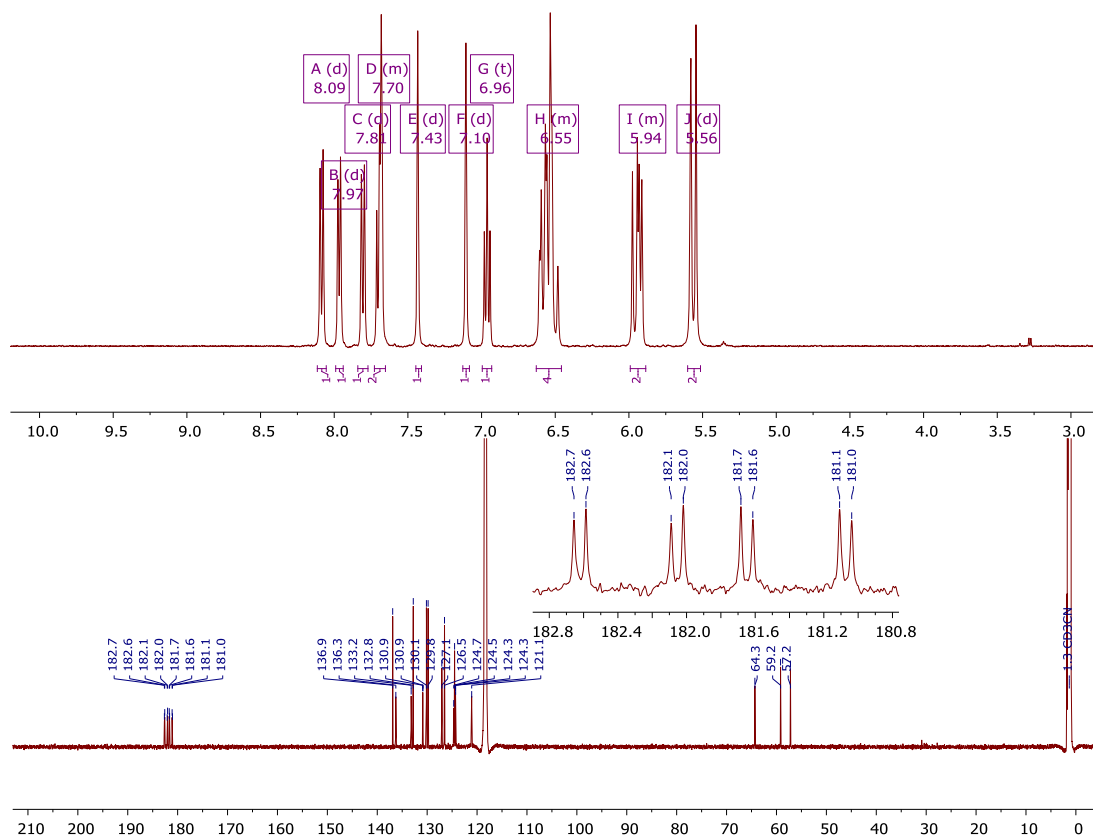


**Figure 4.28.** *Transmetalation of compound 3.2 MeCN.* Spectra recorded in  $\text{CD}_3\text{CN}$ : top spectrum  $^1\text{H}$  NMR spectra (400MHz), lower spectrum  $^{13}\text{C}$  NMR spectrum (201MHz).

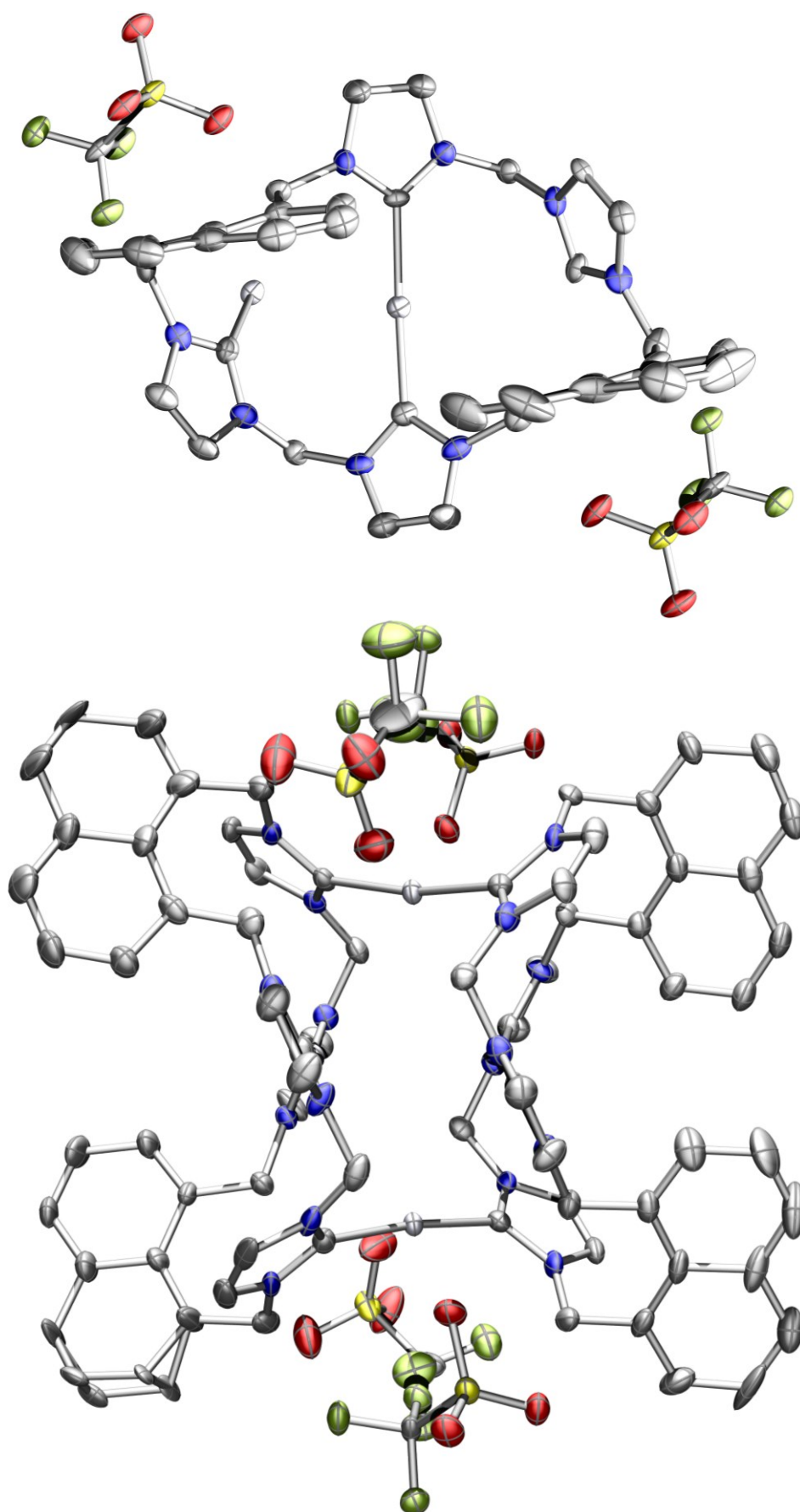


**Figure 4.29.** *Tetrasilver dimer, complex 4.15.* Hydrogen atoms have been omitted for clarity. Thermal ellipsoids are set at a 30% probability level. Atom color-coding: Ag silver, N blue, F yellow-green, S yellow, and C grey.

Unfortunately, the crystals were twinning in multiple planes, which is evident from the presented structure; the naphthalene moiety on the lower left-hand side demonstrate disorder over two positions alongside ill-defined co-crystallized MeCN. We sought to obtain (and are still seeking) better crystals, but we experience similar problems as with **4.13**; extensive twinning, morphological changes during diffraction, in addition to silver-decomposition. While the solid-state work to corroborate connectivity, the low quality precludes meaningful discussion on bond metrics. However, **Figure 4.29** is useful in reconciling the connectivity of the solid state with the entity in the solution.

The signals, their splitting, and relative integration of the  $^1\text{H}$  NMR spectrum, **Figure 4.28**, in conjunction with two well-defined downfield-shifted doublets in the  $^{13}\text{C}$  NMR spectrum, are all consistent with a coordination environment shown in the top part of **Figure 4.29**.

The  $^1\text{H}$  NMR spectrum features different aromatic signals owing to the various positions of a single naphthalene moiety ( $\text{C}_2$  through  $\text{C}_7$ ), the four signals owing to two different ylidene-moieties, and finally, a single distinctive environment for the signals owing to the benzylic and aliphatic linker, respectively.

The  $^{13}\text{C}$  NMR spectrum unequivocally demonstrates two distinctive C coordinating to Ag: **C-1**  $^1J(^{109}\text{Ag}-^{13}\text{C}[182.7, 181.6]) = 209.5\text{Hz}$  and  $^1J(^{107}\text{Ag}-^{13}\text{C}[182.6, 181.7]) = 182.4\text{Hz}$ ; **C-2**  $^1J(^{109}\text{Ag}-^{13}\text{C}[182.1, 181.0]) = 211.4\text{Hz}$  and  $^1J(^{107}\text{Ag}-^{13}\text{C}[182.0, 181.1]) = 183.2\text{Hz}$ . The increase in magnetic field strength helped us in discerning these four signals, which previously were ambiguous, at best.

We were unsuccessful, despite exhaustive attempts, in transforming **4.15** into a heteroleptic NHC-Ag-X complex; the isolable material predominantly consists of various Ag-halide salts and ligand decomposition products.

Compound **3.4** similarly reacts with Ag<sub>2</sub>O in MeOH, furnishing the formation of an isolable white and light-sensitive salt. As evident from the <sup>1</sup>H and {<sup>1</sup>H-<sup>1</sup>H} COSY NMR spectra, shown in **Figure 4.30**, previously observed splitting patterns are observed consistent with metalation *e.g.* two set of signals, each reflecting naphthalene in a distinctive chemical environment: set 1 comprise signals A, B, and C; set 2 comprise signals D, H, and K, as well splitting consistent with geminal and vicinal coupling, *viz.* signals M and N. We successfully obtained a few single-crystals of this adduct, of suitable quality for X-ray diffraction, the structure shown in **Figure 4.31**, revealing a trimeric hexasilver-NHC-complex; each macrocycle tethers to itself by one Ag(I)-atom, which further adjoins to two different macrocycles.

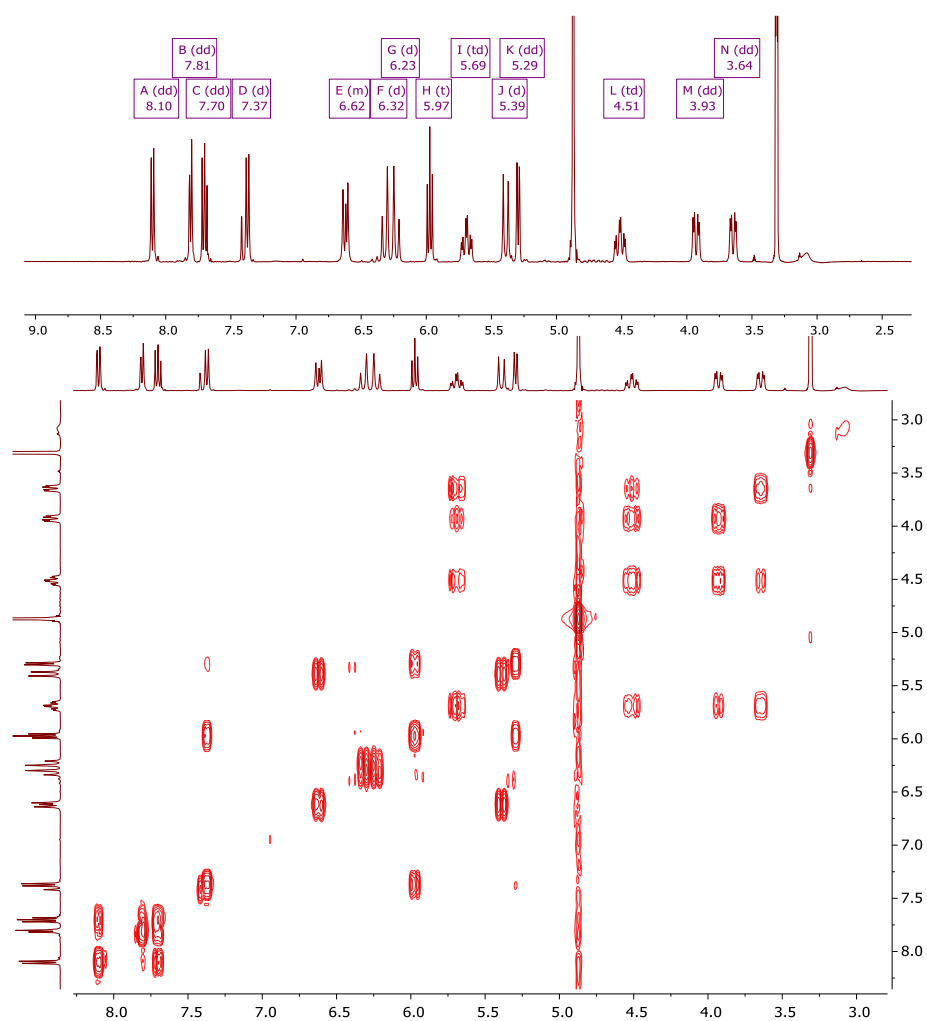


**Figure 4.30.** Reacting compound **3.4** with Ag<sub>2</sub>O in MeOH, isolated material dissolved in MeOH-*d*<sub>4</sub>. Top spectrum: <sup>1</sup>H NMR spectrum, C<sub>6</sub>H<sub>6</sub> residual from lyophilization. Lower spectrum: associated {<sup>1</sup>H-<sup>1</sup>H} COSY spectrum.

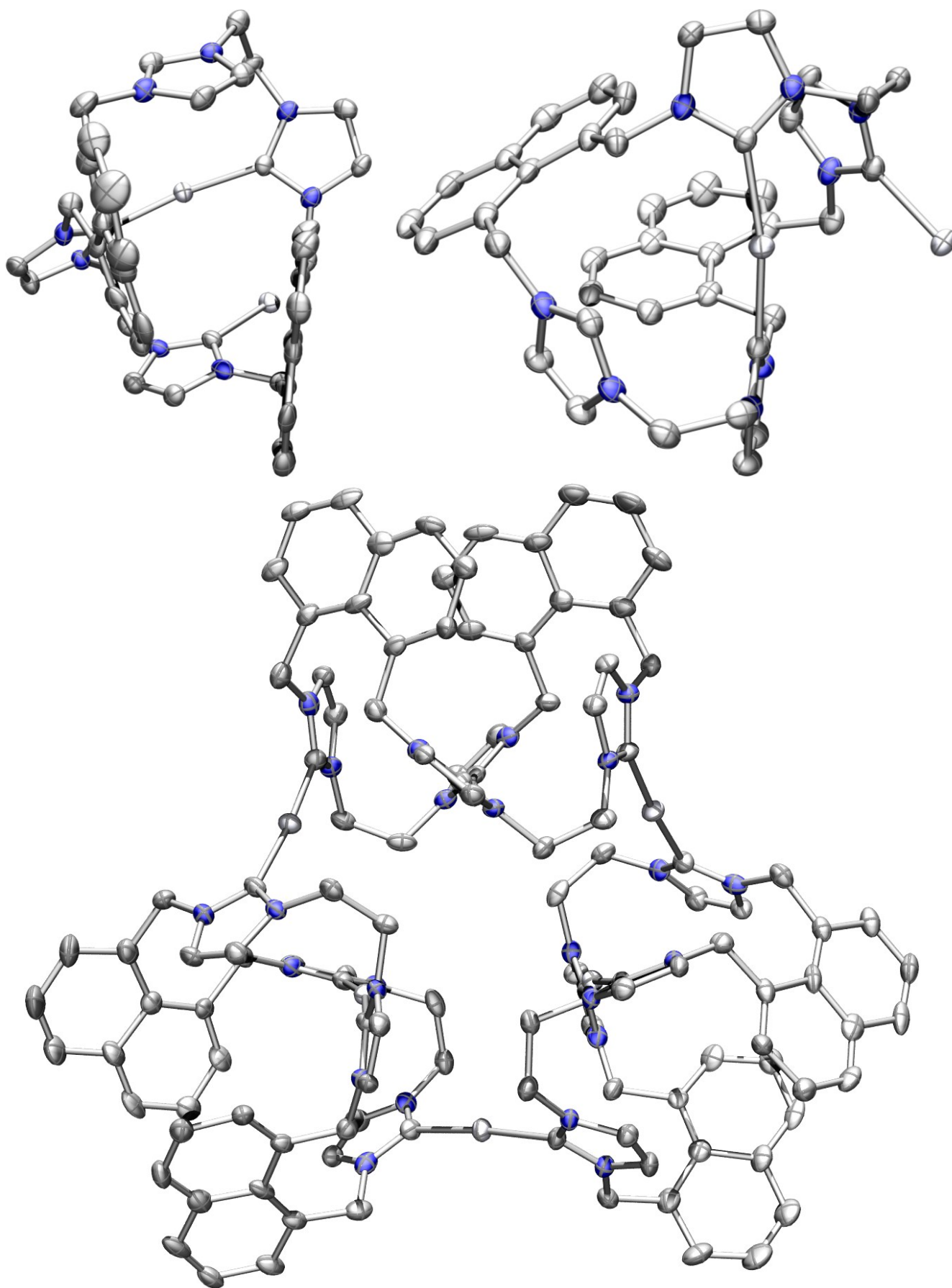
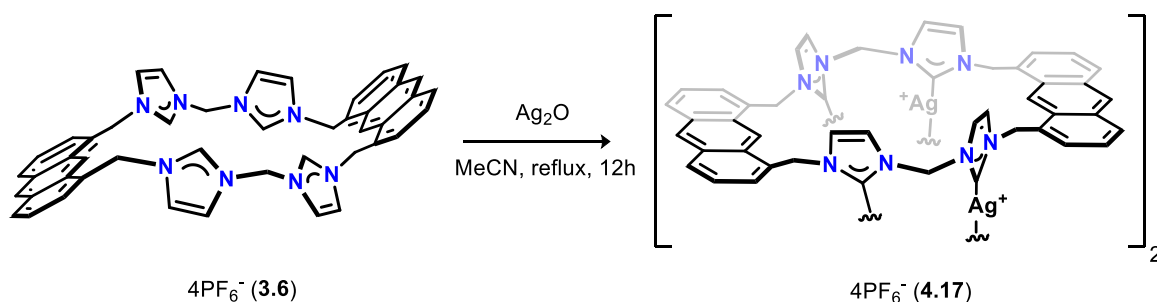


**Figure 4.31.** *Hexasilver trimer, complex 4.16.* Hydrogen atoms have been omitted for clarity. Thermal ellipsoids are set at a 50% probability level. Atom color-coding: Ag silver, N blue, and C grey.



Unfortunately, extensive amounts of ice condensed around the crystal during diffraction, which precludes a meaningful discussion on bond metrics, and bromide ions have not been possible to unequivocally assign.

It is likely that the analogous Ag-salt of **3.1** shares a similar connectivity to this compound, instead as a dimer. Despite exhaustive attempts, the acquisition of other crystals of suitable quality for X-ray diffraction was unsuccessful within the time constraints of this PhD study. Like **4.15**, complex **4.16** neither transform into a corresponding NHC-Ag-X complex.



**Scheme 4.9.** Metalation of compound **3.6**. Suggested connectivity of the intermediary silver complex, which differs from the naphthalene-based macrocycles.

Finally, we then sought to explore the analogous metalation of the anthracene-based macrocycle (**3.6**), as show in **Scheme 4.9**. The amount of material was limited due to the stage of the PhD study which compound **3.6** was isolated at.

Despite this limitation, we can juxtapose spectral differences of this adduct with those of the preceding structures, assess significant differences following transmetalation, and evaluate the likelihood that this complex results in any different transmetalation products.

The isolable salt from the reaction between **3.6** and  $\text{Ag}_2\text{O}$  is as white, light-sensitive, and insoluble in apolar solvents; consistent with the other  $\text{PF}_6$  salts. The  $^1\text{H}$  NMR spectrum (in  $\text{CD}_3\text{CN}$ ) of this Ag-isolate, shown in **Figure 4.32**, features previously described splitting patterns, however, is much simpler than **4.15** and **4.16**.

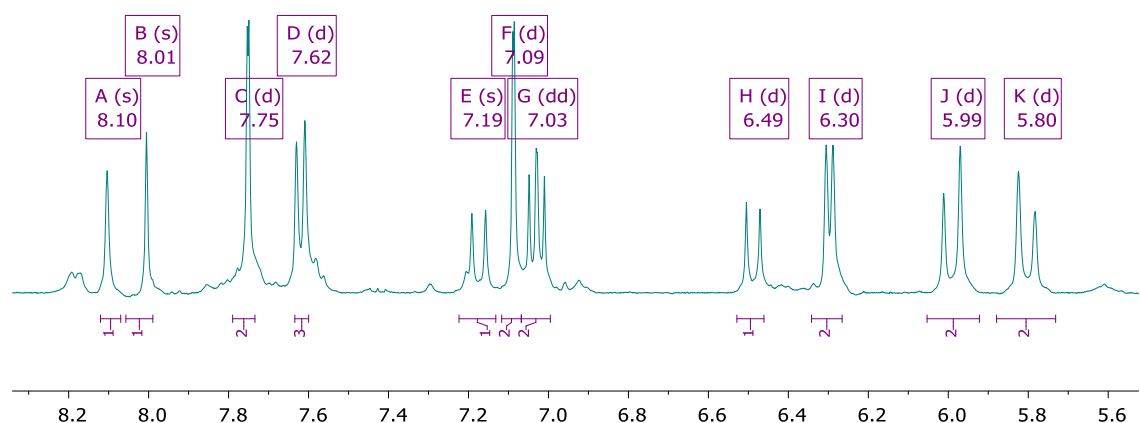


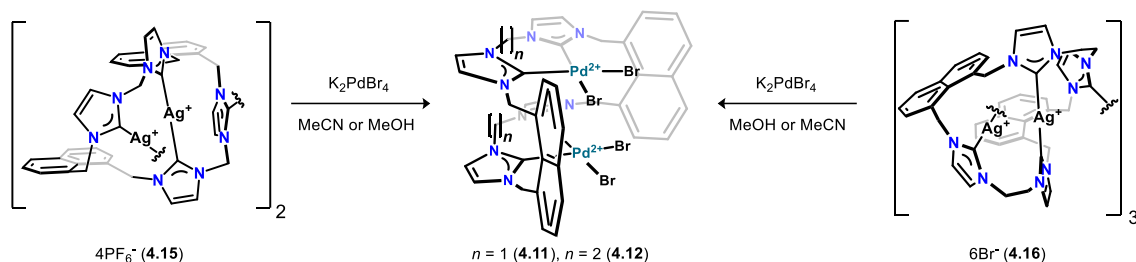
**Figure 4.32.**  $^1\text{H}$  NMR spectral properties (in  $\text{CD}_3\text{CN}$ ) of the silver-adduct following Ag-metalation of compound **3.6**. The spectrum's simplicity suggests that the intermediary silver complex demonstrate a different connectivity from preceding Ag-complexes.

The signals, starting from the left-hand side, feature two singlets owing to the  $\text{C}_{9/10}$  position of the anthracene moiety, followed by the characteristic doublets of the ylidine  $\text{C}_{4/5}$  positions. Two doublets, signals D and I, and a triplet, signal G, are consistent with the periphery of the anthracene  $\text{C}_{2,4}$  positions. Signals J and K demonstrate a diastereotopic splitting and a chemical shift consistent with the benzylic protons, leaving signals E and H; similarly adopting a diastereotopic splitting, these signals are owing to the protons of the and the aliphatic linker. The relative resonance integration further supports such an assignment.

The simplicity of the  $^1\text{H}$  NMR spectrum of **Figure 4.32** is consistent with the center architecture of **Figure 4.5**, in that no Ag binds across a would-be “pocket”, as found in **4.15** and **4.16**. Rather, we instead suggest that this compound is a dimer with four distinctive NHC-Ag-NHC tethers.

Unfortunately, all the material we had decomposed before we were able to submit it to an 800MHz instrument to obtain a meaningful  $^{13}\text{C}$  NMR spectrum, further preventing us from obtaining solid-state structure to support this postulate, as well as subsequent transmetalation studies.

#### 4.4.2 Exploring transmetalation as means of synthesizing dinuclear complexes



**Scheme 4.10.** The conceptual framework for transmetalation towards dinuclear complexes. Utilizing previous findings, an excess of Pd(II)-ate salts were added to NHC-transfer reagents, attempting to access ditopic Pd(II) halido complexes.

From our initial transmetalation studies, *cf.* section 4.2.2,  $[\text{NHC}_2\text{Ag}]\text{-PF}_6^-$  precursors react with  $\text{K}_2\text{PdBr}_4$ , rendering the isolation NHC-chelate Pd(II) dibromido complexes possible. We sought to explore whether any of the silver intermediates of **3.1** and **3.4** would facilitate a similar transformation, as outlined in **Scheme 4.10**.

Exploring transmetalation under reductive conditions was undertaken to probe whether any Pd(II), in the precursor or (partial) transmetalation intermediates, reduces to Pd(I), leading to the formation of Pd-Pd bond, to mitigate porphyrin formation. However, the only products isolable from this approach were complexes consistent with the porphyrin motif, *viz.* **4.13** and **4.14**. The analogous  $\text{PF}_6^-$ -salts of complex **4.17** similarly, react to a great excess (>40 equiv.) of  $\text{K}_2\text{PdBr}_4$  resulting in only the respective macrocyclic complexes, but as mixed salt of bromide and  $\text{PF}_6^-$ . These results support the notion that the “intra macrocyclic” Ag(I) tether predisposes the transmetalation towards thermodynamically favored porphyrin-analogue products.

Following these findings, we instead sought to obtain insight into the Ni(II) structure of **4.13** to understand its coordination to  $3d$  metals, as metal-coordination found in *N*-porphyrin and similar tetra-NHC complexes sometimes feature an ion protruding out of the “pocket”. Exposing complex **4.16** to  $\text{NiCl}_2(\text{glyme})$  furnish the transmetalation into an isolable complex, **4.18**, in excellent yield, as shown in **Figure 4.33**.

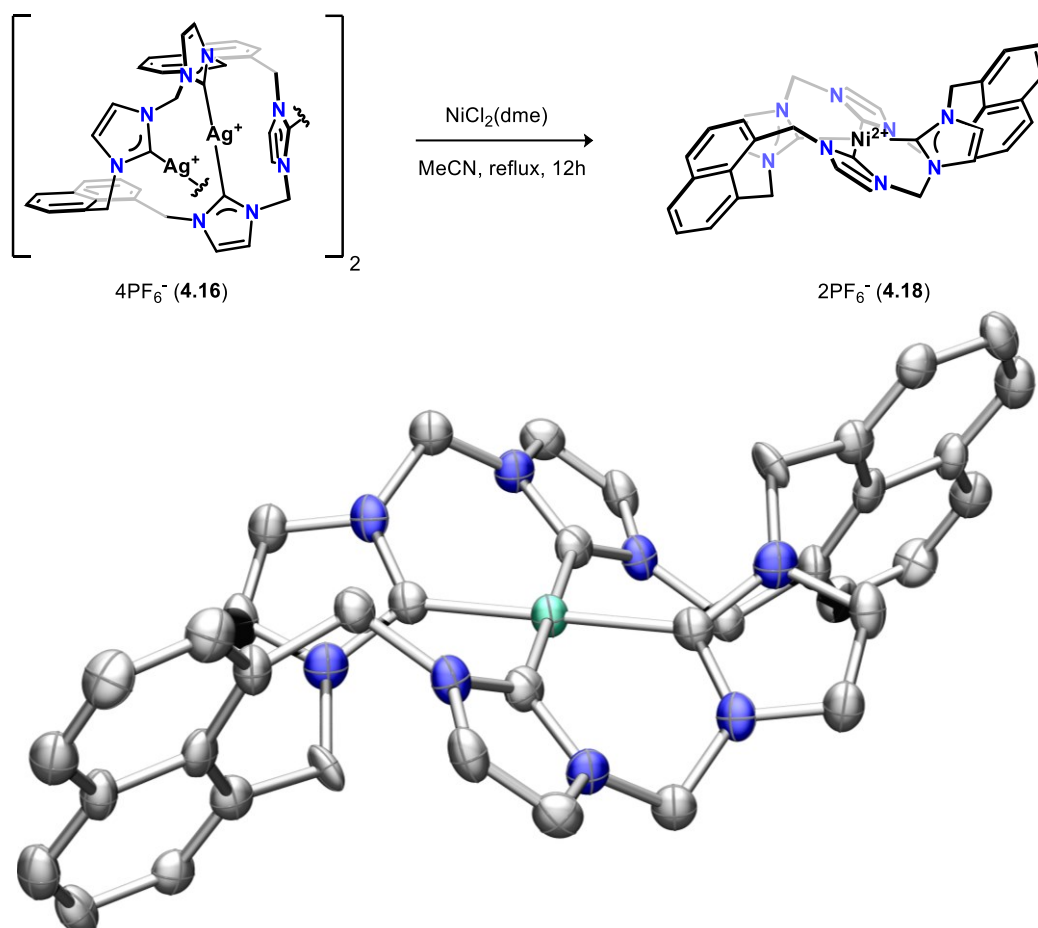


**Figure 4.33.** *Synthesis and solid-state of complex 4.18.* One of the two crystallographic distinctive macrocycles, co-crystallized MeCN, hydrogen atoms, and  $\text{PF}_6^-$ -counterions are omitted for clarity. Thermal ellipsoids are set at a 50% probability level. Atom color-coding: Ni aquamarine, N blue, and C grey.

This complex is white, absent of any electron paramagnetic resonance (EPR) signals, the solid-state demonstrates a square-planar Ni(II), and  $^1\text{H}$  and  $^{13}\text{C}$  NMR spectra, **Figure 4.34**, feature an identical splitting pattern to that observed in the top insert of **Figure 4.19**, telling of change in metal identity featuring the same connectivity. These results, when taken together, corroborate a Ni(II) ion in a low-spin  $d^8$  electronic configuration; a consequence of the strong-field macrocyclic tetra NHC ligand.

#### **Structural characterization of complexes 4.18**

Complex **4.18** crystallizes in the monoclinic  $P2(1)/c$  space group alongside co-crystallized MeCN, and like complex **4.13**, crystals of **4.18** form as thin colorless plates, prone to extensive twinning, and ready evaporation of the co-crystallized solvent.

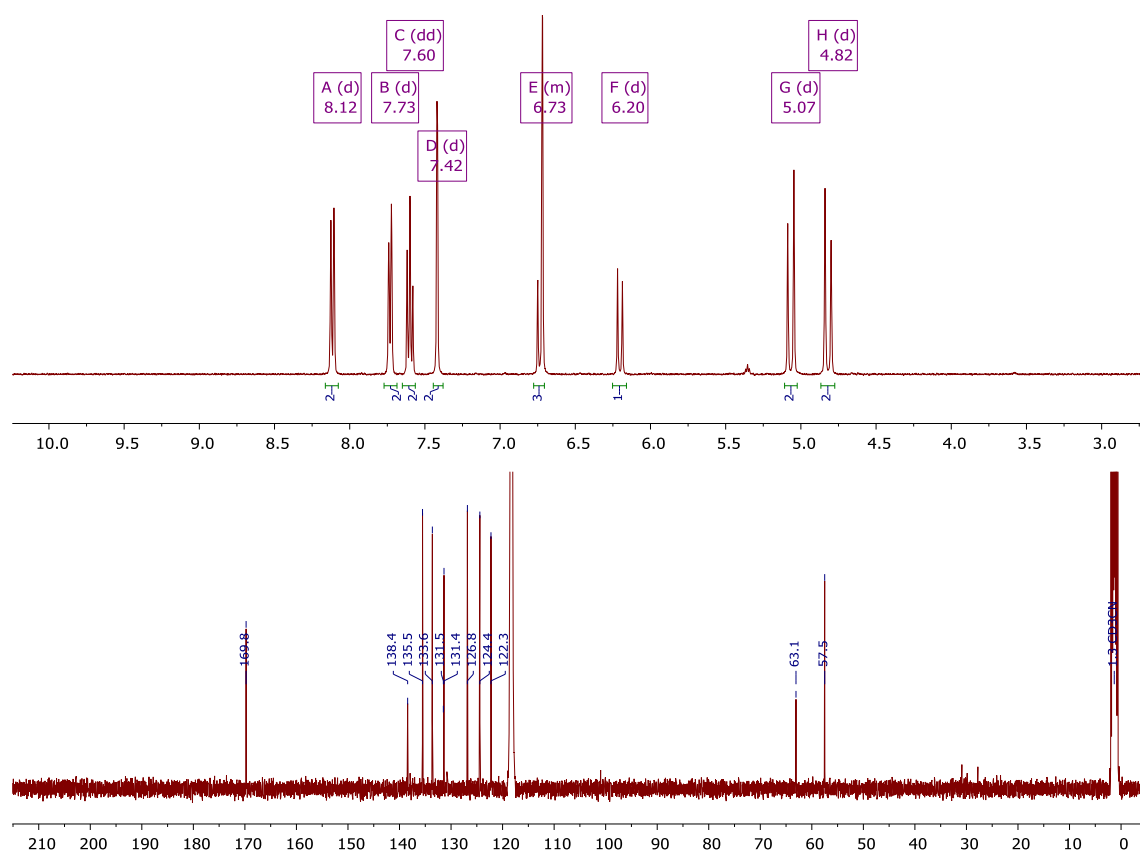


**Figure 4.34.**  $^1\text{H}$  and  $^{13}\text{C}$  NMR ( $\text{CD}_3\text{CN}$ ) spectral properties of complex **4.18**. The complex possess the splitting pattern as the palladium analogue, complex **4.13**, however vary slightly in chemical shift.

However, we were able to obtain crystals of satisfactory quality for X-ray diffraction, which demonstrates two crystallographically distinctive macrocycles in the unit cell. **Figure 4.35** emphasizes the two macrocycle's bonding metrics that each coordinate Ni in a square-planar fashion with inversion through the Ni center. The bond angle across two *trans*-coordinating C atoms in both macrocycles is  $180^\circ$ , and Ni is neither distanced above nor below the mean coordination plane spanned by the ylidenes. These differences are likely a consequence of crystal packing more than anything else, as just a single entity is found by NMR.

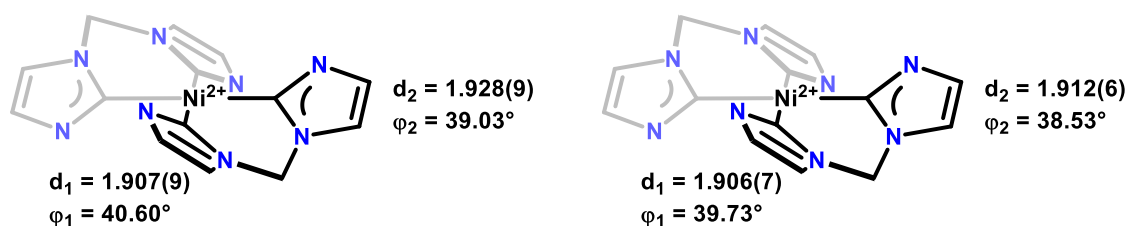


**Figure 4.35.** Bonding metrics pertaining to the core of **4.18**. Two crystallographic distinctive macrocycles were found, and their bond lengths and NHC twist angles are tabulated.

A search in the Cambridge's Crystallographic Data Centre (CCDC on June 30<sup>th</sup> 2022) returns six other Ni(II) complexes bearing distinctive macrocyclic tetra NHC ligands. When comparing lengths between our obtained structure to these, the observed bond lengths fall within the range others have reported, as evident from the tabulated bond lengths listed in **Chart 4.4**<sup>25,30,54–57</sup>, where  $d_n$  denotes the bond length between the central C<sub>2</sub>-C atom to Ni.

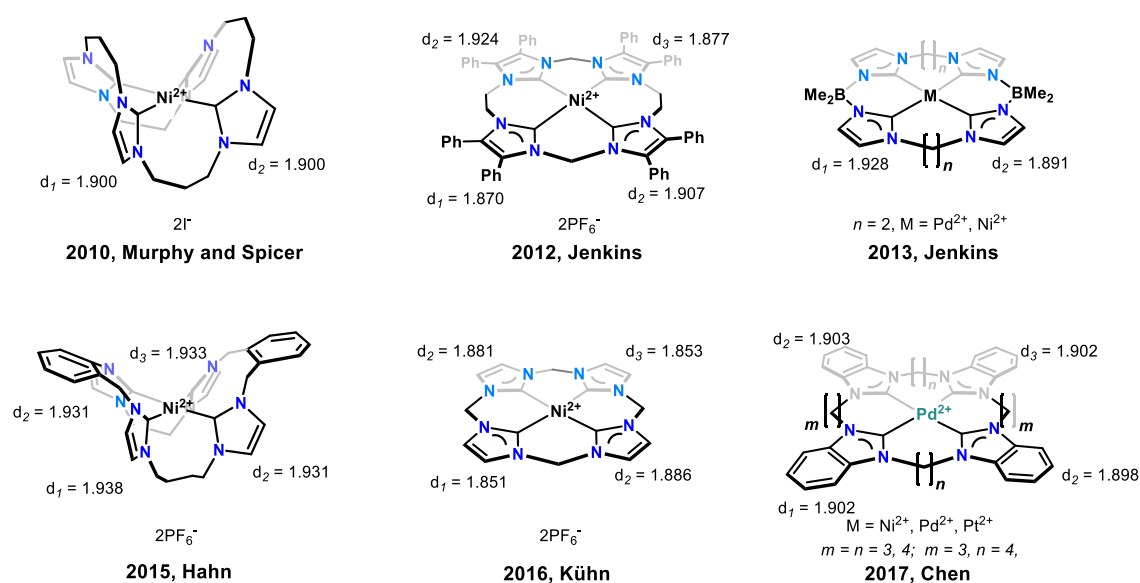
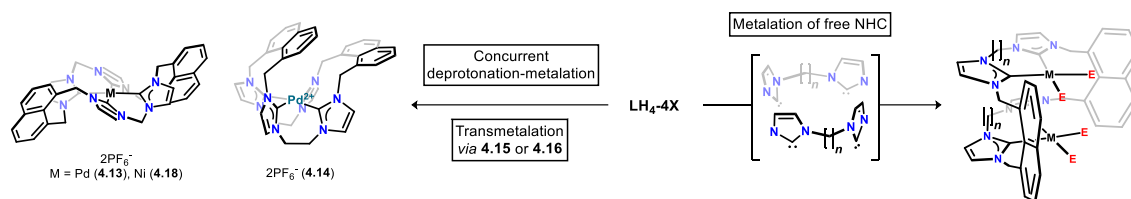


**Chart 4.4.** CCDC structures of Ni(II) complexes bearing macrocyclic tetra NHC ligands. The smallest 16 membered ring unsurprisingly demonstrate by far the shorter Ni-C bond lengths.

Curiously, the structure reported by Hahn in 2015 is quite like our complex **4.14**, and in their analysis of the complex bearing Ni<sup>II</sup>, Pd<sup>II</sup>, and Pt<sup>II</sup>, the authors do not comment on their fluxionality concerning any endo/exo equilibrium. No VT NMR studies were conducted, and evaluating the structure from a space-filling model demonstrate that the benzylic protons completely block any access to the Ni-center.

## 4.5 Seeking dinuclear complexes by metalation of free-carbenes



**Scheme 4.11.** Synthetic approaches investigated in this PhD study, toward dinuclear complexes. Two of the three strategies unequivocally yield tetradentate NHC complexes.

The left-hand side of **Scheme 4.11** presents how we thus far successfully have accounted for metalation of **3.1** and **3.4** with various Pd(II) sources into the respective complexes bearing macrocyclic tetradentate NHC ligands. Similarly, we have successfully identified the respective Ag(I)-intermediates of **3.1** and **3.4**, relevant to transmetalation, and how these complexes are *incompetent* carbene-synthons for our desired dinuclear complexes, leading instead to the formation of the same macrocyclic NHC complexes.

The right-hand side of **Scheme 4.11** conceptually depicts the final metalation route we sought to explore, to probe whether the ligand frameworks of **3.1** and **3.4** adequately accommodate two proximal metal ions: metalation of the preformed carbene. In this setting, we additionally sought to extend our scope of metals to encompass Ni, Rh, and Pt, *vide infra*.

Most of the coming reactions were initially assessed with **3.1**, for a variety of reasons. Firstly, this material is more easily synthesized in large quantities. Secondly, from the coordination differences between **4.13** and **4.14**, and that the latter already demonstrates the desired coordination motif, we envisioned, that in the event of promising results following metalation of **3.1**, the same reaction with **3.4** would have a greater probability of forming the desired product, following their similar coordination chemistry thus far.

Compounds **3.1** and **3.4** react to a slight excess of NaH (4.05 equiv.) in THF, and catalytic amounts of DMSO, to furnish the formation of the free carbene over 2-3 hours (RT), indicated by a cessation in H<sub>2</sub> bubbling. The addition of an excess (>5 equiv.) NaH at first glance, expedites this reaction (1 - 2 hours), however, this mixture seems to slowly undergo decomposition by the color change to brown, and the formation of black solids/deposits. Despite the inherent stability of the free NHC, in absence of O<sub>2</sub> and moisture, no efforts were put into the isolation of the tetra carbenes, apart from separation from NaBr and excess base. Following this step, we sought to drop-wise add a carbene-containing solution into a highly concentrated solution of Pd(OAc)<sub>2</sub> in a great excess (up to >40 equiv.), to probe whether the porphyrin forms as the only product, as acetate is known to demonstrate fluxionality acting as a secondary bridge.

The <sup>1</sup>H NMR spectrum of a red powder, recovered from such a reaction is shown juxtaposed with compound **3.1** and complex **4.13** below, in **Figure 4.36**. The spectrum features additional signals in the aromatic region than those owing to **4.13**, which demonstrate multiple splitting patterns already associated with a successful metalation of the imidazolium salt. Moreover, distinctive signals of this new entity integrate relative to **4.13** in a 1:1 ratio. An encouraging result, however, reproducing this product was inconsistent at best; at times, the resulting powder was just **4.13**, like that as in **Figure 4.36**, or ill-defined insoluble black particles, and difficult to isolate.

Despite our inability to meaningfully disclose the nature of this complex, suggested as a putative dipalladium (II), this spectrum in conjunction with its consistently inconsistent synthesis suggests to us, that dinuclear complexes perhaps could be obtained, given the right combination of metal precursors reacting under the right conditions with the carbene.



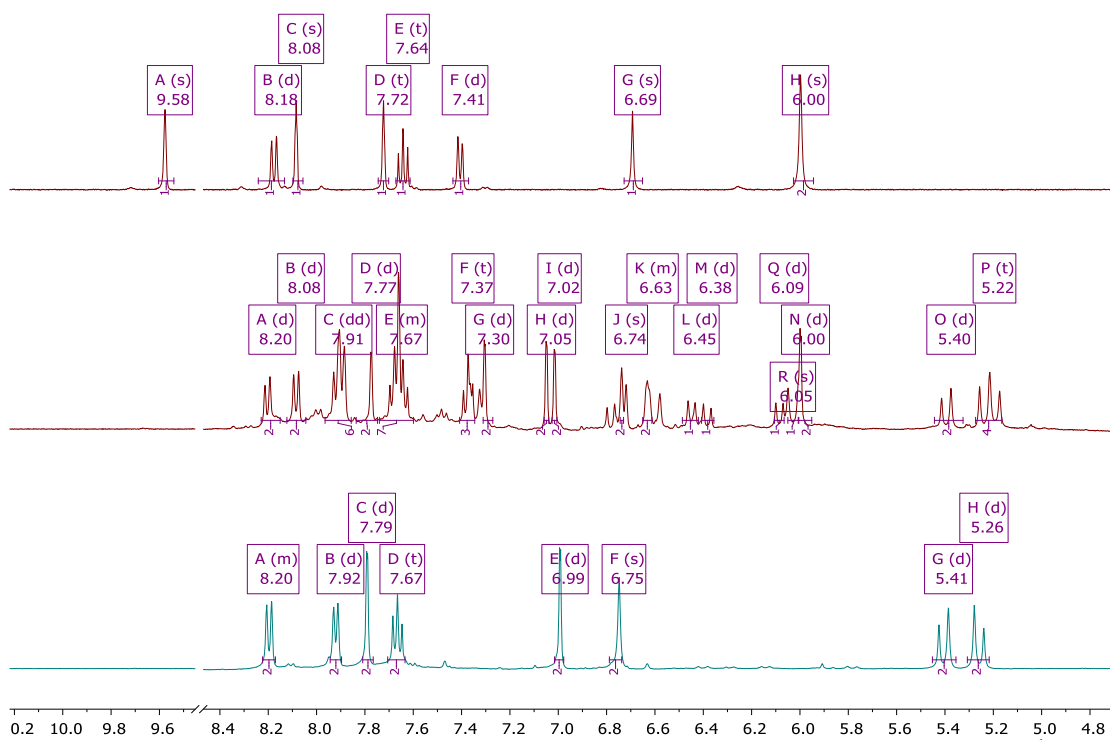


**Figure 4.36.** Metalation of the free-carbene **3.1** with excess  $\text{Pd}(\text{OAc})_2$ . Comparison between the  $^1\text{H}$  NMR spectra ( $\text{DMSO}-d_6$ ) of **3.1** (top spectrum), recovered powder (middle), and **4.13** (lower).

Consequently, our attention turned to the dinuclear metal-precursors shown in **Chart 4.5**. Perhaps naïvely so, we initially sought to answer whether a difference in ligand lability of two proximal palladium ions, can inhibit the macrocycle formation. To this end, two dipalladium (II) paddlewheel complexes  $\text{Pd}_2(\mu\text{-hpp})_4$  and **2.1/2** were reacted with the free carbenes. However, from the isolation of powders with spectral properties identical to **4.13** and **4.14**, under a myriad of different reaction conditions, we found our answer; a stronger force is likely necessitated to retard or fully prevent macrocycle formation.

Such a property is readily achieved in dinuclear complexes, through the formation of (multiple) metal-metal bond(s), which for the late transition-metals, most readily is achieved in complexes, whose “metal-metal-bonded-core”,  $\{\text{M}_2^{n+}\}$ , adopts an electronic configuration consistent with either  $d^9d^9$   $\{\text{M}_2^{2+}\}$  or  $d^7d^7$   $\{\text{M}_2^{6+/4+}\}$  description. To address the former, two parent-dipalladium (I) complexes, top insert of **Chart 4.5**, were isolated, in addition to some *in-situ* prepared dinickel (I) complexes, *vide infra*. Complexes of

dirhodium  $\{\text{Rh}_2^{4+}\}$  and the isoelectronic diplatinum (III)  $\{\text{Pt}_2^{6+}\}$ , lower insert of **Chart 4.5**, were studied in the context of the latter configuration. The interest in low-valent nickel complexes, and Pt (III), was specifically to probe whether the metal size is limiting complex formation.

A key difference between the two electronic configurations relates to the ligand-field each metal adopts. Whereas each metal in the  $d^9d^9$  configuration adopts a strict square-planar and the metal-bond oriented along with one of the coordinate axes, each metal in the  $d^7d^7$  configuration leads to a distorted octahedron, with the metal-bond oriented along with one of the axial coordination sites, as evident in the presented structures in **Chart 4.5**.

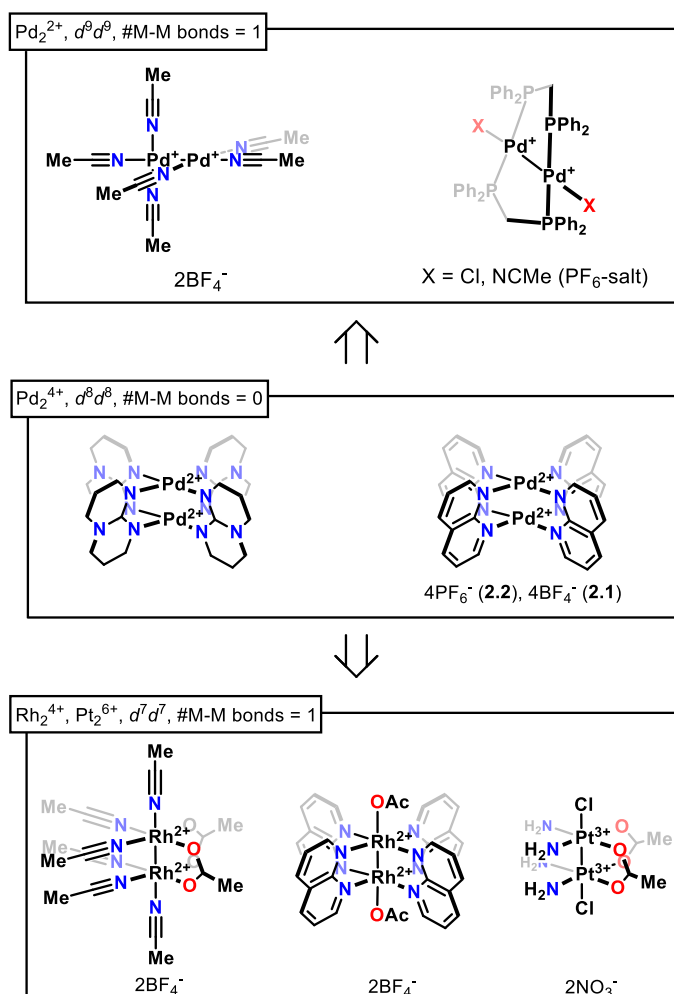


**Chart 4.5.** Dinuclear complexes were investigated in this study. Emphasized in each corner, are info on the electronic configuration and number (#) of metal-metal bonds about each complex' core.

#### 4.5.1 The-not-so-encouraging metalation-results

We initially sought to investigate coordination between the two dipalladium (I) complexes presented in the top insert of **Chart 4.5**. A brick-red powder is recoverable in small amounts (<10%) from these reactions between the carbene of **3.1** with  $\text{Pd}_2(\mu\text{-dppm})_2\text{Cl}_2$ . Tracing the reaction by comparing appropriate  $^{31}\text{P}$  NMR spectra (in  $\text{DMSO-}d_6$ , to ensure solubility), **Figure 4.37**, first appears promising from the noticeable downfield-shift and absence of signals owing to the starting materials in the recovered product. From the top, the first spectrum is free dppm, the second  $\text{Pd}_2(\mu\text{-dppm})_2\text{Cl}_2$ , and the third the powder recovered following an overnight reaction between the free carbene of **3.1** with  $\text{Pd}_2(\mu\text{-dppm})_2\text{Cl}_2$ .

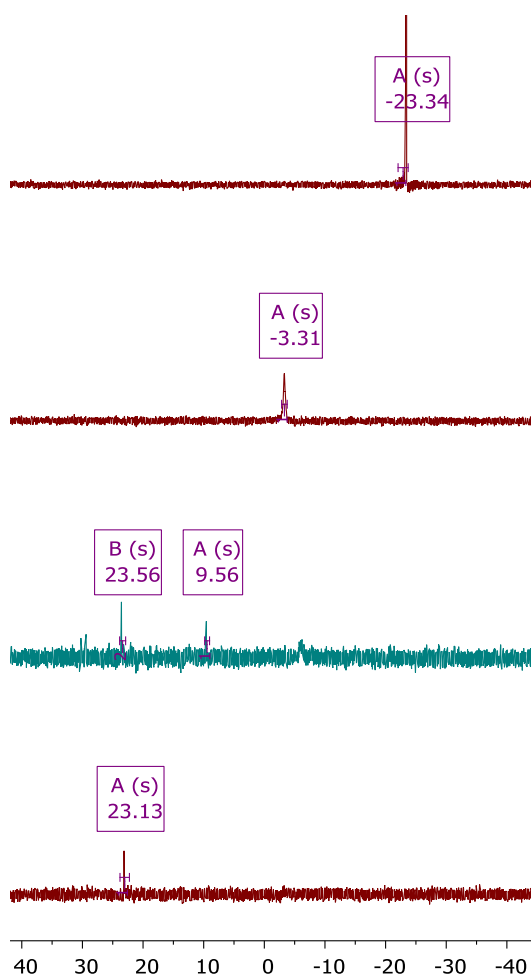


**Figure 4.37.**  $^{31}\text{P}$  NMR spectra of reaction adducts following ligand substitution of  $\text{Pd}_2(\mu\text{-dppm})\text{Cl}_2$  with free carbenes. The left-hand side compares spectra of free dppm (first from the top),  $\text{Pd}_2(\mu\text{-dppm})\text{Cl}_2$  (second), substitution product with carbene of #X (third), and deprotonation of  $\text{Pd}_2(\mu\text{-dppm})\text{Cl}_2$  (bottom).

However, to explore whether this species results from deprotonation of the dppm backbone,  $\text{Pd}_2(\mu\text{-dppm})_2\text{Cl}_2$  was reacted with NaH under the same conditions resulting in the entity at 23.13 ppm. This species is also present in the red powdered obtained from our ligand substitution reactions, leaving a species, 9.56 ppm, which caused us to explore the metalation with **3.4**.

A red-brick powder is similarly obtainable in low amounts, however, the  $^{31}\text{P}$  NMR spectrum contains multiple signals, as shown on the right-hand side of **Figure 4.38**. These compounds comprise mostly of decomposition products.

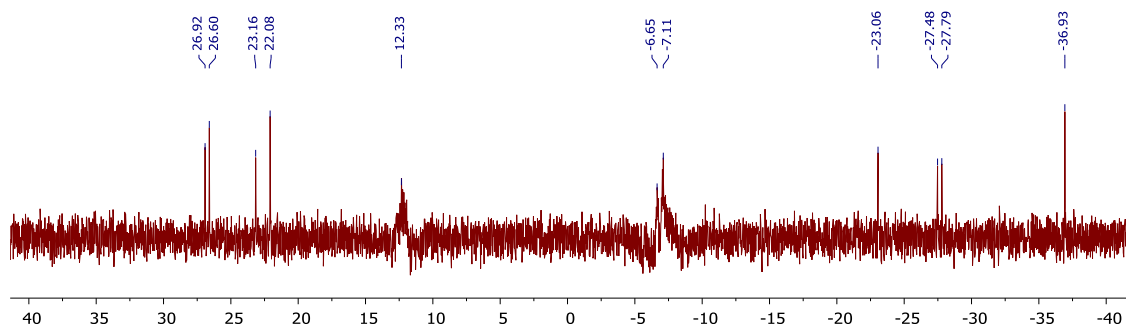


**Figure 4.38.**  $^{31}\text{P}$  NMR spectra of reaction adducts following ligand substitution of  $\text{Pd}_2(\mu\text{-dppm})_2\text{Cl}_2$  with the free carbene of compound **3.4**. A multitude of products were instead found, along with unreacted dipalladium(I), suggesting this neither furnish the desired transformation.

We instead sought to understand the coordination chemistry of the “naked” dipalladium (I)  $[\text{Pd}_2(\text{MeCN})_6] 2\text{BF}_4$ . Treating this complex to either of our carbene yields a blood-red powder, which both are thermally unstable in solution at  $T > -50\text{ }^\circ\text{C}$ , and decompose even as a solid at  $-35\text{ }^\circ\text{C}$ .

We did obtain a  $^1\text{H}$  NMR spectrum, shown in **Figure 4.39**, of just this product from **3.1**, which, evidently is a paramagnetic species. We were unsuccessful in characterizing this product through EPR and Evan’s method, which otherwise would have helped assign the nature of the radical; metal or ligand centered?

Leaving the sample for an additional two minutes at RT provides insight into the decomposition product, which in addition to having formed a Pd-mirror, consists of the protonated macrocycle, and some macrocyclic Pd(II) complex (corroborated by the unit

cell of formed crystals). This is particularly odd, but a source of acid protons is likely explained by a reaction with trace moisture or advantageous protons from the surface of the NMR tube.

Based on the thermodynamic preference towards macrocyclic chelation, it is likely that one Pd is engulfed by four NHCs, which facilitate the disproportionation reaction suggested towards.

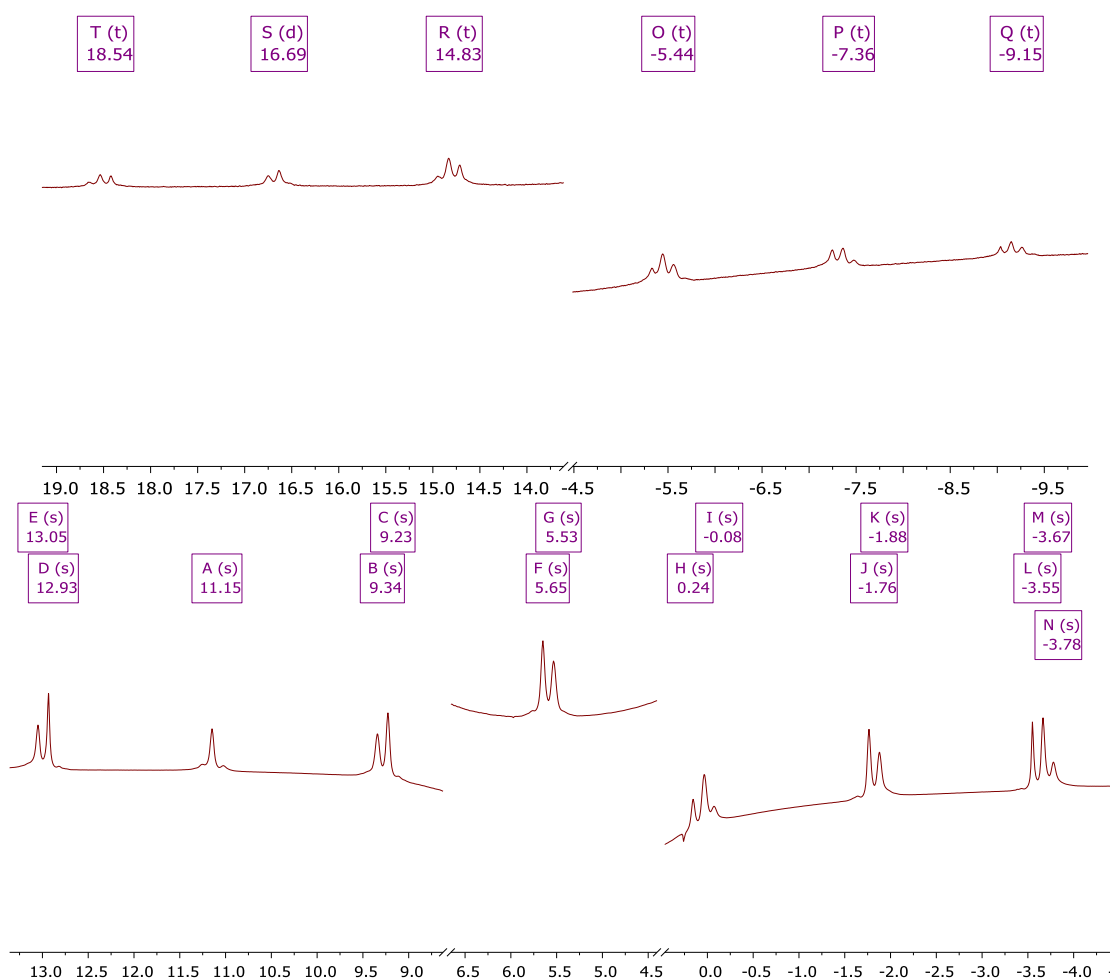
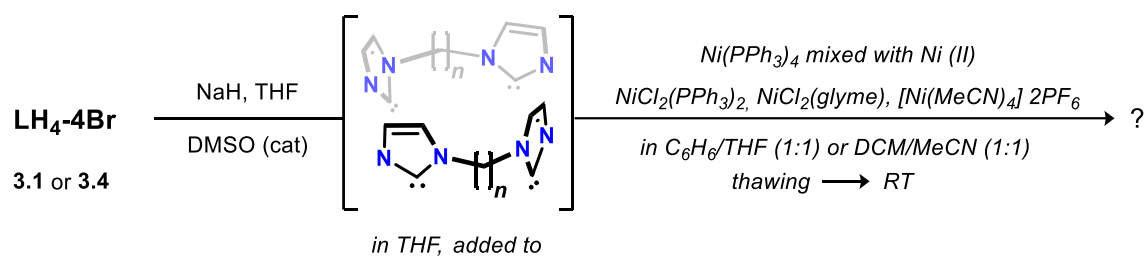


**Figure 4.39.**  $^1\text{H}$  NMR spectra of reaction adducts following ligand substitution of  $[\text{Pd}_2(\text{MeCN})_6] 2\text{BF}_4$  with the free carbene of **3.1**. The spectrum demonstrates a paramagnetic entity.

The same trend was, unfortunately, also observed reacting either **3.1** and **3.4** with the different  $\text{Rh}_2$  and  $\text{Pt}_2$ -complexes: precipitation of black metal particles, ligand decomposition, and trace isolation of macrocyclic intermediates. To exclude the possibility of a transfer of residual dimsyl anion ( $[\text{CH}_3\text{S}(\text{O})\text{CH}_2]^-$ ), and its involvement in the observed decomposition, we replicated the previous experiments with

deprotonation of the PF<sub>6</sub> salts in THF with KO<sup>t</sup>Bu (frozen/thawing) and LiN(SiMe<sub>3</sub>)<sub>2</sub>. However, similar decomposition products were isolated from these reactions.

In closing, we sought to explore whether installation of low-valent Ni(I) was feasible, owing to the Pd(I) ion spatially experiencing a too constrained environment. To this end, with inspiration from Agapie's work<sup>48</sup>, we sought to reach the free carbene to different nickel sources under comproportionation conditions, varying the Ni(II) and Ni(0) sources, as shown in **Scheme 4.11**. However, these reactions consistently led to the formation of Ni(0), either as a Ni(0) mirror on the side of the glassware, or precipitation of Ni-particles, and isolable salts featuring spectral properties consistent with complex **4.18**.



**Scheme 4.12.** The conceptual approach to synthesize dinickel (I) complex. The free carbene, previously accounted for, was drop-wise added to a thawing solution of Ni(PPh<sub>3</sub>)<sub>4</sub> with various Ni(II) sources.

## 4.6 Conclusion

In closing, three different metalation routes, commonly to preparation of NHC complexes, was applied to proligands **3.1** and **3.4**, where the metalation adducts are fully accounted for, whereas proligand **3.6** only was explored in context of transmetalation.

First, we found that the weak base route cleanly forms monopalladium(II) complexes bearing either of the macrocyclic tetra NHC ligands. Metalation of proligand **3.1** yields a square-planar complex of Pd(II), which later also was found to apply to Ni(II). Differently, metalation of proligand **3.4** yields a Pd(II) complex deviating from square-planarity featuring an unsymmetrical binding pocket, which we are seeking to explore in future studies, with *e.g.* Fe or Ru. Moreover, the coordination of Pd demonstrated by complex **4.14** demonstrated that the aliphatic linker worked as the chelate moiety as we wanted in our ditopic system. While weak bases yield isolable complexes, yields are in the range of 40 – 50%, and we sought to explore other syntheses.

Second, we sought to investigate the connectivity of the intermediary Ag(I) complexes, for their application as carbene-transfer reagents. Reacting proligands **3.1** and **3.4** to a source of Ag(I) and base, forms isolable Ag-salts, of which the connectivity was established through single-crystal X-ray diffraction as a dimer and trimer, respectively. More critically, both complexes feature one macrocycle tethered to itself by Ag, and the remaining two NHC moieties bridge; this connectivity is consistent with intermediary silver structures generally observed in macrocyclic poly imidazolium structures, namely motif 3 in **Figure 4.5**. Transmetalation of these homoleptic intermediates,  $[\text{NHC}_2\text{Ag}]_n n\text{X}$ ,  $n = 2, 3$ ,  $\text{X} = \text{Br}, \text{PF}_6$ , exclusively leads to monometallic macrocyclic products, however, isolated in an improved yield, ranging from 80 – 90% relative to the weak base approach. We sought to transform the homoleptic Ag adducts into the heteroleptic halido NHC-Ag-X adducts, as these compounds have been seen to form dinuclear complexes in

transmetalation reactions. However, we were unsuccessful in this endeavor, instead, isolating decomposition products from extrusion of AgX.

We do believe we were successful in synthesizing small amounts of an anthracene-based macrocycle, compound **3.6**, whose Ag(I) adduct we could investigate by  $^1\text{H}$  NMR, inferring trends from the other two systems. The intermediary compound demonstrates different spectral properties, consistent with motif 2 in **Figure 4.5**; in other words, no binding across a would-be pocket. This difference suggests to us, that this compound may transmetalate to form our desired ditopic system, however, remains to be explored more rigorously.

Third, we explored ligand substitution reactions to a variety of dinuclear precursors bearing metal-metal bonds, however, despite recovering some powders demonstrating spectral properties different from the *bona fide* macrocyclic complexes, we were unable to validate whether any authentic ditopic complexes were isolated.

We did identify a thermally unstable, paramagnetic species from the reaction between free tetra NHC and  $[\text{Pd}_2(\text{MeCN})_6] 2\text{BF}_4$ , however, as the decomposition products comprise a mixture of protonated imidazolium, complex **4.13**, and precipitation of Pd(0), we suggest that the macrocyclic coordination motif is thermodynamically too stable to avoid. This suggestion has further support, following the deposition of a pleasingly looking Ni(0) mirror, resulting from the ligand substitution between the free tetra NHC to the comproportionation product of  $\text{Ni}_2^{2+}$ .

All taken together, the introduction of a benzylic  $sp^3$ -C moiety, despite rendering us able to tether two bridging diimidazole units, adds enough flexibility such that only monometallic complexes bearing macrocyclic tetra NHC complexes are isolated.



## 4.7 References

- (1) Igau, A.; Grutzmacher, H.; Baceiredo, A.; Bertrand, G. *J. Am. Chem. Soc.* **1988**, *110*, 6463–6466.
- (2) Arduengo, A. J.; Harlow, R. L.; Kline, M. *J. Am. Chem. Soc.* **1991**, *113*, 361–363.
- (3) Charra, V.; de Frémont, P.; Braunstein, P. *Coord. Chem. Rev.* **2017**, *341*, 53–176.
- (4) Kirmse, W. *Angew. Chem. Int. Ed.* **2010**, *49*, 8798–8801.
- (5) Hopkinson, M. N.; Richter, C.; Schedler, M.; Glorius, F. *Nature* **2014**, *510*, 485–496.
- (6) Bourissou, D.; Guerret, O.; Gabbaï, F. P.; Bertrand, G. *Chem. Rev.* **2000**, *100*, 39–92.
- (7) Arduengo, A. J.; Goerlich, J. R.; Marshall, W. J. *J. Am. Chem. Soc.* **1995**, *117*, 11027–11028.
- (8) Wanzlick, H.-W.; Schikora, E. *Angew. Chem.* **1960**, *72*, 494–494.
- (9) Böhm, V. P. W.; Herrmann, W. A. *Angew. Chem. Int. Ed.* **2000**, *39*, 4036–4038.
- (10) Hu, X.; Castro-Rodriguez, I.; Olsen, K.; Meyer, K. *Organometallics* **2004**, *23*, 755–764.
- (11) Jacobsen, H.; Correa, A.; Poater, A.; Costabile, C.; Cavallo, L. *Coord. Chem. Rev.* **2009**, *253*, 687–703.
- (12) Comas-Vives, A.; Harvey, J. N. *Eur. J. Inorg. Chem.* **2011**, *2011*, 5025–5035.
- (13) Wanzlick, H.-W.; Schönherr, H.-J. *Angew. Chem. Int. Ed.* **1968**, *7*, 141–142.
- (14) Öfele, K. *J. Organomet. Chem.* **1968**, *12*, P42–P43.
- (15) Öfele, K.; Herrmann, W. A.; Mihalios, D.; Elison, M.; Herdtweck, E.; Scherer, W.; Mink, J. *J. Organomet. Chem.* **1993**, *459*, 177–184.
- (16) Herrmann, W. A.; Öfele, K.; Elison, M.; Kühn, F. E.; Roesky, P. W. *J. Organomet. Chem.* **1994**, *480*, c7–c9.
- (17) Scholl, M.; Trnka, T. M.; Morgan, J. P.; Grubbs, R. H. *Tetrahedron Lett.* **1999**, *40*, 2247–2250.
- (18) Huang, J.; Stevens, E. D.; Nolan, S. P.; Petersen, J. L. *J. Am. Chem. Soc.* **1999**, *121*, 2674–2678.
- (19) Herrmann, W. A.; Elison, M.; Fischer, J.; Köcher, C.; Artus, G. R. J. *Angew. Chem. Int. Ed.* **1995**, *34*, 2371–2374.
- (20) Herrmann, W. A.; Schwarz, J.; Gardiner, M. G. *Organometallics* **1999**, *18*, 4082–4089.
- (21) Martynova, E. A.; Tzouras, N. V.; Pisanò, G.; Cazin, C. S. J.; Nolan, S. P. *Chem. Commun.* **2021**, *57*, 3836–3856.
- (22) Wang, H. M. J.; Lin, I. J. B. *Organometallics* **1998**, *17*, 972–975.
- (23) Venkatachalam, G.; Heckenroth, M.; Neels, A.; Albrecht, M. *Helv. Chim. Acta*

**2009**, 92, 1034–1045.

- (24) Liu, S.-T.; Hsieh, T.-Y.; Lee, G.-H.; Peng, S.-M. *Organometallics* **1998**, 17, 993–995.
- (25) Lu, Z.; Cramer, S. A.; Jenkins, D. M. *Chem. Sci.* **2012**, 3, 3081–3087.
- (26) Wanniarachchi, Y. A.; Khan, M. A.; Slaughter, L. M. *Organometallics* **2004**, 23, 5881–5884.
- (27) McKie, R.; Murphy, J. A.; Park, S. R.; Spicer, M. D.; Zhou, S. *Angew. Chem. Int. Ed.* **2007**, 46, 6525–6528.
- (28) Schulte to Brinke, C.; Pape, T.; Hahn, F. E. *Dalt. Trans.* **2013**, 42, 7330–7337.
- (29) Hahn, F. E.; Radloff, C.; Pape, T.; Hepp, A. *Chem. Eur. J.* **2008**, 14, 10900–10904.
- (30) Altmann, P. J.; Weiss, D. T.; Jandl, C.; Kühn, F. E. *Chem. Asian J.* **2016**, 11, 1597–1605.
- (31) Arduengo, A. J.; Dias, H. V. R.; Calabrese, J. C.; Davidson, F. *Organometallics* **1993**, 12, 3405–3409.
- (32) Caballero, A.; Díez-Barra, E.; Jalón, F. A.; Merino, S.; Tejeda, J. *J. Organomet. Chem.* **2001**, 617–618, 395–398.
- (33) Tolman, C. A. *Chem. Rev.* **1977**, 77, 313–348.
- (34) Huynh, H. V.; Han, Y.; Jothibas, R.; Yang, J. A. *Organometallics* **2009**, 28, 5395–5404.
- (35) Teng, Q.; Huynh, H. V. *Dalt. Trans.* **2017**, 46, 614–627.
- (36) Bor, G. *J. Organomet. Chem.* **1967**, 10, 343–359.
- (37) Dorta, R.; Stevens, E. D.; Scott, N. M.; Costabile, C.; Cavallo, L.; Hoff, C. D.; Nolan, S. P. *J. Am. Chem. Soc.* **2005**, 127, 2485–2495.
- (38) Chianese, A. R.; Li, X.; Janzen, M. C.; Faller, J. W.; Crabtree, R. H. *Organometallics* **2003**, 22, 1663–1667.
- (39) Herrmann, W. A. *Angew. Chem. Int. Ed.* **2002**, 41, 1290–1309.
- (40) Hahn, F. E.; Jahnke, M. C. *Angew. Chem. Int. Ed.* **2008**, 47, 3122–3172.
- (41) *N-Heterocyclic Carbenes*; Nolan, S. P., (ed.); (Wiley-VCH Verlag GmbH & Co. KGaA: Weinheim), **2014**.
- (42) Murahashi, T.; Kurosawa, H. *Coord. Chem. Rev.* **2002**, 231, 207–228.
- (43) Boyd, P. D. W.; Edwards, A. J.; Gardiner, M. G.; Ho, C. C.; Lemée-Cailleau, M.-H.; McGuinness, D. S.; Riapanitra, A.; Steed, J. W.; Stringer, D. N.; Yates, B. F. *Angew. Chem. Int. Ed.* **2010**, 49, 6315–6318.
- (44) Scattolin, T.; Bortolamiol, E.; Palazzolo, S.; Caligiuri, I.; Perin, T.; Canzonieri, V.; Demitri, N.; Rizzolio, F.; Cavallo, L.; Dereli, B.; Mane, M. V.; Nolan, S. P.; Visentin, F. *Chem. Commun.* **2020**, 56, 12238–12241.
- (45) Wang, R.; Jin, C.-M.; Twamley, B.; Shreeve, J. M. *Inorg. Chem.* **2006**, 45, 6396–

6403.

- (46) Pirkel, N.; Del Grosso, A.; Mallick, B.; Doppiu, A.; Gooßen, L. J. *Chem. Commun.* **2019**, *55*, 5275–5278.
- (47) Hruszkewycz, D. P.; Guard, L. M.; Balcells, D.; Feldman, N.; Hazari, N.; Tilset, M. *Organometallics* **2015**, *34*, 381–394.
- (48) Tsui, E. Y.; Agapie, T. *Polyhedron* **2014**, *84*, 103–110.
- (49) Arnold, P. L.; Pearson, S. *Coord. Chem. Rev.* **2007**, *251*, 596–609.
- (50) Lee, H. M.; Lu, C. Y.; Chen, C. Y.; Chen, W. L.; Lin, H. C.; Chiu, P. L.; Cheng, P. Y. *Tetrahedron* **2004**, *60*, 5807–5825.
- (51) Spek, A. L. *Acta Crystallogr. Sect. C Struct. Chem.* **2015**, *71*, 9–18.
- (52) Baker, M. V.; Bosnich, M. J.; Brown, D. H.; Byrne, L. T.; Hesler, V. J.; Skelton, B. W.; White, A. H.; Williams, C. C. *J. Org. Chem.* **2004**, *69*, 7640–7652.
- (53) Findlay, N. J.; Park, S. R.; Schoenebeck, F.; Cahard, E.; Zhou, S.; Berlouis, L. E. A.; Spicer, M. D.; Tuttle, T.; Murphy, J. A. *J. Am. Chem. Soc.* **2010**, *132*, 15462–15464.
- (54) Findlay, N. J.; Park, S. R.; Schoenebeck, F.; Cahard, E.; Zhou, S.; Berlouis, L. E. A.; Spicer, M. D.; Tuttle, T.; Murphy, J. A. *J. Am. Chem. Soc.* **2010**, *132*, 15462–15464.
- (55) Bass, H. M.; Cramer, S. A.; McCullough, A. S.; Bernstein, K. J.; Murdock, C. R.; Jenkins, D. M. *Organometallics* **2013**, *32*, 2160–2167.
- (56) Schulte to Brinke, C.; Ekkehardt Hahn, F. *Dalt. Trans.* **2015**, *44*, 14315–14322.
- (57) Fei, F.; Lu, T.; Chen, X.-T.; Xue, Z.-L. *New J. Chem.* **2017**, *41*, 13442–13453.

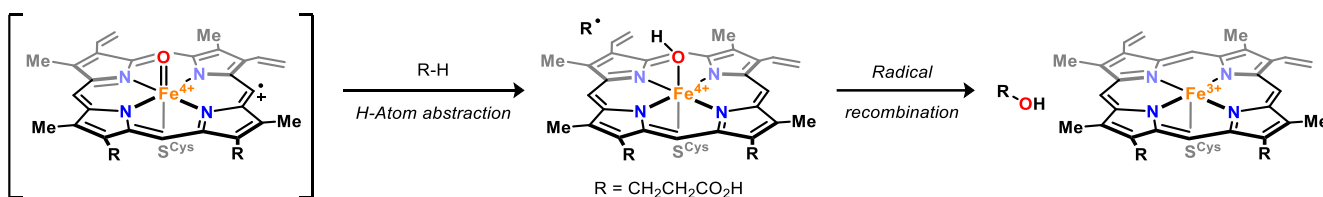
## Chapter. 5. High-valent Ni and Pd complexes bearing a macrocyclic tetra NHC ligand

### 5.1 Introduction

Despite our unsuccessful synthesis of bimetallic complexes with either of the naphthalene ligands, the coordination geometry of complexes **4.13** and **4.18** is quite interesting, in that it closely resembles that of haeme and its synthetic analogues, *viz.* porphyrinates, corrolates, and corrinates. Such complexes are well-known for supporting reactive, high-valent metal centers demonstrating multiple ligand-metal bonds, albeit for early to mid-transition metals<sup>1</sup>. Accordingly, we thought it appropriate to further investigate complexes **4.13** and **4.18** reactivity under oxidative conditions.

#### 5.1.1 Complexes bearing *N*-porphyrin and macrocyclic tetra NHC ligands

High-valent iron(IV)-oxo species are attributed as key intermediates in (catalytic) reactions of dioxygen, mediated by haeme and non-haeme monoiron complexes, for instance in the activation of unreactive C-H bonds *via* alkane hydroxylation, as shown in **Scheme 5.1**<sup>2-4</sup>. Following the first evidence supporting a non-haeme Fe(IV)-oxo complex<sup>5</sup>, several structural elucidations followed, all weak-field *N*-atom donor bearing ligands, *viz.* cyclam<sup>6,7</sup> and tren<sup>8,9</sup>.



**Scheme 5.1.** Hydroxylation of inactive C-H bonds. Proposed involvement of Cytochrome P450, which proceeds *via* a radical-rebound mechanism.

In 2013, Meyer reported the first structure of a Fe (IV)-oxo supported by a macrocyclic tetra NHC ligand, which demonstrates a similar coordination environment to the non-haeme systems as shown in **Figure 5.1**<sup>10</sup>. While both complexes demonstrate a triplet ground-state electron configuration, the ligand-field induced by the macrocyclic tetra NHC results in quite different reactivity, as was later disclosed in joint studies with

the Neese group<sup>11</sup>. While both complexes react as Fe(IV)-oxo species with C-H bonds through an initial H-atom transfer (HAT), resulting in a Fe (III) hydroxyl intermediate following a radical recombination reaction, as in Scheme 5.1, *N*-porphyrin bearing Fe(IV) oxo complexes react *via* a so-called two-state-reactivity between a ground-state triplet state and an excited quintet state. This transition is possible as a consequence following a low-energy barrier between the two states following from the low *d*-manifold perturbation<sup>12</sup>, as emphasized in **Figure 5.1**.

In contrast, the much stronger destabilization of the  $d(x^2-y^2)$  and  $d(z^2)$  orbitals induced by the NHC ligands renders this transition much more energy-intensive and prohibits spin-cross over processes, leading to a single spin-state (triplet) responsible for HAT and oxygen-atom transfer transformations. This subtle difference manifests in terms of C-H bond activation; whereas high-spin *N*-based ligand systems can activate stronger C-H bonds of up to ~100 kcal/mol, the Fe (II) macrocyclic tetra NHC complex only activates C-H bonds of ~80 kcal/mol. However, complexes of the latter type are more stable<sup>13,14</sup>.

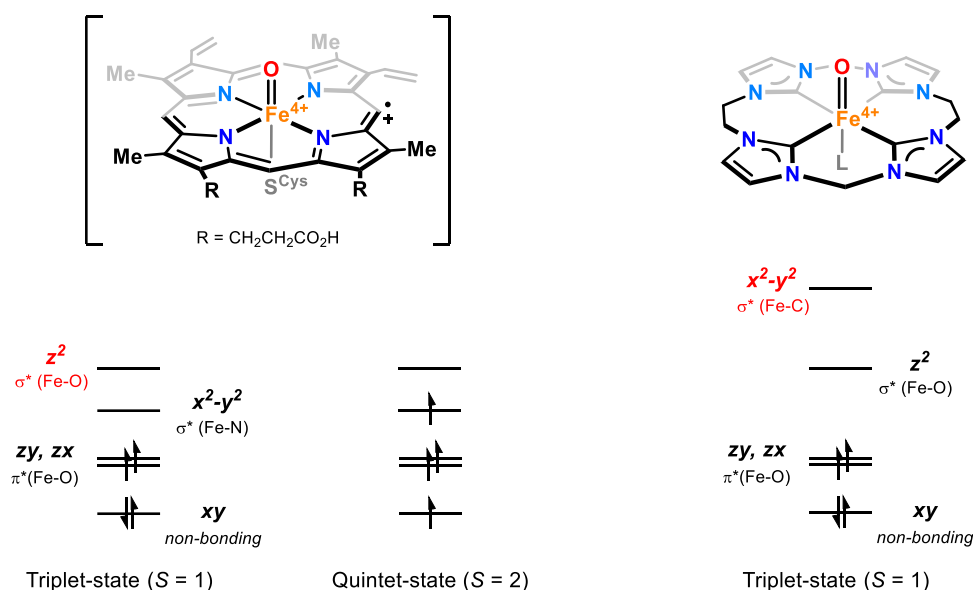


**Figure 5.1.** Electronic differences between complexes bearing *N*-porphyrins and macrocyclic tetra NHC ligands. The strong destabilization of the  $d(x^2-y^2)$  and  $d(z^2)$ -orbitals, pushes these energetically uphill, rendering the reactivity of NHC complexes bound to a single triplet-pathway. The relative orbital energy levels are to provide a qualitative understanding.

Kühn studied the electrochemical properties of a series of Fe (II) complexes bearing various tetradentate ligands, varying in number of NHCs, selected complexes shown in **Figure 5.2**<sup>15</sup>. All complexes demonstrate a single redox event with peak separation ( $\Delta E$ ) between 80 to 100 mV, consistent with a quasi-reversible one-electron process attributed to the  $\text{Fe}^{2+/3+}$ -redox couple. The authors report that the oxidation potential ( $E_{1/2}$ ) linearly decreases following the number of coordinating NHC moieties down from 0.68V vs.  $\text{Fc}^{+/0}$  (single NHC) to 0.08V (four NHCs). The authors further remark that each NHC on average shifts the oxidation potential cathodically by 0.2V, and flexible ligands further lower the oxidation potential, as the distortion of the octahedral coordination environment more readily is accommodated.

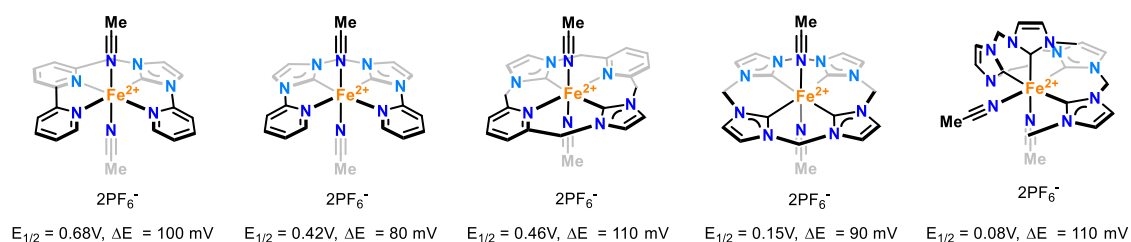
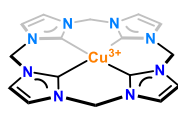


**Figure 5.2.** Half-cell potential of the  $\text{Fe}^{2+/3+}$  redox-couple changes with the number of NHC ligands. Kühn's study provides insight into the electrochemical consequences of multiple NHC ligands.

In the top insert of **Chart 5.1**, complexes featuring unusual metal-oxidation states bearing macrocyclic tetra NHC ligands are shown. Kühn<sup>16</sup> and Cutsail III<sup>17</sup> recently reported Cu-complexes demonstrating the unusual formal oxidation state of 3+; whether the oxidation state of Cu in these complexes truly reflect a metal centered 3+ charge is still not ambiguous, as their data is suggestive of an inverted ligand-field<sup>18</sup> similar to that of  $\text{Cu}(\text{CF}_3)_4$ , opposite what the authors argue in favor of. Additionally, the first five-coordinate Fe(IV) imido-complex is also shown, bearing a macrocyclic tetra NHC ligand, as reported by Jenkins<sup>19</sup>.

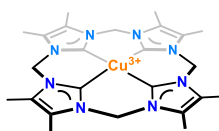
The field of organometallic porphyrin-analogues is still in its infancy, spanning just a few research groups with their own distinctive structure, these are shown in the lower insert of **Chart 5.1**.

Isolated tetra NHC complexes demonstrating an unusually high metal oxidation state



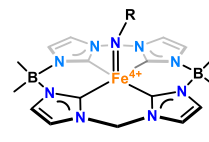
3PF<sub>6</sub><sup>-</sup>

2018, Kühn



3PF<sub>6</sub><sup>-</sup>

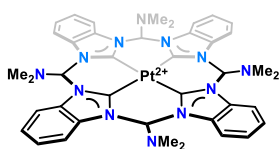
2022, Cutsail III



R = *t*Bu, DiPP, 1-Ad

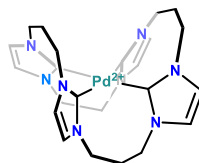
2019, Jenkins

Complexes bearing macrocyclic tetra NHC ligands



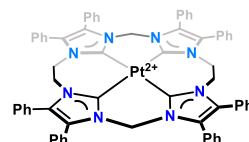
2Cl<sup>-</sup>

2005, Hahn



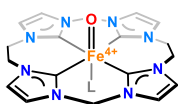
2I<sup>-</sup>

2007, Murphy and Spicer



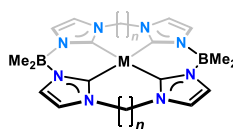
2PF<sub>6</sub><sup>-</sup>

2011, Jenkins



2PF<sub>6</sub><sup>-</sup>

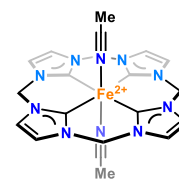
2013, Meyer



$n = 2$ , M = Pd<sup>2+</sup>, Ni<sup>2+</sup>

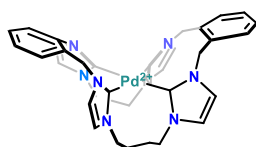
$n = 1$ , M = Fe<sup>2+</sup>

2013 & 2016, Jenkins



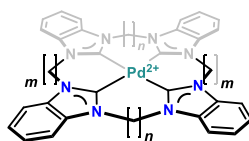
2PF<sub>6</sub><sup>-</sup>

2015, Kühn



2PF<sub>6</sub><sup>-</sup>

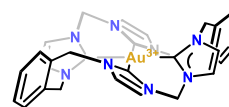
2015, Hahn



M = Ni<sup>2+</sup>, Pd<sup>2+</sup>, Pt<sup>2+</sup>

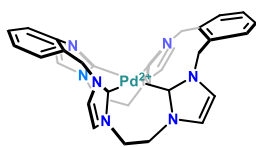
$m = n = 3, 4$ ;  $m = 3$ ,  $n = 4$ ,

2017, Chen



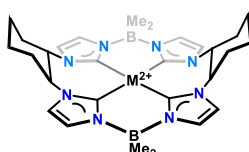
3PF<sub>6</sub><sup>-</sup>

2017, Baker



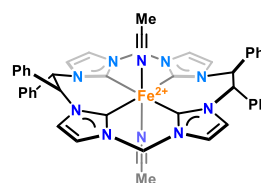
2PF<sub>6</sub><sup>-</sup>

2019, Barnard



M = Pd, Fe

2020, Jenkins



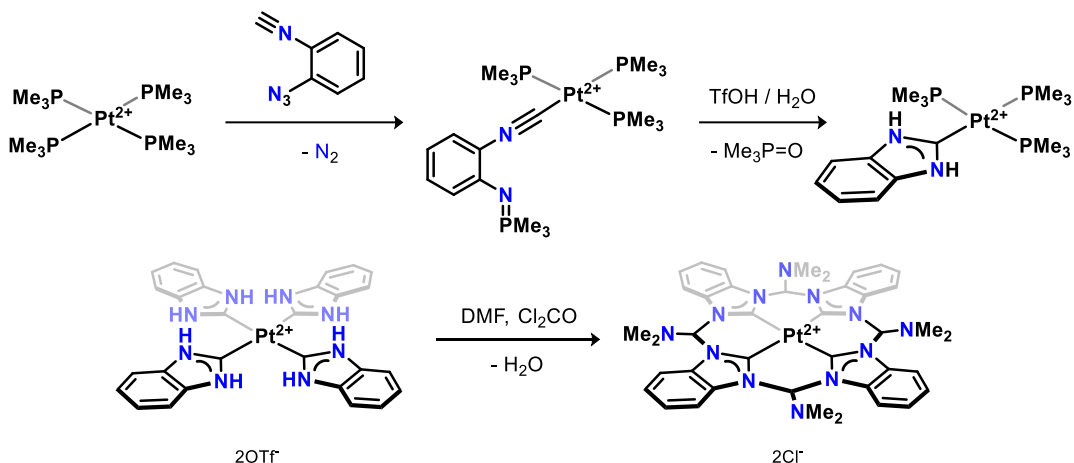
2PF<sub>6</sub><sup>-</sup>

2022, Jenkins

**Chart 5.1.** All the different macrocyclic tetradentate NHC complexes. Three unusually high-valent metal complexes are found in this ligand motif, and all the ligand varieties as per the writing of this dissertation, are heavily represented by the Jenkins group.

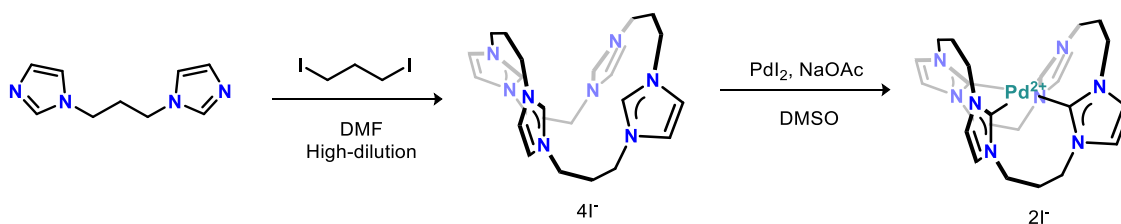
The first such complex was reported by Hahn in 2005 following a metal-templated-annulation between four benzimidazole-2-ylindine moieties coordinating a square-planar Pt (II) complex and DMF. The NHCs were initially generated by reacting *o*-azidoisocyanobenzene with tetrakis(trimethyl phosphine) platinum (II) triflate under acidic

conditions, which furnishes  $\text{N}_2$  extrusion, cleaves the iminophosphorane adduct into phosphine oxide and *o*-functionalized aniline, which subsequently annulate through a nucleophilic attack at isonitrile group, shown in **Scheme 5.2**<sup>20</sup>.



**Scheme 5.2.** Metal-templated synthesis of the first macrocyclic tetradentate NHC bearing complex. Hahn's elegant synthesis of a platinum (II) complex.

Murphy and Spicer two years later reported the structure of a Pd(II) tetra NHC complex, where the tetraimidazolium salt was prepared under high-dilution conditions, reacting 1,3-diimidazole propane with 1,3-diiodopropane, **Scheme 5.3**<sup>21</sup>. The ligand completely envelops the metal center, and a later study on the Ni(II) congener, which demonstrated that the metal is rendered completely inaccessible from an absence of any redox events, and instead, the complex demonstrates ligand-mediated reactivity<sup>22</sup>.



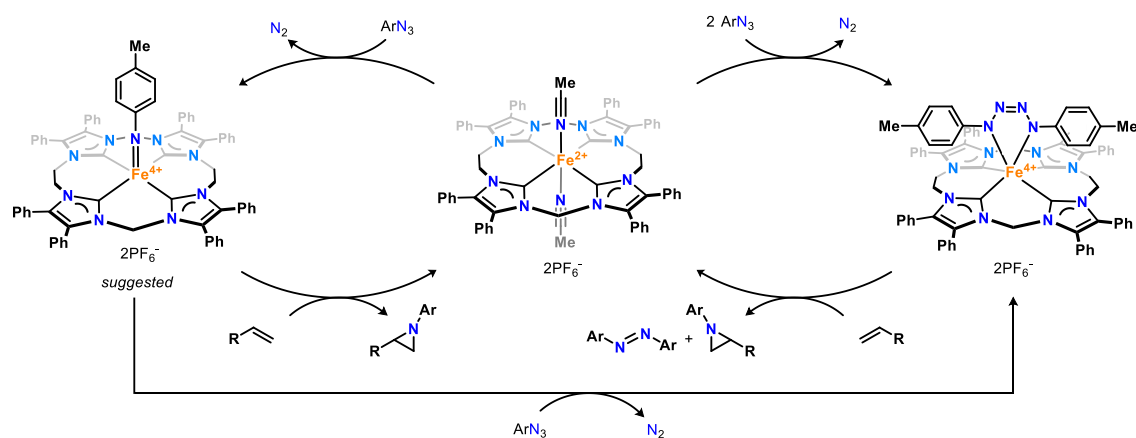
**Scheme 5.3.** High-dilution synthesis of a propyl linked macrocyclic tetra NHC Pd (II) complex. Murphy and Spicer isolated the tetra imidazolium salt in ~15% yield from a high-dilution synthesis.

This synthetic approach to realize the macrocyclic poly imidazolium salts is employed in the remaining complexes; reacting reacting a fragment bearing the bisimidazoles with an appropriate dielectrophile fragment, from dihalido through bistriflate to boranes, and will therefore not be discussed at an individual basis.



The Jenkins group has developed quite a few different macrocyclic tetra NHC ligand systems that support multiple ligand-metal bonds. Their first macrocycle was reported in 2010 on a Pt(II) complex, **Chart 5.1**<sup>23</sup>. The ligand synthesis, similar to Murphy and Spicer, was effected by an S<sub>N</sub>2-substitution reaction between 1,1'-diimidazolemethane and, 1,2-bistriflate ethane. The Pt(II) complex was isolated in a fairly low yield (<15%), which was later amended by isolation of the same complex in >90% yields *via* transmetalation of a Ag(I)-dimer<sup>24</sup>. In this study, they were similarly able to demonstrate redox-neutral transmetalation with a variety of different transition metals, some that seldomly engage in such transformation, such as Cr(II).

Shortly after, Jenkins, as the first group, demonstrated an iron-catalyzed aziridination of unactivated olefins wherein the metal bears a macrocyclic tetra NHC ligand, shown on the left-hand side of **Scheme 5.4**<sup>25</sup>. Despite not having structural evidence, their mass-spectrometry data strongly supports that a Fe(IV) imido intermediate is involved in this transformation. In a later study, the group was able to isolate a Fe(IV) tetrazene complex, catalytically competent in the aziridination reaction, by reacting a parent Fe(II) complex to an excess of aromatic organo azides, shown on the right-hand side of **Scheme 5.4**<sup>26</sup>.



**Scheme 5.4.** First catalytic aziridination reaction with macrocyclic tetra NHC complex. The Jenkins group are actively looking into complex modification to mitigate competitive tetrazene formation.

Further exploring macrocyclic tetra NHC ligand manifolds, Jenkins later reported neutral complexes of Ni(II) and Pd(II) bearing a diborate congener<sup>27</sup>. The anionic diborate groups result in an enhanced NHC donor ability and better charge distribution of the resulting complex, thus better stabilizing reactive high-valent species, as well as improving solubility in apolar solvents. Whereas the neutral macrocycle system is unable in transforming aliphatic azides, this “second-generation” fully furnishes this catalytical transformation<sup>28</sup>. In a later study, the group provides an account of differences between the two complexes, and reported that the diborate complex demonstrates lower activation barriers relevant to key steps, *viz.* initial N<sub>2</sub> extrusion forming the Fe(IV) imido species, and the stability of the metallo-tetrazene *vs.* the aziridine product, of which the latter is energetically favored in alkenes bearing sterically encumbering functional groups<sup>29</sup>. Further corroborating that the diborate moiety imparts desirable properties, manifest from a Cr(II) complex bearing this ligand, which was found to furnish the formation of several multiple Cr-ligands bonds, such as an oxo (triple bond) and imido (double), of which only the imido complexes subsequently reacts in aziridination reactions<sup>30</sup>.

More recently, the group, in collaboration with the Arnold lab, reported several actinide<sup>31</sup> and lanthanide<sup>32</sup> complexes bearing the macrocyclic diborate tetra NHC ligand, as shown in **Figure 5.3**, their successful synthesis attributed to the ligand-centered charge.

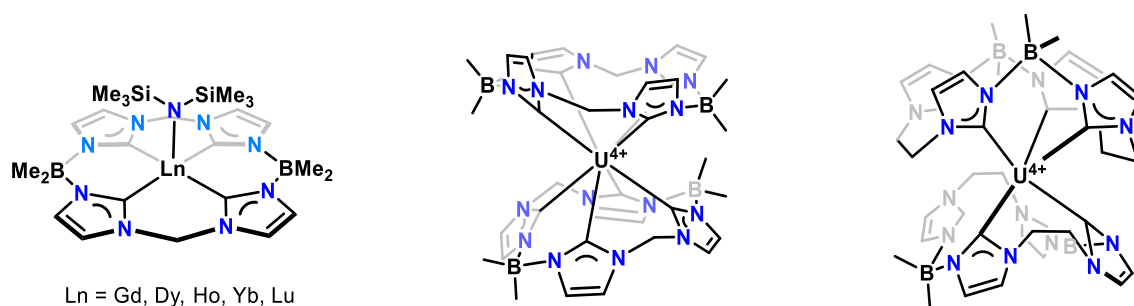
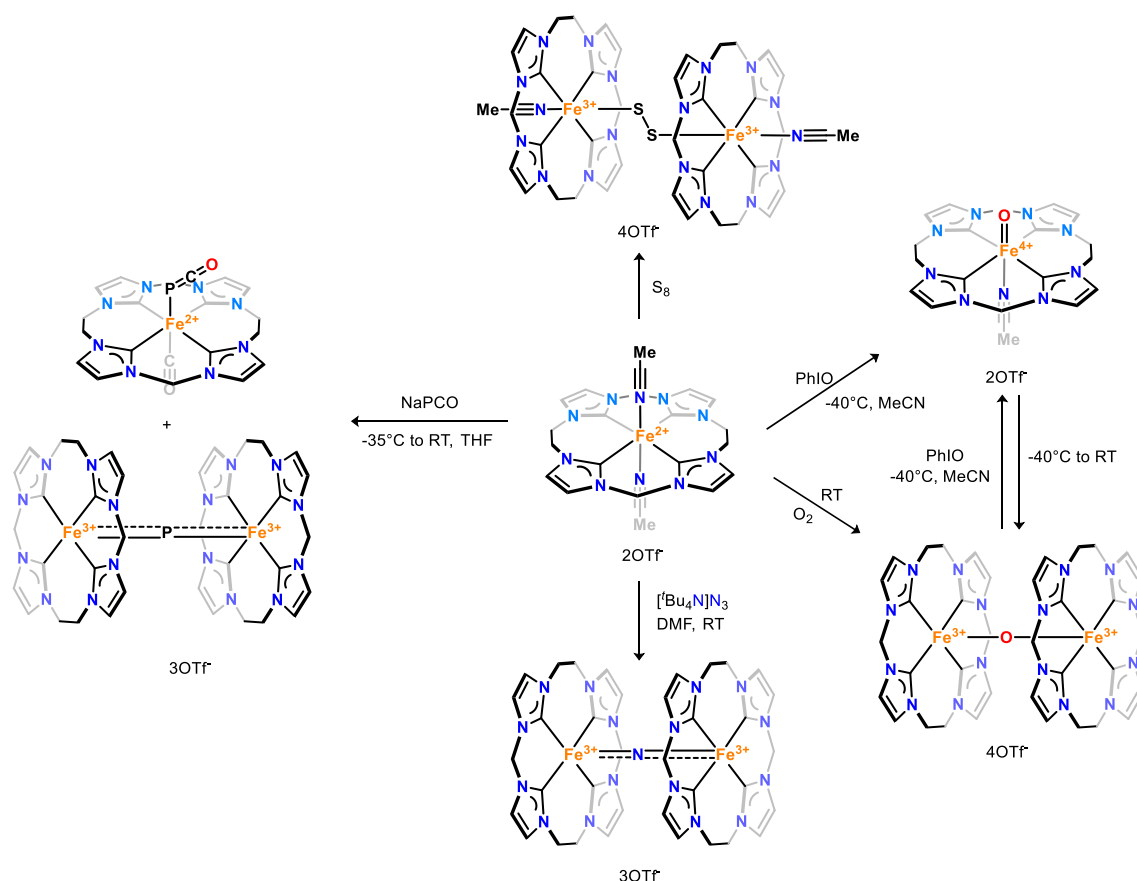


**Figure 5.3.** First lanthanide and actinide complexes bearing macrocyclic tetra NHC ligands. The successful synthesis of these complexes is attributed to the diboronate moieties, to better achieve a match between the Lewis acids and the ligand.

Finally, Jenkins has recently developed two  $D_2$ -symmetric macrocyclic tetra NHC ligands, to induce enantioselectivity in the aziridination reactions, by incorporating  $C_2$ -symmetrical groups in the ethylene-backbone, viz. (1*S*,2*S*)-cyclohexane<sup>33</sup> and (1*S*,2*S*)-1,2-diphenylamine<sup>34</sup>. The latter complex, albeit modestly ( $ee \leq 4\%$ ), successfully catalyzes the stereospecific aziridination reaction between aryl azides and aliphatic alkenes.

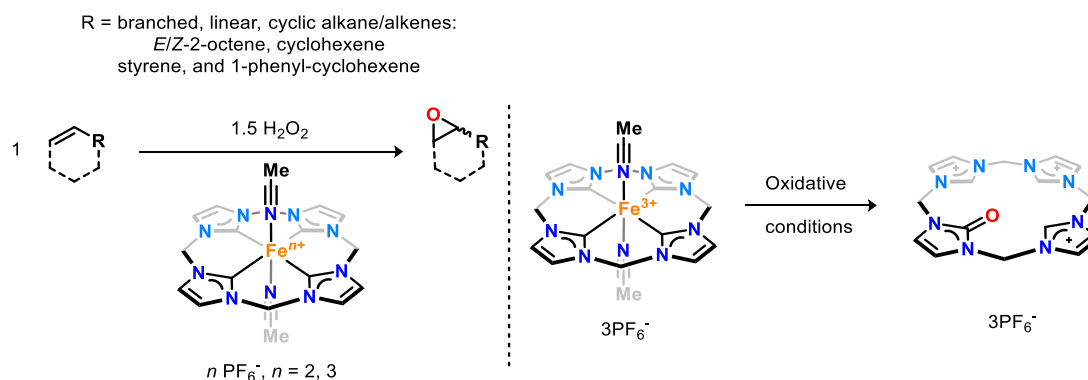
The relatively flat geometry of metal-complexes bearing these ligands often results in dimerization of the reactive intermediates. Meyer's group has done several in-depth studies on how an all-ferrous macrocyclic tetra NHC complex reacts to a variety of different oxidants, outlined in **Scheme 5.5**.



**Scheme 5.5.** Reactivity of all ferrous complex bearing macrocyclic tetra NHC. Meyer's group has demonstrated the transformation taking place under a variety of conditions, leading to the isolation of dimerization products.

Additionally, they have also developed fundamental insights into the reactivity differences, following spin-state dependency as a function of subtle changes in the NHC ring, such as ring-size (16 vs. 18 membered-rings), hybrid donor atoms by exchanging two NHCs for pyridine<sup>35</sup>, mechanistic insights into decomposition products from parent azido, oxo, and anionic P-complexes resulting in bridged nitrido, peroxy, and “naked P” complexes, **Scheme 5.5**<sup>36–38</sup>, to the catalytic activity in small-molecule activation such as C-H bond activation<sup>12,37</sup> and electrocatalytic CO<sub>2</sub> reduction<sup>39</sup>.

The Kühn group has also explored Fe complexes bearing a tetra NHC ligand in a 16 membered ring and their application in the homogenous epoxidation of alkenes using hydrogen peroxide as terminal oxidant, shown on the left-hand side of **Scheme 5.6**<sup>40–43</sup>. Using a Fe(III) (pre)catalyst, they were able to achieve an impressive 183.000 turnovers per hour at RT, and upwards of 4300 turnovers per hour at -30 °C, outcompeting Mo and Re-based (pre)catalysts<sup>42</sup>.



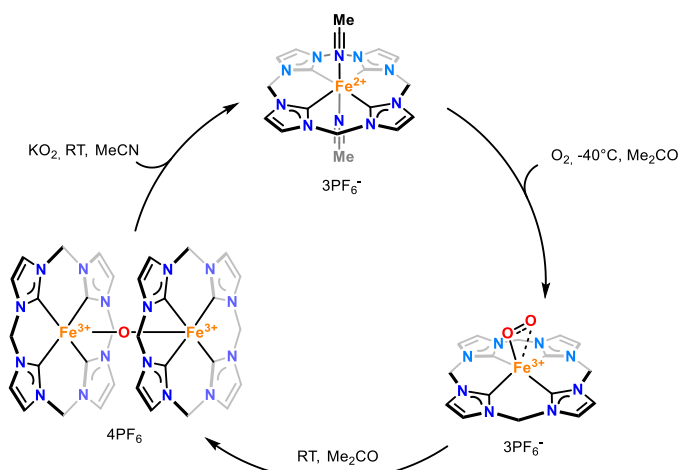
**Scheme 5.6.** Macrocyclic tetra NHC Fe-complexes in epoxidation catalysis. Kühn's group provide further insights into how complexes bearing macrocyclic NHCs mirrors complexes bearing non-haeme N-based ligands.

While the complexes demonstrate high activity, they are prone to deactivation from bridged  $\mu$ -oxo-species, which can be remedied by Lewis acidic additives<sup>40</sup>. In the context of rational catalyst development, the group has investigated relevant decomposition pathways of such Fe complexes under catalytic conditions, and reported that the major

decomposition pathways originate from oxidation of the C<sub>2</sub>-C position leading to the expulsion of Fe from the “binding pocket”, shown on the right-hand side of **Scheme 5.6**<sup>44</sup>.

Continued work by Kühn’s group, focuses on disclosing the reactivity of Fe(II) and Co(II) complexes bearing macrocyclic tetra NHC ligands towards dioxygen in developing biomimetic catalysts *e.g.* synthetic analogues to methane-monooxygenase.

In this context, the Fe(II/III) complex, highly-active in epoxidation catalysis, reacts with O<sub>2</sub> or KO<sub>2</sub>, respectively, to form a transient superoxide Fe(III) complex, which at RT forms a  $\mu$ -oxo-diiron (III) complex, shown on the left-hand side of **Scheme 5.7**<sup>45,46</sup>.

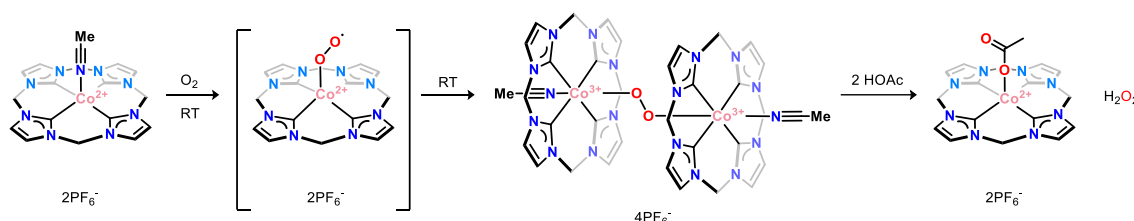


**Scheme 5.7.** The reactivity of an Fe (II) macrocyclic tetra NHC complex with O<sub>2</sub>. The apparent activation of O<sub>2</sub> and subsequent regeneration of the parent Fe(II) complex suggests that the complex may engage in a catalytic capacity.

This superoxide intermediate is isolable in acetone at low temperature, however, and is diamagnetic, precluding a direct assignment *via* EPR. Instead, using a superoxide trapping reagent, 5,5-dimethyl-1-pyrroline *N*-oxide (DMPO), the authors demonstrate that this intermediate transfer of an oxygen-radical from the emergence of a triplet signal  $g = 1.97$ , identical to the reaction by reacting the parent Fe(II) complex with O<sub>2</sub> in presence of DMPO. This complex further undergoes two subsequent single-electron oxidations into a linearly  $\mu$ -oxo-diiron (IV) complex, shown in **Scheme 5.7**, again, demonstrating a high propensity towards dimerization of the reactive intermediates. The

dimeric oxo-complex act as an oxidant, liberating the parent Fe (II) complex, demonstrating that the transformation of O<sub>2</sub> can happen in a catalytical capacity.

The analogous Co(II) complex, shown in **Scheme 5.8**, reacts in a MeCN solution with air, furnishing the reduction of O<sub>2</sub> into a  $\mu$ -peroxo dicobalt (III) complex, which the authors suggest forms *via* an intermediary side-on superoxide species, based on their EPR measurements<sup>47</sup>. The  $\mu$ -peroxo dicobalt complex liberates H<sub>2</sub>O<sub>2</sub> and the parent Co (II) complex upon treatment with an acid.



**Scheme 5.8.** Elucidation on the reactivity of a Co (II) macrocyclic tetra NHC complex with O<sub>2</sub>. The apparent reversibility suggests that the complex can furnish catalytic transformation of O<sub>2</sub>.

The remaining complexes reported by Hahn<sup>48</sup>, Chen<sup>49</sup>, Baker<sup>50</sup>, and Barnard<sup>51</sup> have mostly emphasized the complex synthesis; connectivity of carbene-transfer reagents, resulting macrocyclic tetra NHC complexes, and some applications in the context of anti-cancer activity. Only Baker's Au (III) complex is noteworthy, as Au (III) is a relatively strong oxidant, and only a limited number of Au (III) complexes have been isolated. Unsurprisingly, the complex appears quite stable supported by the macrocyclic tetra NHC crown.

## 5.2 Pd (IV) dihalido complexes bearing a macrocyclic tetra NHC ligand

Complex **4.13** (and **4.18**) is isoelectronic with Vaska's complex and similarly feature a metal coordinated in square-planar geometry, and a HOMO consisting of a  $d(z^2)$ -orbital. However, whereas the basal plane of **4.13** is locked, leaving just the axial sites available to reactivity, Vaska's complex is susceptible to ligand rearrangement, thus facilitating *cis*-oxidative additions of *e.g.*  $H_2$  and  $O_2$ . Moreover, Ir (III) complexes are much more ubiquitous relative to Pd (IV), owing to an inherent stability of the former, and while several complexes of the latter exist, these are often unstable<sup>52</sup>, and occur transiently in transformations where strongly donating ligands bind the Pd-center, *e.g.* alkylation of aromatic C-H bonds, as proposed by Catellani<sup>53</sup>. As such, should complex **4.13** undergo oxidation, it likely is in a limited capacity.

To probe whether complex **4.13** undergoes oxidation to Pd (IV), CV was obtained at different scan-rates, shown in **Figure 5.4**, which pleasingly demonstrates a persisting oxidation wave. In addition, we similarly acquired CV of complex **4.9**, shown in **Figure 5.5**, which in agreement with Kühn's study, demonstrates a different electrochemical profile.

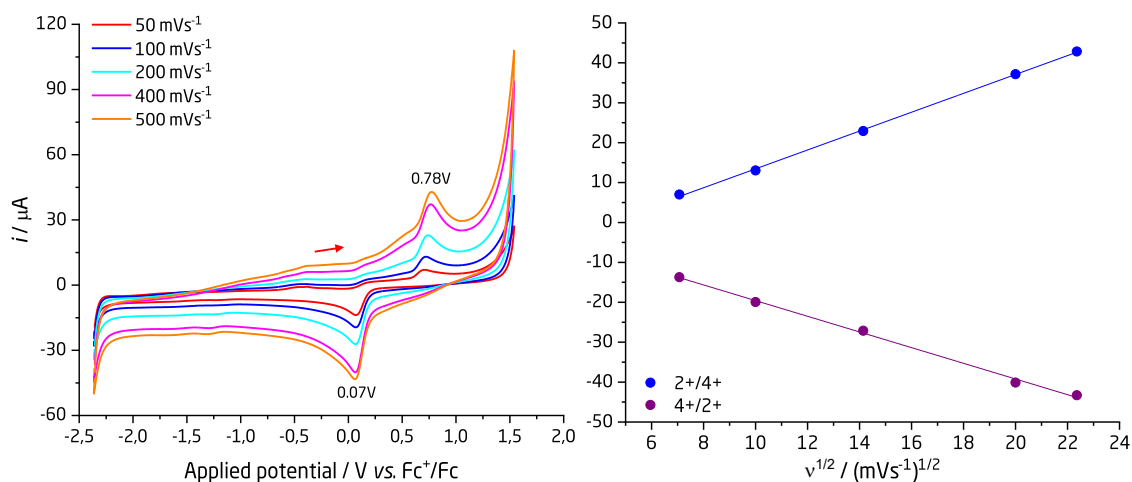


**Figure 5.4.** Cyclic voltammograms of complexes **4.13** at different scan-rates and redox-events relationship with scan-rate. The arrow indicates starting potential and proceeds in the anodic direction. Under an Ar atmosphere, in MeCN, 0.5mM  $[Pd]2PF_6$ , 0.1M TBAPF<sub>6</sub> (supporting electrolyte), working electrode: Glassy Carbon Electrode, Counter electrode: Pt, Potential width: -2.3V to 1.5V  $Ag^{+/0}$ , corrected against the  $Fc^{+/0}$  redox-couple ( $V(Fc^{+/0}) = V(Ag^{+/0}) - 0.36V$ ).

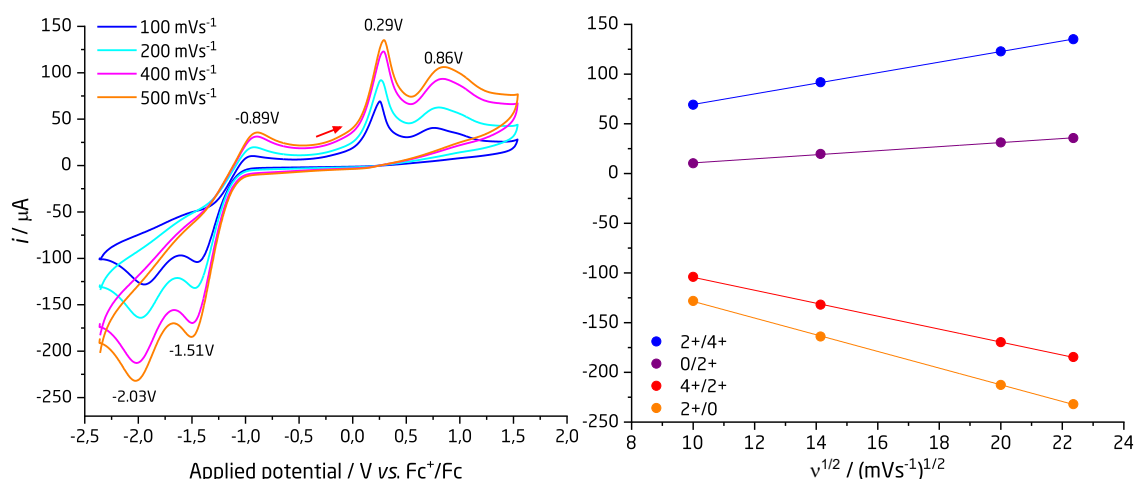


**Figure 5.5.** Cyclic voltammograms of complexes **4.9** at different scan-rates and redox-events relationship with scan-rate. The arrow indicates starting potential and proceeds in the anodic direction. Under an Ar atmosphere, in MeCN, 0.5mM [Pd]2PF<sub>6</sub>, 0.1M TBAPF<sub>6</sub> (supporting electrolyte), working electrode: Glassy Carbon Electrode, Counter electrode: Pt, Potential width: -2.3V to 1.5V Ag<sup>+/0</sup>, corrected against the Fc<sup>+/0</sup> redox-couple ( $V(\text{Fc}^{+/0}) = V(\text{Ag}^{+/0}) - 0.36\text{V}$ ).

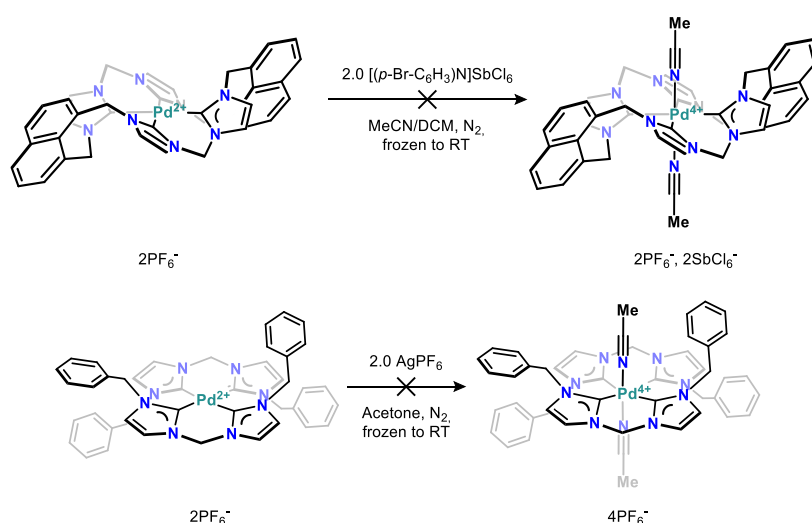
**Figure 5.4** demonstrates the CV of **4.13** over an array of scan-rates, demonstrating what appears as just a single quasi-reversible redox event with no further reduction events, thus suggesting that oxidation to Pd (IV) is possible, whereas reduction to Pd (0) is unlikely. Additionally, an irreversible process appears to take place with on-set at potentials >1.2V for complex **4.13**, which may likely be residual water, as the samples were prepared in a fume hood and sparged with Argon before measurements, and this great oxidation wave is absent in the analogous CV of complex **4.9**, **Figure 5.5**. Under the same conditions, complex **4.9** features an initial oxidation wave at a lower potential, followed by a broad irreversible oxidation wave, which may suggest that the complex oxidizes to Pd (IV), however, suffer from ligand oxidation. This complex does not demonstrate a broad oxidation at potentials >1.2V as **4.13**, suggesting that this process is confined to that complex.

A subsequent scan in the cathodic direction features two strong reduction waves, consistent with the reduction of Pd. The latter reduction wave (-2.03V vs. Fc<sup>+/0</sup>) is accompanied by another oxidation wave, suggesting to us that complex **4.9** electrochemically can shuffle through the Pd<sup>0/II/IV</sup> redox couples, whereas **4.13** only



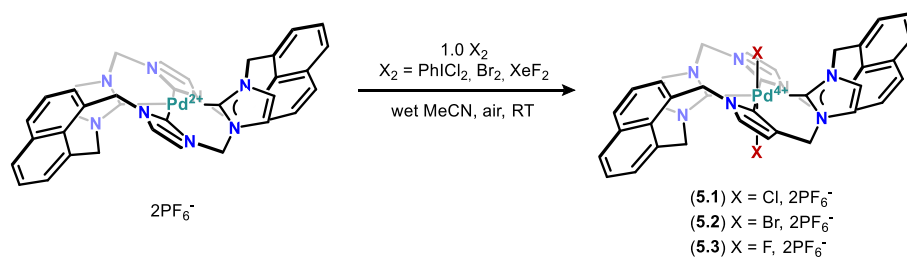
shuffles through  $\text{Pd}^{\text{II/IV}}$ . Each of the redox-events concerning complexes **4.13** and **4.9**, have a linear relationship between the measured current and the scan-rate, indicating that each redox process is for freely dissociating species in solution, and the (quasi) reversible electron-transfer is homogeneous in nature.

Encouraged by these results, we wanted to test whether we could isolate Pd (IV) complexes by reacting **4.13** and **4.9** with outer-sphere oxidants as shown in **Scheme 5.8**<sup>54</sup>. Unfortunately, these oxidants do not furnish any transformation.



**Scheme 5.9.** Initial oxidation reactions targeting Pd (IV) complexes. Neither **4.13** nor **4.9** were reacting with the different oxidants. Complex **4.13** was additionally reacted with NOPF<sub>6</sub>, however, this oxidant neither furnished any transformation.

We instead sought to react the complexes with PhICl<sub>2</sub>, a chlorine surrogate, as this oxidant finds use in the preparation of other high-valent palladium complexes<sup>55</sup>. Complex **4.13** under strictly inert conditions, cleanly and instantaneously reacts with this inner-sphere oxidant transforming the parent Pd (II) complex into the dichlorido Pd (IV) complex at RT. Moreover, Br<sub>2</sub> and XeF<sub>2</sub> furnish a similar transformation of complex **4.13** under inert conditions. More interestingly, this transformation is also facilitated under ambient conditions, as outlined in **Scheme 5.9**. We were able to isolate single crystals of the dibromido (red/brown) and dichlorido (yellow/green) complexes, shown in **Figures 5.6** and **5.7**, respectively.



**Scheme 5.10.** Oxidation of **4.13** with halide (surrogates). Two of the three compounds were unambiguously confirmed as Pd (IV) complexes, through a variety of spectroscopical methods.

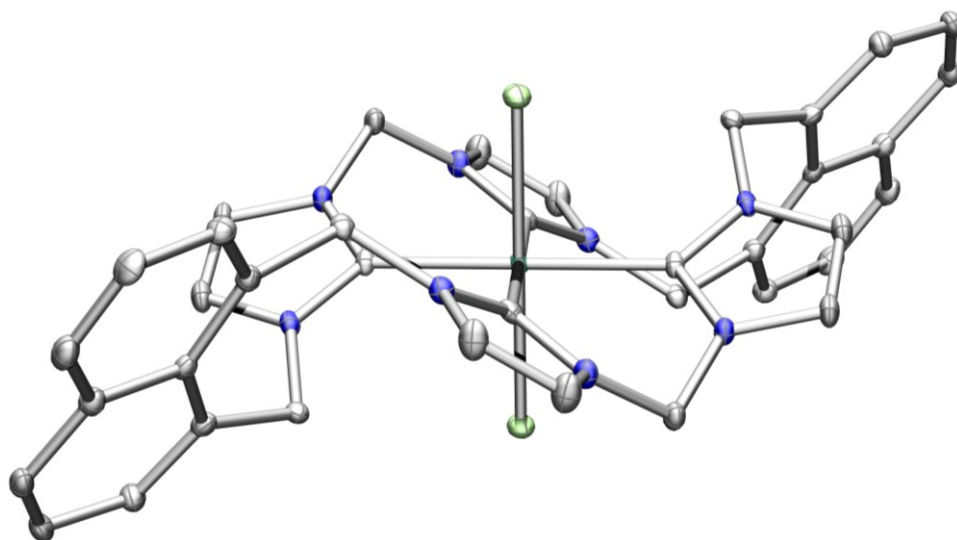


**Figure 5.6.** Solid-state structure of **5.1**. Hydrogen atoms, co-crystallized PhI, and  $\text{PF}_6^-$  counterions are omitted for clarity. Thermal ellipsoids are set at a 50% probability level. Atom color-coding: Pd Seagreen, N blue, Cl yellow-green, and C grey.

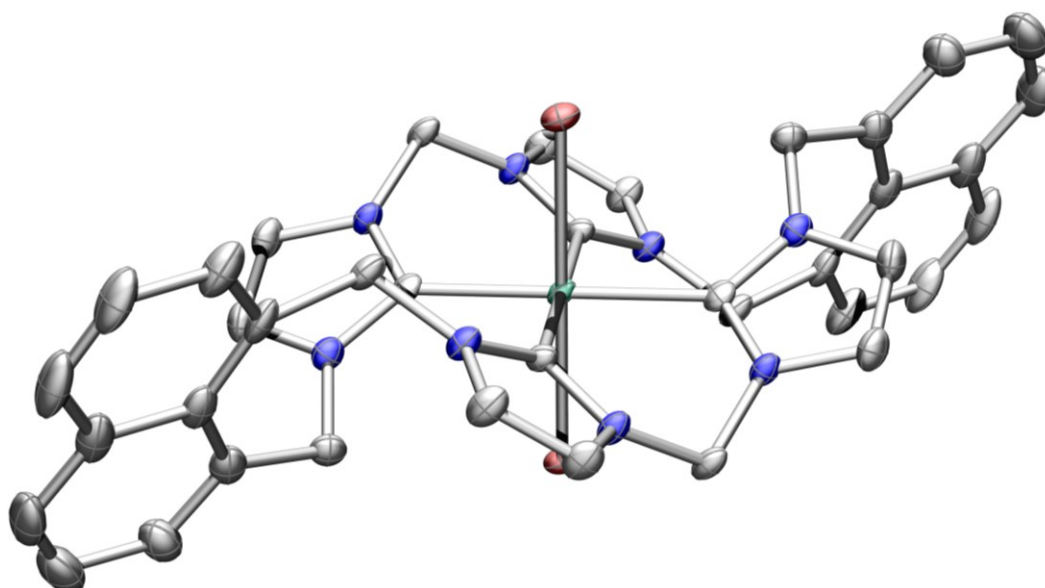


**Figure 5.7.** Solid-state structure of **5.2**. Hydrogen atoms and  $\text{PF}_6^-$  counterions are omitted for clarity. Thermal ellipsoids are set at a 50% probability level. Atom colour-coding: Pd Seagreen, N blue, Br brown, and C grey.

The *bona fide* dichlorido (**5.1**) and dibromido (**5.2**) complexes as their  $\text{PF}_6^-$ -salt are surprisingly stable under ambient conditions (no measurable decomposition in solution

nor solid-state over several weeks), and even at elevated temperatures in dry solvents, under an ambient atmosphere. Reacting **4.9** with the same oxidants under ambient conditions either furnishes no reaction ( $\text{Br}_2$ ,  $\text{PhICl}_2$ ) or complete decomposition ( $\text{XeF}_2$ ). Thus far, we have been unable to produce single crystals of sufficient quality for single-crystal X-ray diffraction of the difluorido complex (**5.3**) following  $\text{XeF}_2$  oxidation (ongoing as of the time of writing).

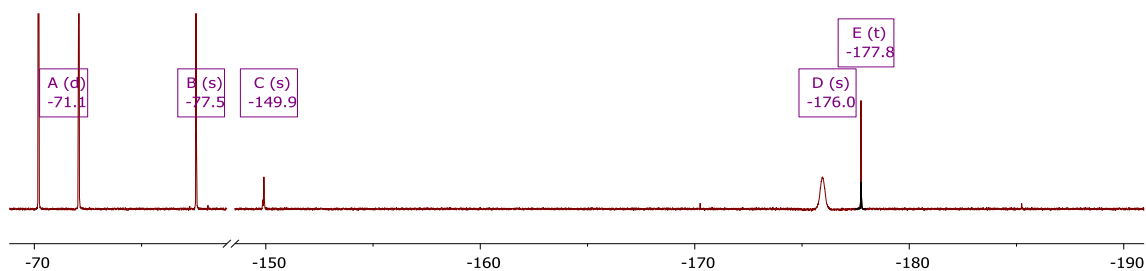


**Figure 5.8.**  $^{19}\text{F}$  NMR spectrum ( $\text{CD}_3\text{CN}$ ) of  $\text{XeF}_2$  oxidation of **4.13**. The spectrum shows signals owing to  $\text{PF}_6^-$  (-71.1),  $\text{F}^-$  (-77.5),  $\text{SiF}_4$  (-149.9), unreacted  $\text{XeF}_2$  (-177.8) and satellites (-170.3, -185.2) owing to  $^1J(^{129}\text{Xe}-^{19}\text{F}) = \sim 5600\text{Hz}$  coupling, leaving -176.0 as a putative Pd-F signal.

However, by acquiring a  $^{19}\text{F}$  NMR spectrum directly after the addition of a slight excess of (1.1 equiv.)  $\text{XeF}_2$  to **4.13** in wet  $\text{CD}_3\text{CN}$ , with reference to the  $\text{PF}_6^-$ -anion (-71.1,  $d$ ,  $^1J(^{19}\text{F}-^{31}\text{P}) = 711\text{Hz}$ )<sup>56</sup>, shown in **Figure 5.8**, we observe the emergence of a new broad signal (-176.0 ppm) owing to the Pd-bound fluoride<sup>57</sup>, in addition to signals owing to the  $\text{PF}_6^-$ -anion,  $\text{MeCN-F}^-$  adduct (-77.5)<sup>58</sup>,  $\text{SiF}_4$  (-149.9), and excess  $\text{XeF}_2$  (-177.8 pseudo-triplet).

$\sim 20\%$  of Pd constitutes  $^{105}\text{Pd}$  ( $I = 5/2$ ), which can explain the line broadening following the coupling between the quadrupole moment and electric field. The pseudo-triplet is a consequence of  $\sim 26\%$  of Xe comprising the NMR spin-active nuclei  $^{129}\text{Xe}$  ( $I = 1/2$ ), which couples to  $^{19}\text{F}$  with a one-bond coupling constant ( $^1J(^{129}\text{Xe}-^{19}\text{F})$ ) magnitude of  $\sim 5600\text{Hz}$ , accounting for the two satellites at -170.3 and -185.2 ppm.

While  $\text{XeF}_2$  is stable in MeCN for several hours, it will react with the silicate glassware, and slowly decompose into HF (-183.5 ppm,  $d$ ,  $^1J(^1\text{H}-^{19}\text{F}) = \sim 400\text{Hz}$ ) in presence of moisture<sup>59</sup>. Moreover, to further support the formation of complex **5.3**, a

comparison between splitting patterns and chemical shift differences upon oxidation is helpful. To this end, differences in the  $^1\text{H}$  NMR spectrum between the *bona fide* dichlorido Pd (IV) complex **5.1** (top spectrum) and complex **4.13** (middle spectrum), **Figure 5.9**, to assess any expected changes.

The splitting patterns of complex **5.1** relative to **4.13** remain unchanged. However, all signals experience a downfield shift, which also holds for complex **5.2**. The extent of the downfield shift can be understood from both through-space and covalent interactions. The naphthalene signals (signals A through C) appear less perturbed than the remaining signals, as these are quite far away from the Pd-center. In contrast, the methylene linker, and the benzylic position each demonstrate a significant downfield shift following their closer proximity, however, the shift is experienced asymmetrically; signals F and G of **5.1** downfield shifts by  $\sim 0.5$  and  $\sim 0.2$  ppm.

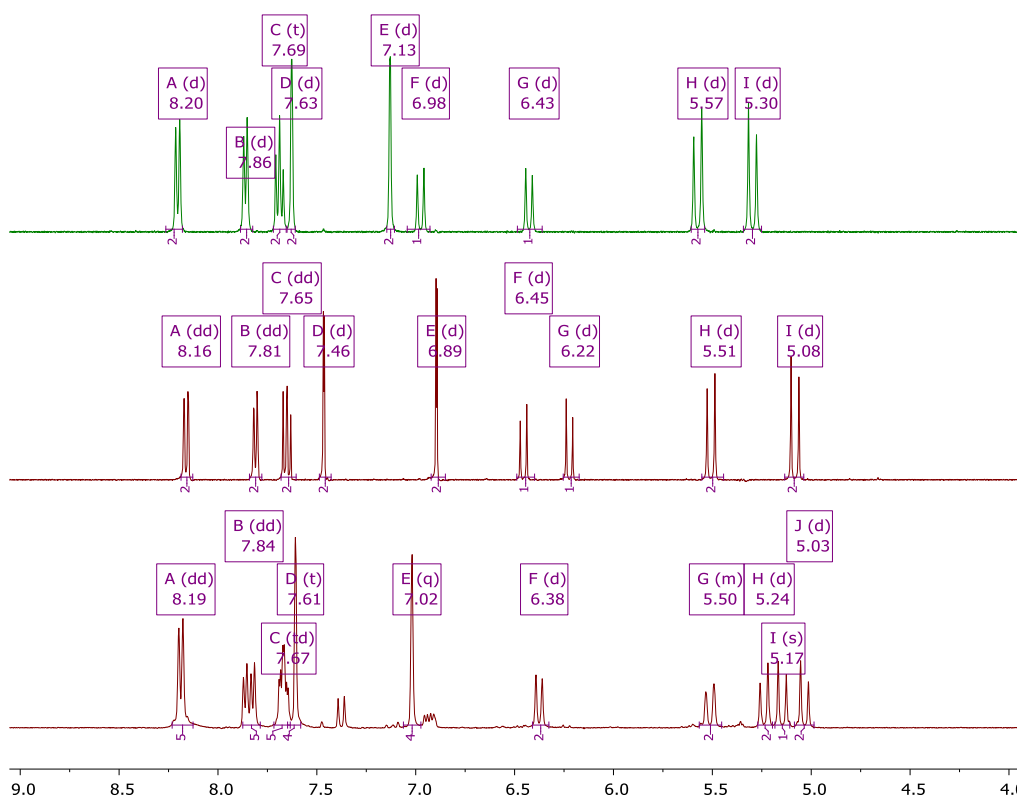


**Figure 5.9.**  $^1\text{H}$  NMR ( $\text{CD}_3\text{CN}$ , ambient atmosphere) spectra comparison of **4.13** to its high-valent Pd (IV) congeners. Top insert: **5.1**, middle insert: **4.13**, and lower insert: **4.13** + 1.1 equiv.  $\text{XeF}_2$  reacted at ambient conditions in  $\text{CD}_3\text{CN}$ .

From the solid-state structure, one proton owing to each of these moieties orient towards the halide, thus experience a greater extent of deshielding thereby experiencing an overall greater downfield shift. Changes to the lower spectrum follow an overall similar downfield shift and substantiate a Pd (IV) species. However, as the splitting pattern is more complex,  $\{^1\text{H}-^1\text{H}\}$  COSY was utilized to unambiguously understand respective coupling partners, shown in **Figure 5.10**.

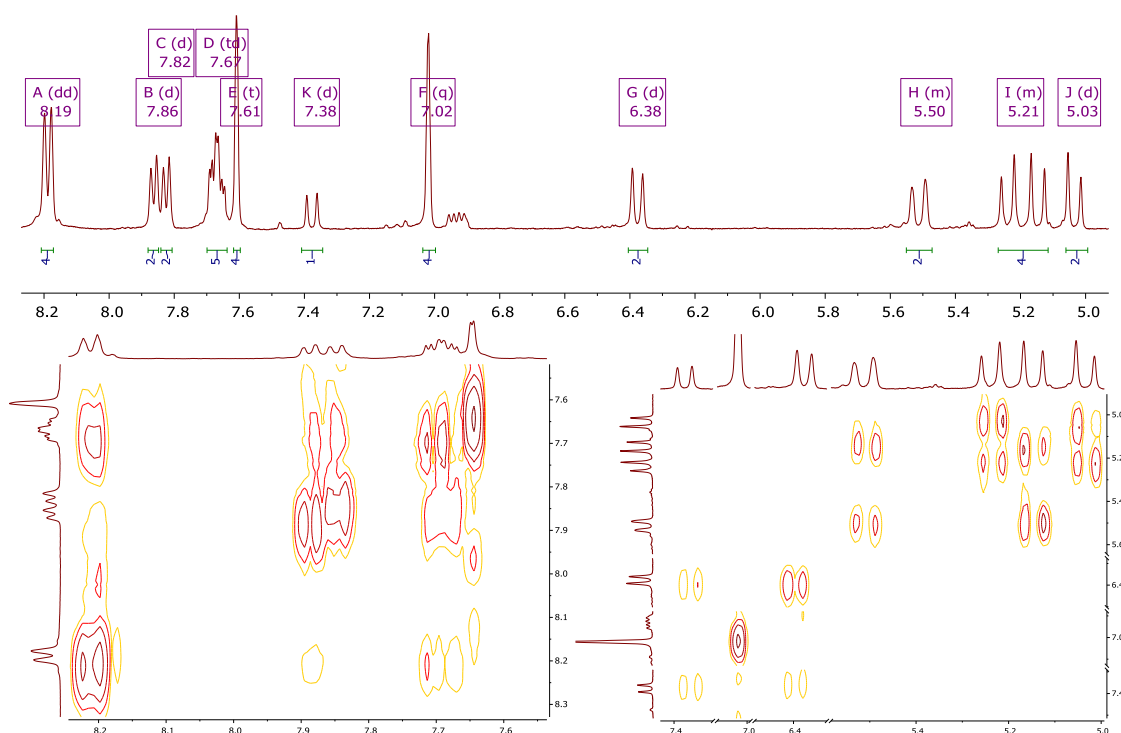


**Figure 5.10.** Combined  $^1\text{H}$  NMR spectrum ( $\text{CD}_3\text{CN}$ ) and  $\{^1\text{H}-^1\text{H}\}$  COSY of **5.3** (putative). The complex demonstrates previously seen splitting patterns consistent with metal complexes bearing the macrocyclic tetra NHC ligand.

The total integration in the top part of **Figure 5.10** amounts to 32 protons, consistent with the total  $^1\text{H}$  count of complex **5.3**. Signal A adopts both a similar splitting pattern and chemical shift as **5.1**, whereas signals B and C appear as two individual signals; if considered as a doublet of doublets, a coupling constant of 15 Hz is found, which is atypical for aromatic compounds. The zoom in the  $\{^1\text{H}-^1\text{H}\}$  COSY spectrum, left-hand side, further suggests two different signals.

The cause of this splitting in two is still uncertain. Signal D integrates five protons, which suggests, that this peak comprises 4 + 1 protons, given the symmetrical nature of the compound. Signals E and F are consistent with the ylidene-moiety, and demonstrate a similar downfield shift found in **5.1**.

Curiously, peak K couples to G as the only resonance, and peak G would otherwise be consistent with a downfield shifted methylene-proton. The remaining coupling patterns of peaks H, I, and J, are easily established by the off-diagonal elements in the  $\{^1\text{H}-^1\text{H}\}$  COSY zoom on the right-hand side, consistent with a geminal coupling pattern owing to the methylene and benzylic positions, however, at fairly upfield shifted chemical shifts. To test the stability of **4.13** and whether the observed splitting arise from ligand fluorination, **4.13** was refluxed in MeCN added a 100-fold excess of  $\text{XeF}_2$  for an hour before being filtered through Celite, and a  $^{19}\text{F}$ -decoupled  $^1\text{H}$  NMR spectrum was acquired, showing the same signals as in the top insert of **Figure 5.8**, suggesting **5.3** is quite stable, and does not undergo H-F exchange. Precipitating this filtrate with  $\text{Et}_2\text{O}$ , yields an off-white powder with spectral properties identical to **4.13**, and recovers ~98 - 99% of the employed mass of **4.13**. The 2 - 1% mass loss may be mechanical in nature, rather than from an actual degradation, working in scales of less than 5 mg.

In trying to rationalize the observed splitting pattern of the  $^1\text{H}$  NMR spectrum, **Figure 5.10**, the Kraft group reported that a tetrachlorido Pd(IV) bis-NHC complex, shown on the left of **Figure 5.11**, facilitates ligand-mediate Cl-atom transfer to alkenes through a cationic  $\text{PdCl}_3^+$  species<sup>60</sup>. The authors report, that excess halide interacts with the NHC-methylene bridge, resulting in significant downfield shifts of the  $\text{H}^5$  and  $\text{H}^{\text{exo}}$  protons, of which  $\text{Cl}^-$  results in the larger downfield shifts relative to  $\text{F}^-$ .

Since this coordination of Kraft's complex resembles that of complex **4.13** (and by extension **5.1-5.3**), it is within reason that any excess  $F^-$  may interact similarly. In addition to the methyl bridging moiety, the benzylic position features a similar disposition to the adjacent naphthalene moiety, which could account for some of the observed coupling patterns.

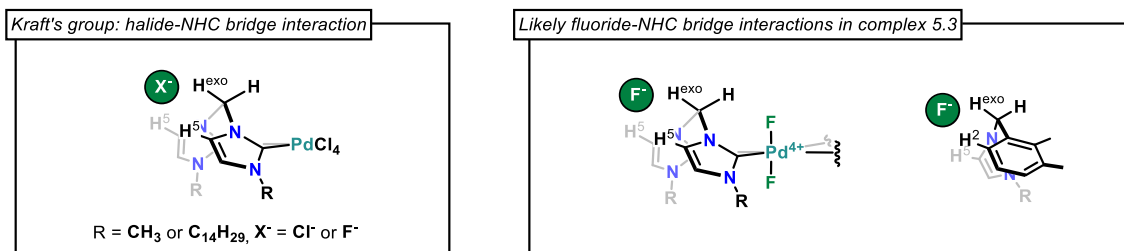


**Figure 5.11.** Halide-NHC bridge interaction was reported by the Kraft group. Envisioned interactions possible in complex **5.3**.

However, probing the chemical shift following different free halides of complexes **5.1 – 5.3**, was not thoroughly investigated in this PhD study. However, while such interactions may exist in solution, none of the  $^{19}F$  NMR signals demonstrates any fine coupling, which is otherwise expected. Likely, any fine coupling patterns resulting from through-space interactions between the Pd-F and the ligand protons are lost due to a rapid quadrupole relaxation induced by  $^{105}Pd$ . In this context, the Sanford group report a related Pd (IV) difluorido complex<sup>57</sup>, and similarly reports a line broadening of Pd-F  $^{19}F$  NMR signals. Moreover, an interaction with rapidly exchanging solvated  $F^-$  anions would result in a similar loss of fine coupling as seen in *e.g.* heteroatoms H/D exchange processes. However, without any solid-state data to obtain insight into F-interactions, it is still unclear what causes the observed splitting.

Other means of trying to obtain **5.3** was attempted following a combined ligand-substitution halide-abstraction of **5.1** (and **5.2**) with AgF under Schlenk conditions. However, these reactions, surprisingly, produce significant quantities of  $F^-$ , and AgX (X = Cl or Br). It is likely the AgF was wet, and the reaction should have been prepared in a

glovebox instead. Nevertheless, the reductant in this situation is still ambiguous. Generally, complex **5.3** appears more sensitive to air and mild reductants, readily reducing into the parent Pd (II) compound, relative to **5.1** and **5.2**.

We noted that the reduction of complex **5.3** is facilitated by precipitation using wet Et<sub>2</sub>O under ambient conditions, corroborated by <sup>1</sup>H and <sup>19</sup>F NMR spectra, as well as multiple isolated single crystals with unit cell matching **4.13**. To probe whether air or moisture reacts with **5.3**, complex **4.13** was reacted with XeF<sub>2</sub> under strictly inert conditions, in dry MeCN, yielding the same <sup>1</sup>H and <sup>19</sup>F NMR spectra as in **Figure 5.10** and **Figure 5.8**, respectively, featuring only trace F<sup>-</sup>, which suggests that any excess fluoride originates from the reaction between XeF<sub>2</sub> and the glassware. Moreover, upon the addition of enough water (degassed by freeze-pump-thaw cycles, cannula addition) at RT, the putative complex **5.3** is fully converted into **4.13** and substantial amounts of HF. Et<sub>2</sub>O precipitation the following filtration through Celite, works to recover >99% of the initially used mass of complex **4.13**, which suggests that complex does not decompose under these extremely oxidative conditions, and that water seems to reduce the complex, *vide infra*.

Finally, we were unable to fully assign whether the iodine adduct in all forms or is thermally unstable. However, as the addition of iodide to **5.1** - **5.3** quickly furnishes the reduction into **4.13** and I<sub>2</sub>, which may suggest that a Pd (IV) iodo complex is consumed as quickly as it is formed.

#### 5.2.1 Structural characterization of complexes **5.1** and **5.2**

Both complexes **5.1** and **5.2** crystallize in the triclinic P-1 spacegroup with co-crystallized PhI (**5.1**) and MeCN (**5.2**), demonstrating differences in bond lengths of Pd-C and Pd-X, as illustrated below in **Figure 5.12**. The crystal quality of **5.1** was quite satisfactory, only iodide of PhI demonstrating some disorder over two positions, and the



associated model converges at  $R_1 = 3.04\%$  and  $wR_2 = 6.93\%$  (all data). The co-crystallized MeCN of **5.2** demonstrate extensive disorder, however, was easily modelled by applying a solvent mask *via* PLATON Squeeze<sup>61</sup>: 70 electrons in a volume of  $275\text{\AA}^3$  were found in 1 void per unit cell, which is consistent with the presence of 3.2 molecules of MeCN per unit cell, accounting for 70 electrons. This solvent mask improves the overall model converging to  $R_1 = 3.62\%$  and  $wR_2 = 8.3\%$  (all data).

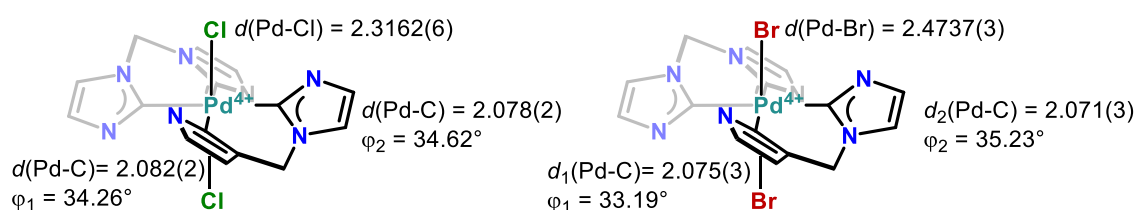


**Figure 5.12.** Bonding metrics of the Pd(IV) core of **5.1** and **5.2**. Complex representation is simplified for sake of clarity.

**Figure 5.6** and **Figure 5.7** both feature Pd in a distorted octahedral coordination environment, where the basal plane is fully occupied by the NHC ligand, and the axial coordination sites are occupied by halides. As the oxidation state changes from Pd (II) to Pd (IV), the corresponding complexes may be expected to undergo bond length contraction leading to shorter Pd-ligand bond lengths. However, as evident from **Figure 5.12**, complexes **5.1** and **5.2** feature Pd-C bond lengths significantly longer than in **4.13** (2.054(4) and 2.053(4)Å, respectively), and the Pd-X bond length seems to counteract any Pd-C contraction; the short Pd-Cl bond leads to longer Pd-C bond lengths, and the longer Pd-Br bond results in a decreased Pd-C bond.

If complexes **5.1** and **5.2** demonstrate electronic properties like Meyer's Fe(IV) complex, *vide supra*, the relative orbital ordering and symmetry should follow that the LUMO predominantly feature antibonding contributions along with the axial ligands, and the LUMO + 1 predominantly is antibonding concerning the basal plane. Moreover, the relative energy difference between the LUMO and LUMO + 1 ( $\Delta E_{\text{rel}}$ ), should decrease accordingly with increasing Pd-C bond lengths, reflecting a lower extent of orbital

destabilization of the LUMO + 1 orbital. Indeed, DFT calculations of complexes **5.1** and **5.2** reflect this trend.

**Figure 5.13** shows that the LUMO of **5.1** and **5.2** comprise a net antibonding interaction between Pd ( $4d(z^2)$ ) to all ligand's  $\sigma$ -orbital, with a larger axial contribution. Further, the LUMO + 1 reflects a net antibonding interaction between Pd ( $4d(x^2-y^2)$ ) and  $\sigma(\text{NHC})$ , following destabilization of the  $d(x^2-y^2)$  orbital following strong Pd-NHC bonds.

$\Delta E_{\text{rel}}$  increases from 1.69 eV (**5.1**,  $d_{\text{avg}}(\text{Pd-C}) = 2.08 \text{ \AA}$ ) to 1.85 eV (**5.2**,  $d_{\text{avg}}(\text{Pd-C}) = 2.073 \text{ \AA}$ ), and it is reasonable to assume that the Pd-F bond of **5.3** would be shorter than the Pd-Cl bond of **5.1**, thus further lowering  $\Delta E_{\text{rel}}$ . It is known that chloride on average binds stronger than bromide following a larger contribution towards  $\pi$ -donation<sup>62</sup>, which also is reflected in the significant difference in Pd-X bond lengths. The mechanistic aspects concerning the formation of the bishalido Pd (IV) complexes **5.1** – **5.3**, were unfortunately not explored in-depth following from time constraints on the PhD study, however, likely proceed similarly to Vaska's complex, following an  $\text{S}_{\text{N}}2$ -like nucleophilic substitution of the X-X bond.

The agreement between the electronic structure of this ligand platform and Meyer's, has implications for the reactivity of the Pd complex, in that the fully occupied  $t_{2g}$  orbitals ( $xy$ ,  $zy$ , and  $zx$ ) constitute a full population of any would-be  $\pi^*(\text{Pd-X})$  orbitals. In other words, the Pd (IV) complex is unable in facilitating multiple metal-ligand bonds, such as oxo or imido ligands, as the  $\pi^*$  orbital is fully occupied. Moreover, neither CV nor reactivity studies with  $\text{XeF}_2$ , suggests the ligand manifold accommodates a  $\text{Pd}^{6+}$ -ion.

Unsurprisingly so, reacting complex **4.13** with different oxo- and imido-transfer reagents *e.g.* PhIO, 1-AdN<sub>3</sub>, (4-F)-PhN<sub>3</sub>, as suggested in **Scheme 5.10**, did not furnish any transformation of **4.13** into the corresponding oxo/imido complexes, instead, the

recovered mass of oxidants were close to 100% of initially used, which further suggests that neither the formation of oxygenoids nor nitrenoids take place<sup>63</sup>.

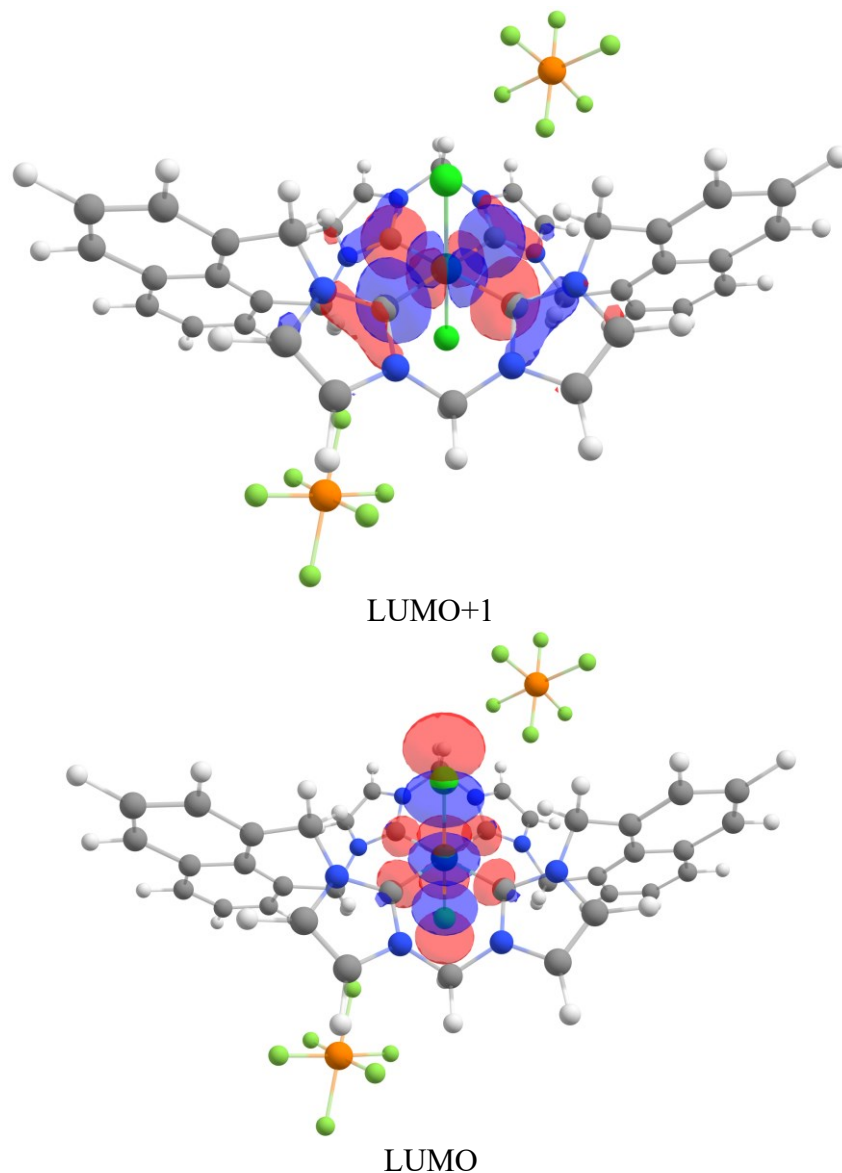
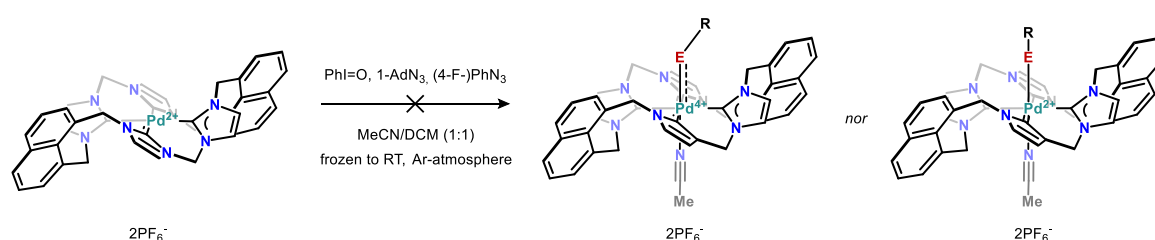


**Figure 5.13.** HOMO/LUMO of Pd (IV) complexes. For clarity, the SALC orbitals reflecting the DFT calculations are shown on the left-hand side of the DFT result.



**Scheme 5.11.** Experiments to verify that **4.13** does not form multiple ligand-metal bonds. The lacking reactivity corroborates the expected electronic configuration.

### 5.3 Water: a peculiar reductant

Our results suggest that complex **4.13** cleanly supports oxidation and reduction, cycling between Pd(II) and Pd(IV), combined with the fact that following oxidation of complex **4.13** with PhICl<sub>2</sub> (using up to 10 equiv.) on humid and hot days, the isolated materials featured a <sup>1</sup>H NMR spectrum consistent with a mixture of complexes **5.1** and **4.13**. This observation, combined with results that suggests complex **5.3** seems to oxidize water, prompted us to explore whether complex **5.1** could act as a (pre)catalyst apt at water oxidation.

To this end, in an Ar-filled glovebox, 1.0 equiv. of **5.1** and 55.0 equiv. of H<sub>2</sub>O (subjected to freeze-pump-thaw cycles prior) was dissolved in MeCN, before the solution quickly was transferred to a J. Young NMR tube and sealed. The tube was brought out of the glovebox, and the reaction was monitored by comparing <sup>1</sup>H NMR spectra acquired at different time intervals, some shown in **Figure 5.14**. At RT no reaction occurs during the first 30 minutes (second insert from the top), and as such, heating was applied.

Encouragingly, after 30 minutes (third spectrum from the top) signals owing to complex **4.13** starts to appear. Continued heating led to a steady decrease in signals owing to **5.1** (*viz.* signals at 5.30 ppm) concurrently with an equal increase in signals owing to **4.13** (*viz.* signals at 5.09 ppm), and a downfield shift in the water signal. After 20 hours (last entry) more than 50% of **5.1** was converted into **4.13**, based on a relative integration of resonances at 5.30 and 5.09 ppm leading to a ratio of 2:2.9, respectively, in addition to water's resonance significantly downfield shifts to 2.42 from 2.13, suggesting the formation of a substantial amount of acid. At no point in time were any metal particles formed.

This reaction is rather slow, which is not unsurprising following a low-spin octahedral d<sup>6</sup> electronic configuration, consistent with a dissociative mechanism of a

kinetically inert complex. This reaction further suggests that **5.1** may be competent in the oxidation of water.

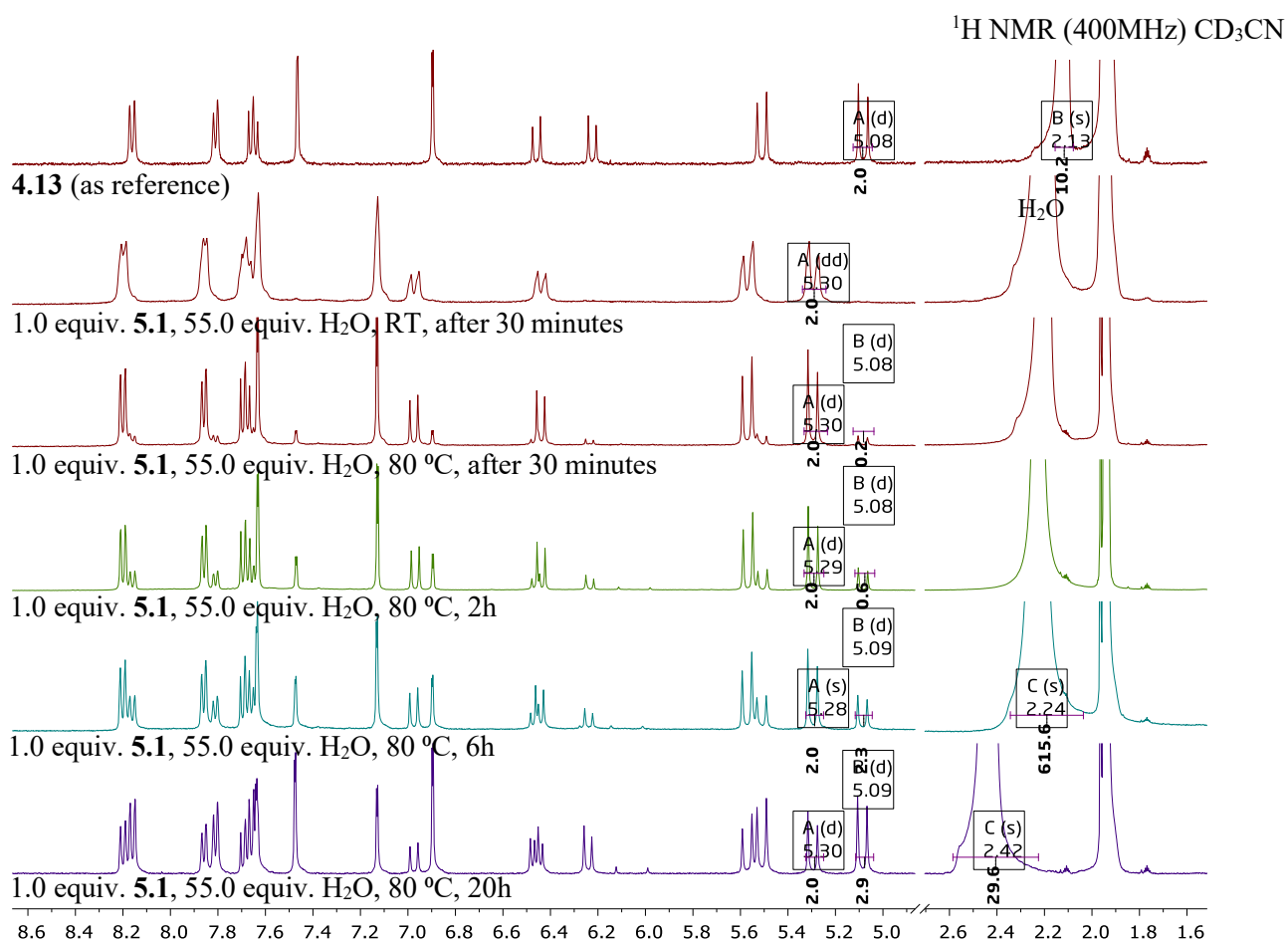


**Figure 5.14.** Progressive reduction of Pd (IV) dichlorido. Continuous heating of complex **5.1** with water yields **4.13** and HCl. Some CH<sub>3</sub>CO<sub>2</sub>H is formed from MeCN hydrolysis.

Accordingly, we scaled the reaction and prepared it for continuous sampling *via* a micro gas chromatograf (GC), assuming the following stoichiometry  $2\text{H}_2\text{O} + 2\text{PhICl}_2 \rightarrow \text{O}_2 + 4\text{HCl} + 2\text{PhI}$ , and after some time, we found a configuration where we could test whether any of the PhICl<sub>2</sub> hydrolysis products generate O<sub>2</sub> or whether it originates from a reaction mediated by **4.13** acting as a precatalyst.

PhICl<sub>2</sub> was weighed out into a flame-dried Schlenk-tube and subjected to several rapid cycles of vacuum/N<sub>2</sub> backfill on a Schlenk line. A solution of H<sub>2</sub>O in MeCN (0.15M) was prepared in a separate tube, and the water was subjected to freeze-pump-thaw cycles prior to being added dry and degassed MeCN. **4.13** was added to such an

H<sub>2</sub>O/MeCN stock solution when tested. The H<sub>2</sub>O/MeCN stock solution was then added to PhICl<sub>2</sub>, and the setup was flushed with N<sub>2</sub> until O<sub>2</sub> levels settled below 1%. The N<sub>2</sub> stream was then disconnected, the tube submerged into a preheated oil bath, and as the reaction mixture's temperature reached the oil bath's, a persisting bubbling ensued. As PhICl<sub>2</sub> is unstable and readily decomposes into PhI and Cl<sub>2</sub> gas, a cold trap was installed prior to a mass-flowmeter and the GC injector to protect the equipment. Moreover, the compound was always prepared immediately prior to its use. With no active flow, apart from the GC's injector, each measurement had consistently about 18 – 20 minutes of waiting time, before any of the gas was detectable at the GC-injector (intake of 200 µL/sample). Moreover, this setup had several weak spots prone to leakages of O<sub>2</sub>.

**Figure 5.15** compares the gas evolution over the span of 1.5 hours, of which the hydrolysis products do not form O<sub>2</sub>. Despite persisting bubbling, the connected flowmeter was unable to register any significant mass flow. Despite several measurements and interference from leakages, one measurement without such was successfully recorded, shown as the red trace in **Figure 5.15**, clearly demonstrating a steady increase in the amount of O<sub>2</sub> content.

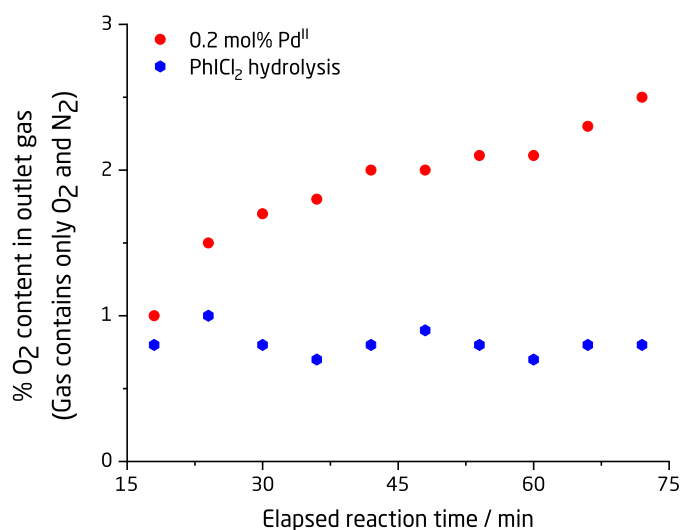


**Figure 5.15.** *Water-oxidation under catalytic conditions.* Even at 0.2 mol% precatalyst loading, the reaction proceeds quite efficiently. Conditions: 0.2 mol% 4.13, 1.0 equiv. PhICl<sub>2</sub>, 1.0 equiv. H<sub>2</sub>O, MeCN (0.2M), 75 °C.

After three hours (leakage was detected after 80 minutes), the reaction was stopped, and an aliquot was taken from the mixture. **Figure 5.16** shows the  $^1\text{H}$  NMR of this mixture, demonstrating that the mixture's content comprises unreacted  $\text{PhICl}_2$  and  $\text{PhICl}$  in a relative integration ratio between  $\text{PhICl}/\text{PhICl}_2$  (integration of the H para to I) of 100:35, suggesting ~65% conversion was obtained relatively fast. In all reactions absent of **4.13** or **5.1** substantial amounts of gaseous  $\text{Cl}_2$  was formed, contrasting our catalytic studies. Although we cannot exclude decomposition, it is unlikely to contribute in a major capacity.

I was able to isolate complex **5.1** consistent with ~99% of the mass initially employed of **4.13**, by concentrating the solution and precipitating out the complex with  $\text{Et}_2\text{O}$ .

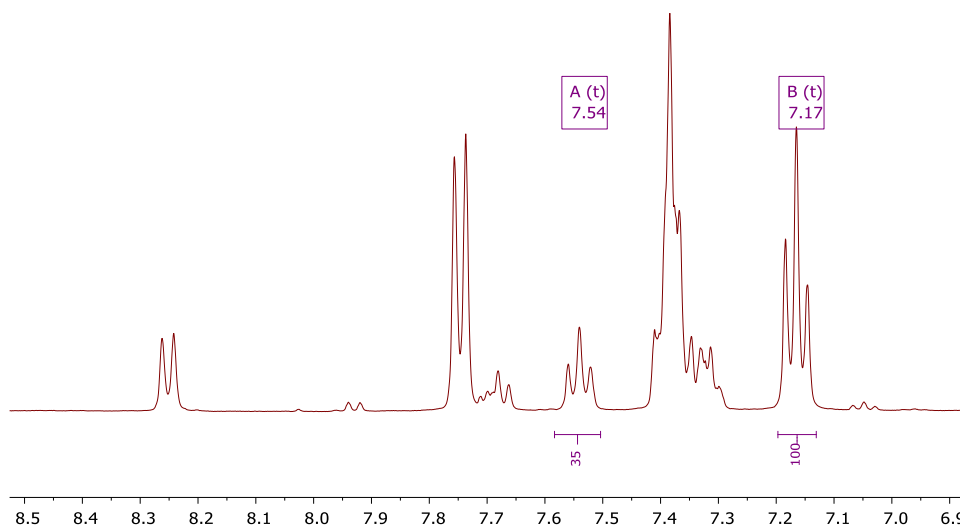
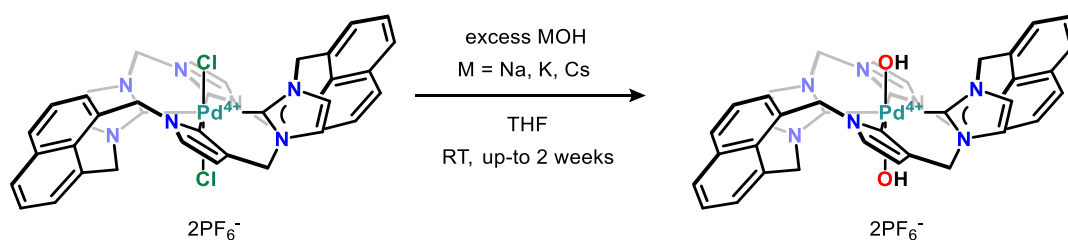


**Figure 5.16.**  $^1\text{H}$  NMR spectra of an aliquot following water oxidation. The relative integration ratio represents  $\text{PhICl}_2$  (35) and  $\text{PhI}$  (100), suggesting ~65% of  $\text{PhICl}_2$  has been consumed in either a productive manner or through decomposition.

To test whether a reaction is homogeneous in nature, it is commonplace to add  $\text{Hg}(0)$  that forms an amalgam with any heterogeneous Pd particles. Any significant changes in the kinetic profile would suggest that the reaction is heterogeneous in nature. We did not perform such a test.  $\text{Hg}(0)$  reacts with  $\text{Cl}_2$  forming  $\text{HgCl}_2$ , and as  $\text{PhICl}_2$  is a  $\text{Cl}_2$  surrogate and a stronger oxidant, it would form  $\text{HgCl}_2$ , rendering said test invalid.

However, since the transformation take place on an NMR appropriate timescale, rate-determination is ideal to pursue using variable-temperature NMR. This approach, will provide insights into any induction periods, and whether the reaction demonstrates different kinetics at various temperatures; which would suggest of different mechanisms. More importantly, the rate-constants at different over a temperature array provide data points for an Eyring analysis, from which critical information about the turn-over limiting (or rate-determining step) can be extracted, such as whether the reaction is uni or bimolecular. Such an analysis was not concluded during this PhD study, however, is the next logical step.

To obtain further insights into the mechanism, an extensive focus was put into the isolation of (reactive) hydroxo intermediates, by reacting **5.1** (and **5.2**) with MOH (M = Na, K, Cs) in THF and MeCN, as outlined in **Scheme 5.12**, however, unsuccessfully so. These reactions led instead to the isolation of unreacted **5.1** and **4.13**, suggesting that any intermediates formed (at RT) quickly react. Another appropriate mechanism may involve the formation of a chloride salt through the displacement of one chlorido ligand by MeCN displacing one, or a concerted hydroxyl formation liberation of HCl.



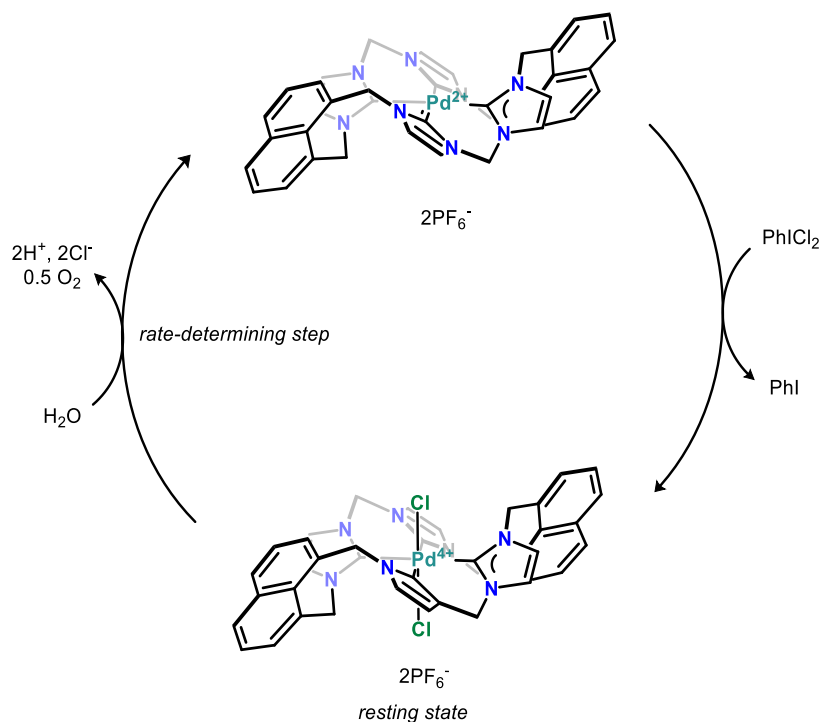
**Scheme 5.12.** A strategy targeting dihydroxy Pd (IV) complex. Qualitative assessments suggest that the reaction proceeds, such as precipitation of THF-insoluble MCl salts.

A different approach to obtain intermediary hydroxyl Pd (IV) species, involves the reaction between complex **5.3** and TMS-OH to facilitate the transformation into a hydroxy species, driven by the formation of a Si-F bond. However, necessitates the unambiguous elucidation of a *bona fide* difluorido Pd (IV) complex.



Nevertheless, these combined results strongly support that the Pd (IV) oxidation state is the resting state, and complexes **5.1** and **5.3** (potentially **5.2**) indeed oxidize water, specifically in an oxygen-evolving reaction, and even in a catalytical capacity, as it first of its kind.

This transformation deserves further attention through mechanistic studies, and in the particular exploration of electro-catalytical water-splitting, based on the strong signal observed in **Figure 5.4** before the onset of MeCN oxidation. However, as of now, a tentative catalytic cycle is presented in **Scheme 5.13**. We can suggest that the transformation is solely located on Pd, as we thus far have no evidence that supports the notion that the NHC ligand acts in a redox non-innocent capacity, which is also unexpected for NHCs. The analogous bischelate complex **4.9** is inactive under the same conditions, suggesting that the macrocyclic ligand imparts necessary electronic properties to facilitate the transformation.



**Scheme 5.13.** Suggested catalytic cycle pertaining to oxygen-evolving reaction. Complex **4.13** readily oxidizes into **5.1**, which acts as the resting-state. Upon heating in presence of a reductant, water, acid, and dioxygen are liberated.

## 5.4 A Ni (III) complex bearing a macrocyclic tetra NHC ligand

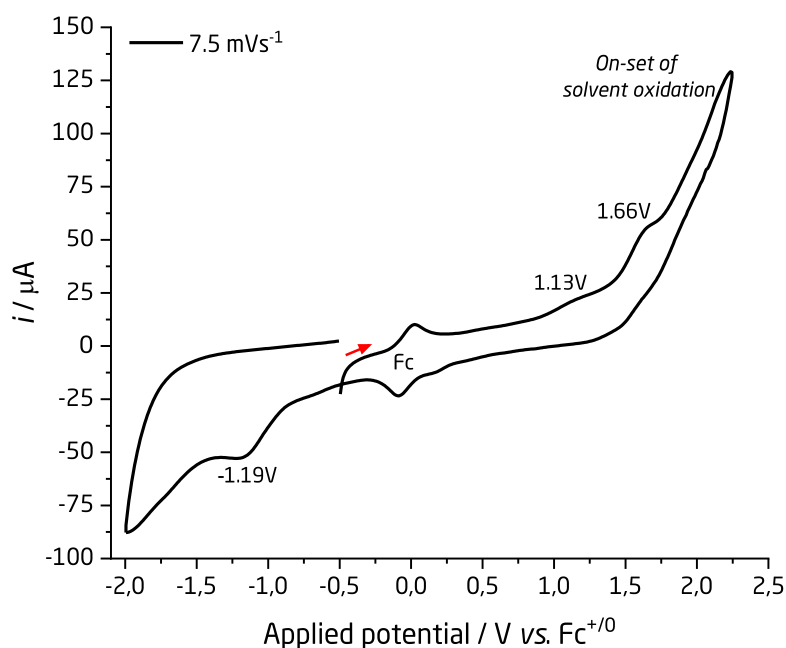


**Figure 5.17.** Cyclic voltammogram of complex **4.18**. The arrow indicates starting potential and proceeds in the anodic direction. Under an  $\text{N}_2$  atmosphere, in MeCN,  $0.25 \text{ mM}$   $[\text{Ni}] \text{ 2PF}_6$ ,  $0.1 \text{ M}$  TBAPF<sub>6</sub> (supporting electrolyte), working electrode: Glassy Carbon Electrode, Counter electrode: Pt wire, Potential width:  $-1.5 \text{ V}$  to  $2.8 \text{ V}$   $\text{Ag}^{+/0}$ , corrected against the  $\text{Fc}^{+/0}$  redox-couple ( $V(\text{Fc}^{+/0}) = V(\text{Ag}^{+/0}) - 0.5 \text{ V}$ ).

The CV of complex **4.18** is shown in **Figure 5.17**, which shows two oxidation events. The first as a broad peak around  $1.13 \text{ V}$  vs.  $\text{Fc}^{+/0}$ , followed by a stronger at  $1.66 \text{ V}$  before the onset of solvent oxidation. The two oxidation waves are putatively attributed to redox couples  $\text{Ni(II/III)}$  and  $\text{Ni(III/IV)}$ . This reactivity would be in line with the general propensity of  $3d$  metals to facilitate single-electron transfers, different from two-electron transfer processes demonstrated by  $4/5d$  metals. Further supporting this notion, is the larger positive potential required to achieve putative oxidation from  $\text{Ni(III)}$  to  $\text{Ni(IV)}$ , following the inherent lower stability of  $\text{Ni(IV)}$  vs.  $\text{Pd(IV)}$ .

Since we were able oxidize complex **4.13** ( $\text{Pd}^{2+}$ ) into **5.2** by addition of  $\text{Br}_2$ , a little surprising given the reduction potential of  $\text{Br}_2$  in MeCN<sup>54</sup> of  $0.07 \text{ V}$  vs.  $\text{Fc}^{+/0}$ , much lower than the expected  $\sim 0.8 \text{ V}$  required, we wanted to explore a similar oxidation of complex **4.18**: specifically, whether any stable high-valent  $\text{Ni}^{2+n}$ -bromido adducts form, and further, whether any such adducts analogously to **4.13**, persist under ambient conditions.

In MeCN, complex **4.18** was reacted with 0.5 equiv. of Br<sub>2</sub> under ambient conditions, a red/orange solid precipitated with Et<sub>2</sub>O, which is a paramagnetic species, as evident by the broad line widths and lack of fine structure featured in the lower spectrum of **Figure 5.18**. No spectral changes occur upon the addition of an additional 0.5 – 5.0 equiv. Br<sub>2</sub>, suggesting that Br<sub>2</sub> is an insufficient oxidant to furnish the formation of the Ni(IV) complex. More curiously, this complex is stable in solution at elevated temperatures under an ambient atmosphere.

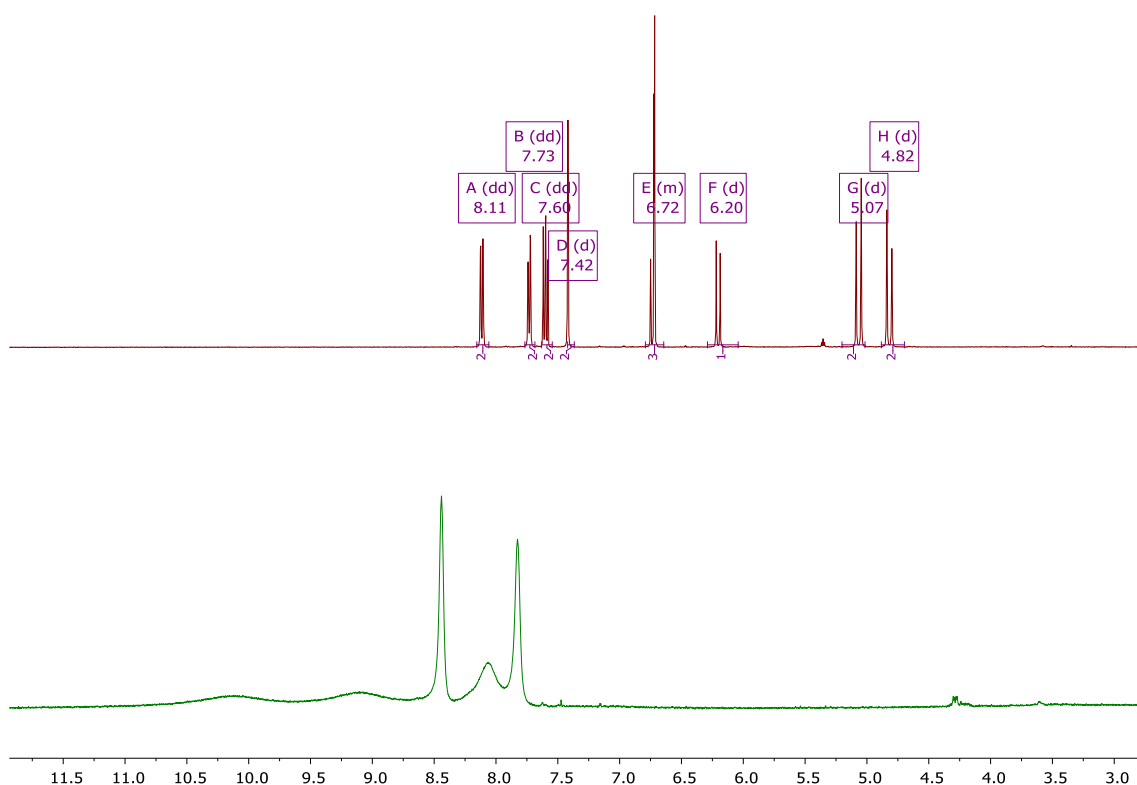


**Figure 5.18.** <sup>1</sup>H NMR spectra (CDCl<sub>3</sub>) of complex **4.18** and its adduct following Br<sub>2</sub> addition. The top spectrum shows that complex **4.18** is diamagnetic, contrasting the lower spectrum, demonstrating 0.5 equiv. of Br<sub>2</sub> furnish the transformation into a paramagnetic species.

#### 5.4.1 Characterization of complex **5.4**

Complex **5.4**, shown in **Figure 5.19**, crystallizes as red/orange crystals in the monoclinic C2/c spacegroup, obtained from slow solvent evaporation from a concentrated MeCN solution of **4.18** and 5.0 equiv. of Br<sub>2</sub> at RT. Contrasting the Pd (IV) complexes **5.1** and **5.2**, solvent occupies the axial coordination sites, surrounded by three outer sphere Br<sub>3</sub>-counterions.

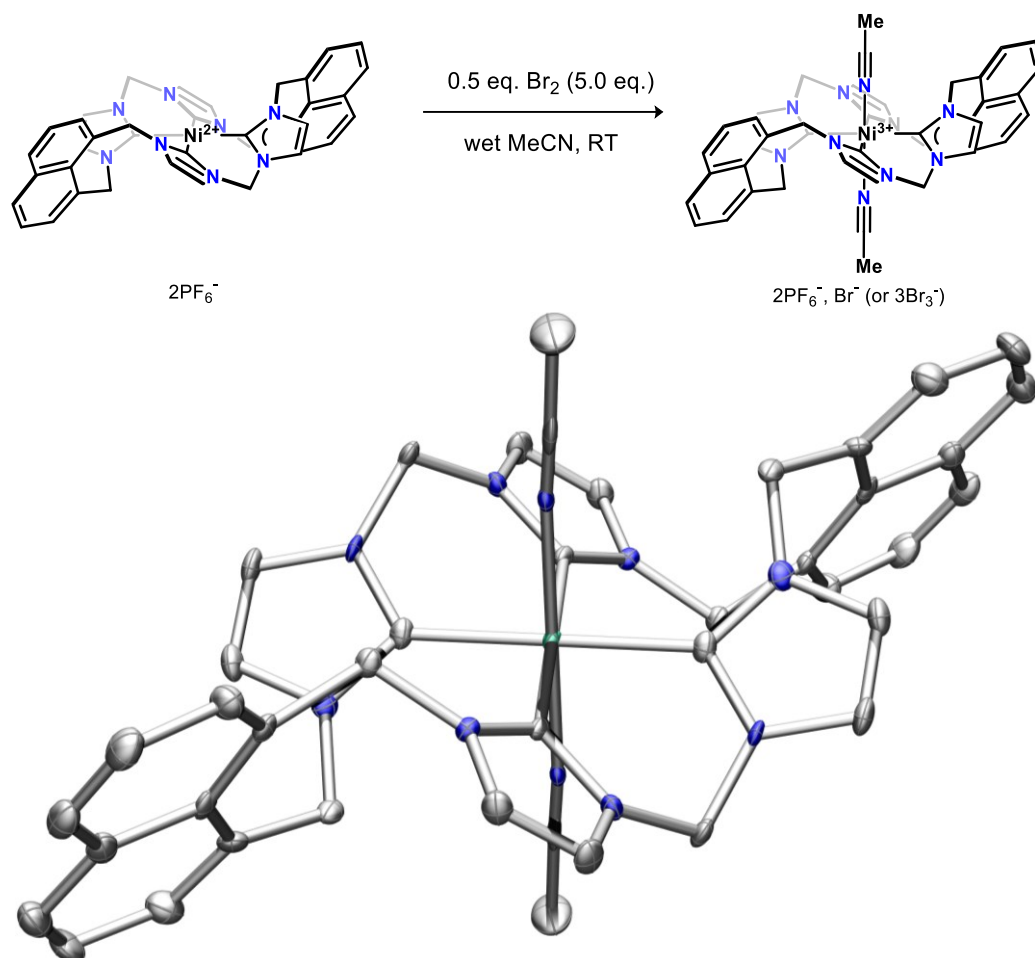


**Figure 5.19.** *Synthesis and solid-state structure of complex 5.4.* Hydrogen atoms, co-crystallized MeCN, and  $\text{Br}_3^-$ -counterions are omitted for clarity. Thermal ellipsoids are set at a 50% probability level. Atom color-coding: N blue, C grey, and Ni aquamarine.

The asymmetric unit cell comprises half a macrocycle and 1.5  $\text{Br}_3^-$ -counterions, of which one counterion demonstrates disorder over two positions. Despite this fact, the crystal quality is of sufficient quality, and the associated model converges at  $R_1 = 3.65\%$  and  $wR_2 = 10.38\%$  (all data).

**Figure 5.20** shows bond lengths pertaining to the Ni-center of complexes **4.18** and **5.4**, which, as evident from **Figure 5.19**, features Ni in a distorted octahedral coordination environment, consistent with a tetragonal distortion from the slight elongation of the ligand bond lengths along the basal plane (Ni-C), and a much larger elongation along the axial direction<sup>64</sup>. Additionally, this distortion is consistent with a low-spin  $d^7$  electronic configuration where the SOMO comprise a Ni-centered  $d(z^2)$ -atomic orbital.

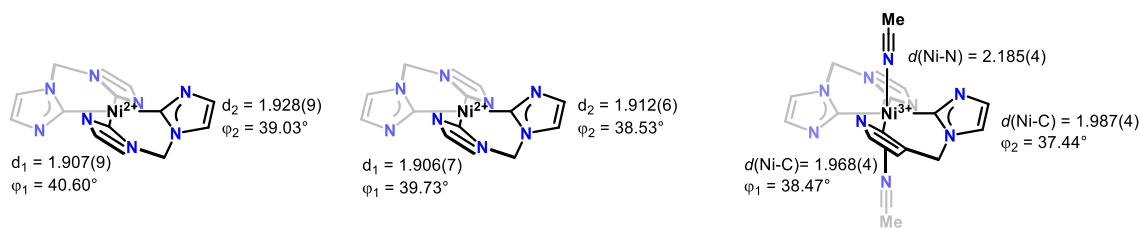


**Figure 5.20.** Bonding metrics pertaining to complexes **4.18** and **5.4**. Upon oxidation the Ni (III) core of **5.4** demonstrates a distorted octahedron following elongation along with the axial coordination sites, consistent with commonly observed tetragonal distortions of Ni (III) and Co (II).

Accordingly, in collaboration with Associate Professor Susanne L. Mossin, DTU Chemistry, complex **5.4** was analyzed through quantitative EPR spectroscopy to assess its electronic properties, and additionally address whether Br<sub>2</sub> genuinely act as an outer sphere oxidant.

Under ambient conditions, complex **4.18** was dissolved in MeCN, and added 1.1 equiv. Br<sub>2</sub>, lightly shaken, and then quickly frozen in liquid N<sub>2</sub> (within 10 seconds) before its EPR spectrum was measured, shown on the left-hand side of **Figure 5.21**. Complex **4.18** is EPR inactive, and quantification of the measured EPR signal, works to establish, that 100% of complex **4.18** is converted into **5.4**.

Complex **5.4** features a metal-centered radical, as the *g*-factor values significantly deviate from 2.00, consistent with a ground state doublet term ( $S = 1/2$ ,  $S_{\text{mult}} = 2$ ) demonstrating axial anisotropy ( $g_{\perp} > g_{\parallel}$ ). The absence of any half-field signals at *g*-values of approximately 4.4 (right-hand spectrum of **Figure 5.21**), further substantiates that the strongly binding NHC ligands induce a low-spin electronic configuration.

The spectrum, however, poorly resolved, demonstrates a super hyperfine coupling to two <sup>14</sup>N (*I* = 1) atoms, owing to MeCN, manifesting in a pentet, readily modelled with EasySpin<sup>65,66</sup>. This super hyperfine coupling corroborates that any bromide ions are an outer sphere. This solution was left in the EPR tube for 48 hours, before re-measuring the EPR spectra as a glass. Freezing this solution, leads to the spectrum on the left-hand side of **Figure 5.22**, featuring the same spectral properties as the “fresh” solution, however,

the super hyperfine coupling to  $^{14}\text{N}$  is much better resolved. This spectrum still lacks splitting owing to hyperfine coupling to  $^{61}\text{Ni}$  ( $I = 3/2$ ), and splitting owing to any super hyperfine coupling to  $^{13}\text{C}$  ( $I = 1/2$ ), a consequence of their low abundance of  $\sim 1\%$ .

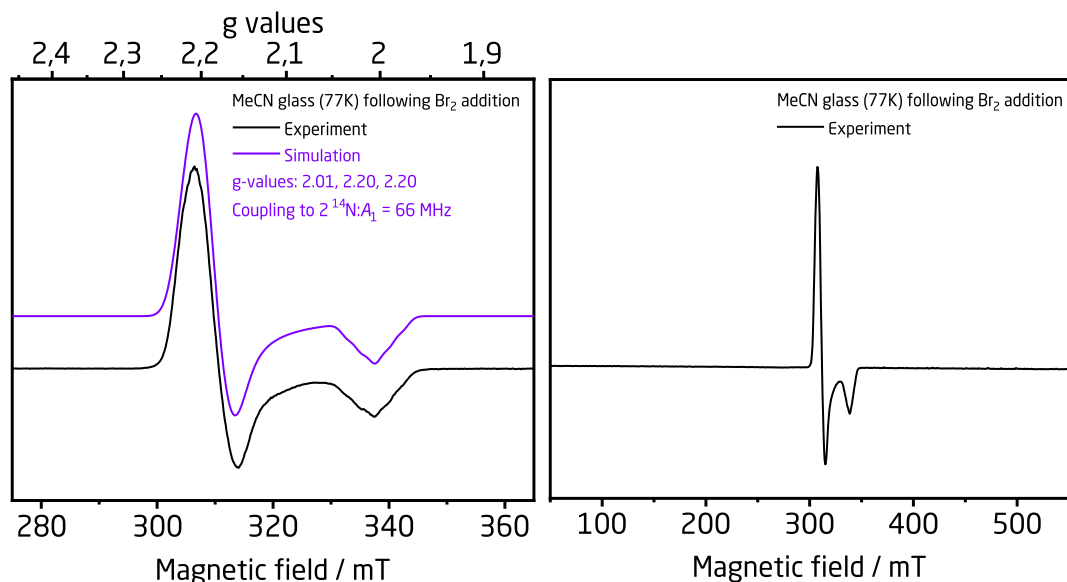


**Figure 5.21.** EPR spectrum following  $\text{Br}_2$  addition to complex **4.18**. The left-hand side figure features poorly-resolved super hyperfine coupling to N, and the wide spectrum (right-hand side) suggests a doublet ground state lacking any resonances at half intensity, double field strength.

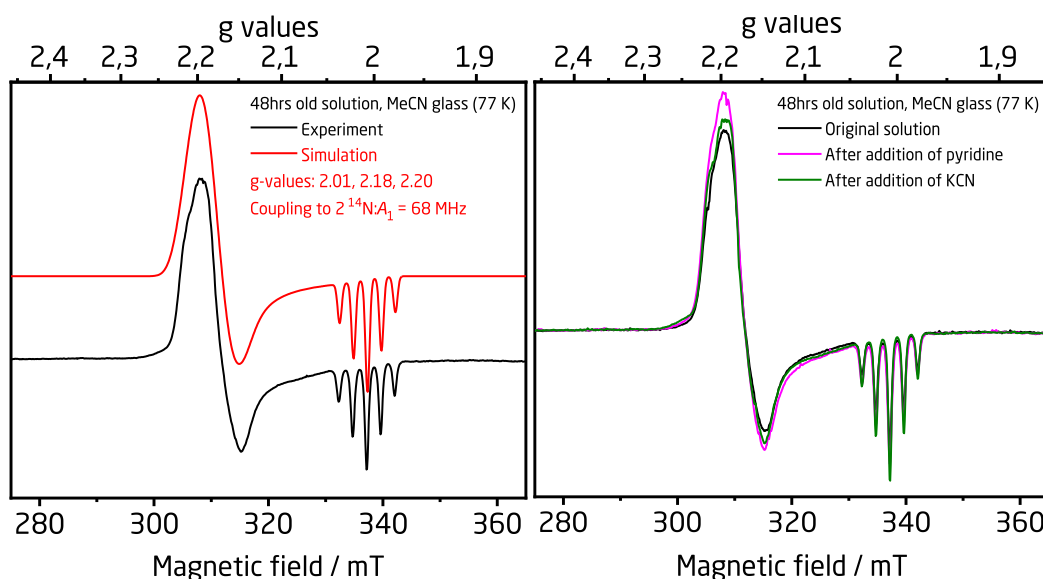


**Figure 5.22.** Complex **5.4** and substitution reactions with various nucleophiles. The left-hand spectrum features the oxidation adduct of **4.18** after 48 hours, to which were added various nucleophiles (right-hand spectrum).

More curiously, the MeCN molecules appear quite strongly bound as evident from the right-hand spectrum of **Figure 5.22**, as no change happens upon addition of pyridine nor KCN. Pyridine may not spatially fit, however, the  $^-\text{CN}$  ion should. We are looking into reproducing these results, also with different a counterion *e.g.*  $\text{BAr}^{\text{F}}_4$  to access PhMe.

DFT calculations further reflect our EPR and solid-state results, consistent with a low-spin  $d^7$  electronic configuration featuring a strong destabilization of the  $x^2-y^2$  orbital and tetragonal distortion demonstrating axial elongation. The metal-centered SOMO and LUMO are shown in **Figure 5.23**.

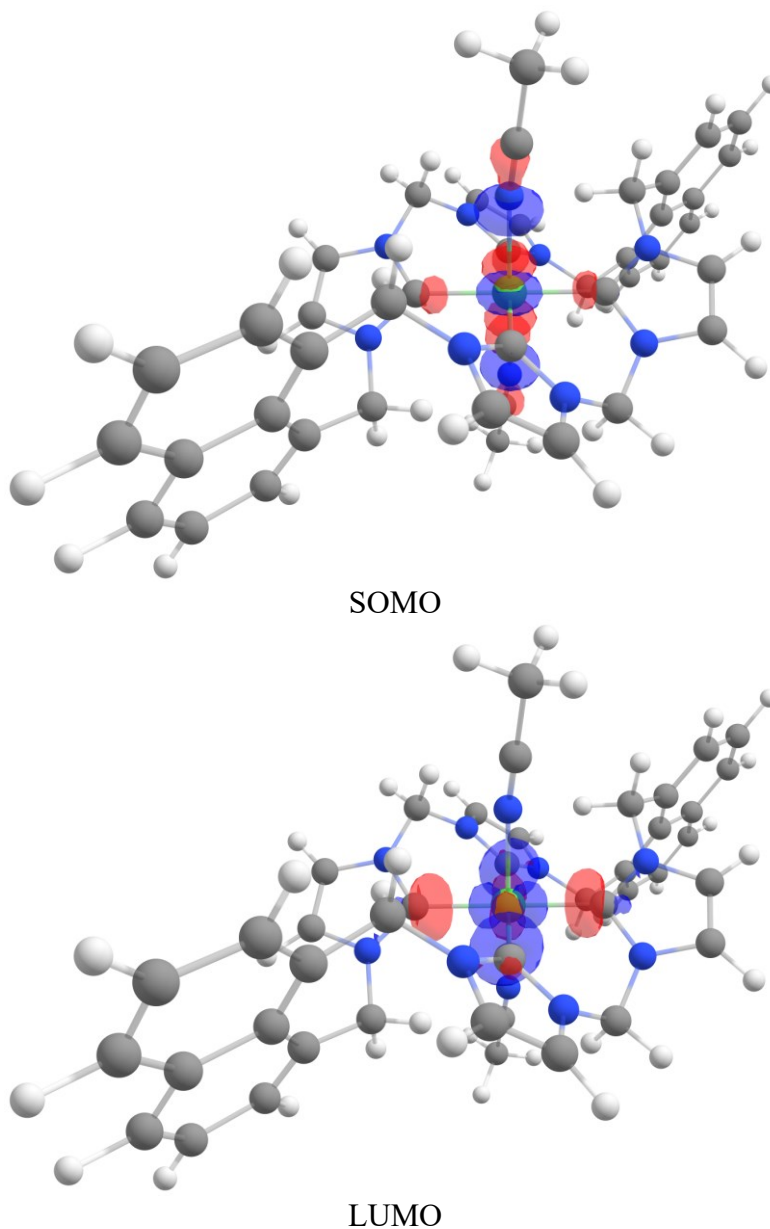


**Figure 5.23.** DFT-calculated metal-centered SOMO and LUMO. Depicted metal-centered orbitals accounts for the SOMO (antibonding  $z^2$  symmetry, left-hand side), and LUMO (antibonding  $x^2-y^2$  symmetry, right-hand side). Isodensity ( $0.065 \text{ e}/\text{\AA}^2$ ) plot.

While the hybrid functional TPPSh generally has been employed throughout the work presented within this dissertation, complex **5.4** was evaluated with various (non) hybrid functionals in collaboration with PhD Mike S. B. Jørgensen, Martin Nielsen group

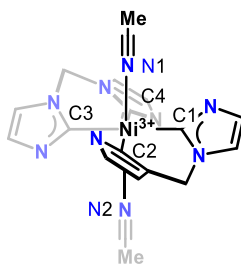
at DTU Chemistry, to best reproduce the experimentally observed properties. This screening, was undertaken to find the functional best describing the bonding to Ni, as we sought to employ DFT to simulate EPR spectra, which is affected by the local ligand field. Generally speaking, hybrid-functionals tend to often better describe metal-complexes, however, including Hartree-Fock (HF) exchange can benifically help to achieve a better bond description, however, the HF extent can lead to significantly overestimations in terms of a too ionic description (~30% HF), to too covalent description (~10%)<sup>67</sup>.

To this end, the single-crystal structure of complex **5.4** absent of counterions was subjected to geometry optimization using six commonly employed functionals. Whereas PBE0 and PBE were used as representatives (hybrid) of non-empirical GGA functionals (25% HF exchange), B3-LYP and B-LYP were employed as (hybrid) functionals including the LYP-correlation (20% HF exchange), and TPSSh and TPSS, were used as representative (hybrid) meta functionals (10% HF exchange)<sup>68</sup>.

**Table 5.1.** *DFT reproduced bond-length of complex 5.4.* The def2-TZVPP basis set was applied to all atoms but Ni, which instead used the def2-QZVP basis set. To account for dispersion forces, Grimme's DFT-D3 approach was applied through the Becke-Johnson dampening implementation<sup>69</sup>. The ChemDraw schematic indicate bond in question.

	$d(\text{Ni} - \text{X}) / \text{\AA}$					
	N1	N2	C1	C2	C3	C4
<i>Solid-state</i>	2.186(4)	2.186(4)	1.986(4)	1.969(4)	1.986(4)	1.969(4)
PBE0 (25% HF)	2.042	2.198	1.988	1.989	1.990	1.990
PBE			1.994	1.995	1.996	1.996
B3-LYP (20% HF)			1.988	1.989	1.990	1.900
B-LYP			2.016	2.017	2.018	2.018
TPSSh (10% HF)			1.990	1.991	1.992	1.992
TPSS			1.992	1.993	1.993	1.994





As evident from the bond lengths shown in **Table 5.1**, neither functional reproduce any of the bond lengths accurately. The bound MeCN molecules demonstrate quite a bond length disparity, which is reproduced in all functionals. If anything, employing hybrid functionals, which employ more than 10% HF seems to better reproduce the basal plane contraction, as the optimized geometries resulting from the PBE0 and B3-LYP functionals demonstrates quite shorter Ni-C bond lengths compared with their non-hybrid functional counterparts, and even relative to the TPPSh functional.

Different functionals were screened to understand, which better reproduce the experimentally observed  $g$ -tensor and hyperfine coupling tensor  $\mathbf{A}$ , the results are presented in **Table 5.2**.

While not fully able to reproduce the experimentally observed values for  $g$  and  $\mathbf{A}$ , the difference in values of  $\mathbf{A}$  reflects the bond length disparity between the two MeCN molecules. However, a trend, the core strength of DFT, is clear: the radical is centered on Nickel, hybrid functionals with a HF contribution to the Slater determinant of >10% is necessary to approximate experimentally observed values, and the basis set “aug\_cc-pVTZ-J”<sup>70</sup> is particularly apt in this context.

Additionally, the spin-density, shown in **Figure 5.24**, reflects the SOMO, **Figure 5.23**, and is consistent with our other experiments: the spin is centered on the Ni-atom, coupling strongly along the axial direction to MeCN.

**Table 5.2.** DFT calculated EPR parameters. Using the TPPS-geometry optimized structure as input structure, variation in basis set and functional produces the following  $g$  and  $\mathbf{A}$  values.

	$g_{zz}$	$g_{yy}$	$g_{xx}$	$g_{iso}$	$\mathbf{A}_{zz}$ (MHz)	$\mathbf{A}_{yy}$ (MHz)	$\mathbf{A}_{xx}$ (MHz)	$\mathbf{A}_{iso}$ (MHz)
MeCN glass (77K)	2.01	2.18	2.20	-	N <sub>1</sub> : 68.0 N <sub>2</sub> : 68.0	<i>Not observable</i>		-
<b>Functional (basis set) {Ni basis set}</b>								
TPSSh (TZVPP){QZVP} implicit MeCN model	2.01	2.11	2.11	2.08	N <sub>1</sub> : 71.5 N <sub>2</sub> : 62.3	71.7 65.5	79.2 69.2	74.1 64.7
TPPS (TZVPP) {QZVP}	2.01	2.10	2.10	2.07	N <sub>1</sub> : 59.9 N <sub>2</sub> : 59.9	59.9 59.9	69.4 69.4	63.1 63.1
B3-LYP (TZVPP) {QZVP}	2.02	2.14	2.14	2.10	N <sub>1</sub> : 61.8 N <sub>2</sub> : 61.8	61.9 61.9	68.6 68.6	64.1 64.1
B3-LYP (TZVPP) {aug_cc-pVTZ-J, also on N}	2.02	2.15	2.15	2.12	N <sub>1</sub> : 55.3 N <sub>2</sub> : 55.3	55.3 55.3	63.7 63.7	58.1 58.1
PBE0 (TZVPP, {QZVP})	2.02	2.15	2.15	2.11	N <sub>1</sub> : 67.5 N <sub>2</sub> : 58.2	67.7 58.4	74.4 64.4	69.9 60.3
PBE0 (TZVPP) {aug_cc-pVTZ-J, also on N}	2.02	2.16	2.16	2.12	N <sub>1</sub> : 63.9 N <sub>2</sub> : 63.9	63.9 63.9	73.6 73.6	67.1 67.1

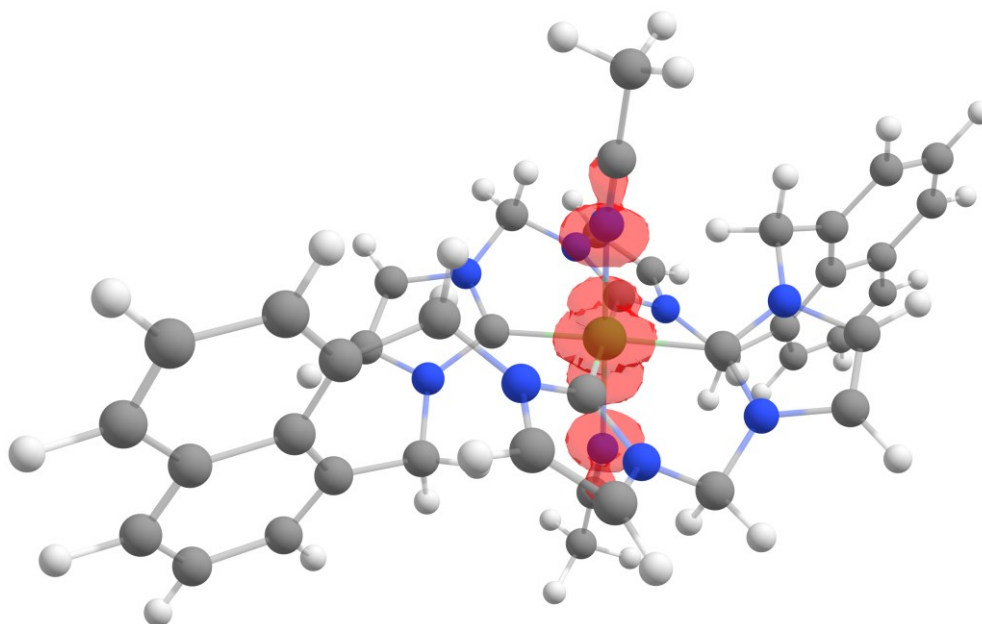
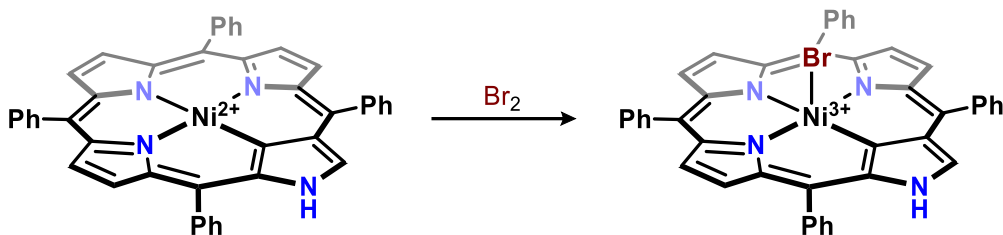


**Figure 5.24.** Spin-density plot of complex 5.4. The plot unequivocally demonstrates that the observed paramagnetism originates from an essential “naked” Ni (III) ion bearing a macrocyclic tetra NHC ligand.

So-called “inverted” *N*-porphyrins are isomers of *N*-porphyrins, which features one inverted pyrrole, resulting in a binding pocket comprising NNNC, apt at stabilizing high metal oxidation states<sup>71</sup>. Latos-Grazynski employed EPR to characterize *in situ* generated Ni (III) adducts following single-electron oxidation by Br<sub>2</sub>, as in **Scheme 5.14**,

and CAN, and subsequent ligand substitution reactions<sup>72</sup>. In each reaction, the Ni (III) adduct is bound by the respective ligand of interest, *e.g.* CN, NO<sub>3</sub>, OH, H<sub>2</sub>O.



**Scheme 5.14.** Oxidation of Ni (II) bearing an inverted *N*-porphyrin. Complexes were only characterized *in situ*, as such the connectivity of is only suggestive of the actual structure.

Two other well-characterized Ni (III) complexes bearing this ligand architecture are known by Dolphin<sup>71</sup>, as well as by Ke, Jiang, and Osuka<sup>73</sup>, shown in **Chart 5.2**. Upon oxidation of the parent Ni (II) complexes, the coordinating C of the binding pockets transforms into a bridging C-Oxide along metal oxidation; exposure of this Ni (III) complex to reductant furnishes the reduction back to the parent structure.

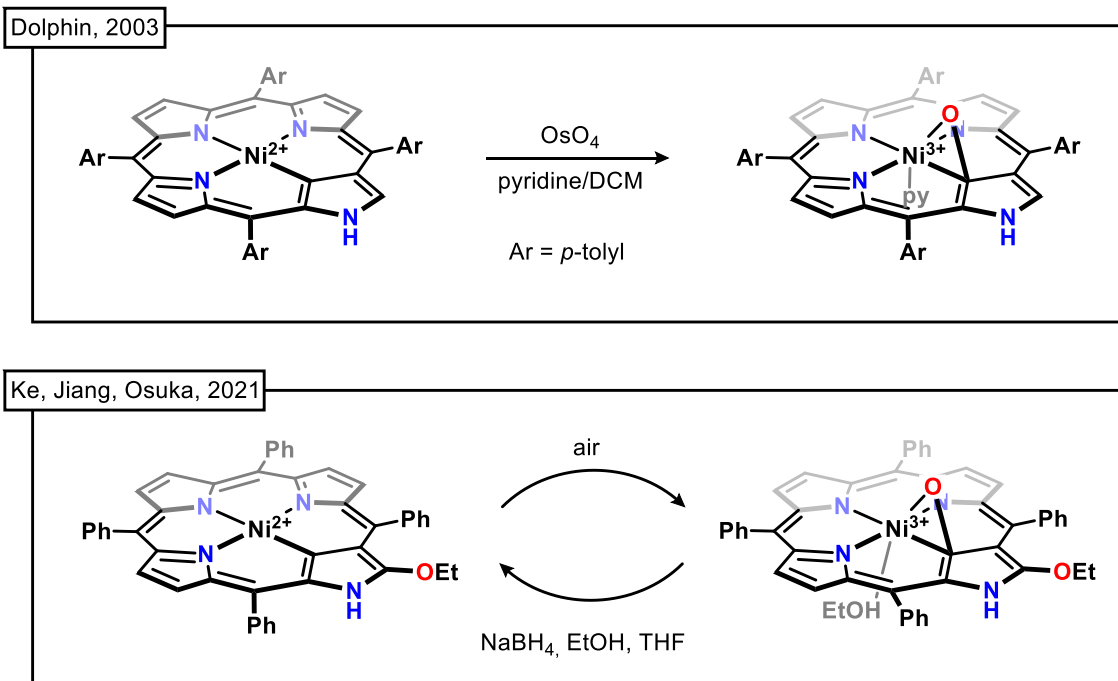


**Chart 5.2.** Oxidation of Ni(II) complexes bearing inverted *N*-porphyrin ligands. The bridging C-Oxide appear to provide stability to the complex.

The reactivity of these related complexes, when juxtaposed to that of **5.4** really emphasize the complex' rather odd reactivity. All taken together, the results corroborates

that the oxidation of complex **4.18** with Br<sub>2</sub> yields a complex bearing a “naked” Ni (III) ion, a rather curious result.

#### 5.4.2 Towards Ni (IV)

To see whether a stable Ni (IV) complex forms, complex **4.18** in a thawing MeCN solution was reacted with increasing equivalents of PhICl<sub>2</sub> under an N<sub>2</sub> atmosphere in a J. Young NMR tube, and their respective <sup>1</sup>H NMR spectra are shown in **Figure 5.25**.

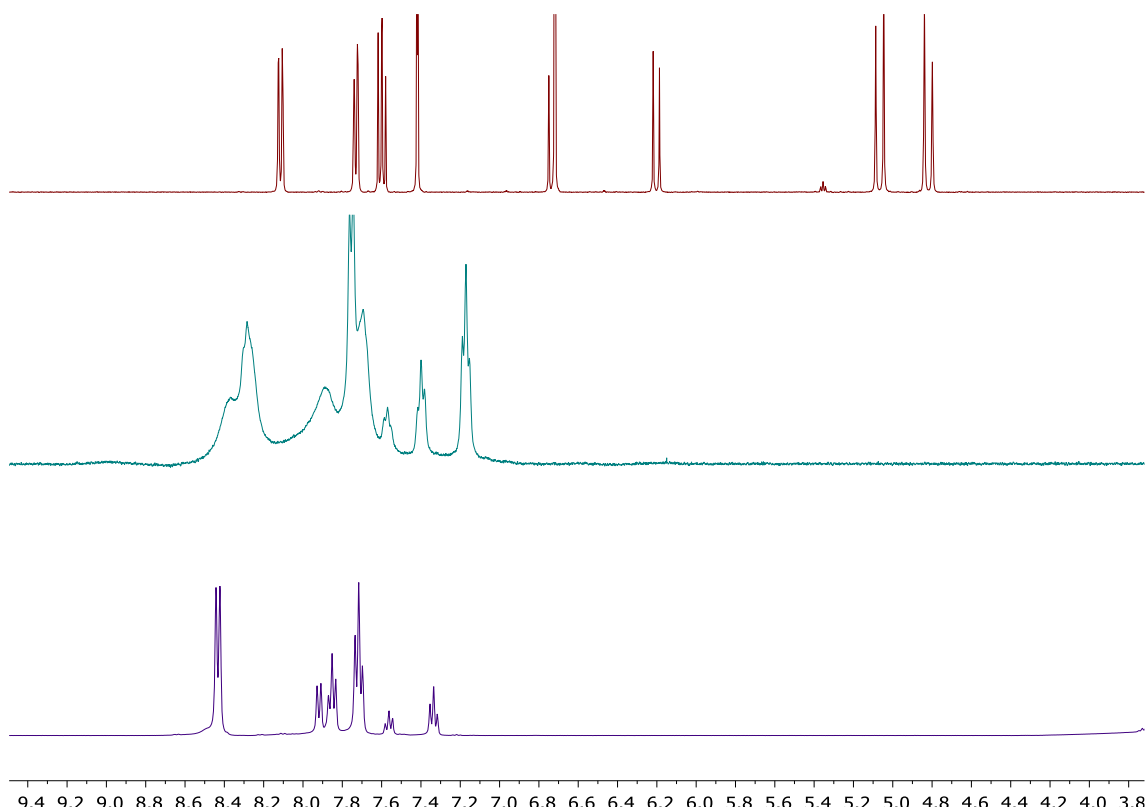


**Figure 5.25.** <sup>1</sup>H NMR spectra (CD<sub>3</sub>CN) of complex **4.18** reacting with increasing equivalents of PhICl<sub>2</sub>. The top insert shows **4.18**, middle insert **4.18** added 0.6 equiv. PhICl<sub>2</sub>, and lower insert show middle insert added an additional 0.6 equiv. PhICl<sub>2</sub>.

Upon addition of 0.6 equiv. of PhICl<sub>2</sub>, a slightly yellow-colored solution forms, slowly transitioning into red, brown, and finally black, giving rise to a paramagnetic species, as evident from the middle spectrum of **Figure 5.25**.

This solution feature EPR signals consistent with a low-spin Ni (III) complex, which does not feature the same super hyperfine splitting patterns owing to MeCN as

complex **5.4**. As of the time of writing, the fate of this complex is still under investigation, which we putatively assign as a Ni (III) chlorido compound.

Upon addition of an additional 0.6 equivalents oxidant, the solution turns yellow, and within 4 - 5 seconds precipitates black particles. The  $^1\text{H}$  NMR spectrum of this mixture, reveals a diamagnetic solution comprising unreacted  $\text{PhICl}_2$  and  $\text{PhI}$ , absent of any complex' signals, thus suggesting a complete decomposition and precipitation of metallic Ni.

These findings suggests to us, that perhaps Ni (IV) adducts are attainable, however, these appear quite thermally unstable and strongly oxidizing.

## 5.5 Conclusion

Macrocyclic tetra NHC ligands provide an electronically distinctive, yet similar, coordination environment to that of *N*-porphyrins, efficient in stabilizing reactive high-valent metal centers relevant to novel substrate transformations. In this context, we sought to explore whether complexes **4.13** and **4.18** undergo oxidation into isolable high-valent adducts.

Complex **4.13** was found to readily undergo two-electron oxidation with halide (surrogates) yielding the corresponding Pd (IV) bishalido complex, of which we corroborated connectivity through single-crystal X-ray diffraction as *bona fide* Pd (IV) dihalido complexes. We were able to extract trends upon oxidation in the  $^1\text{H}$  NMR spectrum, which we could infer onto the difluorido complex to support the notion of oxidation.

We observed that the putative fluorido complex, **5.3**, was susceptible to moisture, readily reducing to the parent complex **4.13**, and sought to explore whether the chlorido congener, complex **5.1**, shared a similar fate. To this end, data pertinent to stoichiometric and catalytic studies strongly support the notion that complex **5.1** indeed is a competent

(pre) catalyst in water-oxidation, specifically oxygen-evolving reaction (O.E.R). Furthermore, we have preliminary data that further suggests that the complex may be an apt electrochemical catalyst to achieve the same process more efficiently, however, this transformation remains to be demonstrated.

Pertaining to the group metals from X, homogeneous water-oxidation have only been demonstrated by a few Ni complexes bearing *N*-based ligands under electrocatalytical conditions, however, there is ambiguity on the nature of the active species, in favor of heterogeneous deposits<sup>74-76</sup>.

Finally, based on DFT-calculations and some stoichiometric studies, the parent Pd (II) compound does not facilitate any transformation towards multiple ligand-metal bonds. As such, to leverage the distinctive binding pocket demonstrated by the ligand, one should instead explore metalation and transformation mediated by early to mid-transition metals; the ligand environment supports high-oxidation states and a lower valence electron count ( $d^0$ - $d^4$ ) is relevant in multiple metal-ligand bonds, relevant in substrate activation, *e.g.* aziridination or epoxidation. Whether these complexes share the same fate as many of the other macrocyclic tetra NHC complexes, dimerization, remains to be proved.

Contrasting these Pd (IV) halido compounds I found that the Ni-analogue undergoes oxidation with Br<sub>2</sub> in a curious fashion, in that it acts as an outer sphere oxidant. The Ni(III) compound was characterized by a myriad of different techniques all corroborating a “naked” Ni (III) complex insofar as that all charge is centered on the Ni-ion; the MeCN ligands appear to strongly bind, as we were unable in substituting them with stronger ligands, *e.g.* <sup>-</sup>CN. Further studies of this complex are in preparation, including whether even stronger ligands may be introduced in place of MeCN and whether the same oxidation occur in apolar solvents.

Some preliminary reactivity studies were performed, pursuant to stable Ni(IV) adducts under ambient conditions, however, these appear highly unlikely, as such adducts likely are quite a temperature sensitive and strongly oxidizing. Instead, modifications to the ligand's electronic environment may be required, such as introducing methyl substituents at the C4 and C5 position of the imidazole-moiety or substituting the methylene linker for the boronate analogues in-line with Jenkins work.

## 5.6 References

- (1) Coelho, P. S.; Brustad, E. M.; Kannan, A.; Arnold, F. H. *Science* **2013**, *339*, 307–310.
- (2) Nam, W. *Acc. Chem. Res.* **2007**, *40*, 522–531.
- (3) Groves, J. T.; McClusky, G. A. *J. Am. Chem. Soc.* **1976**, *98*, 859–861.
- (4) Rittle, J.; Green, M. T. *Science* **2010**, *330*, 933–937.
- (5) Grapperhaus, C. A.; Mienert, B.; Bill, E.; Weyhermüller, T.; Wieghardt, K. *Inorg. Chem.* **2000**, *39*, 5306–5317.
- (6) Rohde, J.-U.; In, J.-H.; Lim, M. H.; Brennessel, W. W.; Bukowski, M. R.; Stubna, A.; Münck, E.; Nam, W.; Que, L. *Science* **2003**, *299*, 1037–1039.
- (7) Thibon, A.; England, J.; Martinho, M.; Young, V. G.; Frisch, J. R.; Guillot, R.; Girerd, J.-J.; Münck, E.; Que, L.; Banse, F. *Angew. Chem. Int. Ed.* **2008**, *47*, 7064–7067.
- (8) Lacy, D. C.; Gupta, R.; Stone, K. L.; Greaves, J.; Ziller, J. W.; Hendrich, M. P.; Borovik, A. S. *J. Am. Chem. Soc.* **2010**, *132*, 12188–12190.
- (9) England, J.; Guo, Y.; Farquhar, E. R.; Young Jr., V. G.; Münck, E.; Que Jr., L. *J. Am. Chem. Soc.* **2010**, *132*, 8635–8644.
- (10) Meyer, S.; Klawitter, I.; Demeshko, S.; Bill, E.; Meyer, F. *Angew. Chem. Int. Ed.* **2013**, *52*, 901–905.
- (11) Ye, S.; Kupper, C.; Meyer, S.; Andris, E.; Navrátil, R.; Krahe, O.; Mondal, B.; Atanasov, M.; Bill, E.; Roithová, J.; Meyer, F.; Neese, F. *J. Am. Chem. Soc.* **2016**.
- (12) Kupper, C.; Mondal, B.; Serrano-Plana, J.; Klawitter, I.; Neese, F.; Costas, M.; Ye, S.; Meyer, F. *J. Am. Chem. Soc.* **2017**, *139*, 8939–8949.
- (13) Singh, R.; Ganguly, G.; Malinkin, S. O.; Demeshko, S.; Meyer, F.; Nordlander, E.; Paine, T. K. *Inorg. Chem.* **2019**, *58*, 1862–1876.
- (14) Lee, J. L.; Ross, D. L.; Barman, S. K.; Ziller, J. W.; Borovik, A. S. *Inorg. Chem.* **2021**, *60*, 13759–13783.
- (15) Weiss, D. T.; Anneser, M. R.; Haslinger, S.; Pöthig, A.; Cokoja, M.; Basset, J.-M.; Kühn, F. E. *Organometallics* **2015**, *34*, 5155–5166.
- (16) Ghavami, Z. S.; Anneser, M. R.; Kaiser, F.; Altmann, P. J.; Hofmann, B. J.; Schlagintweit, J. F.; Grivani, G.; Kühn, F. E. *Chem. Sci.* **2018**, *9*, 8307–8314.
- (17) Geoghegan, B. L.; Liu, Y.; Peredkov, S.; Dechert, S.; Meyer, F.; DeBeer, S.; Cutsail, G. E. *J. Am. Chem. Soc.* **2022**, *144*, 2520–2534.
- (18) DiMucci, I. M.; Lukens, J. T.; Chatterjee, S.; Carsch, K. M.; Titus, C. J.; Lee, S. J.; Nordlund, D.; Betley, T. A.; MacMillan, S. N.; Lancaster, K. M. *J. Am. Chem. Soc.* **2019**, *141*, 18508–18520.
- (19) Anneser, M. R.; Elpitiya, G. R.; Townsend, J.; Johnson, E. J.; Powers, X. B.; DeJesus, J. F.; Vogiatzis, K. D.; Jenkins, D. M. *Angew. Chem. Int. Ed.* **2019**, *58*, 8115–8118.



- (20) Hahn, F. E.; Langenhahn, V.; Lügger, T.; Pape, T.; Le Van, D. *Angew. Chem. Int. Ed.* **2005**, *44*, 3759–3763.
- (21) McKie, R.; Murphy, J. A.; Park, S. R.; Spicer, M. D.; Zhou, S. *Angew. Chem. Int. Ed.* **2007**, *46*, 6525–6528.
- (22) Findlay, N. J.; Park, S. R.; Schoenebeck, F.; Cahard, E.; Zhou, S.; Berlouis, L. E. A.; Spicer, M. D.; Tuttle, T.; Murphy, J. A. *J. Am. Chem. Soc.* **2010**, *132*, 15462–15464.
- (23) Bass, H. M.; Cramer, S. A.; Price, J. L.; Jenkins, D. M. *Organometallics* **2010**, *29*, 3235–3238.
- (24) Lu, Z.; Cramer, S. A.; Jenkins, D. M. *Chem. Sci.* **2012**, *3*, 3081–3087.
- (25) Cramer, S. A.; Jenkins, D. M. *J. Am. Chem. Soc.* **2011**, *133*, 19342–19345.
- (26) Cramer, S. A.; Hernández Sánchez, R.; Brakhage, D. F.; Jenkins, D. M. *Chem. Commun.* **2014**, *50*, 13967–13970.
- (27) Bass, H. M.; Cramer, S. A.; McCullough, A. S.; Bernstein, K. J.; Murdock, C. R.; Jenkins, D. M. *Organometallics* **2013**, *32*, 2160–2167.
- (28) Chandrachud, P. P.; Bass, H. M.; Jenkins, D. M. *Organometallics* **2016**.
- (29) Isbill, S. B.; Chandrachud, P. P.; Kern, J. L.; Jenkins, D. M.; Roy, S. *ACS Catal.* **2019**, *9*, 6223–6233.
- (30) Elpitiya, G. R.; Malbrecht, B. J.; Jenkins, D. M. *Inorg. Chem.* **2017**, *56*, 14101–14110.
- (31) DeJesus, J. F.; Kerr, R. W. F.; Penchoff, D. A.; Carroll, X. B.; Peterson, C. C.; Arnold, P. L.; Jenkins, D. M. *Chem. Sci.* **2021**, *12*, 7882–7887.
- (32) Carroll, X. B.; Errulat, D.; Murugesu, M.; Jenkins, D. M. *Inorg. Chem.* **2022**, *61*, 1611–1619.
- (33) DeJesus, J. F.; Jenkins, D. M. *Chemistry* **2020**, *26*, 1429–1435.
- (34) Blatchford, K. M.; Mize, C. J.; Roy, S.; Jenkins, D. M. *Dalt. Trans.* **2022**, *51*, 6153–6156.
- (35) Schremmer, C.; Cordes (née Kupper), C.; Klawitter, I.; Bergner, M.; Schiewer, C. E.; Dechert, S.; Demeshko, S.; John, M.; Meyer, F. *Chem. Eur. J.* **2019**, *25*, 3918–3929.
- (36) Ghosh, M.; Cramer, H. H.; Dechert, S.; Demeshko, S.; John, M.; Hansmann, M. M.; Ye, S.; Meyer, F. *Angew. Chem. Int. Ed.* **2019**, *58*, 14349–14356.
- (37) Cordes (née Kupper), C.; Morganti, M.; Klawitter, I.; Schremmer, C.; Dechert, S.; Meyer, F. *Angew. Chem. Int. Ed.* **2019**, *58*, 10855–10858.
- (38) Cordes (née Kupper), C.; Klawitter, I.; Rüter, I.; Dechert, S.; Demeshko, S.; Ye, S.; Meyer, F. *Inorg. Chem.* **2022**, *61*, 7153–7164.
- (39) Massie, A. A.; Schremmer, C.; Rüter, I.; Dechert, S.; Siewert, I.; Meyer, F. *ACS Catal.* **2021**, *11*, 3257–3267.
- (40) Dyckhoff, F.; Schlagintweit, J. F.; Reich, R. M.; Kühn, F. E. *Catal. Sci. Technol.*

**2020**, *10*, 3532–3536.

- (41) Bernd, M. A.; Dyckhoff, F.; Hofmann, B. J.; Böth, A. D.; Schlagintweit, J. F.; Oberkofler, J.; Reich, R. M.; Kühn, F. E. *J. Catal.* **2020**, *391*, 548–561.
- (42) Kück, J. W.; Anneser, M. R.; Hofmann, B.; Pöthig, A.; Cokoja, M.; Kühn, F. E. *ChemSusChem* **2015**, *8*, 4056–4063.
- (43) Anneser, M. R.; Haslinger, S.; Pöthig, A.; Cokoja, M.; Basset, J.-M.; Kühn, F. E. *Inorg. Chem.* **2015**, *54*, 3797–3804.
- (44) Dyckhoff, F.; Schlagintweit, J. F.; Bernd, M. A.; Jakob, C. H. G.; Schlachta, T. P.; Hofmann, B. J.; Reich, R. M.; Kühn, F. E. *Catal. Sci. Technol.* **2021**, *11*, 795–799.
- (45) Anneser, M. R.; Haslinger, S.; Pöthig, A.; Cokoja, M.; D’Elia, V.; Högerl, M. P.; Basset, J.-M.; Kühn, F. E. *Dalt. Trans.* **2016**, *45*, 6449–6455.
- (46) Schlachta, T. P.; Anneser, M. R.; Schlagintweit, J. F.; Jakob, C. H. G.; Hintermeier, C.; Böth, A. D.; Haslinger, S.; Reich, R. M.; Kühn, F. E. *Chem. Commun.* **2021**, *57*, 6644–6647.
- (47) Schlagintweit, J. F.; Altmann, P. J.; Böth, A. D.; Hofmann, B. J.; Jandl, C.; Kaußler, C.; Nguyen, L.; Reich, R. M.; Pöthig, A.; Kühn, F. E. *Chem. Eur. J.* **2021**, *27*, 1311–1315.
- (48) Schulte to Brinke, C.; Ekkehardt Hahn, F. *Dalt. Trans.* **2015**, *44*, 14315–14322.
- (49) Fei, F.; Lu, T.; Chen, X.-T.; Xue, Z.-L. *New J. Chem.* **2017**, *41*, 13442–13453.
- (50) Mageed, A. H.; Skelton, B. W.; Baker, M. V. *Dalt. Trans.* **2017**, *46*, 7844–7856.
- (51) Li, Z.; Wiratpruk, N.; Barnard, P. J. *Front. Chem.* **2019**, *7*, 1 - 13.
- (52) Sehnal, P.; Taylor, R. J. K.; Fairlamb, I. J. S. *Chem. Rev.* **2010**, *110*, 824–889.
- (53) Catellani, M.; Frignani, F.; Ranganoni, A. *Angew. Chem. Int. Ed.* **1997**, *36*, 119–122.
- (54) Connelly, N. G.; Geiger, W. E. *Chem. Rev.* **1996**, *96*, 877–910.
- (55) Tierno, A.; Wengryniuk, S. *Molecules* **2017**, *22*, 780.
- (56) Zheng, B.; Tang, F.; Luo, J.; Schultz, J. W.; Rath, N. P.; Mirica, L. M. *J. Am. Chem. Soc.* **2014**, *136*, 6499–6504.
- (57) Ball, N. D.; Sanford, M. S. *J. Am. Chem. Soc.* **2009**, *131*, 3796–3797.
- (58) Gerken, M.; Boatz, J. .; Kornath, A.; Haiges, R.; Schneider, S.; Schroer, T.; Christe, K. . *J. Fluor. Chem.* **2002**, *116*, 49–58.
- (59) Shaw, M. M.; Smith, R. G.; Ramsden, C. A. *Arkivoc* **2011**, *2011*, 221–228.
- (60) McCall, A. S.; Wang, H.; Desper, J. M.; Kraft, S. *J. Am. Chem. Soc.* **2011**, *133*, 1832–1848.
- (61) Spek, A. L. *Acta Crystallogr. Sect. C Struct. Chem.* **2015**, *71*, 9–18.
- (62) Figgis, B. N.; Hitchman, M. A. *Ligand Field Theory and Its Applications*, 1st ed.; Wiley-VCH, **1999**.
- (63) Carsch, K. M.; DiMucci, I. M.; Iovan, D. A.; Li, A.; Zheng, S.-L.; Titus, C. J.; Lee,

- S. J.; Irwin, K. D.; Nordlund, D.; Lancaster, K. M.; Betley, T. A. *Science* **2019**, 365, 1138–1143.
- (64) Grove, D. M.; Van Koten, G.; Mul, P.; Van der Zeijden, A. A. H.; Terheijden, J.; Zoutberg, M. C.; Stam, C. H. *Organometallics* **1986**, 5, 322–326.
- (65) Stoll, S.; Britt, R. D. *Phys. Chem. Chem. Phys.* **2009**, 11, 6614.
- (66) Stoll, S.; Schweiger, A. *J. Magn. Reson.* **2006**, 178, 42–55.
- (67) Bühl, M.; Kabrede, H. *J. Chem. Theory Comput.* **2006**, 2, 1282–1290.
- (68) Nielsen, M. T.; Moltved, K. A.; Kepp, K. P. *Inorg. Chem.* **2018**, 57, 7914–7924.
- (69) Grimme, S.; Ehrlich, S.; Goerigk, L. *J. Comput. Chem.* **2011**, 32, 1456–1465.
- (70) Hedegård, E. D.; Kongsted, J.; Sauer, S. P. A. *J. Chem. Theory Comput.* **2011**, 7, 4077–4087.
- (71) Xiao, Z.; Patrick, B. O.; Dolphin, D. *Inorg. Chem.* **2003**, 42, 8125–8127.
- (72) Chmielewski, P. J.; Latos-Grażyński, L. *Inorg. Chem.* **1997**, 36, 840–845.
- (73) He, H.; Ye, Z.; Shimizu, D.; Sumra, I.; Zhang, Y.; Liang, Z.; Zeng, Y.; Xu, L.; Osuka, A.; Ke, Z.; Jiang, H.-W. *Chem. Eur. J.* **2022**, 28, e202103272.
- (74) Zhang, L.-H.; Yu, F.; Shi, Y.; Li, F.; Li, H. *Chem. Commun.* **2019**, 55, 6122–6125.
- (75) Han, Y.; Wu, Y.; Lai, W.; Cao, R. *Inorg. Chem.* **2015**, 54, 5604–5613.
- (76) Zhang, M.; Zhang, M.-T.; Hou, C.; Ke, Z.-F.; Lu, T.-B. *Angew. Chem. Int. Ed.* **2014**, 53, 13042 – 13048.

## Chapter 6. In pursuit of ruthenium clusters

### 6.1 Introduction

I had the fantastic opportunity to pursue cluster chemistry at Harvard University for around six months, working under Professor Ted Betley's supervision. The following chapter outlines one of two projects that I was working on during my time there.

**Chart 6.1** features representative polymetallic ensembles the Betley lab has studied throughout the years, which center on two hexamine, tritopic ligands,  $^{\text{Me,R}}\text{LH}_6$  and  $^{\text{tbs,R}}\text{LH}_6$ , respectively, where the R denotes any substitution of the diaza catechol moieties<sup>1</sup>, engendering a high-spin environment, resulting in open-shell clusters<sup>2</sup>. As shown in Chapter 1, **Scheme 1.3**, the extensive electron delocalization renders the trimetallic entities apt at facilitating multi-electron transfers<sup>3</sup>; more recently, the group demonstrated that the clusters exhibit size-dependent reactivity<sup>4</sup>.

As outlined in **Chart 6.1**, hexametallic clusters readily form by reacting  $^{\text{Me,R}}\text{LH}_6$  with metal precursors bearing internal bases *viz.* hexamethyl silyl amide, NTMS,  $[\text{Fe}(\text{NTMS})_2]_2$  or mesitylene, mes,  $[\text{Fe}(\text{Mes})_2]_2$ , resulting from dimerization of two trinuclear fragments. Introducing steric encumbrance, by functionalization of the primary anilines, or by addition of exogenous ligands, *e.g.* tertiary phosphines or pyridine, inhibit any dimerization reactions, resulting instead in trimetallic clusters.

As the group has successfully synthesized homotrimetallic complexes of all transition metals from the first row, combined with the triangular predisposition of metals, in particular, is prevalent in CO cluster complexes relevant to cluster catalysis<sup>5,6</sup>, and the propensity to form (stronger) metal-metal bonds increase traversing down a triad<sup>7</sup>, we thought it appropriate to investigate the resulting cluster properties upon a change in metal

identity for its the heavier congener: specifically, what changes occur when substituting iron for ruthenium.

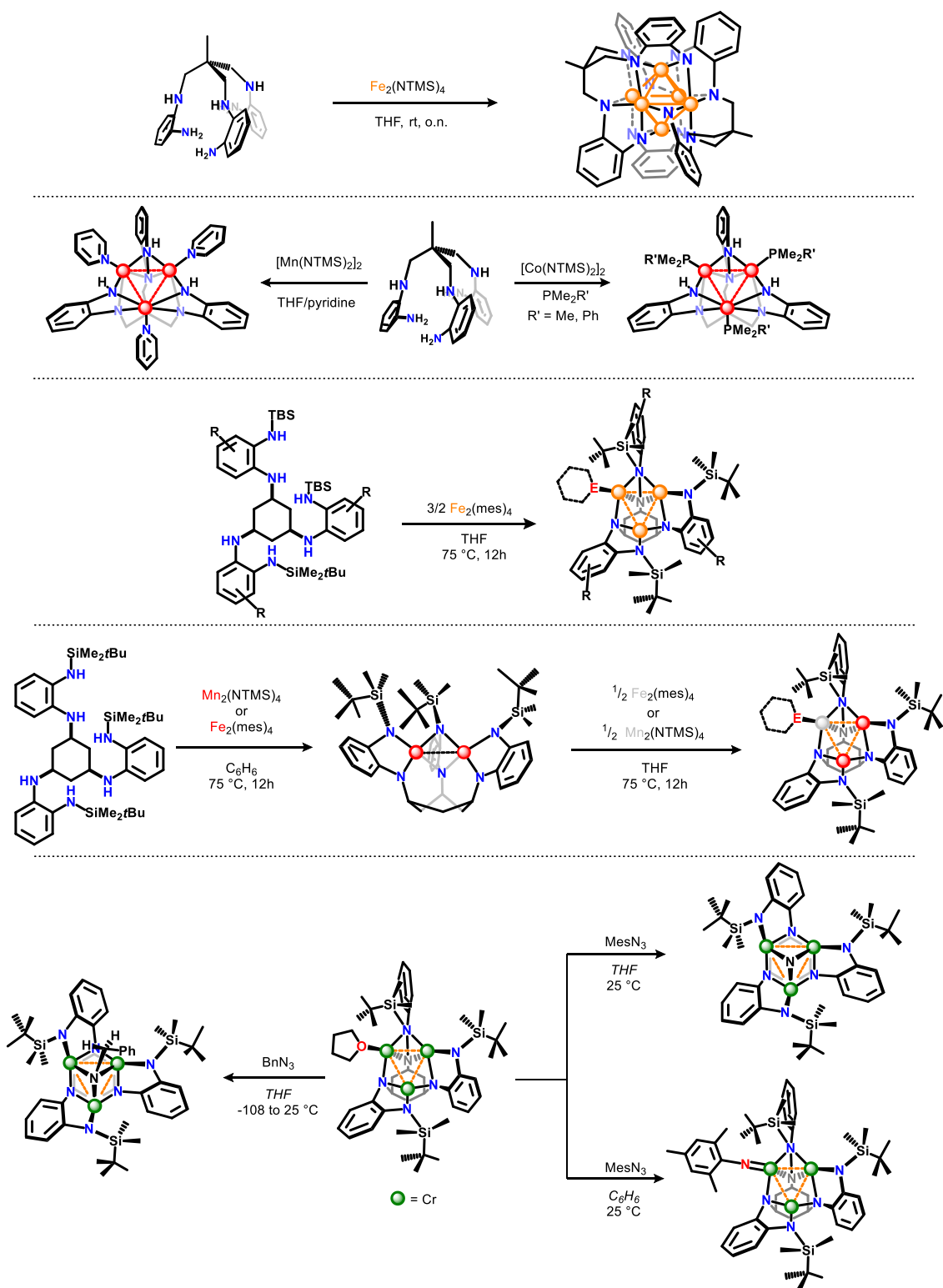
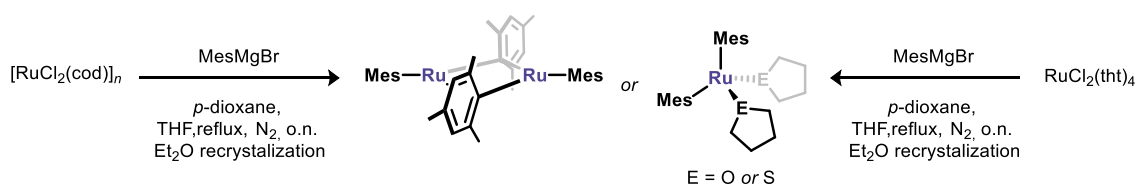


**Chart 6.1.** The tritopic ligand  $^{tbs}\text{LH}_6$  provides the basis for versatile transformations. *a*) 2- and 4e<sup>-</sup> reduction of hydrazine and hydrazone, *b*) ready preparation of trinuclear bimetallic cluster, and *c*) substrate reaction at a single-site or cooperatively.

## 6.2 Synthesis of Ru (II) complexes bearing internal bases

To effect cluster synthesis, we initially sought to explore concurrent deprotonation-metalation using a Ru (II) precursor bearing an internal base; wanting to use the NMTS or mes bearing synthons, as the byproducts are readily separated from the reaction mixture. In contrast to Fe, no preparations, to our knowledge, have been published on the synthesis, isolation, and characterization of neither  $[\text{Ru}(\text{ntms})_2]_2$ ,  $[\text{Ru}(\text{mes})_2]_2$  nor their corresponding monomeric solvato adducts, contrasting  $\text{Ru}(\text{mes})_4$ <sup>8</sup>. We did not pursue metalation using this Ru (IV) compound, as the large charge build-up during complexation may result in competing electron transfer reactions, because the azacatechol of  $^{\text{Me,R}}\text{LH}_6$  has been shown to demonstrate redox-non innocence<sup>9</sup>. However, later realized during the processes of writing, it may have been worth pursuing its preparation with intention of reduction, as this compound demonstrates two reversible one-electron redox waves supporting the redox pairs  $[\text{Ru}(\text{mes})_4]^{\text{III/IV/V}8}$ , in a similar manner to preparation of low-valent Fe(I),  $[\text{K}18\text{-crown-6}][\text{Fe}(\text{ntms})_2]$ <sup>10</sup>.



**Scheme 6.1.** The synthetic strategy targets either organoruthenium (II) complexes. Irrespective of connectivity, the starting material would have been of great interest for further studies.

Initially, we sought to synthesize the organoruthenium (II) mesityl reagent analogous to iron, as either its dimer or solvato adduct,  $[\text{Ru}(\text{mes})_2]_2$  and  $\text{Ru}(\text{mes})_2(\text{thf})_{2/3}$ , respectively, as suggested in **Scheme 6.1**. The iron analogue is readily prepared by reacting  $\text{FeCl}_2(\text{thf})_2$  with two equivalents of  $\text{MesMgBr}$  in the presence of *p*-dioxane<sup>11</sup>; *p*-dioxane greatly benefits the reactions, ensuring transmetalation reaction between  $\text{FeCl}_2(\text{thf})_2$  and  $\text{Mg}(\text{mes})_2(\text{thf})_2$ , and further drives the equilibrium towards the organoiron compound, from the precipitation of insoluble  $\text{MgX}_2(\textit{p}\text{-dioxane})$  salts,  $\text{X} = \text{Cl}, \text{Br}$ ; known as the Schlenk equilibrium.

However, divalent Ru halides are poorly defined molecular entities; instead, Ru (III) tris hydrate,  $\text{RuCl}_3 \cdot 3 \text{H}_2\text{O}$ , forms the basis for obtaining various Ru (II) chloro adducts, such as commercially available tris and tetrakis triphenylphosphine, DMSO<sup>12</sup>, and tetrahydrothiophene (tht) *trans*- $\text{RuCl}_2(\text{tht})_4$ <sup>13</sup>. In addition to the latter complex, we also investigated whether the commercially available  $[\text{RuCl}_2(\text{cod})]_n$  would serve as a source of soluble Ru (II) chlorido. Given the kinetic inertness of Ru (II), any of the employed complexes described within this chapter were reacted for a prolonged time.

First, the Ru-cod precursor was refluxed for an hour in THF, cooled to room temperature and then slowly added MesMgBr; facilitating a noticeable color change, analogous to when the reaction was performed with  $\text{FeCl}_2$ . The addition of *p*-dioxane starts to precipitate out colorless particles, and subsequent steps all suggested the same reactivity in terms of precipitates and colors, albeit slightly lighter. However, the material recovered after multiple recrystallizations from  $\text{Et}_2\text{O}$  strongly contrasts the pyrophoric nature of  $[\text{Fe}(\text{Mes})_2]_2$ : a small quantity was removed from the glovebox, and neither exposure to air nor  $i\text{PrOH}$  resulted in smoke.

We were able to extract some single-crystals suitable for single-crystal X-ray diffraction following recrystallization from  $\text{Et}_2\text{O}$ ; instead of a Ru (II) reagent, these conditions facilitate reduction, yielding a half-sandwich Ru (0) complex, shown in **Figure 6.1**. The complex was isolated from cold ( $-35\text{ }^\circ\text{C}$ )  $\text{Et}_2\text{O}$  in good yields ( $>60\%$ ), however, the complex was not of interest, and consequently, no further analyses were conducted.

The reactivity of this particular Ru (II) diene with Grignard reagents and light is well-described to facilitate the reduction of Ru (0) compounds<sup>14</sup>. In all instances, the cod ligand is maintained; the addition of arenes, leads to isolation of Ru (0) complexes binding

these in  $\eta^6$ -fashion like our observed structure, however, no allylic-functionalization of cod is observed.

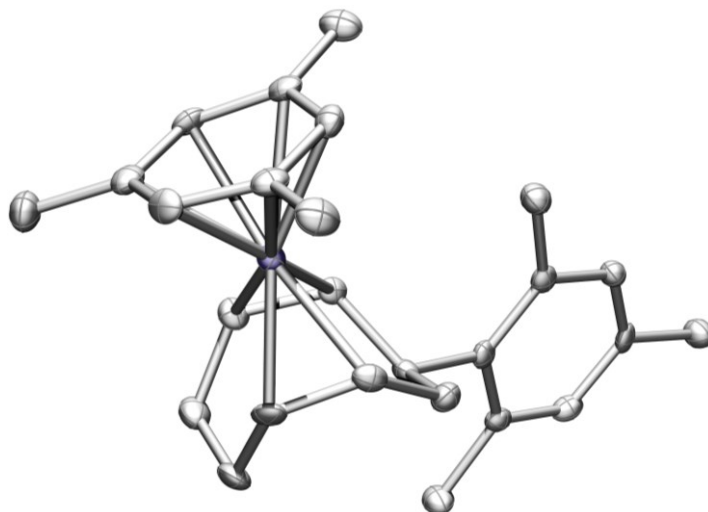
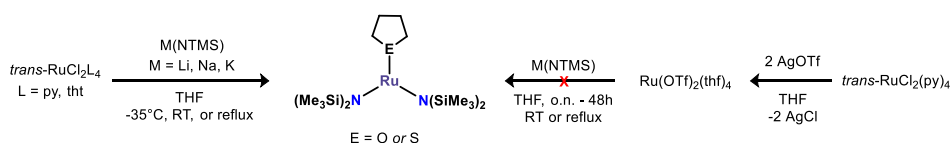


**Figure 6.1.** Single-crystal structure following attempted ligand substitution of  $[RuCl_2(cod)]_n$ , **6.1**. Thermal ellipsoids are shown at a 50% probability level. Color coding scheme: C grey, H white, Ru dark blue.

Instead, we wanted reproduced the same conditions using *trans*- $RuCl_2(thf)_4$ . To our surprise, the only isolable materials were lightly yellow-colored crystals, comprising  $Mg(mes)_2(thf)_2$  covered in oil, which turned out to be a major byproduct, a viscous oil of poorly defined composition. No attempts were made with  $RuCl_2(dmsO)_4$ , as the Grignard will add to the sulfoxide. These findings suggest to us, that a different approach likely is more fruitful within the time constraint of the research exchange. Instead, our attention turned to the preparation of the Ru-NTMS-solvato compound,  $Ru(NTMS)_2(solv)_n$ , as outlined in **Scheme 6.2**, and whereas this material seemed to be pyrophoric, we were unable to obtain a definitive structure to corroborate the connectivity to ruthenium. Critically, despite a qualitative confirmation of the amide functionality, when reacted with the  $^{Me,F}LH_6$  ligand, it did not seem to furnish any transformations, in the same way, reacting the ligand with  $K(NTMS)$  and  $Fe(NTMS)_2(thf)_2$  did.

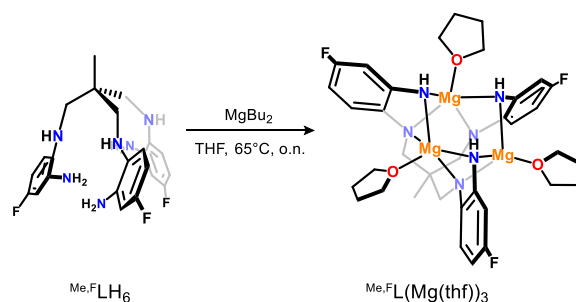


**Scheme 6.2.** The synthetic approach targets the Ru (II)-NTMS base. Irrespective of connectivity, the starting material would have been of great interest for further studies.



### 6.3 Transmetalation reactions

The group encountered a similar problem in their synthesis of the tri nickel cluster bearing the <sup>tb</sup><sub>s</sub>,<sup>F</sup>LH<sub>6</sub> ligand, owing to the instability of the Ni-amide reagent. Instead, reacting the ligand with Mg<sup>''</sup>Bu<sub>2</sub> furnishes the transformation of the ligand into an isolable, diamagnetic trimagnesium cluster decorated by three THF molecules<sup>15</sup>, as outlined in **Scheme 6.3**. Different from the original paper, a fluorine atom was introduced into the diaza catechol, *para* to the secondary aniline to leverage its NMR properties to assess any reactivity from loss in the symmetry; the complex features a single resonance in the <sup>19</sup>F NMR spectrum.



**Scheme 6.3.** Synthesis of trimagnesium cluster synthon. Irrespective of connectivity, the starting material would have been of great interest for further studies.

Consistent with metalation, changes occur to both <sup>1</sup>H and <sup>19</sup>F NMR spectra of the parent <sup>Me,F</sup>LH<sub>6</sub> ligand: signals owing to the secondary aniline, signal C in the top spectrum of **Figure 6.2**, is absent in the lower spectrum, and the resonance owing to the primary aniline, signal E in the top spectrum, signal F in the lower, adopts a singlet splitting and integrates relatively to the methyl group (signal G, lower spectrum) now in a 1:1 ratio. Finally, three THF molecules are accounted for, signals E, and H. The overall C<sub>3</sub>-symmetry is, however, remained consistent with a single <sup>19</sup>F NMR resonance, **Figure 6.3**.

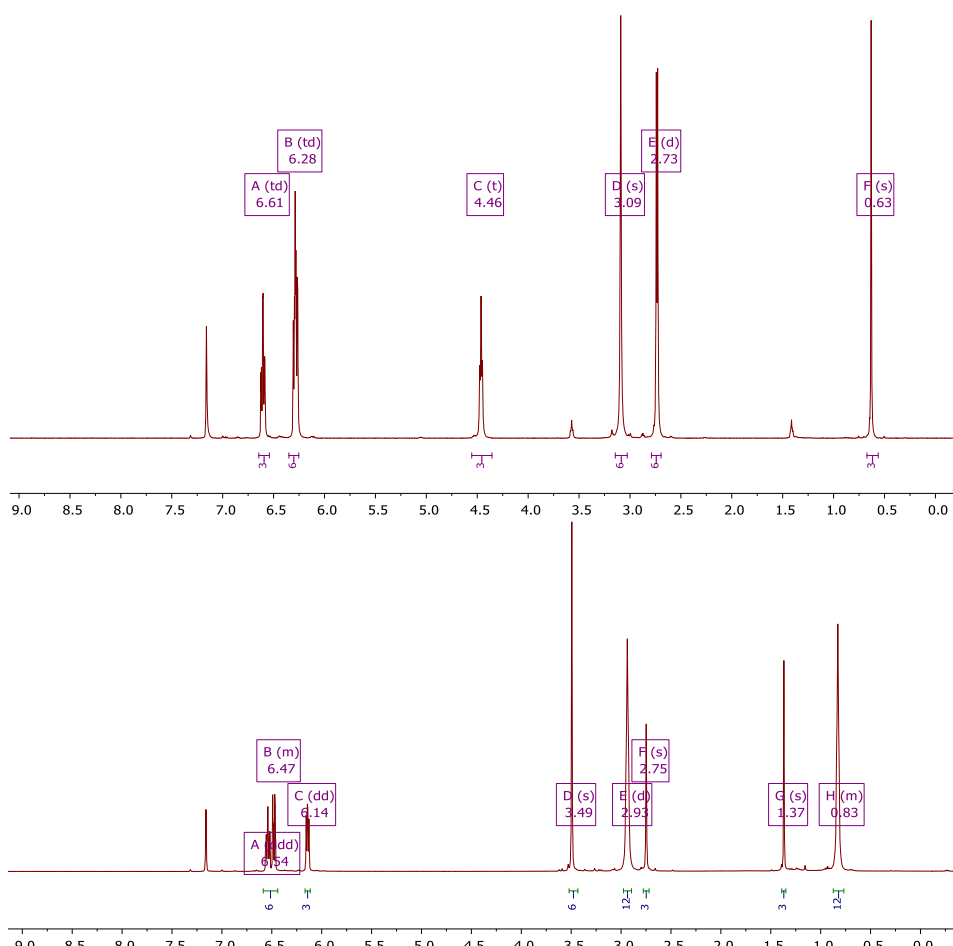


**Figure 6.2.**  $^1\text{H}$  NMR spectra ( $\text{C}_6\text{D}_6$ ) comparing  $\text{Me}_x\text{F}_y\text{LH}_6$  (top) to its Mg-adduct (lower). Upon metalation protons accounting for the aromatics and the primary aniline experience an upfield shift.

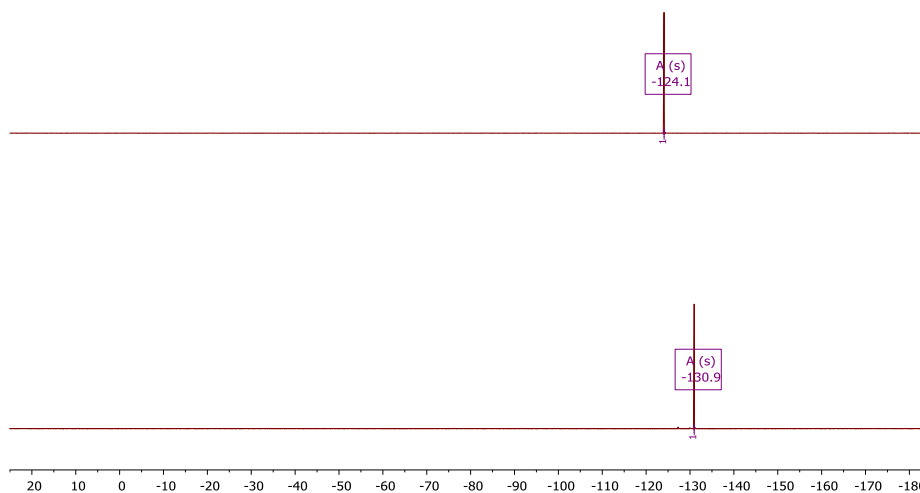
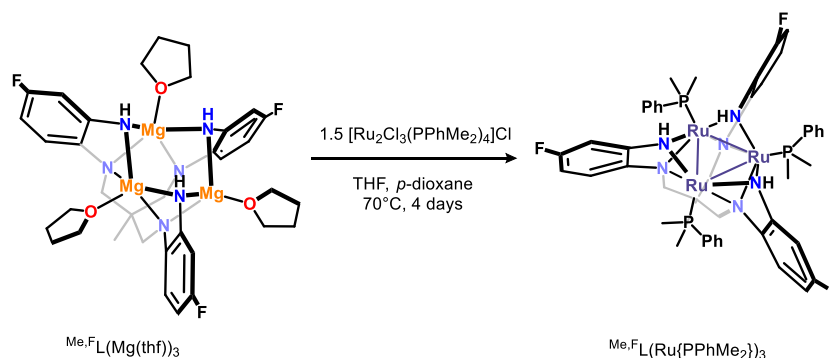


**Figure 6.3.**  $^{19}\text{F}$  NMR spectra ( $\text{C}_6\text{D}_6$ ) comparing  $\text{Me}_x\text{F}_y\text{LH}_6$  (top) to its Mg-adduct (lower). Changes occurring to the singlet support consumption of the starting material, and multiple signals provide insights into reaction products' symmetry.

This ligand was chosen over the cyclohexane from a combination of different elements, including that transmetalation of the Mg-synthon with metal-halido sources may exploit the Schlenk equilibrium through the addition of *p*-dioxane, and that the group

has studied other homotrimetallic clusters in addition to Fe, including Mn and Co<sup>9</sup>; addition of exogenous phosphine or pyridine prevents any dimerization to larger ensembles. Taken together we sought transmetalation as outlined in the below reaction **Scheme 6.4**: seeking to selectively furnish the formation of [Ru<sub>3</sub>] over the [Ru<sub>6</sub>] compound from the presence of exogenous phosphine ligands.



**Scheme 6.4.** *Synthetic strategy concerning transmetalation.* We sought to demonstrate control of the resulting cluster's nuclearity through the absence/presence of ligands impeding cluster dimerization.

We chose to react the Mg-synthon with the Ru (II) dimers bearing PPhMe<sub>2</sub> to furnish the formation of the desired [Ru<sub>3</sub>] complex. The reaction requires several days, owing to the inertness of Ru (II), however, noticeable color changes take place alongside the precipitation of a colorless crystalline material, consistent with MgCl<sub>2</sub>(*p*-dioxane).

Reacting Me,F,L(Mg(thf))<sub>3</sub> with 1.5 equivalents of the chloride salt [Ru<sub>2</sub>Cl<sub>3</sub>(PPhMe<sub>2</sub>)<sub>4</sub>]Cl<sup>16</sup>, transitions from a slightly yellow-colored solution to an intensely blue color; the THF/dioxane solution is readily separated from Mg-salts through filtration, which yields a powder soluble in common organic solvents, however sparingly so in hexane, which helps to remove excess PPhMe<sub>2</sub>. While we were unable to produce single-crystals of suitable quality for X-ray diffraction for connectivity purposes, instead, NMR and mass-spectrometry work to strongly support the notion that a compound consistent with connectivity presented in **Scheme 6.4** was produced and isolated (along with some impurities).

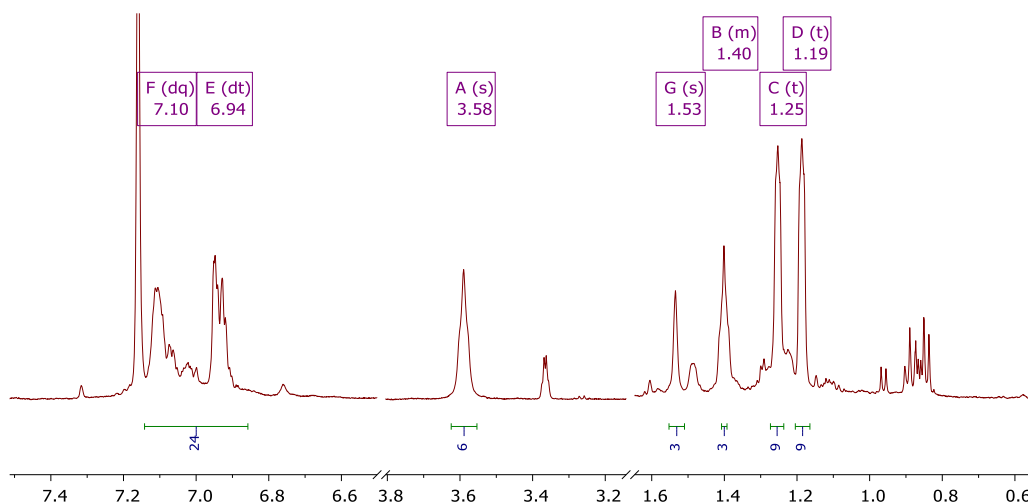


**Figure 6.4.**  $^1\text{H}$  NMR spectra ( $\text{C}_6\text{D}_6$ ) of isolated transmetalation adduct. The spectrum's main entity is consistent with the elements of the desired molecule.

The  $^1\text{H}$  NMR spectrum shown in **Figure 6.4**, integrates relatively to signal A, methylene group of the TAME backbone, suggestive of a different metal occupying the crown, each decorated by a phosphine ligand: First, two signals, C and D, each account 9 protons, consistent with two distinctive methyl groups owing to the phosphine ligand, which is further suggested by aromatic protons integrating to 24.

Second, the primary anilide protons are further upfield shifted compared to in **Figure 6.2**, signal G, consistent with an electron rich metal, *viz.* Ru. However, we did not prepare  $^{\text{Me,F}}\text{L}(\text{Mg}(\text{PPhMe}_2))_3$ , and this compound may be relevant to unambiguously demonstrate that the upfield shift originates from a change in metal identity rather than a difference in ligand *viz.* THF *vs.* phosphine.

Third, in **Figure 6.5**,  $^{19}\text{F}$  (top spectrum) and (decoupled)  $^{31}\text{P}$  (lower spectrum), feature resonances that are sufficiently different from the starting material, however, in a relative integration ratio of 1:2. The Ru-precursor is sparingly soluble in  $\text{C}_6\text{D}_6$  and features a single signal in the  $^{31}\text{P}$  spectrum at 21.04 ppm. Based on discussion with the members of Ted's group, working on related motifs, this spectral feature is not uncommon and often associated with asymmetrical ligand binding. However, without any solid-state

structure, the nature of the asymmetry is difficult to assess, and more speculation than anything.

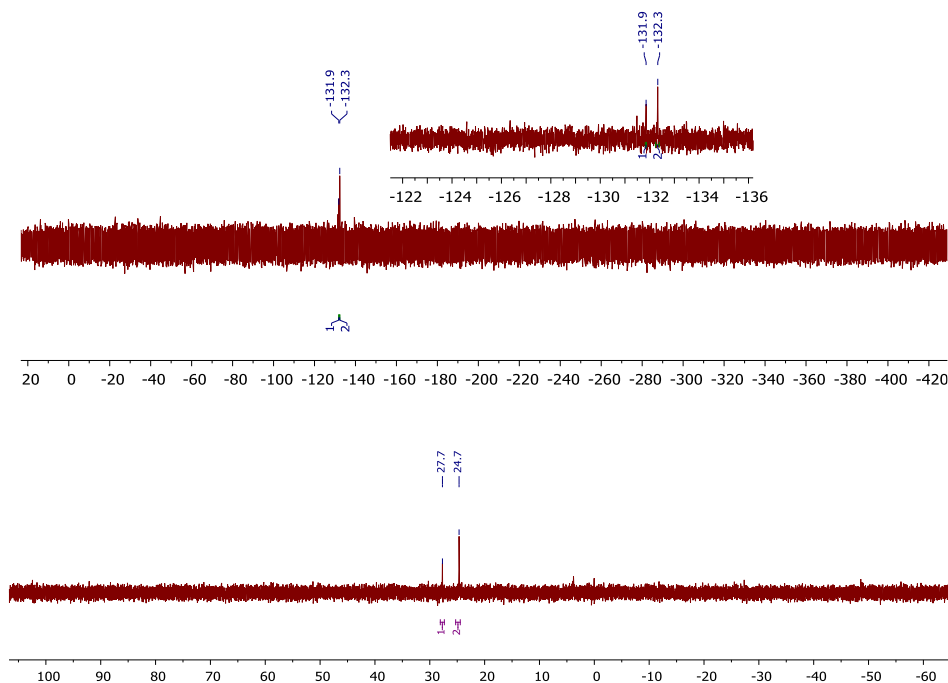


**Figure 6.5.**  $^{19}\text{F}$  (top) and  $^{31}\text{P}$  (lower) NMR spectra ( $\text{C}_6\text{D}_6$ ) of isolated transmetalation adduct. The spectrum's main entity is consistent with the elements of the desired molecule.

Finally, a sample of this material was subjected to high-resolution mass spectrometry, and an ion free of HF was found, shown in **Figure 6.6**, consistent with a compound containing the atoms of our target complex.

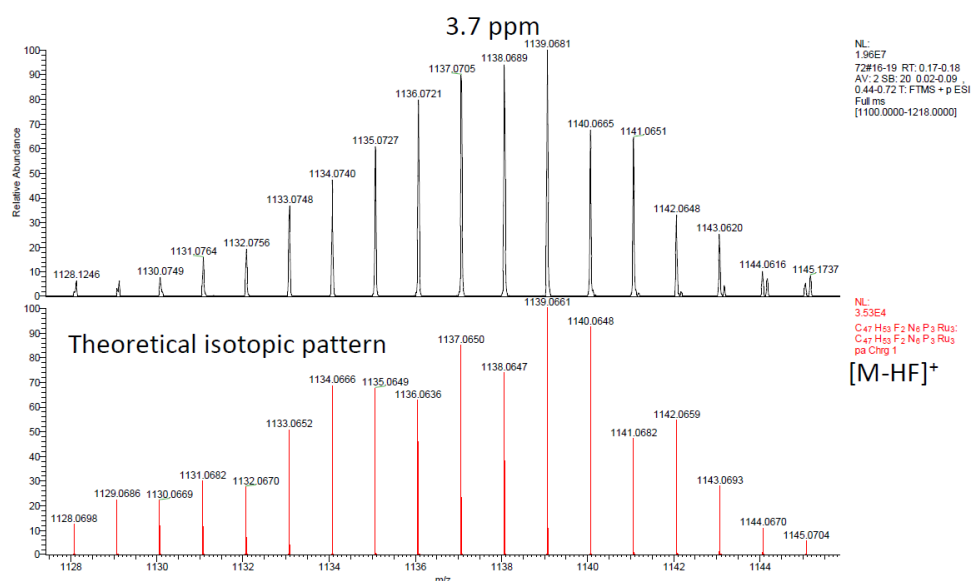


**Figure 6.6.** HR-MS (Maldi-TOF) of isolated transmetalation adduct. An ion consistent with the atoms of our desired intermediate was found, representing a significant portion of the sample.

## 6.4 Conclusion

Polymetallic clusters comprising the base metals, bearing weak-field ligands are of interest in the context of mediating multiple electron transfer reactions. The heavier congeners are of interest from a fundamental aspect in terms of bonding and distinctive properties, such as redox profiles as well as magnetism, and ultimately to understand whether any  $4/5d$  open-shell complexes may be realized.

We initially sought to prepare divalent ruthenium complexes bearing an internal base for metalation purposes, however, found such preparations unsuccessful, despite trying various soluble Ru (II) sources, at least within the timeframe of an external research stay. Instead, based on the groups prior results, we sought to explore transmetalation reactions using a trimagnesium cluster as transfer-reagent.

Reacting this trimagnesium compound to a diruthenium(II) chloride precursor containing  $\text{PPhMe}_2$ ,  $[\text{Ru}_2\text{Cl}_3(\text{PPhMe}_2)_4]\text{Cl}$ , in THF with the addition of *p*-dioxane for 4 days, yields a strongly blue-colored filtrate containing a compound, which when isolated, consistent with NMR and mass-spectrometry, appear to contain all elements. However, as we were unable to produce single-crystals of a sufficient quality for single-crystal X-ray diffraction, the connectivity remains unknown, which is relevant in answering the two singlets, integrating relative to one another in a 1:2 ratio observed in  $^{19}\text{F}$  and  $^{31}\text{P}$  NMR, suggestive of an asymmetric phosphine binding.

Ultimately, we suggests that we have been successful in preparation of a triruthenium cluster bearing the tritopic ligand,  $^{\text{Me,R}}\text{LH}_6$ , bound by three phosphine ligands.

## 6.5 References

- (1) Powers, T. M.; Fout, A. R.; Zheng, S. L.; Betley, T. A. *J. Am. Chem. Soc.* **2011**, *133*, 3336–3338.
- (2) Fout, A. R.; Zhao, Q.; Xiao, D. J.; Betley, T. A. *J. Am. Chem. Soc.* **2011**, *133*, 16750–16753.
- (3) Powers, T. M.; Betley, T. A. *J. Am. Chem. Soc.* **2013**, *135*, 12289–12296.
- (4) Bartholomew, A. K.; Juda, C. E.; Nessralla, J. N.; Lin, B.; Wang, S. G.; Chen, Y.-S.; Betley, T. A. *Angew. Chem. Int. Ed.* **2019**, *58*, 5687–5691.
- (5) Rosenberg, E. R. and Laine, M. in *Catalysis by Di- and Polynuclear Metal Cluster Complexes*; Adams, R. D.; Cotton, F. A. (eds.) (Wiley-VCH, Weinheim) **1998**.
- (6) Nielsen, M. T.; Padilla, R.; Nielsen, M. *J. Clust. Sci.* **2020**, *31*, 11–61.
- (7) *Multiple Bonds Between Metal Atoms*; Cotton, F. A., Murillo, C. A., Walton, R. A., (eds.), (Springer-Verlag: New York), **2005**.
- (8) Hay-Motherwell, R. S.; Wilkinson, G.; Hussain-Bates, B.; Hursthouse, M. B. *J. Chem. Soc., Dalt. Trans.* **1992**, No. 24, 3477–3482.
- (9) Fout, A. R.; Xiao, D. J.; Zhao, Q.; Harris, T. D.; King, E. R.; Eames, E. V.; Zheng, S.-L.; Betley, T. A. *Inorg. Chem.* **2012**, *51*, 10290–10299.
- (10) Werncke, C. G.; Bunting, P. C.; Duhayon, C.; Long, J. R.; Bontemps, S.; Sabo-Etienne, S. *Angew. Chem. Int. Ed.* **2015**, *54*, 245–248.
- (11) Martinez, G. E.; Killion, J. A.; Jackson, B. J.; Fout, A. R.; Petel, B. E.; Matson, E. M.; Gridley, B. M.; Moxey, G. J.; Kays, D. L.; Bryan, A. M.; Power, P. P.; Erickson, J. D.; Riparetti, R.; Power, P. P.; Blundell, T. J.; Ramos, A. M. G.; Sharpe, H. R.; Kays, D. L.; Abraham, M. Y.; Smith, J. C.; Wang, Y.; Robinson, G. H.; Saleh, M.; Osman, K.; Wehmschulte, R. J.; Brennessel, W. W.; Ellis, J. E.; Wolf, R.; Chakraborty, U.; Büschelberger, P.; Rödl, C.; Büschelberger, P.; Rödl, C.; Wolf, R.; Ellis, J. E.; Chakraborty, U.; Wiegel, A.-K.; Wolf, R.; Ellis, J. E. *Inorganic Syntheses*. July 27, **2018**, pp 47–83.
- (12) James, B. R.; Ochiai, E.; Rampel, G. L. *Inorg. Nucl. Chem. Lett.* **1971**, *7*, 781–784.
- (13) Maiti, B. K.; Görls, H.; Klobes, O.; Imhof, W. *Dalt. Trans.* **2010**, *39*, 5713–5720.
- (14) *The Chemistry of Ruthenium: Ruthenium(II)*; Seddon, E. A., and Seddon, K. R. (eds.); Topics in Inorganic Chemistry, Pergamon, **1984**; Vol. 19, pp 341–890.
- (15) Zhao, Q.; Betley, T. A. *Angew. Chem. Int. Ed.* **2011**, *50*, 709–712.
- (16) Chatt, J.; Hayter, R. G. *J. Chem. Soc.* **1961**, 896.

# **Supporting Information**



# 1 Experimental methods

## 1.1 General considerations

All manipulations of metal complexes and proligand syntheses are listed under the appropriate steps. When Schlenk manipulations were involved, all glassware were oven-dried for a minimum of 10 hours or flame-dried using a blowtorch and cooled under a dynamic vacuum. Glassware employed in gloveboxes were similarly dried for a minimum of 10 hours and cooled in an evacuated antechamber prior to use. Et<sub>2</sub>O, THF, MeCN, DMSO, DCM, PhMe, and DMF were dried over activated aluminium oxide using an inert® solvent purification system (SPS), and further stored over 4Å molecular sieves (Sigma). Water and oxygen were removed from hexane and benzene by refluxing over sodium added sodium and benzophenone (0.5 w/v%) until a persisting ketyl radical was established and transferred *via* bulb-to-bulb distillation to a receiver Strauss storage flask. Celite 545 (Sigma, J. T. Baker) was dried in a Schlenk flask for at least 20 h under dynamic vacuum while heating to 200 – 220°C prior to glovebox use. Most chemicals were used as received from Sigma, Strem, Fluorochem, TCI, and VWR. Imidazole was recrystallized from acetone, and further dried over P<sub>2</sub>O<sub>10</sub> in a desiccator standing overnight. Ferrocenium hexafluorophosphate were dried under vacuum overnight and recrystallized from dry THF/MeCN prior to use inside the glovebox.

## 1.2 Characterization and physical measurements

<sup>1</sup>H, <sup>13</sup>C, <sup>19</sup>F, and <sup>31</sup>P NMR spectra were recorded on Bruker Ascend spectrometer with a Prodigy cryoprobe operating at 400 MHz for <sup>1</sup>H-NMR and 101 MHz for <sup>13</sup>C-NMR or, relevant to chapter six only Varian Mercury 400 MHz, or Varian Unity/Inova 500 MHz spectrometers. <sup>1</sup>H and <sup>13</sup>C chemical shifts are reported relative to SiMe<sub>4</sub>, using the residual solvent peak as internal reference<sup>1</sup>. HSQC, HMBC, and COSY experiments were used to verify the structures when <sup>1</sup>H and <sup>13</sup>C NMR were insufficient for characterisation.

The specific deuterated solvent is stated for each compound. Elemental analyses were carried out at Copenhagen University, Department of Chemistry, Niels V. Holst and Pia E. Sørensen. Electrochemical measurements were recorded on an Autolab PGSTAT12 instrument (Eco Chemie, Switzerland) at room temperature (*ca.* 20 °C) with the glassy carbon electrode (GCE), a Pt wire, and a non-aqueous Ag/AgCl electrode as the working, counter, and reference electrode, respectively. Cyclic voltammetry (CV) was conducted in DMF and MeCN containing 0.1 M tetrabutylammonium hexafluorophosphate (TBAPF<sub>6</sub>) and a specified concentration of the analyte within a potential range tabulated under each measurement *vs.* Ag/AgCl at various scan rates typically at 5, 20, 50, 100, 200, 500 and 1000 mV s<sup>-1</sup>, respectively. The potential was then calibrated against the formal potential of the Fc<sup>+</sup>/Fc redox couple by  $E_{vs. Fc^+/Fc} = E_{vs. Ag/AgCl} - 0.36 \text{ V}$ . All electrolytes were degassed with argon for at least 30 min and an argon atmosphere was maintained above the solution throughout the experiments.

The collected attenuated-total-reflectance (ATR) Fourier Transform infrared (FTIR) spectra have been obtained by a VERTEX 80 vacuum FTIR spectrometer from Bruker Optics GmbH. The mid-infrared spectral region (450-5000 cm<sup>-1</sup>) was collected with a Ge on KBr beam splitter, a liquid nitrogen cooled HgCDTe detector and an air-cooled thermal global radiation source employing a single-reflection germanium ATR accessory (IRIS) from PIKE Technologies Inc. The far-infrared (100-500 cm<sup>-1</sup>) recordings were done with a multilayer Mylar beamsplitter, a room temperature DTGS detector and a water-cooled thermal global radiation source employing a single-reflection diamond ATR accessory. The collected spectra of 2 cm<sup>-1</sup> spectral resolution have been corrected for small traces of residual water vapor absorption from the interferometer and the resulting absorption spectra have been corrected for minor baseline drifts. Subsequently,

extended ATR corrections have been applied to account for the wavelength-dependent penetration depth of the infrared probe beam into the solid sample.

The Raman spectra were collected employing the visible lines at 514.5 nm (green) and 488.0 nm (blue) emitted from a LEXEL 95-SHG-QS Argon ion laser (Cambridge Laser Laboratories Inc., USA) as the excitation sources. The continuous laser power was adjusted to ~4 mW, of which about half or less reached the uncovered surface of the sample to avoid sample oxidation. The excitation laser was passing through an InVia Reflex Raman instrument (Renishaw plc, England) via mirrors to an attached Leica DM2700M microscope (Leica Microsysteme Vertrieb GmbH, Germany) equipped with a traditional X5 objective. The scattered light from the sample was collected and sent back through a high-pass filter system dispersed in a single stage spectrograph and detected with a Peltier-cooled high-sensitive CCD device. The entrance slit width was set to 50  $\mu\text{m}$  and the acquisition condition was set to up to 100 s with automatic removal of cosmic spikes. Independent Raman spectra were collected and co-added. The resulting Raman spectrum was not manipulated further and not corrected for monochromator and detector efficiencies. The calibration of the absolute wavenumber scale was done with a diamond slab having its strongest band at  $\sim 1332.4\text{ cm}^{-1}$  and<sup>2</sup> the scale was checked with the ASTM bands of cyclohexane and polystyrene<sup>3,4</sup> to within  $1\text{--}2\text{ cm}^{-1}$  accuracy.

### **1.3 X-ray structure determinations**

A suitable crystal was harvested with a MiTeGen cryo loop and mounted on a goniometer attached to a SuperNova Dual Source CCD-diffractometer. Data were collected at the given temperature K using either Cu  $K\alpha$  or Mo  $K\alpha$  radiation under an active stream of  $\text{N}_2$ . Data integration ranging from 0.84 Å to 0.72 Å resolution was carried out using CrysAlis Pro software with reflection spot size optimization. Using Olex2<sup>5</sup>, the structure was solved with the SHELXT<sup>6</sup> structure solution program using Intrinsic Phasing and

refined with the SHELXL<sup>6</sup> refinement package using Least Squares minimization. The program PLATON was used to confirm an absence of higher symmetries, as well as used to model extensive solvent disorder by applying a solvent mask *via* the PLATON Squeeze<sup>7</sup> implementation.

Non-hydrogen atoms were refined with anisotropic displacement parameters, and hydrogen atoms were added in idealized positions and refined using a riding model. Crystallographic data relevant to a given chapter is listed in the table listed under the “*Crystallographic data*” section header.

## 2 Chapter 2

### 2.1 Synthetic methods

Complexes **2.1** and **2.2**, Starting from  $\text{PdX}_2$ : preparation of the tetraacetonitrile adduct. In air. 1.0 equivalent of  $\text{PdX}_2$  and 2.05 equivalents of  $\text{AgX}'$  were weighed out into a round-bottom flask. The flask was covered in aluminium foil, added a stir bar, MeCN (0.08M w.r.t Pd), fitted a reflux condenser, placed in an oil bath, and brought to reflux for roughly three hours. The flask was cooled to room temperature, the suspension filtered through celite, and transferred to an Erlenmeyer flask.

**Starting from tetraacetonitrile palladium(II) adduct  $2\text{X}' = \text{BF}_4, \text{PF}_6$ .** In air. To an Erlenmeyer flask, 1.0 equivalent of  $[\text{Pd}(\text{MeCN})_4] 2\text{X}'$ , 1.0 equivalent of napy, and MeCN (0.08M w.r.t Pd) was added, the mixture was stirred overnight at room temperature, which occasionally resulted in a yellow suspension. The following day, an additional 1.0 equivalent of napy was added, which after at-least four hours resulted in the formation of a pink/greyish precipitate. An equal volume of  $\text{Et}_2\text{O}$  was added to the Erlenmeyer flask, and the precipitate was collected on a glass frit. The powder was washed with a small amount of cold MeCN, followed by  $\text{Et}_2\text{O}$ , and left to dry in the air resulting in yielding the target dipalladium(II) complex as a grey/pinkish powder in good to excellent yield (50 – 75%). Any black precipitate was removed by re-dissolving the powder in enough MeCN and passing the solution through a glass filter. (This step should be expedited), re-precipitated with  $\text{Et}_2\text{O}$ , and dried on a glassfrit in air. 250 mg  $\text{PdCl}_2$  gave 601.8 mg (65%) of the resulting  $\text{PF}_6$ -complex. 250 mg  $\text{Pd}(\text{MeCN})_4 2\text{BF}_4$  gave 206.8 mg (68%) of the resulting  $\text{BF}_4$ -complex.

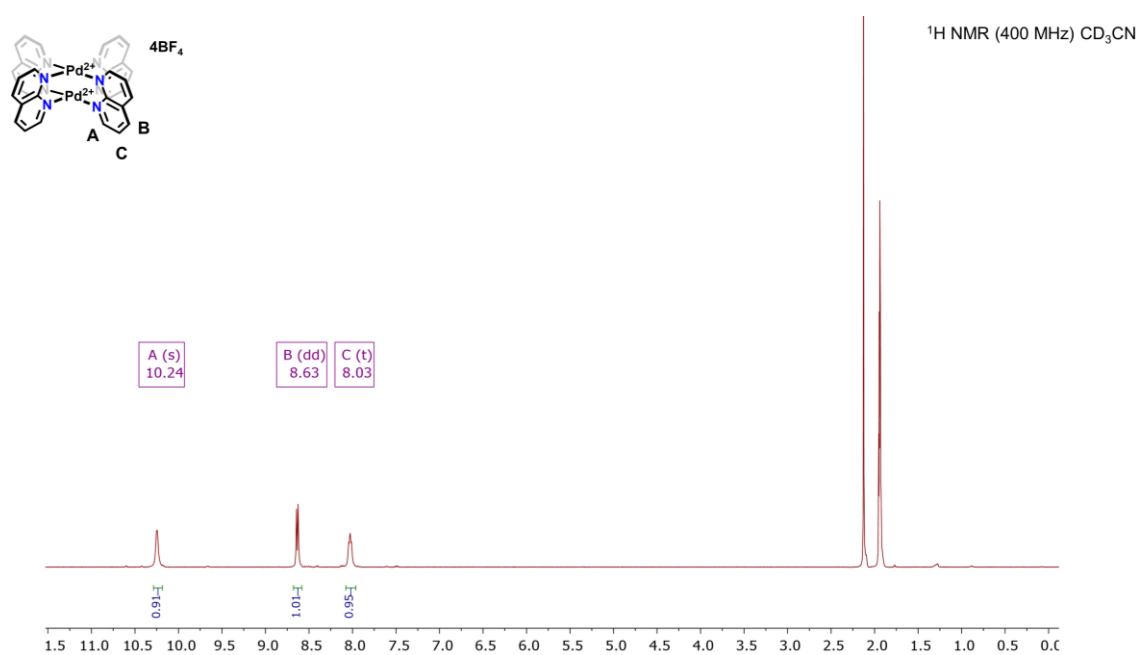
**Complex 2.1**, the  $\text{BF}_4$ -salt.  $^1\text{H}$  NMR (400 MHz,  $\text{MeCN-}d_3$ )  $\delta$  10.24 (broad singlet, 1H), 8.63 (d,  $J = 7.0$  Hz, 1H), 8.03 (t,  $J = 7.0$  Hz, 1H).  $^{13}\text{C}$  NMR (101 MHz,  $\text{CD}_3\text{CN}$ )  $\delta$  161.73,

145.93, 130.04, 127.57.  $^{19}\text{F}$  NMR (377 MHz,  $\text{CD}_3\text{CN}$ )  $\delta$  -151.30, -151.35.  $^1\text{H}$  NMR (400 MHz,  $\text{DMSO}-d_6$ )  $\delta$  10.35 (dd,  $J = 5.4, 1.7$  Hz, 1H), 8.80 (dd,  $J = 8.2, 1.7$  Hz, 1H), 8.15 (dd,  $J = 8.2, 5.4$  Hz, 1H).  $^{19}\text{F}$  NMR (377 MHz,  $\text{DMSO}-d_6$ )  $\delta$  -148.26 (s, F- $^{10}\text{B}$ ), -148.31 (s, F- $^{11}\text{B}$ ). **Elemental analysis** calcd (%) for  $\text{C}_{32}\text{H}_{24}\text{F}_{16}\text{N}_8\text{B}_4\text{Pd}_2$ : C 35.57, H. 2.24, N. 10.37; found: C 35.04, H 2.30, N 10.30. **UV-Vis**:  $\lambda_{\text{max}}$  544 nm, 36.6 ( $\epsilon / \text{M}^{-1}\text{cm}^{-1}$ ). Colorless single-crystals suitable for single-crystal X-ray diffraction were obtained overnight by  $\text{Et}_2\text{O}$  vapor diffusion into a concentrated MeCN solution of complex **2.1** at  $-18^\circ\text{C}$ .

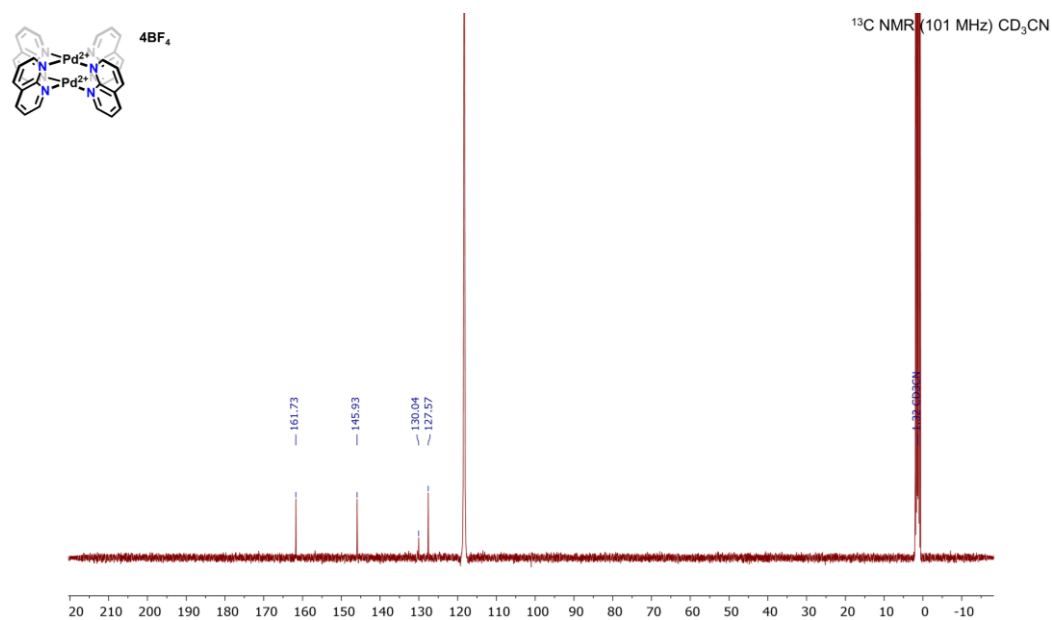
**Complex 2.2**, the  $\text{PF}_6$ -salt.  $^1\text{H}$  NMR (400 MHz,  $\text{DMSO}-d_6$ )  $\delta$  10.36 (dd,  $J = 5.4, 1.7$  Hz, 1H), 8.81 (dd,  $J = 8.2, 1.7$  Hz, 1H), 8.15 (dd,  $J = 8.2, 5.4$  Hz, 1H).  $^{13}\text{C}$  NMR (101 MHz,  $\text{DMSO}-d_6$ )  $\delta$  160.0, 155.6, 144.0, 128.5, 125.9.  $^{19}\text{F}$  NMR (377 MHz,  $\text{DMSO}-d_6$ )  $\delta$  -70.17 (d,  $J = 712.1$  Hz).  $^{31}\text{P}$  NMR (162 MHz,  $\text{DMSO}-d_6$ )  $\delta$  -144.18 (hept,  $J = 712.1$  Hz). **Elemental analysis** calcd (%) for  $\text{C}_{32}\text{H}_{24}\text{F}_{24}\text{N}_8\text{P}_4\text{Pd}_2$ : C 29.27, H. 1.84, N.8.53; found: C 29.24, H 1.58, N 8.53

The following comproportionation reactions were completed in an Argon-filled glovebox, using dried solvents as well as using overnight oven-dried or flame-dried equipment. In a 5 mL vial equipped with a stir bar was 1.0 equivalent of Pd(0) ( $\text{Pd}(\text{PPh}_3)_4$  (25 mg, 21.63  $\mu\text{mol}$ ) or 0.5 equivalent of  $\text{Pd}_2\text{dba}_3(\text{C}_6\text{H}_6)$  initially mixed with 2.0 equivalents of napy in either  $\text{C}_6\text{H}_6$  or DCM for a total volume of 2 mL solvent, and stirred for 5 minutes before a Pd(II)-source ( $\text{PdCl}_2\text{L}_2$  L = MeCN, PhCN or none) was added in one portion. The vial was sealed with a lid and heated to gentle reflux for 30 minutes, which resulted in the deposition of a Pd-mirror. The mixture was filtered through Celite, the Celite was washed with either  $\text{C}_6\text{H}_6$  or DCM. A small number of orange crystals of  $\text{PdCl}_2\text{PPh}_3(\kappa\text{-N-napy})$  was found, crystal yield < 10%. Crystals suitable for X-ray diffraction were grown from slow evaporation of DCM from a concentrated DCM solution.

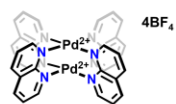
## 2.2 NMR spectra



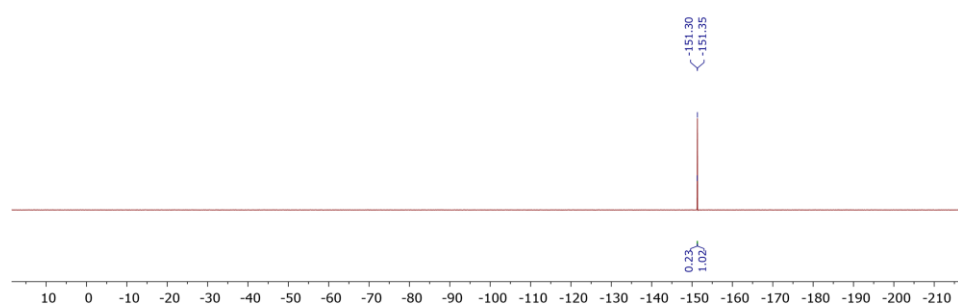
**Supplementary Figure 2.1.** <sup>1</sup>H NMR spectrum of complex **2.1** in CD<sub>3</sub>CN.



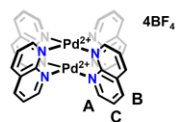
**Supplementary Figure 2.2.** <sup>13</sup>C NMR spectrum of complex **2.1** in CD<sub>3</sub>CN.



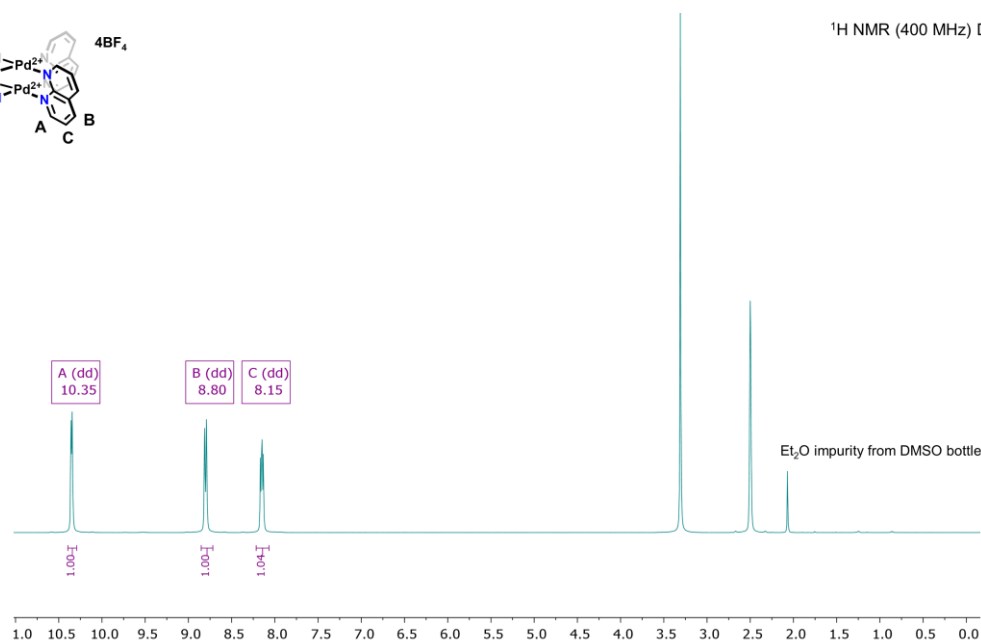
<sup>19</sup>F NMR (377 MHz) CD<sub>3</sub>CN



Supplementary Figure 2.3. <sup>19</sup>F NMR spectrum of complex **2.1** in CD<sub>3</sub>CN

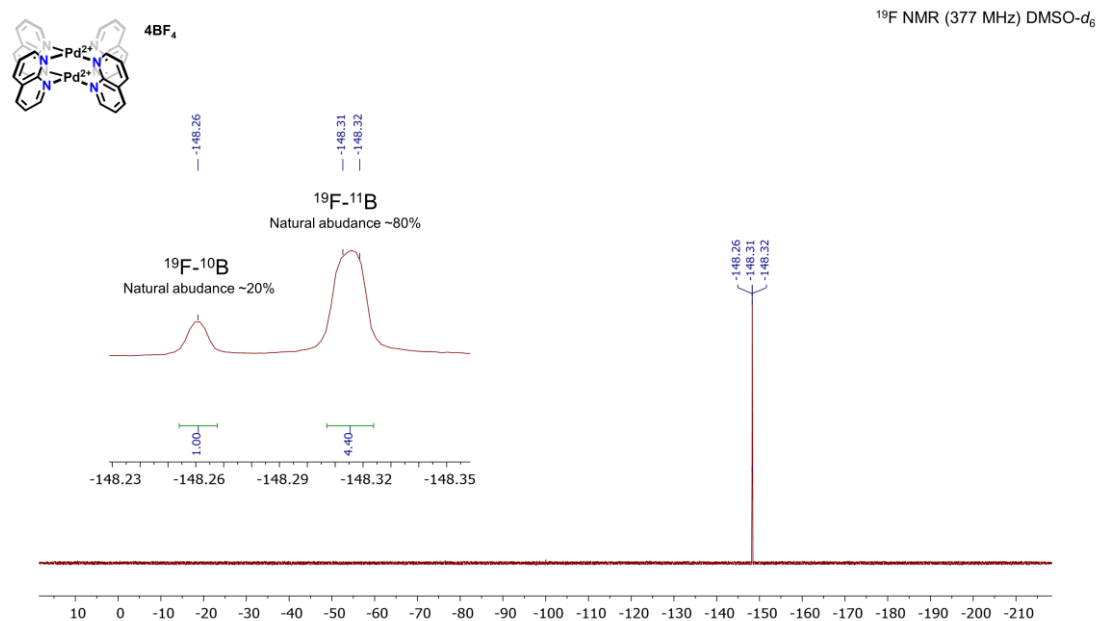


<sup>1</sup>H NMR (400 MHz) DMSO-*d*<sub>6</sub>

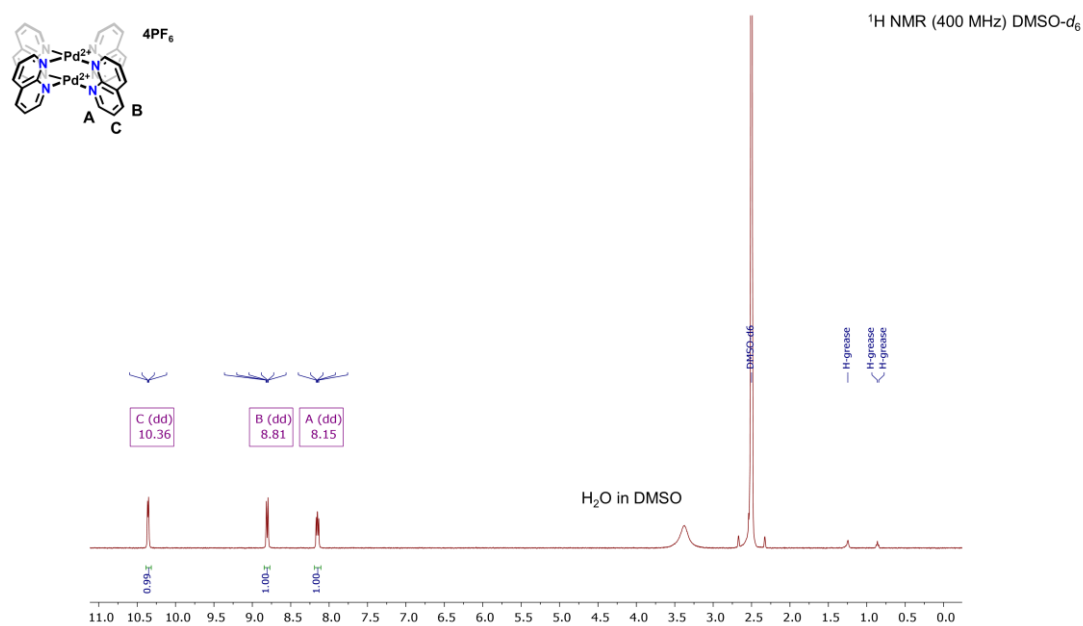


Supplementary Figure 2.4. <sup>1</sup>H NMR spectrum of complex **2.1** in DMSO-*d*<sub>6</sub>.

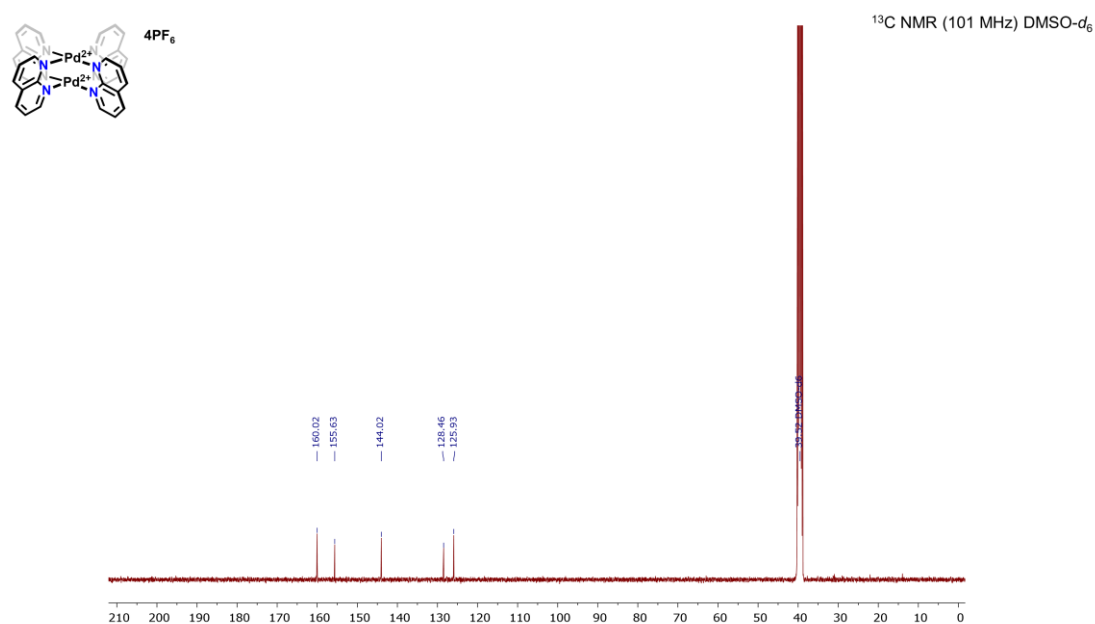




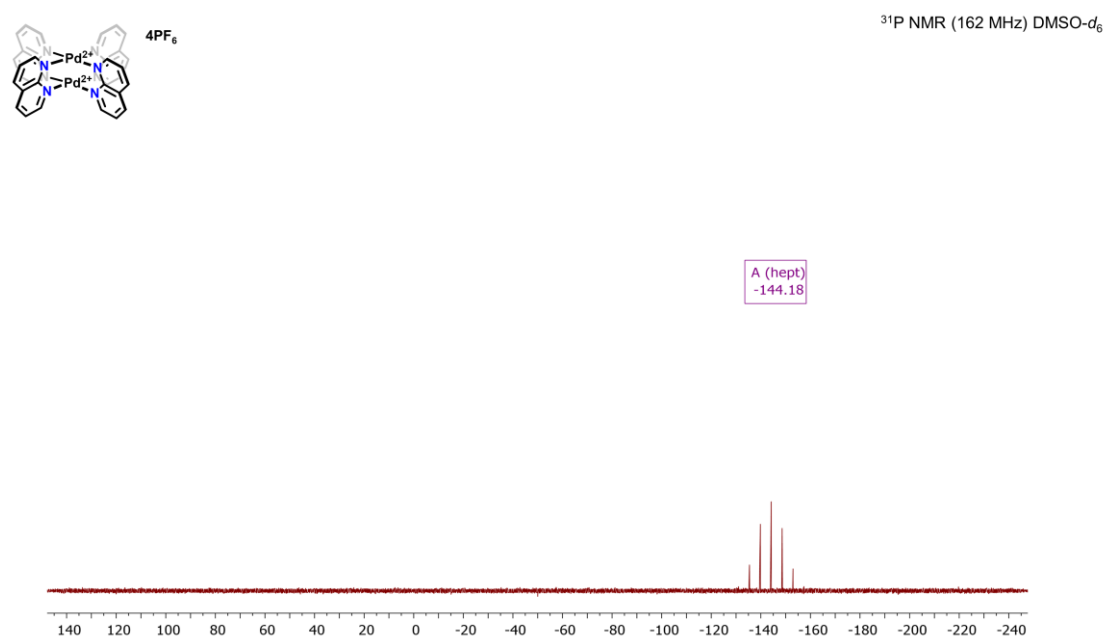
**Supplementary Figure 2.5.** <sup>19</sup>F NMR spectrum of complex **2.1** in DMSO-*d*<sub>6</sub>.



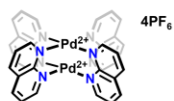
**Supplementary Figure 2.6.** <sup>1</sup>H NMR spectrum of complex **2.2** in DMSO-*d*<sub>6</sub>.



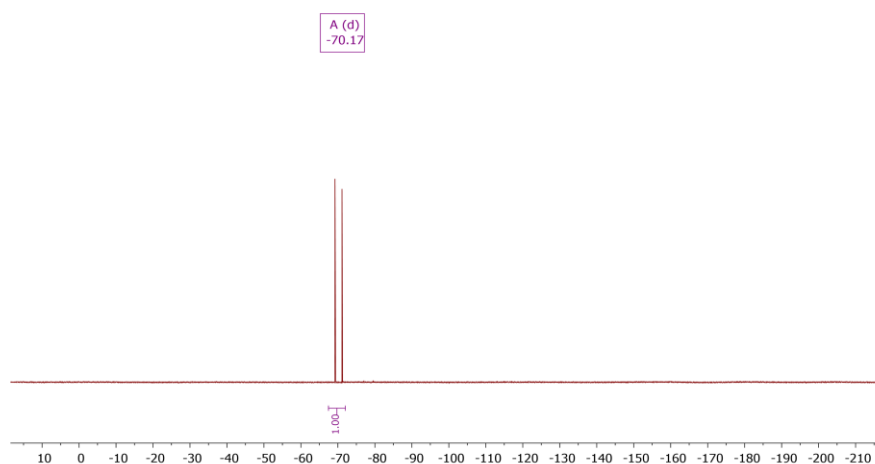
**Supplementary Figure 2.7.** <sup>13</sup>C NMR spectrum of complex **2.2** in DMSO-*d*<sub>6</sub>.



**Supplementary Figure 2.8.** <sup>31</sup>P NMR spectrum of complex **2.2** in DMSO-*d*<sub>6</sub>. <sup>1</sup>*J*(<sup>31</sup>P-<sup>19</sup>F) = 711 Hz.



$^{19}\text{F}$  NMR (377 MHz)  $\text{DMSO}-d_6$



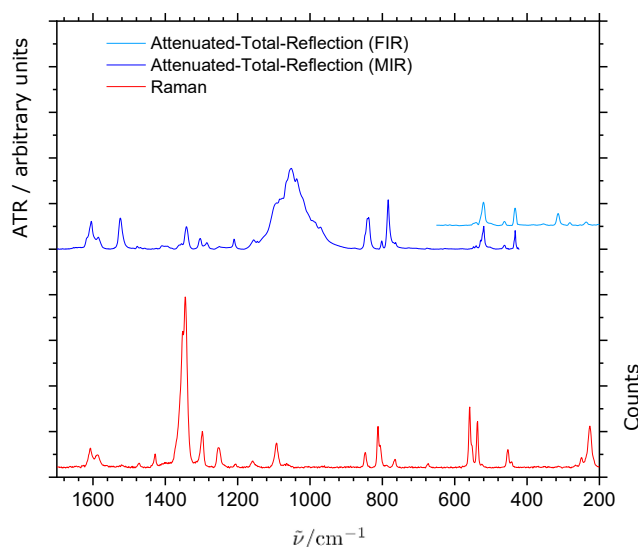
**Supplementary Figure 2.9.**  $^{19}\text{F}$  NMR spectrum of complex **2.2** in  $\text{DMSO}-d_6$ .  $^1J(^{19}\text{F}-^{31}\text{P}) = 711$  Hz.

## 2.3 Computational methods

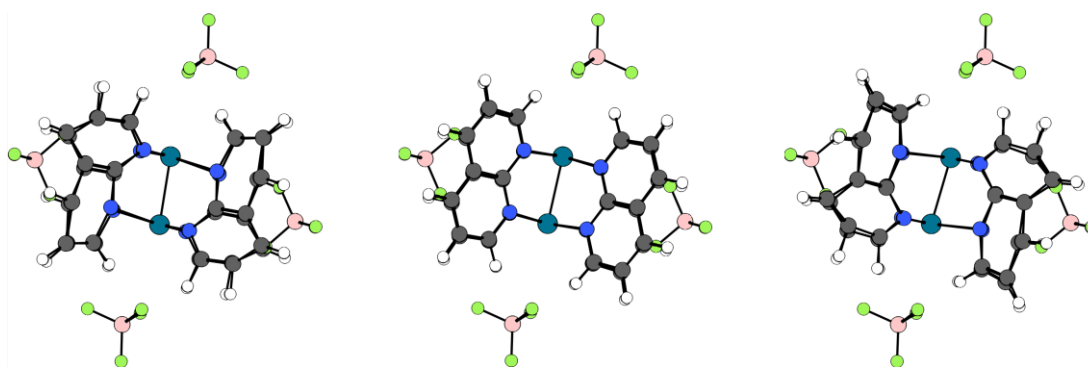
The quantum chemical calculations were performed using the ORCA (5.0)<sup>8</sup> package. Harmonic vibrational frequencies of complex **2.1** molecular unit were calculated using TPSS-D4<sup>9</sup> method with def2-TZVP<sup>10–12</sup> basis set (QZVPP used for Pd). TD-DFT<sup>13</sup> calculations of the excited states transition energies were performed using TPSSh-D4 method with def2-TZVPD (QZVPPD-Pd)<sup>14</sup> basis set on the corresponding minimum geometry of the **2.1**<sup>4+</sup> ionic form of the compound. Solution has been obtained for the first 10 roots.

## 2.4 IR and Raman spectral data

We are still underway in our understanding of the Raman spectrum, hence its absence from the main text.



Supplementary Figure 2.10. Juxtaposed MIR, FIR, and Raman spectra of complex **2.1**.



Supplementary Figure 2.11. Active Raman Pd-N stretching modes.

## 2.5 Crystallographic data

**Supplementary table 2.1.** Crystallographic data for complexes **2.1**, **2.3**, and **2.4**

	<b>2.1</b>	<b>2.3</b>	<b>2.4</b>
Chemical formula	C <sub>44</sub> H <sub>42</sub> B <sub>4</sub> F <sub>16</sub> N <sub>13.5</sub> Pd <sub>2</sub>	C <sub>60</sub> H <sub>56</sub> N <sub>4</sub> Pd <sub>2</sub> S <sub>8</sub>	C <sub>17.99</sub> H <sub>15.32</sub> Cl <sub>2.66</sub> N <sub>1.33</sub> P <sub>0.67</sub> Pd <sub>0.67</sub>
Formula weight	1319.95	1302.36	436.08
Crystal color	Colorless	Slightly yellow	Orange
Crystal system	Triclinic	Triclinic	Triclinic
Space group	P-1	P-1	P-1
<i>a</i> (Å)	11.1375(13)	13.8005(7)	11.2701(4)
<i>b</i> (Å)	11.7457(12)	14.2730(8)	13.4687(8)
<i>c</i> (Å)	12.7482(2)	16.4249(7)	18.8613(10)
$\alpha$ (deg)	76.461(2)	64.481(5)	106.686(5)
$\beta$ (deg)	63.478(10)	72.261(4)	94.923(4)
$\gamma$ (deg)	68.034(10)	83.322(4)	90.772(4)
<i>V</i> (Å <sup>3</sup> )	1297.8(3)	2780.4(3)	2730.2(2)
<i>Z</i>	1	2	6
$\mu$ (mm <sup>-1</sup> )	6.538	8.364	9.782
<i>T</i> (K)	119.99(15)	120.15	119.99(16)
GOF ( <i>S</i> )	1.040	1.179	1.114
<i>R</i> <sup>a</sup> ( <i>wR</i> <sup>b</sup> ) [ <i>I</i> > 2σ( <i>I</i> )]	<i>R</i> <sub>1</sub> = 0.0332 <i>wR</i> <sub>2</sub> = 0.0766	<i>R</i> <sub>1</sub> = 0.0344, <i>wR</i> <sub>2</sub> = 0.0856	<i>R</i> <sub>1</sub> = 0.0434, <i>wR</i> <sub>2</sub> = 0.0977
<i>R</i> <sup>a</sup> ( <i>wR</i> <sup>b</sup> ) [all data]	<i>R</i> <sub>1</sub> = 0.0451, <i>wR</i> <sub>2</sub> = 0.0852	<i>R</i> <sub>1</sub> = 0.0433, <i>wR</i> <sub>2</sub> = 0.0893	<i>R</i> <sub>1</sub> = 0.0593, <i>wR</i> <sub>2</sub> = 0.1134
2θ range for data collection (deg)	8.12 to 133.198	7.08 to 153.244	7.188 to 133.192
Reflections	13444	22682	24381
Radiation type	CuKα (λ = 1.54184)		

$$^a R I = \sum [w(F_o - F_c)] / \sum [wF_o]; ^b wR2 = \left[ \sum [w(F_o^2 - F_c^2)^2] / \sum [w(F_o^2)^2] \right]^{\frac{1}{2}}, w = 1 / [\sigma^2(F_o^2) + (aP)^2 + bP], \text{ where } P = [\max(F_o^2, 0) + 2(F_c^2)] / 3$$

### 3 Chapter 3

#### 3.1 Synthetic methods

**1,1'-bisimidazole methane.** *Adapted from literature*<sup>15</sup>, *in air*. Imidazole (15 g, 220.3 mmol, 1.0 equiv.) and <sup>n</sup>Bu<sub>4</sub>NBr (500 mg, 1.6 mmol, 0.7 mol%) were added to a 500 mL round-bottom flask equipped with a stir bar. KOH (27.2g, 484.7 mmol, 2.2 equiv.), crushed using a pestle and mortar, was added in small portions under vigorous stirring, and the mixture was stirred for 15 – 20 minutes until a liquid without any KOH chunks was obtained. DCM (350 mL) was then added, the flask was equipped with a reflux condenser, and the mixture was brought to gentle reflux overnight. The mixture was filtered while warm over Celite, and the (off)white precipitate was washed with warm DMC (2 x 100 mL). The combined organic fraction was dried over MgSO<sub>4</sub>, concentrated *in vacuo* to ~ 20 mL before adding Et<sub>2</sub>O until precipitation. The precipitate was filtered on a glass-frit (M-coarseness), washed with small amounts of cold (0°C) acetone until the filtrate was colorless, and then dried on the frit in air, yielding a white powder of the title compound (14.9 g, 91% yield). <sup>1</sup>H NMR (400 MHz, DMSO-*d*<sub>6</sub>) δ 7.94 (s, 1H), 7.40 (d, *J* = 1.3 Hz, 1H), 6.92 (d, *J* = 1.3 Hz, 1H), 6.23 (s, 1H). <sup>13</sup>C NMR (101 MHz, DMSO-*d*<sub>6</sub>) δ 137.25, 129.11, 119.05, 54.78.

**1,2-bisimidazole ethane.** *Adapted from literature*<sup>16</sup>. Dry imidazole (14 g, 205.6 mmol, 1.0 equiv.), and <sup>n</sup>Bu<sub>4</sub>NBr (1.7 g, 6.2 mmol, 0.3 equiv.) were added to a 50 mL two-neck round-bottom flask equipped with a stir bar. KOH (13.9 g, 247 mmol, 1.2 equiv.), crushed using a pestle and mortar, was added in small portions under vigorous stirring, and the mixture stirred for upwards of an hour until a liquid without any KOH chunks was obtained. The flask was then equipped with a reflux-condenser, added 1,2-DCE (1,2-dichloroethane) (8.2 mL, 0.5 equiv.), and the small opening fitted a glass-stopper. The mixture was heated to 55°C and stirred at the lowest setting overnight. The next day, an

additional 0.5 equiv. of crushed KOH was portion-wise added, the mixture stirred for another hour before 0.25 equiv. of 1,2-DCE was added, and the mixture stirred for an additional 48 hours at 55°C. The mixture was cooled to rt, added 50 mL EtOH, and transferred to a separatory funnel. The mixture was extracted with additional EtOH (2 x 20 mL), and the solvent was removed from the combined organic phase, leaving a sticky orange oil. Acetone was portion-wise added to the oil, (3 x 100 mL), swirled, and the liquid decanted. The combined acetone fraction was concentrated to ~10 mL, added enough Et<sub>2</sub>O until precipitation of an off-white powder started before the flask was placed at 5°C for 30 minutes. The precipitate was collected on a glass-frit (M-coarseness), washed with small amounts of cold (0°C) acetone until the filtrate was colorless, and then dried on the frit in air, yielding an off-white powder of the title compound (4 g, 24% yield). <sup>1</sup>H NMR (400 MHz, DMSO-*d*<sub>6</sub>) δ 7.36 (s, 1H), 6.99 (d, *J* = 1.3 Hz, 1H), 6.86 (d, *J* = 1.3 Hz, 1H), 4.32 (s, 2H). <sup>13</sup>C NMR (101 MHz, DMSO-*d*<sub>6</sub>) δ 137.32, 128.49, 119.12, 46.63. Variations to this procedure include the use of 1,2-bis(triflato) and bistosylato ethane instead of 1,2-DCE, resulting in an even lower yield.

**1,8-bis(hydroxymethyl)naphthalene.** *Adapted from literature*<sup>17</sup>. LiAlH<sub>4</sub> (25 g, 95 w/w%, 626 mmol, 1.55 equiv.) was added to a flame-dried 2L three-neck round-bottom flask fitted with a stir bar and a thermometer under a stream of N<sub>2</sub>. The flask was submerged into an ice bath, added 1.2L of dry THF, and stirred until the mixture was around 0°C. 1,8-naphthalic anhydride (80 g, 404 mmol, 1.0 equiv.) was portion-wise added at a rate that did not cause the reaction mixture to exceed a temperature of 40°C. The ice bath was replaced with an oil bath, the flask fitted a reflux condenser, and the mixture was brought to gentle reflux for 36 hours. The oil bath was replaced with an ice bath, and the mixture added, *with caution*, dropwise ice-chilled EtOAc and ice-cubes until bubbling subsided. The reaction mixture was transferred to a 1L glass beaker (1/3 of the

volume at a time), added enough 6M HCl was added until all the formed aluminium hydroxides were quenched and dissolved, and the mixture was transferred to a separatory funnel. The combined aqueous fraction was added NaCl (20g) and extracted with THF (2 x 100 mL). The combined organic fractions were dried over MgSO<sub>4</sub>, solvent removed *in vacuo*, and the solid was recrystallized in EtOAc yielding an off-white powder of the title compound (60.4g, 79% yield). <sup>1</sup>H NMR (400 MHz, DMSO-*d*<sub>6</sub>) δ 7.86 (dd, *J* = 8.1, 1.4 Hz, 1H), 7.63 (dd, *J* = 7.0, 1.4 Hz, 1H), 7.46 (dd, *J* = 8.1, 7.0 Hz, 1H), 5.28 (t, *J* = 5.4 Hz, 1H), 5.09 (d, *J* = 5.4 Hz, 2H). <sup>13</sup>C NMR (101 MHz, DMSO-*d*<sub>6</sub>) δ 138.51, 135.07, 130.04, 129.01, 128.09, 124.90, 63.66.

**1,8-bis(bromomethyl)naphthalene.** Commercially available *via* Sigma. A 250 mL flame-dried Schlenk-flask equipped with a stir bar was added 1,8-bis(hydroxymethyl)naphthalene (30g, 160 mmol, 1.0 equiv.) and subjected to vacuum for 45 minutes before being backfilled with N<sub>2</sub>, and added dried glyme (or dioxane, 160 mL, 1M). The suspension was submerged into an ice bath before PBr<sub>3</sub> (19 mL, 200 mmol, 1.25 equiv.) slowly was added under vigorous stirring. The ice bath was removed, and the mixture was stirred for at least 2 hours. The mixture was poured into ice water (400 mL), stirred for 20 minutes, and the precipitate was collected on a glass-frit (M-coarseness), which was washed with MeOH until the filtrate was colorless, and the powder was dried on the frit in air, yielding a light-sensitive white powder of the title compound (46.9g, 94% yield). Upon extended exposure to light, the powder was recrystallized in minimum amounts of benzene. <sup>1</sup>H NMR (400 MHz, CDCl<sub>3</sub>) δ 7.78 (dd, *J* = 8.1, 1.4 Hz, 1H), 7.52 (dd, *J* = 7.1, 1.4 Hz, 1H), 7.35 (t, *J* = 8.1, 7.1 Hz, 1H), 5.20 (s, 2H). <sup>13</sup>C NMR (101 MHz, CDCl<sub>3</sub>) δ 136.25, 133.55, 133.19, 132.07, 129.16, 125.85, 37.34. Spectral data consistent with Sigma's product.



Compound **3.1**, Methylene-linked naphthalene-macrocycle, <sup>Me,Naph</sup>LH<sub>4</sub>-4Br. A 500 mL Schlenk-flask equipped with a stir bar was added 1,1'-bisimidazole methane (7.98 g, 53.9 mmol, 1.0 equiv.), *n*Bu<sub>4</sub>NBr (69.5 g, 215.5 mmol, 4.0 equiv.), and DMF (270 mL, 200 mM w.r.t bisimidazole) before being subjected to degassing for at least an hour. 1,8-bis(bromomethyl)naphthalene (25 g, 53.9 mmol, 1.0 equiv.) was added portion-wise, the mixture was then further degassed for 20 minutes, brought under a slight vacuum, and heated to 110°C for 48 hours under stirring. The reaction mixture was reduced to 1/3 of the original volume of DMF *in-vacuo*, cooled to rt, added 2 times the volume of acetone, and the precipitate collected on an M-coarseness glass-frit. The precipitate was recrystallized in MeOH yielding a white powder of the desired compound in about 10 – 15% yield. Crystals suitable for single-crystal X-ray diffraction were grown from slow solvent evaporation from a concentrated MeOH solution. The powder is somewhat hygroscopic. <sup>1</sup>H NMR (400 MHz, DMSO-*d*<sub>6</sub>) δ 9.69 (s, 2H), 8.17 (d, *J* = 8.2 Hz, 2H), 8.11 (d, *J* = 1.7 Hz, 2H), 7.72 (t, *J* = 1.7 Hz, 2H), 7.64 (t, *J* = 8.2, 7.3 Hz, 2H), 7.43 (d, *J* = 7.3 Hz, 2H), 6.74 (s, 2H), 6.03 (s, 4H). <sup>13</sup>C NMR (101 MHz, DMSO-*d*<sub>6</sub>) δ 138.25, 135.43, 131.39, 130.40, 129.52, 128.82, 125.89, 123.26, 122.93, 59.01, 53.15. **Elemental analysis** calcd (%) for C<sub>38</sub>H<sub>40</sub>Br<sub>4</sub>N<sub>8</sub>O<sub>2</sub>: C 47.52, H 4.20, N 11.67; found: C 47.39, H 4.10, N 11.32. HRMS (ESP+) *m/z* calc. [C<sub>38</sub>H<sub>36</sub>Br<sub>3</sub>N<sub>8</sub>]<sup>+</sup> [M-Br]<sup>+</sup>: 843.058, found: 843.064.

Compound **3.4**, Ethylene-linked naphthalene-macrocycle, <sup>Et,Naph</sup>LH<sub>4</sub>-4Br. A 500 mL flame-dried Schlenk-flask equipped with a stir bar was added 1,2-bisimidazoleethane (10.4, 63.7 mmol, 1.0 equiv.) and 1,8-bis(bromomethyl)naphthalene (20 g, 63.7 mmol, 1.0 equiv.), subjected to vacuum for at least 30 minutes before being backfilled with N<sub>2</sub>, added 320 mL of SPS-quality DMF before the mixture was stirred until everything was dissolved, and then heated to 100°C under a slight vacuum for 48 hours. The reaction mixture was reduced to 1/3 of the original volume of DMF *in-vacuo*, cooled to rt, added

2 times the volume of acetone, and the precipitate collected on an M-coarseness glass-frit. The precipitate was recrystallized in small amounts of MeOH, yielding a white powder of the target compound in about 3 - 10% yield. Crystals suitable for single-crystal X-ray diffraction were grown from slow solvent evaporation from a concentrated MeOH solution. The powder is hygroscopic.  $^1\text{H}$  NMR (400 MHz, DMSO- $d_6$ )  $\delta$  9.34 (s, 2H), 8.06 (d,  $J$  = 8.0 Hz, 2H), 7.97 (t,  $J$  = 1.7 Hz, 2H), 7.76 (t,  $J$  = 1.7 Hz, 2H), 7.54 (t,  $J$  = 8.0, 7.2 Hz, 2H), 6.99 (d,  $J$  = 7.2 Hz, 2H), 6.44 (s, 4H), 4.89 (s, 4H).  $^{13}\text{C}$  NMR (101 MHz, DMSO- $d_6$ )  $\delta$  137.16, 135.21, 130.87, 130.38, 128.71, 126.59, 125.71, 123.88, 123.40, 53.53, 48.80. **Elemental analysis** calcd (%) for  $\text{C}_{40}\text{H}_{56}\text{Br}_4\text{N}_8\text{O}_8$ : C 43.81, H 5.15, N 10.22; found: C 43.69, H 4.89, N 10.09. HRMS (ESP+)  $m/z$  calc.  $[\text{C}_{40}\text{H}_{40}\text{Br}_3\text{N}_8]^+$   $[\text{M}-\text{Br}]^+$ : 873.088, found: 873.097.

**General procedure for salt metathesis.** *In air.* Compound **3.1** or **3.4** (1.0 equiv.) was dissolved in deionized water (10 mM), before a Na/K-salt (4.05 equiv.) of the desired counterion, *e.g.*  $\text{KPF}_6$ ,  $\text{NaOTf}$ , was added to the solution, and the mixture was heated to 80°C overnight under stirring. The suspension was cooled to rt, the solid collected on a glass-frit (M-coarseness), which was washed with  $\text{H}_2\text{O}$ , MeOH, and finally  $\text{Et}_2\text{O}$  before the powder was left to dry in the air on the frit for at least 2 hours. The resulting white powder was redissolved in MeCN, passed through the filter, and MeCN was removed *in vacuo* leaving behind the desired compound as a white solid in nearly quantitative yield (95 – >99%).

Compound **3.2**,  $\text{Me,NaphLH}_4\text{-4PF}_6$ .  $^1\text{H}$  NMR (400 MHz, DMSO- $d_6$ )  $\delta$  9.15 (s, 2H), 8.19 (d,  $J$  = 8.6 Hz, 2H), 8.14 (s, 2H), 7.85 (s, 2H), 7.64 (t,  $J$  = 7.7 Hz, 2H), 7.31 (d,  $J$  = 7.4 Hz, 2H), 6.61 (s, 5H), 5.94 (s, 4H).

Compound **3.3**, <sup>Me,Naph</sup>**LH4-4OTf**. <sup>1</sup>H NMR (400 MHz, DMSO-*d*<sub>6</sub>) δ 9.06 (s, 2H), 8.20 (d, *J* = 8.2 Hz, 2H), 8.16 (t, *J* = 1.8 Hz, 2H), 7.88 (t, *J* = 1.8 Hz, 2H), 7.64 (t, *J* = 8.2, 7.3 Hz, 2H), 7.30 (d, *J* = 7.3 Hz, 2H), 6.60 (s, 2H), 5.93 (s, 4H).

Compound **3.5**, <sup>Et,Naph</sup>**LH4-4PF<sub>6</sub>**. <sup>1</sup>H NMR (400 MHz, DMSO-*d*<sub>6</sub>) δ 8.92 (s, 2H), 8.10 (d, *J* = 8.1 Hz, 2H), 7.94 (t, *J* = 1.8 Hz, 2H), 7.76 (s, 2H), 7.56 (t, *J* = 8.1, 7.3 Hz, 2H), 6.97 (d, *J* = 7.3 Hz, 2H), 5.96 (s, 4H), 4.82 (s, 4H). <sup>13</sup>C NMR (101 MHz, DMSO) δ 137.24, 135.27, 130.79, 130.32, 128.96, 127.26, 125.83, 124.01, 123.44, 52.65, 48.82.

**1,8-dichloroanthracene**. *Spectral data consistent with literature*<sup>18</sup>, *in air*. A 1.5L Erlenmeyer flask equipped with a stir bar was added 1,8-dichloroanthraquinone (20 g, 72 mmol, 1.0 equiv.) and MeOH (750 mL) before NaBH<sub>4</sub> (13.6 g, 359 mmol, 5.0 equiv.) portion-wise was added (slowly), and the mixture stirred for 4 hours at 30°C. 15 mL 12M HCl was added to the mixture, which then stirred for an additional hour, before the yellow precipitate (4,5-dichloro-9-anthrone) was collected, washed with sat. NaHCO<sub>3</sub>, and dried on a glass-frit (F-coarseness). The yellow solid was transferred to a 750 mL round-bottom flask, suspended in *i*PrOH (500 mL), and added additional NaBH<sub>4</sub> (13.6 g, 359 mmol, 5.0 equiv.). The flask was equipped with a reflux condenser before the mixture was brought to gentle reflux and stirred for a minimum of 3 hours. The mixture was then carefully added 15 mL 12M HCl and continued to stir under reflux for an hour. The mixture was cooled to room temperature, diluted with 100 mL H<sub>2</sub>O, causing precipitation of the title compound as bright yellow needles, which were collected on a glass-frit (M-coarseness), washed extensively with sat. NaHCO<sub>3</sub> and H<sub>2</sub>O, and then dried on the frit in air. (15.2g, 86%). Optionally, the crude was recrystallized by dissolving in minimum of refluxing *i*PrOH, added a drop of 12M HCl, and cooled to 5°C overnight. <sup>1</sup>H NMR (400 MHz, CDCl<sub>3</sub>) δ 9.25 (d, *J* = 1.1 Hz, 1H), 8.46 (s, 1H), 7.94 (d, *J* = 8.5 Hz, 2H), 7.63 (dd, *J* = 7.2, 1.1 Hz, 2H), 7.41 (dd, *J* = 8.5, 7.2 Hz, 2H).

**Anthracene-1,8-dicarbonitrile.** *As in literature*<sup>18</sup>. 1,8-dichloroanthracene (15g, 60.8mmol, 1.0 equiv.) and CuCN (23.7g, 265 mmol, 4.36 equiv.) was added to a 250 mL flame-dried Schlenk-flask and subjected to vacuum for at least 45 minutes. The flask was backfilled with N<sub>2</sub> and added dry *N*-methylpyrrolidinone (180 mL), the flask was brought under a slight vacuum, and heated to gentle reflux overnight. After 18 hours, another 23.7g CuCN was added, the mixture was heated for an additional 48 hours. The mixture was poured directly into ice water (360 mL), added 25% ammonium hydroxide, and stirred at room temperature for 96 hours. The resulting brown precipitate was collected on a glass-frit (M-coarseness) sequentially washed with water, diluted NH<sub>3</sub>, 0.6 M NaCN until the NH<sub>3</sub>-filtrate was colorless, and dried in air. The precipitate was dissolved in small amounts of boiling DMF, filtered hot, and placed at 5°C overnight, yielding the title compound as golden needles. (8.87g, 64%). <sup>1</sup>H NMR (400 MHz, CDCl<sub>3</sub>) δ 9.16 (s, 1H), 8.64 (s, 1H), 8.30 (d, *J* = 8.6 Hz, 2H), 8.07 (dd, *J* = 7.0, Hz, 2H), 7.62 (dd, *J* = 8.6, 7.0 Hz, 2H). <sup>13</sup>C NMR (101 MHz, CDCl<sub>3</sub>) δ 134.95, 133.75, 131.38, 130.55, 129.36, 125.41, 122.38, 117.32, 111.22, 100.13.

**Anthracene-1,8-dicarboxylic acid.** *As in literature*<sup>18</sup>. Anthracene-1,8-dicarbonitrile (5g, 21.9 mmol, 1.0 equiv.) and KOH (63g, 1.1 mmol, 63.0 equiv.) in a 250 mL round-bottom flask was suspended in ethylene glycol (135 mL), and under vigorous stirring heated to 150°C for around 30 hours. The mixture was allowed to cool to around 50°C before it was filtered through Celite, which was washed with warm 0.1M KOH (2 x 30 mL). The filtrate was added 0.1 M HCl until a yellow precipitate was formed, which was collected and recrystallized in EtOH leaving bright yellow crystals of the title compound (3.26g, 56%). <sup>1</sup>H NMR (400 MHz, DMSO-*d*<sub>6</sub>) δ 13.20 (s, 2H), 10.47 (s, 1H), 8.78 (s, 1H), 8.34 (d, *J* = 8.5 Hz, 2H), 8.19 (dd, *J* = 7.0, 1.1 Hz, 2H), 7.63 (dd, *J* = 8.4, 7.0 Hz, 2H). <sup>13</sup>C

NMR (101 MHz, DMSO- $d_6$ )  $\delta$  168.61, 132.99, 131.14, 130.45, 128.82, 128.64, 127.89, 124.83, 123.59.

**1,8-bis(hydroxymethyl)anthracene.** Adapted from literature<sup>19</sup>. Anthracene-1,8-dicarboxylic acid (4g, 15 mmol, 1.0 equiv.) was added to flame-dried Schlenk-flask equipped with a stir bar, then subjected to a vacuum for at least 45 minutes before being backfilled with N<sub>2</sub>, which was repeated two times more. The solid was suspended in THF 60 mL and frozen in liquid N<sub>2</sub>. LiAlH<sub>4</sub> (30 mL, 2M in THF) was dropwise added to the mixture (now-thawing), which stirred for an additional 2 hours, slowly coming to room temperature. Ice cubes were *cautiously and slowly* added to the flask until bubbling subsided. The mixture was transferred to a large beaker (500 mL) and added 3M HCl until all the aluminium hydroxides were neutralized and dissolved, leaving a yellow powder of the title compound, which was collected on a glass-frit (M-coarseness) and extensively washed with sat. NaHCO<sub>3</sub>, H<sub>2</sub>O, and finally dried in the air on the frit (2.65g, 74%). <sup>1</sup>H NMR (400 MHz, DMSO- $d_6$ )  $\delta$  8.75 (s, 1H), 8.59 (s, 1H), 7.98 (d,  $J$  = 8.4 Hz, 2H), 7.57 (d,  $J$  = 7.0 Hz, 2H), 7.49 (t,  $J$  = 8.4, 7.0, 2H), 5.40 (t,  $J$  = 5.4 Hz, 2H), 5.13 (d,  $J$  = 5.4 Hz, 4H). <sup>13</sup>C NMR (101 MHz, DMSO- $d_6$ )  $\delta$  138.02, 131.07, 128.77, 127.31, 127.13, 125.11, 123.35, 117.84, 61.29.

**1,8-bis(bromomethyl)anthracene.** As in literature<sup>19</sup>. Preparation is analogous to that of the naphthalene-analogue, crude yield (95%) obtained from 4g of starting material, and was used without further purification. <sup>1</sup>H NMR (400 MHz, DMSO- $d_6$ )  $\delta$  9.01 (s, 1H), 8.74 (s, 1H), 8.15 (d,  $J$  = 8.5 Hz, 2H), 7.79 (d,  $J$  = 6.8, Hz, 2H), 7.51 (dd,  $J$  = 8.5, 6.8 Hz, 2H), 5.40 (s, 4H).

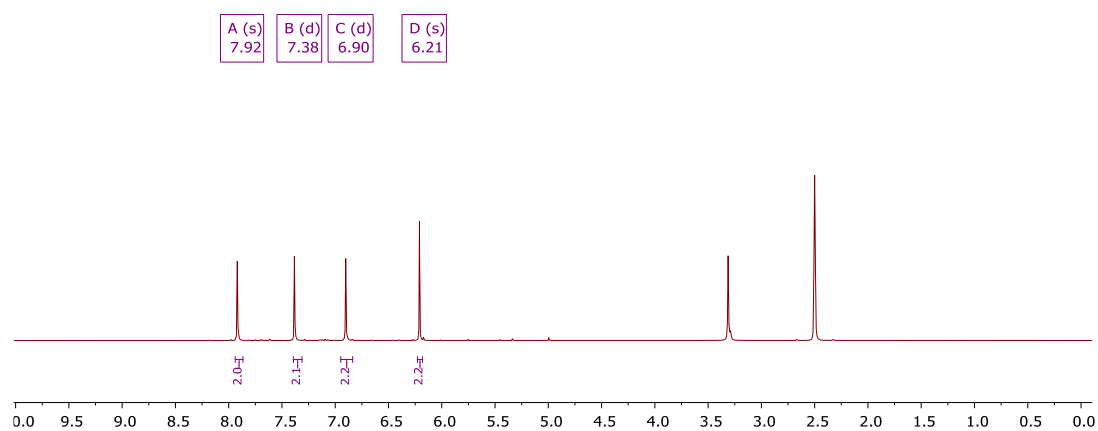
Compound **3.6**, Methylene-linked anthracene-macrocycle, <sup>Me,Anth</sup>LH<sub>4</sub>-4PF<sub>6</sub>. Preparation follows analogous to the naphthalene-congener. After 48 hours, all of the DMF is

removed at elevated temperature, and an equal volume of MeCN is added alongside 8.1 equiv. of Na(K)PF<sub>6</sub>, and the mixture refluxed o.n. The mixture is filtered hot, the filtrate reduced to ~10mL, spread evenly amongst five 5 mL vials, placed inside which are placed inside a scintillation vial filled with Et<sub>2</sub>O, and left for slow vapor diffusion at RT o.n. The powder was then collected on a glass-fiber filter inserted into a Pasteur pipette, washed with small amounts of cold THF, redissolved in MeCN, passed through the filter, and MeCN removed in vacuo, leaving the title compound in ~5% yield (45mg) from 500 mg of 1,8-bis(bromomethyl)anthracene).

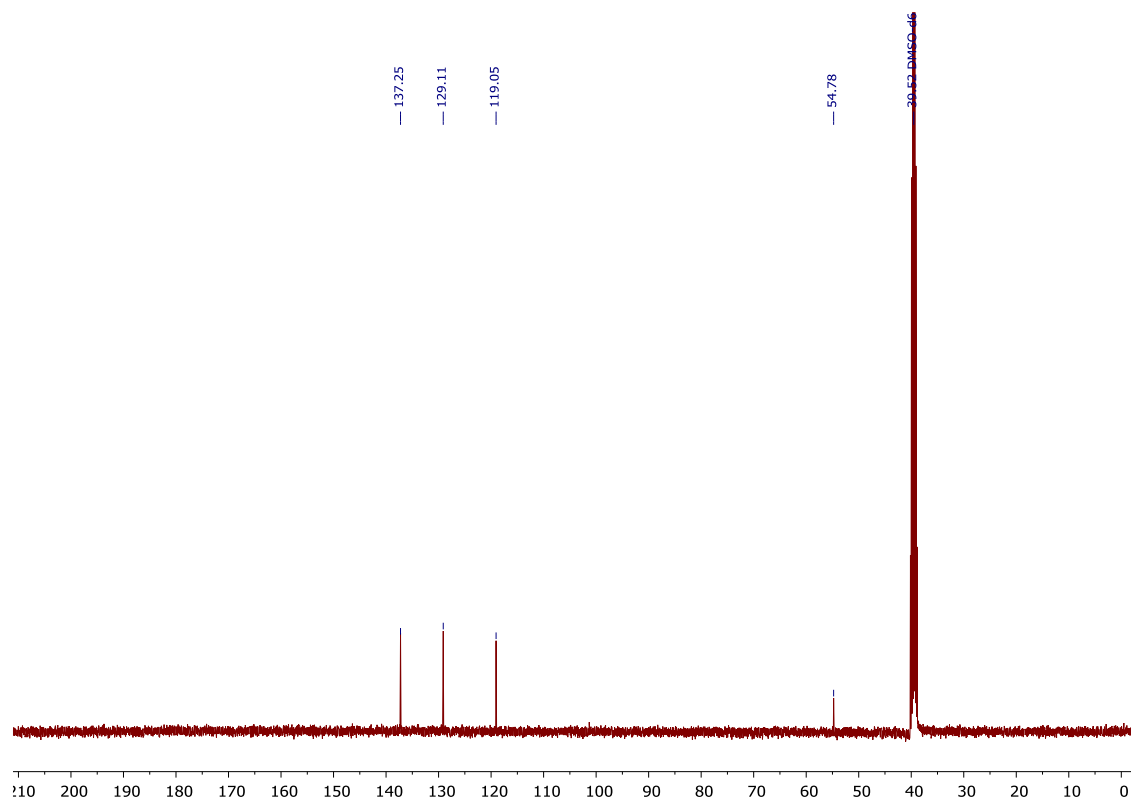
<sup>1</sup>H NMR (400 MHz, DMSO-*d*<sub>6</sub>) δ 9.65 (s, 2H), 8.86 (s, 1H), 8.74 (s, 1H), 8.26 (d, *J* = 8.5 Hz, 2H), 8.19 (d, *J* = 1.8 Hz, 2H), 7.98 (t, *J* = 1.8 Hz, 2H), 7.72 (d, *J* = 6.8 Hz, 2H), 7.65 (dd, *J* = 8.5, 6.8 Hz, 2H), 6.69 (s, 2H), 6.25 (s, 4H). <sup>13</sup>C NMR (101 MHz, DMSO-*d*<sub>6</sub>) δ 137.73, 131.51, 130.30, 129.61, 129.32, 129.07, 125.63, 123.62, 122.25, 58.20, 50.69. <sup>19</sup>F NMR (377 MHz, DMSO-*d*<sub>6</sub>) δ -70.16 (d, *J* = 711.4 Hz). <sup>31</sup>P NMR (162 MHz, DMSO-*d*<sub>6</sub>) δ -144.22 (hept, *J* = 711.4 Hz).

## 3.2 NMR spectra

### 3.2.1 1,1'-bisimidazole methane

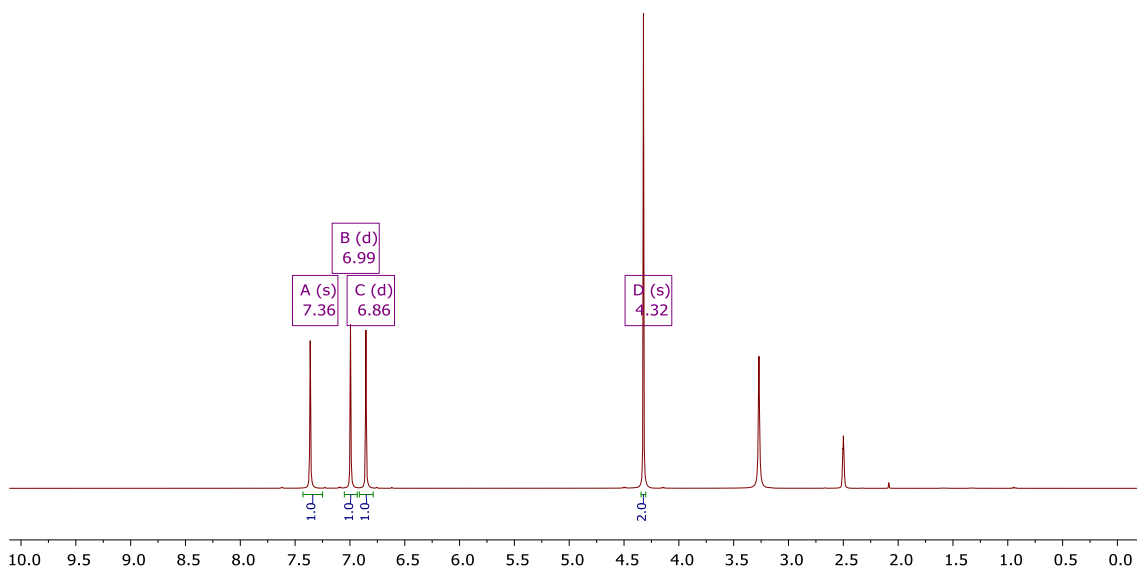


Supplementary Figure 3.1.  $^1\text{H}$ -NMR of 1,1'-bisimidazole methane in  $\text{DMSO-}d_6$ .

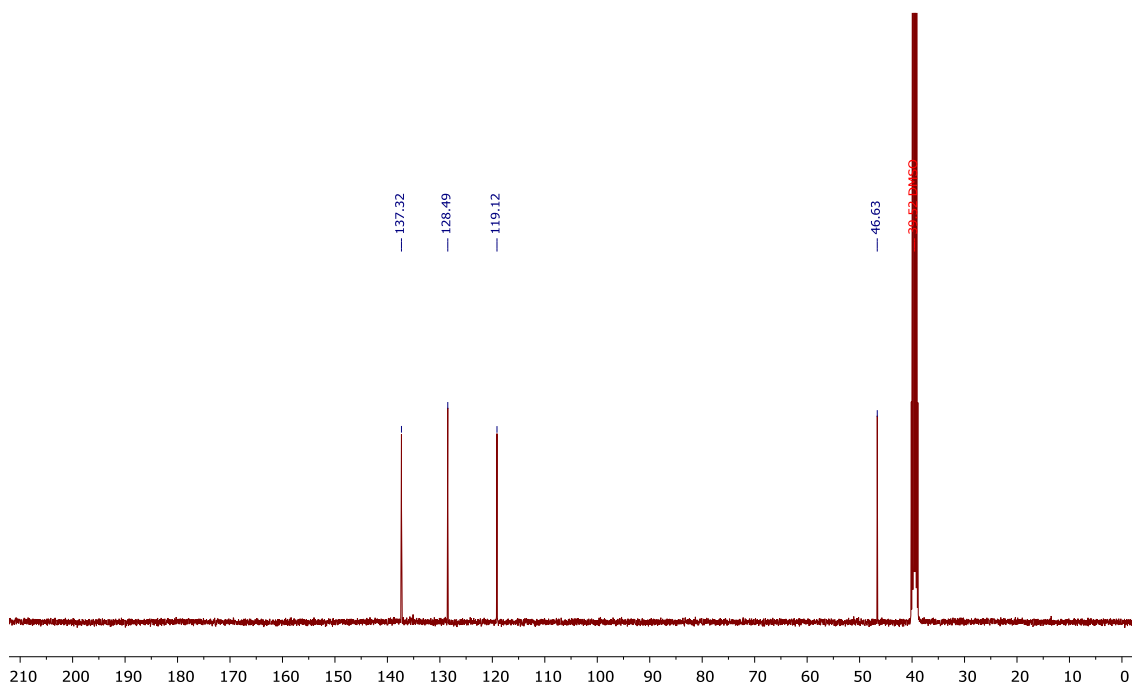


Supplementary Figure 3.2.  $^{13}\text{C}$ -NMR of 1,1'-bisimidazole methane in  $\text{DMSO-}d_6$ .

### 3.2.2 1,2-bisimidazole ethane



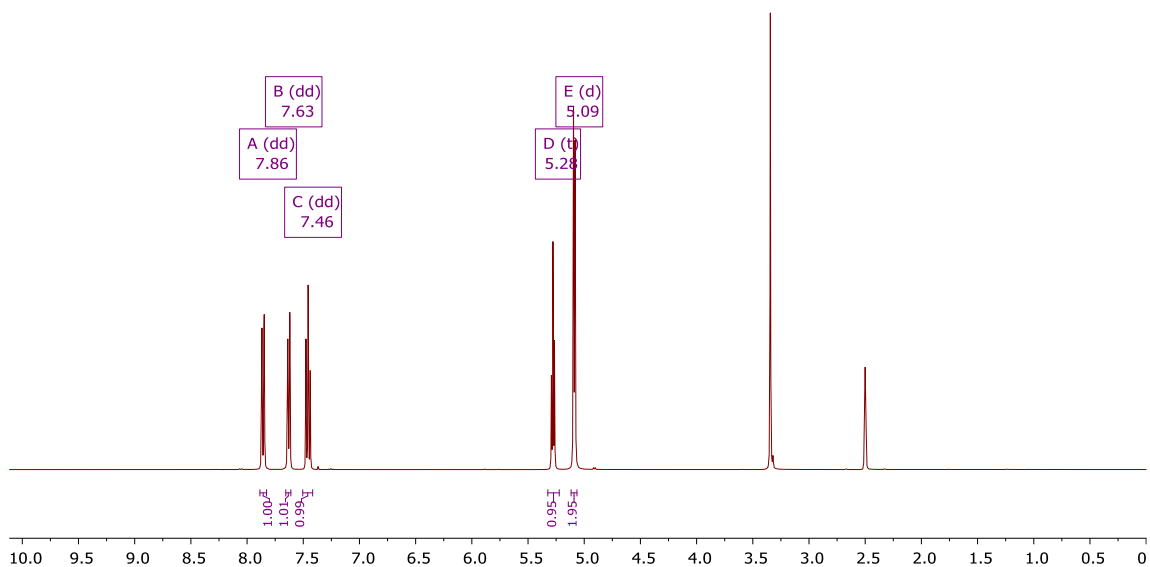
**Supplementary Figure 3.3.** <sup>1</sup>H-NMR of 1,2-bisimidazole ethane in DMSO-*d*<sub>6</sub>.



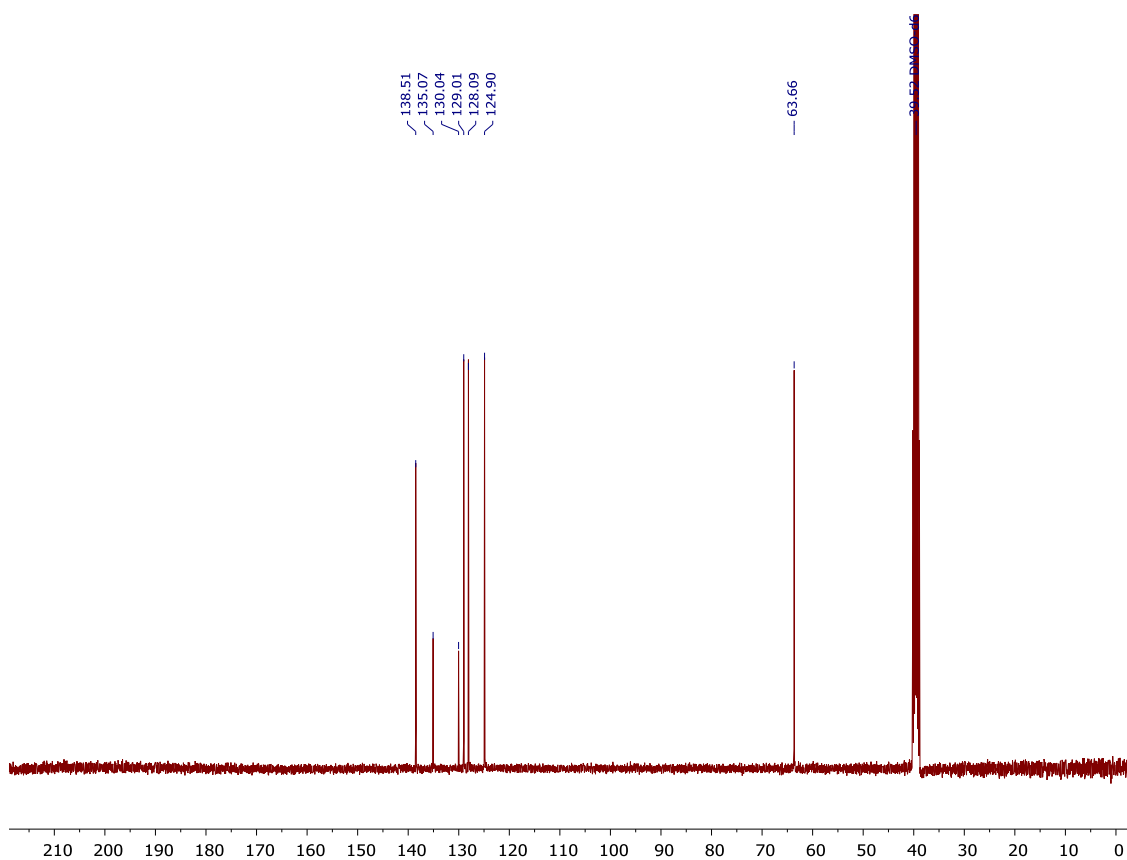
**Supplementary Figure 3.4.** <sup>13</sup>C-NMR of 1,2-bisimidazole ethane in DMSO-*d*<sub>6</sub>.



### 3.2.3 1,8-bis(hydroxymethyl)naphthalene

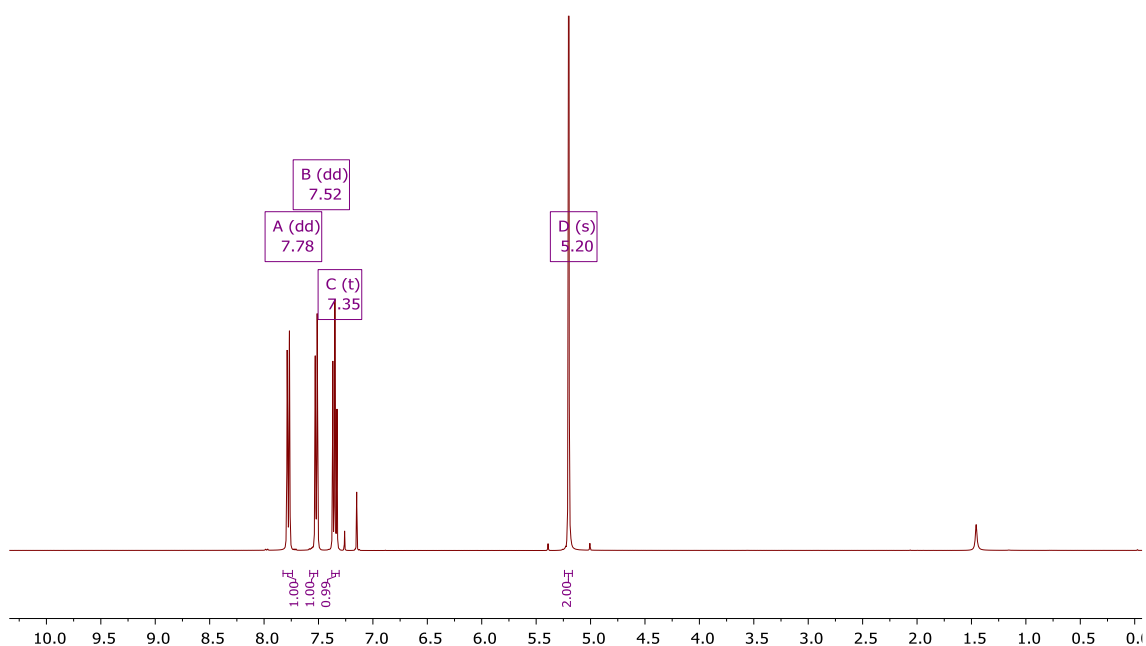


**Supplementary Figure 3.5.** <sup>1</sup>H-NMR of 1,8-bis(hydroxymethyl) naphthalene in DMSO-*d*<sub>6</sub>.

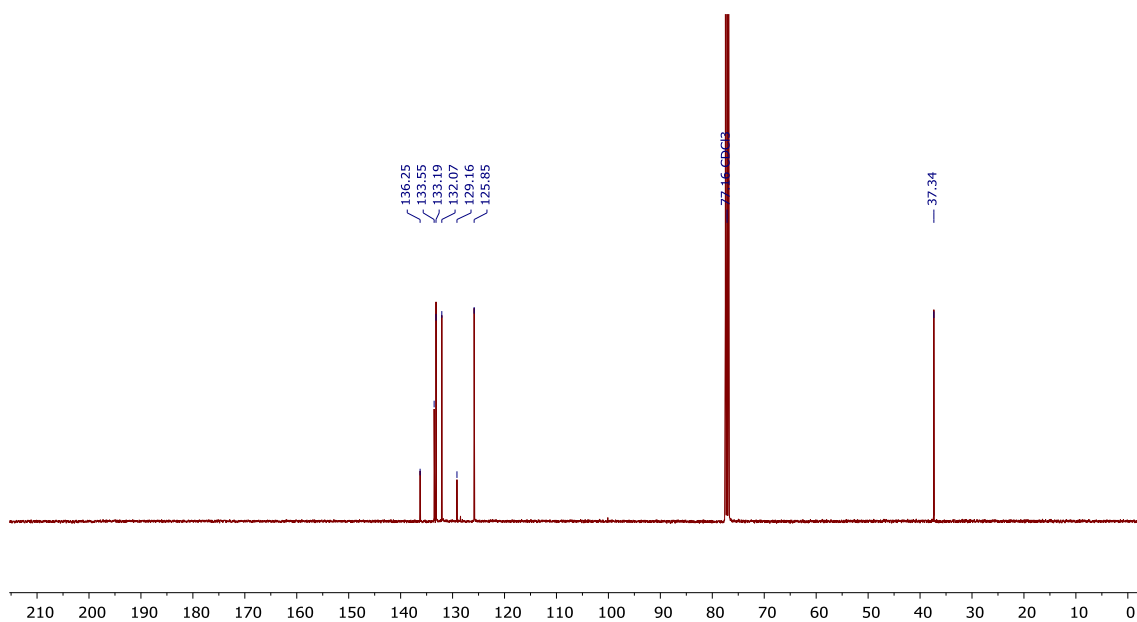


**Supplementary Figure 3.6.** <sup>13</sup>C-NMR of 1,8-bis(hydroxymethyl) naphthalene in DMSO-*d*<sub>6</sub>.

### 3.2.4 1,8-bis(bromomethyl)naphthalene

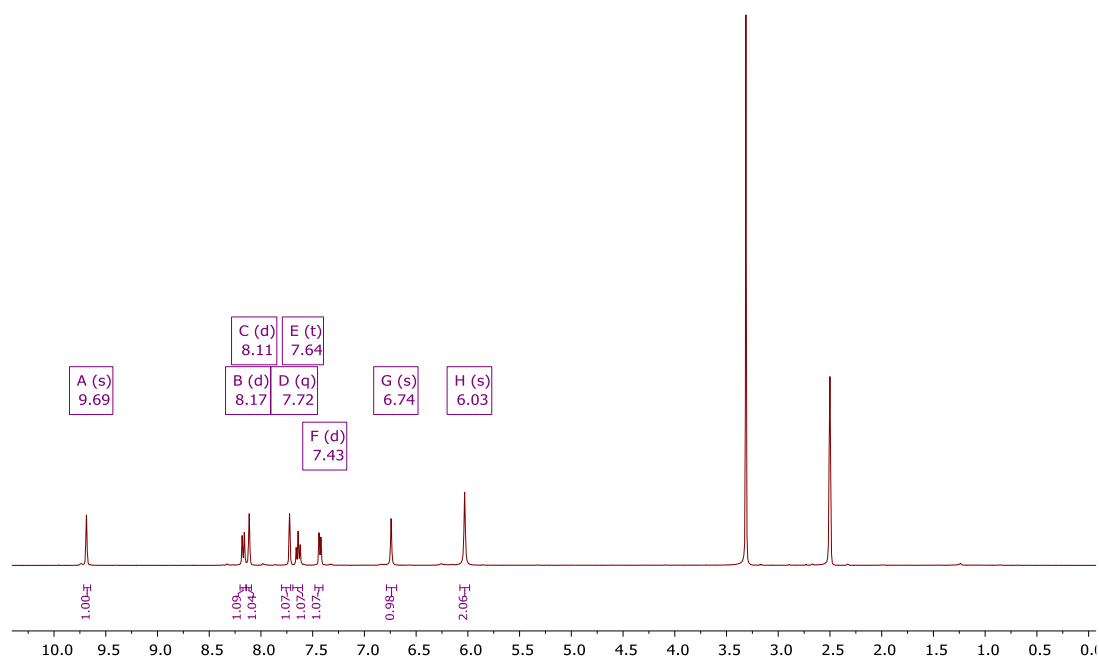


**Supplementary Figure 3.7.** <sup>1</sup>H-NMR of 1,8-bis(bromomethyl)naphthalene in CDCl<sub>3</sub>. Residual C<sub>6</sub>H<sub>6</sub> at 7.13 ppm.

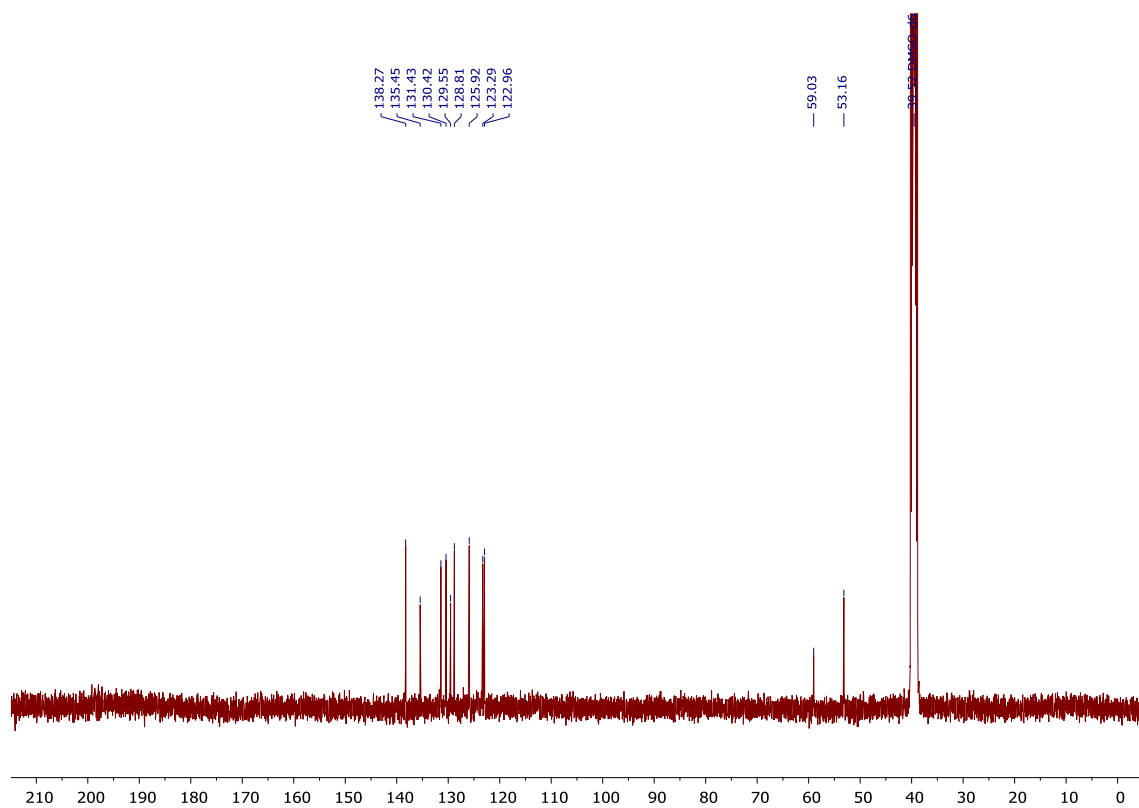


**Supplementary Figure 3.8.** <sup>13</sup>C-NMR of 1,8-bis(bromomethyl)naphthalene in CDCl<sub>3</sub>.

### 3.2.5 <sup>Me</sup>LH<sub>4</sub>-4Br, compound **3.1**

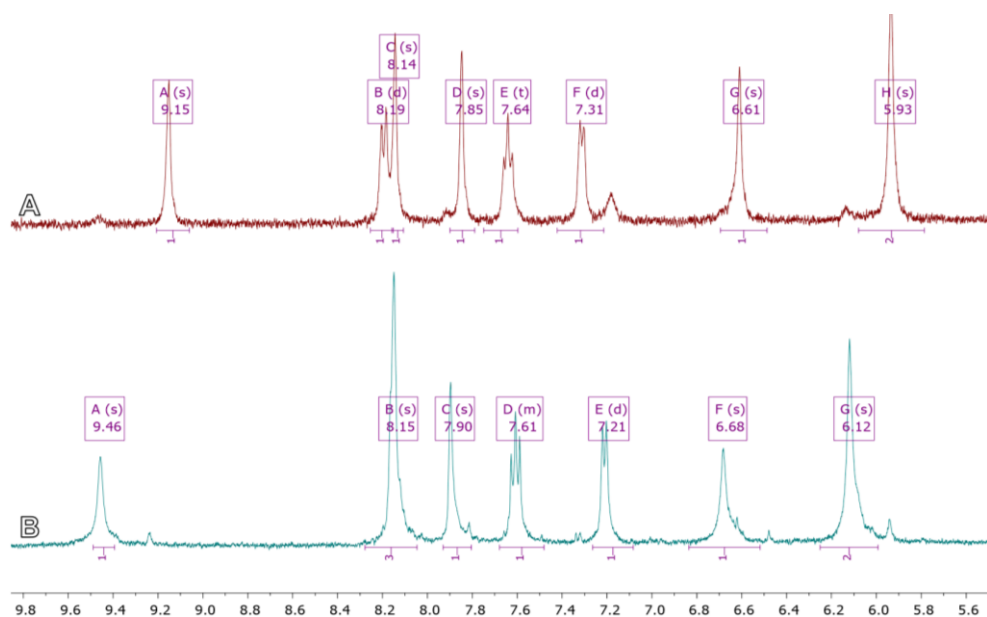


**Supplementary Figure 3.9.** <sup>1</sup>H-NMR of <sup>Me</sup>LH<sub>4</sub>-4Br in DMSO-*d*<sub>6</sub>.



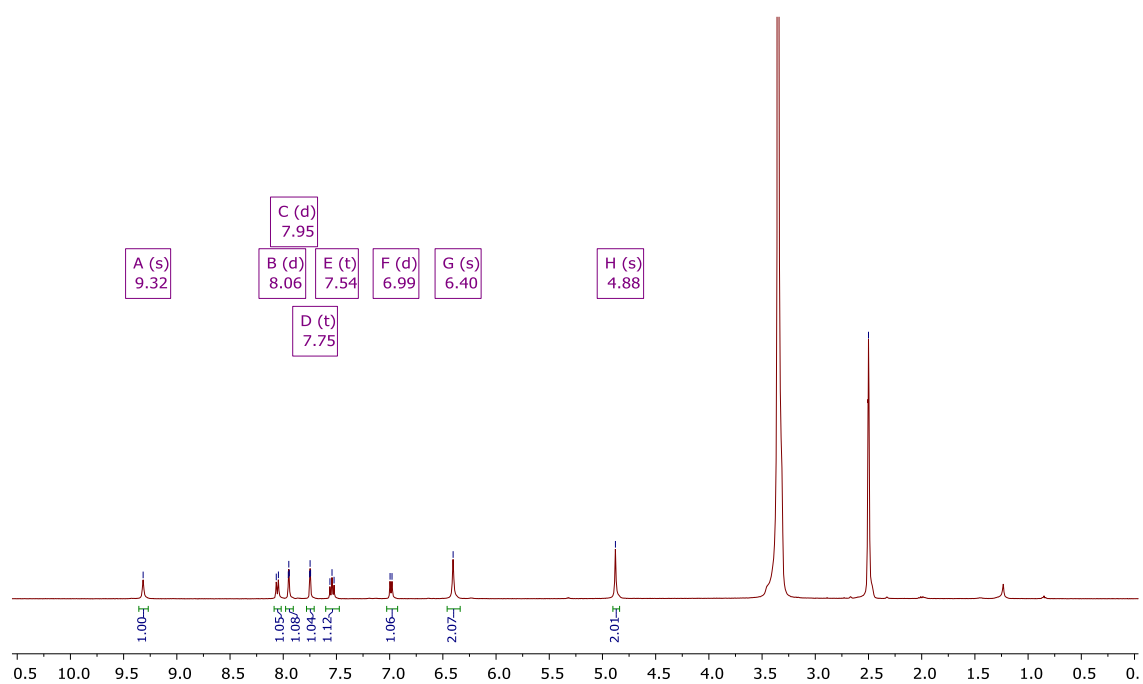
**Supplementary Figure 3.10.** <sup>13</sup>C-NMR of <sup>Me</sup>LH<sub>4</sub>-4Br in DMSO-*d*<sub>6</sub>.

### 3.2.6 Compound 3.2 and larger macrocycle – NMR data

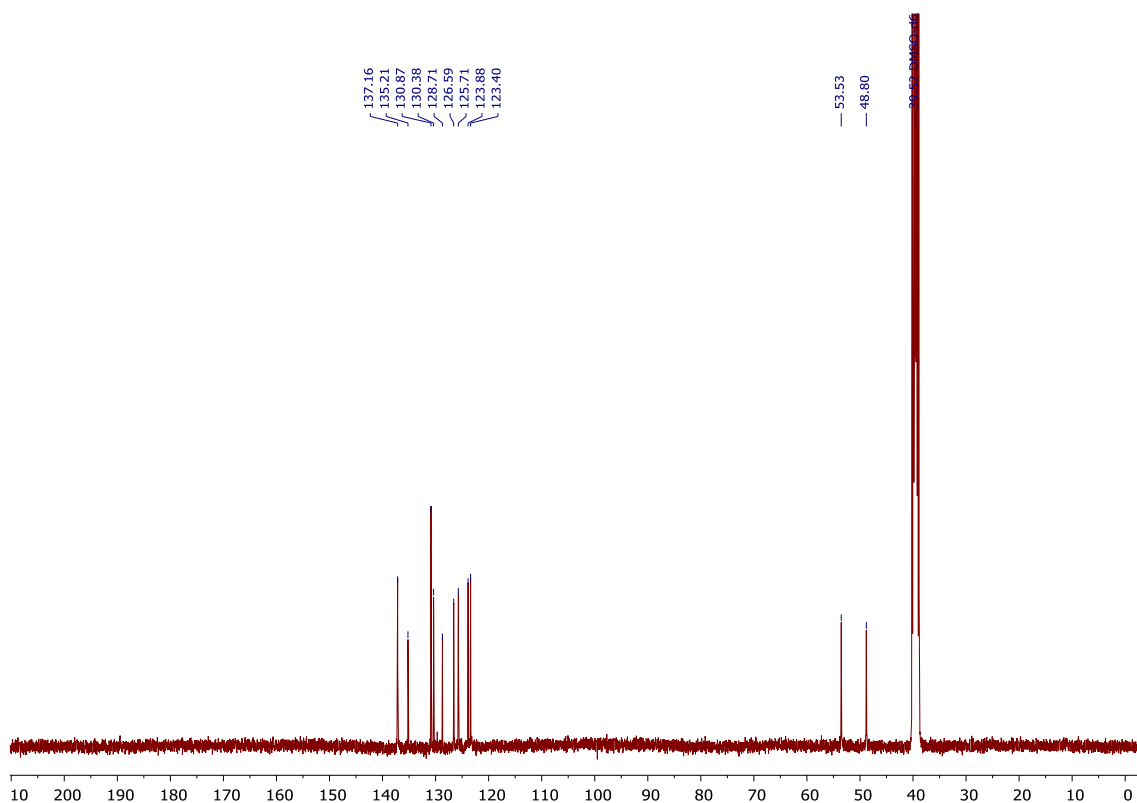


**Supplementary Figure 3.11.** Stacked <sup>1</sup>H NMR of (A) <sup>Me</sup>LH<sub>4</sub>-4PF<sub>6</sub> and (B) the larger macrocycle as a PF<sub>6</sub>-salt in DMSO-*d*<sub>6</sub>.

### 3.2.7 $^{Et}LH_4-4Br$ , compound **3.4**

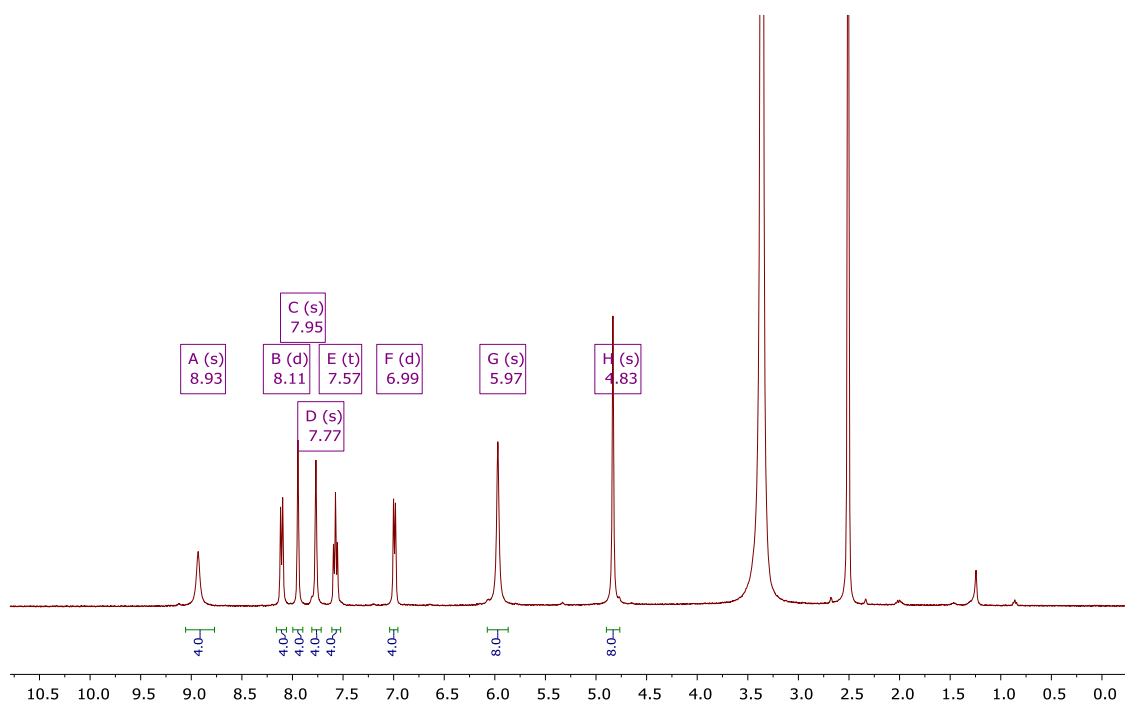


**Supplementary Figure 3.12.**  $^1H$ -NMR of  $^{Et}LH_4-4Br$  in  $DMSO-d_6$ . Residual H-grease at 1.25 ppm.

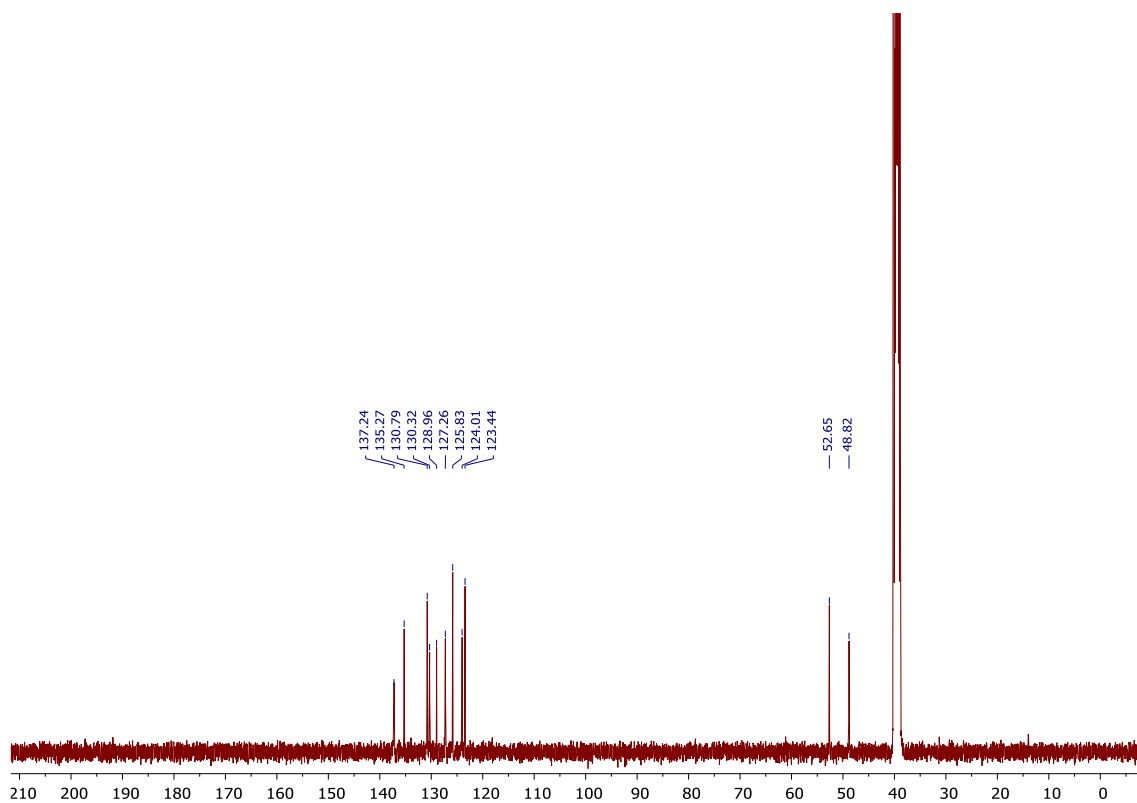


**Supplementary Figure 3.13.**  $^{13}C$ -NMR of  $^{Et}LH_4-4Br$  in  $DMSO-d_6$ .

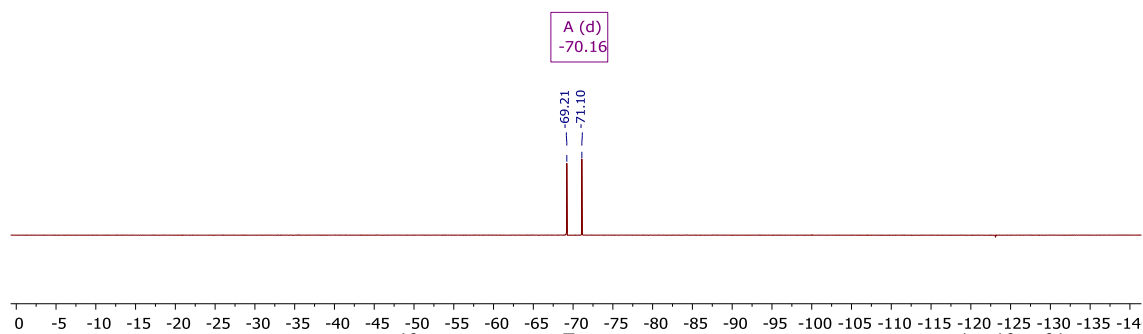
### 3.2.8 $^{Et}LH_4-4PF_6$ , compound **3.5**



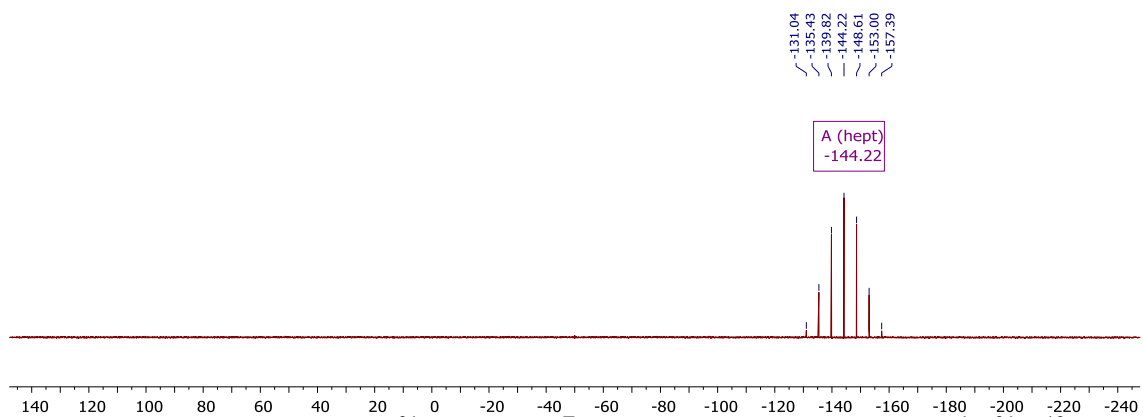
**Supplementary Figure 3.14.**  $^1H$ -NMR of  $^{Et}LH_4-4PF_6$ , **3.5**, in  $DMSO-d_6$ . Residual H-grease at 1.25 ppm.



**Supplementary Figure 3.15.**  $^{13}C$ -NMR (101 MHz) of  $^{Et}LH_4-4PF_6$ , **3.5**, in  $DMSO-d_6$ .

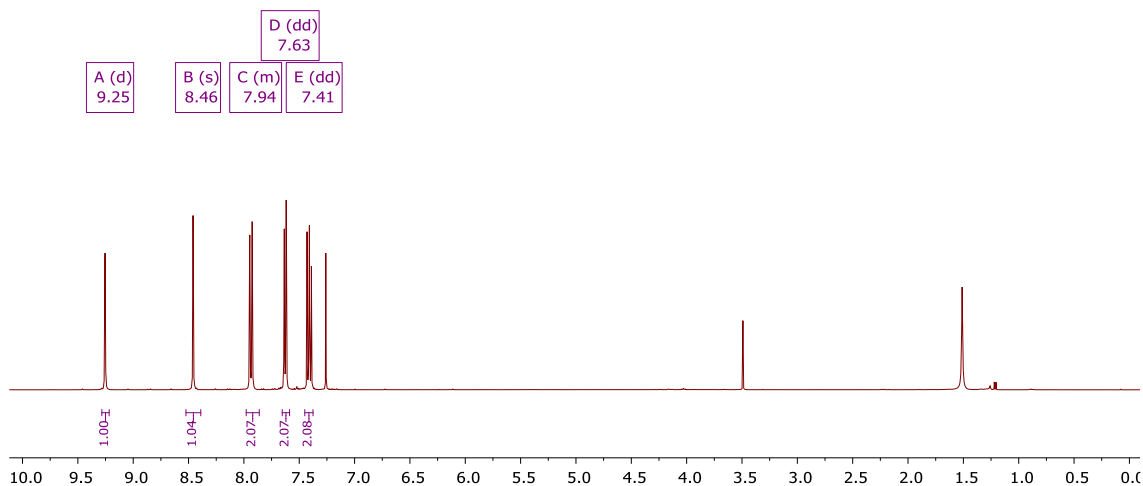


**Supplementary Figure 3.16.**  $^{19}\text{F}$ -NMR of EtLH<sub>4</sub>-4PF<sub>6</sub>, **3.5**, in DMSO-*d*<sub>6</sub>.  $^1J(^{19}\text{F}\text{-}^{31}\text{P}) = 711.4$  Hz.



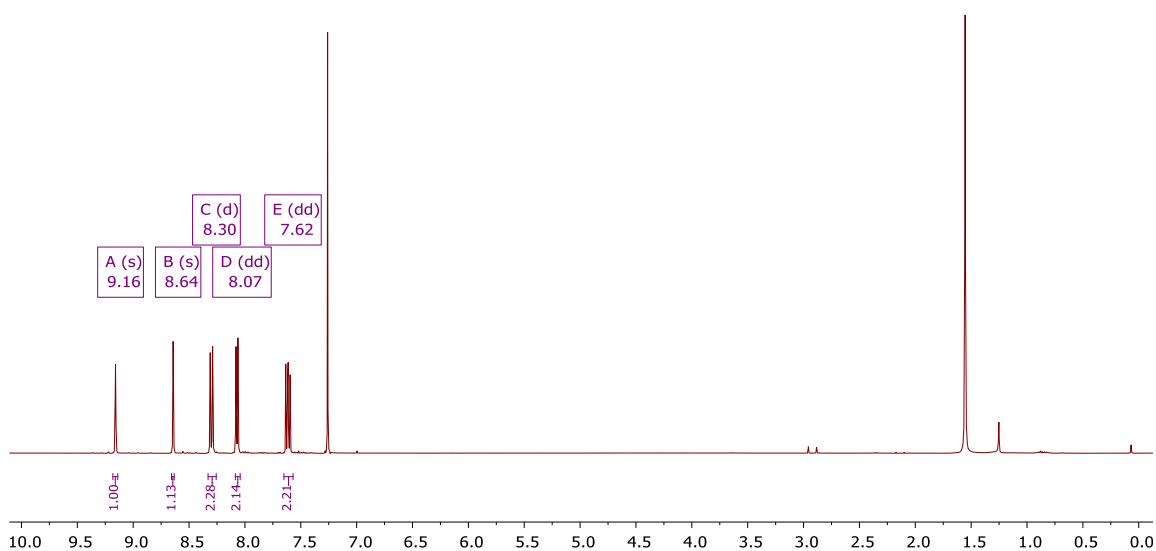
**Supplementary Figure 3.17.**  $^{31}\text{P}$ -NMR of EtLH<sub>4</sub>-4PF<sub>6</sub>, **3.5**, in DMSO-*d*<sub>6</sub>.  $^1J(^{31}\text{P}\text{-}^{19}\text{F}) = 711.4$  Hz.

### 3.2.9 1,8-dichloroanthracene



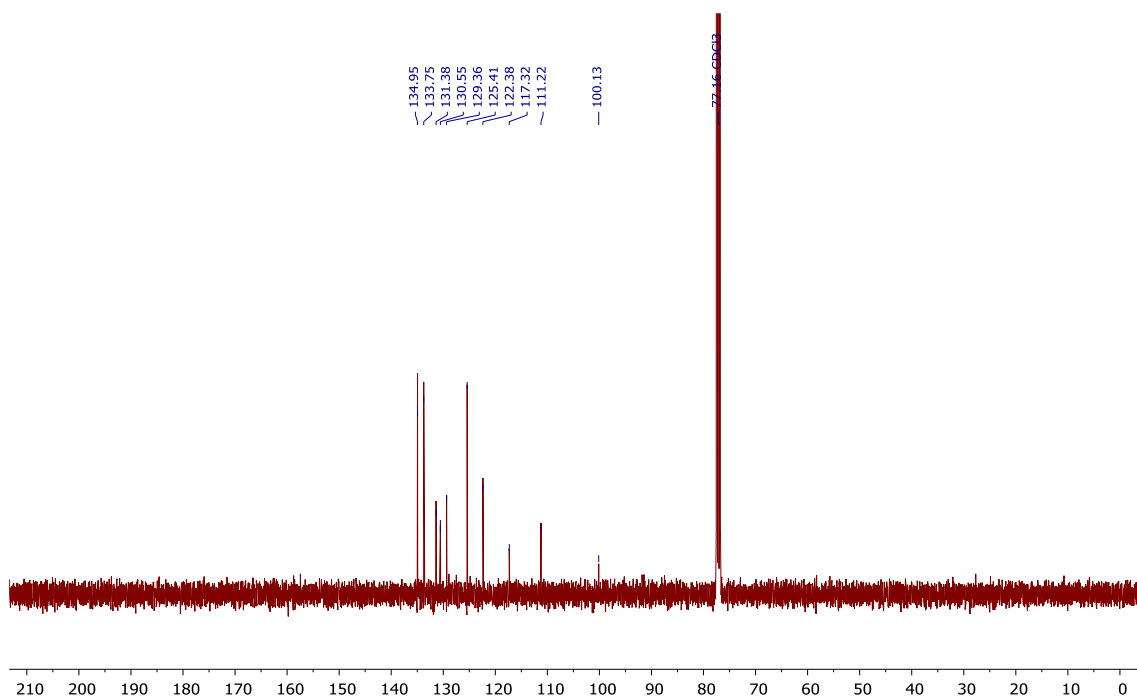
**Supplementary Figure 3.18.** <sup>1</sup>H-NMR of 1,8-bis(chloromethyl)anthracene in CDCl<sub>3</sub>. *i*PrOH residual at 3.49 ppm, and water in CDCl<sub>3</sub> at 1.56 ppm.

### 3.2.10 Anthracene-1,8-dicarbonitrile



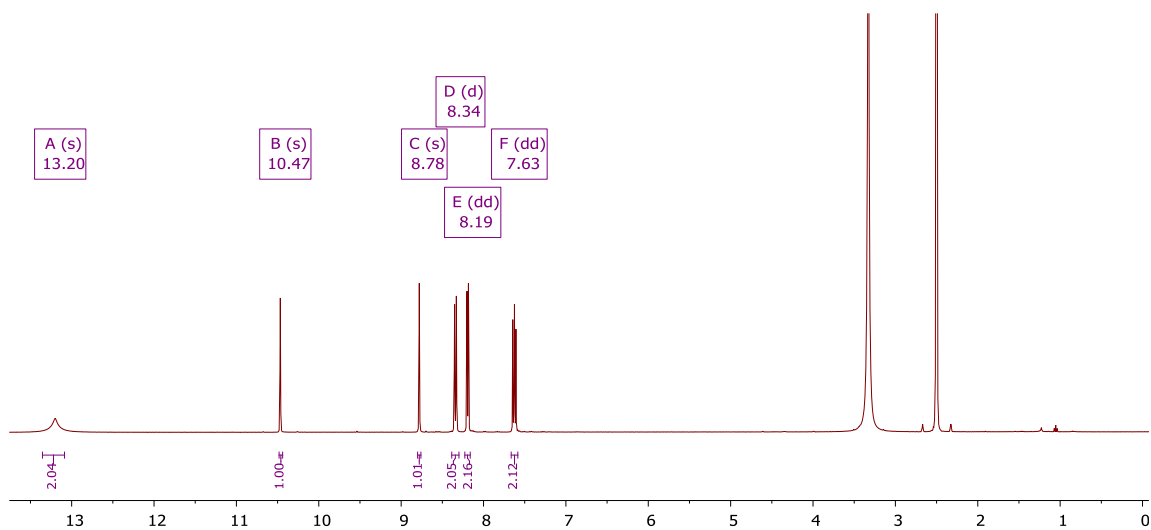
**Supplementary Figure 3.19.** <sup>1</sup>H-NMR of 1,8-bis(cyanomethyl)anthracene in CDCl<sub>3</sub>. Water in CDCl<sub>3</sub> at 1.56 ppm along H-grease at 1.25 ppm.



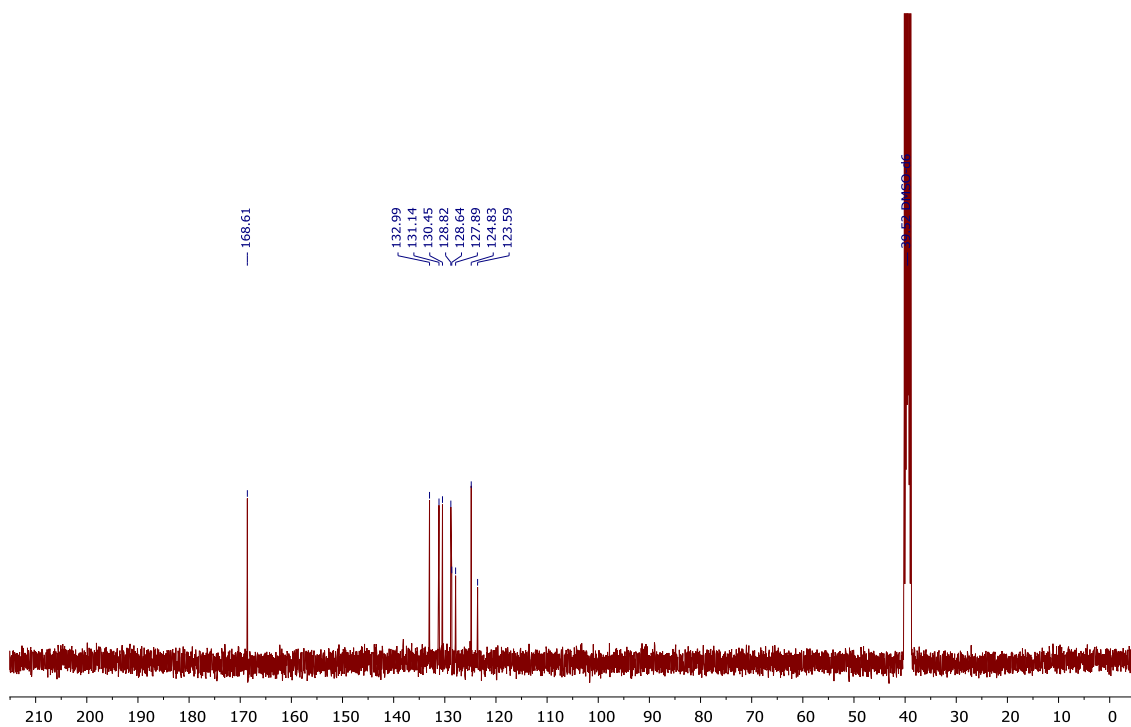


**Supplementary Figure 3.20.** <sup>13</sup>C-NMR of 1,8-biscyanoanthracene in CDCl<sub>3</sub>.

### 3.2.11 Anthracene-1,8-dicarboxylic acid

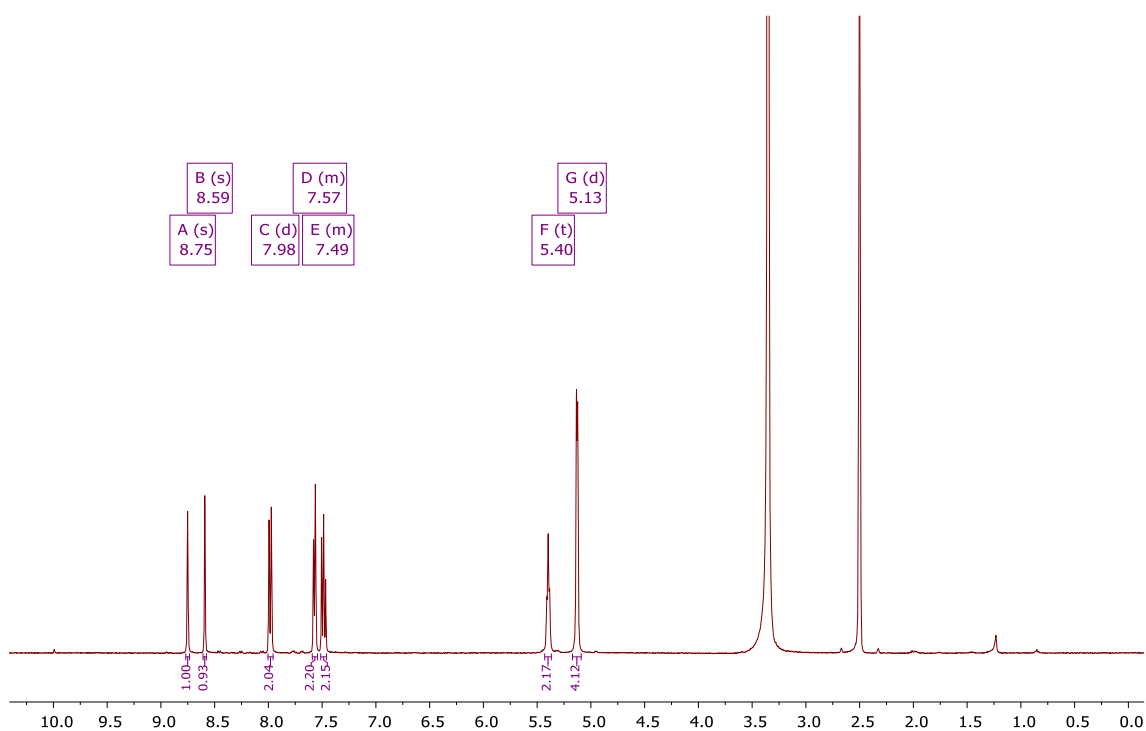


**Supplementary Figure 3.21.** <sup>1</sup>H-NMR of anthracene-1,8-dicarboxylic acid in DMSO-*d*<sub>6</sub>. Pentane residual at 1.04 ppm.

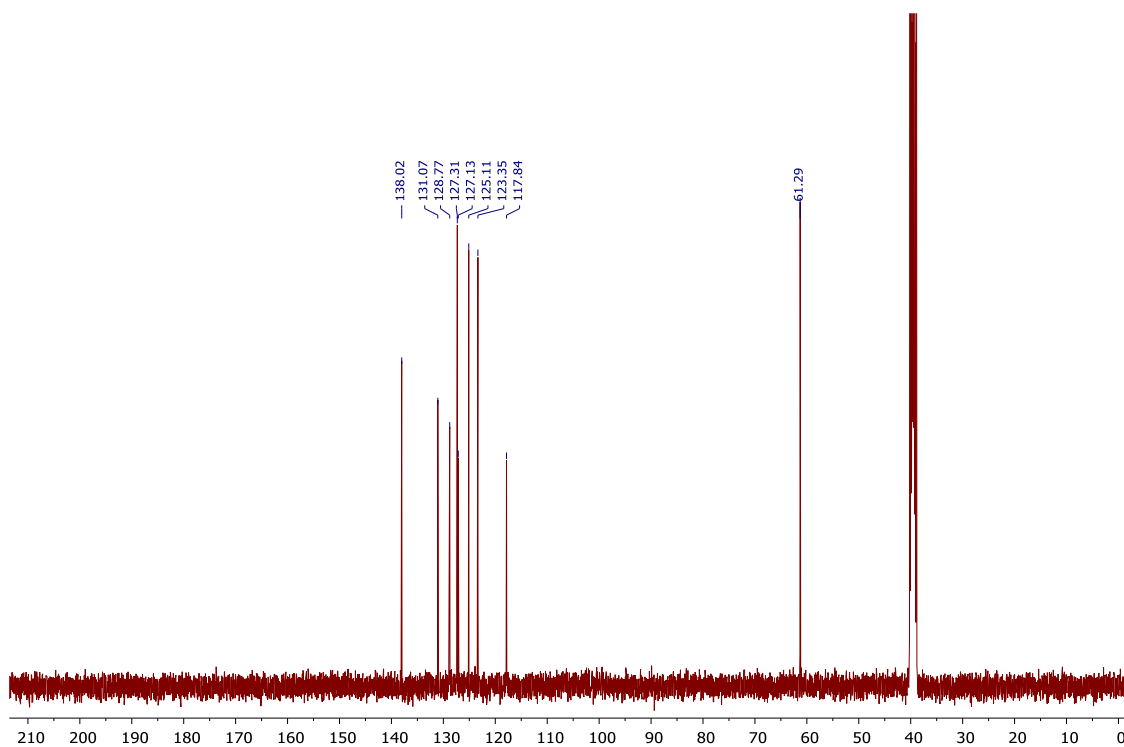


**Supplementary Figure 3.22.**  $^{13}\text{C}$ -NMR of anthracene-1,8-dicarboxylic acid in  $\text{DMSO-}d_6$ .

### 3.2.12 1,8-bis(hydroxymethyl)anthracene

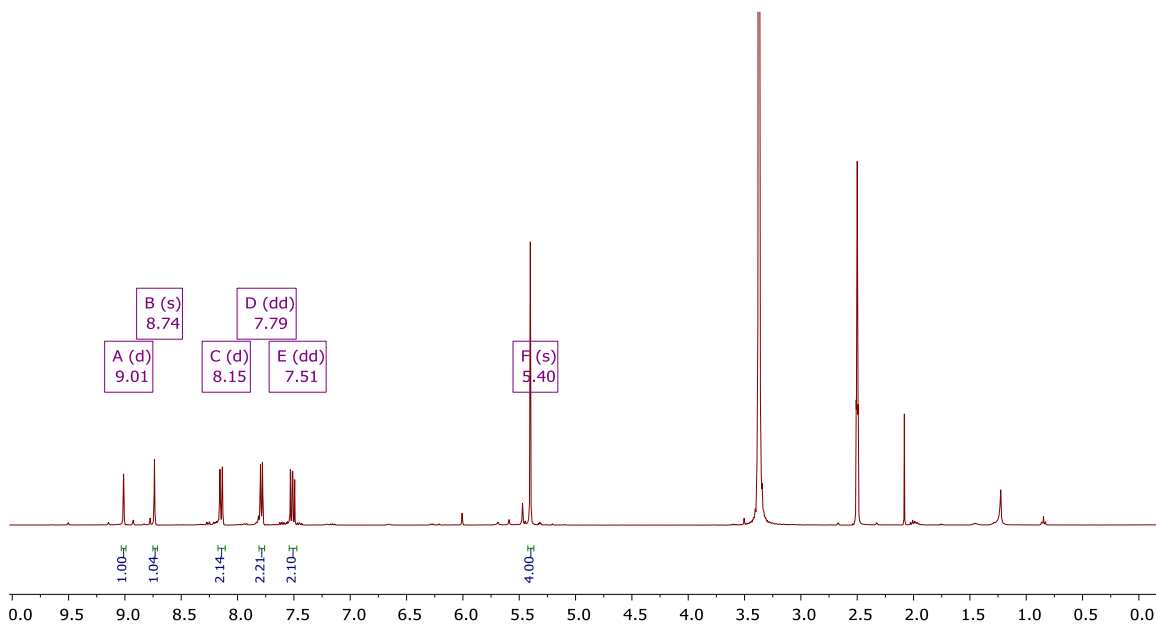


**Supplementary Figure 3.23.**  $^1\text{H}$ -NMR of 1,8-bis(hydroxymethyl)anthracene in  $\text{DMSO-}d_6$ .



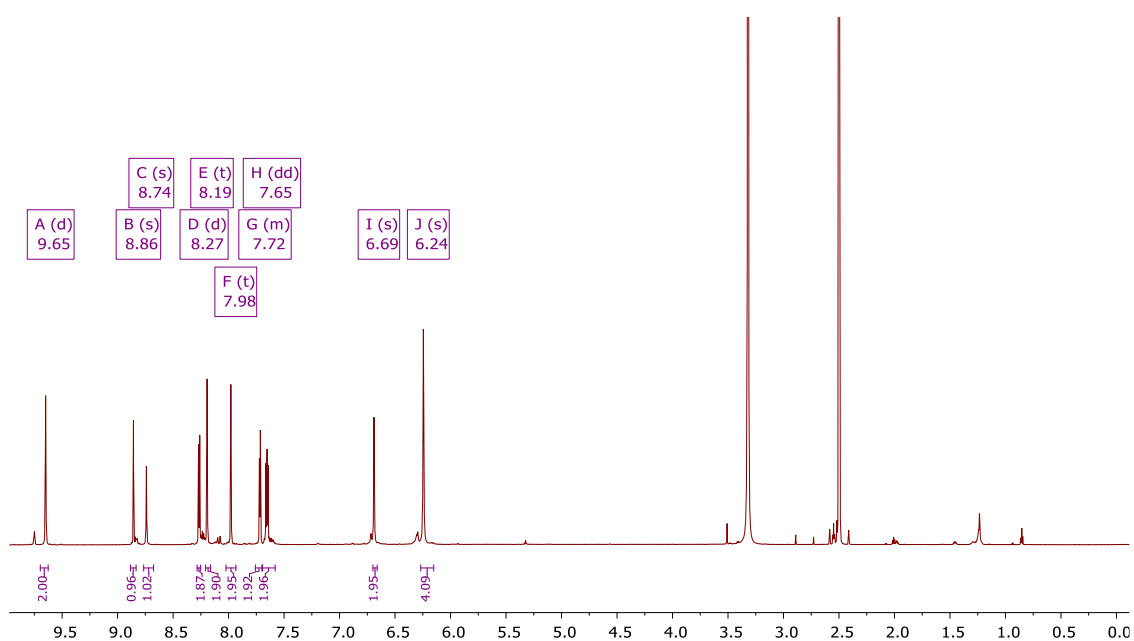
**Supplementary Figure 3.24.**  $^{13}\text{C}$ -NMR of 1,8-bis(hydroxymethyl)anthracene in  $\text{DMSO-}d_6$ .

### 3.2.13 1,8-bis(bromomethyl)anthracene

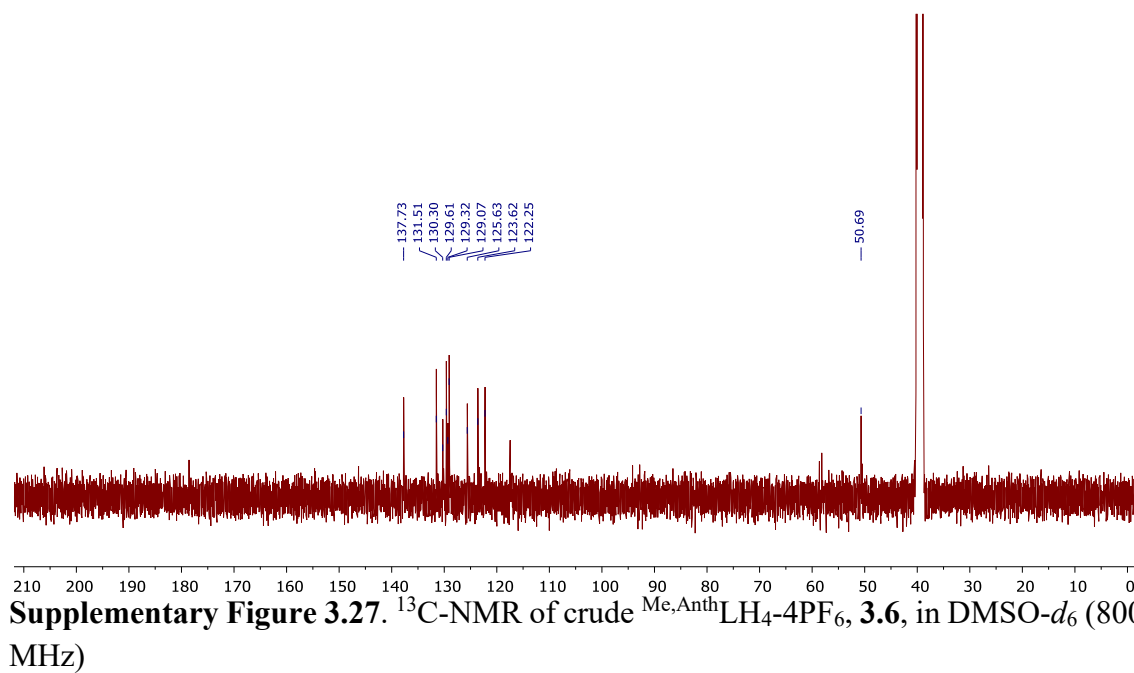


**Supplementary Figure 3.25.**  $^1\text{H}$ -NMR of crude 1,8-bis(bromomethyl)anthracene in  $\text{DMSO-}d_6$ . Residual acetone (2.08 ppm) and H-grease 1.23 ppm.

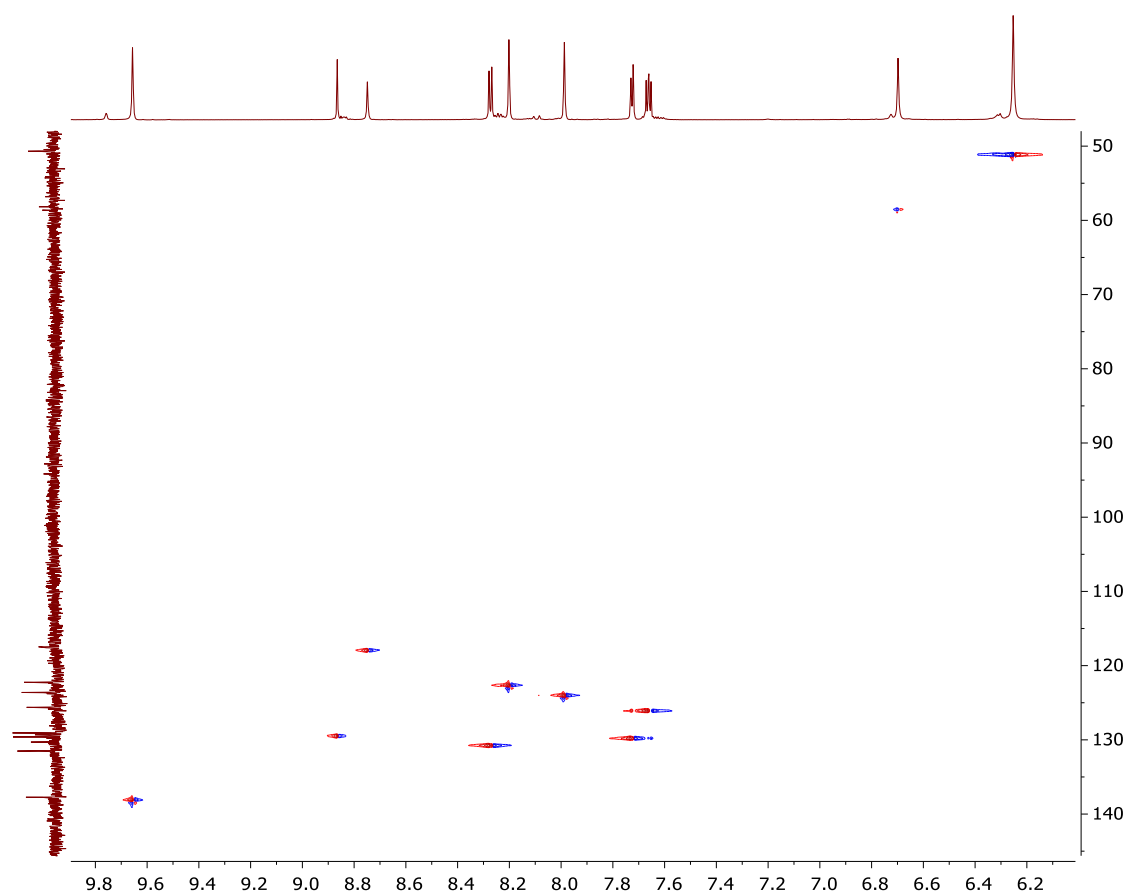
### 3.2.14 <sup>Me,Anth</sup>LH<sub>4</sub>-4PF<sub>6</sub>, compound **3.6**



**Supplementary Figure 3.26.** <sup>1</sup>H-NMR of crude <sup>Me,Anth</sup>LH<sub>4</sub>-4PF<sub>6</sub>, compound **3.6**, in DMSO-*d*<sub>6</sub> (800 MHz).

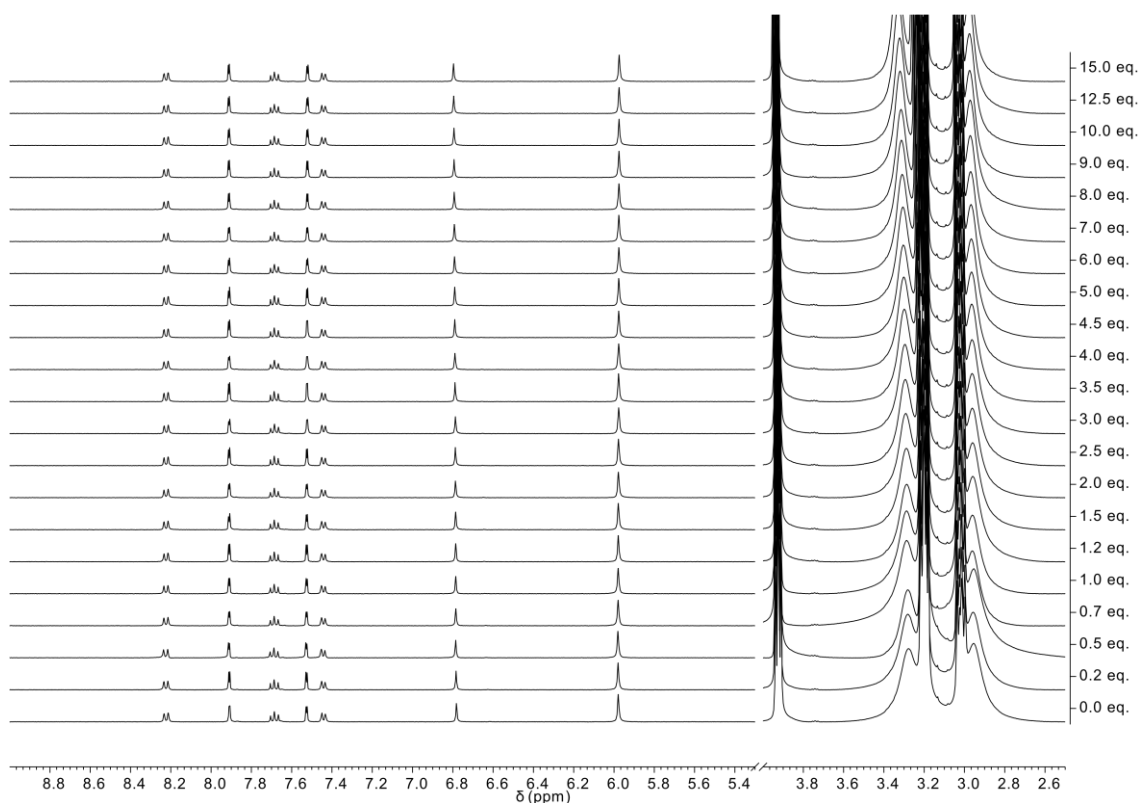


**Supplementary Figure 3.27.** <sup>13</sup>C-NMR of crude <sup>Me,Anth</sup>LH<sub>4</sub>-4PF<sub>6</sub>, **3.6**, in DMSO-*d*<sub>6</sub> (800 MHz)

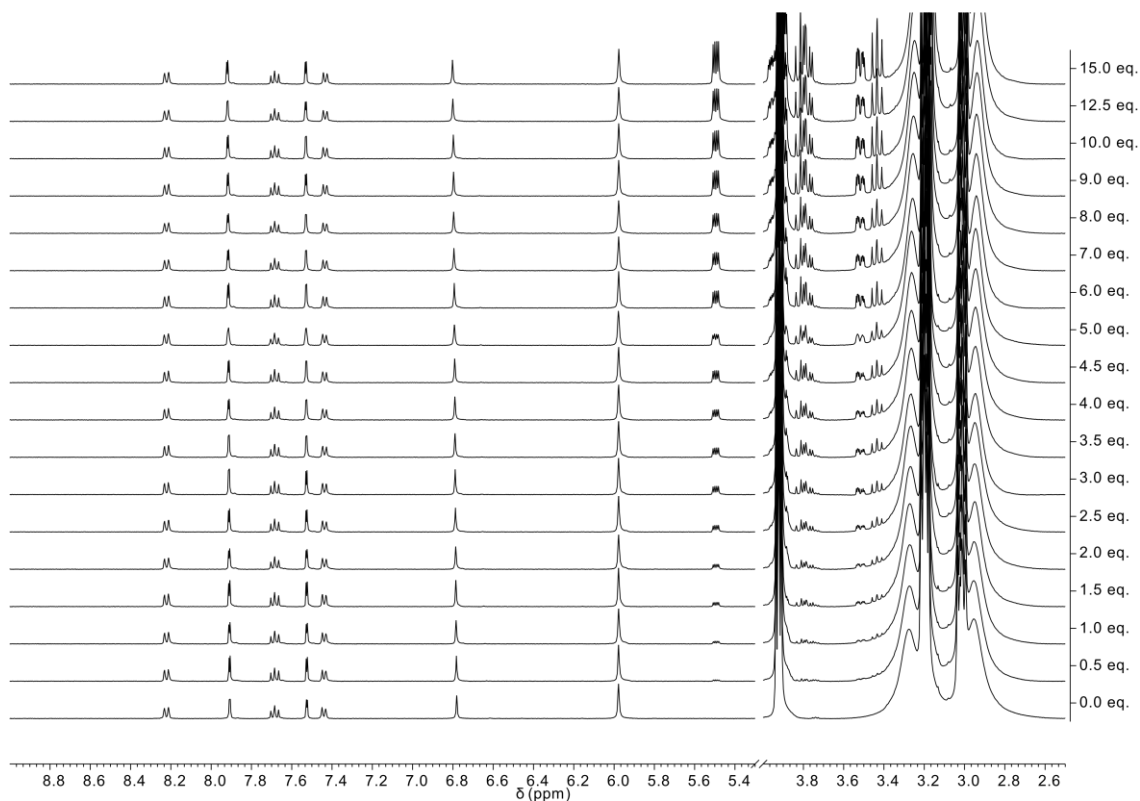


**Supplementary Figure 3.28.** HSQC of crude  $\text{Me,AnthLH}_4\text{-4PF}_6$ , **3.6** in  $\text{DMSO-}d_6$  (800 MHz)

### 3.2.15 NMR titration of compound **3.1**

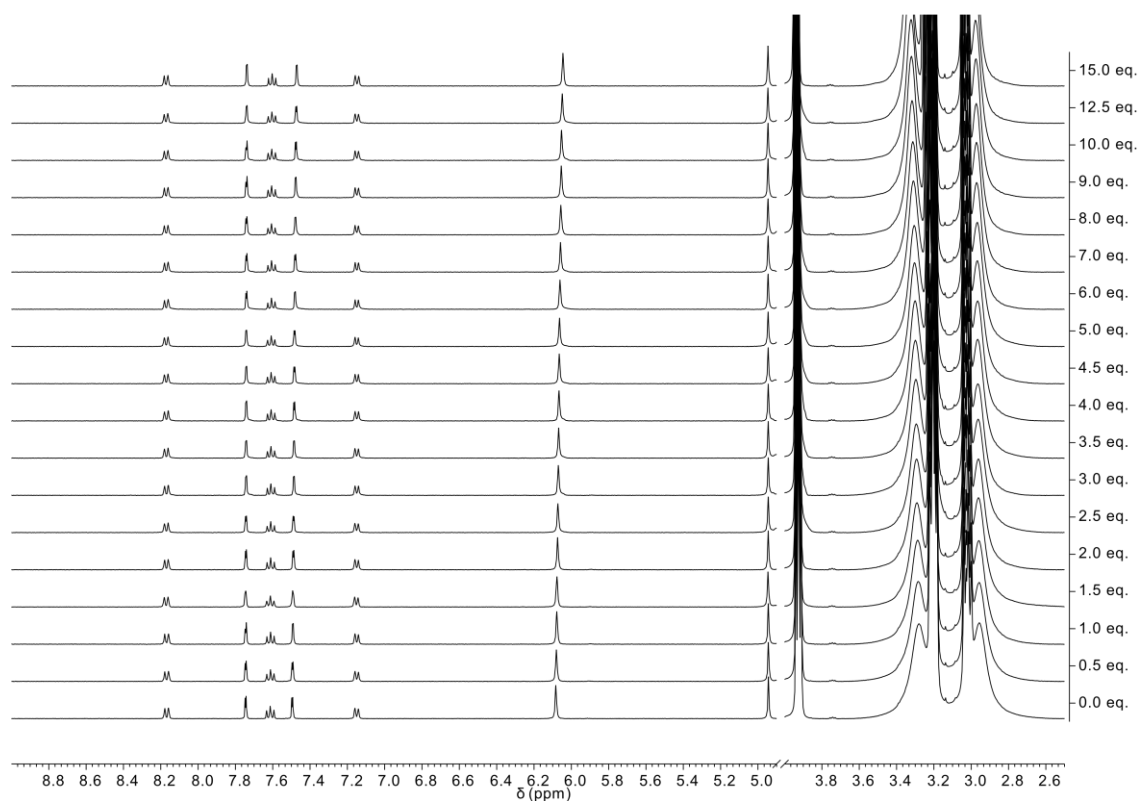


**Supplementary Figure 3.29.** Partial <sup>1</sup>H NMR spectra of **3.1** (1 mM) with increasing concentrations of iP. Supplied by Charlotte Nybro Dansholm.

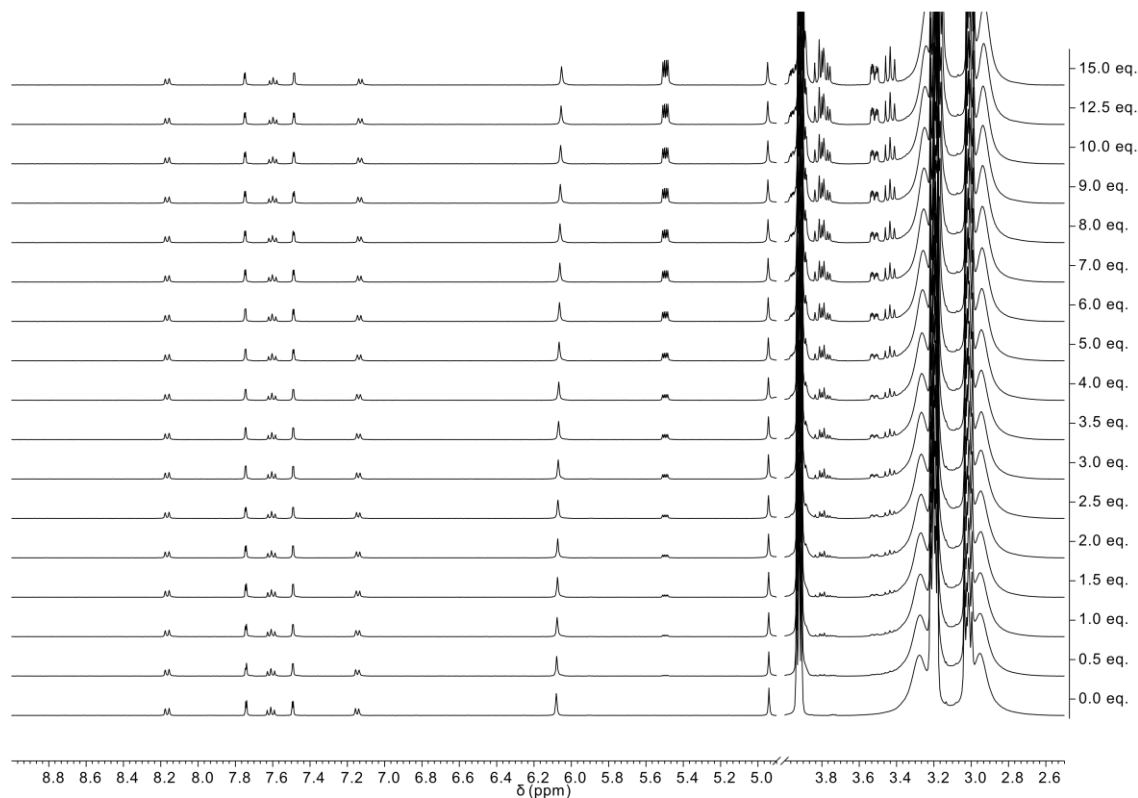


**Supplementary Figure 3.30.** Partial <sup>1</sup>H NMR spectra of **3.1** (1 mM) with increasing concentrations of Glc-1-P. Supplied by Charlotte Nybro Dansholm.

### 3.2.16 NMR titration of compound **3.4**

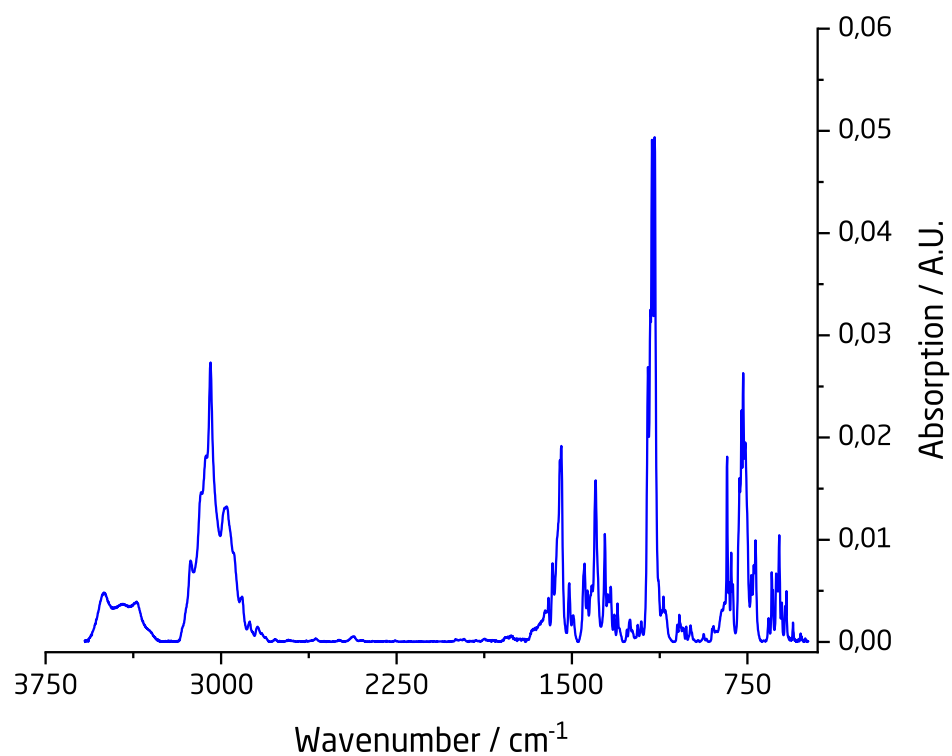


**Supplementary Figure 3.31.** Partial  $^1\text{H}$  NMR spectra of **3.4** (1 mM) with increasing concentrations of iP. Supplied by Charlotte Nybro Dansholm.

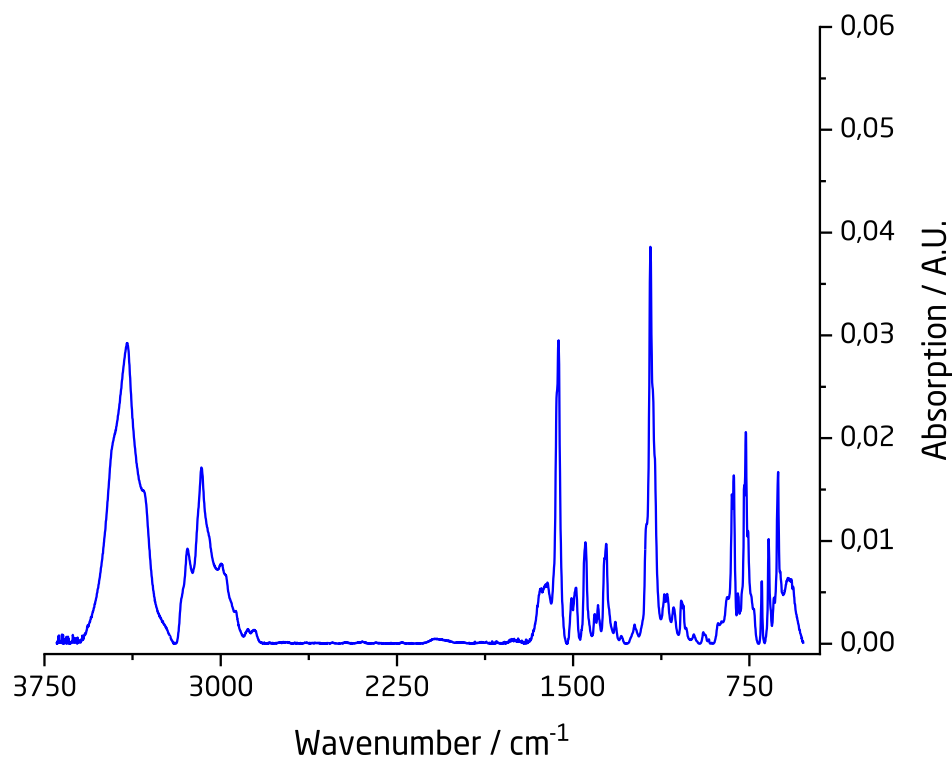


**Supplementary Figure 3.32.** Partial  $^1\text{H}$  NMR spectra of **3.4** (1 mM) with increasing concentrations of Glc-1-P. Supplied by Charlotte Nybro Dansholm.

### 3.3 IR data



**Supplementary Figure 3.33.** IR of compound **3.1**.



**Supplementary Figure 3.34.** IR of compound **3.4**.



### 3.4 Crystallographic data

**Supplementary table 3.1.** Crystallographic data for compounds **3.1** and **3.4**.

	<b>3.1</b>	<b>3.4</b>	<b>3.1, 3 DMSO</b>
Chemical formula	C <sub>38</sub> H <sub>36</sub> Br <sub>4</sub> N <sub>8</sub>	C <sub>40</sub> H <sub>40</sub> Br <sub>3.91</sub> N <sub>8</sub>	C <sub>25</sub> H <sub>36</sub> Br <sub>2</sub> N <sub>4</sub> O <sub>3</sub> S <sub>3</sub>
Formula weight	924.39	944.85	696.58
Crystal color	Colorless	Colorless	Colorless
Crystal system	Triclinic	Triclinic	Triclinic
Space group	P-1	P-1	P-1
<i>a</i> (Å)	7.75860(10)	11.2915(2)	9.1877(2)
<i>b</i> (Å)	12.4837(2)	13.8531(2)	13.0048(3)
<i>c</i> (Å)	12.7482(2)	15.3651(2)	13.1674(2)
<i>α</i> (deg)	76.461(2)	81.173(1)	95.241(2)
<i>β</i> (deg)	85.5210(10)	78.612(1)	100.363(2)
<i>γ</i> (deg)	81.9200(10)	67.890(1)	104.986(2)
<i>V</i> (Å <sup>3</sup> )	1187.20(3)	2174.56(6)	1479.18(5)
<i>Z</i>	1	2	2
<i>μ</i> (mm <sup>-1</sup> )	4.382	4.698	5.731
<i>T</i> (K)	120.15	100.00(10)	120.15
GOF ( <i>S</i> )	1.047	1.031	1.028
<i>R</i> <sup>a</sup> ( <i>wR</i> <sup>2b</sup> )	<i>R</i> <sub>1</sub> = 0.0312	<i>R</i> <sub>1</sub> = 0.0287,	<i>R</i> <sub>1</sub> = 0.0321,
[ <i>I</i> > 2σ( <i>I</i> )]	<i>wR</i> <sub>2</sub> = 0.0753	<i>wR</i> <sub>2</sub> = 0.0675	<i>wR</i> <sub>2</sub> = 0.0876
<i>R</i> <sup>a</sup> ( <i>wR</i> <sup>2b</sup> )	<i>R</i> <sub>1</sub> = 0.0314,	<i>R</i> <sub>1</sub> = 0.0299,	<i>R</i> <sub>1</sub> = 0.0354,
[all data]	<i>wR</i> <sub>2</sub> = 0.0754	<i>wR</i> <sub>2</sub> = 0.0684	<i>wR</i> <sub>2</sub> = 0.0908
2Θ range for data collection (deg)	7.14 to 133.162	8.686 to 133.202	6.898 to 133.186
Reflections	43485	82795	34876
Radiation type	CuKα (λ = 1.54184)		

$$^a R I = \sum [w(F_0 - F_c)] / \sum [wF_0]; \quad ^b wR2 = \left[ \frac{\sum [w(F_0^2 - F_c^2)^2]}{\sum [w(F_0^2)^2]} \right]^{\frac{1}{2}}, \quad w = 1 / [\sigma^2(F_0^2) + (aP)^2 + bP], \quad \text{where } P = [\max(F_0^2, 0) + 2(F_c^2)] / 3$$

## 4 Chapter 4

### 4.1 Synthetic methods

Compound **4.1**, **<sup>Me</sup>LH<sub>2</sub>-2Br**. *As in literature*<sup>20</sup>, *in air*. A round-bottom flask (25 mL) was charged with 1,1'-bisimidazole ethane (500 mg, 3.1 mmol, 1.0 equiv.), which was dissolved in MeCN (15 mL) before a slight excess of BnBr (1.2g (0.84 mL), 2.10 equiv.) was added to the solution. The flask was fitted with a reflux condenser, and the mixture was brought to gentle reflux for 12 hours. The solution was cooled to RT, added enough acetone until precipitation started, stirred for 5 minutes, and the precipitate was collected on an M-coarseness glass-frit (20 mL). The mixture was washed with acetone (3 x 10 mL), Et<sub>2</sub>O (3 x 10 mL), and was left to dry over the glass frit for 2 hours, yielding a white powder of the bromide salt in nearly quantitative yield (1.61g, 98% yield). <sup>1</sup>H NMR (400 MHz, DMSO-*d*<sub>6</sub>) δ 9.61 (s, 1H), 8.07 (s, 1H), 7.91 (s, 1H), 7.48 – 7.40 (m, 5H), 6.68 (s, 1H), 5.50 (s, 2H). <sup>13</sup>C NMR (101 MHz, DMSO) δ 137.72, 134.12, 129.02, 128.93, 128.59, 123.23, 122.58, 58.41, 52.33.

Compound **4.2**, **<sup>Et</sup>LH<sub>2</sub>-2Br**. *As in literature*<sup>20</sup>, *in air*. A round-bottom flask (25 mL) was charged with 1,2-bisimidazole ethane (500 mg, 3.1 mmol, 1.0 equiv.), which was dissolved in MeCN (15 mL, 100mM) before a slight excess of BnBr (1.11 g (0.770 mL), 2.10 equiv.) was added to the solution. The flask was fitted with a reflux condenser, and the mixture was brought to gentle reflux for 12 hours. The solution was cooled to RT, added enough acetone until precipitation started, stirred for 5 minutes, and the precipitate was collected on an M-coarseness glass-frit (20 mL). The mixture was washed with acetone (3 x 10 mL), Et<sub>2</sub>O (3 x 10 mL), and was left to dry over the frit for 2 hours, yielding an off-white powder of the bromide salt in nearly quantitative yield (1.52g, 98% yield). <sup>1</sup>H NMR (400 MHz, DMSO-*d*<sub>6</sub>) δ 9.24 (s, 1H), 7.82 (d, *J* = 1.8 Hz, 1H), 7.68 (t, *J*

= 1.8 Hz, 1H), 7.44 – 7.33 (m, 5H), 5.42 (s, 2H), 4.72 (s, 2H).  $^{13}\text{C}$  NMR (101 MHz, DMSO)  $\delta$  136.74, 134.47, 128.99, 128.80, 128.26, 122.95, 122.86, 52.09, 48.47.

Complex **4.3**,  $^{\text{Me}}\text{LPdBr}_2$ . *As in literature*<sup>20</sup> with the addition of 2.0 equivalents of NaOAc.

The Pd-complex was obtained as a yellow powder in excellent yield (106 mg, 87% yield) from 100 mg compound **3.1**.  $^1\text{H}$  NMR (400 MHz, DMSO- $d_6$ )  $\delta$  7.60 (d,  $J$  = 2.1 Hz, 1H), 7.30 - 7.25 (overlapping multiplets, 6H), 6.35 (broad singlet, 1H), 6.00 (d,  $J$  = 14.7 Hz, 1H), 5.35 (d,  $J$  = 14.7 Hz, 1H).

Complex **4.4**,  $^{\text{Et}}\text{LPdBr}_2$ . *As in literature*<sup>20,21</sup> with the addition of 2.0 equivalents of NaOAc. The Pd-complex was obtained as a yellow powder in excellent yield (105 mg, 86% yield) from 100 mg compound **4.2**.  $^1\text{H}$  NMR (400 MHz, DMSO- $d_6$ )  $\delta$  7.44 (s, 1H), 7.40 – 7.30 (overlapping multiplet, 3H), 7.20 – 7.10 (overlapping multiplet, 2H), 5.42 (d,  $J$  = 15.0 Hz, 1H), 5.28 (broad singlet, 1H), 4.92 (d,  $J$  = 14.9 Hz, 1H), 4.58 (broad singlet, 1H).  $^{13}\text{C}$  NMR (101 MHz, DMSO)  $\delta$  157.47 ( $\text{C}_2\text{-Pd}$ ), 136.34, 128.69, 128.65, 128.45, 128.09, 127.96, 127.78, 123.26, 122.42, 52.99, 46.89.

**General procedure for salt metathesis.** Compound **4.1** or **4.2** (1.0 equiv.) was dissolved in deionized water (50 mM), before a  $\text{NaPF}_6$  (2.02 equiv.), was added to the solution, and the mixture was heated to 80°C overnight under stirring. The suspension was cooled to RT, the solid collected on a glass-frit (M-coarseness), which was washed with  $\text{H}_2\text{O}$ , MeOH, and finally  $\text{Et}_2\text{O}$  before the powder was left to dry in the air on the frit for at least 2 hours. The resulting white powder was redissolved in MeCN, passed through the filter, and MeCN was removed *in-vacuo* leaving behind the desired compound as a white solid in nearly quantitative yield (95 – >99%).

Compound **4.7**,  $^{\text{Me}}\text{LH}_2\text{-2PF}_6$ . Compound **4.1** (250 mg, 0.51 mmol, 1.0 equiv.) dissolved in deionized water (10 mL, 50 mM) was added  $\text{NaPF}_6$  (173 mg, 1.03 mmol, 2.02 equiv.).

310 mg of **4.7** was recovered as white powder (98% yield).  $^1\text{H}$  NMR (400 MHz, DMSO- $d_6$ )  $\delta$  9.45 (d,  $J = 1.9$  Hz, 2H), 7.99 (t,  $J = 1.9$  Hz, 2H), 7.89 (t,  $J = 1.9$  Hz, 2H), 7.53 – 7.35 (overlapping multiplet, 9H), 6.59 (s, 2H), 5.49 (s, 4H). In agreement with A. Schmitzer<sup>22</sup>.

Compound **4.8**,  $^{\text{Et}}\text{LH}_2\text{-2PF}_6$ . Compound **4.2** (400 mg, 0.793 mmol, 1.0 equiv.), dissolved in deionized water (150 mL, 10 mM) was added  $\text{NaPF}_6$  (269.1 mg, 1.6 mmol, 2.02 equiv.). 498.7 mg (99.7% yield).  $^1\text{H}$  NMR (400 MHz, DMSO- $d_6$ )  $\delta$  9.12 (t,  $J = 1.8$  Hz, 2H), 7.81 (t,  $J = 1.8$  Hz, 2H), 7.64 (t,  $J = 1.8$  Hz, 2H), 7.47 – 7.39 (overlapping multiplet, 6H), 7.35 (dd,  $J = 7.6, 1.9$  Hz, 4H), 5.39 (s, 2H), 4.68 (s, 4H).  $^{13}\text{C}$  NMR (101 MHz, DMSO)  $\delta$  136.77, 134.50, 129.08, 128.90, 128.26, 123.08, 122.92, 52.17, 48.56. **Elemental analysis** calcd (%) for  $\text{C}_{22}\text{H}_{24}\text{N}_4\text{F}_{12}\text{P}_2$ : C 41.65, H 3.81, N 8.83; found: C 41.66, H 3.80, N 8.80.

Complex **4.5**,  $[\text{Me}^{\text{e}}\text{LAg}]_2\text{2PF}_6$ . A 50 mL round-bottom flask was wrapped in foil, added compound **4.7** ( $^{\text{Me}^{\text{e}}}\text{LH}_2\text{-2PF}_6$ ) (100 mg, 0.161 mmol, 2.0 equiv.),  $\text{Ag}_2\text{O}$  (47.2 mg (95 w/w%), 0.38 mmol, 2.4 equiv.), and 20 mL MeCN. The mixture was heated overnight at 50°C. The warm mixture was filtered through Celite to remove excess  $\text{Ag}_2\text{O}$ , and the Celite was further washed with an additional 10 mL MeCN. The combined filtrate was dried over  $\text{MgSO}_4$ , passed through a filterpaper, reduced in-vacuo to ~ 5mL before enough  $\text{Et}_2\text{O}$  was added to fully precipitate a white powder, which was collected on a glass frit, and washed with small amounts of  $\text{Et}_2\text{O}$  and hexane, before the powder was moved to a flask covered in foil and dried over-night under vacuum yielding a white powder of the target Ag complex in excellent yield. (87.1 mg, 93%).  $^1\text{H}$  NMR (400 MHz, DMSO- $d_6$ )  $\delta$  7.88 (d,  $J = 1.9$  Hz, 1H), 7.61 (d,  $J = 1.9$  Hz, 1H), 7.24 (mult, 3H), 7.08 (mult, 2H), 5.21 (s, 2H). Methylene proton is absent in DMSO- $d_6$ .  $^{13}\text{C}$  NMR (101 MHz, DMSO)  $\delta$  136.60, 128.72, 128.04, 127.10, 123.53, 122.41, 63.54, 54.44. **Elemental**

**analysis** calcd (%) for  $C_{42}H_{40}Ag_2N_8F_2P_2$ : C 43.39, H 3.47, N 9.64; found: C 43.39, H 3.64, N 9.48. No observable Ag-C coupling patterns.

Complex **4.6**,  $[^{Et}LAg]_2 2PF_6$ . A 50 mL round-bottom flask was wrapped in foil, added compound **4.2** (200 mg, 0.32 mmol, 1.0 equiv.),  $Ag_2O$  (183 mg (95 w/w%), 0.79 mmol, 2.5 equiv.), and 20 mL MeCN. The mixture was heated overnight at 50°C. The warm mixture was filtered through Celite, the Celite was washed with an additional 10 mL MeCN. The combined filtrate was dried over  $MgSO_4$ , filtered, and MeCN was removed *in vacuo* excluding light, yielding a white powder in good yield (165.2 mg, 88% yield).  $^1H$  NMR (400 MHz, DMSO- $d_6$ )  $\delta$  7.49 (d,  $J$  = 1.8 Hz, 1H), 7.42 (d,  $J$  = 1.8 Hz, 1H), 7.25 (dd,  $J$  = 5.0, 1.9 Hz, 3H), 6.97 (dd,  $J$  = 6.6, 2.8 Hz, 2H), 5.13 (s, 2H), 4.64 (s, 2H).  $^{13}C$  NMR (101 MHz, DMSO)  $\delta$  179.92 (d,  $J$  = 211.0 Hz [ $^1J(^{13}C-^{109}Ag)$ ]), 179.91 (d,  $J$  = 181.7 Hz [ $^1J(^{13}C-^{107}Ag)$ ]), 179.01, 136.96, 128.69, 127.90, 126.76, 122.94, 122.54, 54.10, 50.84. Unable to obtain a satisfactory elemental analysis, powder quickly decompose when exposed to light.

Complex **4.9**,  $[(^{Me}L)_2Pd] 2PF_6$ , from transmetalation *via* complex **4.5**. A 20 mL scintillation vial equipped with a stir bar was charged with  $PdCl_2(MeCN)_2$  (other divalent Pd(II) sources work just as well *e.g.*  $PdCl_2(PhCN)_2$ ,  $PdCl_2(PPh_3)_2$ , and  $PdCl_2$ ) (11.7 mg, 45  $\mu$ mol, 1.05 equiv.) and dissolved in MeCN (10 mL). To the now yellow solution was added complex **4.5** (50 mg, 43  $\mu$ mol, 1.0 equiv.), and the mixture was heated to 70°C overnight. The now colorless solution was cooled to RT, filtered through Celite, concentrated to ~1 mL, placed inside a 5 mL glass vial, which was placed inside a 20 mL scintillation vial containing  $Et_2O$ , and left for overnight  $Et_2O$ -vapour diffusion at RT. The resulting white powder was collected on a glass-fiber filter, washed with 2 x 5 mL MeCN/ $Et_2O$  (1:6), redissolved in MeCN, and the solvent removed *in vacuo* leaving a white crystalline material of the Pd-complex in good yield (40.7 mg, 90%). Crystals

suitable for single-crystal X-ray diffraction were obtained from the vapor diffusion.  $^1\text{H}$  NMR (400 MHz,  $\text{CD}_3\text{CN}$ )  $\delta$  7.47 (d,  $J = 2.0$  Hz, 2H), 7.34 – 7.26 (*overlapping multiplet*, 6H), 7.08 (d,  $J = 2.0$  Hz, 2H), 6.95 – 6.88 (*overlapping multiplet*, 4H), 6.05 (d,  $J = 13.6$  Hz, 1H), 5.86 (d,  $J = 13.6$  Hz, 1H), 4.83 (d,  $J = 15.1$  Hz, 2H), 4.63 (d,  $J = 15.1$  Hz, 2H).  $^{13}\text{C}$  NMR (101 MHz,  $\text{CD}_3\text{CN}$ )  $\delta$  170.52, 136.69, 130.00, 129.40, 128.39, 124.13, 123.55, 64.61, 55.06.  $^{19}\text{F}$  NMR (377 MHz,  $\text{CD}_3\text{CN}$ )  $\delta$  -72.95 (d,  $J = 706.7$  Hz).  $^{31}\text{P}$  NMR (162 MHz,  $\text{CD}_3\text{CN}$ )  $\delta$  -144.62 (hep,  $J = 706.7$  Hz). **Elemental analysis** calcd (%) for  $\text{C}_{42}\text{H}_{40}\text{F}_{12}\text{N}_8\text{P}_2\text{Pd}$ : C 47.9, H 3.83, N 10.64; found: C 47.78, H 4.09, N 10.23.

Complex **4.10** [ $(^{\text{Et}}\text{L})_2\text{Pd}$ ]  $2\text{PF}_6$  from transmetalation *via* complex **4.6**. A 20 mL scintillation vial equipped with a stir bar was charged with  $\text{PdCl}_2(\text{MeCN})_2$  (37.6 mg, 0.145 mmol, 1.02 equiv.) and dissolved in MeCN (10 mL). To the now yellow solution was added complex **4.6** (169 mg, 0.142 mmol, 1.0 equiv.), and the mixture was heated to 70°C overnight. The now colorless solution was cooled to RT, filtered through Celite, concentrated to ~1 mL, placed inside a 5 mL glass vial, which was placed inside a 20 mL scintillation vial containing  $\text{Et}_2\text{O}$ , and left for overnight  $\text{Et}_2\text{O}$ -vapour diffusion at RT. The resulting white powder was collected on a glass-fiber filter, washed with 2 x 5 mL MeCN/ $\text{Et}_2\text{O}$  (1:6), redissolved in MeCN, and the solvent removed *in vacuo* leaving a white crystalline material of the Pd-complex in good yield (140 mg, 91%). Crystals suitable for single-crystal X-ray diffraction were obtained from the vapor diffusion.  $^1\text{H}$  NMR (400 MHz,  $\text{CD}_3\text{CN}$ )  $\delta$  7.32 – 7.25 (*overlapping multiplet*, 3H), 7.05 (d,  $J = 2.0$  Hz, 1H), 6.91 (d,  $J = 2.0$  Hz, 1H), 6.72 – 6.65 (*multiplet*, 2H), 4.95 – 4.78 (*multiplet*, 1H), 4.74 (s, 2H), 4.55 – 4.40 (*multiplet*, 1H).  $^{13}\text{C}$  NMR (101 MHz,  $\text{CD}_3\text{CN}$ )  $\delta$  167.82 (C2-Pd), 136.93, 130.01, 128.92, 126.62, 124.73, 124.33, 54.63, 48.69.  $^{19}\text{F}$  NMR (377 MHz,  $\text{CD}_3\text{CN}$ )  $\delta$  -72.95 (d,  $J = 706.7$  Hz).  $^{31}\text{P}$  NMR (162 MHz,  $\text{CD}_3\text{CN}$ )  $\delta$  -144.62 (hep,  $J =$

706.7 Hz). **Elemental analysis** calcd (%) for  $C_{44}H_{44}F_{12}N_8P_2Pd$ : C 48.88, H 4.10, N 10.36; found: C 48.33, H 4.10, N 10.38.

Complex **4.15**,  $[(^{Me,Naph}L)_2Ag_2]_2 4PF_6$ . A 20 mL scintillation vial equipped with a stir bar was added compound **3.2** (150 mg, 126.6  $\mu$ mol, 1.0 equiv.),  $AgPF_6$  (64.7 mg, 64.7  $\mu$ mol, 2.02 equiv.) and  $K_2CO_3$  (175 mg, 1.3 mmol, 10.0 equiv.), before 10 mL of MeCN was added to the powders. The vial was sealed and wrapped in foil and placed atop a stir plat, heating to 55°C overnight. An aliquot was taken to ensure the reaction was completed before the mixture was cool to RT, and the suspension passed through a Celite filter to remove excess  $K_2CO_3$ , which was washed with further 2 x 5 mL MeCN. The combined organic phases were dried over  $MgSO_4$ , the suspension was filtered from  $MgSO_4$ , and the filtrate reduced in vacuo to a total volume of ~2 mL, which was divided into two 5 mL glass vials, which were placed inside a 20 mL scintillation vial covered in foil, containing  $Et_2O$ , and left for overnight  $Et_2O$ -vapour diffusion at RT. The resulting white powder was collected on a glass-fiber filter, washed with 2 x 5 mL MeCN/ $Et_2O$  (1:9), redissolved in MeCN, and the solvent removed *in vacuo* leaving a white light-sensitive crystalline material of Ag complex in good yield (118 mg, 84.2%). Crystals were obtained from slow evaporation of solvent from a concentrated solution of the title compound in MeCN. Unable to obtain a satisfactory elemental analysis.  $^1H$  NMR (400 MHz,  $CD_3CN$ )  $\delta$  8.09 (d,  $J$  = 8.2 Hz, 1H), 7.97 (d,  $J$  = 7.0 Hz, 1H), 7.81 (d,  $J$  = 8.2 Hz, 1H), 7.73 – 7.64 (*overlapping multiplet*, 2H), 7.43 (d,  $J$  = 1.9 Hz, 1H), 7.10 (d,  $J$  = 1.9 Hz, 1H), 6.96 (t,  $J$  = 7.8 Hz, 1H), 6.63 – 6.43 (*overlapping multiplet*, 4H), 6.01 – 5.86 (*overlapping multiplet*, 2H), 5.56 (d,  $J$  = 14.0 Hz, 2H).  $^{13}C$  NMR (201 MHz,  $CD_3CN$ )  $\delta$  182.66, 182.59, 182.09, 182.02, 181.68, 181.61, 181.11, 181.04, 136.91, 136.28, 133.20, 132.78, 130.88, 130.86, 130.15, 129.81, 127.06, 126.52, 124.67, 124.50, 124.32, 124.29, 121.08, 64.33, 59.18, 57.20. C-Ag couplings  $^1J(^{109}Ag-^{13}C[182.7, 181.6]) = 209.5Hz$ ,  $^1J(^{107}Ag-^{13}C[182.6,$

181.7]) = 182.4 Hz;  $^1J(^{109}\text{Ag}-^{13}\text{C})$  [182.1, 181.0]) = 211.4 Hz and  $^1J(^{107}\text{Ag}-^{13}\text{C})$  [182.0, 181.1]) = 183.2 Hz.  $^{19}\text{F}$  NMR (377 MHz,  $\text{CD}_3\text{CN}$ )  $\delta$  -71.1 (d,  $J$  = 711 Hz).  $^{31}\text{P}$  NMR (162 MHz,  $\text{CD}_3\text{CN}$ )  $\delta$  -144.62 (hep,  $J$  = 711 Hz).

**Complex 4.13.** [ $^{\text{Me,Naph}}\text{LPd}$ ]  $2\text{PF}_6$ , from transmetalation *via* complex **4.15**. A 20 mL scintillation vial equipped with a stir bar was added  $\text{PdCl}_2(\text{MeCN})_2$  (33.7 mg, 0.13 mmol, 2.05 equiv.) and 10 mL MeCN, which was stirred for 5 minutes resulting in a yellow/orange solution. Complex **4.15** (140 mg, 63.3  $\mu\text{mol}$ , 1.0 equiv.) was then added, the stir plated heated to 70°C overnight. The following day, an aliquot was taken for NMR corroborating full consumption of the Ag-intermediate, before it was removed and allowed to cool to RT. The suspension was passed through Celite, which was washed with an additional 2 x 5 mL MeCN. The combined organic phases were dried over  $\text{MgSO}_4$ , the suspension was filtered from  $\text{MgSO}_4$ , and the filtrate reduced in vacuo to a total volume of ~2 mL, which was divided into two 5 mL glass vials, which were placed inside a 20 mL scintillation vial covered in foil, containing  $\text{Et}_2\text{O}$ , and left for overnight  $\text{Et}_2\text{O}$ -vapour diffusion at RT. The resulting white powder was collected on a glass-fiber filter, washed with 2 x 5 mL MeCN/ $\text{Et}_2\text{O}$  (1:9), redissolved in MeCN, and the solvent removed *in vacuo* leaving an off-white crystalline material of the Pd complex in excellent yield (117 mg, 93%). Crystals suitable for X-ray diffraction were produced by slow solvent evaporation at RT from a concentrated solution of the complex in MeCN.  $^1\text{H}$  NMR (400 MHz,  $\text{CD}_3\text{CN}$ )  $\delta$  8.16 (d,  $J$  = 8.2 Hz, 2H), 7.81 (d,  $J$  = 6.8 Hz, 2H), 7.65 (t,  $J$  = 8.2, 6.8 Hz, 2H), 7.47 (d,  $J$  = 2.0 Hz, 2H), 6.90 (d,  $J$  = 2.0 Hz, 2H), 6.46 (d,  $J$  = 13.1 Hz, 1H), 6.22 (d,  $J$  = 13.1 Hz, 1H), 5.51 (d,  $J$  = 15.8 Hz, 2H), 5.08 (d,  $J$  = 15.8 Hz, 2H).  $^{13}\text{C}$  NMR (101 MHz,  $\text{CD}_3\text{CN}$ )  $\delta$  167.86, 138.21, 136.45, 133.74, 132.19, 130.32, 127.06, 124.52, 121.36, 63.84, 57.21.  $^{19}\text{F}$  NMR (377 MHz,  $\text{CD}_3\text{CN}$ )  $\delta$  -71.1 (d,  $J$  = 711 Hz).  $^{31}\text{P}$  NMR (162 MHz,  $\text{CD}_3\text{CN}$ )  $\delta$  -144.62 (hep,  $J$  = 711 Hz). **Elemental analysis** calcd (%)



for  $C_{38}H_{32}F_{12}N_8P_2Pd$ :C 45.78 H. 3.24, N.11.24; found: C 46.69 H 3.87, N 10.01. Crystals were obtained from slow solvent evaporation from a concentrated solution of the complex in MeCN.

Complex **4.18**,  $[^{Me,Naph}LNi] 2PF_6$ . Analogous preparation to the Pd-congener, however,  $NiCl_2(dme)$  was used as Ni (II) source.  $NiCl_2(dme)$  (20.4 mg, 93  $\mu$ mol, 2.05 equiv.) was dissolved in 10 mL MeCN, before complex **4.15** (100 mg, 45.2  $\mu$ mol, 1.0 equiv.) was added to the solution and the mixture was heated to 70°C overnight. Recrystallization was achieved by slow diffusion of  $Et_2O$  into a solution of the complex in acetone, leaving a colorless powder in good yield (38.2 mg, 89%). Residual acetone was found in the  $^1H$  NMR spectrum as well as in the E.A.  $^1H$  NMR (400 MHz,  $CD_3CN$ )  $\delta$  8.12 (d,  $J$  = 8.1 Hz, 2H), 7.73 (d,  $J$  = 7.0 Hz, 2H), 7.60 (dd,  $J$  = 8.1, 7.0 Hz, 2H), 7.42 (d,  $J$  = 1.9 Hz, 2H), 6.83 – 6.66 (*overlapping multiplet*, 3H), 6.20 (d,  $J$  = 12.7 Hz, 1H), 5.07 (d,  $J$  = 16.3 Hz, 2H), 4.82 (d,  $J$  = 16.2 Hz, 2H).  $^{13}C$  NMR (101 MHz,  $CD_3CN$ )  $\delta$  169.77, 138.42, 135.54, 133.63, 131.49, 131.37, 126.82, 124.41, 122.25, 63.07, 57.50, 1.32.  $^{19}F$  NMR (377 MHz,  $CD_3CN$ )  $\delta$  -71.1 (d,  $J$  = 711 Hz).  $^{31}P$  NMR (162 MHz,  $CD_3CN$ )  $\delta$  -144.62 (hep,  $J$  = 711 Hz). **Elemental analysis** calcd (%) for  $C_{41}H_{42}F_{12}N_8P_2NiO_3$ :C 47.19, H. 4.06, N.10.74; found: C 47.27 H 4.04, N 11.31. Crystals were obtained from slow solvent evaporation from a concentrated solution of the complex in MeCN.

Complex **4.14**,  $[^{Et,Naph}LPd] 2PF_6$ , from transmetalation *via* complex **4.16**. A 25 mL round-bottom flask wrapped in foil was charged with  $^{Et}LH_4-4Br$  (100 mg, 0.105 mmol, 1.0 equiv.),  $Ag_2O$  (128 mg (95 w/w%, 0.525 mmol, 5.0 equiv.), and added MeOH (25 mL). The flask was fitted with a reflux condenser (also covered in foil), and the mixture was heated to gentle reflux for around 12 hours. The mixture was filtered hot through Celite, washed with MeOH (2 x 5 mL), and all MeOH was removed from the combined fraction leaving behind a black solid. This solid was passed through a silica plug eluting in MeCN,

removed *in vacuo*, leaving behind a highly light-sensitive white powder of the silver trimer [EtLAg<sub>2</sub>]<sub>3</sub> 6Br (83 mg, 89% yield). *The isolation should be expedited as the powder quickly decompose and, if stored, should be kept cold in a foil-wrapped container.* Colorless crystals suitable for X-ray diffraction were obtained over several weeks, in the dark, from slow vapor diffusion at -18°C of Et<sub>2</sub>O into a MeCN solution, as well as from slow evaporation of MeCN from a concentrated solution. <sup>1</sup>H NMR (400 MHz, MeOH-*d*<sub>4</sub>) δ 8.10 (dd, *J* = 8.3, 1.3 Hz, 2H), 7.81 (dd, *J* = 7.2, 1.3 Hz, 2H), 7.70 (dd, *J* = 8.3, 7.2 Hz, 2H), 7.37 (d, *J* = 7.8 Hz, 2H), 6.66 – 6.57 (*overlapping multiplets*, 3H), 6.32 (d, *J* = 15.8 Hz, 2H), 6.23 (d, *J* = 15.8 Hz, 2H), 5.97 (t, *J* = 7.8 Hz, 2H), 5.69 (td, *J* = 13.9, 4.9 Hz, 2H), 5.39 (d, *J* = 15.2 Hz, 2H), 5.29 (d, *J* = 7.8 Hz, 2H), 4.51 (td, *J* = 14.0, 4.9 Hz, 2H), 3.93 (dd, *J* = 15.2, 4.9 Hz, 2H), 3.64 (dd, *J* = 14.0, 4.9 Hz, 2H). <sup>13</sup>C NMR (101 MHz, MeOD-*d*<sub>4</sub>) δ 188.73, 186.80, 186.65, 181.35, 181.19, 179.42, 137.35, 136.27, 133.54, 132.98, 131.43, 129.70, 129.60, 126.65, 125.08, 124.34, 121.17, 59.53, 56.54, 52.19, 51.92. Unable to obtain a satisfactory elemental analysis.

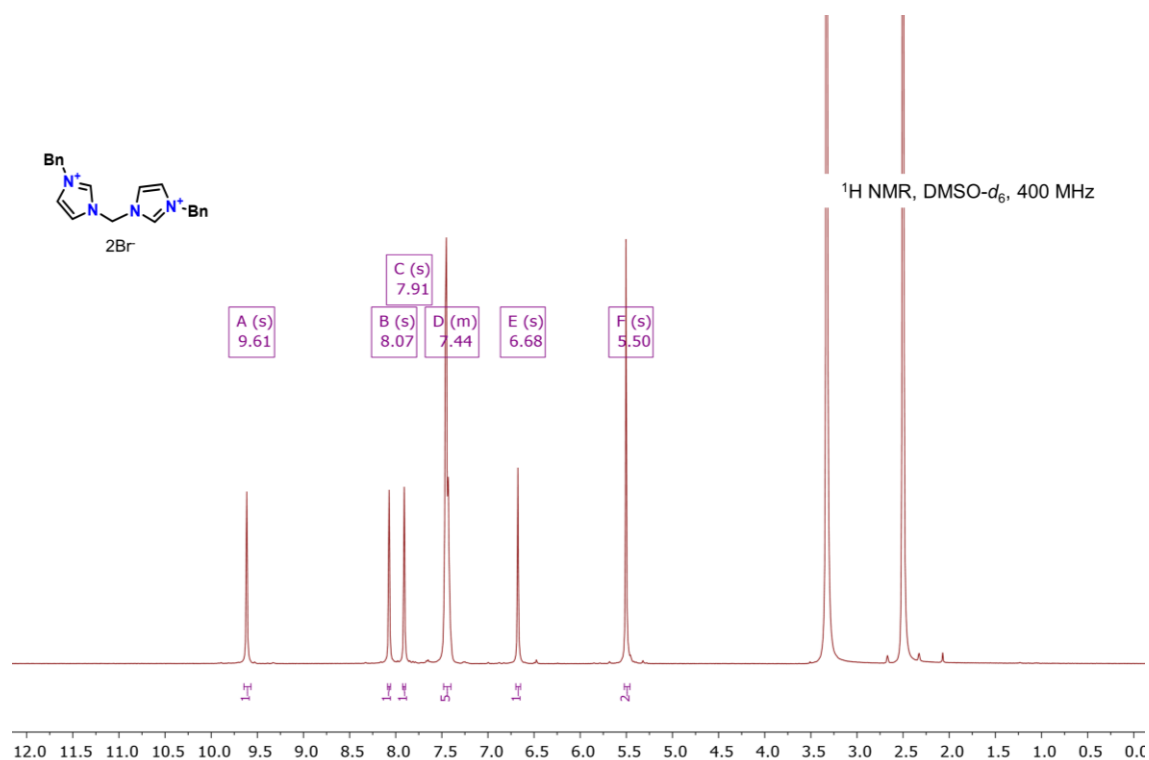
A 25 mL round-bottom flask was charged with PdCl<sub>2</sub> (19.7 mg, 0.11 mmol, 1.06 equiv.), suspended in 10 mL MeCN, before [EtLAg<sub>2</sub>]<sub>3</sub> 6Br (92.8 mg, 37 μmol, 0.33 equiv.) was added, the flask was fitted a reflux condenser before the mixture was brought to gentle reflux for 10 hours. An aliquot was taken for NMR corroborating full consumption of the Ag-intermediate, and the mixture was added NaPF<sub>6</sub> (37 mg, 0.22 mmol, 2.2 equiv.), and heated to reflux for another 2 hours. The solution was cooled to rt, filtered through Celite, concentrated to ~1 mL, placed inside a 5 mL glass vial, which was placed inside a 20 mL scintillation vial containing Et<sub>2</sub>O, and left for overnight Et<sub>2</sub>O-vapour diffusion at rt. The resulting white powder was collected on a glass-fiber filter, washed with 2 x 5 mL MeCN/Et<sub>2</sub>O (1:9), redissolved in MeCN, and the solvent removed *in vacuo* leaving a white crystalline material of the Pd-complex in good yield (85.2 mg, 79%). <sup>1</sup>H NMR (400

MHz, CD<sub>3</sub>CN)  $\delta$  8.00 (dd,  $J$  = 8.0, 1.6 Hz, 2H), 7.88 (dd,  $J$  = 8.0, 1.6 Hz, 2H), 7.68 (dt,  $J$  = 7.0, 1.3 Hz, 2H), 7.65 – 7.53 (*overlapping multiplets*, 8H), 7.29 (d,  $J$  = 2.0 Hz, 2H), 6.99 (d,  $J$  = 2.1 Hz, 2H), 6.80 (d,  $J$  = 2.1 Hz, 2H), 6.06 (d,  $J$  = 15.5 Hz, 2H), 5.61 (d,  $J$  = 15.5 Hz, 2H), 5.13 (ddd,  $J$  = 15.0, 7.3, 4.7 Hz, 2H), 4.89 (ddd,  $J$  = 15.0, 7.3, 4.7 Hz, 2H), 4.55 – 4.33 (*overlapping multiplets*, 6H), 3.92 (d,  $J$  = 15.9 Hz, 2H). <sup>13</sup>C NMR (101 MHz, CD<sub>3</sub>CN)  $\delta$  168.03, 167.93, 137.33, 134.67, 134.31, 133.46, 132.69, 132.48, 131.88, 129.97, 127.88, 126.44, 125.66, 124.55, 123.88, 122.08, 118.30, 54.91, 54.18, 49.74, 48.47. <sup>19</sup>F NMR (377 MHz, CD<sub>3</sub>CN)  $\delta$  -72.95 (d,  $J$  = 711.2 Hz). <sup>31</sup>P NMR (162 MHz, CD<sub>3</sub>CN)  $\delta$  -144.62 (hep,  $J$  = 711.2 Hz).

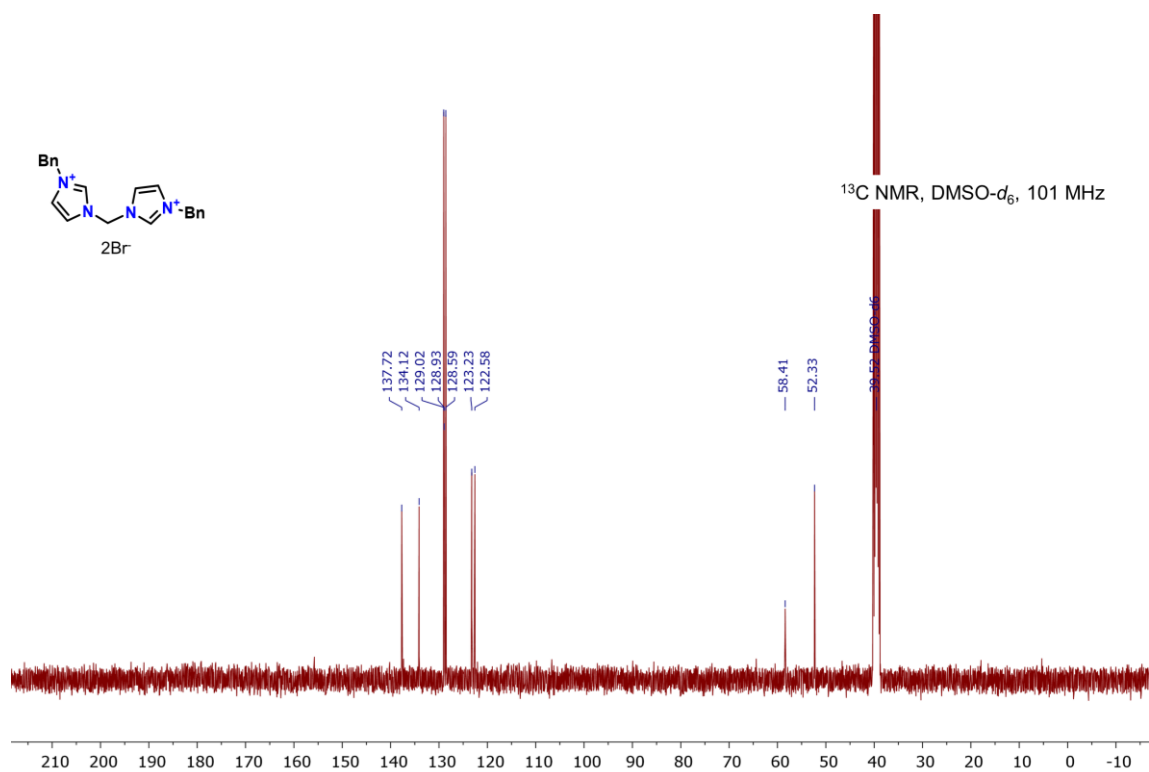
Complex **4.14** as Br salt, [Et<sub>3</sub>Naph]LPd] 2Br. *From deprotonation-metalation.* A 25 mL round-bottom flask was charged with compound **3.4** (100 mg, 0.105 mmol, 1.0 equiv.), K<sub>2</sub>CO<sub>3</sub> (218 mg, 1.57 mmol, 15.0 equiv.), PdCl<sub>2</sub> (19.6 mg, 0.11 mmol, 1.05 equiv.), and the powders were suspended in MeCN (11 mL, ~10 mM w.r.t to macrocycle). The flask was fitted with a reflux condenser, and the mixture was heated to gentle reflux for around 18 hours. The mixture was filtered hot through Celite, washed with MeCN (2 x 5 mL), the combined MeCN fraction was concentrated to ~ 1 mL, placed inside a 5 mL glass vial, which was placed inside a 20 mL scintillation vial containing Et<sub>2</sub>O, and left for overnight Et<sub>2</sub>O-vapour diffusion at rt. The resulting white powder was collected on a glass-fiber filter, washed with 2 x 5 mL MeCN/Et<sub>2</sub>O (1:6), 2 x 5 mL H<sub>2</sub>O, redissolved in MeCN, and the solvent removed *in vacuo* leaving a white crystalline material of the Pd-complex in moderate yield (33.1 mg, 35%). Crystals suitable for single-crystal X-ray diffraction were obtained from slow solvent evaporation of the complex in a MeCN solution at room temperature. <sup>1</sup>H NMR (400 MHz, MeOH-*d*<sub>4</sub>)  $\delta$  8.01 (d,  $J$  = 8.0 Hz, 2H), 7.95 (d,  $J$  = 8.0 Hz, 2H), 7.79 (t,  $J$  = 5.2 Hz, 2H), 7.72 – 7.64 (*overlapping multiplets*, 4H), 7.57 (t,  $J$  = 7.6 Hz, 2H), 6.21 (d,  $J$  = 15.6 Hz, 2H), 5.78 (d,  $J$  = 15.6 Hz, 2H), 5.37 –

5.28 (*overlapping multiplets*, 2H), 5.16 – 5.04 (*overlapping multiplets*, 2H), 4.72 – 4.52 (*overlapping multiplets*, 4H), 4.03 (d,  $J = 15.7$  Hz, 2H).  $^{13}\text{C}$  NMR (101 MHz,  $\text{MeOD-}d_4$ )  $\delta$  167.92, 161.46, 137.93, 137.13, 134.88, 134.60, 133.98, 132.96, 132.25, 130.24, 129.84, 128.08, 126.50, 126.29, 71.35, 55.16, 54.72, 52.72, 52.50, 52.29.

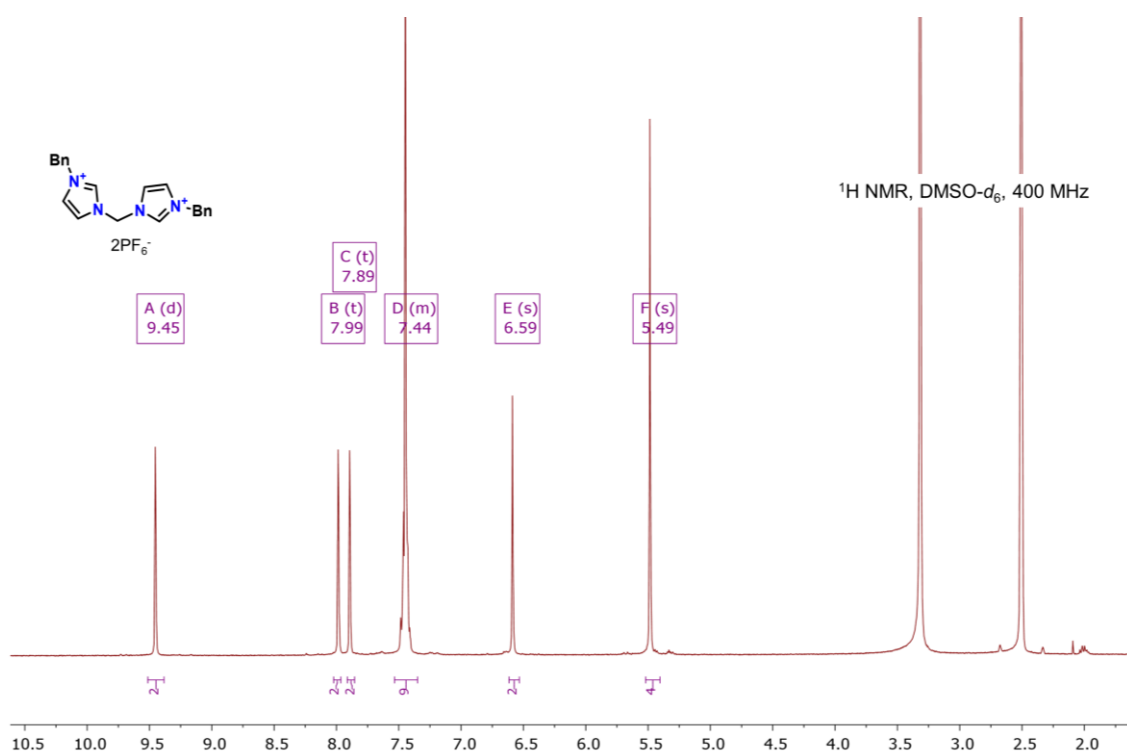
## 4.2 NMR spectra



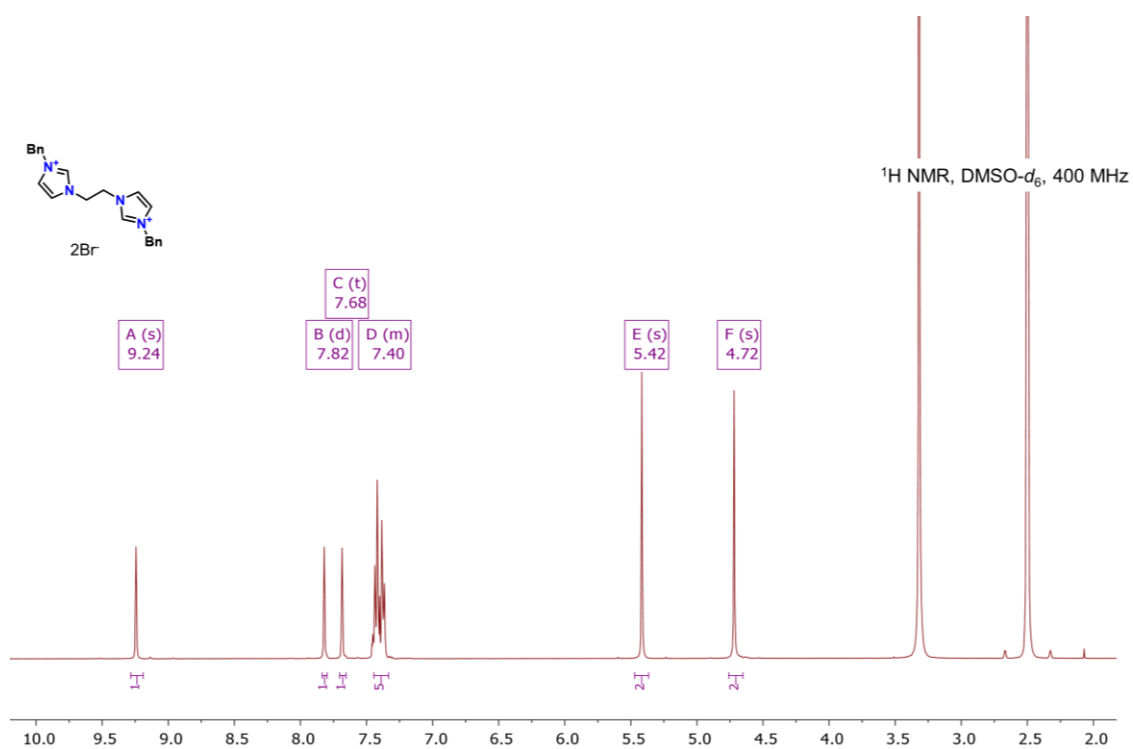
Supplementary Figure 4.1. <sup>1</sup>H NMR spectra of compound 4.1.



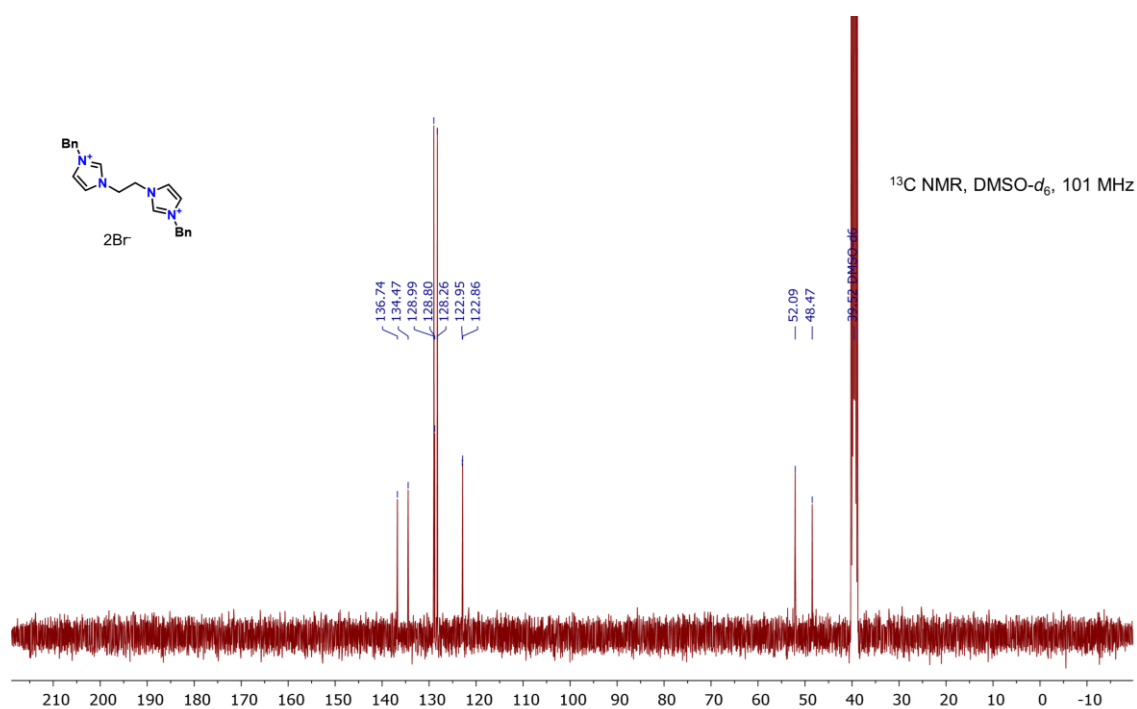
Supplementary Figure 4.2. <sup>13</sup>C NMR spectra of compound 4.1.



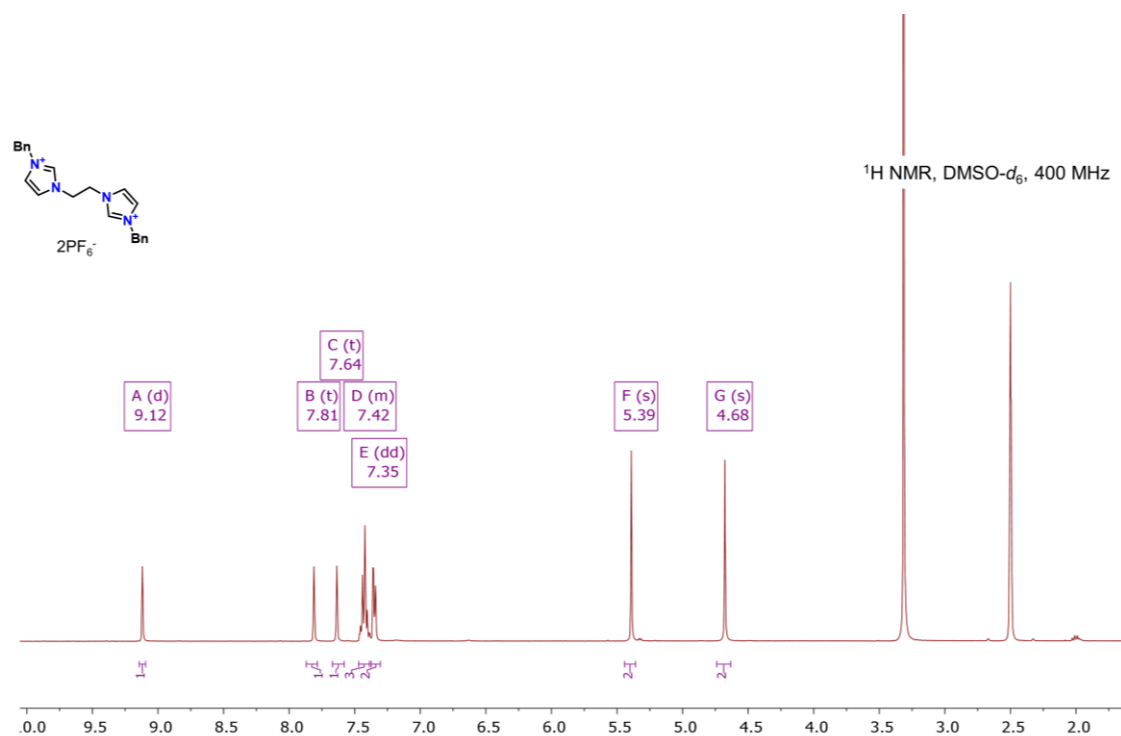
**Supplementary Figure 4.3.**  $^1\text{H}$  NMR spectra of compound 4.7.



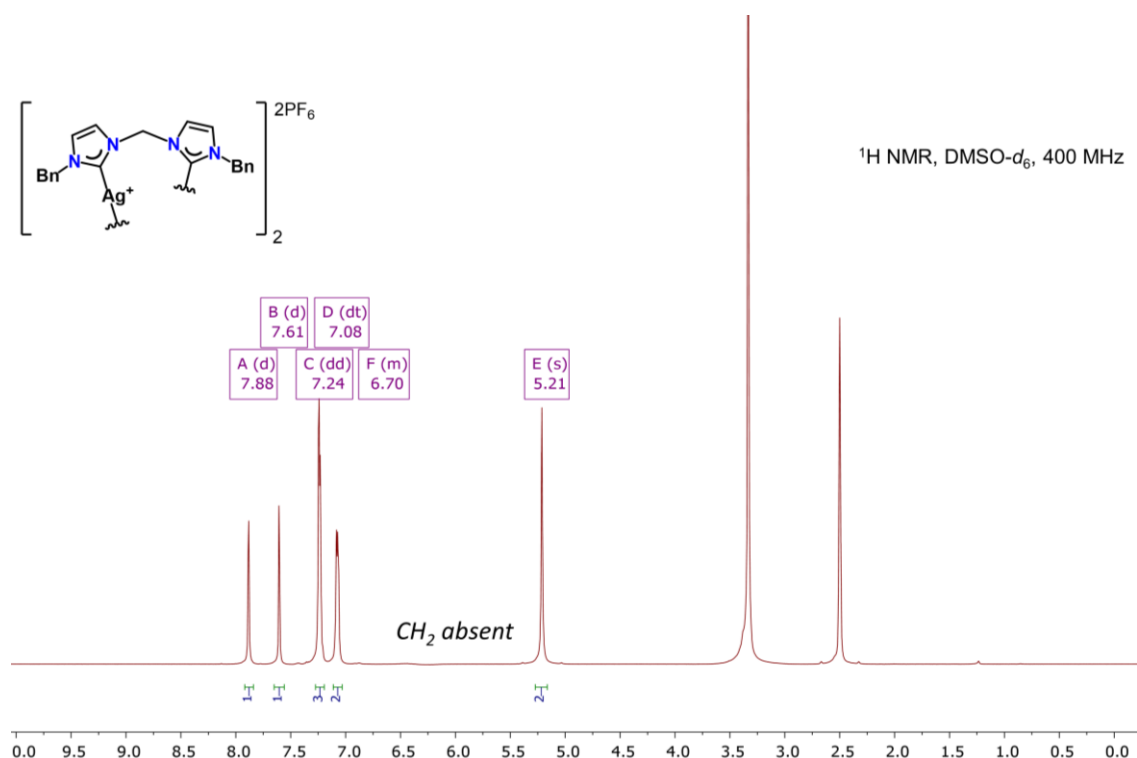
**Supplementary Figure 4.4.**  $^1\text{H}$  NMR spectra of compound 4.2.



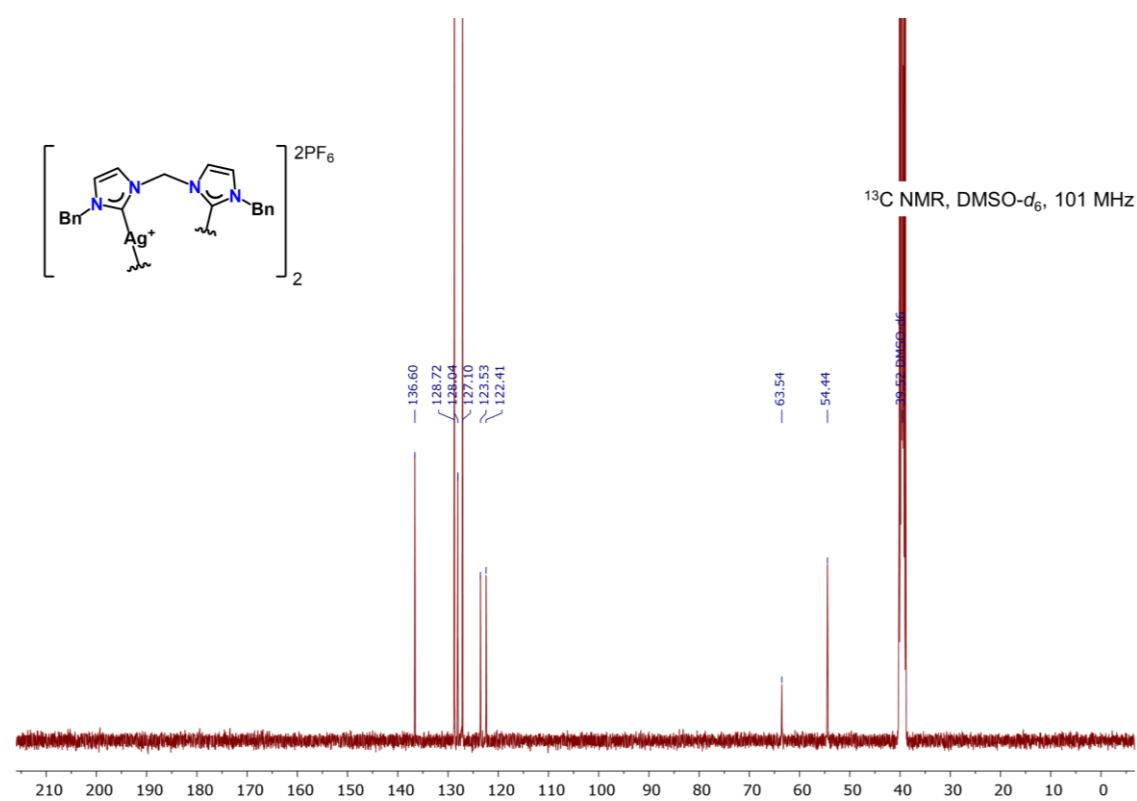
Supplementary Figure 4.5. <sup>13</sup>C NMR spectra of compound 4.2.



Supplementary Figure 4.6. <sup>1</sup>H NMR spectra of compound 4.8.

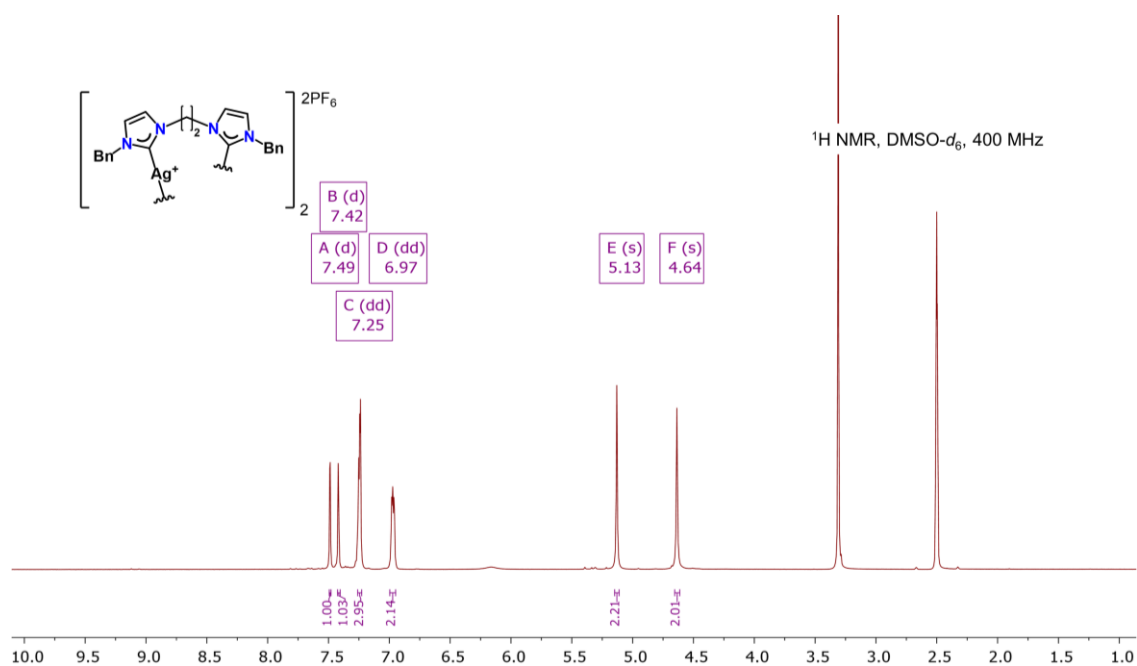


Supplementary Figure 4.7.  $^1\text{H}$  NMR spectra of compound 4.5.

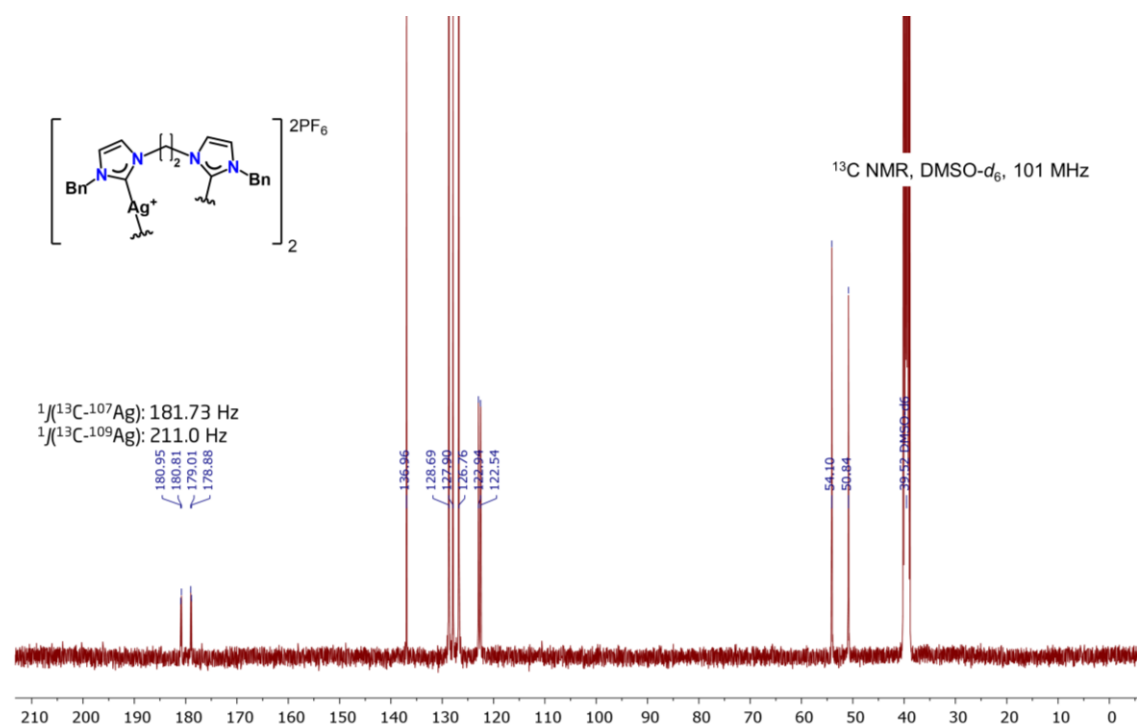


Supplementary Figure 4.8.  $^{13}\text{C}$  NMR spectra of compound 4.5.

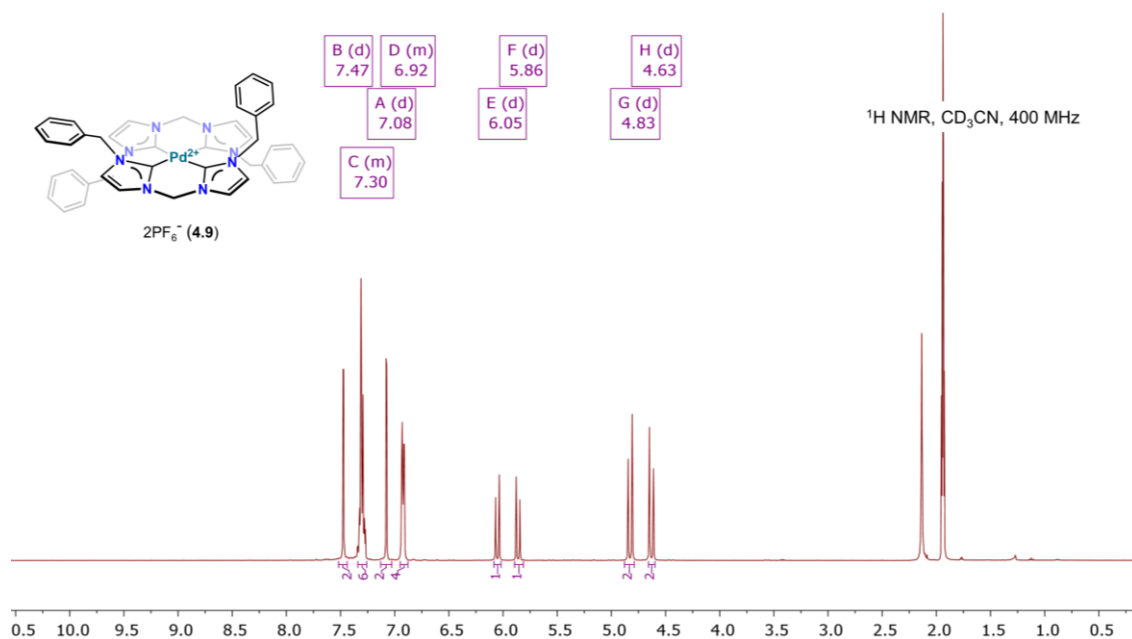




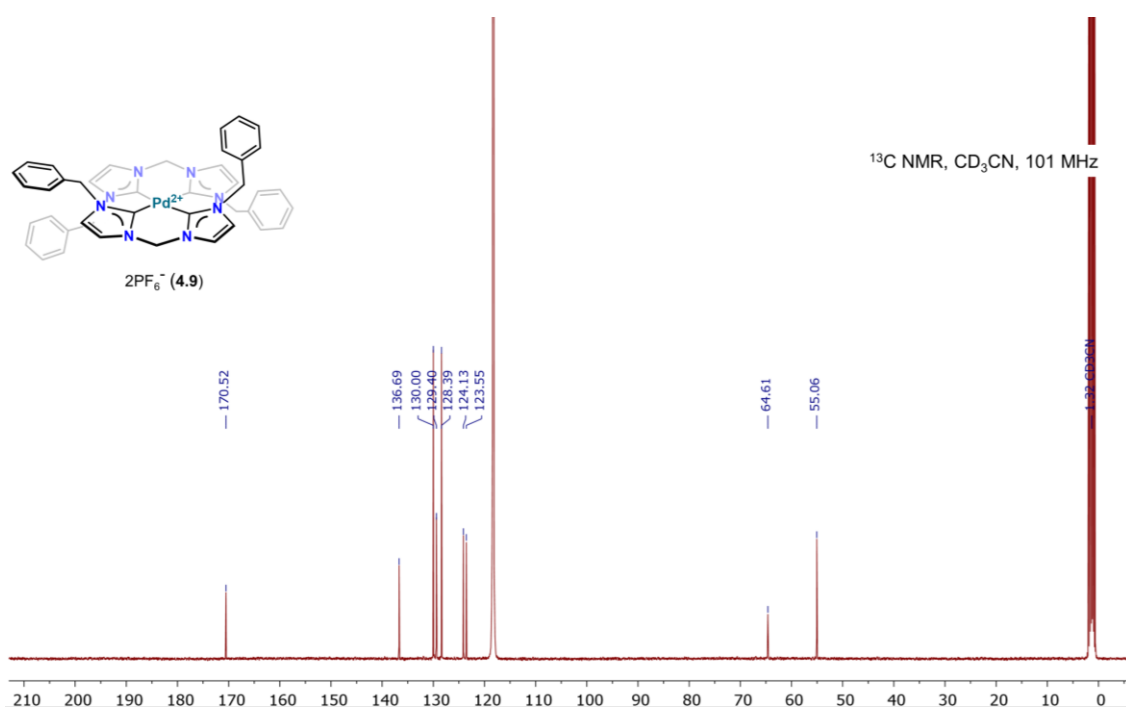
Supplementary Figure 4.9. <sup>1</sup>H NMR spectra of compound 4.6.



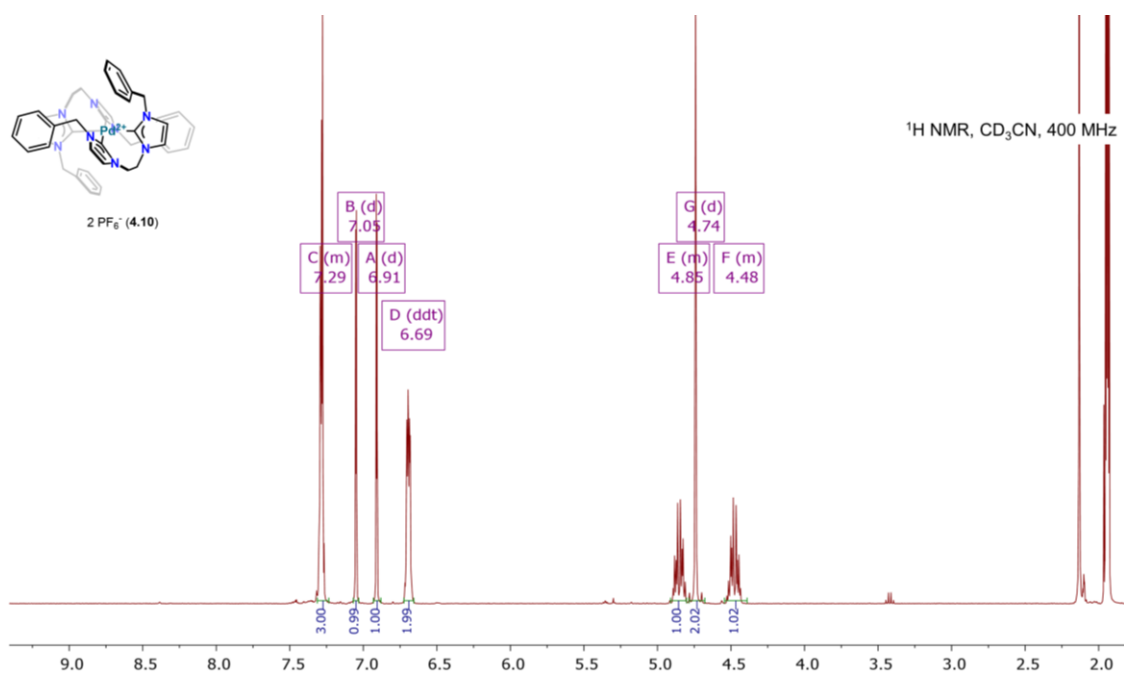
Supplementary Figure 4.10. <sup>13</sup>C NMR spectra of compound 4.6.



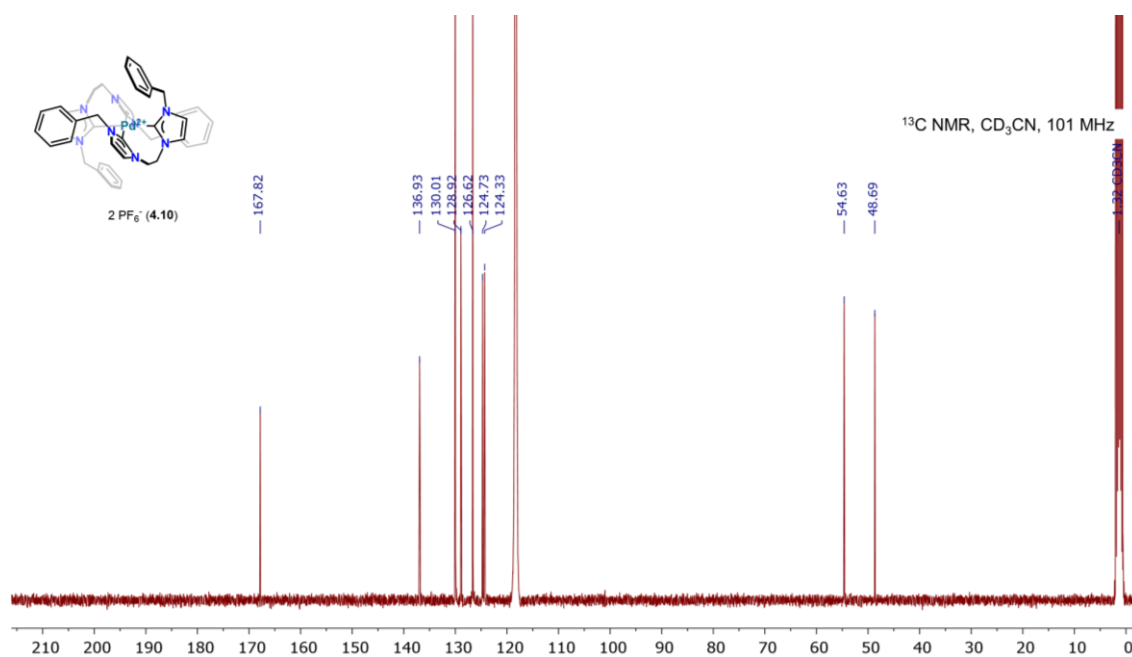
**Supplementary Figure 4.11.** <sup>1</sup>H NMR spectra of compound 4.9.



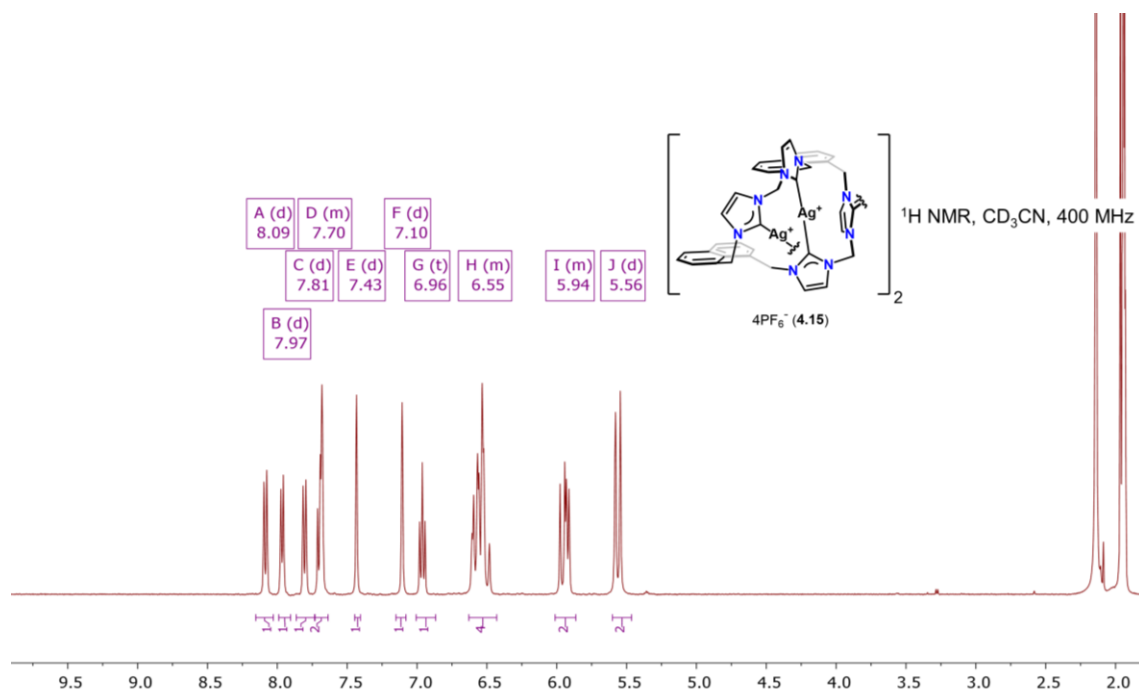
**Supplementary Figure 4.12.** <sup>13</sup>C NMR spectra of compound 4.9.



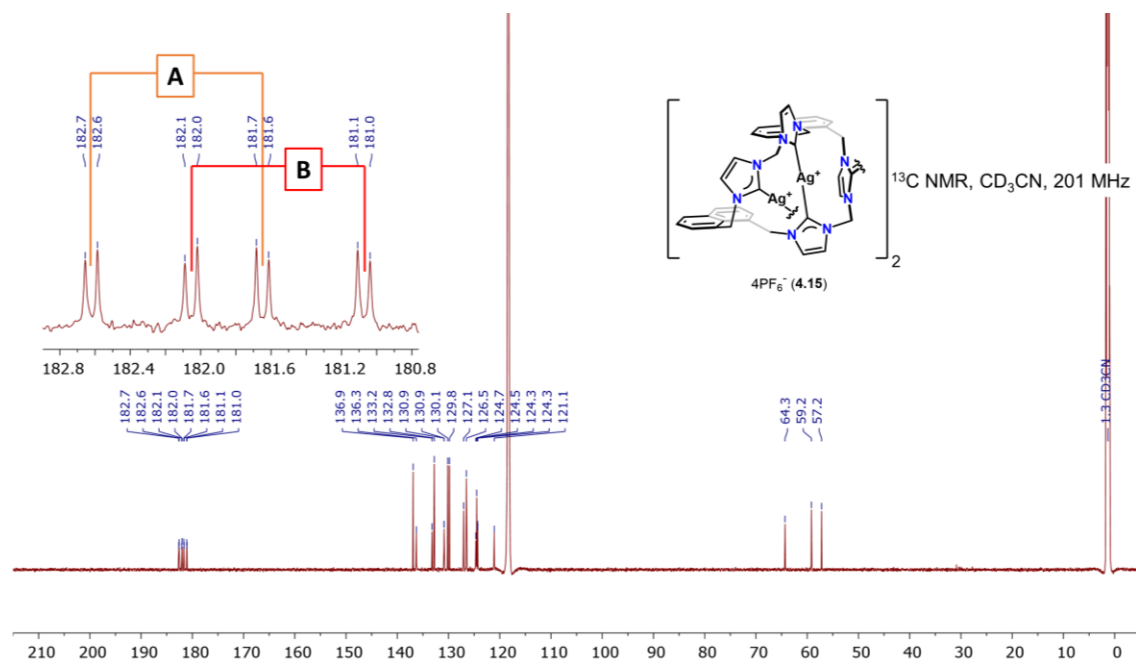
**Supplementary Figure 4.13.** <sup>1</sup>H NMR spectra of compound 4.10.



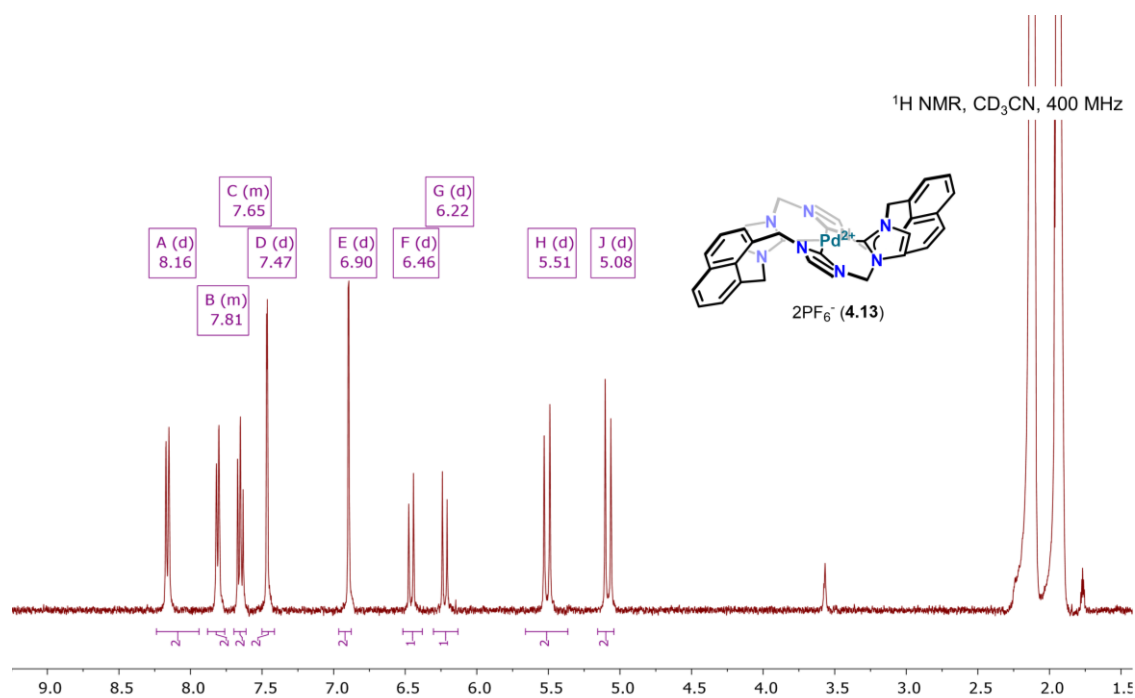
**Supplementary Figure 4.14.** <sup>13</sup>C NMR spectra of compound 4.10.



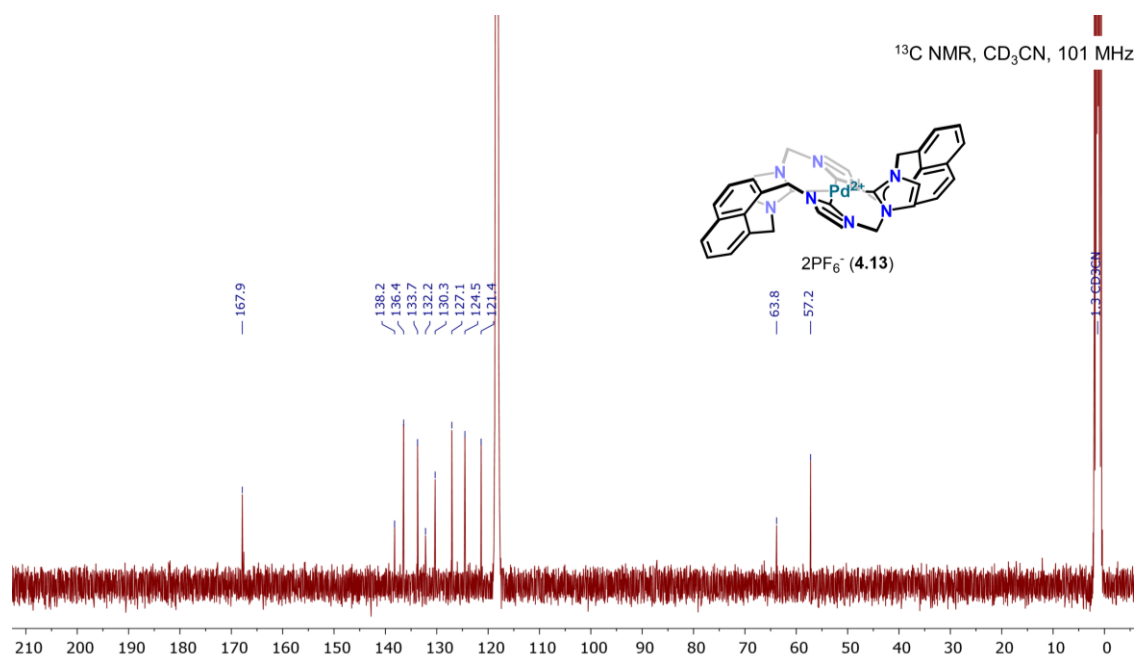
Supplementary Figure 4.15. <sup>1</sup>H NMR spectra of compound 4.15.



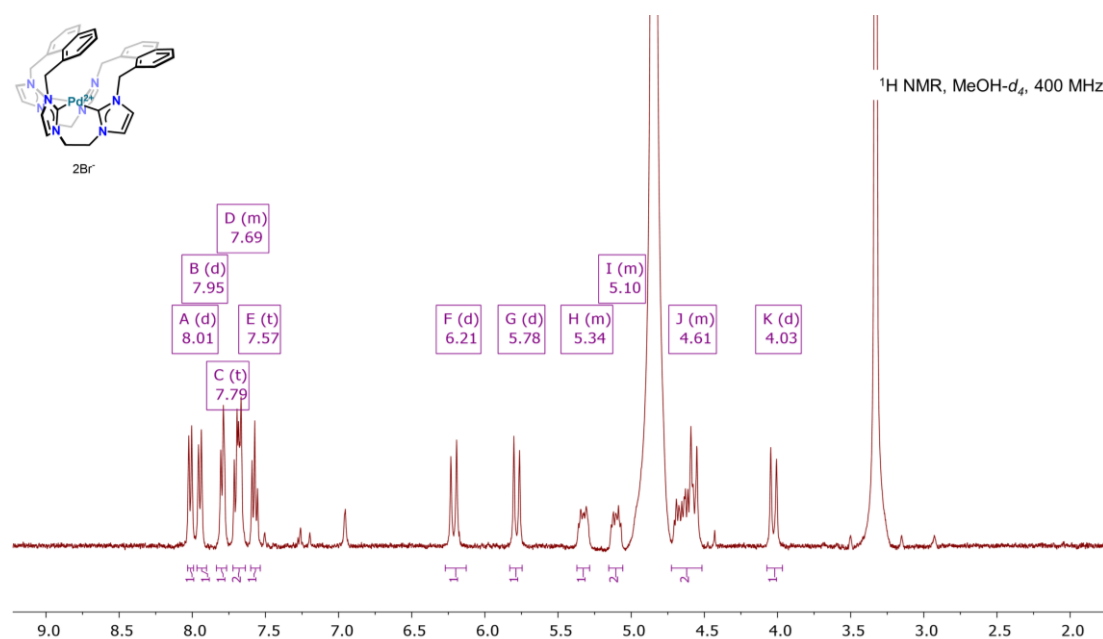
Supplementary Figure 4.16. <sup>13</sup>C NMR spectra of compound 4.15.



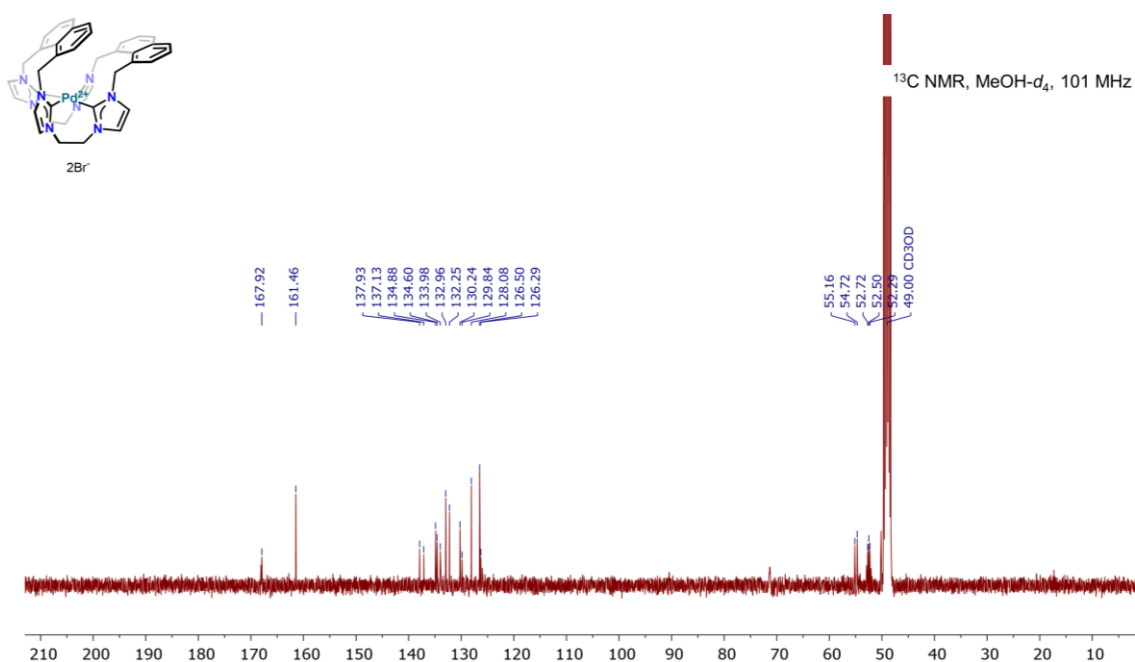
Supplementary Figure 4.17. <sup>1</sup>H NMR spectra of compound 4.13.



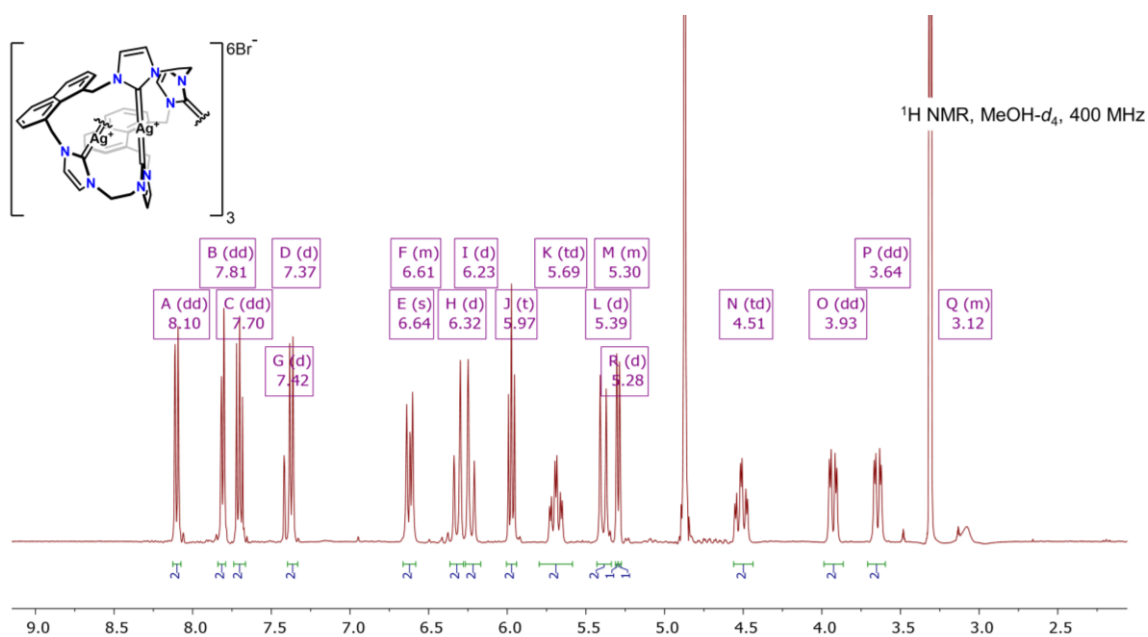
Supplementary Figure 4.18. <sup>13</sup>C NMR spectra of compound 4.13.



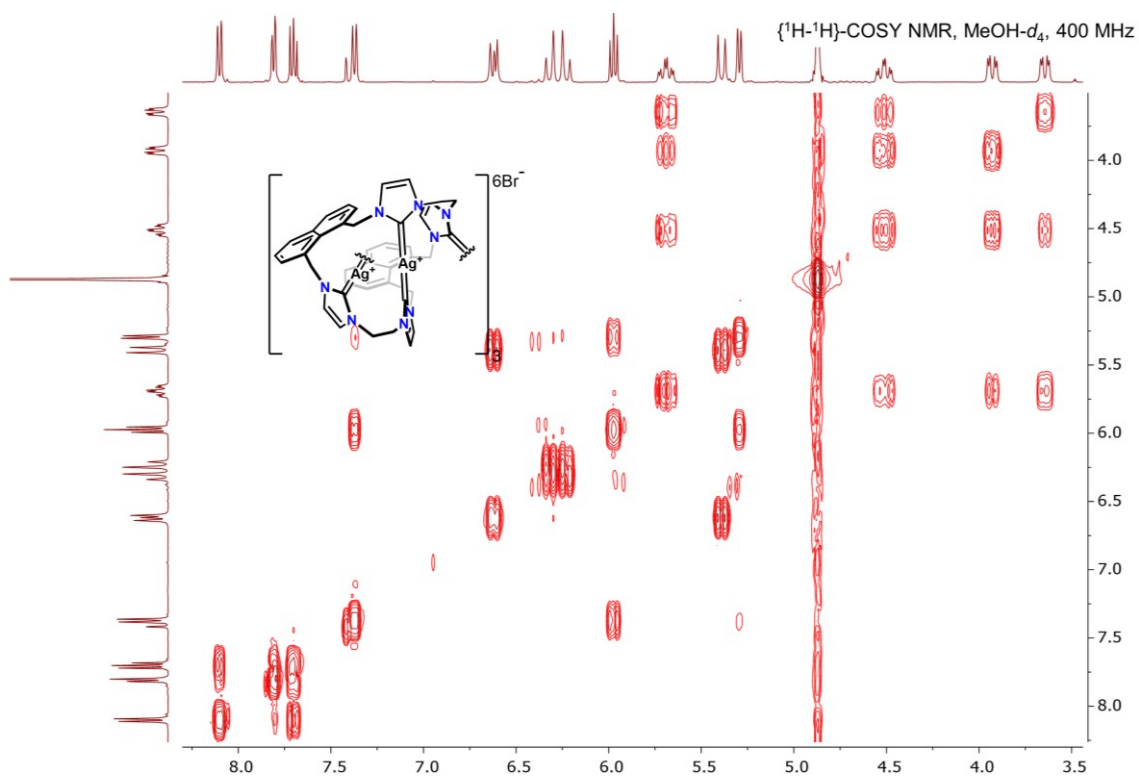
**Supplementary Figure 4.19.** <sup>1</sup>H NMR spectra of compound **4.14** (as bromide salt).



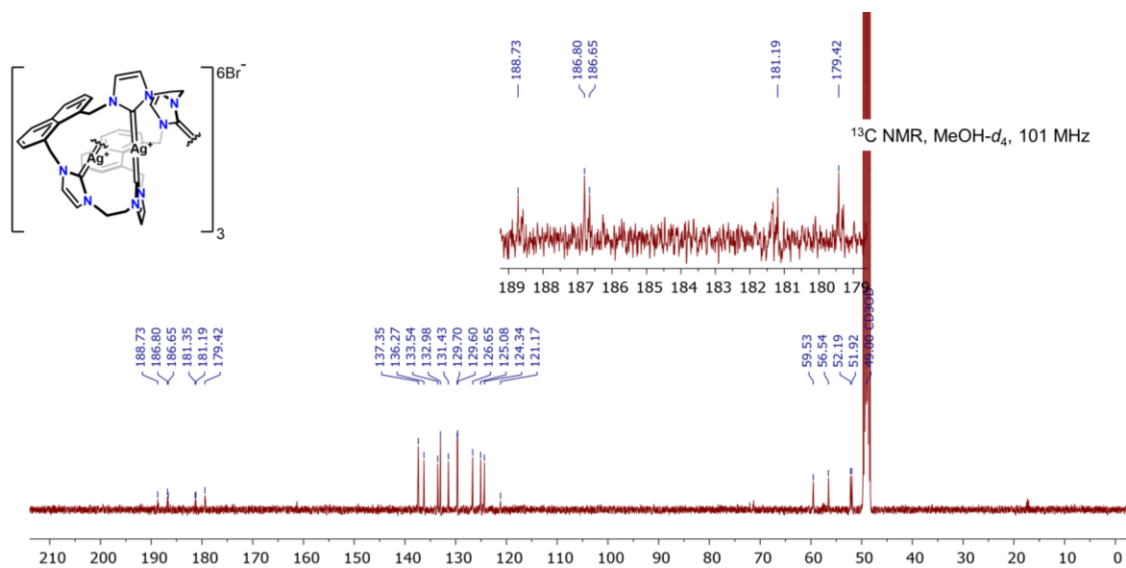
**Supplementary Figure 4.20.** <sup>13</sup>C NMR spectra of compound **4.14** (as bromide salt).



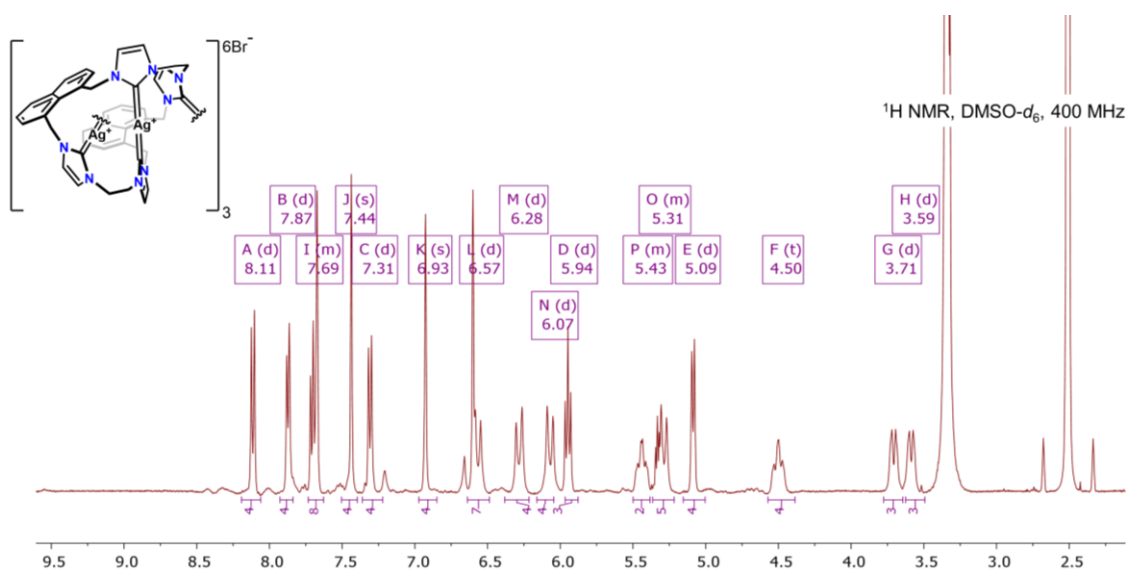
Supplementary Figure 4.21. <sup>1</sup>H NMR spectra of compound 4.16.



Supplementary Figure 4.22. {<sup>1</sup>H-<sup>1</sup>H} COSY NMR spectra of compound 4.16.

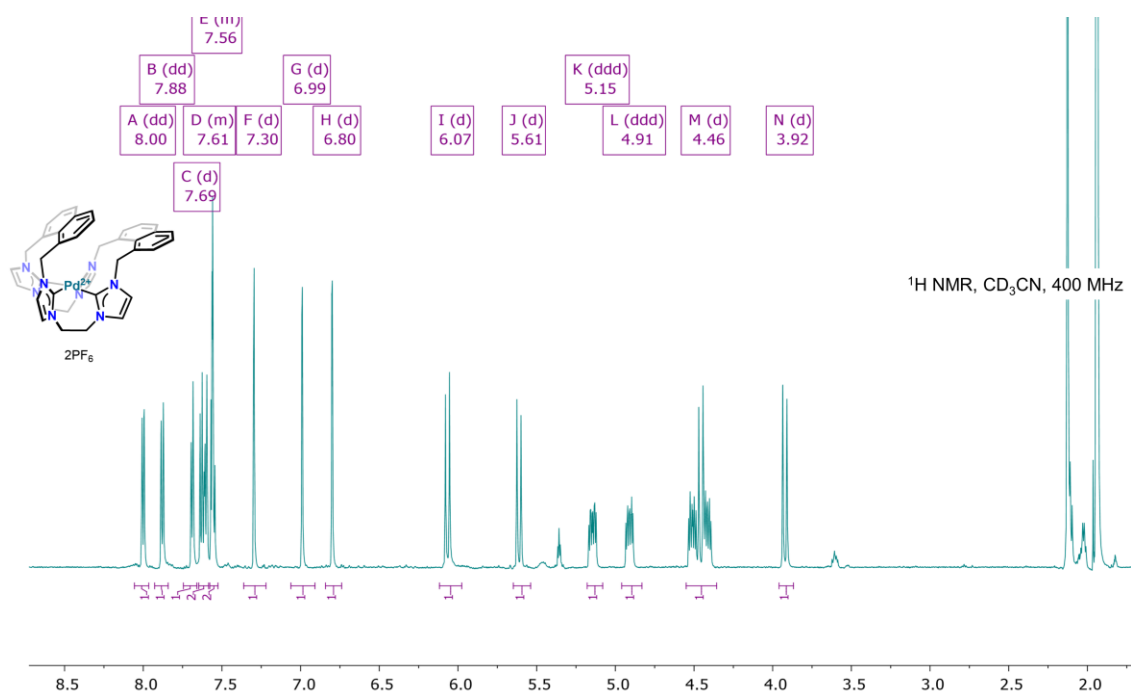


Supplementary Figure 4.23.  $^{13}\text{C}$  NMR spectra of compound 4.16.

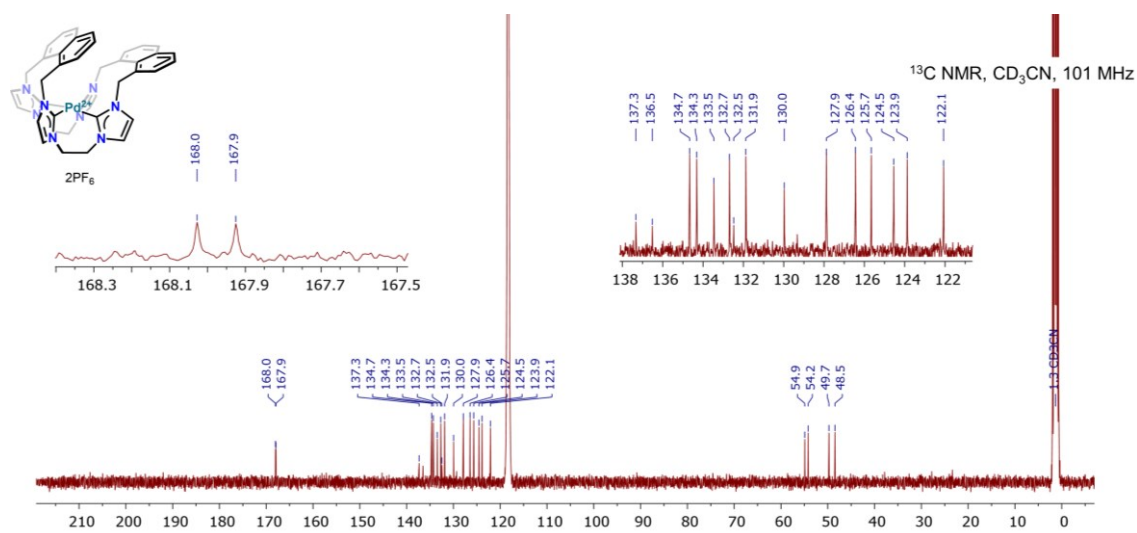


Supplementary Figure 4.24.  $^1\text{H}$  NMR spectra of compound 4.16, in DMSO- $d_6$ .

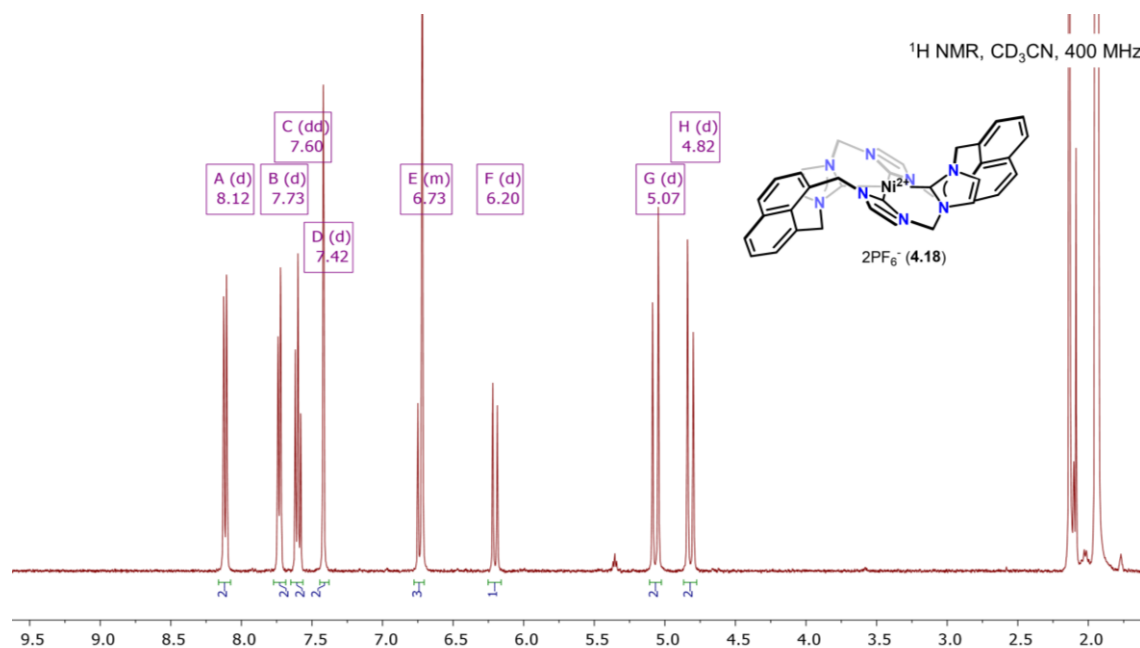




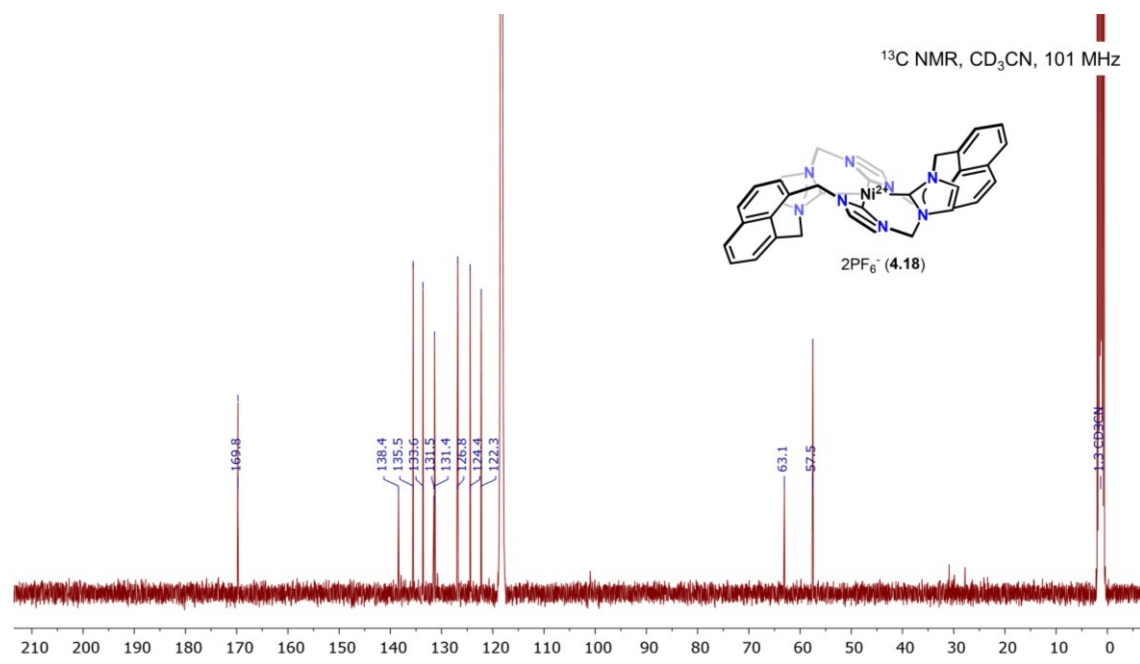
Supplementary Figure 4.25. <sup>1</sup>H NMR spectra of compound 4.14.



Supplementary Figure 4.26. <sup>1</sup>H NMR spectra of compound 4.14.

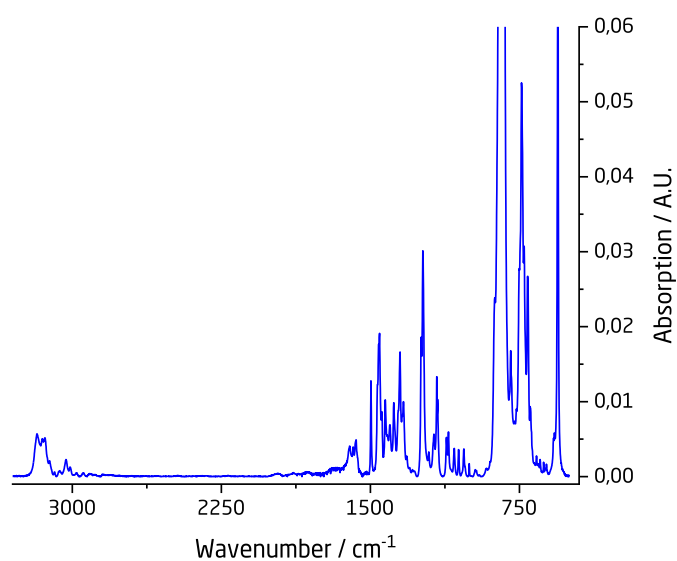


Supplementary Figure 4.27. <sup>1</sup>H NMR spectra of compound **4.18**.

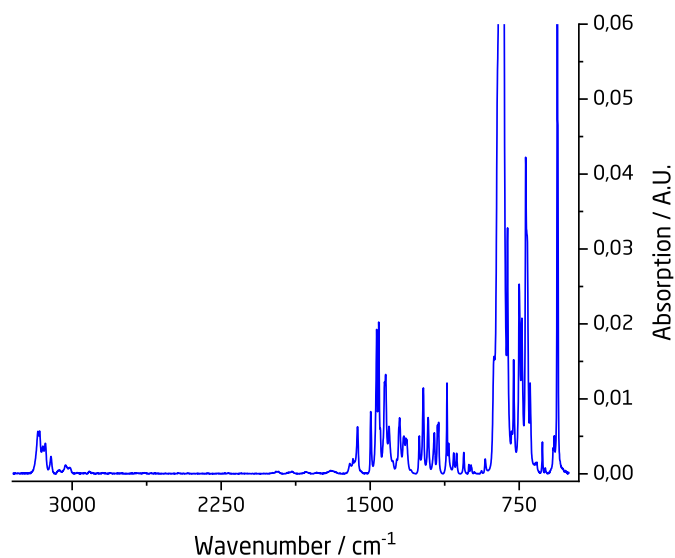


Supplementary Figure 4.28. <sup>13</sup>C NMR spectra of compound **4.18**.

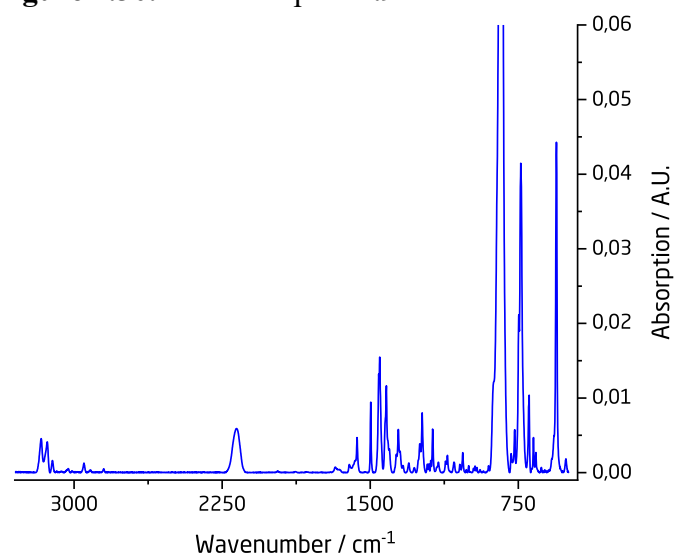
### 4.3 IR Data



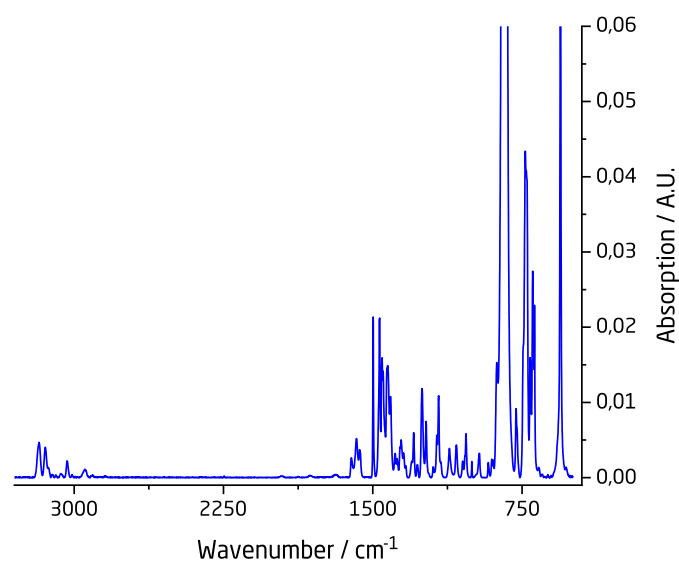
**Supplementary Figure 4.29.** IR of complex 4.5.



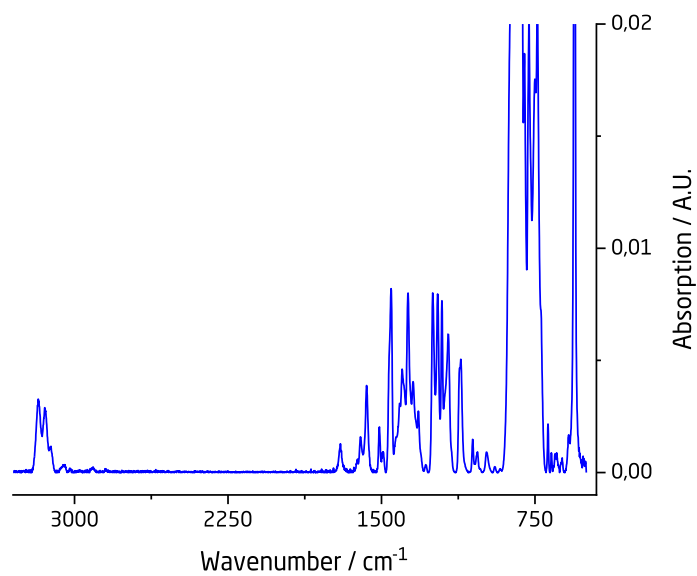
**Supplementary Figure 4.30.** IR of complex 4.9.



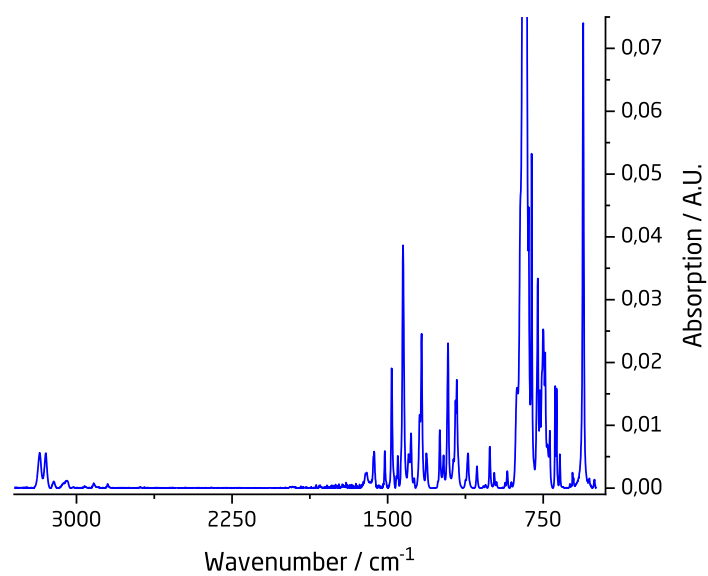
**Supplementary Figure 4.31.** IR of complex **4.6**. Residual MeCN from C-N stretch at approximately  $2250\text{ cm}^{-1}$ .



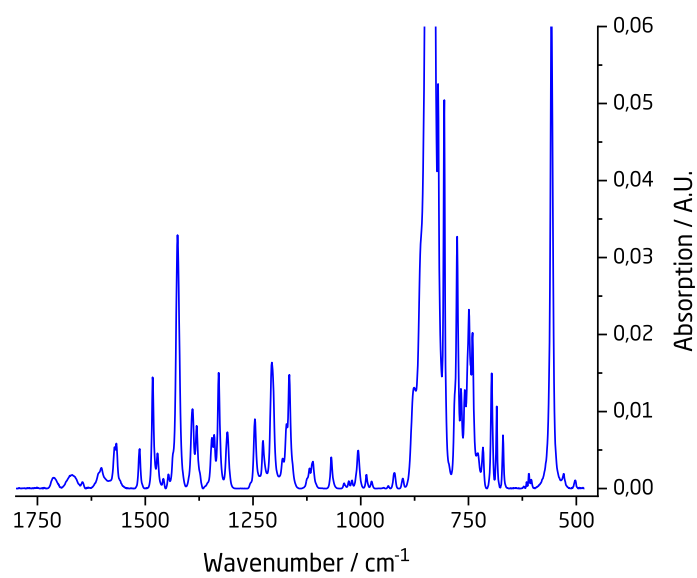
**Supplementary Figure 4.32.** IR of complex **4.10**.



**Supplementary Figure 4.33.** IR of complex **4.13**.



**Supplementary Figure 4.34.** IR of complex **4.15**.



**Supplementary Figure 4.35.** IR of complex **4.18**.

#### 4.4 Crystallographic data

**Supplementary table 4.1.** Crystallographic data for complex, **4.9**, **4.10**, **4.13**, **4.14**, **4.15**, **4.16**, and **4.18**.

	<b>4.9</b>	<b>4.10</b>	<b>4.13</b>
Chemical formula	C <sub>46.69</sub> H <sub>46.97</sub> F <sub>12</sub> N <sub>10.78</sub> P <sub>2</sub> Pd	C <sub>23</sub> H <sub>23.47</sub> F <sub>6.13</sub> N <sub>4.38</sub> PPd <sub>0.5</sub>	C <sub>38</sub> H <sub>32</sub> F <sub>12.03</sub> N <sub>8</sub> P <sub>2</sub> Pd
Formula weight	1155.49	561.75	997.67
Crystal color	Colorless	Colorless	Colorless
Crystal system	Monoclinic	Monoclinic	Orthorhombic
Space group	C2/c	C2/c	Pnma
<i>a</i> (Å)	26.6486(6)	18.1887(5)	18.4595(7)
<i>b</i> (Å)	10.73000(10)	13.1872(4)	17.5028(7)
<i>c</i> (Å)	21.2285(5)	19.5948(7)	12.8966(5)
<i>α</i> (deg)	90	90	90
<i>β</i> (deg)	124.994(3)	91.188(3)	90
<i>γ</i> (deg)	90	90	90
<i>V</i> (Å <sup>3</sup> )	4972.7(2)	4699.0(3)	4166.8(3)
<i>Z</i>	4	8	4
<i>μ</i> (mm <sup>-1</sup> )	4.427	0.557	0.616
<i>T</i> (K)	120.1(2)	120.1(2)	120.15
GOF ( <i>S</i> )	1.041	1.066	1.072
<i>R</i> <sup>1</sup> ( <i>wR</i> <sup>2</sup> <sub>b</sub> )	0.0287	0.0447	0.0479
[ <i>I</i> > 2σ( <i>I</i> )]	0.0713	0.0828	0.1040
<i>R</i> <sup>1</sup> ( <i>wR</i> <sup>2</sup> <sub>b</sub> )	0.0300	0.0690	0.0604
[all data]	0.0724	0.0912	0.1118
2Θ range for data collection (deg)	8.634 to 133.192	6.52 to 59.556	6.416 to 50.054
Reflections	61703	40708	13226
Radiation type	CuKα (λ = 1.54184)	MoKα (λ = 0.71073)	

$$^a R1 = \sum [w(F_0 - F_c)] / \sum [wF_0]; ^b wR2 = [\sum [w(F_0^2 - F_c^2)^2]] / \sum [w(F_0^2)^2]^{1/2}, w = 1 / [\sigma^2(F_0^2) + (aP)^2 + bP], \text{ where } P = [\max(F_0^2, 0) + 2(F_c^2)] / 3$$

**Supplementary table 4.1.** Crystallographic data for complex, **4.9**, **4.10**, **4.13**, **4.14**, **4.15**, **4.16**, and **4.18**.

	<b>4.14</b>	<b>4.15</b>	<b>4.16</b>	<b>4.18</b>
Chemical formula	C <sub>44</sub> H <sub>42</sub> Br <sub>2</sub> N <sub>10</sub> Pd	C <sub>122.78</sub> H <sub>99.79</sub> Ag <sub>6.36</sub> F <sub>9</sub> N <sub>25</sub> . 6O <sub>9</sub> S <sub>3</sub>	C <sub>73.85</sub> H <sub>66.46</sub> Ag <sub>3</sub> . 56Br <sub>0.63</sub> N <sub>14.77</sub>	C <sub>42</sub> H <sub>38</sub> F <sub>12</sub> N <sub>10</sub> Ni P <sub>2</sub>
Formula weight	977.09	3031.47	1595.27	1031.47
Crystal color	Colorless	Colorless	Colorless	Colorless
Crystal system	monoclinic	orthorhombic	cubic	monoclinic
Space group	P2 <sub>1</sub> /c	Amm2	Pa-3	P2 <sub>1</sub> /c
<i>a</i> (Å)	9.4574(3)	26.7906(4)	30.98650(10)	19.2100(11)
<i>b</i> (Å)	10.3831(3)	26.9565(4)	30.98650(10)	12.1739(7)
<i>c</i> (Å)	40.6214(10)	26.2626(4)	30.98650(10)	18.3817(11)
$\alpha$ (deg)	90	90	90	90
$\beta$ (deg)	91.428(2)	90	90	94.8150(10)
$\gamma$ (deg)	90	90	90	90
<i>V</i> (Å <sup>3</sup> )	3987.7(2)	18966.4(5)	29752.1(3)	4283.6(4)
<i>Z</i>	4	5	13	4
$\mu$ (mm <sup>-1</sup> )	6.471	7.402	1.066	0.627
<i>T</i> (K)	120.15	120.15	120.15	100(2)
GOF (S)	1.060	1.014	1.095	1.043
R1 <sup>a</sup> (wR2 <sup>b</sup> ) [ <i>I</i> > 2σ( <i>I</i> )]	0.0354 0.0898	0.0492, 0.1247	0.0564 0.1562	0.0701 0.1756
R1 <sup>a</sup> (wR2 <sup>b</sup> ) [all data]	0.0427 0.0940	0.0591 0.1346	0.0776 0.1834	0.1016, 0.1976
2θ range for data collection (deg)	8.71 to 158.274	8.102 to 133.19	6.442 to 50.04	3.964 to 50.136
Reflections	27076	34013	233351	7811
Radiation type	CuKα (λ = 1.54184)		MoKα (λ = 0.71073)	
Flack parameter	-	0.030(6)	-	-

## 5 Chapter 5

### 5.1 Synthetic methods

Compound **5.1**. *In a fume hood, in air.* A 20 mL scintillation vial was added complex **4.13** (25 mg, 25.1  $\mu\text{mol}$ , 1.0 equiv.) and dissolved in 5 mL MeCN with a Pasteur glass pipette before  $\text{PhICl}_2$  (13.8 mg, 50.2  $\mu\text{mol}$ , 2.0 equiv.) was added and the mixture was mixed with the pipette quickly turning yellow. An aliquot was taken aside for crystallization; Crystals suitable for X-ray diffraction were obtained by slow solvent evaporation at RT from this solution, and isolated as yellow/greenish crystals. The mixture was layered with  $\sim 12$  mL of  $\text{Et}_2\text{O}$  and placed in-side a refrigerator for 30 minutes resulting in the precipitation of a yellow/greenish powder. The powder was collected on a glass-fiber frit, F-coarseness, and washed with more  $\text{Et}_2\text{O}$ , before it was redissolved in minimum amounts of MeCN, collected in a new vial, and dried in vacuo for a couple of hours, affording the desired complex in excellent yield (26 mg, 97%). For long term storage, the vial was filled with an  $\text{N}_2$  atmosphere and kept in the dark.  $^1\text{H}$  NMR (400 MHz,  $\text{CD}_3\text{CN}$ )  $\delta$  8.20 (d,  $J = 8.2$  Hz, 2H), 7.86 (d,  $J = 7.0$  Hz, 2H), 7.69 (t,  $J = 8.2$ , 7.0 Hz, 2H), 7.63 (d,  $J = 2.1$  Hz, 2H), 7.13 (d,  $J = 2.1$  Hz, 2H), 6.98 (d,  $J = 13.3$  Hz, 1H), 6.43 (d,  $J = 13.3$  Hz, 1H), 5.57 (d,  $J = 16.1$  Hz, 2H), 5.30 (d,  $J = 16.1$  Hz, 2H).  $^{13}\text{C}$  NMR (151 MHz,  $\text{CD}_3\text{CN}$ )  $\delta$  150.03, 138.16, 136.91, 134.05, 132.08, 129.46, 127.24, 126.44, 123.25, 63.24, 57.66.  $^{19}\text{F}$  NMR (377 MHz,  $\text{CD}_3\text{CN}$ )  $\delta$  -71.1 (d,  $J = 711$  Hz).  $^{31}\text{P}$  NMR (162 MHz,  $\text{CD}_3\text{CN}$ )  $\delta$  -144.62 (hep,  $J = 711$  Hz). Unable to obtain a satisfactory elemental analysis.

Compound **5.2**. *In a fume hood, in air.* A 20 mL scintillation vial was added complex **4.13** (50 mg, 50.2  $\mu\text{mol}$ , 1.0 equiv.), dissolved in 8 mL MeCN with a Pasteur glass pipette before a couple of droplets of  $\text{Br}_2$  was added, mixed through a push-pull motion, resulting in the mixture now turning red/brown. An aliquot was taken aside for crystallization;

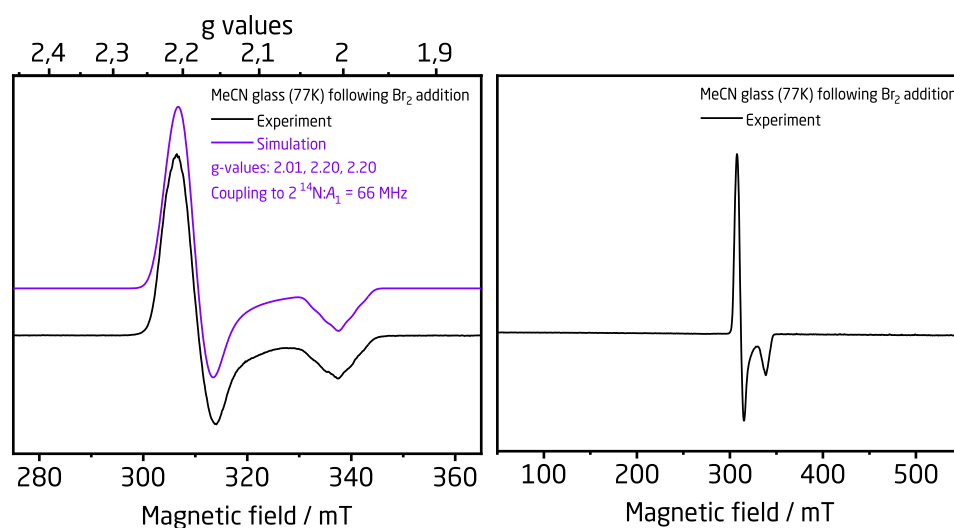


Crystals suitable for X-ray diffraction were obtained by slow solvent evaporation at RT from this solution, and isolated as orange/brown crystals. The mixture was layered with ~ 10 mL of Et<sub>2</sub>O and placed in-side a refrigerator for 30 minutes resulting in the precipitation of a red/brown powder. The powder was collected on a glass-fiber frit, F-coarseness, and washed with more Et<sub>2</sub>O, before it was redissolved in minimum amounts of MeCN, collected in a new vial, and dried in vacuo for a couple of hours, affording the desired complex in excellent yield (55.2 mg, 95%). For long term storage, the vial was filled with an N<sub>2</sub> atmosphere and kept in the dark. <sup>1</sup>H NMR (400 MHz, CD<sub>3</sub>CN) δ 8.20 (dt, *J* = 8.3, 2.6, 1.8 Hz, 2H), 7.88 (dt, *J* = 7.0, 2.6, 1.8 Hz, 2H), 7.70 (td, *J* = 8.3, 7.0, 2.6 Hz, 2H), 7.63 (t, *J* = 2.4 Hz, 2H), 7.16 (t, *J* = 2.4 Hz, 2H), 7.05 (dd, *J* = 13.6, 2.6 Hz, 1H), 6.46 (dd, *J* = 13.6, 2.6 Hz, 1H), 5.56 (dd, *J* = 16.0, 2.6 Hz, 2H), 5.32 (dd, *J* = 16.0, 2.6 Hz, 2H). <sup>13</sup>C NMR (101 MHz, CD<sub>3</sub>CN) δ 146.88, 138.05, 136.91, 133.94, 132.20, 129.44, 127.25, 126.52, 123.60, 64.26, 58.57. <sup>19</sup>F NMR (377 MHz, CD<sub>3</sub>CN) δ -71.1 (d, *J* = 711 Hz). <sup>31</sup>P NMR (162 MHz, CD<sub>3</sub>CN) δ -144.62 (hep, *J* = 711 Hz). Unable to obtain a satisfactory elemental analysis.

Compound **5.4**. *In a fume hood, in air*. A 20 mL scintillation vial was added complex **4.18** (25 mg, 26.3 μmol, 1.0 equiv.), dissolved in 5 mL MeCN with a Pasteur glass pipette before a couple of droplets of Br<sub>2</sub> was added, mixed through a push-pull motion, resulting in the mixture now turning red/brown. An aliquot was taken aside for crystallization; Crystals suitable for X-ray diffraction were obtained by slow solvent evaporation at RT from this solution, and isolated as orange/brown crystals. The mixture was layered with ~ 12 mL of Et<sub>2</sub>O and placed in-side a refrigerator for 30 minutes resulting in the precipitation of a red/brown powder. The powder was collected on a glass-fiber frit, F-coarseness, and washed with more Et<sub>2</sub>O, before it was redissolved in minimum amounts of MeCN, collected in a new vial, and dried in vacuo for a couple of hours, affording the

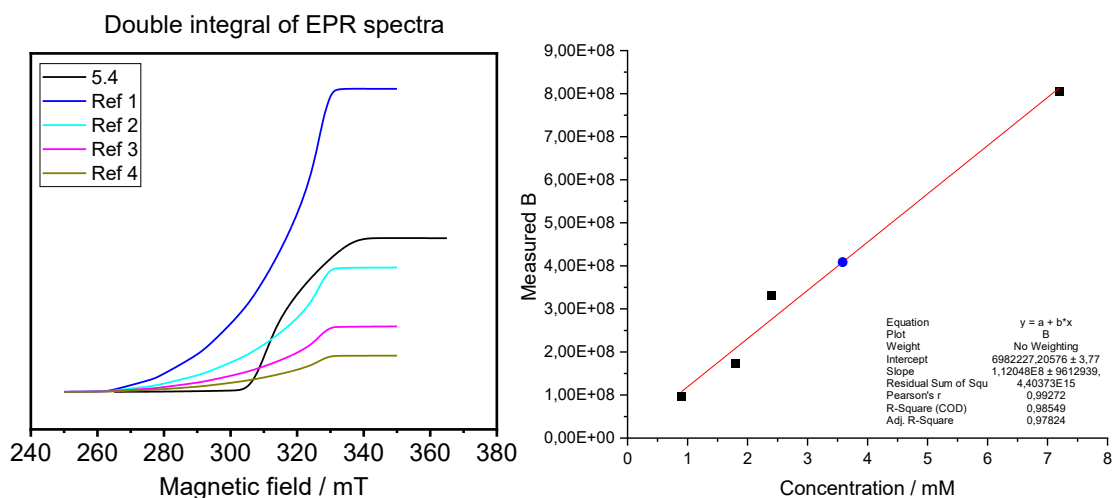
desired complex in excellent yield (26 mg, 96%). For long term storage, the vial was filled with an N<sub>2</sub> atmosphere and kept in the dark. Redissolution in MeCN-d<sub>3</sub>, reveals a paramagnetic species; Evan's method was not employed to determinate magnetic moment. From MeCN (77K) EPR:  $A_{||} = 66$  MHz (pentet),  $g$ -values: 2.01, 2.20, 2.20.

The EPR spectrometer used is a Bruker EMX with an ER 4012ST cavity. The spectral data was collected using a liquid nitrogen finger dewar at 77K with the following spectrometer settings: Microwave power = 6.65 mW; frequency 9.48 GHz, center field = 315 mT, sweep width = 100 mT, modulation frequency = 100 KHz, modulation amplitude = 0.5 mT, time constant = 20 ms, conversion time = 20 ms.. All spectra were baseline corrected by subtracting the spectrum of the empty dewar. The spectra shown are averaged over 3 sweeps.



**Supplementary Figure 5.1.** EPR spectrum following Br<sub>2</sub> addition to complex **4.18**.

## 5.2 EPR quantification



**Supplementary Figure 5.2.** Quantification of complex **5.3**.

*Standard solution of  $\text{Cu}(\text{NO}_3)_2$ .* 1.002 mg  $\text{Cu}(\text{NO}_3)_2 \cdot 5\text{H}_2\text{O}$  was weighed out into a LCMS vial, to which was added 0.5 mL of 1M  $\text{HClO}_4$ . Using a precision pipette, a volume of this standard solution was measured out into an LCMS vial which was diluted with MiliQ water until the desired concentration was met, **Supplementary table 5.1**. 80  $\mu\text{L}$  of these solutions were then transferred into an EPR tube, frozen, and its spectrum recorded, to obtain the double integral shown in **Supplementary Figure 5.2**, for concentrations of 0.9, 1.8, 2.41, and 7.22 mM, resulting in measured magnetic field values of 0.95, 1.75, 3.25, and 7.95, respectively.

0.27 mg of complex **4.18** was dissolved in MeCN to which was added an excess of  $\text{Br}_2$ ; upon shaking, the EPR tube was quickly frozen, and a spectrum was recorded. We were able to determine a concentration of the formed complex **5.4**, from a linear regression between the Cu (II) standard, which deviates from the expected concentration of ~10%. This deviation is within the acceptable window in quantitative EPR; however, we seek to reproduce these measurements. Despite this deviation, we can confirm that complex **4.18** is fully oxidized to complex **5.4**, which is responsible for the observed EPR signal.

**Supplementary table 5.1.** Standard solution for EPR quantification.

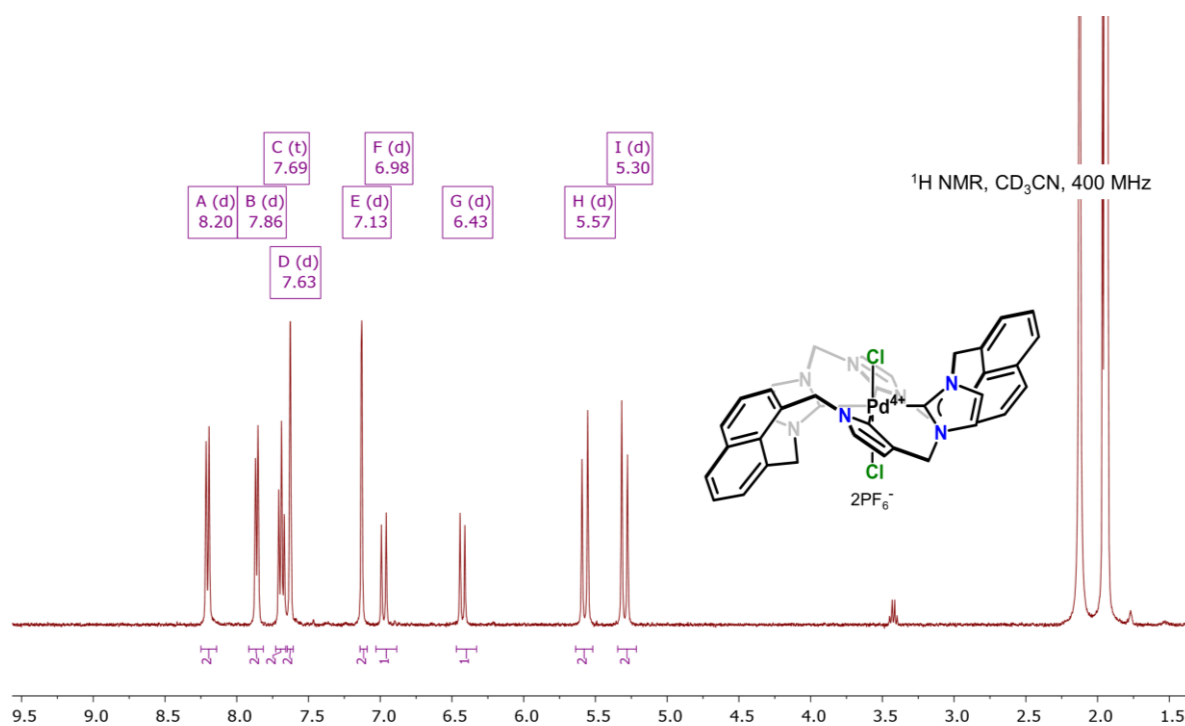
Volume from standard	Diluted with $x$ $\mu\text{L H}_2\text{O}$	Concentration / mM	$\mu\text{L}$ from this solution used in measurement	Concentration / mM	Measured B value
80	0	7.22		80	7.22
40	80	2.41		80	2.41
50	150	1.80		80	1.80
25	175	0.90		80	0.90

### 5.3 Computational methods

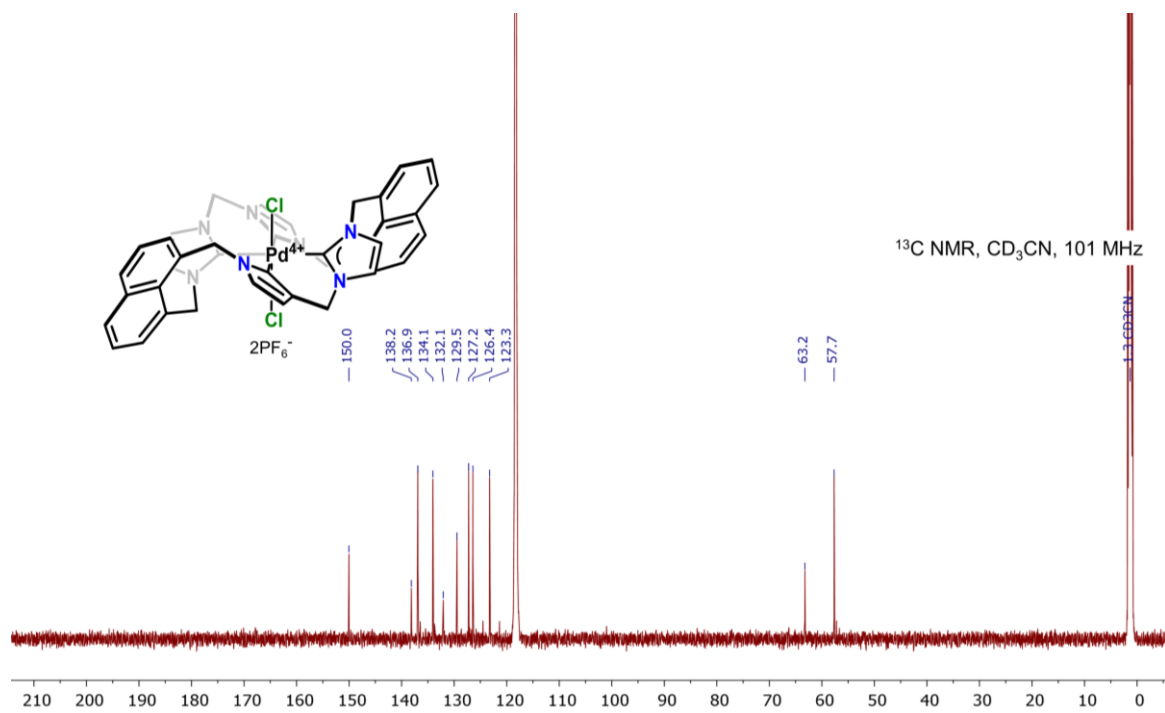
The quantum chemical calculations were performed using the ORCA (5.0)<sup>8</sup> package. Harmonic vibrational frequencies of complexes **5.1** and **5.2** molecular units were calculated using TPSS-D4<sup>9</sup> method with def2-TZVP<sup>10–12</sup> basis set (QZVPP used for Pd). Solution has been obtained for the first 10 roots.

Harmonic vibrational frequencies of complex **5.4** was calculated using PBE, B-LYP, TPSS, PBE0, B3-LYP, and TPSSh D3<sup>23</sup> methods with def2-TZVP<sup>10–12</sup> basis set (QZVPP used for Ni). Solution has been obtained for the first 10 roots. EPR spectra and spin-densities were obtained using various combinations of levels of theory and functionals listed in the body in chapter 5, using the implementation accessible through the ORCA (5.0) software.

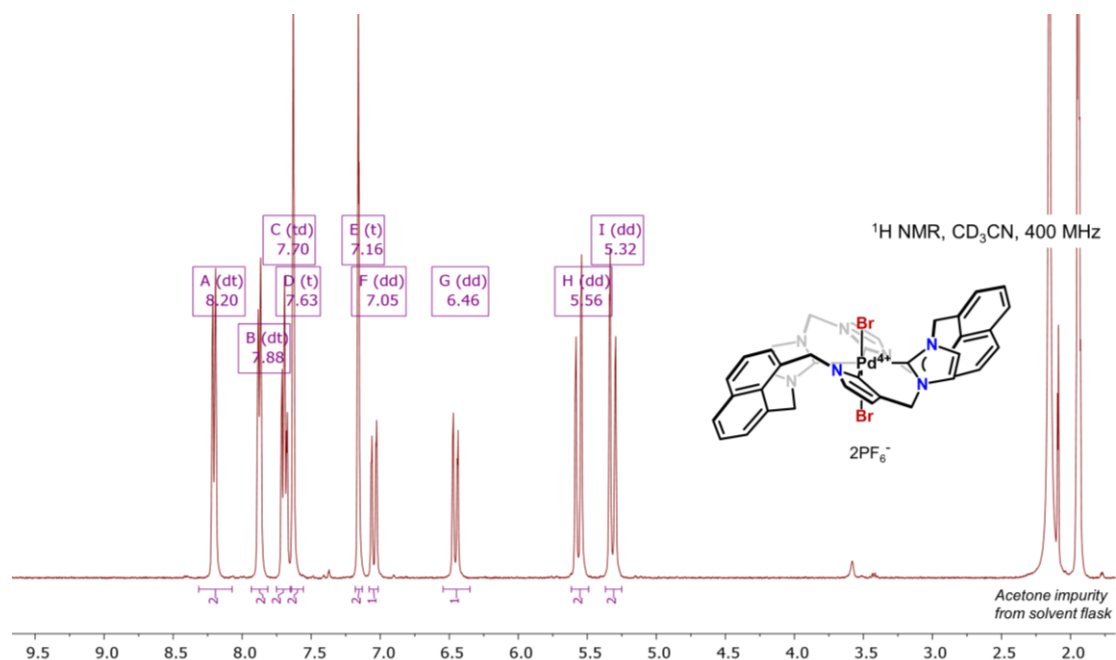
## 5.4 NMR spectra



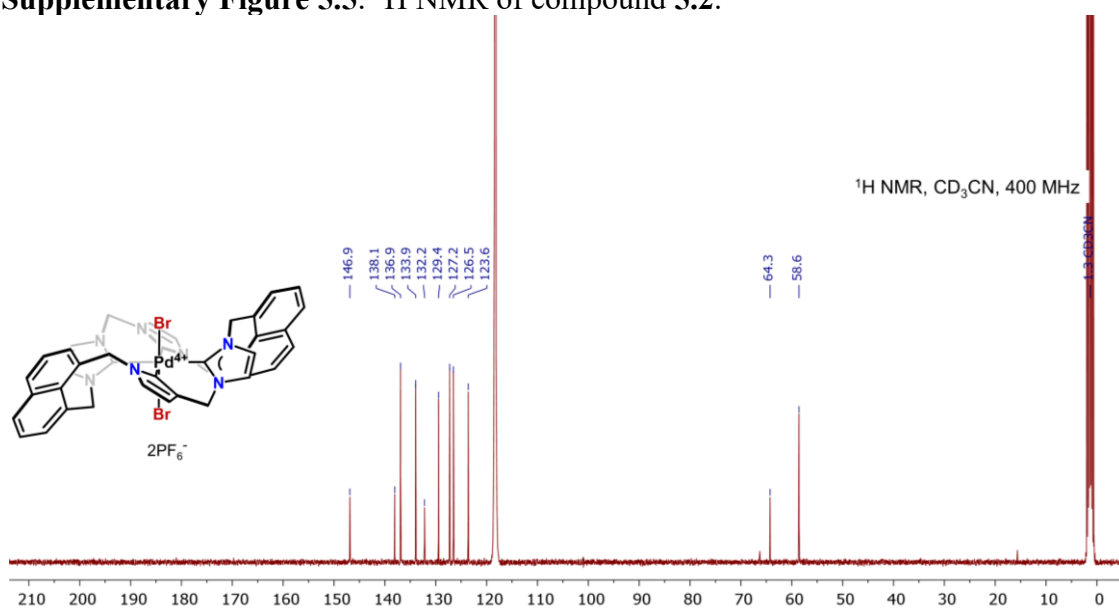
Supplementary Figure 5.3. <sup>1</sup>H NMR of compound 5.1.



Supplementary Figure 5.4. <sup>13</sup>C NMR of compound 5.1.



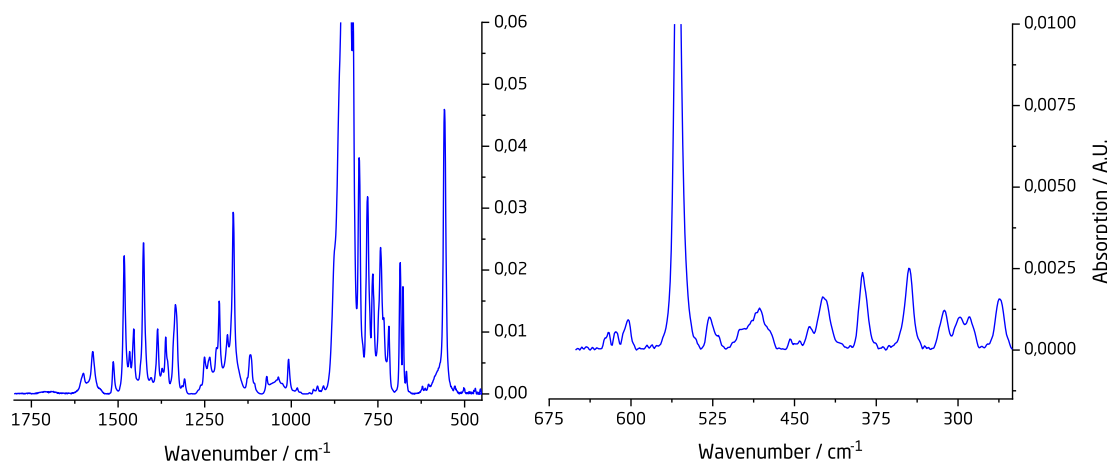
Supplementary Figure 5.5. <sup>1</sup>H NMR of compound 5.2.



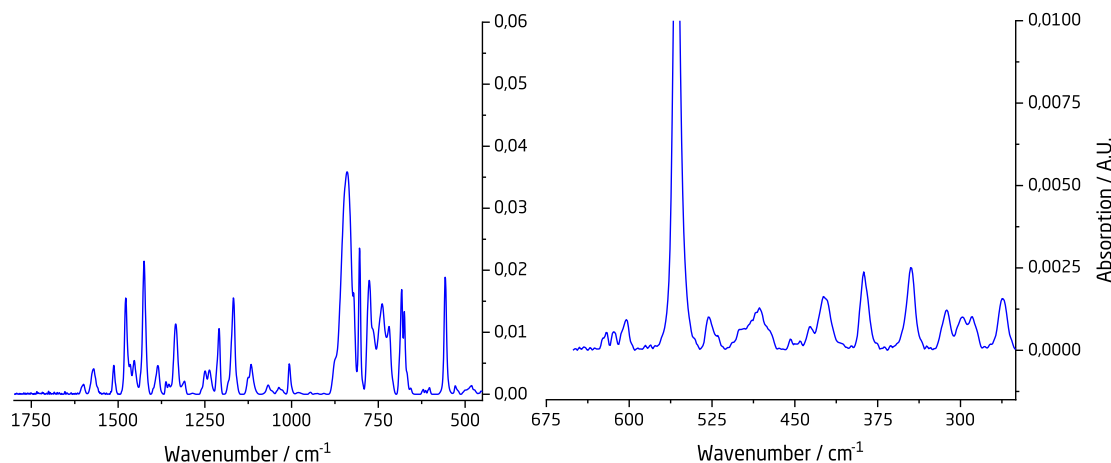
Supplementary Figure 5.6. <sup>13</sup>C NMR of compound 5.2.

## 5.5 IR Data

MIR and FIR data have been obtained for complexes **5.1** and **5.2**, as we are underway in understanding Pd-C and Pd-X bonding. Ultimately, we were unable to finish this investigation during the time of the PhD study, and as such, is not involved in the main body.



**Supplementary Figure 5.7.** MIR (left) and FIR (right) spectra of complex **5.1**.



**Supplementary Figure 5.8.** MIR (left) and FIR (right) spectra of complex **5.2**.

## 5.6 Crystallographic data

**Supplementary table 5.2.** Crystallographic data for compounds **5.1**, **5.2**, and **5.4**.

	<b>5.1</b>	<b>5.2</b>	<b>5.4</b>
Chemical formula	C <sub>25</sub> H <sub>21</sub> ClF <sub>6</sub> IN <sub>4</sub> PPd 0.5	C <sub>38</sub> H <sub>32</sub> Br <sub>2</sub> F <sub>12</sub> N <sub>8</sub> P 2Pd	C <sub>42</sub> H <sub>38</sub> Br <sub>8.97</sub> N <sub>10</sub> N i
Formula weight	737.98	1156.87	1458.72
Crystal color	Yellow/green	Orange/brown	Orange/brown
Crystal system	Triclinic	Triclinic	Monoclinic
Space group	P-1	P-1	C2/c
<i>a</i> (Å)	8.2065(3)	8.4055(3)	19.7283(7)
<i>b</i> (Å)	12.3787(6)	11.7123(5)	11.3849(4)
<i>c</i> (Å)	14.2333(8)	13.4793(6)	21.3581(10)
<i>α</i> (deg)	113.449(5)	99.957(4)	90
<i>β</i> (deg)	103.650(4)	107.238(3)	100.068(4)
<i>γ</i> (deg)	95.745(4)	103.102(3)	90
<i>V</i> (Å <sup>3</sup> )	1258.13(12)	1192.58(9)	4723.3(3)
<i>Z</i>	2	1	4
<i>μ</i> (mm <sup>-1</sup> )	1.858	2.215	8.047
<i>T</i> (K)	120.15	120.15	120.15
GOF (S)	0.962	1.043	1.060
R1 <sup>a</sup> (wR2 <sup>b</sup> )	0.0304	0.0362	0.0365
[ <i>I</i> > 2σ( <i>I</i> )]	0.0645	0.0767	0.1015
R1 <sup>a</sup> (wR2 <sup>b</sup> )	0.0376	0.0481	0.0485
[all data]	0.0693	0.0832	0.1038
2Θ range for data collection (deg)	6.588 to 59.538	6.552 to 59.076	4.73 to 50.092
Reflections	12766	11005	17506
Radiation type	MoKα (λ = 0.71073)		

$$^a R1 = \sum[w(F_0 - F_c)] / \sum[wF_0]; ^b wR2 = [\sum[w(F_0^2 - F_c^2)^2]] / \sum[w(F_0^2)^2]^{1/2}, w = 1 / [\sigma^2(F_0^2) + (aP)^2 + bP], \text{ where } P = [\max(F_0^2, 0) + 2(F_c^2)] / 3$$



## 6 Chapter 6

### 6.1 Synthetic methods

*1,1,1-tris(p-toluenesulfonyloxy)methyl)ethane*. Adapted from Beaufort *et al.*<sup>24</sup> Trihydroxymethylethane (30.04g, 250 mmol, 3.0 equiv.) was suspended in cold pyridine (500 mL) in an ice-bath and cooled for 30 minutes. To the solution was slowly added TsCl (214.3 g, 1.13 mol, 13.5 equiv.) and the yellow solution transitioned to an off-white precipitate. The mixture was stirred o.n. and the suspension was added to a solution of H<sub>2</sub>O (300 mL), HCl (300 mL, 12 M), CH<sub>3</sub>OH (700 mL) and filtered on a Büchner funnel. The powder was washed with 3 x 100 mL of each H<sub>2</sub>O and CH<sub>3</sub>OH and dried o.n. *in vacuo*, affording 1,1,1-tris(*p*-toluenesulfonyloxy)methyl)ethane (46.5g, 95.8% yield). <sup>1</sup>H NMR (400 MHz, CDCl<sub>3</sub>)  $\delta$  7.76 – 7.63 (d, *J* = 8.1 Hz, 6H), 7.35 (d, *J* = 8.1 Hz, 6H), 3.76 (s, 6H), 2.46 (s, 9H), 0.88 (s, 3H).

*1,1,1-tris((benzylamino)methyl hydrochloride) ethane*. Adapted from Qin *et al.*<sup>25</sup> a.: (1) (58.3 g, 100 mmol, 3.0 equiv.) was dissolved in benzylamine (132 mL, 1.2 mol, 36.0 equiv.) and the mixture was purged with N<sub>2</sub> for at least 10 minutes. The mixture was heated to 180°C for 2 hours and allowed to cool to rt. Excess benzylamine was removed under vacuum distillation. 200 mL heptane was added to the crude product which was refluxed for 15 minutes, allowed to cool to rt and subsequently cooled to 5°C. The mixture was refrigerated o.n. and the suspension was filtered, and the solids were washed with hexane (4 x 20 mL). Combined filtrate was with H<sub>2</sub>O (3 x 30 mL) and dried over MgSO<sub>4</sub> and dried *in vacuo* affording a yellow tinted oil, which was dissolved in 250 mL MeOH and HCl (50 mL, 12 M) was added, forming a purple solution. Solvent was removed *in vacuo* and addition of ethanol was continued until almost of the water was gone. The purple crude was dissolved in as little possible EtOH (100 mL) under reflux and refrigerated o.n. at 5°C. The powder was filtered on M-frit and washed with EtOH (5 x

20 mL) until the powder was completely white and was dried *in vacuo* overnight affording the title compound in good yield (45.7g, 92%). <sup>1</sup>H NMR (400 MHz, D<sub>2</sub>O) δ 7.58 – 7.45 (overlapping multiplet, 15H), 4.31 (s, 6H), 3.25 (s, 6H), 1.29 (s, 3H).

*tris-(aminomethyl hydrochloride)ethane*. Synthesis adapted from Qin *et al.*<sup>25</sup> (**2**) (12.42 g, 25.0 mmol, 3 equiv.) was dissolved in CH<sub>3</sub>OH (750 mL, 0.03 L/mmol) and the solution was purged with N<sub>2</sub> for at least 10 minutes. Pd/C (10%, 2.66 g, 3.0 equiv.) and NH<sub>4</sub>HCO<sub>2</sub> (23.65 g, 375 mmol, 45 equiv.) were added and a reflux-adaptor was attached. The reaction mixture was evacuated and purged with N<sub>2</sub> at least 3 times, and the mixture was heated to 60°C for 4 hours. The mixture was allowed to cool to rt and filtered through a Celite pad, washed with CH<sub>3</sub>OH and the combined organic phase was concentrated *in vacuo* affording a white powder of the trishydrochloride salt, which was recovered from a recrystallization from EtOH in good yield (4.932g, 87%). <sup>1</sup>H NMR (400 MHz, D<sub>2</sub>O) δ 3.23 (s, 6H), 1.29 (s, 3H).

Compound <sup>F,Me</sup>L(NO<sub>2</sub>)<sub>3</sub>. Synthesis adapted from Betley and co-worker<sup>26</sup>. Inside a N<sub>2</sub> filled glovebox, tris-(aminomethyl hydrochloride)ethane (5 g, 22.1 mmol, 1.0 equiv.), K<sub>2</sub>CO<sub>3</sub> (24.4 g, 0.18 mol, 8 equiv.), 2,5-difluoro-nitrobenzene (15 mL, 132.4 mmol, 6.0 equiv.), were added to a bomb flask equipped with a stirbar. 250 mL of MeCN was added to the flask, which was sealed, brought out of the glovebox, placed inside an oil bath, and heated under stirring to 110°C for 3 days, under vigorous stirring. The mixture was allowed to cool to RT, the solids collected on glass-frit, M-coarseness, and the motherliquid was collect and reduced in volume by ~60%, to which was added water. The resulting red-precipitate was added back to the original filter cake, which was sequentially washed with H<sub>2</sub>O, heptane, and small amounts of acetone, which was repeated for to a total of 6 times, until the filtrate no longer contained any black/dark red materials, and dried *in vacuo* affording an orange powder of the title compound in good

yield (10.5g, 89%).  $^1\text{H}$  NMR (400 MHz,  $\text{DMSO-}d_6$ )  $\delta$  8.17 (t,  $J$  = 6.0 Hz, 3H, Ar-NH), 7.82 (dd,  $J$  = 9.4 (H-F), 3.1 Hz, 3H,  $\text{O}_2\text{NC}(\text{CH})\text{CF}$ ), 7.46 (ddd,  $J$  = 10.3, 7.4 (H-F), 3.1 Hz, 3H), 7.20 (dd,  $J$  = 10.3, 4.7 (H-F) Hz, 3H), 3.56 (d,  $J$  = 6.0 Hz, 6H, NH-CH<sub>2</sub>), 1.16 (s, 3H, CH<sub>3</sub>).  $^{19}\text{F}$  NMR (377 MHz,  $\text{DMSO-}d_6$ )  $\delta$  -127.9 (td,  $J$  = 9.4, 7.4, 4.7 Hz).

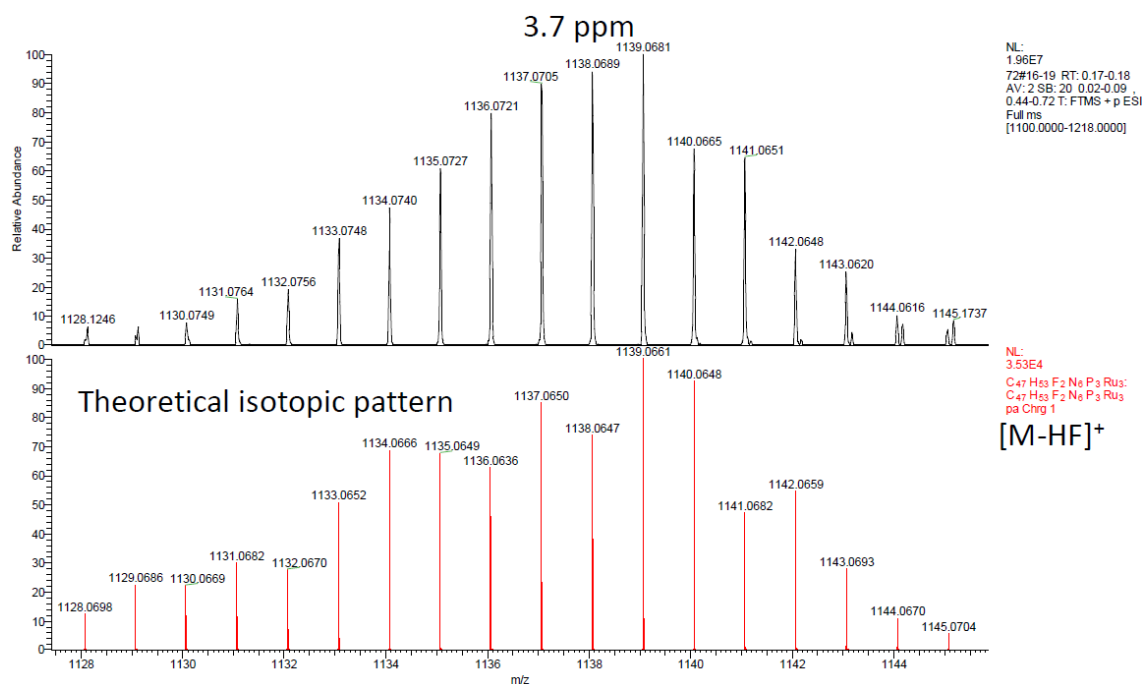
Compound  $^{\text{F,Me}}\text{LH}_6$ . The following step was done in a  $\text{N}_2$  filled glovebox. Compound  $^{\text{F,Me}}\text{L}(\text{NO}_2)_3$  (11.25 g, 21.1 mmol, 1.0 equiv.) and Pd/C (10 w/w%, 1.4 g) were placed inside a mason jar, equipped with a stir bar, that fitted inside a Parr reactor before THF (100 mL) was added. The reactor was purged thrice with  $\text{H}_2$  gas (40 psi), and subsequently back filled until 100 psi was reached. The Parr reactor was placed atop a heating plate and stirred for 2 hours at  $65^\circ\text{C}$ , which caused the pressure to drop to 40 psi. The reactor was removed from the heat, allowed to cool to RT, and refilled with  $\text{H}_2$  to 100 psi. The morning after the pressure was  $\sim 5$  psi  $\text{H}_2$ . The autoclave was once again filled to 100 Psi and stirred until the mixture no longer consumed  $\text{H}_2$  ( $\sim 4$  hours). The mixture was then allowed to cool to RT before residual  $\text{H}_2$  was evacuated under purging. The mixture was filtered through Celite, and the pad washed with THF (10 x 2 mL). The filtration flask was subjected to vacuum resulting in an off-white liquid forming, which after some time crystallized a white powder, which was scraped down with a spatula. 5 x 2 mL benzene was added to the filtration flask to help transfer the suspension to a new filter. The powder was washed with benzene until the filtrate ran clear, leaving the title compound as a white powder in good yield (7.08g, 76%).  $^1\text{H}$  NMR (500 MHz,  $\text{C}_6\text{D}_6$ )  $\delta$  6.61 (td,  $J$  = 8.6, 2.9 Hz, 3H), 6.34 – 6.24 (*mult*, 6H), 4.46 (t,  $J$  = 6.6 Hz, 3H), 3.09 (s, 6H), 2.73 (d,  $J$  = 6.5 Hz, 6H), 0.63 (s, 3H).  $^{13}\text{C}$  NMR (126 MHz,  $\text{C}_6\text{D}_6$ )  $\delta$  159.19, 157.32, 138.25, 138.17, 133.95, 113.96, 113.88, 105.87, 105.70, 104.15, 103.95, 55.10, 36.94, 23.65.  $^{19}\text{F}$  NMR (470 MHz,  $\text{C}_6\text{D}_6$ )  $\delta$  -124.05.

Complex  $^{\text{F,Me}}\text{L}(\text{Mg}\{\text{thf}\})_3$ . Adapted from Betley and co-worker<sup>26</sup>. Compound  $^{\text{F,Me}}\text{LH}_6$  (250 mg, 0.56 mmol, 1.0 equiv.) was added to a 20 mL scintillation vial equipped with a stirbar and dissolved in ~8 mL of THF before  $^{\text{n}}\text{Bu}_2\text{Mg}$  (350.6mg, 2.53 mmol, 4.5 equiv.) slowly was added causing the mixture to bubble vigorously. The vial was heated on a stir plate overnight at 55°C. The mixture was cooled to RT, a vacuum was applied to remove all solvent, and the remaining gooye material was suspended in *n*-hexane and stirred for 5 minutes. The mixture was then allowed to settle for 5 minutes, and the hexane decanted off. This procedure was repeated until all of the off-yellow goo was a yellow powder. Once a powder was achieved, 2 mL of benzene was added to lyophilize the mixture under vacuum. The desired thf-solvato trimagnesium complex was collected as an off-yellow powder in good yields (262mg, 64%).  $^1\text{H}$  NMR (500 MHz,  $\text{C}_6\text{D}_6$ )  $\delta$  6.54 - 6.44 (m, 6H), 6.14 (dd,  $J = 8.1, 5.6$  Hz, 3H), 3.49 (s, 6H), 2.93 (d,  $J = 6.4$  Hz, 12H), 2.75 (s, 3H), 1.37 (s, 3H), 0.88 – 0.76 (m, 12H).  $^{19}\text{F}$  NMR (470 MHz,  $\text{C}_6\text{D}_6$ )  $\delta$  -130.92.

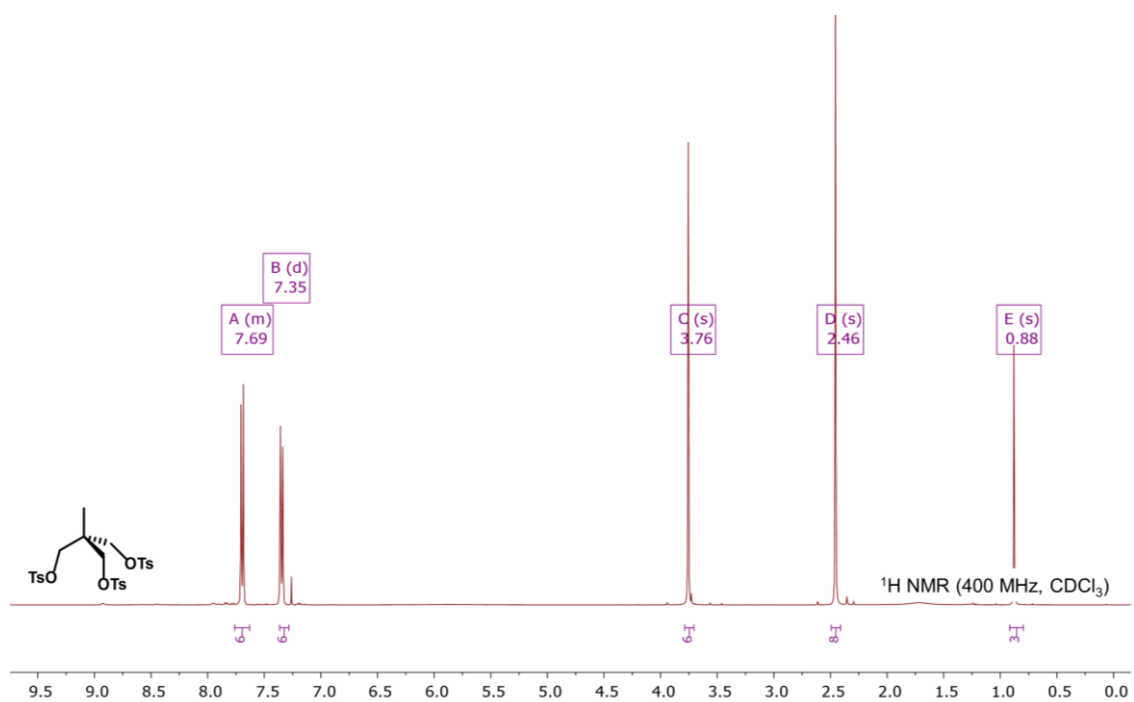
Putative complex  $^{\text{F,Me}}\text{L}(\text{Ru}\{\text{PPhMe}_2\})_3$ . Inside a  $\text{N}_2$ -filled glovebox,  $^{\text{F,Me}}\text{L}(\text{Mg}\{\text{thf}\})_3$  (200 mg, 0.275 mmol, 1.0 equiv.) and  $[\text{Ru}_2\text{Cl}_3(\text{PPhMe}_2)_4]\text{Cl}$  (516 mg, 0.44 mmol, 1.6 equiv.) were added to a bomb-flask equipped with a stirbar. The solids were added 50 mL of THF and 8 mL of *p*-dioxane, before the vessel was sealed and brought out of the glovebox, emerged into an oil bath, which was heated to 70°C for at least 4 days. During this time, the color changes from pale yellow to an intense blue/purple. The mixture was cooled to RT, wiped free from oil, and brought back into the glovebox, where reaction volume was reduced to ~50% of its original volume. The mixture was passed through Celite, the pad was washed with THF until the filtrate ran clear, and solvent from the combined filtrate was removed in vacuo. The remaining solid was re-dissolved in minimum amounts of warm hexane (~55°C), which was transferred to a clean vial, which was placed in-side a freezer overnight. The morning after, the liquid was decanted off,

and the solid subjected to vacuum, and transferred to a new vial. This procedure was repeated two times more, leaving a black/intensely blue-colored powder of the desired complex in about 30%.  $^1\text{H}$  NMR (500 MHz,  $\text{C}_6\text{D}_6$ )  $\delta$  7.0 (*overlapping multiplet*, 24), 3.58 (s, 6H), 1.53 (s, 3H), 1.40 (broad singlet, 3H), 1.25 (t,  $J = 3.3$  Hz, 9H), 1.19 (t,  $J = 3.5$  Hz, 9H).  $^{19}\text{F}$  NMR (470 MHz,  $\text{C}_6\text{D}_6$ )  $\delta$  -131.85, -132.33.  $^{31}\text{P}$  NMR (202 MHz,  $\text{C}_6\text{D}_6$ )  $\delta$  27.69, 24.66.

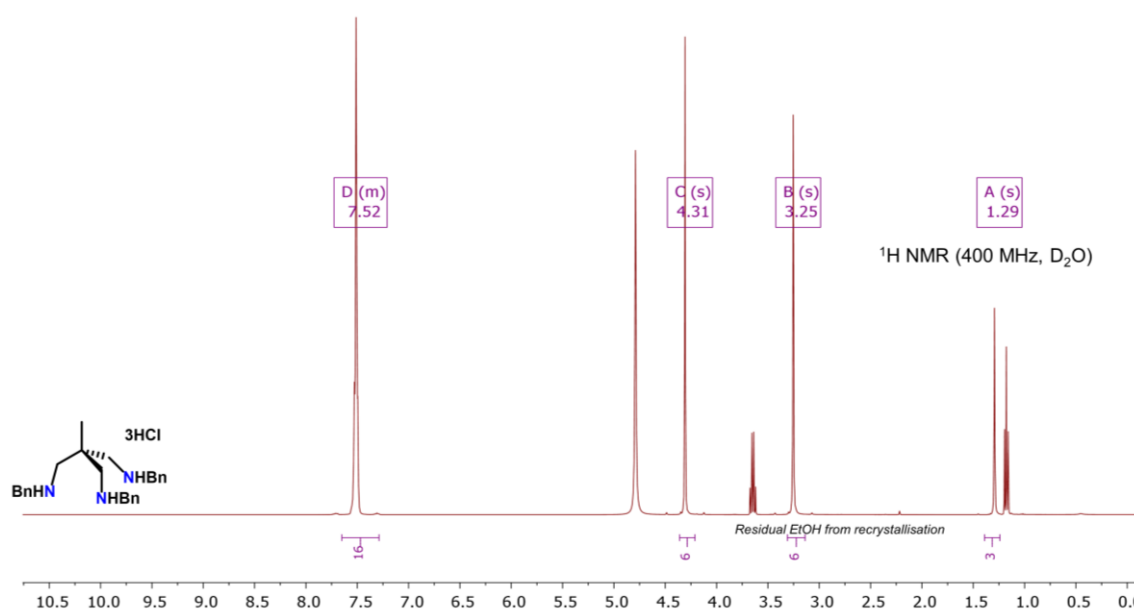
Mass spectrometry was performed at the Harvard University FAS Center for Systems Biology Mass Spectrometry and Proteomic Resource Laboratory on an Agilent 6210 TOF LC/MS with a dual nublizer ESI source for HRMS and on a Water Q-TOF Micro LC/MS/MS with an ESI source for yield determination.



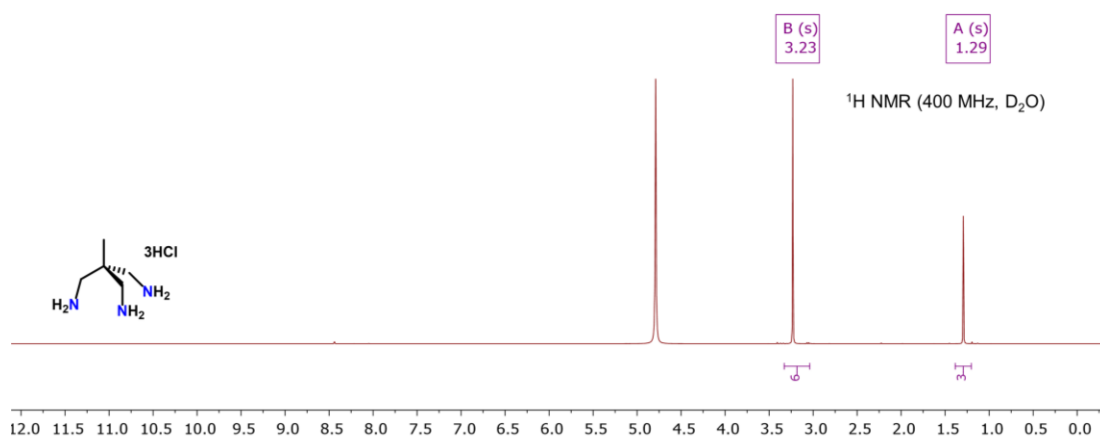
## 6.2 NMR spectra



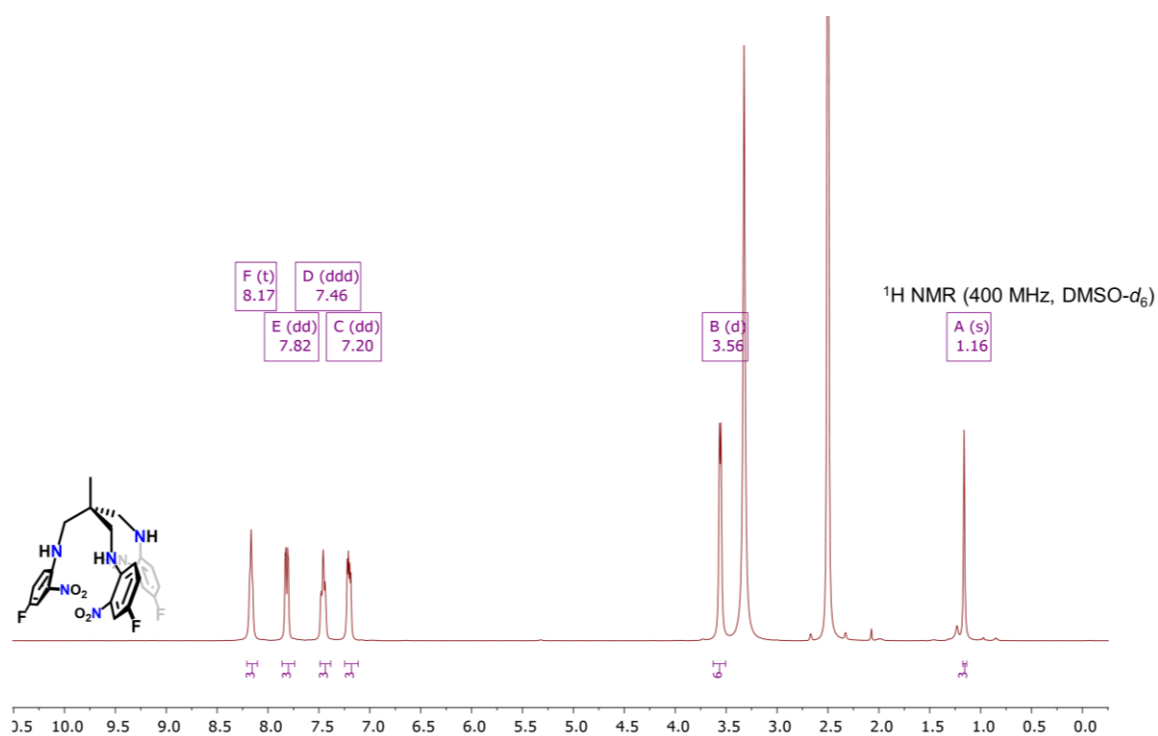
**Supplementary Figure 6.1.** <sup>1</sup>H NMR spectrum of 1,1,1-tris(p-toluenesulfonyloxy)methyl)ethane.



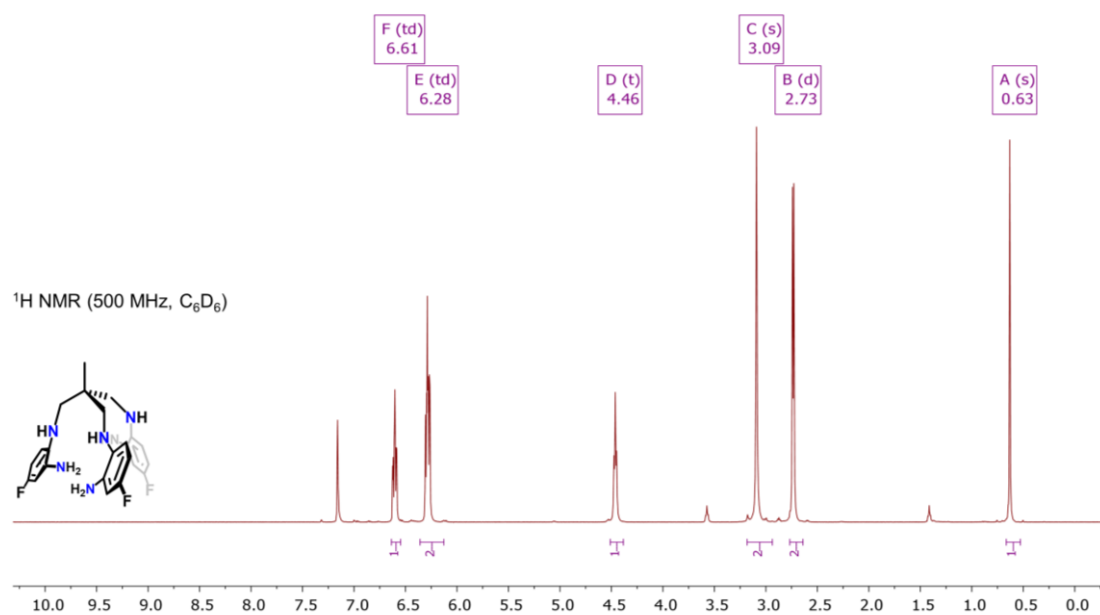
**Supplementary Figure 6.2.** <sup>1</sup>H NMR spectrum of 1,1,1-tris((benzylamino)methyl)ethane hydrochloride.



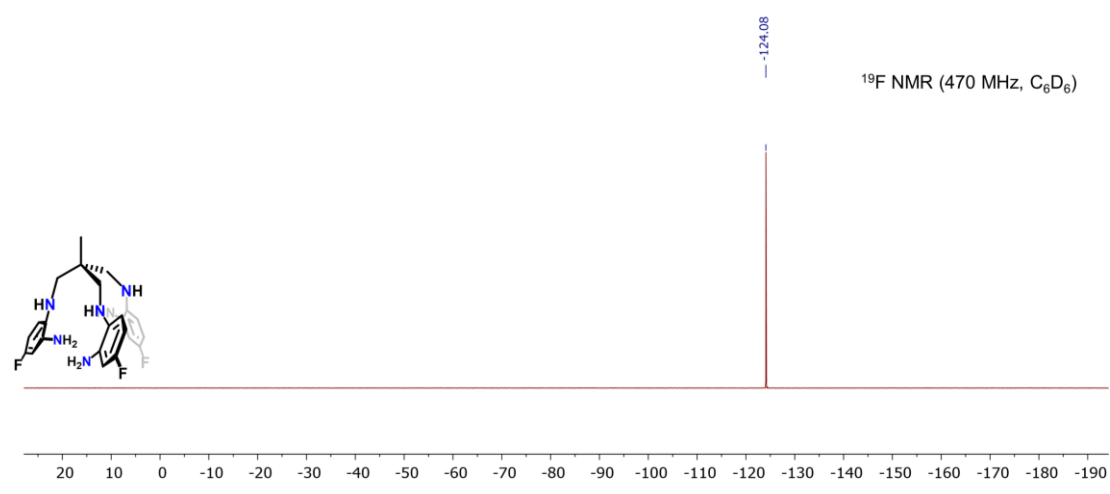
**Supplementary Figure 6.3.** <sup>1</sup>H NMR spectrum of tris-(aminomethyl)ethane hydrochloride.



**Supplementary Figure 6.4.** <sup>1</sup>H NMR spectrum of compound F,MeL(NO<sub>2</sub>)<sub>3</sub>.

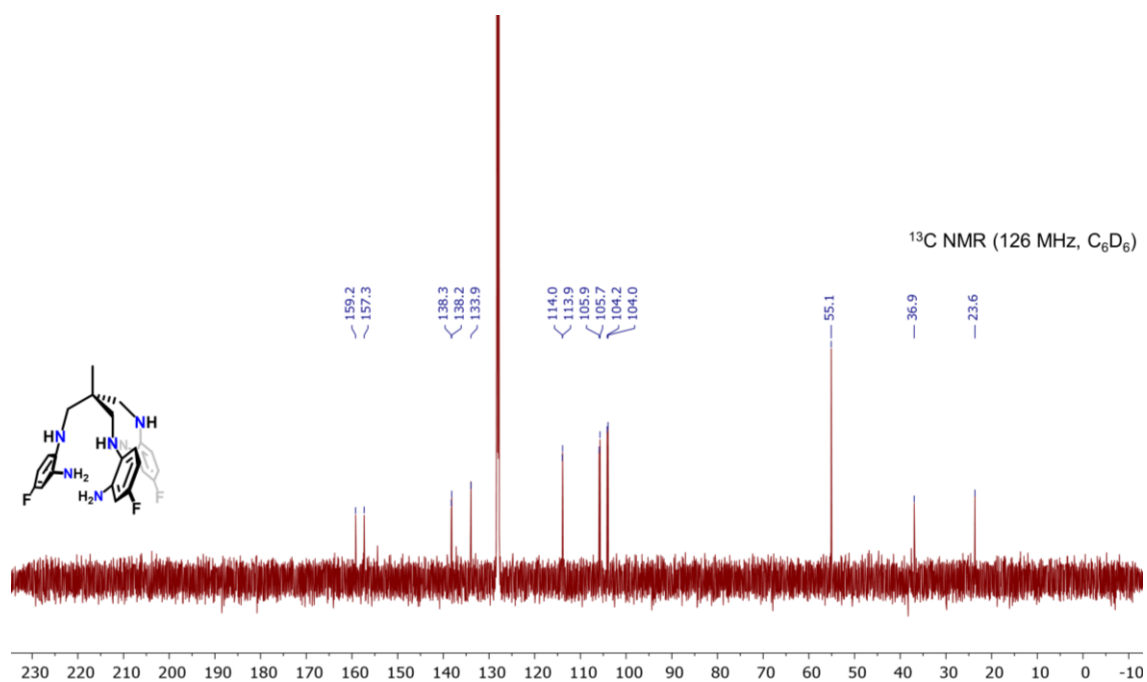


Supplementary Figure 6.5. <sup>1</sup>H NMR spectrum of compound **F,MeLH<sub>6</sub>**.

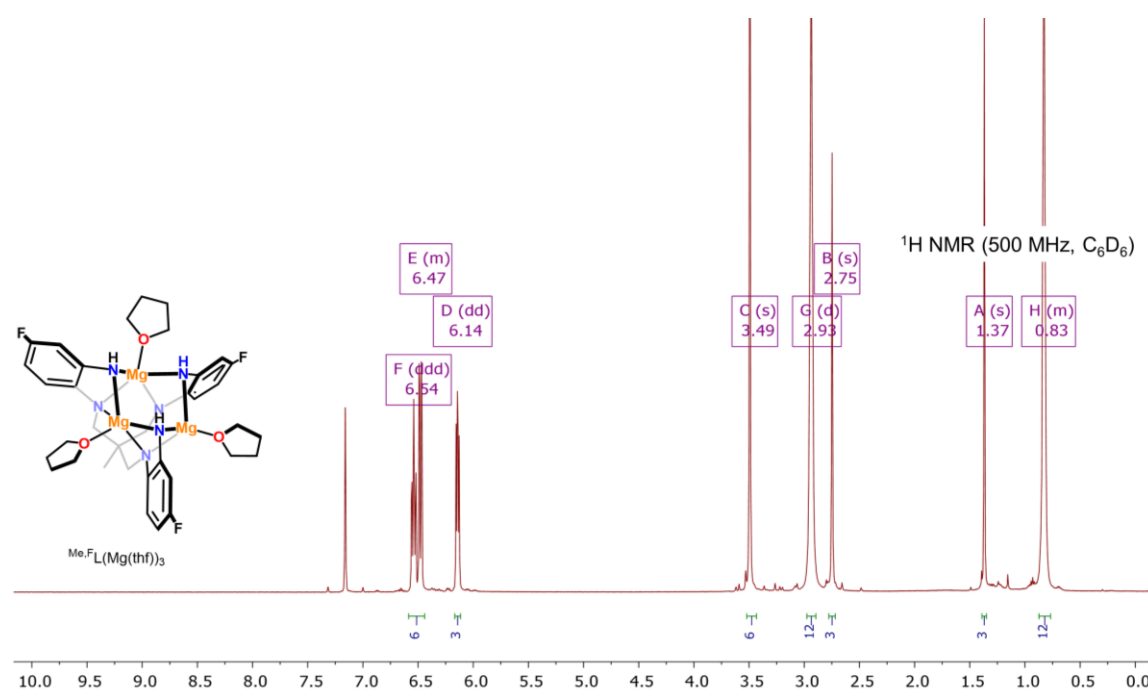


Supplementary Figure 6.6. <sup>19</sup>F NMR spectrum of compound **F,MeLH<sub>6</sub>**.

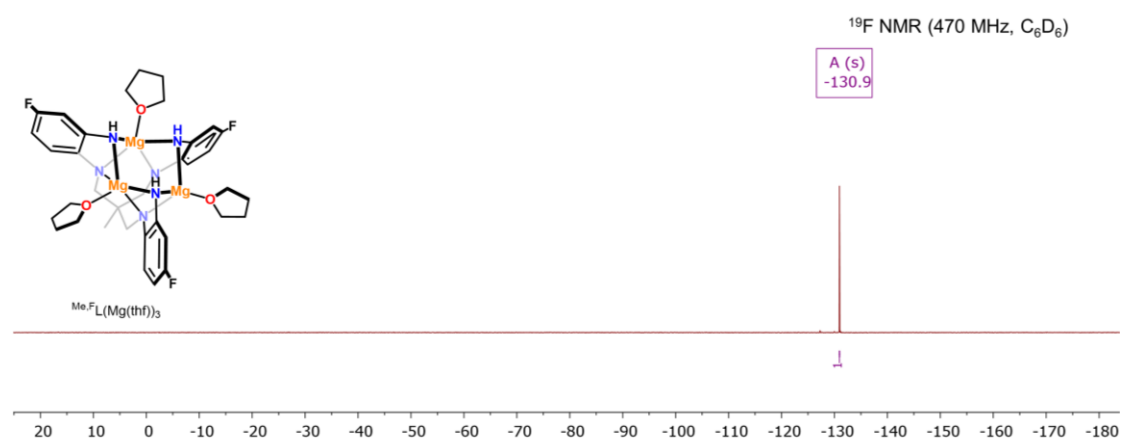




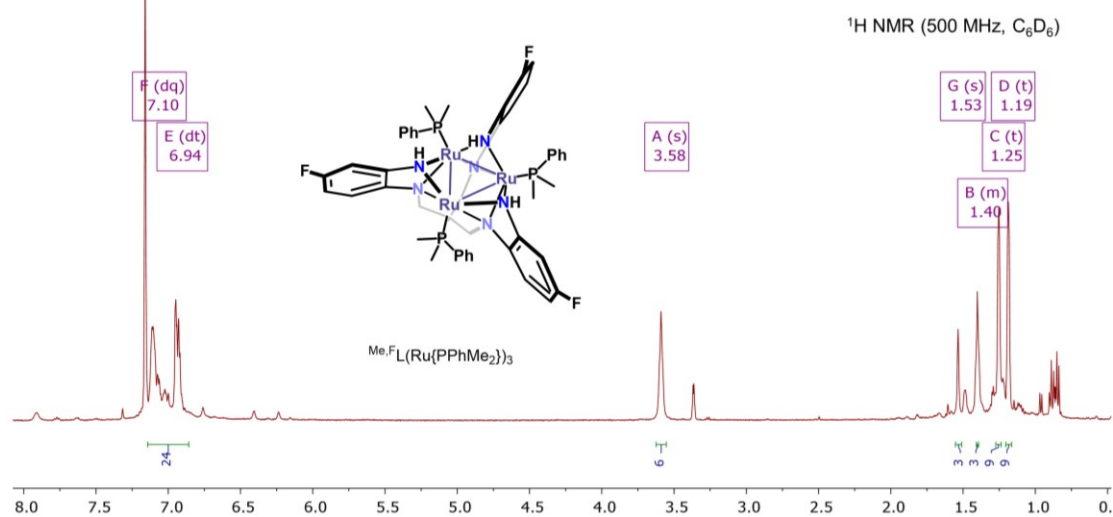
Supplementary Figure 6.7. <sup>13</sup>C NMR spectrum of compound **F,MeLH<sub>6</sub>**.



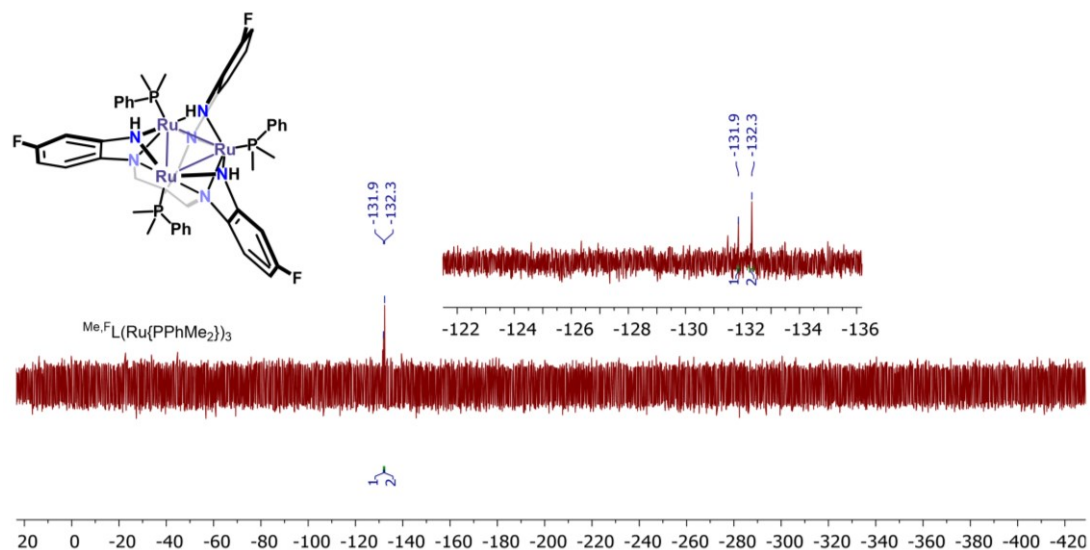
Supplementary Figure 6.8. <sup>1</sup>H NMR spectrum of compound **F,MeL(Mg{thf})<sub>3</sub>**.



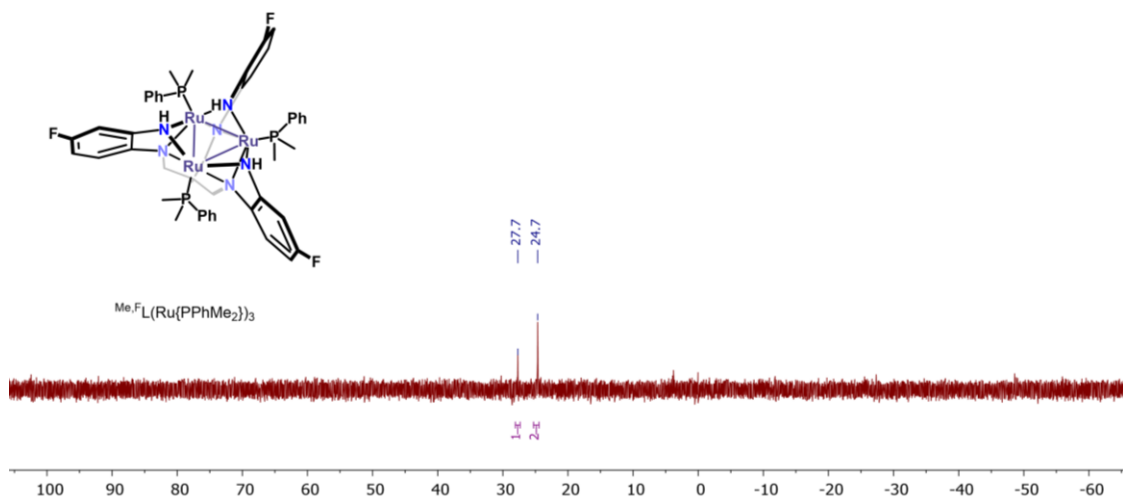
**Supplementary Figure 6.9.**  $^{19}\text{F}$  NMR spectrum of compound  $\text{F}_3\text{MeL}(\text{Mg}\{\text{thf}\})_3$ .



**Supplementary Figure 6.10.**  $^1\text{H}$  NMR spectrum of compound  $\text{F}_3\text{MeL}(\text{Ru}\{\text{PPhMe}_2\})_3$  (putative).



**Supplementary Figure 6.11.**  $^{19}\text{F}$  NMR (470 MHz,  $\text{C}_6\text{D}_6$ ) spectrum of compound  $\text{F}_2\text{Me}_2\text{L}(\text{Ru}\{\text{PPhMe}_2\})_3$  (putative).



**Supplementary Figure 6.12.**  $^{31}\text{P}$  NMR (202 MHz,  $\text{C}_6\text{D}_6$ ) spectrum of compound  $\text{F}_2\text{Me}_2\text{L}(\text{Ru}\{\text{PPhMe}_2\})_3$  (putative).

### 6.3 Crystallographic data

**Supplementary table 6.1.** Crystallographic data for compounds **5.1**, **5.2**, and **5.4**.

6.1	
Chemical formula	C <sub>26</sub> H <sub>34</sub> Ru
Formula weight	447.60
Crystal color	Yellow/green
Crystal system	Triclinic
Space group	P-1
<i>a</i> (Å)	8.8436(12)
<i>b</i> (Å)	11.3404(15)
<i>c</i> (Å)	12.1292(17)
<i>α</i> (deg)	67.597(13)
<i>β</i> (deg)	70.172(13)
<i>γ</i> (deg)	74.722(12)
<i>V</i> (Å <sup>3</sup> )	1045.3(3)
<i>Z</i>	2
<i>μ</i> (mm <sup>-1</sup> )	0.758
<i>T</i> (K)	120.15
GOF (S)	1.094
<i>R</i> <sup>a</sup> ( <i>wR</i> <sup>b</sup> )	0.0464
[ <i>I</i> > 2σ( <i>I</i> )]	0.0897
<i>R</i> <sup>a</sup> ( <i>wR</i> <sup>b</sup> )	0.0628
[all data]	0.1026
2Θ range for data collection (deg)	6.786 to 50.034
Reflections	15104
Radiation type	MoKα (λ = 0.71073)

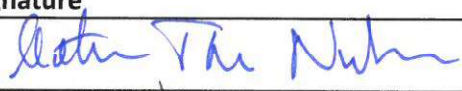


$$^a R I = \sum [w(F_0 - F_c)] / \sum [wF_0]; \quad ^b wR2 = \left[ \frac{\sum [w(F_0^2 - F_c^2)^2]}{\sum [w(F_0^2)^2]} \right]^{\frac{1}{2}}, \quad w = \frac{1}{[\sigma^2(F_0^2) + (aP)^2 + bP]}, \quad \text{where } P = [\max(F_0^2, 0) + 2(F_c^2)]/3$$

## 7 References

- (1) Fulmer, G. R.; Miller, A. J. M.; Sherden, N. H.; Gottlieb, H. E.; Nudelman, A.; Stoltz, B. M.; Bercaw, J. E.; Goldberg, K. I. *Organometallics* **2010**, *29*, 2176–2179.
- (2) Prawer, S.; Nemanich, R. J. *Philos. Trans. R. Soc. London. Ser. A Math. Phys. Eng. Sci.* **2004**, *362*, 2537–2565.
- (3) Berg, R. W.; Nørbygaard, T. *Appl. Spectrosc. Rev.* **2006**, *41*, 165–183.
- (4) Liu, C.; Berg, R. W. *Appl. Spectrosc.* **2012**, *66*, 1034–1043.
- (5) Dolomanov, O. V; Bourhis, L. J.; Gildea, R. J.; Howard, J. A. K.; Puschmann, H. *J. Appl. Crystallogr.* **2009**, *42*, 339–341.
- (6) Sheldrick, G. M. *Acta Crystallogr. Sect. A Found. Adv.* **2015**, *71*, 3–8.
- (7) Spek, A. L. *Acta Crystallogr. Sect. C Struct. Chem.* **2015**, *71*, 9–18.
- (8) Neese, F.; Wennmohs, F.; Becker, U.; Riplinger, C. *J. Chem. Phys.* **2020**, *152*, 224108.
- (9) Perdew, J. P.; Kurth, S.; Zupan, A.; Blaha, P. *Phys. Rev. Lett.* **1999**, *82*, 2544–2547.
- (10) Schäfer, A.; Horn, H.; Ahlrichs, R. *J. Chem. Phys.* **1992**, *97*, 2571–2577.
- (11) Weigend, F.; Häser, M.; Patzelt, H.; Ahlrichs, R. *Chem. Phys. Lett.* **1998**, *294*, 143–152.
- (12) Andrae, D.; Häußermann, U.; Dolg, M.; Stoll, H.; Preuß, H. *Theor. Chim. Acta* **1990**, *77*, 123–141.
- (13) CASIDA, M. E. In *Recent Advances in Density Functional Methods; Recent Advances in Computational Chemistry*; WORLD SCIENTIFIC, 1995; Vol. Volume 1, pp 155–192.
- (14) Rappoport, D.; Furche, F. *J. Chem. Phys.* **2010**, *133*, 134105.
- (15) Claramunt, R. M.; Elguero, J.; Meco, T. *J. Heterocycl. Chem.* **1983**, *20*, 1245–1249.
- (16) Ortiz, A.; Gómez-Sal, P.; Flores, J. C.; de Jesús, E. *Organometallics* **2018**, *37*, 3598–3610.
- (17) Boekelheide, V.; Vick, G. K. *J. Am. Chem. Soc.* **1956**, *78*, 653–658.
- (18) Guillard, R.; Lopez, M. A.; Tabard, A.; Richard, P.; Lecomte, C.; Brandes, S.; Hutchison, J. E.; Collman, J. P. *J. Am. Chem. Soc.* **1992**, *114*, 9877–9889.
- (19) Suzuki, M.; Fujii, T.; Naito, Y.; Yamoto, K.; Matsuoka, S.; Takagi, K.; Sugiyama, H.; Uekusa, H. *Bull. Chem. Soc. Jpn.* **2017**, *91*, 343–348.

- (20) Lee, H. M.; Lu, C. Y.; Chen, C. Y.; Chen, W. L.; Lin, H. C.; Chiu, P. L.; Cheng, P. Y. *Tetrahedron* **2004**, *60*, 5807–5825.
- (21) Ortiz, A.; Gómez-Sal, P.; Flores, J. C.; de Jesús, E. *Organometallics* **2018**, *37*, 3598–3610.
- (22) Noujeim, N.; Leclercq, L.; Schmitzer, A. R. *J. Org. Chem.* **2008**, *73*, 3784–3790.
- (23) Grimme, S.; Ehrlich, S.; Goerigk, L. *J. Comput. Chem.* **2011**, *32*, 1456–1465.
- (24) Beaufort, L.; Delaude, L.; Noels, A. F. *Tetrahedron* **2007**, *63*, 7003–7008.
- (25) Qin, C. J.; James, L.; Chartres, J. D.; Alcock, L. J.; Davis, K. J.; Willis, A. C.; Sargeson, A. M.; Bernhardt, P. V.; Ralph, S. F. *Inorg. Chem.* **2011**, *50*, 9131–9140.
- (26) Zhao, Q.; Betley, T. A. *Angew. Chem. Int. Ed.* **2011**, *50*, 709–712.

<b>Title of article</b>		
Homogeneous Catalysis by Organometallic Polynuclear Clusters (review article)		
<b>Journal/conference</b>		
Journal of Cluster Science		
<b>Author(s)</b>		
Mathias T. Nielsen, Rosa Padilla, Martin Nielsen		
<b>Name (capital letters) and signature of PhD student</b>		
MATHIAS THOR NIELSEN		
<b>PhD student's date of birth</b>		
12-06-94		
<b>Declaration of the PhD student's contribution</b>		
<i>For each category in the table below, please specify the PhD student's contribution to the article as appropriate (please do not fill in with names or x's)</i>		
<b>Category</b>	<b>Minor contribution to the work</b> <i>(please specify the nature of the PhD student's contribution)</i>	<b>Substantial contribution to the work</b> <i>(please specify the nature of the PhD student's contribution)</i>
Formulation of the conceptual framework and/or planning of the design of the study including scientific questions		Literature review: <ul style="list-style-type: none"> <li>Finding the most pertinent literature relevant to the review</li> <li>Defining the scope of the review</li> </ul>
Carrying out of experiments/data collection and analysis/interpretation of results		<ul style="list-style-type: none"> <li>Assessing appropriate articles by evaluating each article's content to deem fit;</li> </ul>
Writing of the article/revising the manuscript for intellectual content		<ul style="list-style-type: none"> <li>Provided all figures, tables, and the first draft on one half of the review;</li> <li>Revising the would-be final draft in conjunction with supervisor;</li> <li>Evaluated on Editor's comments and updated review accordingly</li> </ul>
<b>Signatures</b>		

<b>Title of article</b>			
Homogeneous Catalysis by Organometallic Polynuclear Clusters (review article)			
<b>Journal/conference</b>			
Journal of Cluster Science			
<b>Author(s)</b>			
Mathias T. Nielsen, Rosa Padilla, Martin Nielsen			
<b>Name (capital letters) and signature of PhD student</b>			
MATHIAS THOR NIELSEN			
<b>PhD student's date of birth</b>			
12-06-94			
<b>Date</b>	<b>Name</b>	<b>Title</b>	<b>Signature</b>
20/10/2020	Mathias Thor Nielsen	PhD student	
20/10/2020	Rosa María Padilla Paz	Postdoc	
20/10/2020	Martin Nielsen	Associate Professor	

Please note that by signing this declaration, co-authors permit the PhD student to reuse whole or parts of co-authored articles in their PhD thesis, under the condition that co-authors are acknowledged in connection with the reused text or figure.





# Homogeneous Catalysis by Organometallic Polynuclear Clusters

Mathias T. Nielsen<sup>1</sup> · Rosa Padilla<sup>1</sup> · Martin Nielsen<sup>1</sup>

Received: 22 May 2019 / Published online: 18 July 2019  
© Springer Science+Business Media, LLC, part of Springer Nature 2019

## Abstract

Homogeneous polynuclear metal clusters constitute a broad class of coordination compounds with important applications in catalysis. The current interest of synthetic chemistry in this field demands the exploration of new strategies to develop catalytic methods that work under mild conditions and maximize atom utilization. This review covers the application of polynuclear clusters of nuclearity  $\geq 3$  in homogeneous catalytic processes, with focus on providing an array of examples of various reaction types within cluster catalysis.

**Keywords** Polynuclear cluster · Ligand scaffold · Homogeneous catalysis

## Introduction

Polynuclear metal clusters constitute a broad class of coordination compounds with numerous applications in catalysis. As is true for traditional mononuclear organometallic catalysis, polynuclear clusters may perform complex transformations in homogeneous solution. The principal objective of both fields is the exploration of new strategies to develop novel catalytic atom-efficient transformations that work under mild conditions. The typical approach towards this goal is to employ a transition metal or -ion with specific fundamental features, and then fine-tune the catalytic behavior by proper modification of the ligand scaffold. In this regard, compared to mononuclear complexes, the study of polynuclear cluster catalysis offers the potential of tuning an entirely new dimension, namely the interaction between several transition metals.

The chemistry involved in activation of small molecules, such as alkenes, alkynes, CO, and H<sub>2</sub>, by metal-(hydrido)carbonyl clusters is well reported [1–5]. The binding of substrate to these clusters varies from analogous to monometallic complexes, to simultaneous interactions of the substrate with multiple metal centers resulting in unique chemo-, regio- and stereoselectivities, see for

example Scheme 1 [6–8]. These scenarios provide many opportunities for novel transformations and, as such, demonstrate that the combined application of more than one metal offers appealing new opportunities for the synthetic community.

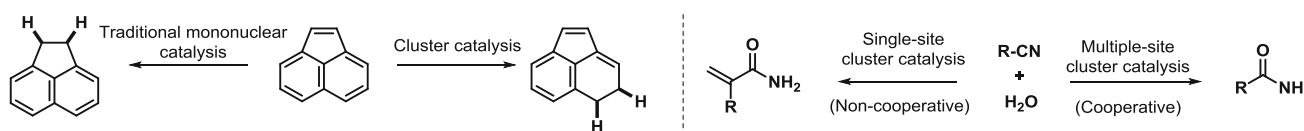
In this review, we focus on catalysis based on homogeneous polynuclear transition metal clusters with nuclearities of three or higher. We do so because dinuclear clusters have recently been extensively discussed in excellent reviews [9, 10]. In the course of analyzing the definitions and criteria discussed below, we have sought to provide pertinent literature, which serves to deliver excellent illustrations on current state-of-the-art within cluster catalysis.

## Cluster Catalysis

The term *cluster* was introduced in 1964 by F. A. Cotton to designate a finite number of metal atoms held together to a certain extent, either by metal–metal interactions or metal–nonmetal bonds [11–13]. The nuclearity defines the total number of metal atoms comprising the cluster, and further classification is made with respect to the number of different metals. For example, a hexanuclear bimetallic cluster refers to a complex comprising of six metals of two different natures, such as [Ru<sub>5</sub>Pt] [14]. In addition, it may be practical to state whether a cluster comprises metal–metal interactions [15]. The proximity between metal centers permits unique substrate transformations as

✉ Martin Nielsen  
marnie@kemi.dtu.dk

<sup>1</sup> Department of Chemistry, Technical University of Denmark, 2800 Kgs. Lyngby, Denmark



**Scheme 1** Examples of unique cluster catalyzed transformations compared to traditional mononuclear catalysis (left scheme) and between different types of cluster catalysis (right scheme) [6–8]

multiple binding sites are available, and each metal center potentially provides additional redox-active electrons.

A given cluster's electronic properties and catalytic proficiency largely relate to three parameters, namely (i) electronic properties of the parent metals, (ii) the combination of metal and ligand, and (iii) the extent of metal–metal interactions. Cluster frameworks consisting of early-transition metals predominantly comprise high valent metals combined with  $\sigma/\pi$ -donating ligands, such as halides and chalcogenides (*high valent clusters*) [16, 17]. The ligands act as a source of electrons that promote bonding interactions between the metals, as well as stabilizing the positive oxidation states. Such electropositive clusters often act as potential Lewis acidic catalysts. Contrary, late-transition metal clusters mainly comprise low valent metals combined with  $\pi$ -accepting ligands (*low valent clusters*) [18]. Hereof, CO represents the more common ligand albeit other examples of  $\pi$ -accepting ligands have been reported, such as phosphines, alkenes, alkynes, and heteroaromatics. These typically redox-active compounds may undergo oxidative addition and can catalyze reactions such as hydrogenation, hydroformylation and C–H bond activation.

The propensity to form M–M bonds increases when going from 3d, through 4d, to 5d metals, which reflects the increased possible  $d$ – $d$  orbital overlap when going down a transition metal triad. A range of [MRu<sub>2</sub>], M=Ni, Pd, Pt, clusters work to demonstrate the effect on catalysis when substituting one metal for another in a triad. Thus, for the catalytic oxidation of benzylic alcohol to benzaldehyde, the

activity was observed to increase up to fivefold when substituting either [PdRu<sub>2</sub>] or [PtRu<sub>2</sub>] with [NiRu<sub>2</sub>] [19]. Interestingly, the effect of substituting Pt with Ni was also reflected in the structures of the cluster cores. As such, the NiRu<sub>2</sub> core in [NiRu<sub>2</sub>] is asymmetric with Ni–Ru bond lengths of 2.90 and 3.12 Å, respectively, whereas in [PtRu<sub>2</sub>] the PtRu<sub>2</sub> core is symmetric with equidistant Pt–Ru bond lengths of 3.16 Å.

Clusters containing first-row transition metals are significantly more affected by ligation than the corresponding second and third row metals. Perturbation of the  $d$ -orbital splitting and the properties derived hereof, thus relates to the ligand, and whether this induces a low field-splitting (*weak field*), or a large field-splitting (*strong field*) environment. However, the majority of cluster catalysts comprises 4d and 5d metals coordinated by strong-field ligands.

Laine proposed a three-level scale to reflect the involvement of a given cluster in the catalytic cycle as schematized in Fig. 1 [20]. The highest level of sophistication necessitate that at least two of the cluster's metal centers are mechanistically required for the transformation. The combination of multiple metals (identical or different in chemical nature) typically leading to a distinct chemo-, regio- and stereoselectivity, as well as a significantly different activity from a mere additive effect, is considered as *synergism* or *cooperativity*. In this regard, specific combinations of various transition metals can afford clusters with unique stereoelectronic environments to satisfy a certain set of criteria for reactivity. On the other hand, a single metal center may mechanistically account for the

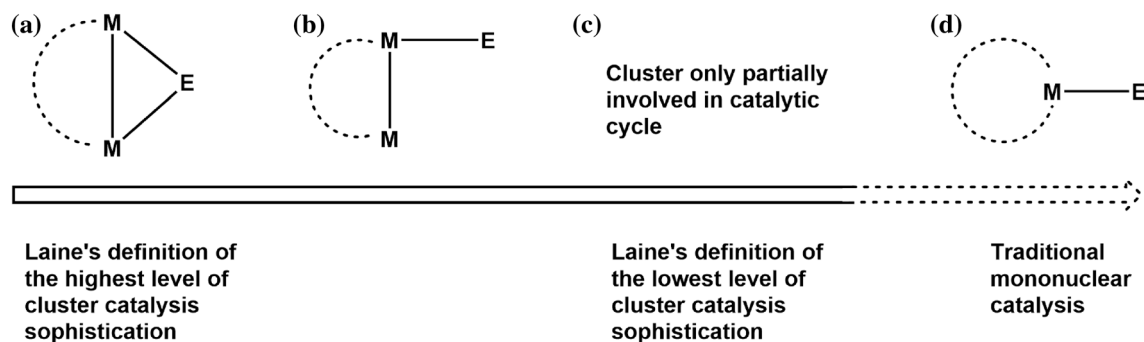
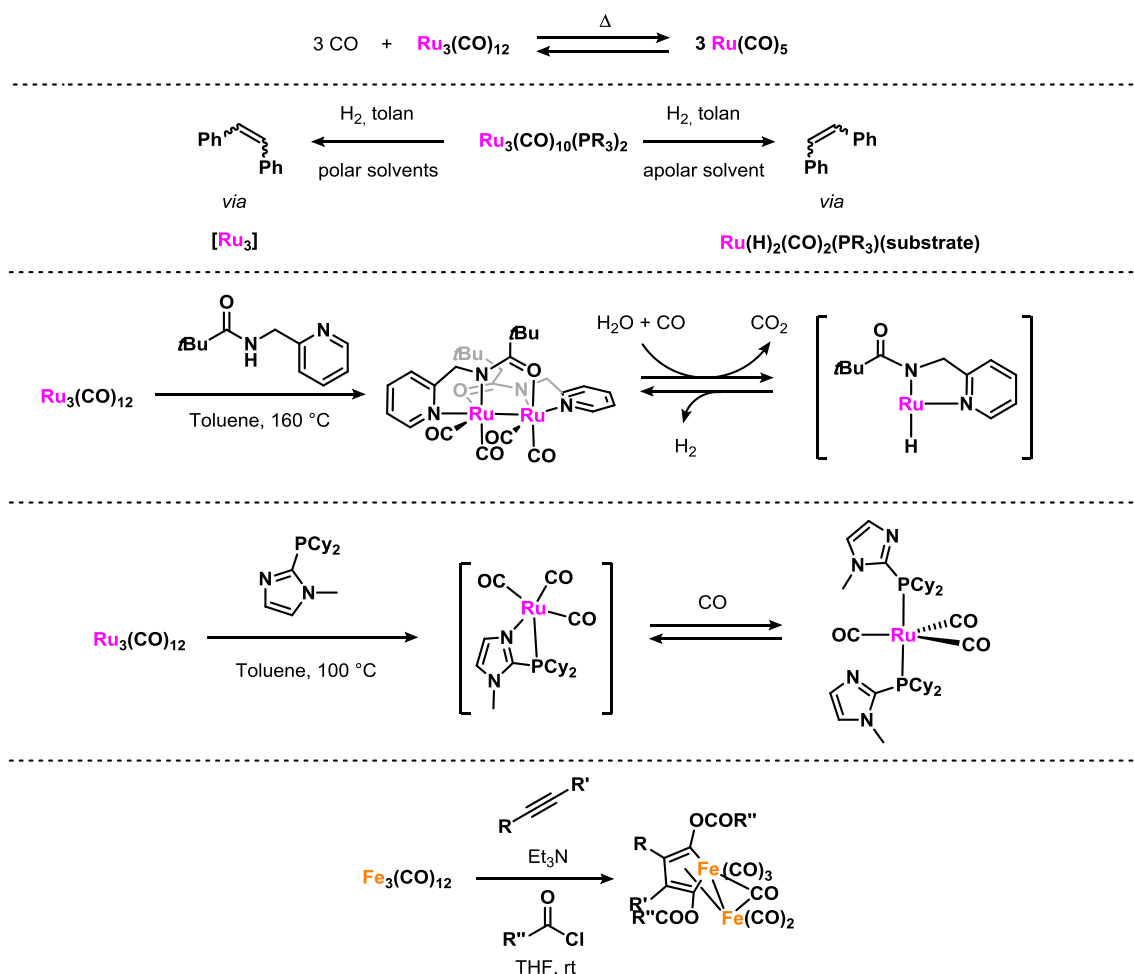


**Fig. 1** Three levels of sophistication **a** multiple metal interactions with a substrate, **b** a metal–substrate interaction is influenced by a vicinal metal center either electronic, sterically or both, and **c** cluster only partially involved in the catalytic cycle [20]. Finally, **d** represents traditional mononuclear organometallic catalysis



**Scheme 2** Selected examples of fragmentations for catalyst precursors  $\text{Ru}_3(\text{CO})_{12}$  and  $\text{Fe}_3(\text{CO})_{12}$ . Starting from the top, through the bottom, the reactions follow [39, 43, 44, 46–54], respectively

transformation, while interacting with vicinal centers. The other metal thus acts as an *extended ligand*. The nature of this interaction may be explained from both a steric and an electronic perturbation of the center bound to the substrate, and thereby enhance the overall catalytic performance. Finally, the lowest level of sophistication suggests a cluster be required in at least one of the catalytic steps.

Laine's three-level scale of sophistication provides the basis for the following separate five criteria, also proposed by Laine, that suggest cluster mediated catalysis as:

1. An increasing amount of added catalysts results in a corresponding increase in turnover frequency (TOF).
2. Differences in product selectivity due to the use of a cluster catalyst (precursor), which mechanistically cannot be justified by a mononuclear compound.
3. A change in reaction conditions, or change in the catalyst, which favors metal–metal bond formation, induces an increased catalytic activity.
4. Mixed-metal cluster catalysis is suggested given a combination of at least two different metals enhance the rate of reaction or change product selectivity, which either fails to provide alone.
5. Chiral induction achieved employing asymmetric metal cluster (pre)catalysts. Chirality may reside on the basic skeletal- or metal-framework.

While these criteria provide an indirect indication of cluster catalysis, supplementary measurements are often required to ascertain the true nature of the catalyst. Such further measurement can include testing for agglomeration of colloids and nanoparticles, for example by a  $\text{Hg}(0)$  poisoning test. In addition, a catalyst (precursor) inhibition test, as well as recovery and recycling experiments, may provide even further insights into the nature of the true catalyst [21]. Moreover, it is important to emphasize that no methods alone should form the conclusion on the nature of the true catalyst, as immature conclusions may potentially be drawn [22].

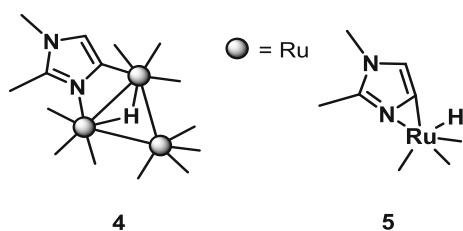


**Fig. 2** Two compounds with different nuclearity assumed to be central for the activation of C–H bond activation in 1,2-dimethylimidazole. Terminal CO molecules have been omitted for clarity [62]

### Clusters: Catalysts or Precatalysts?

Polynuclear cluster catalysts are more often isolated as their corresponding precatalyst rather than as one of the catalytically active intermediates because of the high reactivity of the latter. Thus, the binary metal carbonyl dodecacarbonyl triruthenium,  $\text{Ru}_3(\text{CO})_{12}$ , has been extensively used in small molecule activation, for example of  $\text{H}_2$  [23–25] or CO [26–30], as well as more complex transformations, such as (cyclo)carbonylation [31–34] and C–H bond activation [35–38]. However, while highly active systems have been reported, mechanistic studies on these

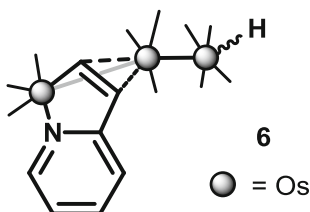


**Fig. 3** 5-membered metallacycle obtained from reaction of  $\text{Os}_3(\text{CO})_{10}(\text{CH}_3\text{CN})_2$  with 2-vinylpyridine. Terminal CO molecules have been omitted for clarity [67]

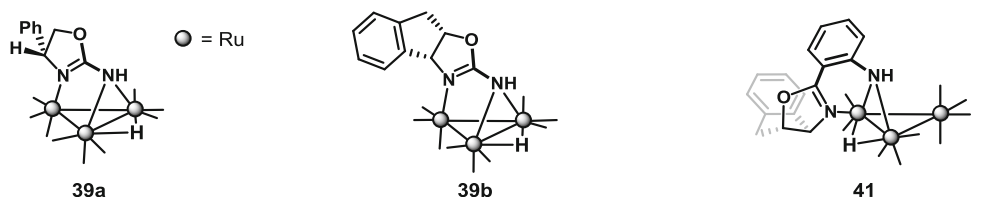
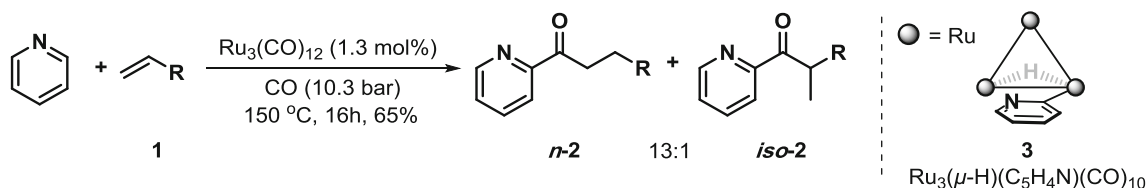


**Fig. 4** Three triruthenium clusters **39–40** derived from chiral aminooxazolines. Terminal CO molecules have been omitted for clarity [90]



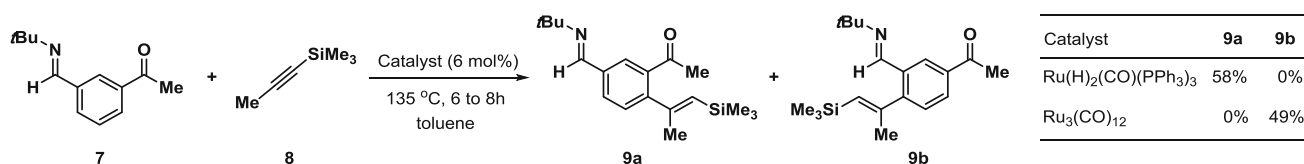
**Scheme 3** Acylation of pyridine using  $\text{Ru}_3(\text{CO})_{12}$  as precatalyst [61]

$\text{Ru}_3(\text{CO})_{12}$  catalyzed reactions strongly suggest that the cluster acts as a precatalyst and transforms into the active species prior to catalysis.

At high pressures of CO,  $\text{Ru}_3(\text{CO})_{12}$  is in equilibrium with its mononuclear congener  $\text{Ru}(\text{CO})_5$ , see Scheme 2 [39]. This equilibrium has been shown to be highly accelerated by the presence of chloride [40]. Geoffroy and Dombek reported various nuclearity ruthenium structures resulting from different equilibria depending on temperature, CO pressure and the nature of a halide additive [41]. Thermal treatment afford tetranuclear butterfly structures in presence of chloride and bromide, whereas iodide promotes loss of CO resulting in a triruthenium- $(\mu_3\text{-I})$  species.

Treating  $\text{Ru}_3(\text{CO})_{12}$  with dppe resulted in formation of the mononuclear species  $\text{Ru}(\text{CO})_3(\text{dppe})$  [42]. Interestingly, work by Dyson and Duckett demonstrates that, in polar solvents, the  $[\text{Ru}_3]$ -core stays intact despite the presence of phosphine, whereas apolar solvents induce cluster fragmentation, forming  $\text{Ru}(\text{H})_2(\text{CO})_2(\text{PPh}_3)_2$  [43, 44]. Krische was able to isolate a mononuclear Ru-metallacycle from the fragmentation of  $\text{Ru}_3(\text{CO})_{12}$  in presence of  $\text{PCy}_3$  [45]. Chatani found that, under carbonylation of C–H bonds, fragmentation of the precatalyst  $\text{Ru}_3(\text{CO})_{12}$  into mononuclear Ru-complexes occurs [46–48]. Beller reported precatalytic amounts of  $\text{Ru}_3(\text{CO})_{12}$  mixed with phosphine ligands in situ forms a mononuclear species [49–51]. Thus, there is significant evidence suggesting that  $\text{Ru}_3(\text{CO})_{12}$  behaves as a precatalyst for a variety of catalytically active mononuclear Ru-species.

In a similar fashion, treatment of  $\text{Fe}_3(\text{CO})_{12}$  with amine in THF was reported by Periasamy to fragment into two different compounds, a dinuclear  $\text{Fe}_2(\text{CO})_8$  and an amine- $\text{Fe}(\text{CO})_4$  species [52–54]. Chini and Martinengo reported that the binary tetrarhodium carbonyl cluster,  $\text{Rh}_4(\text{CO})_{12}$

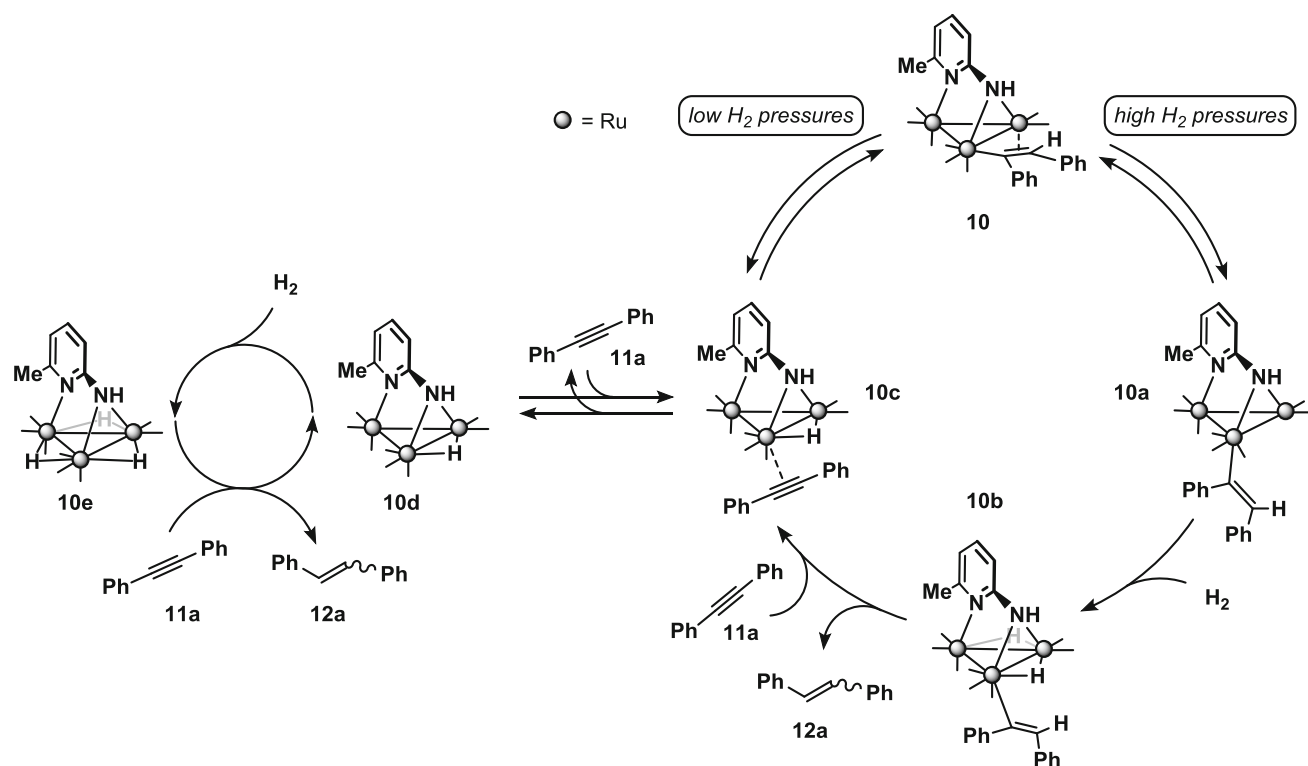


**Scheme 4** Catalyst nuclearity affect the regioselectivity in vinylation of functionalized benzenes [71]

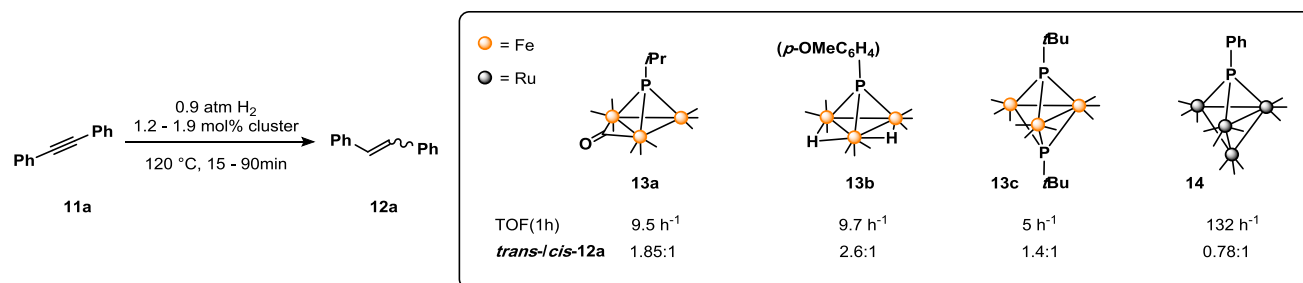
undergoes thermal decomposition (130–140 °C) under  $\text{N}_2$ , affording  $\text{Rh}_6(\text{CO})_{16}$  [55]. This decomposition was also observed to occur slowly in MeOH. The reaction of either tetra- or hexarhodium cluster with  $\text{PPh}_3$  under a CO atmosphere afforded the dirhodium compound,  $\text{Rh}_2(\text{CO})_4(\text{PPh}_3)_4$ . Chini later reported that  $\text{Rh}_4(\text{CO})_{12}$  forms an array of clusters varying in nuclearity at increasingly reducing conditions under a CO atmosphere [56]. Likewise,  $\text{Rh}_6(\text{CO})_{16}$  reacts with CO under reducing conditions to form anionic compounds of lower nuclearities, namely  $[\text{Rh}_4(\text{CO})_{11}]^{2-}$  and  $[\text{Rh}(\text{CO})_4]^-$  [57]. Fragmentation of  $\text{Rh}_4(\text{CO})_{12}$  was corroborated by Matsuda, who reported degradation under silylformylation of terminal alkynes using  $\text{Rh}_4(\text{CO})_{12}$  as precatalyst [58]. Longoni demonstrated that the transformation of tetracobalt dodecacarbonyl,  $\text{Co}_4(\text{CO})_{12}$ , to a dicobalt compound,  $\text{Co}_2(\text{CO})_8$ , is feasible at room temperature under approximately 1 bar of CO in

$i\text{PrOH}$  [59]. The equilibrium was further pushed towards the dicobalt in the presence of halide ions. These findings corroborate previously established decomposition patterns of the tetracobaltate clusters  $[\text{Co}_4(\text{CO})_{11}\text{X}]^-$ ,  $\text{X} = \text{Br}, \text{I}$ , or  $\text{SCN}$ , in Lewis-basic solvents.

Watanabe studied various Ru-complexes as (pre)catalysts for the hydroacylation of olefins with an array of aldehydes [60]. The authors were able to recover  $\text{Ru}_3(\text{CO})_{12}$  from the reaction mixture where mononuclear complexes, such as  $\text{Ru}(\text{COD})(\text{COT})$  and  $\text{Ru}(\text{COD})_2$ , had been employed as precatalysts. Among the screened potential catalysts,  $\text{Ru}_3(\text{CO})_{12}$  showed the best activity with 95% conversion and 50% yield. Moreover, changing the composition of the atmosphere significantly affected the amount of recovered  $\text{Ru}_3(\text{CO})_{12}$ . Approximately 50 bar of Ar afforded a merely 5% recovery, whereas 20 bar of CO resulted in 60% recovery. The authors suggest that CO

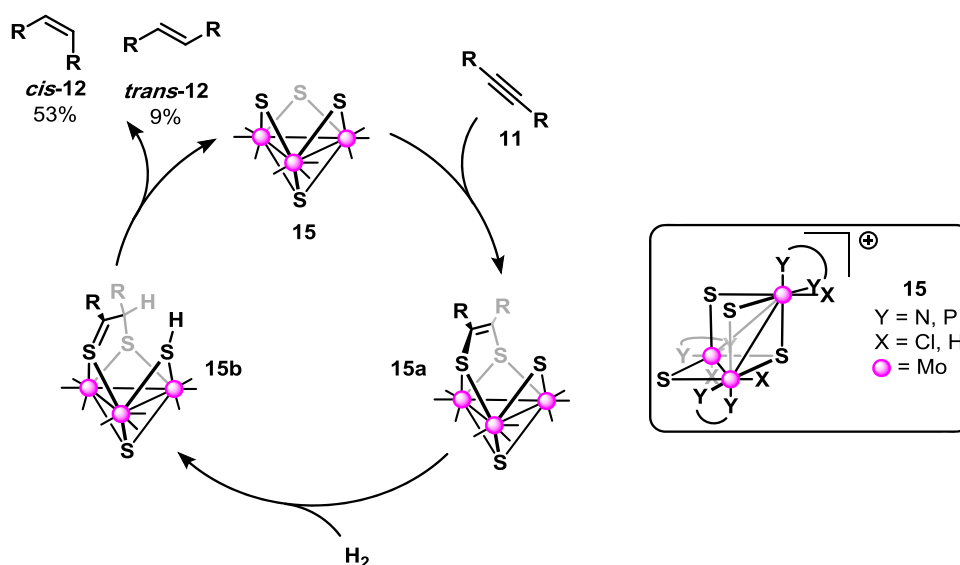


**Scheme 5** Proposed mechanism by Cabeza of the hydrogenation of tolan (**11a**) to stilbene (**12a**) catalyzed by **10**. Terminal CO molecules have been omitted for clarity [72, 73]



**Scheme 6** Three structurally related face-capped triiron cluster compared to a face-capped tetraruthenium cluster for the hydrogenation of **11a** to *trans*-**12a** and *cis*-**12a**. Terminal CO molecules have been omitted for clarity [75]

**Scheme 7** Partial hydrogenation of **11** via bridging sulfur atoms, rather than the metals of **15**. Terminal CO molecules have been omitted for clarity [76]



stabilize  $\text{Ru}(\text{CO})_5$  and  $\text{Ru}_3(\text{CO})_{12}$ , either of which may be the active catalyst.

Similarly, Moore investigated the acylation of pyridine with CO and olefins **1** using  $\text{Ru}_3(\text{CO})_{12}$  as precatalyst, Scheme 3 [61]. Under 10.3 bar of CO pressure and at 150 °C, 65% of a 13:1 mixture of *n*-**2** and *iso*-**2** was produced. During their studies, they observed that the ortho-metalated compound **3** decomposed to  $\text{Ru}_3(\text{CO})_{12}$  under the given reaction conditions albeit in the absence of an olefin. Thus, even though **3** was not observed in the catalytic reaction mixture, they inferred that the catalytic cycle is based on a triruthenium hydride species. They further corroborated their finding by performing kinetic studies that showed a first-order rate dependence on the  $\text{Ru}_3(\text{CO})_{12}$  concentration.

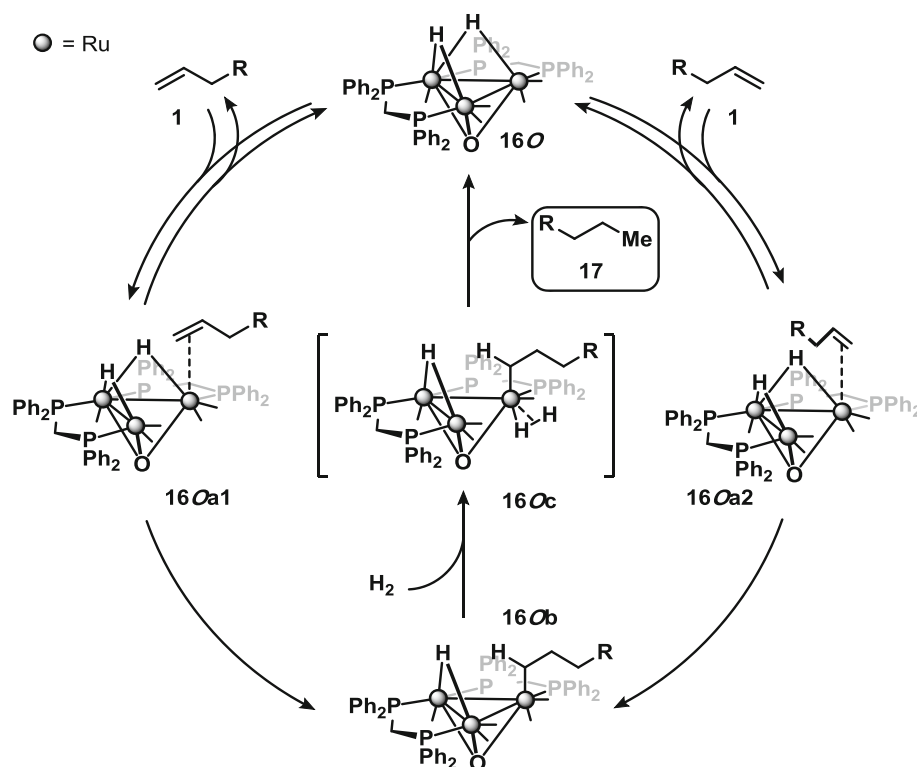
Related transformations exploiting chelate assisted C–H bond activation using  $\text{Ru}_3(\text{CO})_{12}$  as (pre)catalyst has since been reported by the groups of Murai and Chatani. This includes the reaction of 1,2-dimethylimidazole with *n*-hexene (**1a**) under CO affording catalytic acylation of the imidazole with yields up to 77% of predominantly the

linear product (up to > 99:1) [62]. Interestingly, the authors propose the left triruthenium species **4** in Fig. 2 to be a key component in the catalytic cycle. However, it could not be ruled out that the monoruthenium complex **5** is catalytically active as well. Moreover, the two structures were suggested from a related triosmium cluster,  $\text{Os}_3(\text{C})_{10}(\text{CH}_3\text{CN})_2$  [63], as well as the ortho-metalated species discussed by Moore in Scheme 3, to rationalize for the observed products.

The general difficulty in ascertaining the true nature and nuclearity of the catalysts in various reactions is reflected in discussions in several subsequent reports using  $\text{Ru}_3(\text{CO})_{12}$  as precatalyst. One examples is the *N*-directed Ru-catalyzed carbonylation at a C–H bond in pyridylbenzenes, where analyses suggest the mononuclear species to be the catalytically active species [64]. Another example is the cyclocarbonylation of yne-aldehydes forming bicyclic  $\alpha,\beta$ -unsaturated  $\gamma$ -butyrolactones, where the catalyst was merely defined as a Ru dihydride species [65]. In a third example, both  $\text{Ru}_3(\text{CO})_{12}$  and  $\text{Rh}_4(\text{CO})_{12}$  were found active in catalytic carbonylation at olefinic pyridylolefins



**Scheme 8** Face-capping oxygen and dpmm ligands of **16O** provide positive interactions that ensures the cluster integrity throughout the catalytic hydrogenation of olefins as proposed by Bonnet. Terminal CO molecules have been omitted for clarity [77]



via chelate assisted  $sp^2$  C–H bond activation [66]. In this study, the reactivity patterns of the precatalysts were rationalized based on a previously reported triosmium structure **6** shown in Fig. 3 [67]. Likewise, Ru-catalyzed carbonylation of imidazoles via  $sp^2$  C–H bond activation adjacent to the  $sp^2$  N proceeds in high yields (up to 96%) and excellent linear selectivity (up to > 99:1). The authors rationalize the observed products via an ortho-metalated trinuclear Ru-cluster as in **4** [68]. Finally, Ru-catalyzed carbonylation of aza-heterocycles provided C–H bond activation  $\beta$  to a directing nitrogen proceeding via **5** [69].

In this context, Chatani found that carbonylation of pyridin-2-ylmethylene *N*-substituted aromatic amides using  $\text{Ru}_3(\text{CO})_{12}$  as precatalyst produced a diruthenium complex with the substrate providing a chelating *N,N*-coordination environment to one of the Ru-centers [70]. While catalytically active, the compound was attributed as the resting state, as the presence of  $\text{H}_2\text{O}$  was necessary for a significant reactivity. As such, merely 16% product was observed after 3 days without the presence of  $\text{H}_2\text{O}$ , which should be compared to 55% after the same time span in the presence of two equivalents of  $\text{H}_2\text{O}$ . Moreover, the authors rationalized that the dinuclear species reacted under water–gas-shift conditions. A similar dinuclear species, also attributed as the resting state, was found in later studies on carbonylation of aromatic amides [46–48]. This compound, too, was fragmented in the presence of water, forming the mononuclear species.

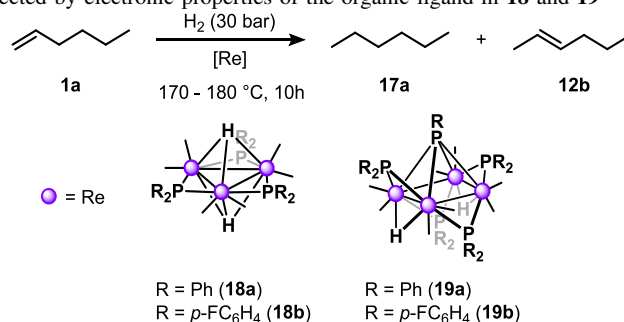
Interestingly, work by Murai and Chatani on alkylation and vinylation of aromatic compounds revealed a catalyst nuclearity influence on the product regioselectivity [71]. Thus, as shown in Scheme 4,  $\text{Ru}(\text{H})_2(\text{CO})(\text{PPh}_3)_3$  provides C–C bond formation *ortho* to the acetyl group of **7** leading to **9a**, whereas  $\text{Ru}_3(\text{CO})_{12}$  affords a selectivity *ortho* to the imine leading to **9b**. Hence, even though no further detailed mechanistic investigation were carried out, these observation suggest cluster catalysis based on, at least, the second criterion according to Laine.

These examples are meant to demonstrate the need for thorough mechanistic investigations to account for cluster catalysis and, if cluster catalysis is indicated, to elucidate the structure of the catalytically active cluster(s). Moreover, a trend is that polydentate ligands provide means of stabilizing a cluster framework during the catalytic cycle. They do so by enabling sufficient structural fluxionality for the various bond cleavages and formations throughout the catalytic transformation while retaining cluster integrity.

## Homonuclear Clusters in Catalysis

### Hydrogenation

Cabeza provided an example of a well-defined triruthenium cluster active in catalysis, where the preformed complex **10** catalyzes the hydrogenation of tolan (**11a**) to stilbene

**Table 1** Treatment of **1a** with H<sub>2</sub> is affected by electronic properties of the organic ligand in **18** and **19**

Catalyst	Loading (mol%)	Conversion (%) [TOF (h <sup>-1</sup> )]	
		17a	12b
18a	$1.6 \times 10^{-2}$	28.6 (184)	40.4 (260)
19a	$8.3 \times 10^{-3}$	23.8 (288)	39.6 (480)
18b	$9.0 \times 10^{-3}$	56.4 (630)	8.3 (92)
19b	$8.5 \times 10^{-3}$	63.5 (750)	21.1 (250)

Terminal CO molecules have been omitted for clarity [78]


(**12a**), as shown in Scheme 5 [72, 73]. The authors emphasize that the ampy-NH moiety affords a substrate coordination-wise regioselectivity towards the *cis* position to the NH coordinated ruthenium center, as CO substitution was consistently observed at this site. To elucidate the catalytic cycle, varying pressures of H<sub>2</sub> were used to establish rate-order dependence of substrate/catalyst ratio. At low H<sub>2</sub> pressures (low substrate to catalyst ratios), **10** undergoes  $\beta$ -hydride elimination to yield **10c**, followed by dissociation of tolan leading to **10d**. Subsequently, **10e** is formed by oxidative addition of H<sub>2</sub> to **10d**, followed by a fast hydrogenation of an incoming **11a**. Contrary, at high H<sub>2</sub> pressures (high substrate to catalyst ratios), **10** rearranges to **10a**, which then undergoes oxidative addition of H<sub>2</sub> forming **10b**. Hydride transfer and loss of **12a** with subsequent association of **11a** then leads to **10c**. Finally, a 1,2-migratory insertion completes the cycle. A later study of a structurally related cationic ruthenium cluster,  $[\text{Ru}_3(\mu\text{-H})(\mu_3\text{-ampy})(\mu, \eta^1, \eta^2\text{-PhCH=CHPh})(\text{CO})_8]^+$ , was reported by Cabeza as a catalyst precursor that promotes homogeneous catalytic hydrogenation of **11a** as well [74]. From kinetic studies indicating a first order rate-dependence with respect to the cluster, as well as spectroscopic analyses corroborating a trinuclear ruthenium complex as the only species in solution, the authors suggest a catalytic scheme analogous to the right hand side of Scheme 5.


Sappa investigated a series of face-capping phosphinidene-bridged triiron clusters **13**, Scheme 6, as catalysts for the hydrogenation of **11a** as well as isomerization of *cis*-**12a** [75]. The catalytic activities of one of these clusters, Fe<sub>3</sub>(CO)<sub>9</sub>(μ<sub>3</sub>-PtBu)<sub>2</sub> (**13c**), was compared with

that of a shape-wise similar tetraruthenium cluster, Ru<sub>4</sub>(-CO)<sub>13</sub>(μ<sub>3</sub>-PPh) (**14**), which showed that for hydrogenation of **11a**, **14** is greater than one order of magnitude more active albeit with loss of *trans*-**12a** selectivity. Thus, whereas the iron-based **13c** had a TOF(1 h) of 5 h<sup>-1</sup> with a *trans*-/cis-**12a** ratio of 1.4:1, the ruthenium-based **14** showed a TOF(1 h) of approximately 130 h<sup>-1</sup> with a ratio of close to 1:1. It is difficult to assess the precise role and effect of the metal core due to the difference in nuclearities. However, the use of phosphinidene-bridging ligands demonstrates the cluster stabilizing power of μ<sub>3</sub>-bridging X<sub>2</sub>L-type ligands.

More recently, Algarra, Llsuar, and Basallote reported the incomplete cubane-type Mo<sub>3</sub>S<sub>4</sub> cluster **15**, Scheme 7, as catalyst for the partial hydrogenation of alkynes (**11**) [76]. The authors rationalize a mechanism based on experimental and computational studies, which invoke transformation via the edge-bridging sulfur groups rather than at the metal centers. A dithiolene adduct (**15a**) is formed between two of the bridging sulfurs and the alkyne, analogous to adsorption to MoS<sub>2</sub> surfaces. The remaining edge-bridging sulfur cleaves the σ-bond in H<sub>2</sub>, resulting in intermediate **15b** with one (μ-S)-H and a C-H bond. Two competing pathways account for formation of either of the (*E*) or (*Z*) alkene. The former undergoes an isomerization step and subsequently reductive elimination, whereas the latter forms without prior isomerization. Using 12 mol% of the catalyst for 65 h under 100 bars pressure of H<sub>2</sub> at 150 °C in CH<sub>3</sub>CN resulted in 62% conversion of **11a**, of which 85% was *cis*-**12a**.



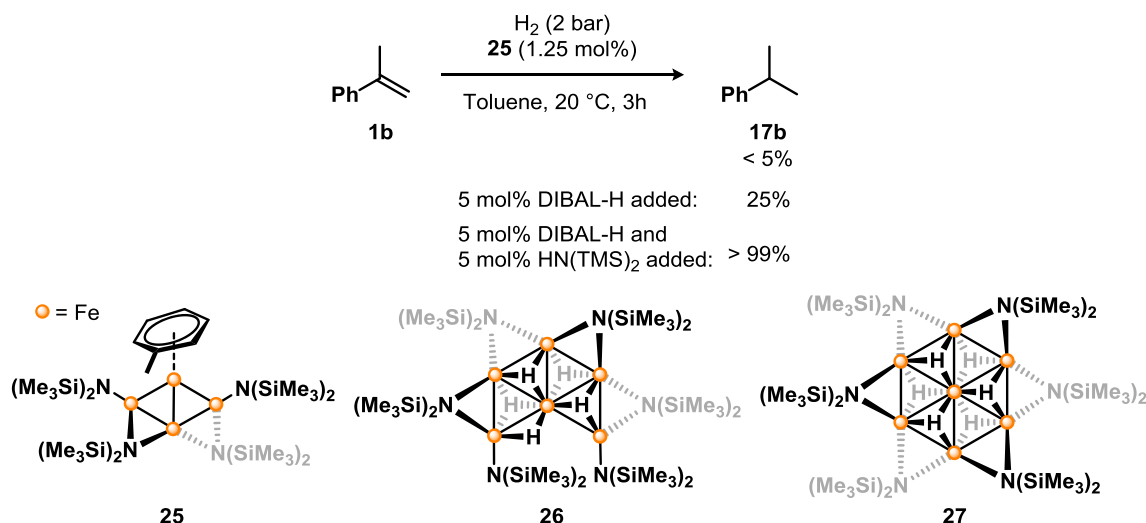

  
C1=CCCCC=C1  $\xrightarrow[\text{[Ir]}]{\text{H}_2 (20 \text{ bar}), 110^\circ\text{C}, 4 \text{ h}}$  C1=CCCCC=C + C1=CCCCC=C + C1=CCCCC=C + C1CCCCCCC1
  
**20** **21** **22a** **22b** **23**


  
 ● = Ir
   
**24** **Ir<sub>4</sub>(CO)<sub>12</sub>**

Catalyst	Conversion (%)	Selectivity (%)			
		<b>21</b>	<b>22a</b>	<b>22b</b>	<b>23</b>
Ir on activated carbon	100	–	–	–	100
IrCl(CO)(PPh <sub>3</sub> ) <sub>2</sub>	100	–	–	1	99
<b>24</b>	44	47	18	33	2
Ir <sub>4</sub> (CO) <sub>12</sub>	40	58	14	14	14

Bonnet studied chalcogenide face-capped triruthenium hydrido clusters,  $(\mu\text{-H})_2\text{Ru}_3(\mu_3\text{-Y})(\text{CO})_5(\text{dppm})_2$   $\text{Y} = \text{O}$  (**16O**), S (**16S**), as precatalysts for the hydrogenation of **1** to alkanes **17** as seen in Scheme 8 [77]. The authors discuss possible mechanisms for the observed products, and suggests a transient species, **16Oa1** and **16Oa2**, wherein a Ru–Ru bond is broken to accommodate alkene coordination. While substitution of  $\mu_3\text{-O}$  with  $\mu_3\text{-S}$  did not increase catalytic activity, they did not provide sufficient framework stability as some fragmentation product was observed. However, no fragmentation was observed for the clusters where the one or two of the edges was bridged by a dppm-ligand. As such, the authors conclude a synergism between

Haupt reported that the treatment of dirhenium complexes,  $\text{Re}_2(\mu\text{-P}(p\text{-XC}_6\text{H}_4)_2)(\text{CO})_8$ ,  $\text{X} = \text{H}, \text{F}$ , with  $\text{H}_2$  afforded tri- and tetranuclear rhenium clusters (**18** and **19**, respectively) [78]. These were found to be active catalysts in both hydrogenation and isomerization of **1a**, of which a

 Springer

**Table 3** 2D heteroleptic planar Mn<sub>6</sub> cluster **28** as catalyst for the hydrogenation of **1b** and **21a** [80]

Catalyst	<i>t</i> Bu <sub>2</sub> AlH (mol%)	<b>17b</b> (%)	<b>23a</b> (%)
<b>28</b>	–	0	–
<b>28</b>	5	97	–
Mn(hmds) <sub>2</sub>	10	97	–
Mn(hmds) <sub>2</sub>	5	–	–
Mn(hmds) <sub>2</sub>	10	–	> 99

distinct selectivity for hydrogenation was observed for the fluorine-substituted arenes (**18b** and **19b**), Table 1. Ligand substitution for *p*-FC<sub>6</sub>H<sub>4</sub> resulted in an increase in TON along with suppression of isomerization reaction. Cluster **18b** and **19b** are evidently stronger Lewis acids, thus resulting in a more facile coordination to **1a**. The authors suggest cluster catalysis based on the recovered amount of intact clusters. A catalytic cycle was rationalized based on their observations, and comparing the reactivity to that of the known trisium cluster, Os<sub>3</sub>(μ-H)<sub>2</sub>(CO)<sub>10</sub> [4]. As such, the proposed cycle proceeds analogously to traditional mononuclear catalysis; (i) formation of cluster-alkene π-complex, (ii) alkene insertion into the (μ-H)–Re bond, (iii) oxidative addition of H<sub>2</sub>, and finally (iv) reductive elimination of **17a**.

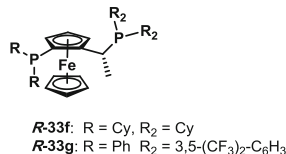
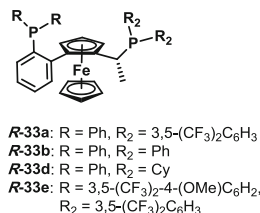
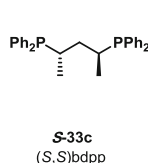
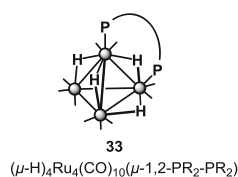
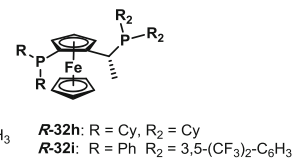
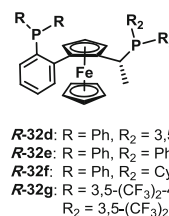
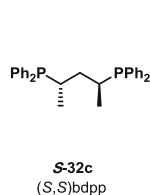
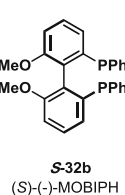
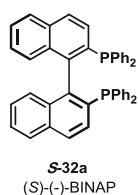
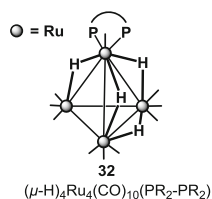
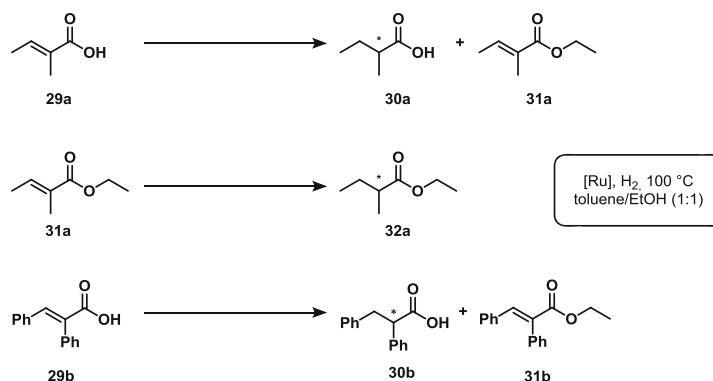
Araujo investigated the selectivity in the catalytic partial hydrogenation of 1,5-cyclooctadiene (**20**) employing a range of tetrairidium clusters [25]. While bulk iridium as well as mononuclear IrCl(CO)(PPh<sub>3</sub>)<sub>2</sub> afforded full hydrogenation to cyclooctane (**23**), Ir<sub>4</sub>(CO)<sub>11</sub>PPh<sub>2</sub>H (**24**) and Ir<sub>4</sub>(CO)<sub>12</sub> afforded partial hydrogenation to **21** and **22** with up to 58% selectivity albeit at a lower conversion, Table 2. Kinetic measurements established a first-order rate-dependency with respect to **20**, whereas the various iridium clusters had a similar value (~ 0.0015 min<sup>–1</sup>) suggesting a transformation of the catalyst precursors. The lack of nanoparticles, a lack of change in reactivity in presence of Hg, and an observed product selectivity difference, work in support of cluster catalysis.

From Wangelin's studies on Fe(hmds)<sub>2</sub>, hmds=N(SiMe<sub>3</sub>)<sub>2</sub>, for the catalytic hydrogenation of alkenes, discrete metal clusters ranging from four to seven in nuclearity were obtained, each containing metal–metal

bonds, Scheme 9 [79]. Preliminary reactions demonstrated that **25** afforded catalytic hydrogenation of α-methylstyrene **1b** to the alkane **17b** of merely 5%. However, under reducing conditions (5 mol% DIBAL-H) 25% yield was achieved, which in presence of additional reductant resulted in > 99% yield.

Wangelin synthesized a low-valent 2D heteroleptic planar Mn<sub>6</sub> cluster **28**, and provided an account on its catalytic properties for the hydrogenation of alkenes, alkynes and imines under reducing conditions [80]. Preparation of the cluster, or in situ formation, afforded the same yields of **17b** (97%) from **1b** using equimolar amount of the reductant DIBAL-H:Mn in *n*-hexane at 20 °C. On the contrary, hydrogenation of sterically encumbered alkenes (or alkynes), such as **21a** to **23a**, was achieved using reductant/Mn in 2:1, Table 3. Moreover, it was unclear whether the cluster or a mononuclear Mn species was responsible for the catalysis.

Matteoli investigated the influence of two different chiral phosphine-ligated tetraruthenium clusters in asymmetric hydrogenation of olefins, as well as α,β-unsaturated acids **29**, such as tiglic acid (**29a**) and **29b**, and their corresponding esters, such as **31a** [81]. The difference in electronic properties of the substrates was sought to provide mechanistic insight, such as competing isomerization reactions, enhanced substrate–catalyst interactions, and steric congestion. The structures of the precursors were determined by both single-crystal X-ray diffraction, as well as <sup>1</sup>H and <sup>31</sup>P NMR, which demonstrated a *P,P*-coordination environment at a single Ru center, **32**, Table 4. Based on these experimental findings, the authors emphasize that the presence of a carboxylic moiety in the substrate enhances the substrate–catalyst interaction. Moreover, they

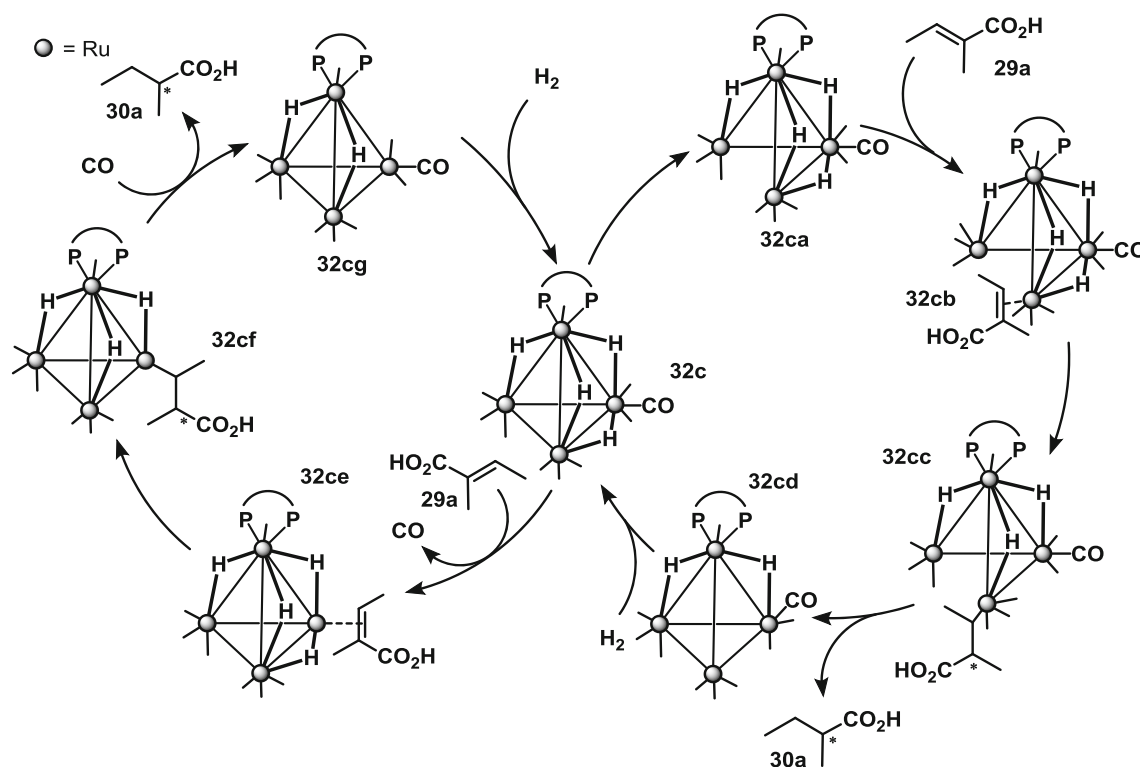
**Table 4** Asymmetric hydrogenation of **29a**, **29b**, and **31a** using tetraruthenium clusters **32** or **33** having chiral ligands as catalysts

Substrate	Catalyst (loading (mol%))	H $_2$ pressure (bar)	Reaction time (h)	Conversion (%)	Product	Selectivity (%)	Yield (%)	ee (%)	Configuration
<b>29a</b>	<b>S-32a</b> (0.05)	130	93	91	<b>30a</b>	—	85	29	(R)
<b>29a</b>	<b>S-32b</b> (0.05)	130	72	100	<b>30a</b>	—	94	17	(S)
<b>31a</b>	<b>S-32a</b> (0.05)	130	234	87	<b>32a</b>	—	87	3	(R)
<b>31a</b>	<b>S-32b</b> (0.05)	130	253	100	<b>32a</b>	—	100	2	(S)
<b>29a</b>	<b>R-32c</b> (0.1)	50	48	85	<b>30a</b>	94	—	45	(R)
<b>29a</b>	<b>S-32c</b> (0.1)	50	48	75	<b>30a</b>	92	—	43	(S)
<b>29a</b>	<b>R-33c</b> (0.4)	50	48	100	<b>30a</b>	95	—	42	(R)
<b>29a</b>	<b>S-33c</b> (0.4)	50	48	100	<b>30a</b>	92	—	44	(S)
<b>29a</b>	<b>R-32d</b> (0.4)	50	24	100	<b>30a</b>	100	—	93	(S)
<b>29a</b>	<b>R-33a</b> (0.4)	50	24	99	<b>30a</b>	99	—	82	(S)
<b>29a</b>	<b>R-33a</b> (0.4) + Hg(0)	50	24	100	<b>30a</b>	100	—	87	(S)
<b>29a</b>	<b>R-33b</b> (0.4)	50	24	100	<b>30a</b>	100	—	58	(S)
<b>29a</b>	<b>R-33b</b> (0.4) + Hg(0)	50	24	100	<b>30a</b>	100	—	62	(S)
<b>29b</b>	<b>R-33a</b> (0.4)	50	24	100	<b>30b</b>	90	—	66	(R)
<b>29b</b>	<b>R-33b</b> (0.4)	50	24	100	<b>30b</b>	83	—	63	(R)
<b>29a</b>	<b>R-33d</b> (0.4)	50	24	99	<b>30a</b>	100	—	54	(R)
<b>29a</b>	<b>R-33e</b> (0.4)	50	24	87	<b>30a</b>	100	—	77	(S)
<b>29a</b>	<b>R-33f</b> (0.4)	50	24	100	<b>30a</b>	90	—	—	—

**Table 4** (continued)

Substrate	Catalyst (loading (mol%))	H <sub>2</sub> pressure (bar)	Reaction time (h)	Conversion (%)	Product	Selectivity (%)	Yield (%)	ee (%)	Configuration
<b>29a</b>	<b>R-33 g</b> (0.4)	50	24	100	<b>30a</b>	96	—	—	—

Terminal CO molecules have been omitted for clarity [81, 82, 84, 85]

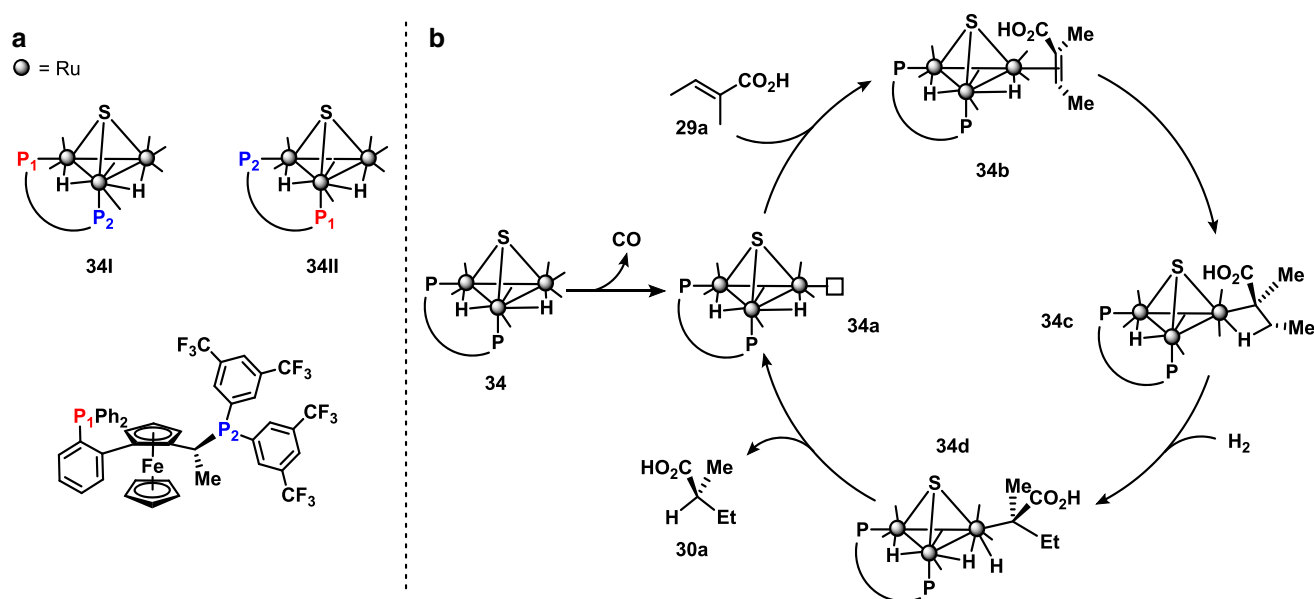


**Scheme 10** Catalytic cycles involved in hydrogenation of **29a** leading to **30a** by cluster **32c** as proposed by Nordlander. The low CO pressure is suggested to disfavor the left hand pathway, as CO reassociation is unlikely. Remaining terminal CO molecules have been omitted for clarity [82]

conclude the BINAP ligated cluster (**32a**) in general affords the better properties, and the presence of an additional ligand may increase catalytic activity. No elaborate studies on nuclearity and retention hereof were reported, nor was any tentative mechanism proposed.

Nordlander investigated two sets of stereoenriched tetraruthenium clusters,  $(\mu\text{-H})_4\text{Ru}_4(\text{CO})_{10}\{\mu\text{-1,1-}(R/S, R/S)\text{-bdpp}\}$  (**R-32c** or **S-32c**, respectively) and  $(\mu\text{-H})_4\text{Ru}_4(\text{CO})_{10}\{1,2\text{-(}R/S, R/S\text{)-bdpp}\}$  (**R-33c** or **S-33c**, respectively), as catalysts for the asymmetric hydrogenation of **29a** under milder conditions [82]. Lowering the pressure of H<sub>2</sub> from 130 to 50 bar resulted in three distinct observations: high conversion (75–100%), interconversion from the bridging **33c** to the chelating **32c**, and a product distribution strongly affected by the ligand enantiomer; (*R, R*)

forms (*R*), likewise (*S, S*) resulting in (*S*). As the activities of **S/R-33c** were nearly identical to **S/R-32c**, and the recovered cluster was of the latter structure, cluster catalysis by structure **S/R-32c** was argued. While the possibility of lower-nuclearity species forming from degradation is not excluded, the activity of these being responsible for the conversion is unlikely. The authors argue that in such a scenario, the activity of  $[\text{H}_4\text{Ru}_4(\text{CO})_{12}]$ -systems would be independent of the ligands, whereas they find the opposite to be true. Despite not having determined the exact sequence of elementary steps, a tentative account on the experimental findings is presented in Scheme 10. Starting from **32cg**, the oxidative addition of H<sub>2</sub> is discussed to be stereoselective due to the orientation of *P*-phenyl substituents. Accordingly, introduction of **29a** to the



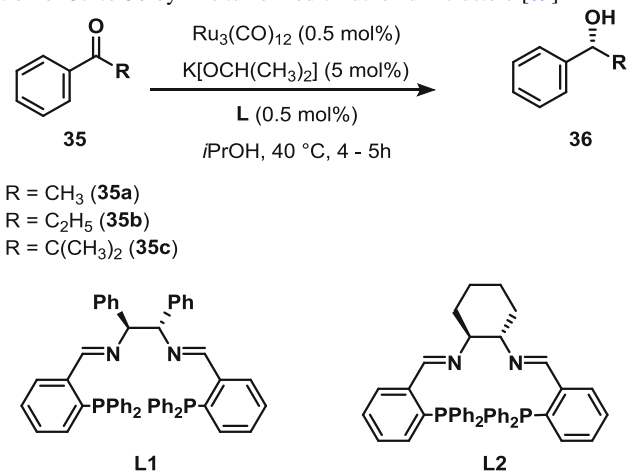
**Scheme 11** a The two Ru<sub>3</sub>-cluster diastereomers **34I** and **34II**. b Catalytic scheme for the asymmetric hydrogenation of **29a** to **30a** as proposed by Nordlander. Terminal CO molecules have been omitted for clarity [87]

coordination-sphere of **32c** follows either of two pathways: (i) ligand substitution forming **32ce**, or (ii) homo or heterolytic cleavage of a Ru–Ru bond forming **32ca**, permitting coordination of **29a**, resulting in **32cb**. Stepwise hydride insertion is followed by reductive elimination, regenerating **32c**. The latter route is argued to be more probable because of a low CO pressure makes reassociation unlikely.

Continued work by Nordlander investigated the changes in cluster stability and activity in the asymmetric hydrogenation of **29a** induced by various chiral phosphine ligands [83]. While improvement was observed over the parent hydrido cluster, (μ-H)<sub>4</sub>Ru<sub>4</sub>(CO)<sub>12</sub>, the authors noted varying conversion (70–95%), with poor increase in enantioselectivity (up to 23% *ee*), along with thermal decomposition. Cluster catalysis is invoked, as the decomposition products were insufficient in providing similar catalytic activity, as well as provided different products than those observed. The authors relate these findings to their prior study, and suggest that a better enantioselectivity can be achieved by employing ligands with a significant steric bulk proximal to the substrate. To this end, Nordlander prepared Walphos substituted tetraruthenium clusters (**33a,b**) and reported up to excellent enantioselectivity (30–93% *ee*) in the hydrogenation of various α,β-unsaturated carboxylic acids [84]. From spectroscopical and single-crystal X-ray diffraction analysis, an unusual bonding of the phosphine ligand was found; one coordinates equatorially whilst the other axially, resulting in chiral cluster frameworks and thus potential diastereomeric mixtures. Nevertheless, NMR analysis corroborates

the presence of only a single diastereomer. A Hg(0) poisoning test and recovery experiment suggest (small amounts of) cluster fragmentation albeit the authors dismiss the significance of the colloidal material, due to the significantly difference observed in catalyst activity with respect to yield and selectivities. Moreover, the authors emphasize an interconversion of isomers of chelating and bridging diphosphines during catalysis, and they suggest suppressing this interconversion may result in even higher stereoselectivity.

A series of tetraruthenium hydrido clusters was substituted with Josiphos-(**32h**, **i** and **33f**, **g**) and Walphos phosphines (**32d**, **e**, **f**, **g** and **33d**, **e**) to assess the steric and electronic influence of the ligand on the hydrogenation of **29a** [85]. Whereas the Josiphos substituted clusters demonstrated poor catalytic properties as well as degradation, the Walphos clusters demonstrated both excellent conversion (99–100%), product selectivity (99–100%), and enantioselectivity (92% *ee*), Table 4. Interestingly, an interconversion opposite to that previously established was observed, transforming the 1,1-chelating into 1,2-bridging diphosphines (**32** to **33**). This observation is argued by the authors to origin in strain relief transitioning from a nine membered “dimetallacycle” ring to the eight membered ring. Suppression of this isomerization is suggested to result in an increased enantioselectivity. While spectroscopic analyses and catalyst poisoning tests demonstrated that the combination of cluster, hydrogen pressure and temperature afforded the majority of the transformation, the free ligand was found to promote the reaction with 68% *ee* albeit at a mere conversion of 23% after 72 h.

**Table 5** Asymmetric transfer hydrogenation of **35** to **36** by in situ formed triruthenium clusters [89]

R	Ligand	Base present	Time (h)	Yield (%)	ee (%)
CH(CH <sub>3</sub> ) <sub>2</sub>	L1	No	5	48	> 99
		Yes	4	79	> 99
	L2	No	5	30	94
		Yes	4	66	90
C <sub>2</sub> H <sub>5</sub>	L2	No	5	72	92
		Yes	4	93	92
CH <sub>3</sub>	L1	No	5	91	81
		Yes	4	96	82

Nordlander explored the analogous phosphine-rhenium clusters of the Josiphos and Walphos-families and observed that, as for the ruthenium clusters, the Walphos-family ligand afforded better catalyst precursors in the asymmetric hydrogenation of **29a** [86]. While the trirhenium clusters demonstrated poor conversion (15%) and enantioselectivity (13% *ee*), the corresponding dinuclear complexes afforded superior conversion (88%) and selectivity (57%). Moreover, the ligand discrepancy is suggested to relate to a potential wider bite angle of the Walphos.

Furthermore, Singh and Nordlander investigated the effect of a face-capping chalcogenide to provide stability of the cluster framework in a triruthenium cluster under hydrogenation of **29a** [87]. Thus, employing the Walphos-ligand affords two diastereomers of the Ru<sub>3</sub>-cluster **34**, Scheme 11a. Cluster mediated catalysis is strongly suggested based on spectroscopic analyses demonstrating an intact organometallic species in solution and neither diastereomers had interconverted after the reaction. The authors provide mechanistic insights by combining their experimental observations with DFT calculations, and rationalize a catalytic cycle invoking an initial dissociation of a CO *trans*-positioned to the phosphine leading to **34a**, Scheme 11b. Thereby an unsaturated cluster is formed, permitting the formation of a  $\pi$ -complex (**34b**), which

undergoes alkene insertion (**34c**). Subsequent oxidative addition of H<sub>2</sub> at the same Ru-center (**34d**) results in reductive elimination regenerating the cluster concurrently with formation of the hydrogenation product (**30a**). Moreover, the authors conclude that the face-capping chalcogenide ensures cluster integrity throughout the transformation.

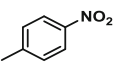
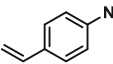
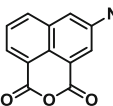
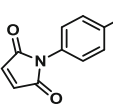
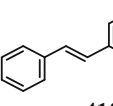
A more recent study by Nordlander investigated the use of chiral binaphthyl mono-substituted phosphiranes as ligands in use with the tetra-ruthenium hydrido cluster for asymmetric hydrogenation of **29a** [88]. While the clusters demonstrated catalytic activity, no enantioselectivity was observed. As no products associated with cluster fragmentation was found, cluster catalysis is suggested by the authors. Moreover, based on their comprehensive studies, Nordlander suggests that asymmetric induction in cluster catalyzed alkene hydrogenation reactions is, in large, determined by the properties of the ligand and that bidentate phosphine provides more beneficial properties relative to the monodentate congeners.

Gao and Ikariya investigated the asymmetric Meerwein-Ponndorf-Verley reduction of ketones **35** to alcohols **36** by mixing Ru<sub>3</sub>(CO)<sub>12</sub> with chiral diiminodiphosphine ligands in the presence of isopropanol, Table 5 [89]. Evidence in support of in situ formation of a triruthenium cluster is

presented by combining spectroscopic measurements, reactivity differences compared to a mononuclear ruthenium complex (the latter is inactive), as well as preparation and test of catalytic competence of a related anionic species. Additionally, kinetic studies suggest first-order rate-dependency with respect to the cluster concentration. Moreover, while the addition of base affected the conversion of the sterically encumbered ketone **35c**, the enantioselectivity remained generally similar. Thus, treating **35c** with  $\text{Ru}_3(\text{CO})_{12}$  in presence of **L2** and base afforded 90% *ee*, whereas in the absence of base 94% *ee* was obtained.

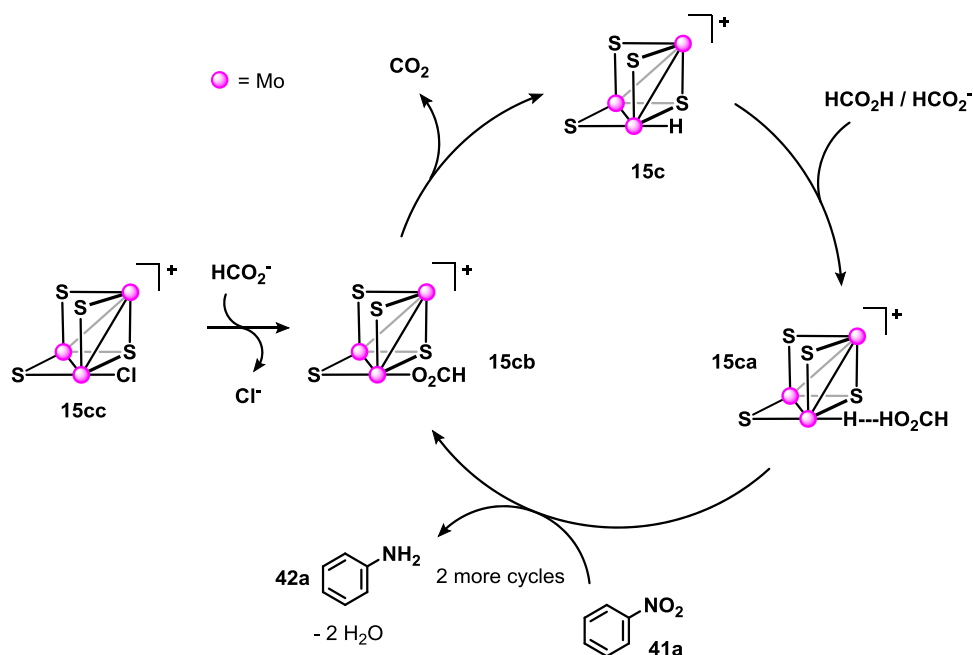
Rio and Gossage investigated the asymmetric hydrogenation of acetophenone **35a**, as well as the asymmetric Diels–Alder reaction of cyclopentadiene **37** and acrolein **38a**, employing catalytic amounts of each of the compounds **39–40** (0.5 mol%) acquired from treating  $\text{Ru}_3(\text{CO})_{12}$  with three different chiral aminooxazolines, Fig. 4 [90]. Single-crystal X-ray diffraction revealed that two of the three clusters possess a triangular face-capped  $\text{Ru}_3$ -core (**39a** and **39b**), where the amido unit binds two Ru-centers and the oxazoline nitrogen atom coordinates to the remaining Ru-center. In the third complex (**40**), the amido and hydrido spans the same Ru–Ru edge. The authors tested the mentioned reactions using  $\text{Ru}_3(\text{CO})_{12}$  as precatalyst mixed with the respective ligands. They observed conversions lower than 5% in the hydrogenation reaction, whereas the Diels–Alder reaction showed up to 20% conversion. Contrary, when using either of the preformed precatalysts **39–40**, excellent conversion is seen (99%) with TOF(10 h) values of 144–200  $\text{h}^{-1}$  albeit with poor

**Table 6** Chemoselective reduction of functionalized **41** to **42** catalyzed by **15e** [93]

$\text{R}-\text{C}_6\text{H}_4-\text{NO}_2 \xrightarrow[\text{MeOH}]{\text{H}_2 (20 \text{ bar}), \text{15e (5 mol\%)}, 70^\circ\text{C, 18h}} \text{R}-\text{C}_6\text{H}_4-\text{NH}_2$		
<b>41</b>	Conversion (%)	Yield (%)
	> 99	> 99
	98	85
	> 99	99
	> 99	70
	> 99	95

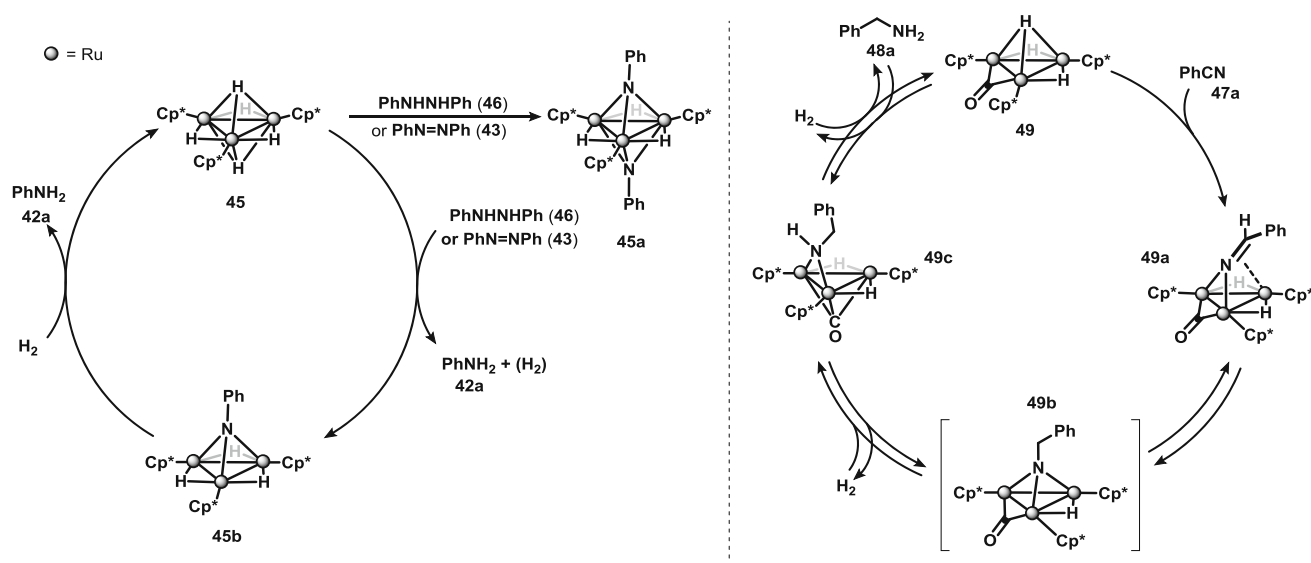
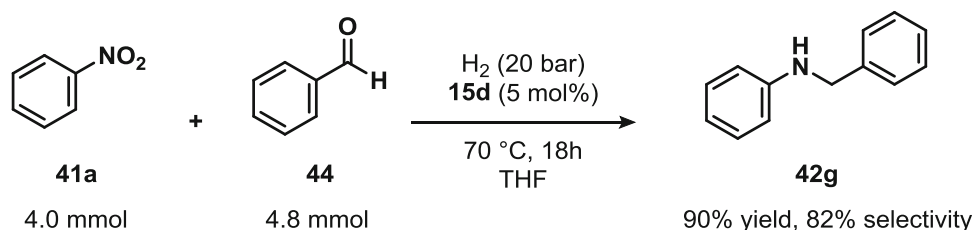
**Scheme 12** Catalytic scheme proposed by Llusar and Beller for the cubane-type cluster **15** catalyzing the reduction of **41a** to **42a**.

Terminal, chelating phosphines, and hydrides/chlorides have been omitted for clarity [91]





**Scheme 13** Reductive amination using incomplete cubane **15d** as catalyst precursor [94]



**Scheme 14** Catalytic schemes for the hydrogenation of hydrazine as proposed by Suzuki [95], and of benzonitrile as proposed by Takao [96]. Structural modification via a bridging carbonyl resulted in a compound with better catalytic behavior

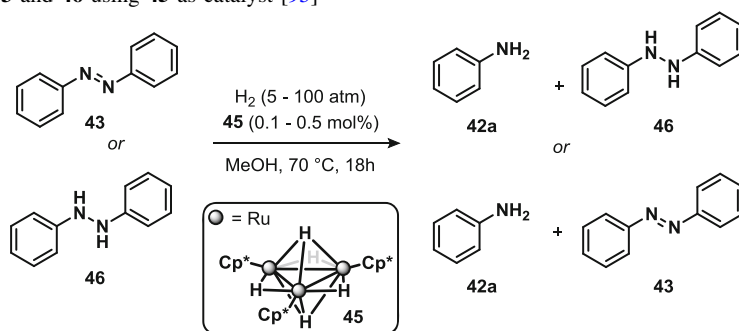
enantioselectivities ranging between 18 and 20% ee in the hydrogenation. The authors suggest that the prepared clusters form catalytically active hydrido compounds in situ. They rationalize their conclusion based on the observation that addition of KOH increases the TOF(10 h) from 65 to 200  $\text{h}^{-1}$  and elevates the conversion from 51 to 99%. In the absence of catalyst precursors, the [4 + 2]-cycloaddition achieved approximately 20% conversion within 2 h, whereas the use of the precursors afforded 80% conversion in the same timespan, with a TOF(10 min) of 25  $\text{h}^{-1}$ .

Llusar and Beller employed the incomplete cubane-type  $\text{Mo}_3\text{S}_4$ -cluster,  $[\text{Mo}_3\text{S}_4\text{X}_3(\text{Y}_2)_3]^+$  (**15**), Scheme 7, in several settings with variation of the terminal ligands, X and Y. The hydrido dmpe ligated  $[\text{Mo}_3\text{S}_4]$  cluster,  $[\text{Mo}_3\text{S}_4\text{H}_3(\text{dmpe})_3]\text{BPh}_4$  (**15c**), was found to catalytically reduce functionalized nitroarenes **41** to aminoarenes **42**, and the extent of conversion was affected by the source of reductant [91]. While  $\text{H}_2$  provided merely 5% yield, a mixture of  $\text{HCO}_2\text{H}/\text{Et}_3\text{N} = 5:2$ , afforded up to > 99% conversion with yields up to > 99% of the corresponding **42** for an array of compounds as shown in Scheme 12. In a later study, they reported chemoselective reduction of **41** and azoarenes **43**

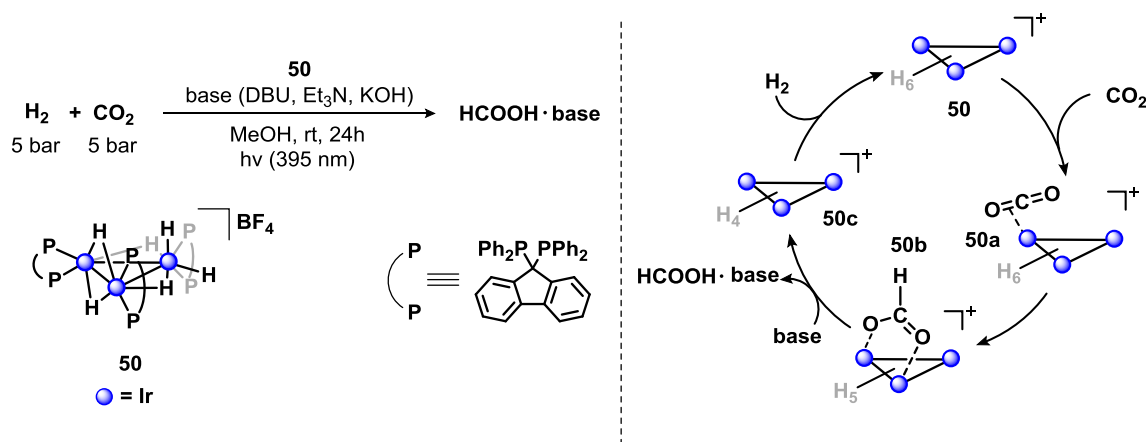
in the presence of other reduction-susceptible functional groups, such as ketones and esters, using the trihydrido-cluster  $[\text{Mo}_3\text{S}_4\text{Cl}_3(\text{dmen})_3][\text{BF}_4]$  **15d**, dmen = *N,N'*-dimethylethylenediamine [92]. Later, the scope was expanded to include additional functional groups, Table 6 [93]. Of the screened catalyst precursors, the cluster having a *N,N*-bidentate ligand,  $[\text{Mo}_3\text{S}_4\text{Cl}_3(\text{dnbpy})_3][\text{PF}_6]$  **15e**, was found to provide the optimal conditions. When using a 5 mol% catalyst loading, quantitative yields were obtained under 20 bar of  $\text{H}_2$  and 70 °C in MeOH. To account for cluster integrity during the transformation, the reaction mixture was analyzed after 4 h by ESI-MS, and no other ions corresponding to species of lower-nuclearity were observed. Further, the catalyst was recovered and reused, which afforded a modest yield of 52%.

The incomplete cubane-type cluster **15d** was also found by Llusar and Beller to afford catalytic reductive amination of **41a** with benzaldehyde **44** using 6 mol% catalyst loading under approximately 20 bar of  $\text{H}_2$  at 70 °C in THF on a 4 mmol scale to form *N*-benzylaniline **42g**, Scheme 13 [94]. The authors account for cluster integrity throughout the transformation based on ESI-MS showing no ions of lower-nuclearity as well as  $^1\text{H}$  NMR of the reaction



**Table 7** Hydrogenation of **43** and **46** using **45** as catalyst [95]

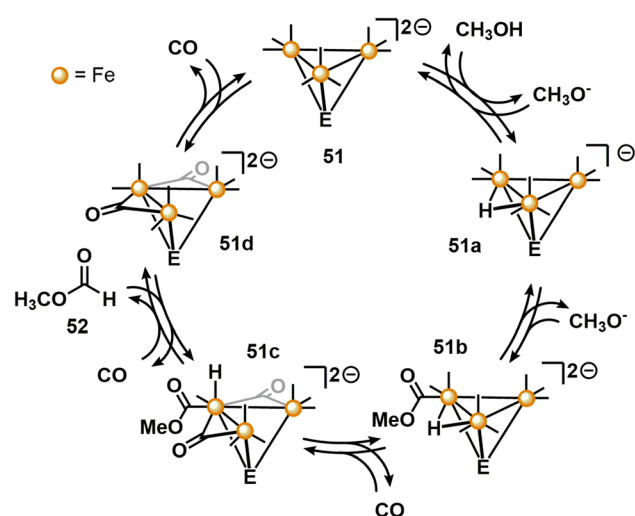
Loading of <b>45</b> (mol%)	Pressure H <sub>2</sub> (atm)	Substrate	Conversion (%)	Selectivity ( <b>42a/46</b> ) or ( <b>42a/43</b> )
0.50	5	<b>43</b>	13	3.5:1
0.40	100	<b>43</b>	68	9.1:1
0.10	5	<b>46</b>	72	1.7:1
0.10	100	<b>46</b>	31	14.9:1

**Scheme 15** Catalytic hydrogenation of CO<sub>2</sub> using trinuclear complex **50** as proposed by Inagaki. The diphosphine ligands are omitted for clarity [101]

mixture revealing intact cluster. Moreover, the cluster was recovered and used in a recycling experiment, which afforded full conversion with 90% yield of **42g**.

Suzuki studied the neutral polyhydrido triruthenium cluster,  $\{(\text{Cp}^*\text{Ru}(\mu\text{-H}))_3(\mu_3\text{-H})_2\}$ , **45** in Scheme 14, for the hydrogenation of diazenes **43** and hydrazines **46**, Table 7 [95]. As such, **45** activated the *N*–*N* bond of **46** to afford asymmetric capped bis- and mono- $(\mu_3\text{-imido})$  clusters, **45a** and **45b**, respectively (left hand side of Scheme 14). Only the latter reacted with H<sub>2</sub> to provide **42a** and regenerate **45**. Under catalytic amounts of **45** (0.12 mol%), H<sub>2</sub> (approximately 100 bar), at 100 °C in EtOH, **46** was converted to **42a** in 31%. Despite the high pressure of H<sub>2</sub> suppressing the formation of the inactive complex **45a**, most of **45** was converted into this inactive species over time.

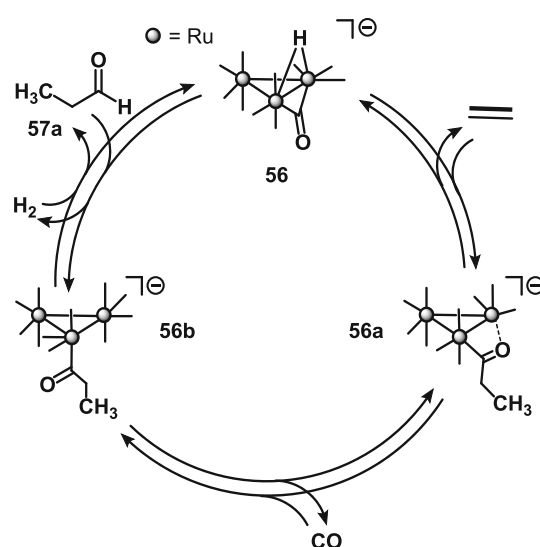
Cluster **45** was also reported by Takao as an active catalyst for the hydrogenation of benzonitrile **47a**, as shown on the right hand side of Scheme 14 [96]. At approximately 10 bar of H<sub>2</sub> and 110 °C in MeOH, 93% conversion of **47a** was achieved with 82% selectivity towards benzylamine **48a**. Further increase in temperature to 130 °C achieved 98% conversion albeit at a lower product selectivity of 48%. Introducing a bridging carbonyl to **45**, thus affording cluster **49**, resulted in a higher catalytic performance, allowing the transformation to occur at lower temperatures as well as providing a higher selectivity. The authors speculate that the CO withdraws sufficient electron density from the Ru<sub>3</sub>-core to prevent a simultaneous coordination of two **47a** substrates. Thus, at approximately 10 bar of H<sub>2</sub> and 120 °C in THF, 98% conversion was



**Scheme 16** The catalytic cycle in carbonylation of MeOH using the triiron chalcogenide cluster **51** homologue series (E = S, Se or Te) as proposed by Whitmire. Terminal CO molecules have been omitted for clarity [102]

observed with a 93% selectivity towards **48a**. Based on extensive analyses, including crystal-structures, (decomposition) products obtained from stoichiometric reactions, the authors rationalize a catalytic cycle shown on the right hand side in Scheme 14.

Research into efficient CO<sub>2</sub> hydrogenation catalysis is an active area of research, and while typical examples comprise mononuclear complexes based on, for example, iron [97], cobalt [98], ruthenium [99], and iridium [100], Inagaki recently reported a trinuclear iridium cluster **50** working as a photocatalytic CO<sub>2</sub> hydrogenation catalyst [101]. Whereas conventional catalysis invoke high pressure and temperature for this reaction, **50** provided approximately 60% yield under 10 bars of pressure (H<sub>2</sub>/CO<sub>2</sub> = 1:1) at room temperature. The authors suggest a



**Scheme 17** Mechanism of the hydroformylation of ethylene to **57a** catalyzed by **56** as proposed by Süß-Fink. Terminal CO molecules have been omitted for clarity [105]

catalytic cycle as shown Scheme 15, invoking initial coordination of CO<sub>2</sub> leading to **50a**, which is followed by insertion into the Ir-H bond leading to **50b**. Reductive elimination leads to **50c** while concomitantly forming an acid-basic adduct. Finally, subsequent oxidative addition of H<sub>2</sub> regenerates **50**. While both irradiation and base are necessary for the reaction to proceed, the effect of irradiation remains unclear. The authors suggest that its involvement is to facilitate hydride dissociation forming a vacant coordination-site for CO<sub>2</sub>. However, evidence is presented that suggests further involvement by enhancing the reaction with CO<sub>2</sub>.

**Table 8** Cross carbonylation of **53** with **11b** [104]

Catalyst	Solvent	Yield (%)	
		54	55
Ru <sub>3</sub> (CO) <sub>12</sub>	Toluene	61	35
	THF	51	32
	<i>N</i> -Methylpiperidine	85	Trace
[RuCl <sub>2</sub> (CO) <sub>3</sub> ] <sub>2</sub>	<i>N</i> -Methylpiperidine	76	4
RuCl <sub>2</sub> (PPh <sub>3</sub> ) <sub>3</sub>	<i>N</i> -Methylpiperidine	Trace	Trace

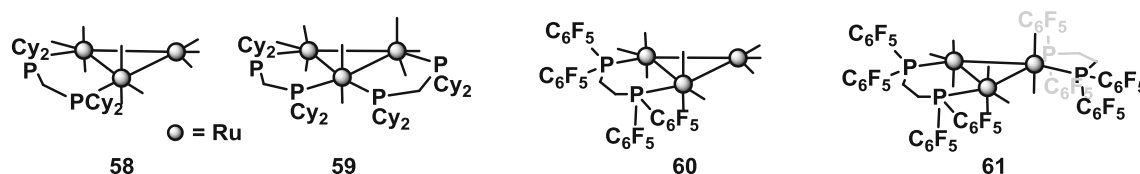


**Fig. 5** Various ligated triruthenium clusters as catalysts for the hydroformylation of **1**. Terminal CO molecules have been omitted for clarity [107]

**Table 9** Hydroformylation of 1-pentene by tri- and tetracobalt clusters, **62** and **63** [108–110]

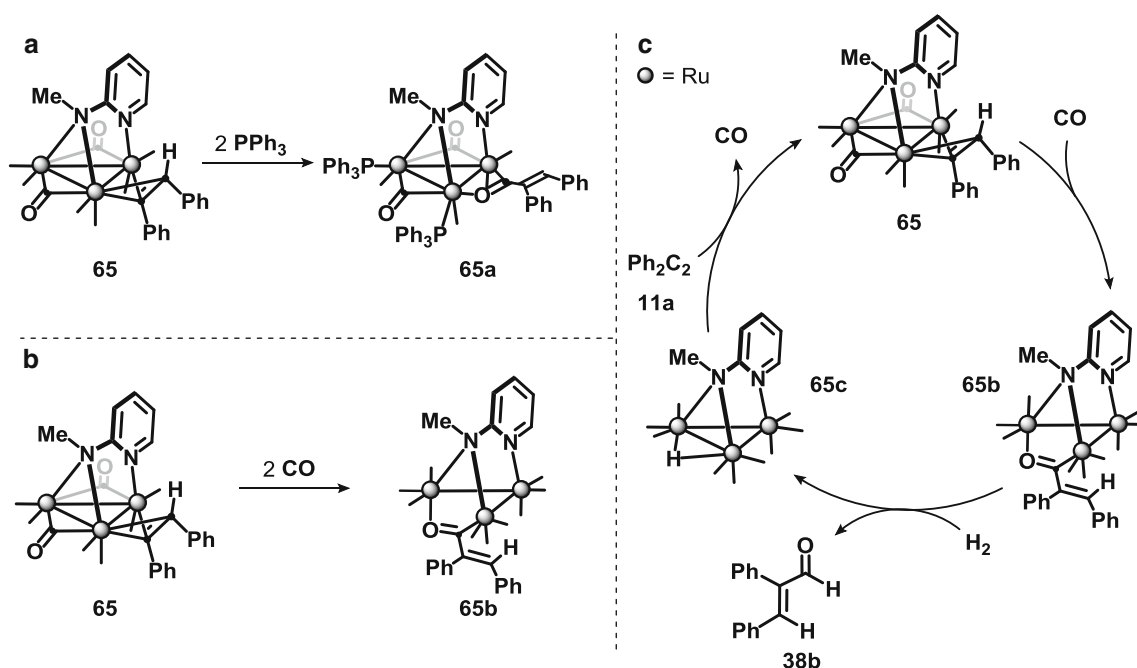
Cluster								
Cluster	Loading (mol%)	Substrate	Temp (°C)	Pressure (bar)	Solvent	Time (h)	Yield aldehyde (%)	Selectivity n-57b/(iso-57c + iso-57c)
<b>62</b>	0.36	<b>1c</b>	90	61–56	C <sub>6</sub> H <sub>6</sub>	104	57.5	5.4
			130	63–54		22	99.7	2.2
<b>63</b>	0.36	<b>1c</b>	130	48–44	C <sub>6</sub> H <sub>6</sub>	88	62.5	2.6
			150	50–44		23.5	84.2	1.9

## Carbonylation

Whitmire studied the homologous series of chalcogenide capped triironclusters,  $[\text{Et}_4\text{N}]_2[\text{Fe}_3(\text{CO})_9\text{E}]$ ,  $\text{E} = \text{S}$  (**51S**),  $\text{Se}$  (**51Se**), and  $\text{Te}$  (**51Te**), for the carbonylation of methanol to methyl formate **52**, while concurrently providing insight into the effect of main-group chalcogenides on cluster stability, as well as on the reactivity pattern [102]. Kinetic studies established a first-order rate dependence with respect to cluster concentration, that in conjunction with a lack of activity of the related mononuclear iron complexes,  $\text{Fe}(\text{CO})_5$  and  $[\text{HFe}(\text{CO})_4]^-$ , worked to support cluster catalyzed transformation. Despite the almost identical rates in formation of **52** between the various chalcogenide clusters, the authors find substantial differences in activation energy (43, 76 and 72 kJ for **51S**, **51Se** and **51Te**, respectively). This discrepancy between formation rates and activation energies are explained by the deduced preexponential factors, where  $\text{E} = \text{S}$  contains a less favorable value ( $3.5 \times 10^3$  for **51S**, vs. approximately  $2.0 \times 10^7$  for **51Se** and **51Te**, respectively). From these values, and in addition to a readily isolation of the open  $\text{Te}$  complex

$[\text{Te}\{\text{Fe}(\text{CO})_4\}_3]^{2-}$  [103] not observed for **51S**, the authors conclude a variation in the rate-determining step, despite a similar rate-law. The proposed catalytic scheme shown in Scheme 16, invoke a catalytically active species that undergoes  $\text{Fe-Fe}$  bond breakage, which **51S** strongly disfavor. While a tentative mechanism involving rupture of a  $\text{Fe-Fe}$  bond, the authors limit the discussion to on  $\text{M-M}$  bond opening of a dianionic species in presence of  $\text{CO}$ .

By using  $\text{Ru}_3(\text{CO})_{12}$  as catalyst precursor in junction with *N*-methylpiperidine, Mitsudo was able to afford cross carbonylation affording hydroquinones **54** from alkynes **11** and 2-norbornenes **53** [104]. While catalyst (precursor) screening demonstrated a distinct catalyst activity between triruthenium (up to 85% yield) and the mononuclear complex (trace), thus satisfying Laine's second criterion, diruthenium complexes afforded only a slightly lower yield (up to 76%) compared to the polynuclear precursor, Table 8. Moreover, no studies into the concrete structure of the active catalyst were provided.



**Scheme 18** Hydroformylation of **11a** using face-capped triruthenium cluster **65** as catalyst as proposed by Lavigne. Terminal CO molecules have been omitted for clarity [111, 112]

**Table 10** Hydroesterification of **66** catalyzed by an in situ mixture of  $\text{Ru}_3(\text{CO})_{12}$  and 2-pyridinemethanol [113]

Catalyst	Additive	Temperature (°C)	Yield (%)
$\text{Ru}_3(\text{CO})_{12}$		170	97
$\text{Ru}_3(\text{CO})_{12}$	None	170	0
$[\text{Ru}(p\text{-cymene})\text{Cl}_2]_2$		150	0
$\text{Rh}_4(\text{CO})_{12}$		170	0

## Hydroformylation

Süss-Fink found indirect evidence that the anionic cluster  $[\text{Ru}_3(\mu\text{-H})(\text{CO})_{11}]^-$  **56** remained intact while catalyzing hydroformylation of ethylene to yield aldehyde **57a**, as shown in Scheme 17 [105]. The authors were able to ascertain the sequence of elementary steps in the catalytic cycle using an isotopic labeling method. Thus, by mixing **56** with  $\text{CF}_3\text{CO}_2\text{D}$  and ethylene in THF, they were successful in trapping the deuterated intermediate,  $[\text{Ru}_3(\mu\text{-D})(\mu\text{-}\eta^2\text{-OCCH}_2\text{CH}_3)(\text{CO})_{10}]$ , which enabled them to locate the position of the bridging hydride by  $^1\text{H}$  and  $^2\text{H}$  NMR. In addition, they were able to establish that the

hydride transfer to ethylene precedes hydrogen incorporation.

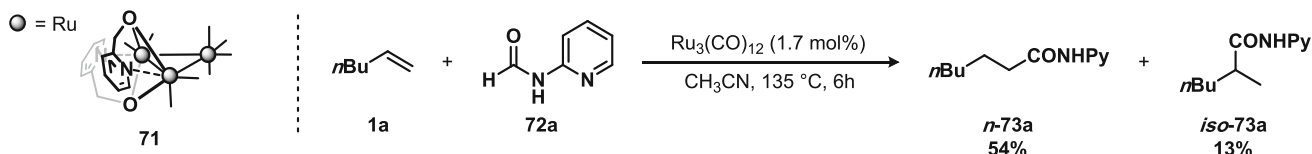
Further studies, using propylene (**1c**) as substrate probed the selectivity as a function of temperature, pressure and solvent [106]. Generally, the cluster was found to provide chemoselective formation of aldehydes rather than alcohols independent of the conditions. On the contrary, control of regioselectivity (*n* over *iso*) was feasible, and under 10 bar of total pressure ( $\text{CO}/\text{H}_2 = 2:1$ ) at 75 °C in diglyme, *n*-butanal (**57b**) was produced in practically quantitative yield (*n/iso* = 73). Importantly, the authors provided spectroscopically evidence that no fragmentation occurs during the reaction.

**Table 11** Hydroesterification of **1a** using  $\text{Ru}_3(\text{CO})_{12}$  as catalyst precursor [114]

Catalyst	Solvent	Conversion (%) ( <i>n</i> : <i>iso</i> )	Decarbonylation (%)
$\text{Ru}(\text{COD})\text{Cl}_2$	Toluene	8	5
$[\text{RuCl}_2(p\text{-cymene})]_2$	Toluene	4	—
$\text{Ru}_3(\text{CO})_{12}$	Toluene	99 (57:43)	53
	DMF	> 99 (74:26)	< 1

**Table 12** Alkene insertion into formyl bond using anionic triruthenium cluster [119]

Catalyst	Conversion (%)	Yield (%)	<i>exo</i> : <i>endo</i>
$\text{Ru}_3(\text{CO})_{12}$	26	18	84/16
<b>75</b>	100	97	71/29
$[\text{Ru}(\eta^6\text{-C}_6\text{H}_6)\text{Cl}_2]_2$	91	—	—
$\text{Ru}(\text{COD})(\text{COT})$	74	16	82/18

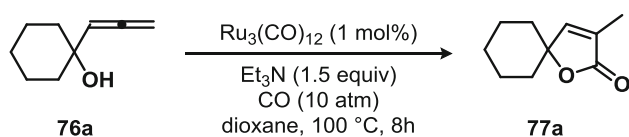
**Scheme 19** Stoichiometric reaction of pyridylmethylalcohol with  $\text{Ru}_3(\text{CO})_{12}$  resulting in a *N,O*-chelated cluster. Hydroamidation **1a** with **72a** leading to mixtures of *n*-**73a** and *iso*-**73a**, respectively, using

$\text{Ru}_3(\text{CO})_{12}$  as precatalyst. Terminal CO molecules have been omitted for clarity [117]

Süss-Fink further investigated the hydroformylation of olefins (**1**), and changes resulting from substituting CO in  $\text{Ru}_3(\text{CO})_{12}$  with sterically demanding diphosphines [107]. Single-crystal X-ray diffraction unambiguously established four structures, one of which was found having an unusual  $\mu_1\text{-}\eta^2$  coordination (chelating) **58**, opposed to  $\mu_2\text{-}\eta^2$  (bridging) **59–61**, Fig. 5. In DMF at 80 °C, both cluster-types demonstrated catalytic activity towards hydroformylation. Moreover, the clusters were largely recovered unaltered. The maximum TON value in the hydroformylation of ethylene was observed for  $\text{Ru}_3(\text{CO})_{10}(\text{F-dppe})$ , F-dppe = bis(perfluoro-diphenylphosphino)ethane **60**, obtaining 429 cycles, compared to merely 157 cycles for  $\text{Ru}_3(\text{CO})_{12}$ .

Pittman reported the use of two different cobalt clusters, **62**, and **63**, catalysts for achieving hydroformylation of 1- and 2-pentene with a predominantly linear selectivity, Table 9 [108, 109]. A high yield of the intact cluster, as

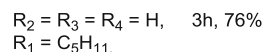
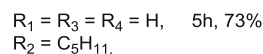
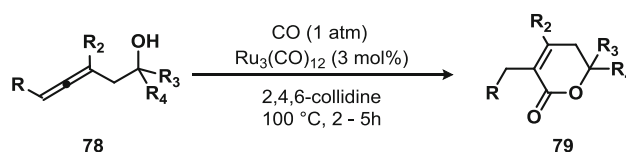
well as a different reactivity compared to  $\text{Co}_2(\text{CO})_8$ , work to support cluster mediated catalysis. The authors suggest that the  $\mu_3\text{-C}$  ligand of cluster **62**, and the bridging  $\text{PC}_6\text{H}_5$  ligands of cluster **63**, discourages fragmentation into lower nuclearity species. A small selectivity difference (*n*/*iso*) was observed between **62** and **63**, 5.4 vs. 2.6 in favour of the *n*-isomer *n*-**57b**, respectively. Further, the authors note that whereas an elevated temperature reduced selectivity, a pressure increase enhanced the selectivity. For cluster **62**, at 90 °C a selectivity of 5.4 was achieved, which was more than halved to 2.2 at 130 °C, despite reaching almost full conversion at roughly a fifth of the time. The authors further investigated cluster **63**, and the catalytic properties of a phosphine-substituted homologue **64** for hydroformylation of 1- and 2-pentene [110]. The high yield of recovered cluster **63** (95%), the lack of other organometallic species, as well as a reactivity difference compared to  $\text{Co}_2(\text{CO})_8$ , works to support cluster-mediated catalysis. Moreover,



**Scheme 20** Triruthenium  $\text{Ru}_3(\text{CO})_{12}$  of **76** affording  $\gamma$ - and  $\delta$ -lactones [120]

single-crystal X-ray diffraction was used to establish the structural configuration of cluster **64**. Interestingly, only cluster **63** was recovered from the reaction mixture were **64** was used originally.

Lavigne observed **65** in Scheme 18c, as a catalyst for the hydroformylation of tolan (**11a**), forming  $\alpha$ -phenylcinnamaldehyde **38b** [111, 112]. Ligand substitution demonstrated two distinct reactivities, of which one was important in the catalytic cycle. Whereas  $\text{PPh}_3$  resulted in migratory insertion of CO to **11a** leading to **65a**, coordination of CO afforded the vinyl group to undergo migratory insertion leading to **65b**. This step is described to occur by an  $\sigma$ - $\pi$  motion. As such, under sufficient CO pressure the migration of the vinylic group is argued to constitute an important intermediate in the catalytic cycle. Oxidative addition of  $\text{H}_2$  then enables reductive elimination, forming **38b** and hydride compound **65c** that can react with **11a** and conclude the cycle. Moreover, the cluster was active for up to six catalytic cycles.

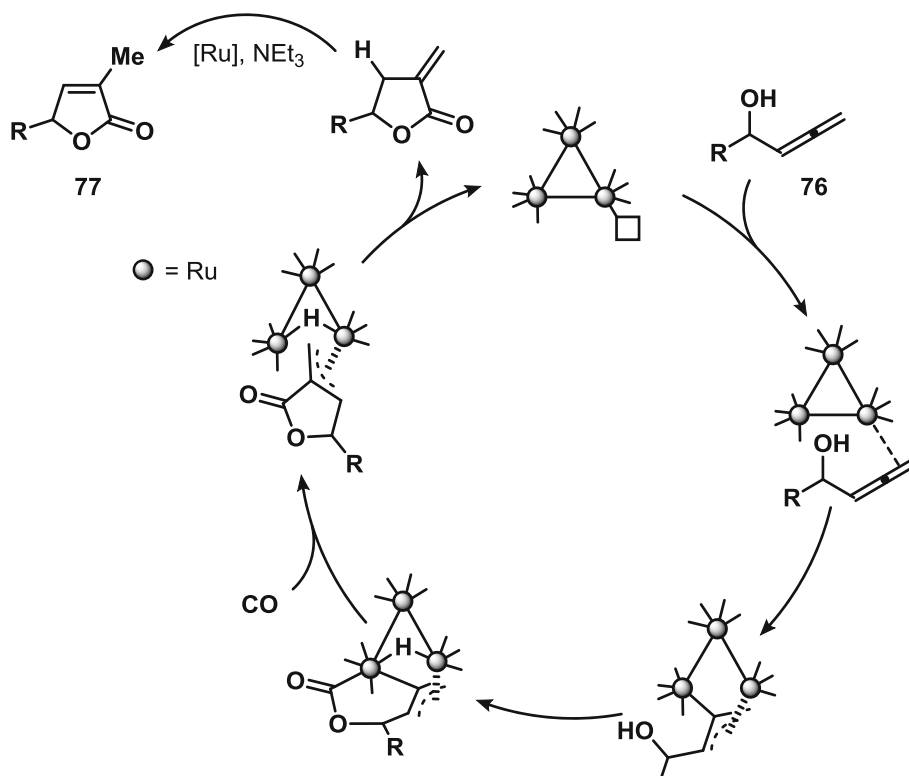


**Scheme 22** Cyclocarbonylation of **78** to **79** under atmospheric pressure of CO using  $\text{Ru}_3(\text{CO})_{12}$  as (pre)catalyst [122]

## Hydrocarbonylation

Jun reported a chelation-assisted hydroesterification of **66** using sodium formate **67** as the  $\text{C}_1$ -source and 2-phenylethanol **68** as alcohol to provide ester **32b**, Table 10 [113].  $^{13}\text{C}$ -labeling experiments established the carbonylic carbon in **69** originated from **67**. Thermal decomposition of **67** was further substantiated by pH measurements showing an increase from 6.9 to 9.1 after an hour of heating at  $170^\circ\text{C}$ , as well as trapping of CO in a Rh(I) complex. The role of 2-pyridinemethanol is explained in terms of a five-membered metallacycle, concluding the mechanism to consists of a chelation-assisted hydroesterification, and transesterification. While the nuclearity of the catalyst(s) was not addressed directly, considering the various precatalysts

**Scheme 21** The catalytic cycle for cyclocarbonylation of **76** to yield **77** using  $\text{Ru}_3(\text{CO})_{12}$  as catalyst, as proposed by Takahashi. Terminal CO molecules have been omitted for clarity [121]



employed, the difference in product distributions satisfy Laine's second criterion, thus suggesting cluster catalysis.

Chang demonstrated the hydroesterification of various alkenes (**1**) employing catalytic amounts of  $\text{Ru}_3(\text{CO})_{12}$  to afford products *n*-**32c** or *iso*-**32c** with predominantly linear selectivity (up to > 99:1), Table 11 [114]. Comparing a number of catalyst precursors resulted in a significant product variation between the triruthenium species relative to di- and monoruthenium compounds, with the two latter severely lacking activity. No further studies to ascertain the nature of the catalyst were provided.

A later study by Chang found that using  $\text{Ru}_3(\text{CO})_{12}$  in DMSO worked to provide conditions for regioselective catalytic hydroesterification of alkynes, whereas DMF provided beneficial conditions for dienes [115]. No experiments were done to address the structure of the catalyst, nor was ruthenium-sources of varying nuclearities investigated. However, a triruthenium species **71**, shown in Scheme 19, was isolated from another study on cooperative coupling using Ru and Pd, thus suggesting a polynuclear nature of the catalyst [116]. A later study found that, whereas DMF suppressed decarbonylation for hydroesterification, the opposite was true in hydroamidation [117]. Utilizing  $\text{CH}_3\text{CN}$  as solvent provided conditions affording varying yields (53–76%) of predominantly linear selectivity.

Following these results, Chang demonstrated that cocatalytic amounts of halide salts worked to enhance the ruthenium-catalyzed hydroesterification of olefins **1** and alkynes such as *n*-Pr-CC-*n*-Pr **11b** [118]. While the presence of halide has been reported to promote cluster fragmentation (vide supra), the authors invoke that this equilibrium is relevant only at high pressures of CO, as opposed to their conditions (absence of CO, and a maximum of 110 °C in DMSO). Rather, based on spectroscopic data, the role of halide was argued to promote dissociation of CO ligand. As such, using  $\text{Bu}_4\text{NI}$  as additive afforded excellent yields (up to 99%) with predominantly linear selectivity (up to > 98:2) in the hydroesterification of **1**.

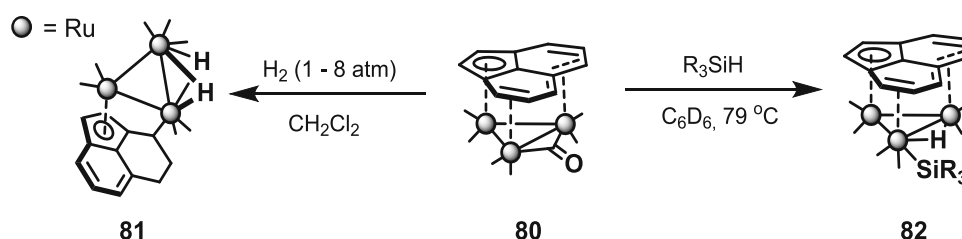
Formyl addition of **72b** to **53** leading to **74** was successfully achieved by Kondo and Mitsudo using a catalyst

precursor system comprising the anionic triruthenium hydrido cluster **75**,  $[\text{PPN}][\text{Ru}_3\text{H}(\text{CO})_{11}]$ , PPN = bis(triphenylphosphine)iminium, and  $\text{PCy}_3$ , Table 12 [119]. From screening a range of catalyst precursors, the mononuclear compound  $\text{Ru}(\text{COD})(\text{COT})$  demonstrated good conversion and similar regioselectivity (*exo:endo*) to that of **75**, albeit at a significantly reduced yield of 16% compared to 97%. The more simple  $\text{Ru}_3(\text{CO})_{12}$  also showed a *exo:endo* regioselectivity in the same range (84/16), but with significantly lower conversion of merely 26%. While these differences in conversions and product distributions satisfies Laine's second criterion, further studies could potentially shed more light on the nature of the catalytically active species.

### Cyclocarbonylation

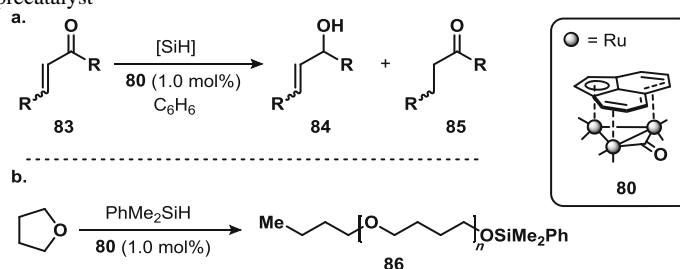
Takahashi demonstrated that  $\text{Ru}_3(\text{CO})_{12}$  is an efficient catalyst (precursor) for cyclocarbonylation to selectively afford  $\gamma$ - and  $\delta$ -lactones, such as **77a**, from allenyl alcohols, such as **76a** (91–99% yield), Scheme 20 [120]. When substituting to mononuclear ruthenium complexes, such as  $\text{RuCl}_3 \cdot x\text{H}_2\text{O}$  and  $\text{RuCl}_2(\text{PPh}_3)_3$ , catalytic activity was observed albeit with lower yields of 82% and 41%, respectively. Additionally, related metalcarbonyls demonstrated no activity. Investigation of the reaction conditions found that absence of additive  $\text{Et}_3\text{N}$  reduced the yield to approximately 60%. Moreover, while the nuclearity of the actual catalyst was not addressed, the catalyst precursor nuclearity was shown to affect the yield of product formation.

A subsequent study on the same reaction demonstrated a linear correlation of TOF with respect to the  $\text{Ru}_3(\text{CO})_{12}$ , in accordance with Laine's first criterion [121]. Labelling studies revealed the formation of two furanone-based products, of which tautomerisation to **77** occurs at elevated temperature in presence of  $\text{Et}_3\text{N}$  and ruthenium. To conclude their findings to a catalytic cycle, Scheme 21, the authors argue for an initial formation of a  $\pi$ -allyl complex. This suggestion is based on two observations, (i) excess addition of MeOH did not increase the rate of



**Scheme 23** Treatment of triruthenium-acenaphthylene cluster **80** with molecular hydrogen affording a distinct hydrogenation of the ligand **81**, or provides an oxidative addition adduct with silanes **82**. Terminal CO molecules have been omitted for clarity [6, 7, 123]



**Table 13** Initial discovery using **80** as precatalyst

a.

Substrate	[SiH] (1 equiv.)	Time (h)	Yield (%)	<b>84:85</b>
	(HSiMe <sub>2</sub> ) <sub>2</sub> (CH <sub>2</sub> ) <sub>2</sub>	1	80	12:88
	Ph <sub>2</sub> SiH <sub>2</sub>	4	93	91:9
	(HSiMe <sub>2</sub> ) <sub>2</sub> (CH <sub>2</sub> ) <sub>2</sub>	1	94	94:6
	Ph <sub>2</sub> SiH <sub>2</sub>	2.5	74	100:0

b.

THF/SiH	Temperature (°C)	Time (h)	Yield (%)	M <sub>n</sub>	M <sub>w</sub> /M <sub>n</sub>
20	40	20	40	5500	1.4
100	40	20	44	16,000	1.5

Terminal CO molecules have been omitted for clarity [123]

**Scheme 24** Catalytic scheme for the polymerization of ethers to **91**, exemplified by polymerization of vinyl ether **83**, as proposed by Nagashima [129]. Terminal CO molecules have been omitted for clarity

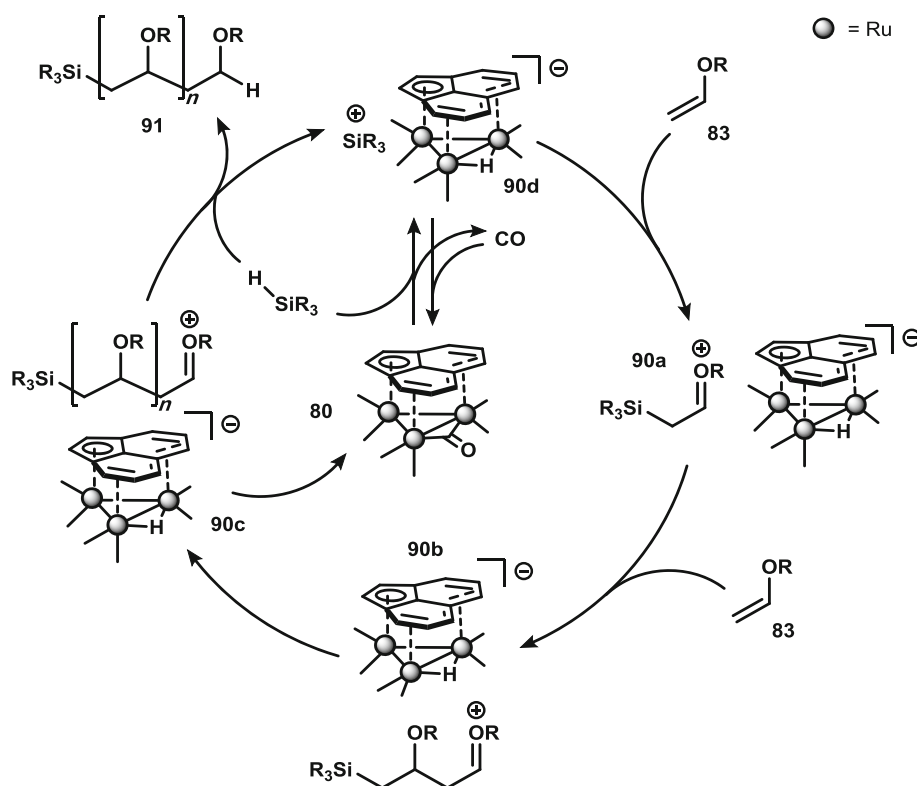




**Table 14** Alkoxy substituent promoting rearrangement over polymerization [130]

Substrate	[SiH] (mol%)	Catalyst (mol%)	T (°C)	t (h)	Conv. (%)	Yield (%)	<b>88:89</b>
	PhMe <sub>2</sub> SiH (10)	0.1	50	1	> 99	88	100:0
	(130)	1	50	1	> 99	91	0:100
	PhMe <sub>2</sub> SiH (20)	0.1	50	3	12	12	100:0

carbonylation, and (ii) the isolation of  $\pi$ -allyl adducts of both Fe<sub>2</sub>(CO)<sub>9</sub> and Os<sub>3</sub>(CO)<sub>12</sub>.

With reference to the work by Takahashi, Tsubuki and Honda reported that the use of Ru<sub>3</sub>(CO)<sub>12</sub> in catalytic amounts under atmospheric pressure of CO selectively affords cyclocarbonylation of homoallylic alcohols **78** to either five- or six-membered lactones, such as **76**, Scheme 22 [122]. The nature of the solvent was found to affect the formation of *endo* vs. *exo* product. Whereas acyclic tertiary amines resulted in complex mixtures, using cyclic tertiary amines resulted in a predominantly *endo* selectivity in varying yields 58–76%. Of the various solvents, 2,4,6-collidine resulted in a *endo-exo* distribution of 3.0:1. Additionally, the solvent affected the necessary pressure for cyclocarbonylation. Using Et<sub>3</sub>N, pressures below five atmospheres resulted in approximately 10% yield, while 2,4,6-collidine afforded up to 79% yield under

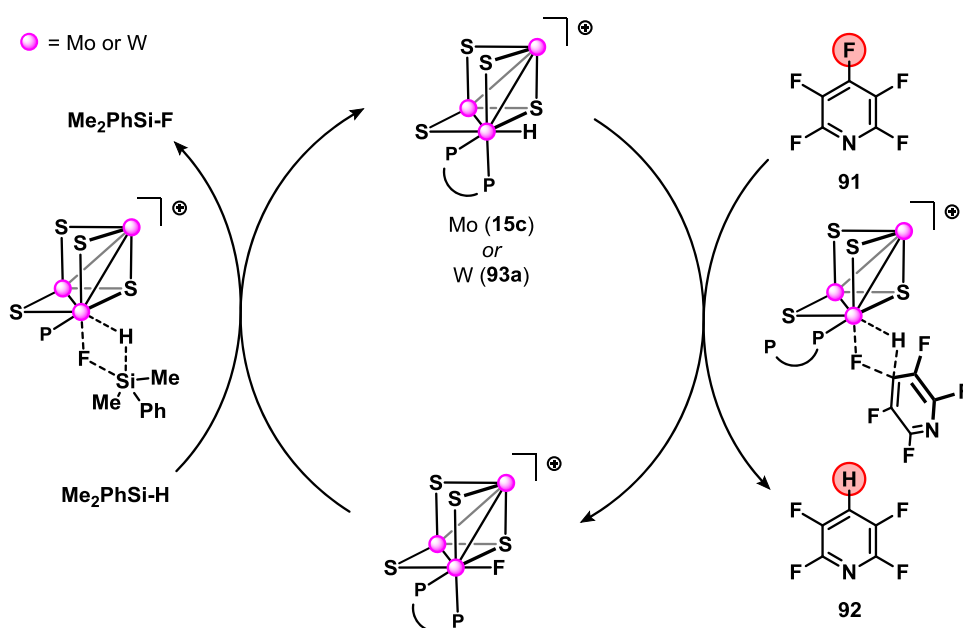
atmospheric pressure of CO. The catalyst nuclearity was not addressed, nor was any other ruthenium sources investigated as potential catalysts.

## Miscellaneous

### Hydroosilylation

Nagashima reported that the acenaphthylene face-capped triruthenium cluster, **80** [6], undergoes a distinct hydrogenation of the arene-moiety, affording hydrogenation of the C–C double bond within the six membered ring of the ligand to provide **81**, shown in Scheme 23 [7]. A later study revealed the resultant oxidative addition adduct of silanes to **75** provided clusters with retained integrity, **82** [123].

**Scheme 25** Catalytic regioselective hydrodefluorination of **91** to **92** using the high valent clusters **15c** or **93a**, as proposed by Llusar. For clarity, ligands have been omitted on residual metal centers [131]



The same study disclosed **80** as an efficient catalyst precursor for the hydride addition to  $\alpha,\beta$ -unsaturated carbonyls **83** to afford either **84** or **85**, as well as for ring-opening polymerization of THF to polymeric ether **86**, Table 13. Up to full selectivity of the hydride addition was achieved by pairing **83** with the appropriate silane. As such, employing diphenylsilane resulted in 1,2-addition to yield **84**, whereas dihydrosilanes resulted in 1,4-addition providing **85**. Interestingly, ring-opening polymerization of THF provided a selective  $M_n$  in the range of  $10^3$ – $10^5$ , a process commonly initiated in strongly acidic media. The authors suggest a transient species, structurally resembling **82**, based on an induction period, as well as  $^1\text{H}$  NMR studies of the reaction mixture showing similar resonances. Moreover, **82** was preparatively synthesized albeit under thermally different conditions than those in the catalytic cycle (79 °C vs. 40 °C). These observations thus suggests cluster catalysis.

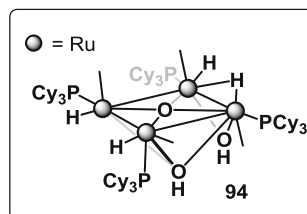
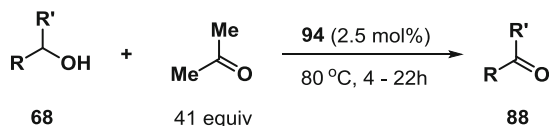
Nagashima provided further reports on selective reduction of functional groups using **80** as catalyst precursor. For example, addition of tertiary amines, such as  $\text{Et}_3\text{N}$ , as additive afforded selective reduction of the amide unit in ketoamide compounds [124]. In another example, the presence of  $\text{Me}_2\text{S}$  in mixtures of aldehydes and ketones selectively suppressed reduction of the ketones [125]. Furthermore, under neutral conditions **80** catalyzes the

cleavage of the C–O bond in a range of functionalities containing the C–O<sup>t</sup>Bu unit, including *N*- and *O*-Boc as well as <sup>t</sup>Bu-esters and <sup>t</sup>Bu-ethers [126]. Further substrate

**Table 16** Tandem one-pot dehydrogenation-alkene insertion using two ruthenium catalysts [135]

1	95	TON
		364
		310
		284

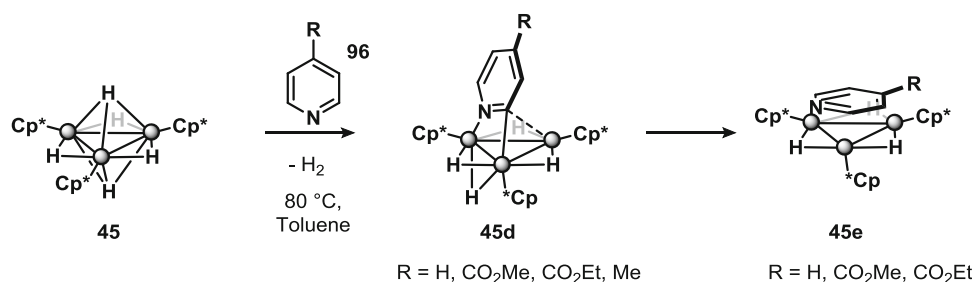
**Table 15** Dehydrogenation of **68** to **88** using a tetra ruthenium cluster **94** as catalyst



Substrate	Time (h)	Conversion (%)	Yield (%)
	18	100	62
	18	100	94
	3.5	95	85
	16	83	79
	6	100	98

Terminal CO molecules have been omitted for clarity [133]

**Scheme 26** Transformation of the pentahydrido triruthenium cluster **45** with pyridines [136]



selectivity was demonstrated by varying the source of silane. To this end, reduction of carboxylic acids using monofunctional silanes afforded the corresponding silyl ether, whereas bifunctional silanes provided the aldehyde [127]. Finally, bifunctional silanes were further employed in dehydration of amides [128].

Variation of the substituents changes the reactivity from vinyl ether polymerization to a [1, 3] O to C rearrangement. A stereo-electronic-activity relationship of the substituents in the substrate **87** concluded that, H as  $\alpha$ -substituent ( $\text{R}'$ ) generally results in polymerization, shown in Scheme 24 [129, 130]. On the other hand, when  $\text{R}'$  is different from H, in addition to a vinyl substituent that form a stable cation, such as furfuryl vinyl ether or *p*-methoxybenzyl vinyl ether, rearrangement was observed, Table 14. Moreover, the addition of excess hydrosilane resulted in a step-wise formation of the corresponding silyl ether going through an initial [1, 3] O to C rearrangement to the corresponding carbonylic moiety, followed by reduction, finally forming the silyl ether. While using 10 mol%  $\text{PhMe}_2\text{SiH}$  selectively provide **88**, a complete reversal in selectivity was achieved using 130% of the silane and using 1 mol% **80** providing **89**.

The polymerization is described by a cationic mechanism initiated by a heterolytic cleavage of the H-SiR<sub>3</sub> bond, resulting in an ion pair consisting of  $\text{R}_3\text{Si}^+[\text{H-Ru}_3]^-$  (**90d**). The siliconium ion then adds to the terminal carbon of **83** leading to **90a**, which is followed by propagation of the monomer (**90b** and **90c**) and terminated by hydride transfer providing the polymerization product **91**, as shown in Scheme 24. The Lewis acidity of the siliconium species is proposed to be insufficient for activating compounds bearing electron withdrawing substituents. End group analysis using deuterium corroborates the authors' suggested mechanism and observations regarding insertion of alkene between the Si and H bond in  $\text{R}_3\text{Si-H}$ .

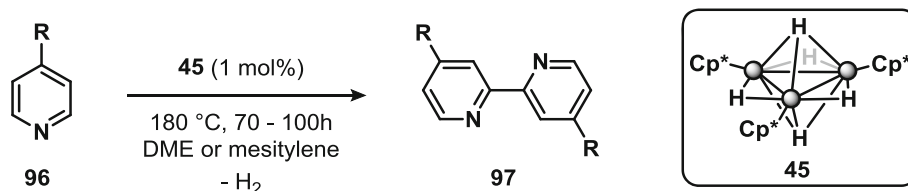
### Hydrodefluorination

Catalytic hydrodefluorination of perfluoropyridine **91** to tetrafluoropyridine **92** was achieved using the incomplete cubane-type cluster,  $[\text{M}_3\text{S}_4\text{H}_3(\text{dmpe})_3]^+$   $\text{M}=\text{Mo}$  (**15c**),  $\text{W}$  (**93a**), of which **93a** was reported by Llusar to afford a

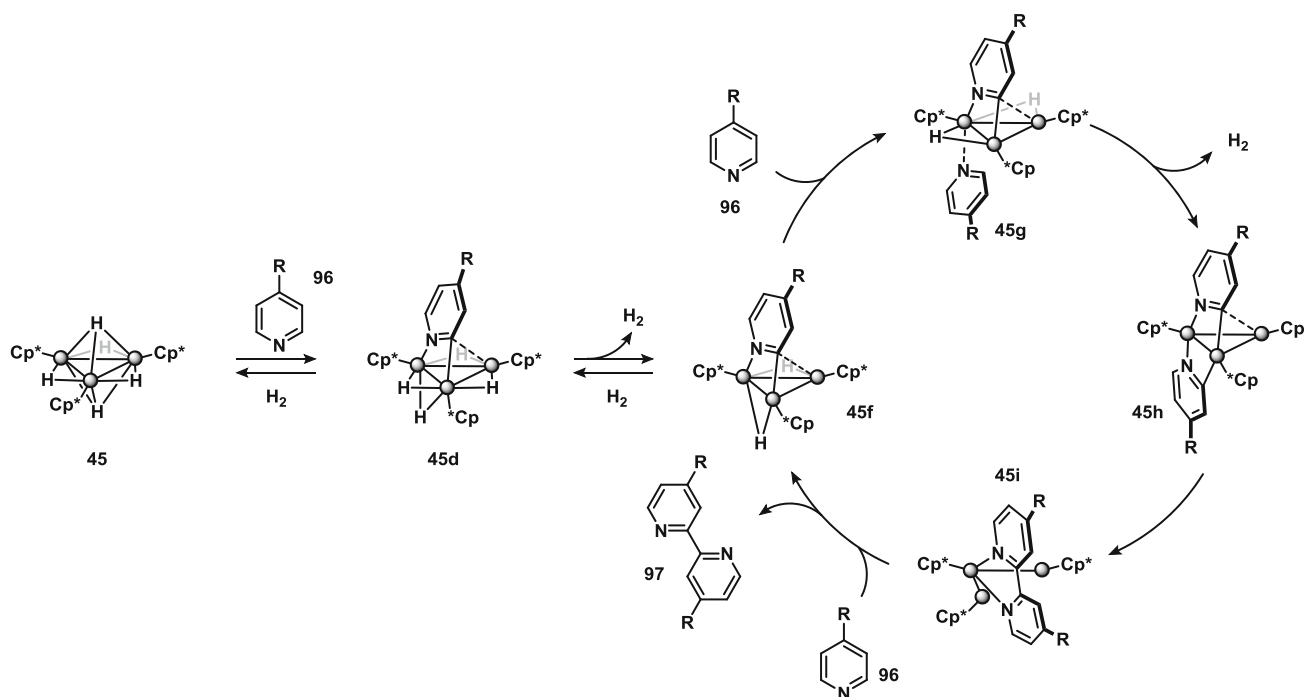
superior TON value of 90 [131]. Using 1 mol% catalyst loading and  $\text{Me}_2\text{PhSiH}$  as silane source afforded 90% yield under microwave conditions. Under the applied conditions, no cluster degradation was observed, and any reaction was only observed in the presence of the cluster. Mechanistic accounts were rationalized from DFT studies suggesting an initial phosphine dissociation from the cluster permitting M-H/C-F  $\sigma$ -bond metathesis. This compound, in turn, undergoes M-F/Si-H  $\sigma$ -bond metathesis that is concluded by re-coordination of the phosphine ligand as shown in Scheme 25. To assess the influence of the phosphine ligands on catalytic activity, Llusar reported in a later study the activity of the dppe congeners,  $[\text{M}_3\text{S}_4\text{H}_3(\text{dppe})_3]^+$ ,  $\text{M}=\text{Mo}$  (**15f**),  $\text{W}$  (**93b**) [132]. Approximately 90% yield was achieved at a significantly lower temperature (115 vs. 180 °C) and catalyst loading (0.7 vs. 1.0 mol%, respectively). Thus, substitution for less basic chelating phosphine was found to afford higher catalytic activity.

### Dehydrogenation Reactions

Yi demonstrated that the tetraruthenium complex,  $\{[(\text{PCy}_3)(\text{CO})\text{RuH}]_4(\mu_4\text{-O})(\mu_3\text{-OH})(\mu_2\text{-OH})\}$ , **94**, is a highly effective catalyst for the Oppenauer oxidation of primary (62–85%) and secondary alcohols (79–98%), Table 15 [133]. The authors were able to recover **94** after the reaction, which by  $^1\text{H}$  NMR spectra showed no changes. Further, the activity was found to remain the same throughout five cycles. In addition, the activity of **94** was greater than either of the parent compounds,  $\text{RuHCl}(\text{CO})(\text{PCy}_3)_2$  and  $[(\text{PCy}_3)_2(\text{CO})\text{RuH}](\mu\text{-H})(\mu\text{-OH})[\text{RuH}(\text{CO})\text{PCy}_3]$ , which afforded merely 30% and trace conversions, respectively. Additional two mononuclear ruthenium complexes were tested, of which neither afforded any oxidation. This drastic difference suggests cluster catalysis according to Laine's second criterion. Moreover, the transformation was concluded to proceed by cooperative interaction, as Hammett studies demonstrate an outer-sphere mechanism, as well as a sigmoidal curve-shape for the initial reaction rates. As such, the substrate seemingly binds to multiple ruthenium centers. Finally, a  $\text{Hg}(0)$  poisoning test indicates homogeneous-phase catalysis.

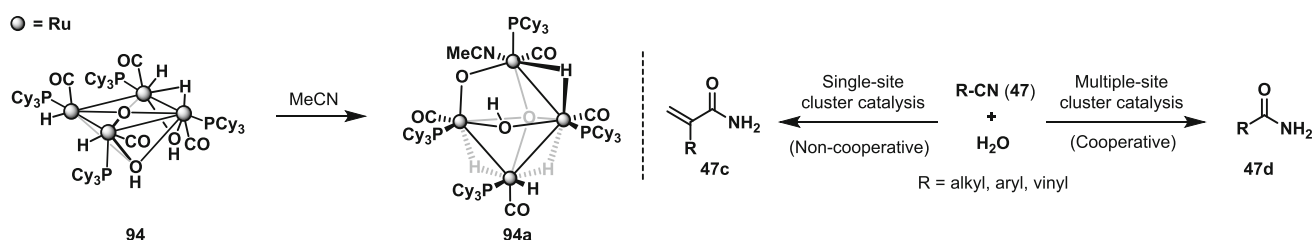
**Table 17** Dehydrogenative coupling of **96** leading to **97** using **45** as catalyst precursor [136]

R	Time (h)	Solvent	Yield (h)
Me	72	DME	2
Me	72	Mesitylene	20
Me	100	Mesitylene	43
4-pyridyl			27
NMe <sub>2</sub>			23
CO <sub>2</sub> Et			Trace
OMe			8

**Scheme 27** Tentative mechanism involved in dehydrogenative coupling of **96** leading to **97** using **45** as catalyst precursor, as proposed by Suzuki [136]

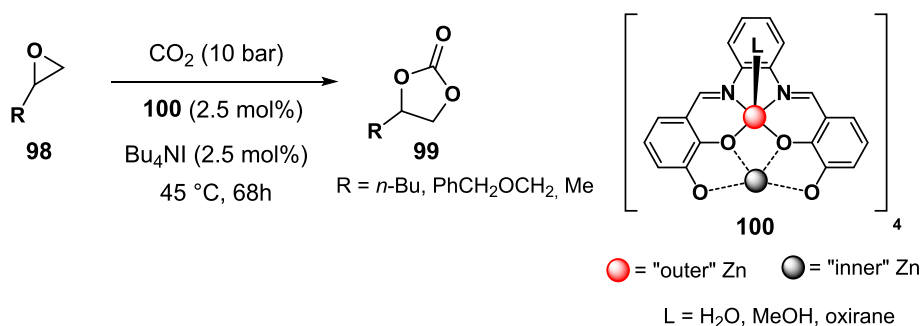
Using the same ruthenium cluster, **94**, Yi demonstrated its ability as an efficient catalyst for the dehydrogenation of unreactive C–H bonds in amines and carbonyls, resulting in TON values up to 20,000 within 2 h at 200 °C [134]. Additional mechanistic insights were obtained by phosphine inhibition and labeling studies, demonstrating that the cluster undergoes dissociative activation, as a significant reduction in TON was observed following increasing equivalents of phosphine. Further, the transformation was

established to occur via a reversible C–H activation at the vinylic position of *tert*-butylethylene (TBE). From these findings, Yi later reported a tandem one-pot setup for dehydrogenation-alkylation of hydrocarbons to provide a variety of aromatic compound, using a combination of tetraruthenium cluster **94** and the cationic monoruthenium species  $[(\eta^6\text{-C}_6\text{H}_6)\text{RuH}(\text{CO})(\text{PCy}_3)]\text{BF}_4$  [135]. This method worked to afford a highly regio- and



**Scheme 28** MeCN adduct of tetraruthenium cluster (**94**) demonstrating retention of nuclearity. Electronic properties of the nitrile affects the interaction with the cluster, electron-poor resulting in multiple-site catalysis [8]

**Scheme 29** Using an octazinc cluster **100** for the cycloaddition of  $\text{CO}_2$  to oxiranes **99** [137]



stereoselective protocol for the one-pot dehydrogenation-alkylation and insertion of **1** to ketones, such as **88a**, Table 16.

Suzuki reported that cluster **45** is active for the catalytic dehydrogenative coupling of electron-donating 4-substituted pyridine compounds **96** to yield 4,4'-dimethylbipyridine **97**, Scheme 27 [136]. Cluster **45** treated with excess pyridine reacted via a C–H bond cleavage at the  $\alpha$ -position resulting initially in the formation of an edge-bridge pyridyl species **45d**, which for electron-withdrawing functional groups transformed into the thermodynamically favored face-capped  $\mu_3$ -pyridyl complex, **45e**, Scheme 26.

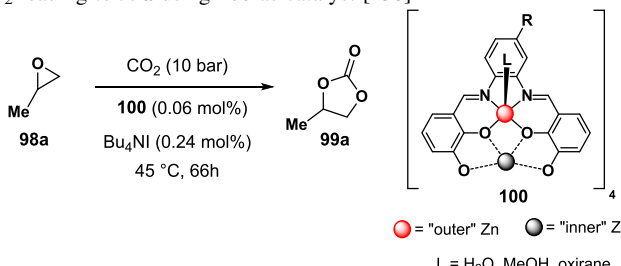
Using 0.2 mol% of **45** at  $180^\circ\text{C}$ , dehydrogenative coupling forming **97** was achieved in turn-over number of 80 after 120 h. The reaction in general provided moderate yields of the coupling products. However, it constitutes a rare example of reactions that utilize C–H bond activation for C–C bond formation, Table 17. The authors noted strongly coordinating solvent suppressed the reaction, as demonstrated by the difference in yields by one order magnitude between DME (2%) and mesitylene (20%). Moreover, the lack of products observed for electron-withdrawing substituents is suggested to relate to formation of **45e**.

While a full mechanistic account remained unclear, the authors provide a tentative mechanism based on an initial oxidative addition of a C–H bond at the  $\alpha$ -position to give **45f**, Scheme 27. This is followed by the coordination of a second pyridine compound giving **45g**, which promotes loss of hydrido ligands as  $\text{H}_2$ . The second pyridine

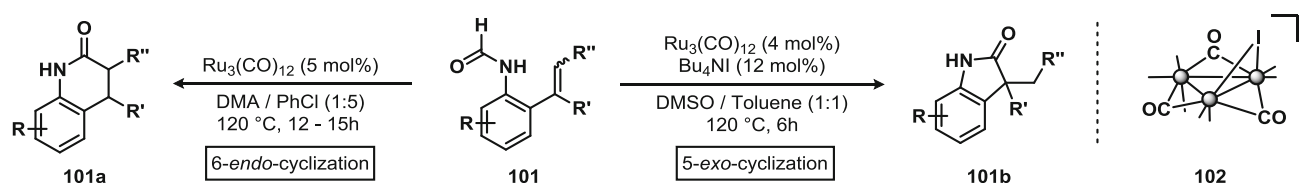
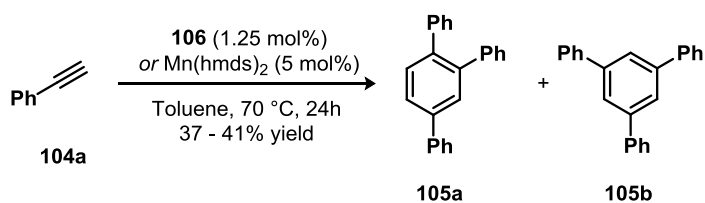
compound undergo C–H bond scission to provide **45h**, which via a rupture of a Ru–Ru bond permits for reductive elimination (**45i**). Finally, regenerating the Ru–Ru bond, releasing **97**, and allowing oxidative addition of a new pyridine compound closes the catalytic cycle by reforming **45g**.

### Hydration

Subsequent studies disclosed insights into the nature of the cooperative catalytic interactions by employing cluster **94** in the hydration of nitriles **47** to amides (either **47c** or **47d**), Scheme 28 [8]. By comparing the binding differences between benzonitrile **47a** and methacrylonitrile **47b** to **94**, and based on a Hill coefficient of approximately three, it was found that likely only **47a** demonstrated multiple binding interactions. Thus, three sites are able to bind **47a**, whereas **47b** was found to have a lower binding affinity. Consequently, **94** does only demonstrate cooperativity when reacting with **47a**. Single-crystal X-ray structure of a tetraruthenium-MeCN adduct **94a** revealed insight into the nature of the cluster, which upon MeCN coordination undergoes transformation of three structural features: (i)  $\mu_3$ -OH to  $\mu$ -OH, (ii) rearrangement of hydrides from terminal to bridging, and (iii) increased bond length between the ruthenium centers opposite to the nitrile. Moreover, the same adduct was found to provide four times the catalytic activity compared to **94**. From kinetic studies, it was demonstrated that only electron-poor arenes undergo cooperative transformation to a significant extent. This

**Table 18** Cycloaddition of **98a** with CO<sub>2</sub> leading to **99a** using **100** as catalyst [138]


R	Yield (%)	Selectivity (%)	TON
H	61	> 99	254
OMe	100	> 99	417
NO <sub>2</sub>	65	> 99	271

**Scheme 30** Regioselective cyclocarbonylation of **101** to yield either **101a** or **101b**. Terminally bound CO ligands have been omitted for clarity [139]**Scheme 31** Cyclotrimerization of **104a** to either **105a** or **105b** using cubane Mn<sub>4</sub>-Alkynyl cluster **103** as catalyst. Hmids ligands have been omitted for clarity [140]

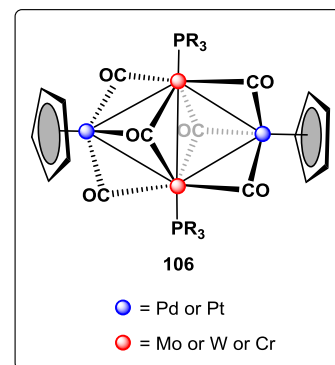
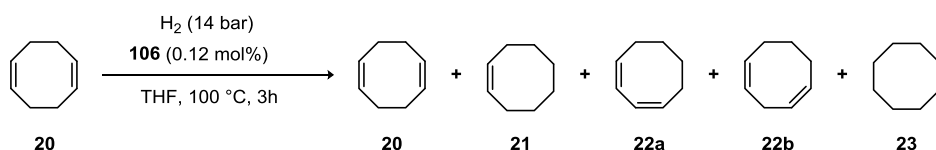
observation is suggested by the authors to relate to Ru–Ru bond rupture leading to cluster fragmentation from electron-rich arenes. Furthermore, DOSY NMR studies demonstrated that the active species is mononuclear under transformations of electron-rich arenes, corroborating the postulate. Finally, a Hg(0) poisoning test concluded homogenous phase catalysis.

### Cycloaddition

Kleij investigated the octanuclear zinc clusters **100**, resulting from a conglomeration of four symmetrical Zn<sub>2</sub>-Schiff-bases, as potential catalyst precursors for the cycloaddition of CO<sub>2</sub> to oxiranes **98** leading to carbonates **99**, Scheme 29 [137]. Single-crystal X-ray diffraction demonstrated two distinct zinc sites, of which the coordination environment and geometry of the “inner” site, was

argued to be a consequence of the nature of the “outer” site. Moreover, the former has a single water molecule associated, whereas the latter is exclusively coordinated by the phenoxo ligands. Spectroscopic and chromatographic analyses established an intact spherical cluster-entity. In methylethylketone, after 68 h of reaction time, 0.63 mol% of **100** afforded 87% yield of **99**, Scheme 29.

A later study by Kleij assessed the catalytic activity of **100** by introducing functional groups varying in electronic properties, as well as using asymmetric Schiff bases as building blocks, Table 18 [138]. Higher TON values were observed when employing electron-donating groups, which was accounted for in terms of a lower Lewis acidity of the zinc metals. On the contrary, employing electron-poor ligand backbone substituents resulted in a facile ligand dissociation and thus lower substrate turnover. Comparing the turnover number reveal a difference by a factor of

**Table 19** Planar triangulated low valent heterometallic cluster used as selective hydrogenation catalyst of **20** using **106** as catalyst (precursor) [141]

M	M'	R	Selectivity (%)				
			<b>20</b>	<b>21</b>	<b>22a</b>	<b>22b</b>	<b>23</b>
Pd	W	Et	7.0	24.5	61.3	7.2	Trace
		Ph	7.7	4.4	79.0	7.9	1.0
Pd	Mo	Et	2.6	70.4	23.7	3.0	0.4
		Ph	12.9	22.2	51.1	13.0	0.7
Pt	W	Et	–	18.7	77.7	Trace	3.6
		Ph	–	0.6	95.6	Trace	3.8
Pt	Mo	Et	Trace	61.1	32.1	–	6.8
		Ph	0.3	19.3	79.5	Trace	0.9
Pd	Cr	Et	–	15.7	83.8	Trace	0.5

approximately 1.5 between the methoxy and nitro-substituted cluster, at 417 vs 271, respectively. Notably, mononuclear Zn-salen complexes showed similar activities as **100** did.

Using iodide as additive, Chang reported reaction conditions that selectively afford either 5-*exo*-, or 6-*endo*-cyclization of formamides **101** using catalytic amounts of  $\text{Ru}_3(\text{CO})_{12}$ , Scheme 30 [139]. Based on their prior results combined with those of Geoffroy and Dombek [41], the authors suggest the halide bridged triruthenium species **102**,  $[\text{Ru}_3(\text{CO})_{10}(\mu\text{-I})]^-$ , as the catalytically active species for producing the 5-*exo*-cyclization **101b**. The lack of either product using other catalyst precursors, such as  $\text{Os}_3(\text{CO})_{12}$ , and  $\text{Ru}(\text{PPh}_3)_4\text{H}_2$ , combined with their prior findings, supports cluster mediated catalysis.

Exploring the chemistry of alkyne ligands for polynuclear architectures, Wangelin prepared the first examples of a heteroleptic alkynyl-Mn cubane structure **103**, shown in Scheme 31 [140]. Based on their previous studies on  $\text{Fe}(\text{N}(\text{SiMe}_3)_2)_2$  complexes in cyclotrimerization of phenylacetylene **104a** to provide either **105a** or **105b**, cluster **103** was employed as catalyst. Both the cluster and the parent compound,  $\text{Mn}(\text{hmds})_2$  was found to be moderately active in the same reaction. While  $\text{Mn}(\text{hmds})_2$  achieved 37%

yield with a distribution of **105a/105b** of 1.5:1, cluster **103** afforded 41% yield with the same product distribution.

Further catalytic studies on **103** found that the cluster is active in the hydrogenation of alkenes, such as  $\alpha$ -methylstyrene **1b**. Using 1.3 mol% cluster in toluene at 70 °C under 5 bars pressure of  $\text{H}_2$  for 20 h resulted in full hydrogenation. Interestingly, a significant difference between **103** and  $\text{Mn}(\text{hmds})_2$  in the hydrogenation of **11a** was observed. Whereas  $\text{Mn}(\text{hmds})_2$  afforded full conversion, **103** afforded merely 30%.

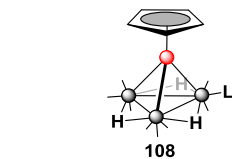
## Heteronuclear Clusters in Catalysis

### Hydrogenation

For the selective hydrogenation of COD (**20**), low valent heterometallic clusters were studied by Pittman and Braunstein, Table 19 [141]. All of the clusters **106** were moderately active as hydrogenation catalysts, however considerable amount of isomerization products were observed as well. To assess whether the ligand ( $\text{PEt}_3$  vs.  $\text{PPh}_3$ ) or the combination of metals was more influential on the activity, the clusters' activities were compared at 100 °C. Of the group six metals, the Mo- $\text{PEt}_3$  clusters



H<sub>2</sub> (0.9 bar)



Terminal CO molecules have been omitted for clarity [142–144]

catalyst loading, approximately 70% selectivity of the mono hydrogenated product was achieved using the  $(\eta^5\text{-Cp})_2\text{Pd}_2(\mu_3\text{-CO})_2(\mu\text{-CO})_4\text{Mo}_2(\text{PET}_3)_2$  cluster.

Cluster mediated hydrogenation and isomerization of diolefins **107** were established by Sappa and Tiripicchio, using tetrahedral heterometallic clusters **108** comprising a



triangular array of the group eight metals capped by a Ni-Cp unit,

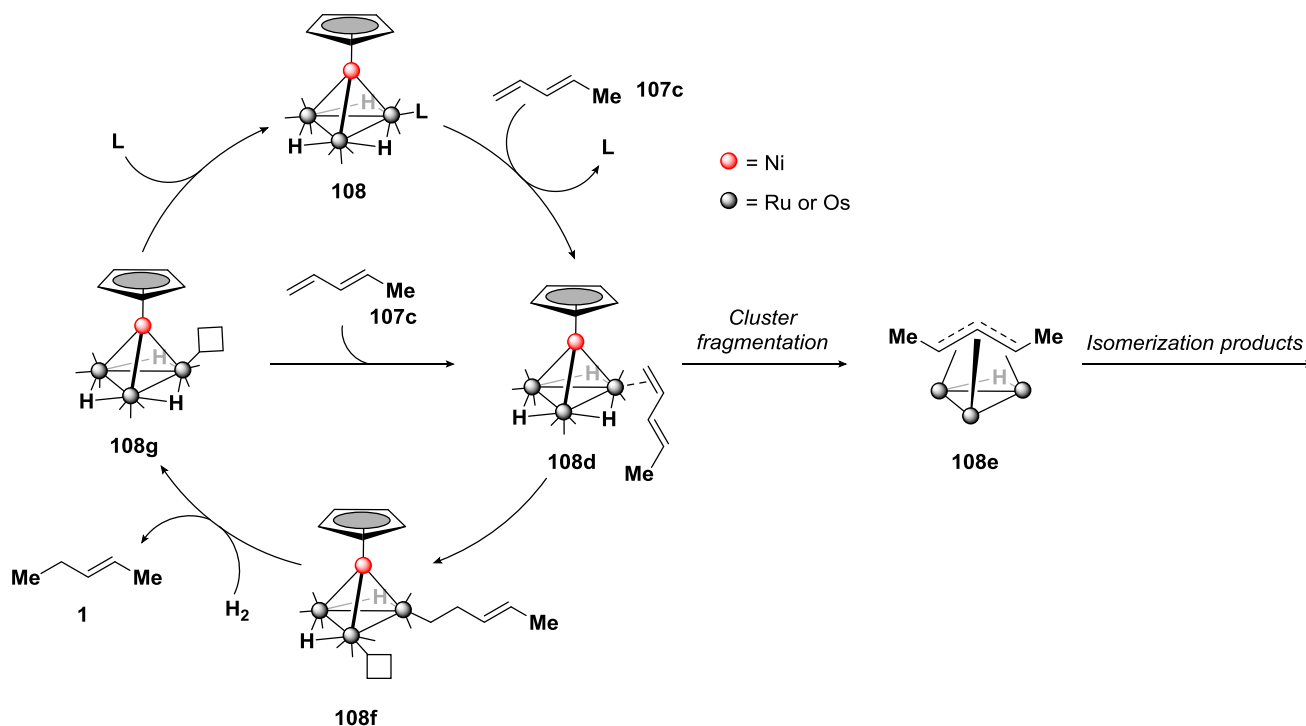
Table 20 [142, 143]. From the well-defined tetrahedral bimetallic osmium cluster,  $\text{CpNiOs}_3(\mu\text{-H})_3(\text{CO})_9$  **108Osa**, the authors hypothesise a similar structure of the ruthenium congener,  $\text{CpNiRu}_3(\mu\text{-H})_3(\text{CO})_9$  **108Rua**. While both **108Osa** and **108Rua** were found catalytically active, spectroscopic analysis established a poor stability of **108Rua**, as decomposition was observed within 40 min. Fragmentation is further supported by comparing the amount of **1c** found using **108Osa** and **108Rua**. While **108Osa** provide up to 22% after 240 min, only 2% is found for the **108Rua** within the first 30 min. The authors suggests the role of the capping group to provide a “trans-effect” that promotes the dissociation of CO, as isomerization predominantly was observed as it was lost. Comparing the reactivity of  $\text{HRu}_3(\text{CO})_7(\mu\text{-PPh}_3)_3$  to  $(\text{Cp})\text{NiRu}_3(\mu\text{-H})_3(\text{CO})_7(\text{PPh}_3)_2$  **108Rud** a similar selectivity for isomerization is seen.

Further insights were disclosed on changes in catalytic activity induced by various phosphine ligands, by substituting the tetrahedral bimetallic **108Ru** and **108Os** clusters [144]. The ruthenium clusters were again observed to decompose within the first 40 min. While monosubstituted  $\text{PPh}_3$  clusters,  $(\text{Cp})\text{NiRu}_3(\mu\text{-H})_3(\text{CO})_8(\text{PPh}_3)$  **108Rub**, were less active than **108Rua**, the doubly substituted clusters, such as **108Rud**, clusters generally demonstrate a higher

turnover than the respective parent clusters. This observation led the authors to conclude that isomerization precedes hydrogenation. The lack of recovered degradation  $\text{Ru}_3(\text{-CO})_{12-n}\text{L}_n$  products from the reaction mixture supports catalysis by an intact  $[\text{Ru}_3]$ -cluster framework. Moreover, the phosphine is suggested to lower hydride acidity rather than promoting the dissociation of CO ligands.

Concluding their studies on hydrogenation and isomerization of (cyclic) dienes, the combined findings are summarized by the authors who suggest a catalytic cycle shown in Scheme 32. Either  $[\text{NiRu}_3]$  or  $[\text{NiOs}_3]$  act in the cycle that initially work by ligand substitution of a terminally bound ligand **L** from **108** with **107c** leading to **108d**. Substitution is followed by either of two pathways. Loss of the CpNi unit results in cluster degradation forming **108e** and cluster-mediated isomerization products, whereas hydride insertion results in a vacant site (**108f**), which permit for oxidation addition of  $\text{H}_2$ , followed by reductive elimination. This step generates product **1** and cluster **108g**, which undergoes ligand association by either **L** or **107c**, thus closing the cycle.

Hydrogenation of **103a** was demonstrated by Pittman and Braunstein by employing the same triangulated planar clusters **106** as in Table 19 to selectively afford partial hydrogenation of **103a** to styrene **1d** [141]. Of the various combinations, the use of  $(\eta^5\text{-Cp})_2\text{Pt}_2(\mu_3\text{-CO})_2(\mu\text{-CO})_4\text{-Mo}_2(\text{PEt}_3)_2$  achieved 99% selectivity at 60 °C under



**Scheme 32** Catalytic scheme for the selective hydrogenation of **107** in presence of **108** as proposed by Sappa and Tiripicchio. Fragmentation of the cluster results in isomerization products. Terminal CO molecules have been omitted for clarity [142–144]

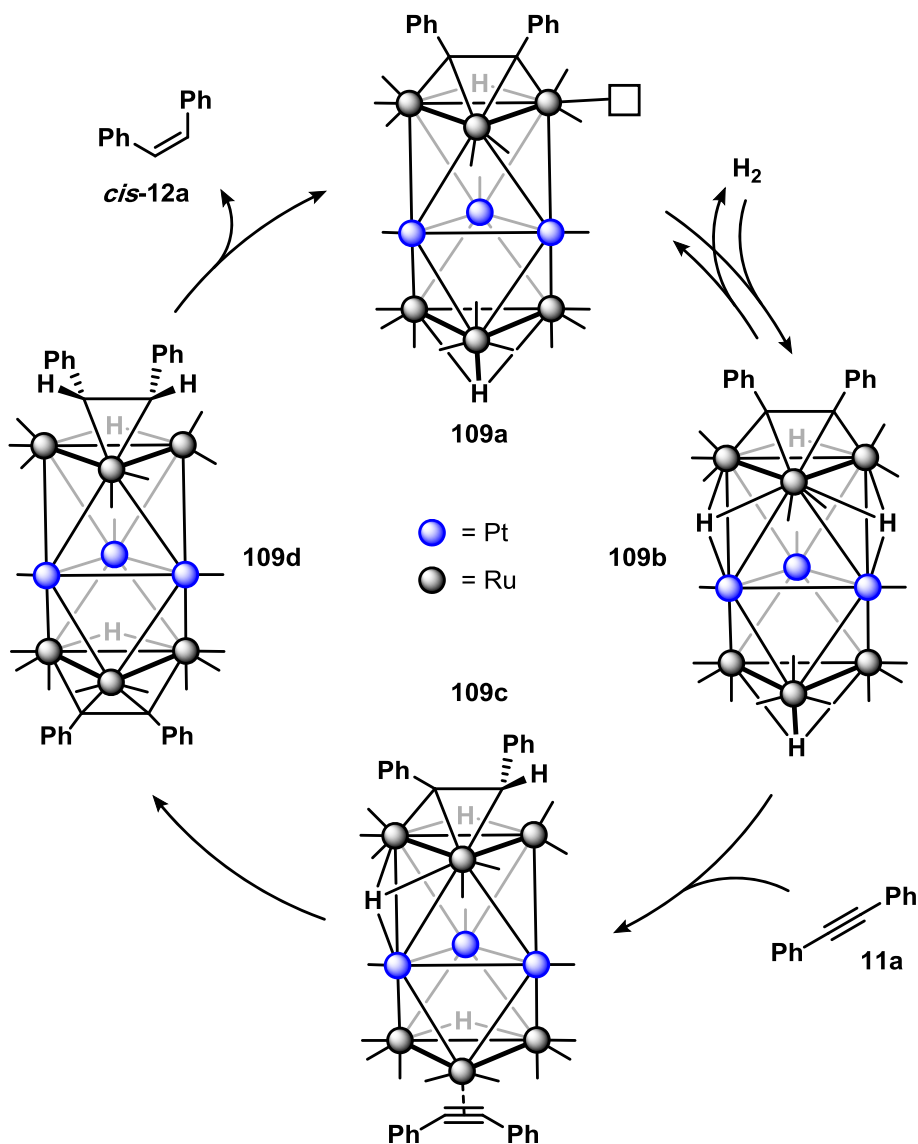
approximately 14 bar of  $\text{H}_2$ . Hydrogenation of *n*-hexyne **103b** demonstrated that terminal alkyl alkynes readily hydrogenated to the corresponding alkene as well.

A mixed-metal Ru-Pt cluster **109**,  $\text{Pt}_3\text{Ru}_6(\text{CO})_{20}(\mu_3\text{-PhC}_2\text{Ph})(\mu_3\text{-H})(\mu\text{-H})$ , was prepared by Adams as a catalyst precursor for the selective partial hydrogenation of **11a** [145]. To assess ligand exchange, and to provide evidence in support of cluster catalysis, **109** as well as the ditolylacetylene homologue **110**,  $\text{Pt}_3\text{Ru}_6(\text{CO})_{20}(\mu_3\text{-TolC}_2\text{-Tol})(\mu_3\text{-H})(\mu\text{-H})$ , were used in labelling studies, that demonstrated incorporation of reagents [146]. Additionally, kinetic studies revealed first order rate-dependence with respect to cluster concentration, whereas CO had an inverse first order dependence. Further kinetic studies of appropriate (fragmentation) species afforded TOF values of insufficient magnitude (up to  $3\text{ h}^{-1}$  vs. up to  $82.4\text{ h}^{-1}$  for **109**). Thus, the empirically derived activation parameters

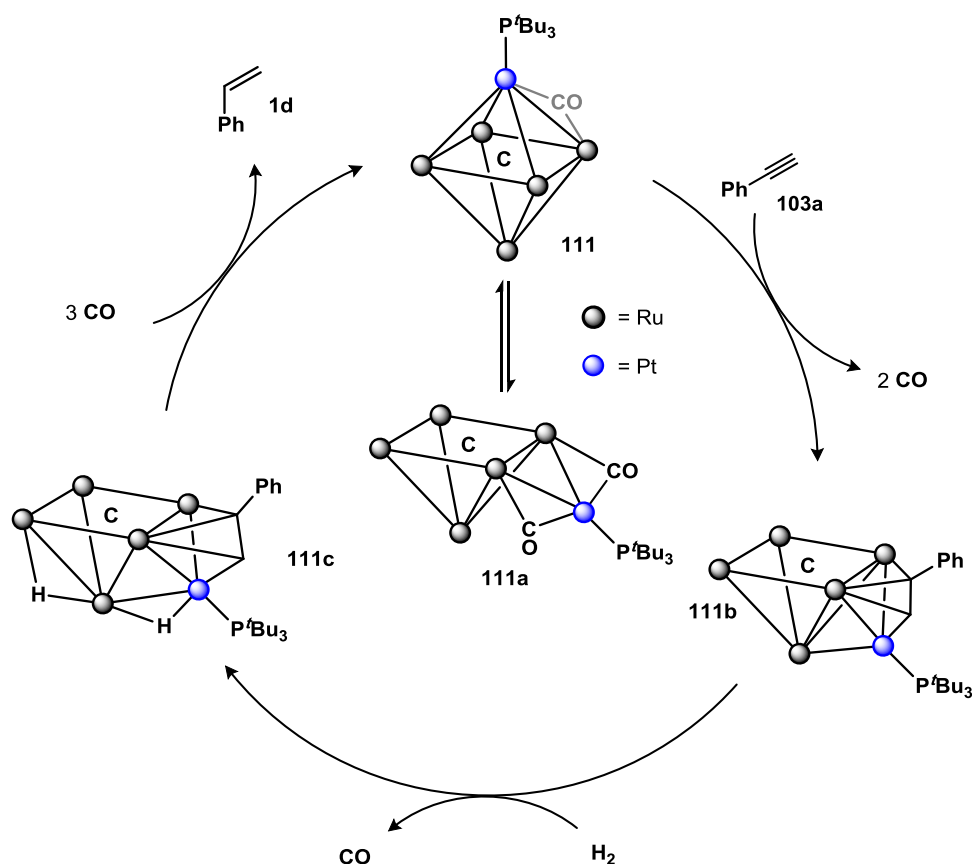
suggest cluster catalysis. Similar results with respect to rate order dependency, as well as labelling studies, were observed when using **109** as catalyst precursor for the hydrosilylation of **11a** [147].

To ascertain the active site for the transformation, and to account for the interplay between Ru-Pt, a homologue of **109** containing the labile ligand  $\text{Me}_2\text{S}$  was used for the partial hydrogenation of **11a** [148]. The initial reaction rate (20 min) was three times as large using this homologue, which the authors argue is a result of more facile ligand dissociation. In spite of the high catalytic activity, the cluster interconverts back to **109** under the reaction conditions, which precluded a detailed kinetic account. The authors conclude that the transformation of both  $\text{H}_2$  and **11a** necessarily must take place at the  $\text{Ru}_3$ -triangle, with a tentative explanation that the Ru-Pt interaction originates in an electron donation from the latter transition metal.

**Scheme 33** Catalytic scheme for hydrogenation of **11a** by a formation of a vacant coordination site, followed by formation of two triply bridging hydrides as proposed by Adams. Coordination of **11a** to the unencumbered ruthenium triangle promotes insertion of one hydride to the originally coordinated alkyne. Terminal CO molecules have been omitted for clarity [148]



**Scheme 34** Probing the role Pt plays in transformation of alkynes in the related layer segregated Ru–Pt cluster, Adams prepared a hexanuclear Ru–Pt compound, in which Pt is connected to substrate activation rather than an extended ligand. Terminal CO molecules have been omitted for clarity [14]



Thus, a catalytic transformation of **11a** is proposed to follow the mechanism shown in Scheme 33. The initial step proceeds via ligand (CO) dissociation resulting in an electronically unsaturated species with a vacant coordination site (**109a**), which then undergoes oxidative addition of  $H_2$  to provide **109b**. A  $\mu_3$ -bridging H is argued based on structures of related fragments, and the subsequent interaction to **11a** at the free ruthenium triangle promotes the formation of a C–H bond from the hydride and the originally coordinated alkyne. The resulting vinyl ligand, with *cis*-positioned phenyl groups, then becomes triply coordinated to the cluster (**109c**), that further promote a hydride transfer to form the *cis*-**12a**. Moreover, steric encumbering was found to favor product dissociation. The authors note that at a high substrate loading and after several catalytic cycles, fragmentation and alkene adducts play a significant role in the loss of catalytic activity.

Further insight on the Ru–Pt interaction was provided using the mixed-metal hexanuclear cluster **111**,  $Ru_5(-CO)_{14}(\mu-H)_2(\mu_6-C)[Pt(P^tBu_3)]$ , demonstrating that the Pt was involved in activation of hydrogen and **103a** [14]. The hexanuclear  $[Ru_5Pt]$  was found in an equilibrium with the open structure **111a**, Scheme 34. Treatment of **111** with **103a** at 40 °C resulted in a platinum-capped square-pyramidal pentaruthenium cluster, with the alkyne bridging a

$PtRu_2$  triangle **111b**. Subsequent treatment with  $H_2$  at elevated temperature (80 °C) regenerated **111** along with the production of **1d**. Overall, the TOF was  $20\ h^{-1}$ .

## Carbonylation

Echavarren studied a series of polynuclear gold clusters, of which the pentabimetallic  $Au_4Ag^I$  cluster **112** was found to catalyze carbonylation of various primary amines **42** to ureas **113** with up to 99% yield [149]. In support of cluster catalysis, **112** was recovered and reused, which afforded a yield of 73%. In addition, the lack of an induction period suggests that catalysis is taking place in the homogeneous phase. Conducting a  $Hg(0)$  poisoning test was precluded as the mercury reacted with **112**. From the optimized reaction conditions, a broad scope of **42**, including sterically demanding examples, were carbonylated to the corresponding urea compounds **113**, Table 21.

## Hydroformylation

Pittmann and Braunstein found that two different clusters containing Co and Pt, a triangular (**114**) and a butterfly cluster (**115**), respectively, Table 22, was active in hydroformylation of *n*-pentene (**1c**) to mixture of *n*-**57b** and *iso*-

**Table 21** Catalytic carbonylation of primary amines using  $\text{Au}_4\text{Ag}^{\text{I}}$  cluster [149]

$\text{R-NH}_2 \xrightarrow[\text{THF, 60}^\circ\text{C, 24h}]{\text{CO (5 bar), air, 112 (2 mol\%)}} \text{R-NH-CO-NH-R}$		
42	113	
42	113	Yield [%]
 42h	 n-Hex-NH-CO-NH-n-Hex	93
 42i		88
 42j		92
 42k		89

**57b** [141]. The chemical nature of the coordinating atoms in the chelating ligand was found to significantly influence the activity of **114**. Comparing the reactivities between complexes of dppe,  $\text{Ph}_2\text{P}(\text{CH}_2)_2\text{PPh}_2$  (**114P**), and dpae,  $\text{Ph}_2\text{As}(\text{CH}_2)_2\text{AsPh}_2$  (**114As**), ligated clusters respectively, showed that whereas **114As** was inactive, **114P** afforded a yield of approximately 39% at 80 °C (*n/iso* = 3.7:1). The authors suggest the reactivity difference to origin from retention of cluster integrity, of which only dppe aids towards this, based on the amount of recovered compound. Using 0.11 mol% catalyst loading of **115** provided 85% conversion with a predominantly linear selectivity (*n/iso* = 4:1) at 100 °C.

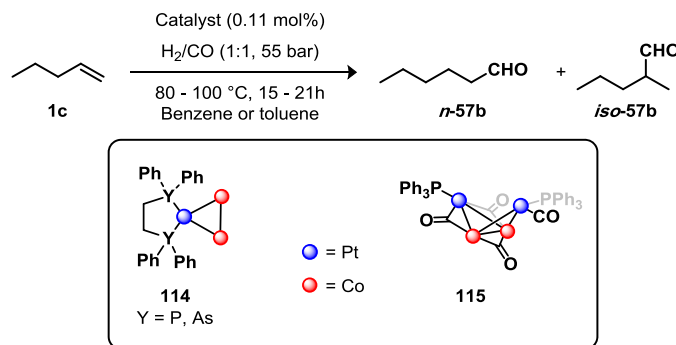
To investigate the postulate that polydentate  $\mu_3$ -ligands suppress cluster fragmentation, whilst accommodating M–M bond rupture to facilitate (catalytic) transformations, a series of face-capped triangular mixed-metal clusters **116**–**121**, Table 23, were prepared by Pittman for the catalytic hydroformylation of **1c** to mixtures of *n*-**57b** and *iso*-**57b** [150]. Under the conditions for transformation of **1c**, isomerization competition was observed. Most notably for the clusters **116**, **119**, and **121**. While cluster **116** initially (7 h) catalyze the hydroformylation of **1c**, extending the reaction time (24 h) significantly lowers the selectivity, due to hydroformylation of the 2-penten-1-ynes (**1**). Fragmentation was

suspected for **121** and, as such, its activity was compared to that of  $\text{Co}_2(\text{CO})_8$ . Interestingly, they showed nearly identical activities, thereby indeed indicating a fragmentation of **121** to a lower nuclearity complex. Moreover, the authors conclude cluster mediated catalysis for clusters **116** through **120** based on a lack of evidence supporting the presence of lower nuclearity species, as well as the amount of recovered cluster (> 90% yield). Finally, the transformation is suggested to proceed via a metal–metal bond cleavage, and the  $\mu_3$ -ligand likely works to retain cluster integrity throughout the catalytic cycle.

Gervais and Kalck observed that the heterometallic  $d^0$ – $d^8$   $[\text{ZrRh}_2]$  cluster **122** ( $\eta^5\text{-Cp}$ ) $_2\text{Zr}(\text{CH}_2\text{PPh}_2)_2\text{Rh}_2(\mu\text{-S}^t\text{-Bu})_2(\text{CO})_2$  afforded catalytic hydroformylation of **1a**, under mild reaction conditions [151, 152]. Approximately 90% conversion to mixtures of *n*-**57c** and *iso*-**57d** was achieved at 80 °C at a pressure of approximately 5 bars of  $\text{H}_2/\text{CO}$  (1:1), with predominantly linear selectivity (*n/iso* = 2:1), Table 24. The authors speculate that the role of Zr is to act as an electron reservoir. Choukroun provided further insight on the role of Zr by introducing sterically encumbered zirconocene substituents at the cyclopentadienyl group [153, 154]. Single-crystal X-ray diffraction of the *t*-Bu homologue of **122** revealed a disruption of the Zr–S interactions, consequently changing the coordination environment of Zr from a pentacoordinate to that of pseudo-tetrahedron. However, the role of Zr is in large suggested to ensure that the Rh-centres remain vicinal thereby warranting a cooperativity between the two Rh-centers.

Similarly, Ciriano, Oro and Claver provided insight on cluster compounds **123** comprising the early transition metal titanium and late transition metal rhodium,  $[\text{TiRh}_3]$ , in the hydroformylation of **1a** and **1d** [155]. Probing **123** with monodentate phosphine and phosphites, the authors were able to ascertain the active catalyst to exist in an equilibrium between a bis- (**123a**) and a tris ligated (**123b** and **123c**) compound type, as shown in Scheme 35. A previous study by Ciriano and Oro on the iridium homologue further corroborated this equilibrium [156]. Thus, using 0.5 mol% of precatalyst **123** at 80 °C under approximately 5 bar of  $\text{H}_2/\text{CO}$  (1:1) in toluene with  $\text{PPh}_3$  in a P/Rh ratio of four, **1a** was converted in 96% to **57c** with a predominantly linear selectivity of 78%. On the contrary, 88% conversion of **1d** to **57d** was achieved, at a slightly higher pressure of approximately 30 bar in THF, with an interestingly *iso*-selectivity of 89%.

Haupt investigated the synergism between Rh and Mn as well as between Rh and Re,  $[\text{M}_2\text{Rh}(\mu\text{-PCy}_2)(\mu\text{-CO})_2(-\text{CO})_8]$ , M = Re (**124Re**), Mn (**124Mn**), Table 25, for the hydroformylation of **1a** [157]. The Rh–Mn cluster **124Mn** was found to catalyze isomerization to **1e** and **1f** with predominantly *trans*-selectivity with TOF values of up to

**Table 22** Triangular (**114**) and butterfly (**115**) PtCo mixed-metal complexes as catalysts for the hydroformylation of **1c** to mixtures of *n*-**57b** and *iso*-**57b**

Catalyst	Temperature (°C)	Time (h)	Conversion (%)	Yield (%)	
				<i>n</i> - <b>57b</b>	<i>iso</i> - <b>57b</b>
<b>114P</b>	80	21	39	3.7	8.2
<b>114As</b>	80	22	0	–	–
<b>115</b>	62	17	Trace	Trace	Trace
	75	18	16.5	14	2.5
	100	17	85.4	63.5 (+ 7.3% 1-hexanol)	14.6

Terminal CO molecules have been omitted for clarity [141]

473 h<sup>−1</sup>. On the contrary, the Rh-Re complex **124Re** achieved hydroformylation to **57c** with TOF values of up to 246 h<sup>−1</sup> with predominantly linear selectivity (*n*/*iso* = 3.4).

## Miscellaneous

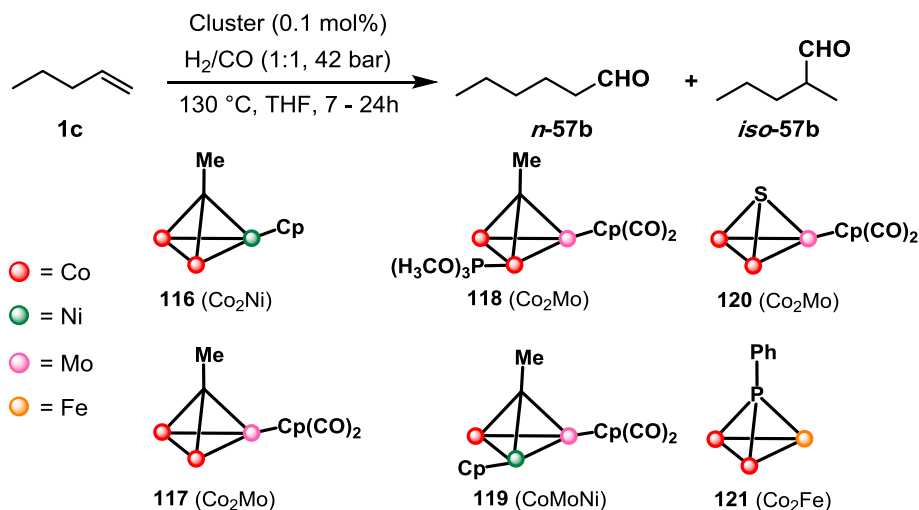
### Hydrosilylation

As previously discussed by Pittman, the use of non-fluxional ligands in metal-carbonyl clusters, such as the face capping  $\mu_3$ -ligands used in Table 23, serve to inhibit cluster fragmentation under thermal catalysis. Pittman and Vahrenkamp present evidence to support this proposal by using such  $\mu_3$ -ligated clusters as catalyst precursors in the photoinitiated reaction between Et<sub>3</sub>SiH and acetophenone (**35a**) leading to either hydrosilylation (**125**) or Mukaiyama silyl enol ether formation (**126**) [158]. In the absence of both **121** and irradiation ( $\lambda$  = 254 or 355 nm) no reaction was observed, and the amount of recovered **121** after photolysis was up to 98%. A higher quantum yield was observed using irradiation at 254 nm, which is discussed in relation to a possible mechanism invoking loss of a CO ligand. Whereas high-energy irradiation results in a metal–ligand charge transfer that consequently destabilizes the M–CO bonds, low energy light merely results in M–M bond cleavage that readily reform, Scheme 36.

### Dehydrogenation Reactions

Shapley investigated the activity of a trinuclear bimetallic cluster **127** complex comprising Ru and the group ten metals, (dppe)M( $\mu_3$ -S)<sub>2</sub>{Ru(N)Me<sub>2</sub>}<sub>2</sub>, M=Ni (**127Ni**), Pd (**127Pd**), and Pt (**127Pt**), for the dehydrogenation of **65f** to **44**, Table 26 [19]. A bond length variance of approximately 0.2 Å between Ni and Ru centers was observed in **127Ni**, of which the shorter distance (2.9 Å) was suggested by the authors to stem from a two-electron interaction from Ru to Ni. This is rationalized based on the relative small HOMO–LUMO gap between Ni and Ru. On the contrary, the Pt–Ru bonds were both found to be equidistant (3.16 Å) in **127Pt** [159]. Comparing the activity of **127Pt** cluster at 18.8 and 44 bars pressures of O<sub>2</sub>, respectively, the authors established that an increase in O<sub>2</sub> pressure does not increase the oxidation rate. This observation is suggested to be due to that O<sub>2</sub> and **65f** likely compete between the same binding sites at the cluster. Additionally, an increase in the concentration of O<sub>2</sub> lowers the CO<sub>2</sub> and thus the cluster solubility. While **127Ni** demonstrates a direct metal–metal interaction, its effect on catalytic activity is not addressed. The conversion difference of approximately 20% (in toluene) is also not addressed in detail [19].

Takao studied the homologue series of triangular trimetallic clusters comprising the group nine metals and Ru, Ru<sub>2</sub>M( $\mu$ -H)<sub>3</sub>( $\mu_3$ -H)( $\eta^5$ -Cp)<sub>3</sub>, M=Co (**128Co**), Rh (**128Rh**) and Ir (**128Ir**), for the dehydrogenative coupling of 4-substituted pyridines **96** to bipyridines **97**, Table 27

**Table 23** Tetrahedral clusters with  $\mu_3$ -bridging ligands **116–121**, investigated by Pittman as catalyst (precursors) for the hydroformylation of **1c** to mixtures of *n*-**57b** and *iso*-**57b**

Catalyst	Time (h)	Alcohols (%)	<b>57b</b> (%)	Selectivity ( <i>n/iso</i> )
<b>116</b>	7		21	2.6
	24	11	88	0.6
<b>117</b>	24		14	2.4
<b>118</b>	24		26	2.9
<b>119</b>	24		8	3.2
<b>120</b>	24		2	Only <i>n</i> - <b>57b</b>
<b>121</b>	24	1.2	90	1.4
$\text{Co}_2(\text{CO})_8$	24	1.0	92	1.5

Terminal CO molecules have been omitted for clarity [150]

[160]. Compared to the all ruthenium cluster **45**, a significant increase in TOF (3 h) (from 0.1 to 0.3  $\text{h}^{-1}$ ) was achieved by substituting one Ru-atom for Co. Interestingly, poor to no reactivity was observed for **128Rh** and **128Ir**, respectively.

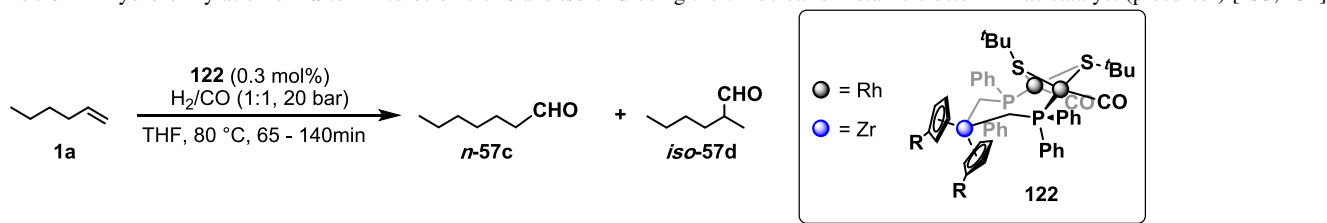
Analysis of the intermediate **128Coa** was indicative of an electron transfer from the Co center to the ligand forming monoanionic dmbpy<sup>−</sup> species, which was supported by spin-density DFT calculation demonstrating a negative value residing at the ligand, and positive values at the Co-center. As such, the Co is suggested to be in oxidation state 2+, adopting a  $d^7$  electron configuration. Evan's method was used to determine a  $\mu_{\text{eff}}$  (297.7 K) of  $2.5\mu_{\text{B}}$ , consistent with a triplet state of **128Coa**. For unsubstituted bipyridines, the lower LUMO energy level hampers the electron-transfer. Treatment of **128Coa** with pyridine demonstrated a facile ligand dissociation of dmbpy, Scheme 37. Prior to dissociation of dmbpy, electron transfer from the dmbpy<sup>−</sup> species to the  $\text{Co}^{2+}$  is required.

Using a 5 mol% catalyst loading in heptane at 140–180 °C for 3 days afforded up to 87% yield. To

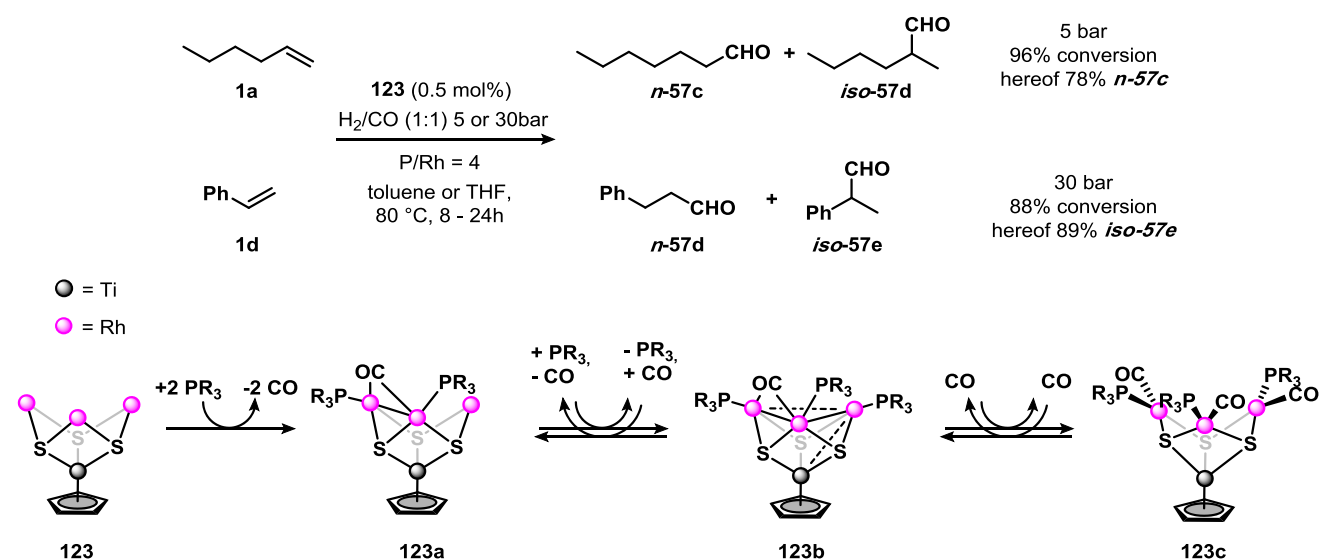
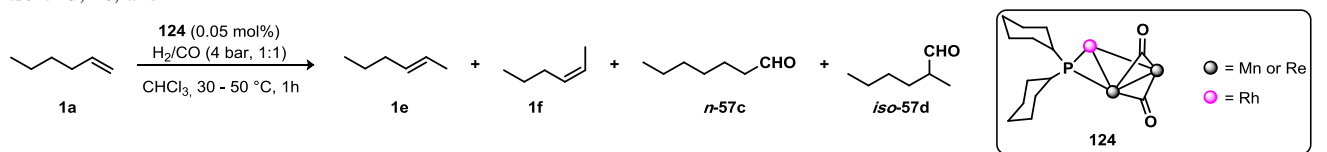
support cluster catalysis, the authors monitored the reaction by  $^1\text{H}$  NMR to analyze the reaction products. In addition, a key intermediate was structurally characterized using single-crystal X-ray diffraction, showing cobalt coordinated in a chelating-fashion by the bipyridine adduct. Moreover, **128Co** was completely converted at the end of the reaction, and loss of catalytic activity stem from fragmentation to mononuclear species, which the authors found to be catalytically inert.

Wong reported the pentanuclear bimetallic cluster  $\text{Os}_4\text{Au}(\mu\text{-H})_3(\text{CO})_{12}(\text{PPh}_3)_3$ , **129**, as catalyst towards oxidative carbonylation of aniline (**42a**) in methanol [161]. Catalytic formation of methyl phenylcarbamate **130** was effected using **129** with 93% conversion and an 82% selectivity, compared to approximately 40% selectivity demonstrated by the two tetraosmium clusters,  $\text{Os}_4(\mu\text{-H})_4(\text{CO})_{12}$  and  $[\text{N}(\text{PPh}_3)_2]\text{Os}_4(\mu\text{-H})_3(\text{CO})_{12}$ , Table 28. Moreover, the two latter clusters formed the byproducts *N*-methylaniline **42h** and formaniline **67b** not observed for **129**. Lowering the concentrations of substrate and cluster in MeOH resulted in an increase of conversion at the expense of the selectivity



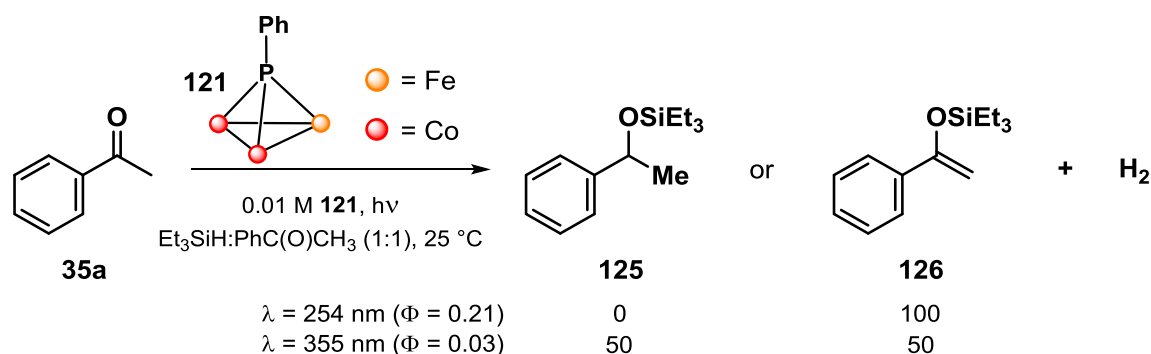
**Table 24** Hydroformylation of **1a** to mixtures of *n*-**57c** and *iso*-**57d** using the trinuclear bimetallic cluster **122** as catalyst (precursor) [153, 154]


R	Time (min)	Conversion (%)	Selectivity ( <i>n</i> / <i>iso</i> )
H	65	56	2.1
	115	96	2.0
<sup>t</sup> Bu	70	38	2.2
	140	97	1.8

**Scheme 35** Hydroformylation of **1a** to mixtures of *n*-**57c** and *iso*-**57d** as well as of **1d** to mixtures of *n*-**57d** and *iso*-**57e** using **123** as catalyst precursor. Terminal CO molecules have been omitted for clarity [156]**Table 25** Triangular mixed-metal  $\text{RhM}_2$ , M = Mn (**124Mn**) and Re (**124Re**) as catalysts for the hydroformylation of **1a** to mixtures of *n*-**57c**, *iso*-**57d**, **1e**, and **1f**


124	Temperature [°C]	<b>1f</b> TOF ( $\text{h}^{-1}$ )	<b>1e</b> TOF ( $\text{h}^{-1}$ )	<i>n</i> - <b>57c</b> TOF ( $\text{h}^{-1}$ )	<i>iso</i> - <b>57d</b> TOF ( $\text{h}^{-1}$ )
<b>124Re</b>	30	5	20	58	26
	50	79	162	190	56
<b>124Mn</b>	30	104	152	12	4
	50	187	286	43	12

Terminal CO molecules have been omitted for clarity [157]



**Scheme 36** Photoinitiated catalytic (dehydrogenative) silylation of **35a** leading to **125** or **126** using **121** as catalyst. Terminal CO molecules have been omitted for clarity [158]

towards **130**. The lack of byproducts formed by **129** lead the authors to suggest two different mechanisms for **129** relative to the tetraosmium clusters.

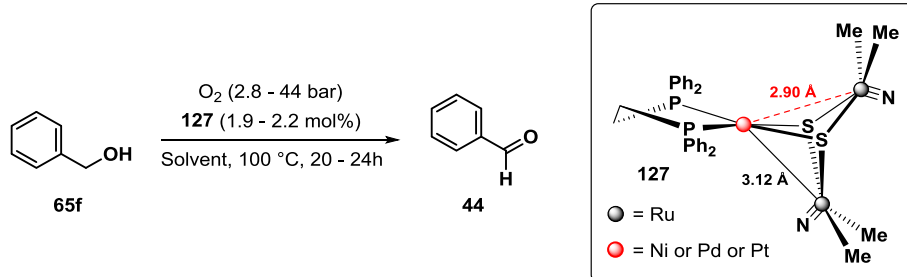
### Addition Reactions

Hidai has provided several accounts on the mixed-metal sulfide cubane-type cluster  $[\text{MMo}_3\text{S}_4]$  as catalyst precursors for various transformation of alkynes (**104**, **132**, **142**, **144**), olefins (**1d**, **157**), and hydrazines (**46**). For example,  $[\text{PdMo}_3\text{S}_4(\text{H}_2\text{O})_9\text{Cl}]\text{Cl}_3$  (**133**) and  $[\text{PdMo}_3\text{S}_4(\text{tacn})_3\text{Cl}]\text{Cl}_3$  (**134**), tacn = 1,4,7-triazacyclononane, cubane-type clusters were found to be highly regioselective towards *trans*-addition of alcohols to alkynoic acid esters **132** leading to **135**, Table 29 [162]. Cluster catalysis is suggested based on the combined observations that spectroscopic analyses indicate

a single organometallic species in the reaction mixture, and that neither of the parent compounds  $[\text{Mo}_3\text{S}_4(\text{H}_2\text{O})_9]\text{Cl}_4$  nor Pd-black provide sufficient catalytic activity.

Cluster **134** was reported to catalyze the stereoselective addition of alkyl and aryl substituted hydrogen carbonates **137** to electron-deficient alkynes, such as **136a**, Table 30 [163]. To support the suggestion of cluster catalysis, the reactivity of **134** was compared to that of **133**, as well as to those of other appropriate mononuclear Pd, Ru, and Rh complexes. Whereas **133** provided transformation at a much lower rate than **134** did, neither of the mononuclear complexes resulted in any detectable transformation, which satisfies Laine's second criterion on cluster-mediated catalysis. Additionally, spectroscopic analyses substantiate a single organometallic species in the reaction mixture. Moreover, **134** demonstrated a TON(18 h) of 2500. The

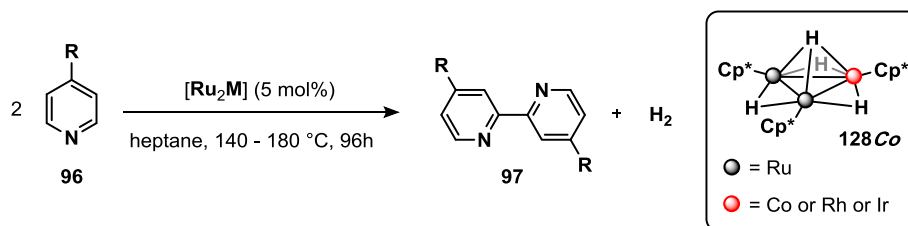
**Table 26** Catalytic dehydrogenation of **65f** leading to **44** employing hetero-trinuclear cluster **127** as catalyst



<b>127</b>	Solvent	Pressure O <sub>2</sub> (total pressure) (bar)	Time (h)	Conversion (%)	TON	TOF (h <sup>-1</sup> )
<b>127Ni</b>	Toluene	2.8 (2.8)	24	53	18.5	0.8
<b>127Pd</b>				32	3.63	0.2
<b>127Pt</b>				35	7.06	0.3
<b>127Ni</b>	scCO <sub>2</sub>	10 (120)	20	19	9.57	0.5
<b>127Pt</b>				11	5.97	0.3
<b>127Pt</b>		18.8 (120)	20	32	15.99	0.8
<b>127Pt</b>		44 (129)	20	22	10.70	0.5

scCO<sub>2</sub> denote supercritical CO<sub>2</sub> [19]



**Table 27** Catalytic dehydrogenation of **96** to **97** using **128Co** as catalyst [160]

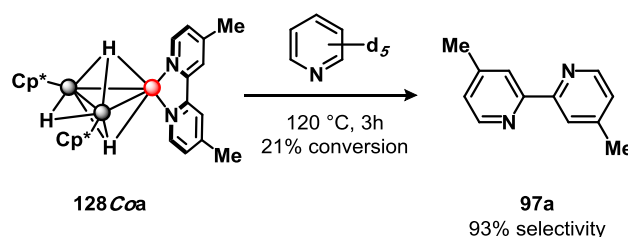
Ru <sub>2</sub> M	R	Temperature (°C)	Yield (%)
Ir	Me	180	Trace
Rh	Me	180	16
Co	Me	180	87
	<sup>t</sup> Bu	180	76
	NMe <sub>2</sub>	140	58
	OMe	140	Trace
	CO <sub>2</sub> Et	140	0
	CF <sub>3</sub>	180	0

role of the cubane-type cluster is twofold and is suggested to (i) activate the acetylenic species, and (ii) suppress side reactions. The mechanism suggested by the authors follow analogously to that in Table 29.

Regioselective addition of alcohols across triple bonds was catalyzed by the triangular mixed-metal sulfide cluster comprising Ir<sub>2</sub>M, M=Pd (**139Pd**), Pt (**139Pt**), Table 31 [164], where substituting Pd for Pt afforded a less selective cluster. Cluster catalysis is suggested based on the combination of recovered cluster, and lack of selectivity when employing lower nuclearity catalysts. A later study by Hidai provided further insights to the transformation, where it was shown that the electronic properties of the arene in **104** affected the selectivity, as electron donating groups in the *p*-position was found to decrease the regioselectivity [165]. The authors suggest a catalytic cycle that is initiated by ligand substitution at the palladium center of chloride for the alkyne **104**, resulting in **139a**. Addition of the first equivalent of alcohol and protonolysis results in a alkoxyvinyl cluster **139b**, which further undergoes addition of alcohol to form **140**.

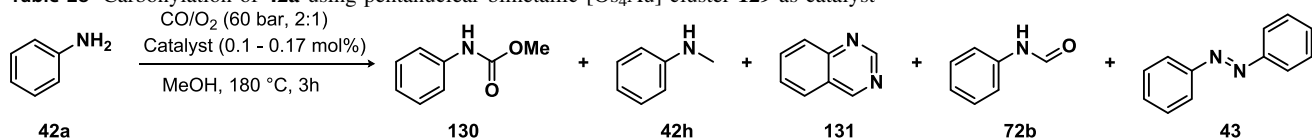
### Cycloaddition

In a later study, Hidai employed cluster **134** to demonstrate its applicability in the cyclization of various alkynoic acids **142a** to furanone type product **143a**, Scheme 38 [166]. Cluster catalysis is strongly implied based on kinetic studies revealing a first order rate-dependence with respect to the cluster, an approximately 20-fold rate enhancement relative to mononuclear Pd complex, PdCl<sub>2</sub>(PhCN)<sub>2</sub>, as

**Scheme 37** Release of dmbpy ligand from **128Coa** by substitution with pyridine [160]

well as spectroscopic measurement showing intact catalyst throughout the reaction. A TON(19 h) value of 100,000 was reported in the cyclization of the simplest compound, using a 0.001 mol% catalyst loading in MeCN at 40 °C (97% yield).

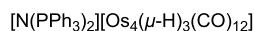
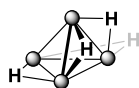
Continued efforts to provide insight into the catalytic activity of cubane-type clusters **134** were provided by Hidai in the cyclization of aminoalkynes **144** to **146**, Scheme 39 [167]. Changing the Pd-precursor to either Pd(dba)<sub>2</sub>, dba=bis(dibenzylideneacetone), or Pd(ma)(nbd), ma=maleic anhydride, and nbd=nobornadiene, resulted in corresponding cubane-type clusters [(Cp\*Mo)<sub>3</sub>PdS<sub>4</sub>(-dba)][PF<sub>6</sub>], **145a** and [(Cp\*Mo)<sub>3</sub>PdS<sub>4</sub>(ma)][PF<sub>6</sub>]**145b**, respectively. Both **145a** and **145b** showed a high catalytic activity in the intramolecular cyclization of **144**, affording up to 98% yield. These findings are in stark contrast with when employing PPh<sub>3</sub>, which afforded merely 6% yield. This observation was accounted for as to due to a difficult ligand-substrate substitution in the former systems. Insights on the mixtures was provided by UV–vis measurements

**Table 28** Carbonylation of **42a** using pentanuclear bimetallic [Os<sub>4</sub>Au] cluster **129** as catalyst

Catalysts

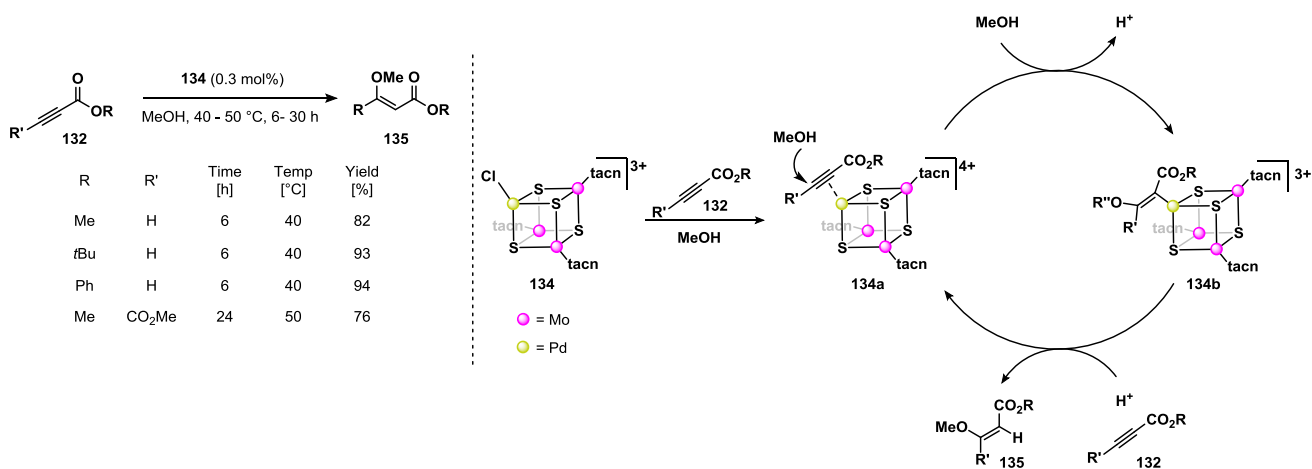
● = Os

● = Au

**129**

Cluster	Loading (mol%)	TOF (h <sup>-1</sup> )	MeOH (mL)	Conversion (%)	Selectivity (%)				
					130	42h	131	72b	43
<b>129</b>	0.13	248	3	93	82	—	10	—	—
	0.13	267	20	100	—	—	37	—	39
Os <sub>4</sub> (μ-H) <sub>4</sub> (CO) <sub>12</sub>	0.17	42	3	21	41	30	4	8	5
	0.17	126	20	63	—	12	—	—	28
[N(PPh <sub>3</sub> ) <sub>2</sub> ][Os <sub>4</sub> (μ-H) <sub>3</sub> (CO) <sub>12</sub> ]	0.10	33	3	10	43	37	8	7	5
	0.10	333	20	35	—	22	—	—	78

Terminal CO molecules have been omitted for clarity [161]

**Table 29** Proposed catalytic cycle for conversion of **132** to **135** using **134** as catalyst precursor [162]

substantiating an intact cluster entity. Using a 1 mol% catalyst loading of [(Cp\*Mo)<sub>3</sub>PdS<sub>4</sub>(dba)][PF<sub>6</sub>]**145a** in THF at 60 °C led to near quantitative yields.

Substituting Ni for Pd and tacn for Cp\* in **134** provided the COD-dimer of the cluster [(Cp\*Mo)<sub>3</sub>(μ<sub>3</sub>-S)<sub>4</sub>Ni]<sub>2</sub>(-μ,η<sup>2</sup>:η<sup>2</sup>-cod)[PF<sub>6</sub>]<sub>2</sub>, **147** [168]. A monomeric cluster was generated by treating **147** with dimethyl acetylenedicarboxylate, resulting in the singly alkyne-Ni coordinated cluster **148**, Scheme 40. The alkyne coordination to the Ni-

center is suggested to result from the π-accepting properties of the Mo<sub>3</sub>S<sub>4</sub>-framework, thus lowering the electron-density at the Ni center. While both **147** and **148** demonstrated catalytic activity, neither of the parent compounds, [(Cp\*Mo)<sub>3</sub>(μ<sub>2</sub>-S)<sub>3</sub>(μ<sub>3</sub>-S)][PF<sub>6</sub>] and Ni(COD)<sub>2</sub>, provided any activity in the cyclization. Based on the lack of catalytic activity of the parent compounds as well as prior observations, the authors propose the catalytic cycle by a single cluster shown in the Scheme 41.

**Table 30** Stereoselective catalytic addition of carboxylic acids to electron deficient alkynes [163]

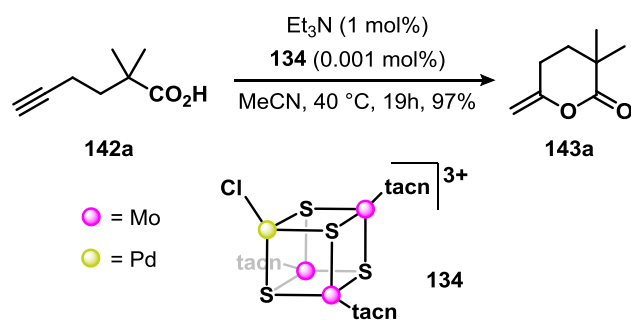
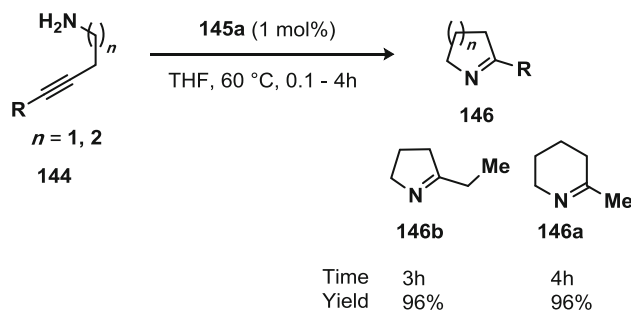
R'	Time (h)	Conversion (%)	Yield (%)	cis:trans
Me	8	90	62	98/2
Ph	5	92	76	98/2
<i>m</i> -ClC <sub>6</sub> H <sub>4</sub>	10	96	72	97/3

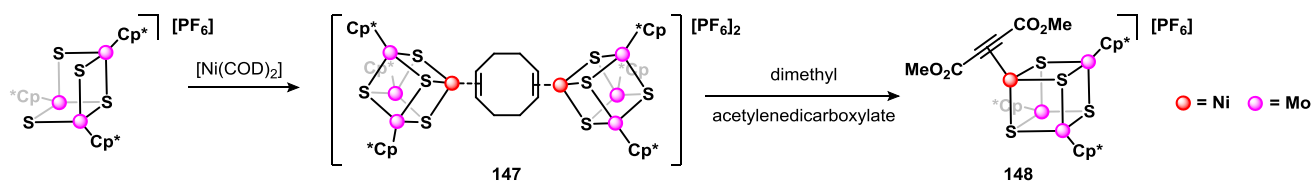
**Table 31** Regioselective alcohol addition to **104** leading to **140** or **141** using **139** as catalyst precursor [164, 165]

Yield	89%	50%	95%	59%
Distribution	97:3	13:87	97:3	66:34
	139Pd (2 mol%)			

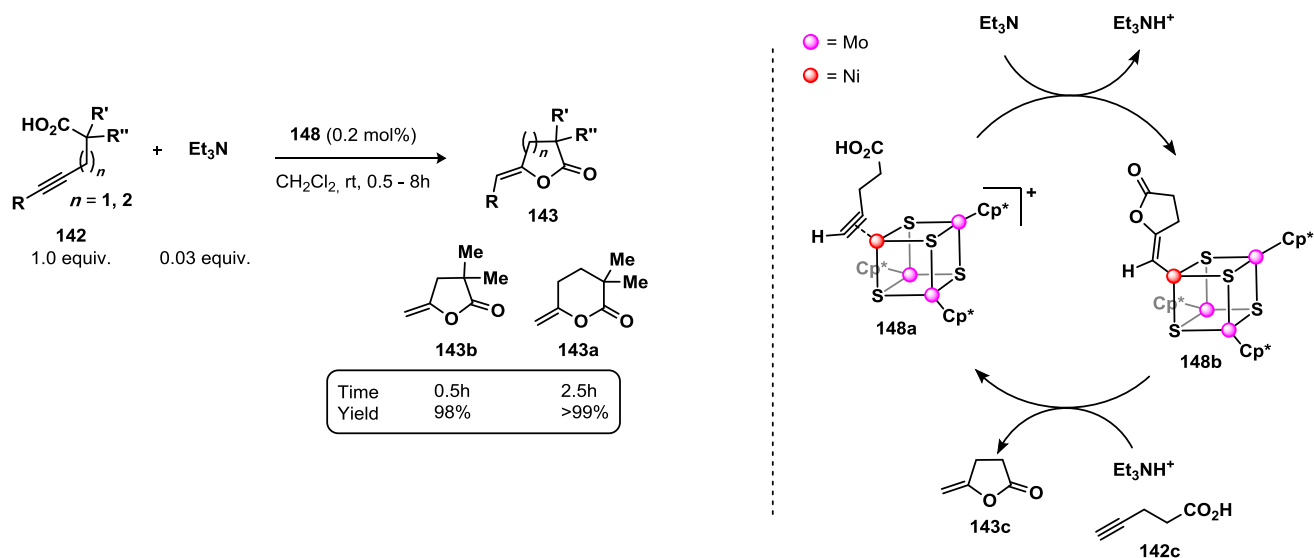
Llusar and Pérez-Prieto reported asymmetric induction in the catalytic intra- and intermolecular cyclopropanation of olefins, such as **149** and **1d**, with  $\alpha$ -diazoketo units leading to **150** and **152**, respectively, by using catalytic amounts of stereo-enriched mixed-metal cubane-type CuMo<sub>3</sub>S<sub>4</sub>-clusters, **153–156**, Table 32 [169]. Optically pure trinuclear frameworks were prepared stereoselectively via cluster excision of the polymeric unit, {Mo<sub>3</sub>S<sub>7</sub>Cl<sub>4</sub>}<sub>n</sub>, using the chiral chelating phosphine ligand, (*R/S*, *R/S*)-Me-BPE. The resulting cluster chirality was preserved as Cu was introduced to the framework. Single-crystal X-ray diffraction in combination with circular dichroism was used to establish two enantiopure compounds. Preliminary studies of the intramolecular cyclopropanation reaction showed that the parent Mo<sub>3</sub>S<sub>4</sub>-framework **15** was catalytically inactive. Furthermore, spectroscopic analysis confirmed the racemic cubane-cluster, **156**, stayed intact throughout the reaction. Based on the preliminary results of the racemic cluster, the chiral cluster **153** was employed under the same reaction conditions, affording a low enantiomeric excess of merely 25% *ee*.

Additionally, clusters **153–156** were employed in an intermolecular cyclopropanation, resulting in *E/Z* ratio of up to 2.6 and with low enantioselectivity. The low

**Scheme 38** Cyclization of **142a** to **143a** using **134** as catalyst precursor [166]**Scheme 39** Catalytic intramolecular aminoalkyne cycloaddition of **144** leading to **146** using **145a** as catalyst precursor [167]



**Scheme 40** Preparation of [NiMo<sub>3</sub>S<sub>4</sub>]-cubane type clusters **147** and **148** [168]



**Scheme 41** Left: Intramolecular cyclization of **142** leading to **143** using **148** as catalyst precursor. Right: Catalytic cycle for the cyclization of **142** to **143** using **148** as catalyst, as proposed by Hidai [168]

**Table 32** Chiral induction using enantiopure CuMo<sub>3</sub>S<sub>4</sub>-clusters **153** and **156** as catalyst precursors for the cyclopropanation of **149** [169], as well as the intermolecular cyclopropanation of **1d** [170]

149

Cluster (1 mol%)

CH<sub>2</sub>Cl<sub>2</sub>, reflux, 24h

150

Cluster	Yield [%]	ee [%]
156	95	-
153	84	25
[Mo <sub>3</sub> S <sub>4</sub> ]	-	-

● = Mo

● = Cu

1d

151

Cluster (1 mol%)

CH<sub>2</sub>Cl<sub>2</sub>, reflux, 4 - 12h

84

Ph

CO<sub>2</sub>Et

Z-152

Ph

CO<sub>2</sub>Et

E-152

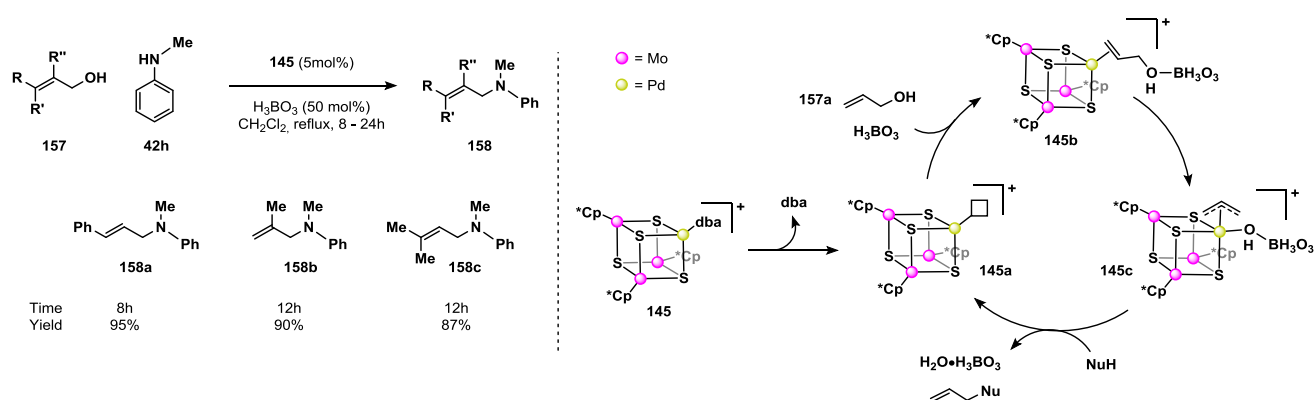
Cluster	Time [h]	Yield [%]	E/Z	Z-152 ee [%]	E-152 ee [%]
156	80	80	2.4	-	-
		88	2.6	21	20
153	5	77	2.3		
154	5	41	2.6		
155	12	70	2.6		

E = S, X = Cl (156)

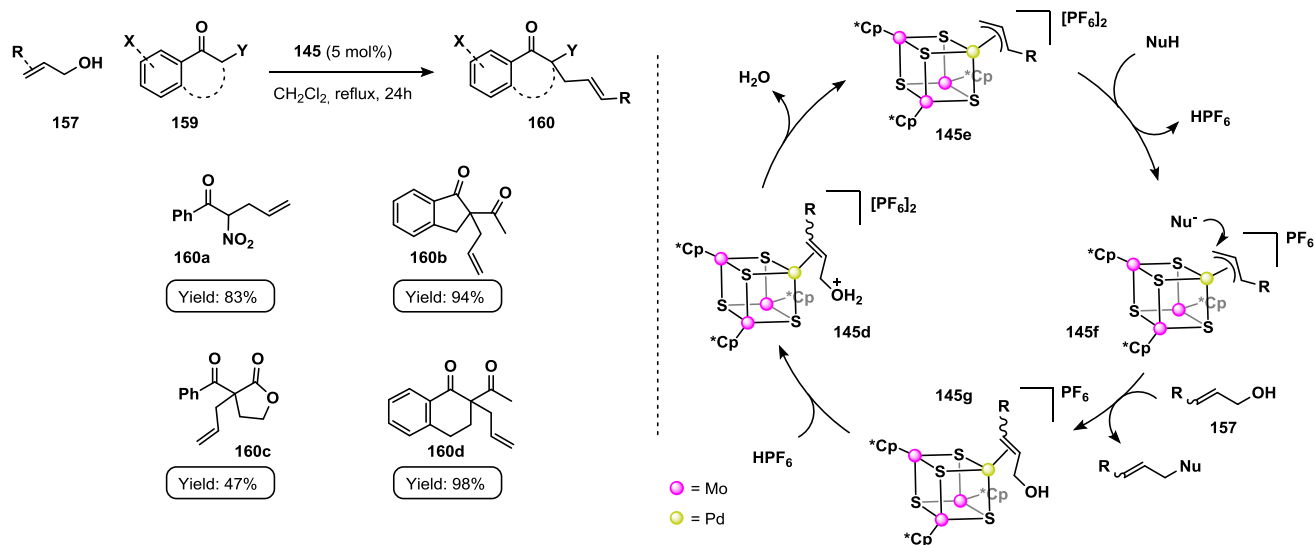
E = S, X = Cl (153)

E = S, X = Br (154)

E = Se, X = Cl (155)



**Scheme 42** Left: Allylation of **42 h** leading to **158** using **145** as catalyst precursor. Right: Catalytic cycle for allylation of various nucleophiles as proposed by Qu [171]

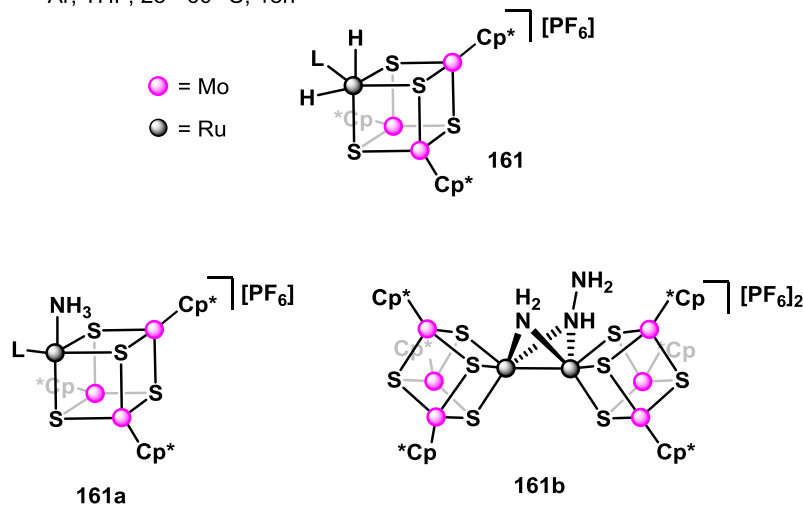
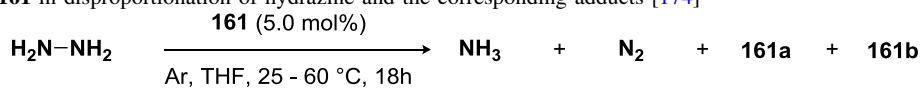


**Scheme 43** Left: allylation of **159** to **160** using **145** as catalyst precursor. Right: Catalytic cycle in allylation of amines and Friedel–Crafts-type reaction as proposed by Qu [172, 173]

selectivity is suggested to relate to the addition of alkenes to the Cu-carbene species, which is insufficiently sterically encumbered. As such, the authors suggest that an increase of steric bulk at the coordination-sphere of the Cu-center likely will be beneficial for the stereoselectivity. Pérez-Prieto proposed the involvement of the cluster **153** to occur by either of two mechanisms, namely (i) halide dissociation [at the Cu-center], or by (ii) Cu–S/Se bond cleavage [170]. To this end, analogues were prepared; substituting Cl with Br, and S for Se. Whereas the enantiomeric ratios were effectively identical for the chloride- and bromide cluster, the rate was decreased by substitution of S for Se, Table 32, indicating that the latter mechanism is more likely.

## Allylation

Cluster **145** was further used to afford regioselective allylation of amines, such as **42 h**, leading to **158**, Scheme 42 [171]. Using 50 mol%  $\text{H}_3\text{BO}_3$  as additive, near quantitative yields were reported within 4 h with 5 mol% catalyst loading. As in the aforementioned study, the ligation was found to affect the catalytic activity, and only dba afforded a catalytically active cluster. Of the mononuclear compounds, only  $\text{Pd}(\text{PPh}_3)_4$  was able to provide any transformation albeit at lower yield (70 vs. 96%). The authors concluded that the  $\text{Mo}_3\text{S}_4$ -framework act as a sterically encumbered ligand, thus suppressing formation of branched product. A tentative mechanism was

**Table 33** [RuMo<sub>3</sub>S<sub>4</sub>] **161** in disproportionation of hydrazine and the corresponding adducts [174]

L	Temperature (°C)	TON	Equiv. of			
			NH <sub>3</sub>	N <sub>2</sub>	<b>161a</b>	<b>161b</b>
PPh <sub>3</sub>	25	3.4	3.1	0.9	0.56	0.07
PCy <sub>3</sub>		3.6	4.0	1.2	–	0.19
PPh <sub>3</sub>	60	5.9	6.6	1.6	0.38	0.15
PCy <sub>3</sub>		15.2	20	4.7	–	0.23

provided by the authors, initiated by ligand substitution going from **145** to **145b**. The allylic hydroxyl group in turn coordinates to the boric acid. Subsequent nucleophilic attack to the  $\pi$ -allyl intermediate **145c** regenerates **145a** concurrently with product formation. The authors suggest the [(Cp\*Mo)<sub>3</sub>S<sub>4</sub>] unit may be regarded in terms of an extended ligand.

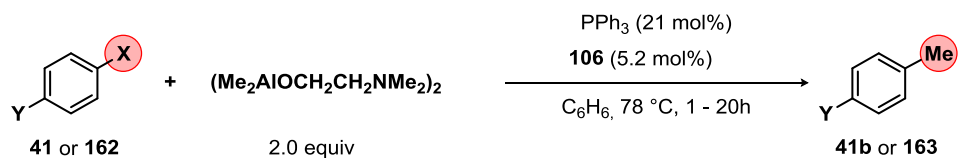
Continued studies of **145** was done by Qu, who reported an extended substrate scope for the allylation reaction, to include additional amines as well as active methylene compounds **159**, such as 2-nitro-acetophenone, leading to **160** (Scheme 43, left) [172]. High yields up to 98% were obtained using a 5 mol% catalyst loading. In a later study, they demonstrated that the same cluster is an efficient catalyst precursor for the Friedel–Crafts-type allylation of both anilines and indoles with allylic alcohols, Scheme 43, right [173]. In both studies, the lack of catalytic activity of related lower nuclearity species, combined with previous findings by Hidai, led the authors to propose cluster catalysis as shown in the scheme. Nucleophilic attack to **145e** is directed by the [(Cp\*Mo)<sub>3</sub>S<sub>4</sub>] unit that acts an extended ligand **145f**, rather than the hindered allylic carbon, resulting. Subsequent ligand substitution with **157** forms **145g** that undergoes protonation of the allylic alcohol moiety (**145d**).

### Disproportionation

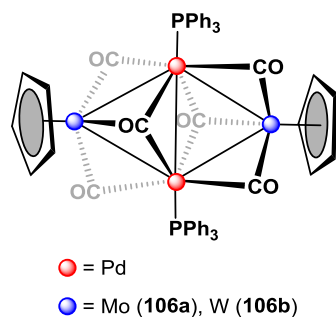
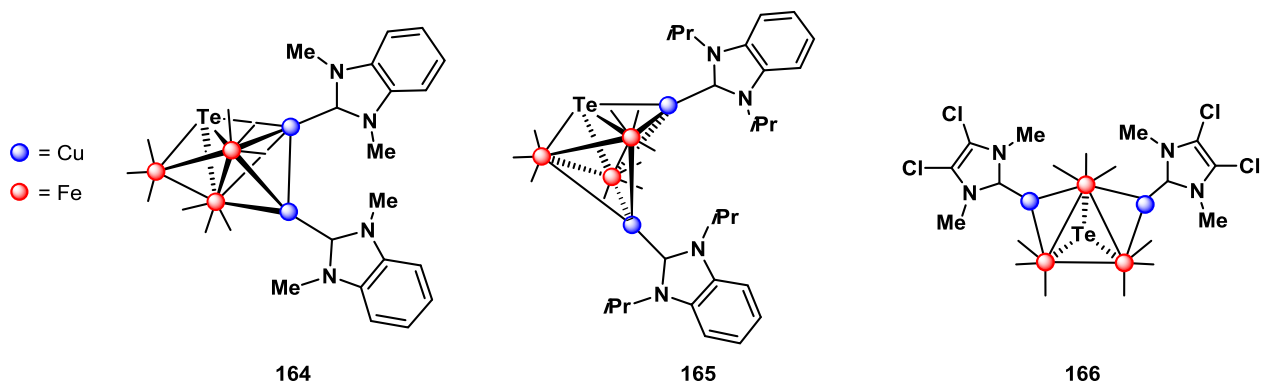
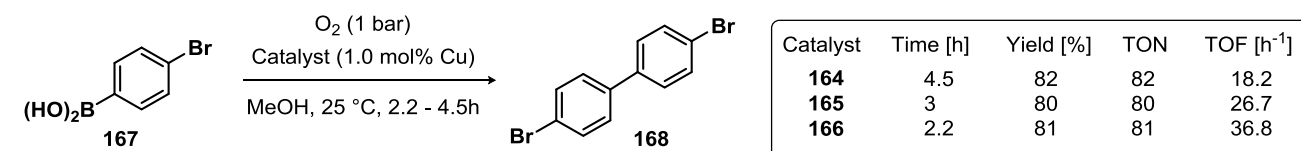
Hidai reported the cubane-cluster **161** containing Ru as an efficient catalyst for cleaving of N–N bonds in hydrazines [174]. Thus, catalytic disproportionation of hydrazine occurs from treatment with **161**, Table 33. In addition to the disproportionation products (NH<sub>3</sub> and N<sub>2</sub>), an ammonia ligated cluster, **161a**, along with a di-cubane cluster **161b** bridged by both an amido and hydrazido ligand,  $\mu$ -NH<sub>2</sub> and  $\mu$ -NHNH<sub>2</sub>, were observed. Substitution of PPh<sub>3</sub> with PCy<sub>3</sub> resulted in a catalytically more active cluster in the disproportionation reaction whilst suppressing the formation of **161a**. The authors conclude a low reactivity of the clusters compared to a mononuclear molybdenum [175], and a dinuclear ruthenium thiolate-complex [176].

### Cross-Alkylation

Blum reported the triangulated mixed-metal clusters **106a** and **106b** as an efficient catalyst precursors for the cross-alkylation of (pseudo)-halide arenes by group thirteen-stabilized alkylation agents, Table 34 [177]. The authors provide evidence in support of cluster catalysis. Thus, the use of either catalyst precursor **106a** or **106b**, exclusively afford methylation products, whereas mononuclear Pd-

**Table 34** Methylation of aryls using either **106a** or **106b** [177]

Substrate	Catalyst	Time [h]	Yield [%]
<b>41g</b>	<b>106a</b>	20	99
	<b>106b</b>	20	99
<b>41h</b>	<b>106a</b>	1	25
	<b>106b</b>	1	11
<b>162a</b>	<b>106a</b>	2	100
	<b>106b</b>	2	65
<b>162b</b>	<b>106a</b>	1	89
	<b>106b</b>	1	63

**Table 35** Mixed-metal clusters **164–166** stabilized by Te in Suzuki homocross-coupling of **167** leading to **168** [178]

Terminal CO molecules have been omitted for clarity



compounds promote both homocoupling and hydrogenolysis. Moreover, the authors note that whereas conventional Pd-catalysts do not activate chloroarenes, both clusters demonstrated 99% yields when using **41g** as substrate. The authors further suggest that side-reactions are suppressed based on a synergistic interaction between Pd and Mo or W.

### Aryl Homocoupling

Shieh investigated three *N*-heterocyclic (NHC) functionalized mixed-metal pentanuclear clusters **164–166**, which provided catalytic activity under Suzuki conditions for the homocoupling of *p*-bromoboronic acid **167** to biphenyl product **168** [178]. Comparing the reactivity the three clusters **164**, **165**, and **166**, the authors conclude that the steric encumbering at the Cu center affords a greater activity in **166** (18.2 h<sup>-1</sup> in **164** vs. 36.8 h<sup>-1</sup> **166**), Table 35. Furthermore, based on DFT and spectroscopical data (<sup>13</sup>C NMR), the authors suggest a facile oxidation of Cu(I), with the NHC groups stabilizing a Cu(III) intermediate during the catalytic cycle.

### Conclusion

During the past decades, the homogeneous catalytic research community has witnessed an impressive development within the use of polynuclear clusters as catalysts for a plethora of organic transformations. Interestingly, it has been demonstrated on numerous occasions that these clusters bear the potential to provide unique product selectivities, and thus represent a highly exciting rising methodology.

In this review, we have presented multiple examples of successes in homogeneous cluster catalysis. We have shown how the use of either homonuclear or heteronuclear clusters, respectively, may provide increased catalyst activity as well as different chemo-, regio-, and stereoselectivities than those seen with traditional mononuclear organometallic catalysts. Furthermore, several accounts shed light on the effect on catalysis when substituting among the members of a transitional metal triad of a single metal center in a heteronuclear cluster. Finally, throughout the review we have presented the Laine criteria for cluster catalysis and highlighted how the structures of the true catalysts have been addressed by use of a multitude of analytical tools. These investigations have led to several mechanistic proposals, which have been discussed here as well.

Many of the examples shown in this review demonstrate a fundamental challenge relating to cluster catalysis, namely the lack of framework stability, resulting from

fluxional ligands, such as carbonyls and hydrides, often leading to cluster fragmentation. On the other hand, considerable evidence already supports that polynucleating ligands provide the necessary rigidity to retain cluster integrity while accommodating the essential geometric rearrangements during catalysis.

Cluster catalyzed reactions have the potential to open new avenues in chemical transformations stemming from the synergistic interaction between several vicinal metal centers, and their ability to mediate multiple electron transfers. Despite a wide range of cluster structures found in literature, their provision has largely relied on (serendipitous) self-assembly of appropriate metal and strong-field ligand combinations. Moreover, the majority of catalytic transformations are dictated by the parent cluster structure, thus limiting the scope. Consequently, the development of cluster catalyst that are structurally dictated by their polynucleating ligands are of high interest.

**Funding** This study was supported by Det Frie Forskningsråd, Natur og Univers (Grant Number 8102-00004B).

### References

1. D. F. Shriver and M. J. Sailor (1988). *Acc. Chem. Res.* **21**, 374–379.
2. R. Giordano, E. Sappa, and S. A. R. Knox (1996). *J. Clust. Sci.* **7**, 179–190.
3. E. Sappa, A. Tiripicchio, and P. Braunstein (1983). *Chem. Rev.* **83**, 203–239.
4. J. B. Keister and J. R. Shapley (1975). *J. Organomet. Chem.* **85**, C29–C31.
5. E. L. Muetterties and J. Stein (1979). *Chem. Rev.* **79**, 479–490.
6. H. Nagashima, T. Fukahori, K. Aoki, and K. Itoh (1993). *J. Am. Chem. Soc.* **115**, 10430–10431.
7. H. Nagashima, A. Suzuki, M. Nobata, and K. Itoh (1996). *J. Am. Chem. Soc.* **118**, 687–688.
8. C. S. Yi, T. N. Zeczycki, and S. V. Lindeman (2008). *Organometallics* **27**, 2030–2035.
9. P. Buchwalter, J. Rosé, and P. Braunstein (2015). *Chem. Rev.* **115**, 28–126.
10. I. G. Powers and C. Uyeda (2017). *ACS Catal.* **7**, 936–958.
11. F. A. Cotton (1964). *Inorg. Chem.* **3**, 1217–1220.
12. F. A. Cotton (1966). *Q. Rev. Chem. Soc.* **20**, 389.
13. E. R. Rosenberg, M. Laine. in *Catalysis by di- and polynuclear metal cluster complexes*. R. D. Adams and F. A. Cotton (eds.), (Wiley-VCH, Weinheim, 1998), p. 4.
14. R. D. Adams, B. Captain, and L. Zhu (2004). *J. Am. Chem. Soc.* **126**, 3042–3043.
15. S. Sculfort and P. Braunstein (2011). *Chem. Soc. Rev.* **40**, 2741–2760.
16. T. G. Gray (2003). *Coord. Chem. Rev.* **243**, 213–235.
17. R. A. Walton (2004). *J. Clust. Sci.* **15**, 559–588.
18. E. L. Muetterties and M. J. Krause (1983). *Angew. Chem. Int. Ed.* **22**, 135–148.
19. J. L. Kuiper, P. A. Shapley, and C. M. Rayner (2004). *Organometallics* **23**, 3814–3818.
20. R. M. Laine (1982). *J. Mol. Catal.* **14**, 137–169.



21. D. R. Anton and R. H. Crabtree (1983). *Organometallics* **2**, 855–859.
22. C. M. Hagen, L. Vieille-Petit, G. Laurenczy, G. Süß-Fink, and R. G. Finke (2005). *Organometallics* **24**, 1819–1831.
23. P. M. Lausarot, G. A. Vaglio, and M. Valle (1982). *J. Organomet. Chem.* **240**, 441–445.
24. P. M. Lausarot, G. A. Vaglio, and M. Valle (1984). *J. Organomet. Chem.* **275**, 233–237.
25. F. C. C. Moura, R. M. Lago, E. N. dos Santos, and M. Helena Araujo (2002). *Catal. Commun.* **3**, 541–545.
26. T. Joh, K. Doyama, K. Onitsuka, T. Shiohara, and S. Takahashi (1991). *Organometallics* **10**, 2493–2498.
27. L. Alvila, T. A. Pakkanen, T. T. Pakkanen, and O. Krause (1992). *J. Mol. Catal.* **73**, 325–334.
28. N. Chatani, A. Kamitani, M. Oshita, Y. Fukumoto, and S. Murai (2001). *J. Am. Chem. Soc.* **123**, 12686–12687.
29. S. Inoue, K. Yokota, H. Tatamidani, Y. Fukumoto, and N. Chatani (2006). *Org. Lett.* **8**, 2519–2522.
30. K. M. Driller, H. Klein, R. Jackstell, and M. Beller (2009). *Angew. Chem. Int. Ed.* **48**, 6041–6044.
31. T. Morimoto, N. Chatani, Y. Fukumoto, and S. Murai (1997). *J. Org. Chem.* **62**, 3762–3765.
32. T. Kondo, N. Suzuki, T. Okada, and T. Mitsudo (1997). *J. Am. Chem. Soc.* **119**, 6187–6188.
33. T. Kondo, A. Nakamura, T. Okada, N. Suzuki, K. Wada, and T. Mitsudo (2000). *J. Am. Chem. Soc.* **122**, 6319–6320.
34. T. Kondo, Y. Kaneko, Y. Taguchi, A. Nakamura, T. Okada, M. Shiotsuki, Y. Ura, K. Wada, and T. Mitsudo (2002). *J. Am. Chem. Soc.* **124**, 6824–6825.
35. H. Yamazaki and P. Hong (1983). *J. Mol. Catal.* **21**, 133–150.
36. N. Chatani, Y. Ie, F. Kakiuchi, and S. Murai (1997). *J. Org. Chem.* **62**, 2604–2610.
37. Y. Ishii, N. Chatani, F. Kakiuchi, and S. Murai (1997). *Organometallics* **16**, 3615–3622.
38. N. Chatani, T. Asaumi, S. Yorimitsu, T. Ikeda, F. Kakiuchi, and S. Murai (2001). *J. Am. Chem. Soc.* **123**, 10935–10941.
39. R. Koelliker and G. Bor (1991). *J. Organomet. Chem.* **417**, 439–451.
40. F. Ragaini, A. Ghitti, and S. Cenini (1999). *Organometallics* **18**, 4925–4933.
41. S. H. Han, G. L. Geoffroy, B. D. Dombek, and A. L. Rheingold (1988). *Inorg. Chem.* **27**, 4355–4361.
42. R. A. Sanchez-Delgado, J. S. Bradley, and G. Wilkinson (1976). *J. Chem. Soc. Dalton. Trans.* <https://doi.org/10.1039/DT9760000399>.
43. D. Blazina, S. B. Duckett, P. J. Dyson, and J. A. B. Lohman (2001). *Angew. Chem. Int. Ed.* **40**, 3874–3877.
44. D. Blazina, S. B. Duckett, P. J. Dyson, and J. A. B. Lohman (2003). *Chem. Eur. J.* **9**, 1045–1061.
45. B. Y. Park, T. P. Montgomery, V. J. Garza, and M. J. Krische (2013). *J. Am. Chem. Soc.* **135**, 16320–16323.
46. N. Hasegawa, V. Charra, S. Inoue, Y. Fukumoto, and N. Chatani (2011). *J. Am. Chem. Soc.* **133**, 8070–8073.
47. K. Shibata, N. Hasegawa, Y. Fukumoto, and N. Chatani (2012). *ChemCatChem* **4**, 1733–1736.
48. N. Hasegawa, K. Shibata, V. Charra, S. Inoue, Y. Fukumoto, and N. Chatani (2013). *Tetrahedron* **69**, 4466–4472.
49. I. Fleischer, L. Wu, I. Profir, R. Jackstell, R. Franke, and M. Beller (2013). *Chem. Eur. J.* **19**, 10589–10594.
50. I. Fleischer, K. M. Dyballa, R. Jennerjahn, R. Jackstell, R. Franke, A. Spannenberg, and M. Beller (2013). *Angew. Chem. Int. Ed.* **52**, 2949–2953.
51. J. Liu, C. Kubis, R. Franke, R. Jackstell, and M. Beller (2016). *ACS Catal.* **6**, 907–912.
52. C. Rameshkumar and M. Periasamy (2000). *Tetrahedron Lett.* **41**, 2719–2722.
53. M. Periasamy, A. Mukkanti, and D. S. Raj (2004). *Organometallics* **23**, 619–621.
54. M. Periasamy, A. Mukkanti, and D. S. Raj (2004). *Organometallics* **23**, 6323–6326.
55. P. Chini and S. Martinengo (1969). *Inorg. Chim. Acta* **3**, 315–318.
56. S. Martinengo, A. Fumagalli, P. Chini, V. G. Albano, and G. Clani (1976). *J. Organomet. Chem.* **116**, 333–342.
57. S. Martinengo, A. Fumagalli, and P. Chini (1985). *J. Organomet. Chem.* **284**, 275–279.
58. I. Matsuda, Y. Fukuta, T. Tsuchihashi, H. Nagashima, and K. Itoh (1997). *Organometallics* **16**, 4327–4345.
59. Longoni G, Campanella S, Ceriotti A, Chini P, Albano VG, Braga D (1980). *J. Chem. Soc. Dalton Trans.* pp. 1816–1819.
60. T. Kondo, M. Akazome, Y. Tsuji, and Y. Watanabe (1990). *J. Org. Chem.* **55**, 1286–1291.
61. E. J. Moore, W. R. Pretzer, T. J. O’Connell, J. Harris, L. LaBounty, L. Chou, and S. S. Grimmer (1992). *J. Am. Chem. Soc.* **114**, 5888–5890.
62. N. Chatani, T. Fukuyama, F. Kakiuchi, and S. Murai (1996). *J. Am. Chem. Soc.* **118**, 493–494.
63. R. Agarwala, K. A. Azam, R. Dilshad, S. E. Kabir, R. Miah, M. Shahiduzzaman, K. I. Hardcastle, E. Rosenberg, M. B. Hursthouse, and K. M. Abdul Malik (1995). *J. Organomet. Chem.* **492**, 135–144.
64. M. I. Bruce, B. L. Goodall, F. Gordon, and A. Stone (1973). *J. Organomet. Chem.* **60**, 343–349.
65. N. Chatani, T. Morimoto, Y. Fukumoto, and S. Murai (1998). *J. Am. Chem. Soc.* **120**, 5335–5336.
66. N. Chatani, Y. Ishii, Y. Ie, F. Kakiuchi, and S. Murai (1998). *J. Org. Chem.* **63**, 5129–5136.
67. K. Burgess, H. D. Holden, B. F. G. Johnson, J. Lewis, M. B. Hursthouse, N. P. C. Walker, A. J. Deeming, P. J. Manning, and R. Peters (1985). *J. Chem. Soc. Dalton. Trans.* <https://doi.org/10.1039/DT9850000085>.
68. N. Chatani, T. Fukuyama, H. Tatamidani, F. Kakiuchi, and S. Murai (2000). *J. Org. Chem.* **65**, 4039–4047.
69. T. Fukuyama, N. Chatani, J. Tatsumi, F. Kakiuchi, and S. Murai (1998). *J. Am. Chem. Soc.* **120**, 11522–11523.
70. S. Inoue, H. Shiota, Y. Fukumoto, and N. Chatani (2009). *J. Am. Chem. Soc.* **131**, 6898–6899.
71. F. Kakiuchi, T. Sato, T. Tsujimoto, M. Yamauchi, N. Chatani, and S. Murai (1998). *Chem. Lett.* **27**, 1053–1054.
72. J. A. Cabeza, J. M. Fernandez-Colinas, A. Llamazares, V. Riera, S. Garcia-Granda, and J. F. Van der Maelen (1994). *Organometallics* **13**, 4352–4359.
73. J. A. Cabeza, I. del Rio, J. M. Fernández-Colinas, A. Llamazares, and V. Riera (1995). *J. Organomet. Chem.* **494**, 169–177.
74. J. A. Cabeza, I. del Río, J. M. Fernández-Colinas, and V. Riera (1996). *Organometallics* **15**, 449–451.
75. M. Castiglioni, R. Giordano, and E. Sappa (1991). *J. Organomet. Chem.* **407**, 377–389.
76. A. G. Algarra, E. Guillellamón, J. Andrés, M. J. Fernández-Trujillo, E. Pedrajas, J. Á. Pino-Chamorro, R. Llusar, and M. G. Basallote (2018). *ACS Catal.* **8**, 7346–7350.
77. C. Bergounhou, P. Fompeyrine, G. Commenges, and J. J. Bonnet (1988). *J. Mol. Catal.* **48**, 285–312.
78. H.-J. Haupt, R. Wittbecker, and U. Flörke (1996). *J. Organomet. Chem.* **518**, 213–219.
79. T. N. Gieshoff, U. Chakraborty, M. Villa, and A. Jacobi von Wangelin (2017). *Angew. Chem. Int. Ed.* **56**, 3585–3589.
80. U. Chakraborty, E. Reyes-Rodriguez, S. Demeshko, F. Meyer, and A. Jacobi von Wangelin (2018). *Angew. Chem. Int. Ed.* **57**, 4970–4975.

81. U. Matteoli, V. Beghetto, and A. Scrivanti (1996). *J. Mol. Catal. A. Chem.* **109**, 45–50.
82. P. Homanen, R. Persson, M. Haukka, T. A. Pakkanen, and E. Nordlander (2000). *Organometallics* **19**, 5568–5574.
83. V. Moberg, P. Homanen, S. Selva, R. Persson, M. Haukka, T. A. Pakkanen, M. Monari, and E. Nordlander (2006). *Dalton Trans.* <https://doi.org/10.1039/B515273A>.
84. V. Moberg, M. Haukka, I. O. Koshevoy, R. Ortiz, and E. Nordlander (2007). *Organometallics* **26**, 4090–4093.
85. V. Moberg, R. Duquesne, S. Contaldi, O. Röhrs, J. Nachtigall, L. Damoense, A. T. Hutton, M. Green, M. Monari, D. Santelia, M. Haukka, and E. Nordlander (2012). *Chem. Eur. J.* **18**, 12458–12478.
86. A. F. Abdel-Magied, M. S. Patil, A. K. Singh, M. Haukka, M. Monari, and E. Nordlander (2015). *J. Clust. Sci.* **26**, 1231–1252.
87. A. F. Abdel-Magied, A. K. Singh, M. Haukka, M. G. Richmond, and E. Nordlander (2014). *Chem. Commun.* **50**, 7705–7708.
88. A. F. Abdel-Magied, M. H. Majeed, M. F. Abelairas-Edesa, A. Ficks, R. M. Ashour, A. Rahaman, W. Clegg, M. Haukka, L. J. Higham, and E. Nordlander (2017). *J. Organomet. Chem.* **849–850**, 71–79.
89. H. Zhang, C.-B. Yang, Y.-Y. Li, Z.-R. Donga, J.-X. Gao, H. Nakamura, K. Murata, and T. Ikariya (2003). *Chem. Commun.* <https://doi.org/10.1039/B209974H>.
90. J. A. Cabeza, I. da Silva, I. del Río, R. A. Gossage, D. Miguel, and M. Suárez (2006). *Dalton Trans.* <https://doi.org/10.1039/B517758H>.
91. I. Sorribes, G. Wienhöfer, C. Vicent, K. Junge, R. Llusar, and M. Beller (2012). *Angew. Chem. Int. Ed.* **51**, 7794–7798.
92. E. Pedrajas, I. Sorribes, K. Junge, M. Beller, and R. Llusar (2015). *ChemCatChem* **7**, 2675–2681.
93. E. Pedrajas, I. Sorribes, A. L. Gushchin, Y. A. Laricheva, K. Junge, M. Beller, and R. Llusar (2017). *ChemCatChem* **9**, 1128–1134.
94. E. Pedrajas, I. Sorribes, K. Junge, M. Beller, and R. Llusar (2017). *Green Chem.* **19**, 3764–3768.
95. Y. Nakajima and H. Suzuki (2005). *Organometallics* **24**, 1860–1866.
96. T. Takao, S. Horikoshi, T. Kawashima, S. Asano, Y. Takahashi, A. Sawano, and H. Suzuki (2018). *Organometallics* **37**, 1598–1614.
97. C. Federsel, A. Boddien, R. Jackstell, R. Jennerjahn, P. J. Dyson, R. Scopelliti, G. Laurency, and M. Beller (2010). *Angew. Chem. Int. Ed.* **49**, 9777–9780.
98. C. Federsel, C. Ziebart, R. Jackstell, W. Baumann, and M. Beller (2012). *Chem. Eur. J.* **18**, 72–75.
99. S. Wesselbaum, T. vom Stein, J. Klankermayer, and W. Leitner (2012). *Angew. Chem. Int. Ed.* **51**, 7499–7502.
100. J. F. Hull, Y. Himeda, W.-H. Wang, B. Hashiguchi, R. Periana, D. J. Szalda, J. T. Muckerman, and E. Fujita (2012). *Nat. Chem.* **4**, 383.
101. S. Shitaya, K. Nomura, and A. Inagaki (2019). *Chem. Commun.* **55**, 5087–5090.
102. I. Y. Guzman-Jimenez, J. W. Van Hal, and K. H. Whitmire (2003). *Organometallics* **22**, 1914–1922.
103. R. E. Bachman and K. H. Whitmire (1994). *Inorg. Chem.* **33**, 2527–2533.
104. N. Suzuki, T. Kondo, and T. Mitsudo (1998). *Organometallics* **17**, 766–769.
105. G. Süß-Fink and G. Herrmann (1985). *J. Chem. Soc. Chem. Commun.* <https://doi.org/10.1039/C39850000735>.
106. G. Süß-Fink and G. F. Schmidt (1987). *J. Mol. Catal.* **42**, 361–366.
107. E. L. Diz, A. Neels, H. Stoeckli-Evans, and G. Süß-Fink (2001). *Polyhedron* **20**, 2771–2780.
108. R. C. Ryan, C. U. Pittman, and J. P. O'Connor (1977). *J. Am. Chem. Soc.* **99**, 1986–1988.
109. C. U. Pittman and R. C. Ryan (1978). *Chemtech* **8**, 170–175.
110. C. U. Pittman, G. M. Wilemon, W. D. Wilson, and R. C. Ryan (1980). *Angew. Chem. Int. Ed.* **19**, 478–479.
111. P. Nombel, N. Lugan, F. Mulla, and G. Lavigne (1994). *Organometallics* **13**, 4673–4675.
112. P. Nombel, N. Lugan, B. Donnadieu, and G. Lavigne (1999). *Organometallics* **18**, 187–196.
113. D.-S. Kim, W.-J. Park, C.-H. Lee, and C.-H. Jun (2014). *J. Org. Chem.* **79**, 12191–12196.
114. S. Ko, Y. Na, and S. Chang (2002). *J. Am. Chem. Soc.* **124**, 750–751.
115. Y. Na, S. Ko, L. K. Hwang, and S. Chang (2003). *Tetrahedron Lett.* **44**, 4475–4478.
116. S. Ko, C. Lee, M.-G. Choi, Y. Na, and S. Chang (2003). *J. Org. Chem.* **68**, 1607–1610.
117. S. Ko, H. Han, and S. Chang (2003). *Org. Lett.* **5**, 2687–2690.
118. E. J. Park, J. M. Lee, H. Han, and S. Chang (2006). *Org. Lett.* **8**, 4355–4358.
119. T. Kondo, T. Okada, and T. Mitsudo (1999). *Organometallics* **18**, 4123–4127.
120. E. Yoneda, T. Kaneko, S.-W. Zhang, K. Onitsuka, and S. Takahashi (2000). *Org. Lett.* **2**, 441–443.
121. E. Yoneda, S.-W. Zhang, D.-Y. Zhou, K. Onitsuka, and S. Takahashi (2003). *J. Org. Chem.* **68**, 8571–8576.
122. M. Tsubuki, K. Takahashi, and T. Honda (2009). *J. Org. Chem.* **74**, 1422–1425.
123. H. Nagashima, A. Suzuki, T. Iura, K. Ryu, and K. Matsubara (2000). *Organometallics* **19**, 3579–3590.
124. H. Sasakuma, Y. Motoyama, and H. Nagashima (2007). *Chem. Commun.* <https://doi.org/10.1039/B711743D>.
125. S. Yumino, T. Hashimoto, A. Tahara, and H. Nagashima (2014). *Chem. Lett.* **43**, 1829–1831.
126. S. Hanada, A. Yuasa, H. Kuroiwa, Y. Motoyama, and H. Nagashima (2010). *Eur. J. Org. Chem.* **2010**, 1021–1025.
127. K. Miyamoto, Y. Motoyama, and H. Nagashima (2012). *Chem. Lett.* **41**, 229–231.
128. S. Hanada, Y. Motoyama, and H. Nagashima (2008). *Eur. J. Org. Chem.* **2008**, 4097–4100.
129. H. Nagashima, C. Itonaga, J. Yasuhara, Y. Motoyama, and K. Matsubara (2004). *Organometallics* **23**, 5779–5786.
130. N. Harada, T. Nishikata, and H. Nagashima (2012). *Tetrahedron* **68**, 3243–3252.
131. T. F. Beltrán, M. Feliz, R. Llusar, J. A. Mata, and V. S. Safont (2011). *Organometallics* **30**, 290–297.
132. C. Alfonso, T. F. Beltrán, M. Feliz, and R. Llusar (2015). *J. Clust. Sci.* **26**, 199–209.
133. C. S. Yi, T. N. Zeczycki, and I. A. Guzei (2006). *Organometallics* **25**, 1047–1051.
134. C. S. Yi and D. W. Lee (2009). *Organometallics* **28**, 947–949.
135. J. Kim, N. Pannilawithana, and C. S. Yi (2016). *ACS Catal.* **6**, 8395–8398.
136. T. Takao, T. Kawashima, H. Kanda, R. Okamura, and H. Suzuki (2012). *Organometallics* **31**, 4817–4831.
137. R. M. Haak, A. Decortes, E. C. Escudero-Adán, M. M. Belmonte, E. Martin, J. Benet-Buchholz, and A. W. Kleij (2011). *Inorg. Chem.* **50**, 7934–7936.
138. N. Kielland, E. C. Escudero-Adán, M. Martínez Belmonte, and A. W. Kleij (2013). *Dalton Trans.* **42**, 1427–1436.
139. B. Li, Y. Park, and S. Chang (2014). *J. Am. Chem. Soc.* **136**, 1125–1131.
140. U. Chakraborty, S. Demeshko, F. Meyer, and A. Jacobi von Wangelin (2019). *Angew. Chem. Int. Ed.* **58**, 3466–3470.

141. C. U. Pittman, W. Honnick, M. Absi-Halabi, M. G. Richmond, R. Bender, and P. Braunstein (1985). *J. Mol. Catal.* **32**, 177–190.
142. M. Castiglioni, R. Giordano, E. Sappa, A. Tiripicchio, and M. T. Camellini (1986). *J. Chem. Soc. Dalton Trans.* <https://doi.org/10.1039/DT9860000023>.
143. M. Castiglioni, R. Giordano, and E. Sappa (1987). *J. Organomet. Chem.* **319**, 167–181.
144. M. Castiglioni, R. Giordano, and E. Sappa (1988). *J. Organomet. Chem.* **342**, 111–127.
145. R. D. Adams, Z. Li, P. Swepston, W. Wu, and J. Yamamoto (1992). *J. Am. Chem. Soc.* **114**, 10657–10658.
146. R. D. Adams, T. S. Barnard, Z. Li, W. Wu, and J. H. Yamamoto (1994). *J. Am. Chem. Soc.* **116**, 9103–9113.
147. R. D. Adams and T. S. Barnard (1998). *Organometallics* **17**, 2567–2573.
148. R. D. Adams and T. S. Barnard (1998). *Organometallics* **17**, 2885–2890.
149. E. S. Smirnova, J. M. Muñoz Molina, A. Johnson, N. A. G. Bandeira, C. Bo, and A. M. Echavarren (2016). *Angew. Chem. Int. Ed.* **55**, 7487–7491.
150. M. G. Richmond, M. Absi-Halbi, and C. U. Pittman (1984). *J. Mol. Catal.* **22**, 367–371.
151. F. Senocq, C. Randrianalimanana, A. Thorez, P. Kalck, R. Choukroun, and D. Gervais (1984). *J. Chem. Soc. Chem. Commun.* <https://doi.org/10.1039/C39840001376>.
152. D. Gervais, J. Jaud, P. Kalck, R. Choukroun, and F. Senocq (1986). *Organometallics* **5**, 67–71.
153. R. Choukroun, D. Gervais, and C. Rifaï (1989). *Polyhedron* **8**, 1760–1761.
154. R. Choukroun, F. Dahan, D. Gervais, and C. Rifaï (1990). *Organometallics* **9**, 1982–1987.
155. M. A. Casado, J. J. Pérez-Torrente, M. A. Ciriano, L. A. Oro, A. Orejón, and C. Claver (1999). *Organometallics* **18**, 3035–3044.
156. M. A. Casado, M. A. Ciriano, A. J. Edwards, F. J. Lahoz, L. A. Oro, and J. J. Pérez-Torrente (1999). *Organometallics* **18**, 3025–3034.
157. H. J. Haupt, R. Wittbecker, and U. Florke (2001). *Z. Anorg. Allg. Chem.* **627**, 472–484.
158. C. U. Pittman Jr., M. G. Richmond, M. Absi-Halabi, H. Beurich, F. Richter, and H. Vahrenkamp (1982). *Angew. Chem. Int. Ed.* **21**, 786–787.
159. P. A. Shapley, H.-C. Liang, and N. C. Dopke (2001). *Organometallics* **20**, 4700–4704.
160. M. Nagaoka, T. Kawashima, H. Suzuki, and T. Takao (2016). *Organometallics* **35**, 2348–2360.
161. Y. Li, W.-X. Pan, and W.-T. Wong (2002). *J. Clust. Sci.* **13**, 223–233.
162. T. Murata, Y. Mizobe, H. Gao, Y. Ishii, T. Wakabayashi, F. Nakano, T. Tanase, S. Yano, and M. Hidai (1994). *J. Am. Chem. Soc.* **116**, 3389–3398.
163. T. Wakabayashi, Y. Ishii, T. Murata, Y. Mizobe, and M. Hidai (1995). *Tetrahedron Lett.* **36**, 5585.
164. D. Masui, Y. Ishii, and M. Hidai (1998). *Chem. Lett.* **27**, 717–718.
165. D. Masui, T. Kochi, Z. Tang, Y. Ishii, Y. Mizobe, and M. Hidai (2001). *J. Organomet. Chem.* **620**, 69–79.
166. T. Wakabayashi, Y. Ishii, K. Ishikawa, and M. Hidai (1996). *Angew. Chem. Int. Ed.* **35**, 2123–2124.
167. I. Takei, Y. Enta, Y. Wakebe, T. Suzuki, and M. Hidai (2006). *Chem. Lett.* **35**, 590–591.
168. I. Takei, Y. Wakebe, K. Suzuki, Y. Enta, T. Suzuki, Y. Mizobe, and M. Hidai (2003). *Organometallics* **22**, 4639–4641.
169. M. Feliz, E. Guillamón, R. Llusar, C. Vicent, S.-E. Stiriba, J. Pérez-Prieto, and M. Barberis (2006). *Chem. Eur. J.* **12**, 1486–1492.
170. E. Guillamón, R. Llusar, J. Pérez-Prieto, and S.-E. Stiriba (2008). *J. Organomet. Chem.* **693**, 1723–1727.
171. Y. Tao, Y. Zhou, J. Qu, and M. Hidai (2010). *Tetrahedron Lett.* **51**, 1982–1984.
172. Y. Tao, B. Wang, B. Wang, L. Qu, and J. Qu (2010). *Org. Lett.* **12**, 2726–2729.
173. Y. Tao, B. Wang, J. Zhao, Y. Song, L. Qu, and J. Qu (2012). *J. Org. Chem.* **77**, 2942–2946.
174. I. Takei, K. Dohki, K. Kobayashi, T. Suzuki, and M. Hidai (2005). *Inorg. Chem.* **44**, 3768–3770.
175. B. P. Hitchcock, L. D. Hughes, J. M. Maguire, K. Marjani, L. R. Richards (1997). *J. Chem. Soc. Dalton Trans.* pp. 4747–4752.
176. S. Kuwata, Y. Mizobe, and M. Hidai (1994). *Inorg. Chem.* **33**, 3619–3620.
177. M. Shenglof, G. A. Molander, and J. Blum (2006). *Synthesis (Stuttg)* **2006**, 111–114.
178. M. Shieh, Y. H. Liu, Y. H. Li, C. N. Lin, and C. C. Wang (2018). *J. Organomet. Chem.* **867**, 161–169.

**Publisher's Note** Springer Nature remains neutral with regard to jurisdictional claims in published maps and institutional affiliations.

1 The paddlewheel complex of 1,8-naphthyridine and  
2 palladium(II). Synthesis, characterization, and  
3 reactivity studies.

4 *Mathias T. Nielsen, Dmytro Mihrin, Mike S. B. Jørgensen, Xiaomei Yan, Rolf W. Berg, Xinxin*  
5 *Xiao, René W. Larsen, and Martin Nielsen\**

6 **AUTHOR ADDRESS** (Word Style “BC\_Author\_Address”).

7 Department of Chemistry, Technical University of Denmark, 2800 Kgs. Lyngby, Denmark

8 **KEYWORDS** (Word Style “BG\_Keywords”). If you are submitting your paper to a journal that  
9 requires keywords, provide significant keywords to aid the reader in literature retrieval.

10 **ABSTRACT** (Word Style “BD\_Abstract”). All manuscripts must be accompanied by an abstract.

11 The abstract should briefly state the problem or purpose of the research, indicate the theoretical or  
12 experimental plan used, summarize the principal findings, and point out major conclusions.

13 Abstract length is one paragraph.

14

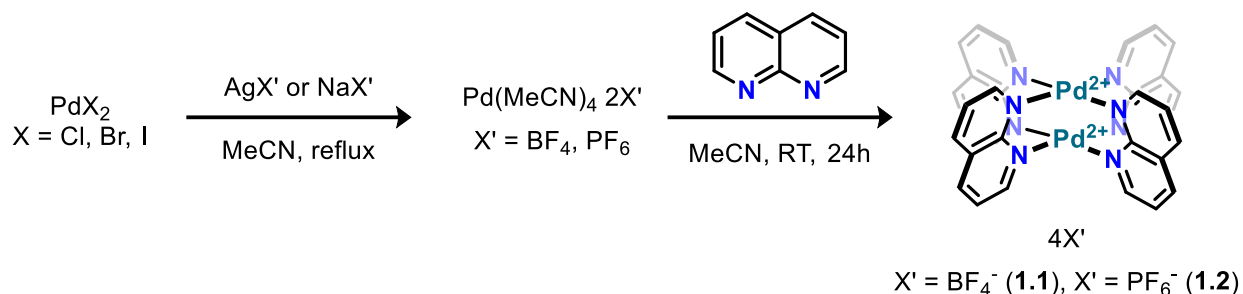
## Introduction

Transition-metal paddlewheel complexes are well-known bimetallic entities with a distinct electronic configuration that presents an opportunity for multiple metal-metal bonds, and the metal-metal proximity results in interesting redox chemistry<sup>1</sup>. Additionally, this arrangement of two proximal metal centers provides a unique reactivity different from monometallic analogues as exemplified by Gray's seminal work on a Rh(I)-dimer, demonstrating a two-center oxidative addition of I<sub>2</sub> with the concurrent formation of a Rh-Rh bond<sup>2</sup>. These complexes often employ rigid anionic ligands, such as guanadinate derivatives, carboxylates, and formamidinate, as the ligand imparts directionality during complex synthesis as well as stabilization of the metal in higher oxidation states. Fundamentally, it is of interest to investigate whether formally neutral ligands facilitate a similar complex formation; aggregation of two non-metal-metal bonded ions that subsequently supports the formation of a metal-metal-bonded complex-core, in which the ancillary ligands subsequently can undergo substitution. In this context, 1,8-naphthyridine (abbreviated napy) is of interest, as the close disposition of the two parallel *N*-centered lone pairs, serves as a rigid template to direct metal ions closely together. Indeed, literature provides a plethora of napy-based dinuclear homoleptic<sup>3-8</sup> and heteroleptic complexes<sup>9-16</sup>. Moreover, examples of napy coordinating bidentate<sup>17</sup> as well as in a monodentate<sup>4</sup> fashion, are also found.

In this paper, we explore the use of the napy ligand to furnish the formation of a non-metal-metal-bonded cationic dipalladium (II)-tetranapy paddlewheel complex, [Pd<sub>2</sub>( $\mu$ -napy)<sub>4</sub>] 4BF<sub>4</sub>, followed by an exploration of subsequent oxidation and reduction to the corresponding the [Pd<sub>2</sub>( $\mu$ -napy)<sub>4</sub>]<sup>6+</sup> and [Pd<sub>2</sub>( $\mu$ -napy)<sub>4</sub>]<sup>2+</sup> complex, respectively. The spectroscopic and electrochemical properties of the [Pd<sub>2</sub>( $\mu$ -napy)<sub>4</sub>]<sup>4+</sup>-complex are disclosed, in addition to the crystal structure of PdCl<sub>2</sub>PPh<sub>3</sub>( $\kappa$ -*N*-napy).

## Results and discussion

*Synthesis and solid-state structure.* The tetracationic paddlewheel-dipalladium complex of tetra- $\mu$ -napy-dipalladium(II) tetrafluoroborate,  $[\text{Pd}_2(\mu\text{-napy})_4] 4\text{BF}_4$ , abbreviated **1.1**, precipitates as a lightly-pink colored powder (**Scheme 1**), following a sequential addition of napy to tetraacetonitrilepalladium(II) tetrafluoroborate,  $[\text{Pd}(\text{MeCN})_4] 2\text{BF}_4$ , in acetonitrile over 30 hours.



**Scheme 1.** *Synthetic route for preparation of 1.* Different counterions than  $\text{BF}_4$  are readily prepared demonstrated by a halide abstraction of  $\text{PdX}_2$ ,  $\text{X} = \text{Cl}, \text{Br}, \text{I}$ .

Alternatively, the same complex bearing counterions different from  $\text{BF}_4$ , *e.g.* hexafluorophosphate (**1.2**), is readily realized from an initial halide abstraction of  $\text{PdX}_2$  ( $\text{X} = \text{Cl}, \text{Br}, \text{I}$ ) using two equivalents of either  $\text{AgX}'$  or  $\text{NaX}'$  ( $\text{X}' = \text{BF}_4, \text{PF}_6$ ) in MeCN. The two compounds show diamagnetic behavior from well-resolved NMR spectra ( $^1\text{H}$ ,  $^{13}\text{C}$ ,  $^{19}\text{F}$ , and  $^{31}\text{P}$ ), which further reflects a high symmetry from the presence of only three resonances in the  $^1\text{H}$  NMR spectrum. The three resonances, upon ligand substitution or extrusion of a Pd center from complexes **1.1** and **1.2**, split into six; our attempts to prepare the diplatinum (II) congener under the same conditions, yields instead the dicationic salt of tetra-( $\kappa$ -*N*-napy) platinum(II) hexafluorophosphate,  $[\text{Pt}(\text{napy})_4] 2\text{PF}_6$ . This complex, shows six resonances comprising four individual and two overlapping peaks, one for each of the  $\text{C}_2$  through  $\text{C}_7$  position of the napy-backbone, in agreement with findings reported by Biffis<sup>8</sup>. The salts of complexes **1.1** and **1.2** are stable towards the air, moisture, and light. Leaving either reaction mixtures to stir for an additional 16 hours consumes any powders, likely from the transformation of **1.1** into a mixture of monopalladium MeCN adducts. This

suggestion is based on the isolated complexes of **1.1** and **1.2** slowly undergoing ligand substitution in strongly coordinating solvents, *e.g.*, DMSO, MeCN, and DMF (over several hours, rt).

**Figure 1** shows that each palladium (II) center of **1.1** is coordinated in a square planar fashion by four symmetry-related napy ligands in a paddlewheel geometry. The average Pd-N bond length is 2.043 Å and the Pd-Pd separation is 2.5639(5) Å, significantly shorter than Pd's van der Waals radius of 3.26 Å<sup>18</sup>. While these distances compare well to the platinum congener, [Pt<sub>2</sub>(μ-napy)<sub>4</sub>] 4OTf<sup>8</sup>, they are on average shorter. Pt<sub>2</sub>(μ-napy)<sub>4</sub> 4OTf feature average bond distances of Pt-N (napy) 2.050(4) Å and a Pt-Pt' separation of 2.5841(4) Å, respectively. The napy ligands in **1.1** bridge the two metal centers planarly, as in the molybdenum<sup>13</sup>, rhodium<sup>7</sup>, and platinum<sup>8</sup> analogs. Finally, comparing the same distances of **1.1** to that of the neutral dipalladium(II) triazabicyclodecene (hpp) complex reported by Cotton and co-workers<sup>19</sup>, reveals bond distances more comparable than to that in the Pt-congener. This complex features an average Pd-N (hpp) bond length of 2.038 Å and Pd-Pd' separation of 2.554 Å. Curiously, a tetrafluoroborate-counterion appear to reside above and below each Pd (II) center forming interacting with the *ortho*-hydrogen atoms of the napy ligand.

We sought to better understand the electronic structure of **1.1** (and by extension **1.2**) with respect to the nature of the Pd-Pd interaction given the short metal-metal distance and the complex' high symmetry. Optical absorption spectroscopy, **Figure 2** features an absorption in the visible region,  $\epsilon(543.8 \text{ nm } (\lambda_{\text{max}})) = 36.6 \text{ M}^{-1} \text{ cm}^{-1}$ , and further absorptions are present in the UV-region, likely relating to metal-to-ligand charge-transfer (MLCT). In this context, various dinuclear napy-complexes feature strong MLCT in the region from 450 to 330 nm<sup>3,5</sup>. Interestingly, the dimolybdenum(II) napy complex, [Mo<sub>2</sub>(μ-napy)<sub>4</sub>(MeCN)<sub>2</sub>]<sup>4+</sup>, feature an additional low-energy transition ( $\lambda = 699 \text{ nm}$ ,  $\epsilon = 717 \text{ M}^{-1} \text{ cm}^{-1}$ ), which the authors assign to a  $\delta \rightarrow \delta^*$  transition<sup>13</sup>.



Differently, in the dipalladium formamidinate complex,  $\text{Pd}_2(\text{DAni})_4$  ( $\text{DAni}$  = di-*p*-anisylformamidinate)<sup>20,21</sup>, a low-energy transition is observed in the visible region ( $\lambda \sim 500$  nm), which disappears upon oxidation to the corresponding  $\text{Pd}_2^{5+}$ -core.

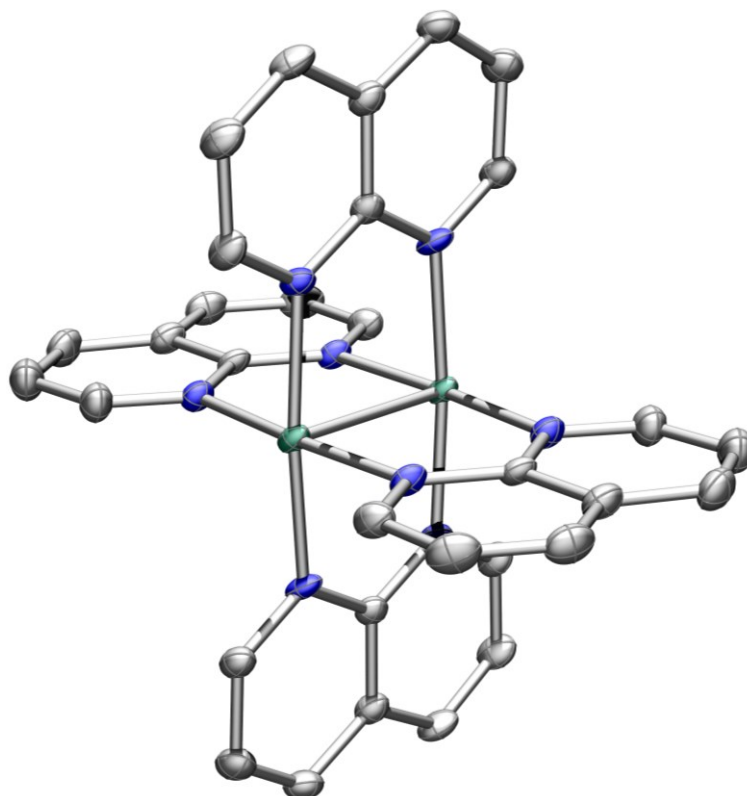


**Figure 1.** Single-crystal X-ray structure of the paddlewheel complex. The solid-state structure of **1.1** with thermal ellipsoids at 50% probability level.  $\text{BF}_4^-$ -counterions, co-crystallized MeCN, and H-atoms are omitted for clarity. Color coding: C grey, N blue, Pd sea green.

These examples, combined with the magnitude of the absorption coefficient of the low-energy transition found in **Figure 2**, suggests that this transition may originate from a spin-allowed, Laporte-forbidden transition between the HOMO (highest-occupied molecular orbital) and the LUMO (lowest-unoccupied molecular orbital), where the orbital symmetries as expected following the paddlewheel disposition. To further explore this transition, we sought to apply Density-Functional Theory (DFT) calculations to gain further insight into the electronic properties of **1.1**.



<b>Table 1.</b> Summary of crystallographic data for <b>1.1</b>	
Chemical formula	C <sub>44</sub> H <sub>42</sub> B <sub>4</sub> F <sub>16</sub> N <sub>13.5</sub> Pd <sub>2</sub>
Formula weight	1319.95
Crystal color	Colorless
Crystal system	Triclinic
Space group	P-1
<i>a</i> (Å)	11.1375(13)
<i>b</i> (Å)	11.7457(12)
<i>c</i> (Å)	12.7482(2)
<i>α</i> (deg)	76.461(2)
<i>β</i> (deg)	63.478(10)
<i>γ</i> (deg)	68.034(10)
<i>V</i> (Å <sup>3</sup> )	1297.8(3)
<i>Z</i>	1
<i>μ</i> (mm <sup>-1</sup> )	6.538
<i>T</i> (K)	119.99(15)
Radiation type	CuKα ( <i>λ</i> = 1.54184)
GOF ( <i>S</i> )	1.040
<i>R</i> <sub>1</sub> <sup>a</sup> ( <i>wR</i> <sub>2</sub> <sup>b</sup> ) [ <i>I</i> > 2σ( <i>I</i> )]	<i>R</i> <sub>1</sub> = 0.0332, <i>wR</i> <sub>2</sub> = 0.0766
<i>R</i> <sub>1</sub> <sup>a</sup> ( <i>wR</i> <sub>2</sub> <sup>b</sup> ) [all data]	<i>R</i> <sub>1</sub> = 0.0451, <i>wR</i> <sub>2</sub> = 0.0852
2Θ range for data collection (deg)	8.12 to 133.198
Reflections	13444
Largest diff. peak/hole / e Å <sup>-3</sup>	1.20/-0.75
Index ranges	-13 ≤ <i>h</i> ≤ 11, -13 ≤ <i>k</i> ≤ 13, -14 ≤ <i>l</i> ≤ 14
<sup>a</sup> <i>R</i> <sub>1</sub> = Σ(  <i>F</i> <sub>o</sub>   -   <i>F</i> <sub>c</sub>  )/Σ  <i>F</i> <sub>o</sub>  , <i>wR</i> <sub>2</sub> = {Σ[ <i>w</i> ( <i>F</i> <sub>o</sub> <sup>2</sup> - <i>F</i> <sub>c</sub> <sup>2</sup> ) <sup>2</sup> ]/Σ <i>w</i> ( <i>F</i> <sub>o</sub> <sup>2</sup> ) <sup>2</sup> } <sup>1/2</sup> <i>w</i> = 1/[σ <sup>2</sup> ( <i>F</i> <sub>o</sub> <sup>2</sup> ) + ( <i>aP</i> ) <sup>2</sup> + <i>bP</i> ], where <i>P</i> = [max( <i>F</i> <sub>o</sub> <sup>2</sup> , 0) + 2( <i>F</i> <sub>c</sub> <sup>2</sup> )]/3	

98  
99

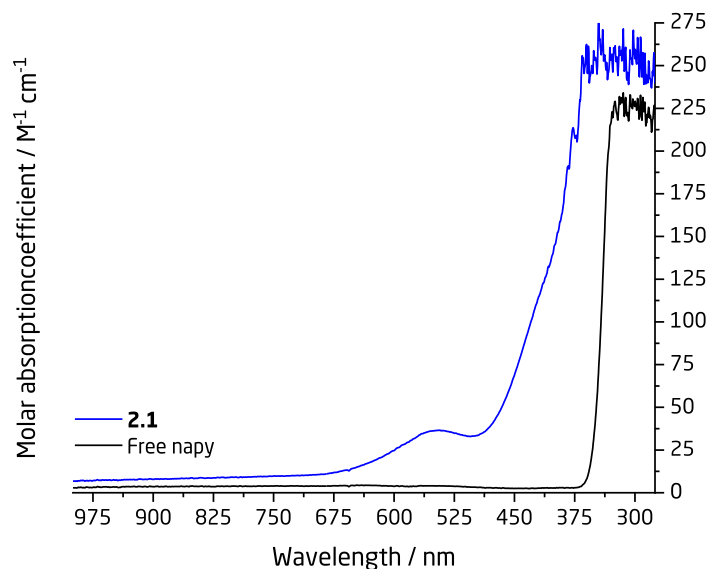


**Figure 2.** Optical absorption spectra of **1.1** and napy in DMF. The stacked UV-Vis spectra of the paddlewheel complex and free napy demonstrate a small absorption coefficient ( $\epsilon(543.8 \text{ nm } (\lambda_{\text{max}})) = 36.6 \text{ M}^{-1} \text{ cm}^{-1}$ ). DMF solutions (in mM) of **1.1** (10.0, blue) and napy (10.0, black).

**Figure 3** shows that the frontier-molecular orbitals of the ground-state: the HOMO comprises an antibonding interaction ( $\sigma^*$ ) between the two Pd atomic  $d(z^2)$  orbitals, whereas the LUMO comprises an antibonding interaction between the two atomic  $d(x^2-y^2)$  orbitals and the ligands ( $\sigma^*(\text{M-L}), d(x^2-y^2)\text{-L}(\sigma^*)$ ). This deviation from an expected stabilizing  $\delta$  interactions between the two  $d(x^2-y^2)$  orbitals, renders an expected transition between the HOMO-LUMO Laporte forbidden, following both orbital's *ungerade* parity. We were able to obtain further insights into the orbitals involved in the excitations observed in **Figure 2**, through time-dependent DFT (TD-DFT), as well as on the mid and far infrared spectra, *vide infra*. The quantum chemical calculations (in a vacuum) predict two transitions; a low-energy, low-intensity transition, at 484 nm, followed by a high-energy transition at 338 nm, in line with commonly observed MLCT for napy-complexes, both relating to an MLCT transition. The former comprises a transition from the HOMO to the LUMO+2 and the LUMO+3, whereas the higher-energy transition is between HOMO-1 to LUMO+2, and HOMO-2 to LUMO+3, respectively.

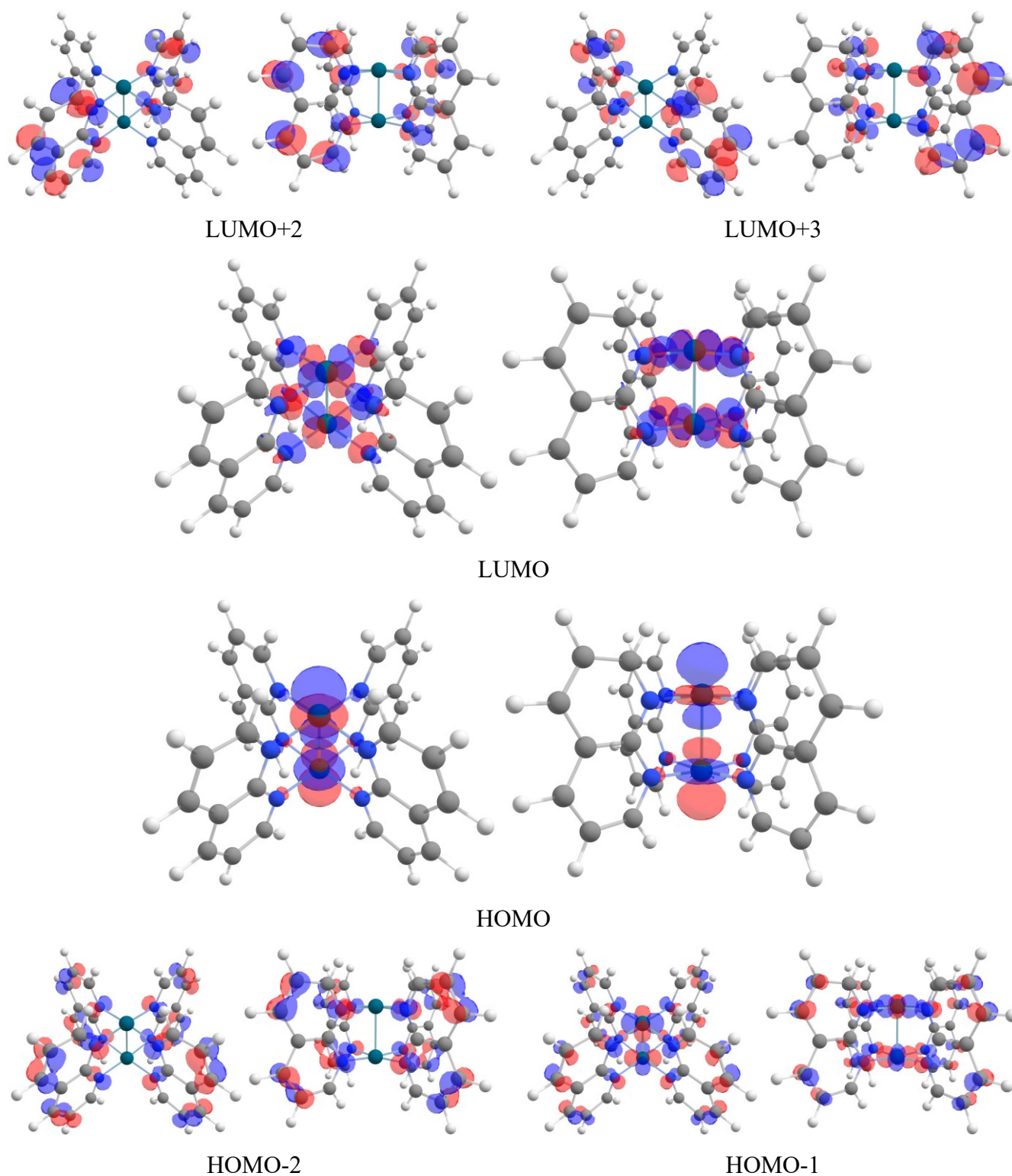


**Figure 3.** *DFT-calculated frontier molecular orbitals.* Depicting orbitals involved in electronic transitions calculated by TD-DFT for UV-Vis spectra: HOMO  $\rightarrow$  LUMO+2,+3 and HOMO-1,-2  $\rightarrow$  LUMO+2,3 for transition in the visible and UV spectral range, respectively. Isodensity ( $0.040 \text{ e}/\text{\AA}^2$ ) plot.

To account for a polar solvation shell present in the experimentally observed excitation, which potentially could stabilize an excited charge-distribution centered on the ligand, two implicit DMF models were investigated: conductor-like polarizable continuum model (CPCM), and cavity-dispersion-solvent structure (CDS) term, respectively. These calculations suggest the UV transition redshifts to 590 nm, which, despite a somewhat crude model, from the lacking hydrogen bonds, provides some insight into how solvent polarity affects the spectrum. Based on these findings, we suggest that the absorption spectrum of complex **1.1** displays a transition from the HOMO(-1,-2) to the ligand's  $\pi^*$ -system, although the magnitude of the observed MLCT are lower than usually encountered. Moreover, TD-DFT corroborates that no  $\sigma$ -orbitals originating from mixing of two  $5p_z$  orbitals are involved in any transitions, suggesting that application of the complex in photolytic reactions will be of limited success.

*FIR, Raman, and DFT-calculated spectra.* The complete vibrational spectrum of free napy ligand has previously been reported in a combined Raman/infrared investigation of napy embedded in a Nujol mull<sup>22</sup>, later in a surface-enhanced Raman spectroscopic (SERS) investigation of napy adsorbed on silver colloids<sup>23</sup>, and the reported vibrational assignments of monomeric napy were inspired by the assignments for the structurally similar naphthalene molecule. The attenuated-total-reflectance (ATR) spectra of **1.1** collected in the mid-infrared (MIR) fingerprint (600-1700  $\text{cm}^{-1}$ ) and the far-infrared (150-600  $\text{cm}^{-1}$ ) (FIR) spectral regions are shown in **Figure 4**. The mid-infrared fingerprint region of the spectra features mostly vibrational fundamental transitions associated with slightly perturbed intramolecular normal modes of the napy ligands, whereas the far-infrared part of the spectra additionally features several fundamental transitions associated with large-amplitude vibrational motion involving the metal-ligand bonds.

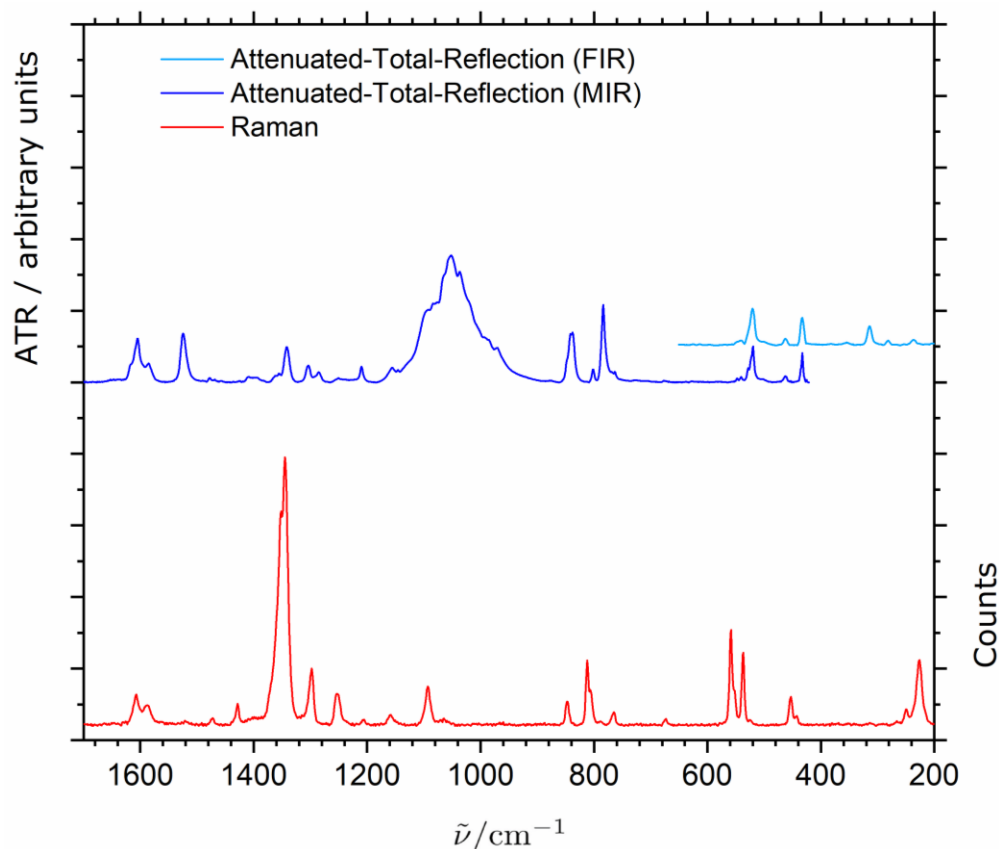


**Figure 4.** The attenuated-total-reflectance (ATR) infrared (blue trace) and Raman spectra (red trace) of **1.1** in the mid-infrared fingerprint and the far-infrared spectral regions.

Our infrared and Raman spectroscopic observations for **1.1** agree rather well with the literature, although the mid-infrared part of the spectrum is significantly blurred in the 900–1175 cm<sup>-1</sup> range due to the very strong and broad absorption feature resulting from the B-F stretching modes of the BF<sub>4</sub> counter-ion. A complete list of observed infrared and Raman band positions of distinct bands is provided in the supplementary material.

The far-infrared spectrum reveals several absorption bands, which have previously been assigned to different modes involving the torsional and bending motion of the aromatic rings of the napy monomer. Three bands observed at 169, 433, and 463 cm<sup>-1</sup>, respectively, relates directly to the torsional motions of the ring, and gain intensity in napy due to the asymmetry introduced by the *N*-heteroatoms. Additionally, the two bands observed at 521 and 543 cm<sup>-1</sup>, respectively, have both

previously been assigned to bending motions of the aromatic rings<sup>22,23</sup>. The non-zero infrared activity is the result of the different vibrational amplitudes of the involved C and N atoms. More interestingly, the observation of three distinctive vibrational transitions, not previously observed in monomeric napy, at, 236, 281 and 314  $\text{cm}^{-1}$ , respectively, are indicative of the complexation between napy and Pd (II).

Some ambiguity exists on the particular far-infrared assignments of the N··Pd··N bending and Pd··N stretching modes for palladium (II) complexes, as different of studies have assigned vibrational transitions associated with large-amplitude Pd··N stretching modes in the 400-550  $\text{cm}^{-1}$  range<sup>24</sup> and other investigations have assigned these stretching transitions in the 200-300  $\text{cm}^{-1}$  range<sup>25</sup>. However, a normal mode analysis of the present harmonic vibrational predictions at the TPSS-D4/def2-TZVP [Pd def2-QZVP] level of theory provides further insight into the observed transitions, as these are associated with concerted large-amplitude N··Pd··N bending motion. The theoretical simulation of the far-infrared spectrum based on this level of theory is shown in **Figure 5** together with the experimental spectrum. The agreement between the simulation and experiment is surprisingly good although the undertaken harmonic vibrational predictions clearly are more challenging for the N··Pd··N bending modes due to the more anharmonic character for this class of large-amplitude vibrational motion. Two of the three transitions, 236 and 314  $\text{cm}^{-1}$ , respectively, are associated with two different concerted out-of-plane N··Pd··N bending modes involving all four napy subunits. The last transition at 281  $\text{cm}^{-1}$  is associated with a concerted in-plane N··Pd··N bending mode. A normal mode animation of the highest-energy out-of-plane N··Pd··N bending mode is illustrated in **Figure 6**.

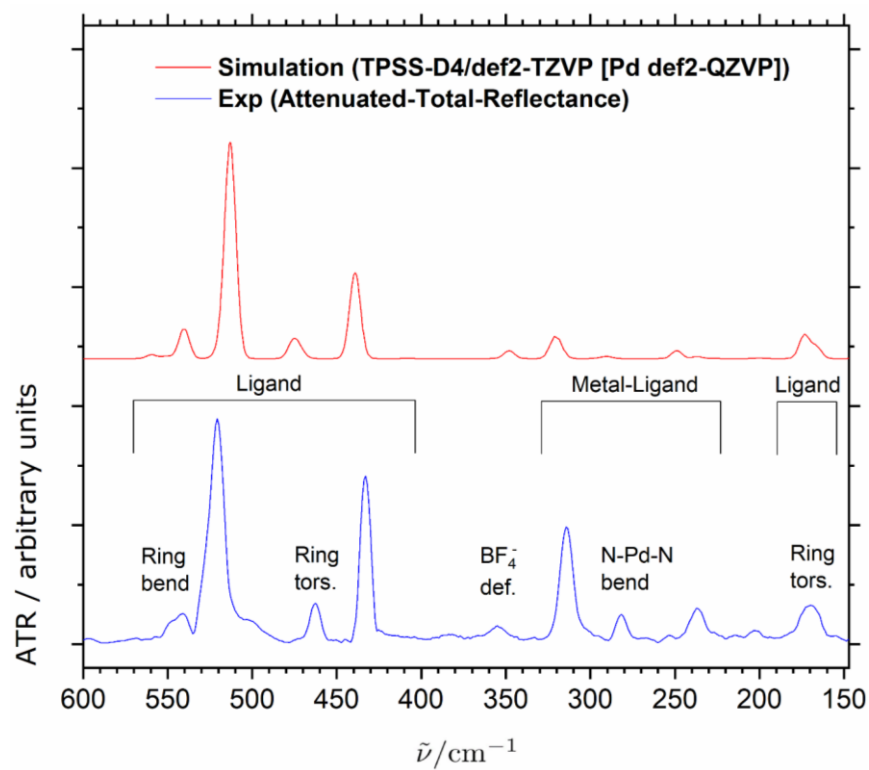


**Figure 5:** The experimental far-infrared attenuated-total-reflectance spectrum of **1.1** (blue trace) together with a simulation of the spectrum at the TPSS-D4/def2-TZVP [Pd def2-QZVP] level of theory (red trace). The present vibrational assignments of the intramolecular ring modes from the napy ligands, the deformation of the counter-ions  $\text{BF}_4$  and the large-amplitude concerted  $\text{N}\cdots\text{Pd}\cdots\text{N}$  bending modes of **1.1** are indicated.

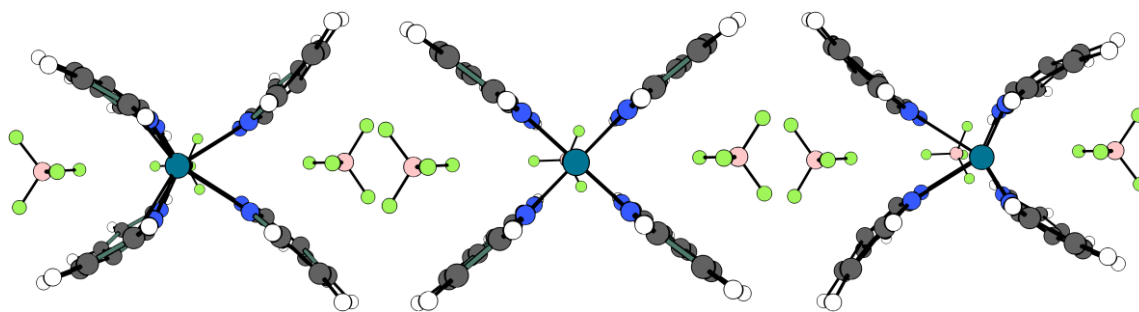


**Figure 6.** The animation of the large-amplitude concerted out-of-plane  $\text{N}\cdots\text{Pd}\cdots\text{N}$  bending mode of **2.1** predicted by the TPSS-D4/def2-TZVP level of the theory. The equilibrium configuration of **2.1** is shown (center) together with the configurations at the two outer vibrational turning points of the normal mode (left and right). Front counter-ion omitted for clarity

Based on predicted Raman activities at the same level of theory, we tentatively assign the vibrational transition observed at  $673\text{ cm}^{-1}$  in the Raman spectrum to concerted large-amplitude

N··Pd··N stretching motion involving all the metal-ligand bonds. The normal mode animation of the predicted vibration motion (with three-fold amplified vibrational displacements) is shown in **Figure 7**, which demonstrates that this concerted N··Pd··N stretching motion does not involve any change of the overall dipole moment and is therefore only slightly Raman-active.

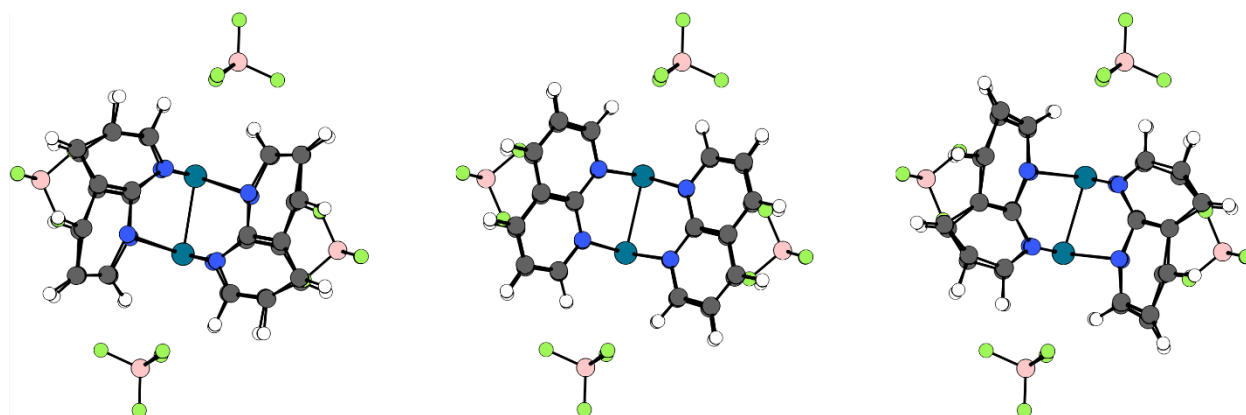


**Figure 7.** The animation of a large-amplitude (concerted N··Pd··N stretching mode of **1.1** predicted by the TPSS-D4/def2-TZVP [Pd def2-QZVP] level of the theory (with three-fold amplified vibrational displacements). The equilibrium configuration of **1.1** is shown (center) together with the configurations at the two outer vibrational turning points of the normal mode (left and right).

*Electrochemical studies.* Motivated by the spectroscopic and computational results, we sought to gain insight into the electrochemical properties of complex **1.1/2**, specifically concerning any distinctive oxidation events owing to the formation of a Pd<sub>2</sub><sup>6+</sup>-core. Concerning paddlewheel complexes, the ligand's electronic properties play a pivotal role in the stabilization of dipalladium(III). In this context, Cotton demonstrated that *N,N'*-tolylamidinato ligands enable the electrochemical preparation of such a Pd<sub>2</sub><sup>6+</sup>-core<sup>26</sup>, while Bear instead found that the phenyl-congener only gave rise to the mixed-valent Pd<sup>II</sup>Pd<sup>III</sup>-complex<sup>27</sup>. From a systematic comparison of the oxidation potentials of monopalladium, clamshell dipalladium, and paddlewheel palladium complexes, Budnikova reports a linear decrease in oxidation potential following the Pd-Pd distance<sup>28</sup>, of which paddlewheel complexes demonstrate lower oxidation potentials, typically in



210 the range of  $\sim 0.4$  to  $0.6$  V vs.  $\text{Fc}^+/\text{Fc}$ , with electron-rich bridging units at the lower end.  
211 Accordingly, should **1.1** (or **1.2**) thus facilitate multiple oxidation events towards dipalladium (III),  
212 these events would be expected within this range, perhaps with an onset of oxidation at  $\sim 0.8$  V.  
213 The left-hand side of **Figure 8**  
214 **Figure 2.8** show our initial voltammograms of napy (blue trace) and **1.2** (black and red traces),  
215 which clearly demonstrate that any redox events are a consequence of the complex. Unfortunately,  
216 no reversible oxidations events are measurable within the expected range attributable to the  
217 Pd(II/III) redox couple. Instead, we find several reduction events. However, the associated  
218 oxidation peaks are difficult to fully discern at the given scan rate ( $20 \text{ mVs}^{-1}$ ), and as such, we  
219 repeated the measurement at a higher concentration with varying scan rates to probe the stability  
220 of any formed species, as seen on the right-hand side of the figure, and these voltammograms better  
221 demonstrates the redox events owing to **1.2**. The broad oxidation wave onset of  $\sim 0.4 \text{ V}$  vs.  $\text{Fc}^{+/0}$ , is  
222 consistent with a quasi-reversible ligand-based oxidation. In Biffis' analysis of  $[\text{Pt}_2(\text{napy})_4] 4\text{OTf}$ ,  
223 the authors account for two ligand-centered oxidation events: a quasi-reversible oxidation at  $1.12 \text{ V}$   
224 vs SCE (MeCN), and an irreversible oxidation at  $1.5 \text{ V}$  vs SCE, respectively<sup>8</sup>. In this context, we  
225 did characterize napy-oxidation products, while we were unable to isolate a mixed-valent  $\text{Pd}^{\text{II}}\text{Pd}^{\text{III}}$   
226 compound. These findings suggest that oxidation to the  $\text{Pd}_2^{6+}$ -core is highly unlikely, and napy is  
227 a poorly suited ligand to support strongly oxidizing metal-centres<sup>29</sup>.

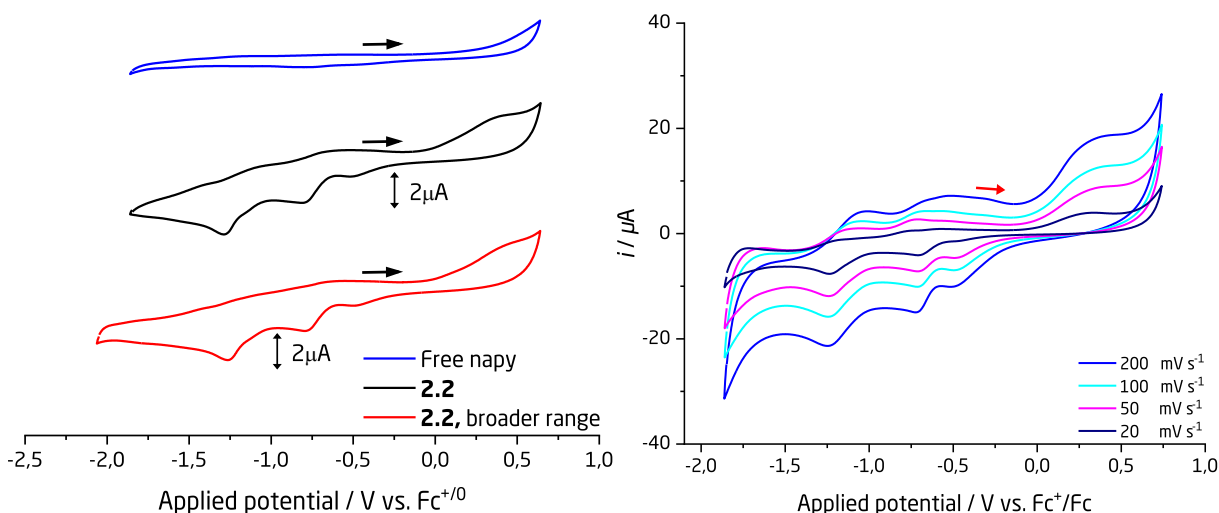
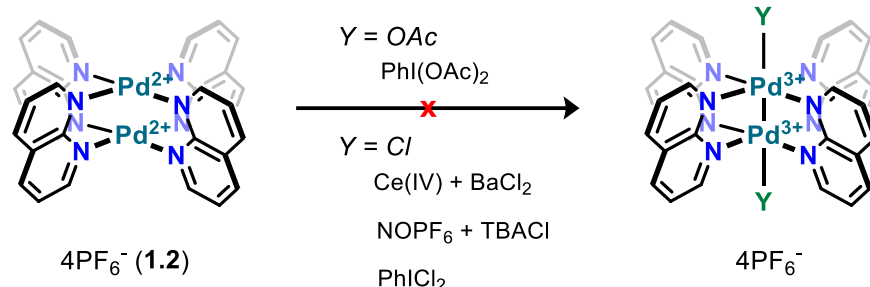


**Figure 8.** Voltammogram of **2.2** over various scan rates. Increasing the scan-rate results in a species that demonstrate electrochemical reversibility with respect to oxidation/reduction. The left-hand graph depicts the average of three scans. The scan starts at -0.36V and proceeds in the cathodic direction.

Two pronounced reduction events follow, at approximately -0.7V and -1.25V, with accompanying oxidation events. Both pairs follow a linear relationship between the peak current ( $i_p$ ) and square-root of the scan-rate ( $v^{1/2}$ ), right-hand of **Figure 2.9**, with peak separations of 67 mV, and 65 mV, respectively. The oxidation events appear frequency dependent, appear to anodically shift and broaden following increasing scan-frequency, and at 20 mVs<sup>-1</sup> they are gone, as found in **Figure 2.8**. Both redox events also appear to relate to a two-electron transfer, estimated from the relationship between the half-peak potential ( $E_{p/2}$ ) and midpoint redox potential ( $E_{1/2}$ ),  $E_{p/2} = E_{1/2} \pm \frac{28 \text{ mV}}{n}$ . These redox events significantly differ from the other complexes presented by Budnikova, as those predominantly demonstrate irreversible reductions. However, while the presence of two reduction waves additionally differ from monopalladium complexes, the observed potentials do fall within the range of reduction potentials (DMF) of monopalladium complexes, varying between >-2.03 to -0.88V vs. Fc<sup>+/0</sup>. We therefore suggest that this distinctive electrochemical profile is a consequence of a combination of the napy ligand and metal proximity, contrasting redox properties affected solely by metal proximity.

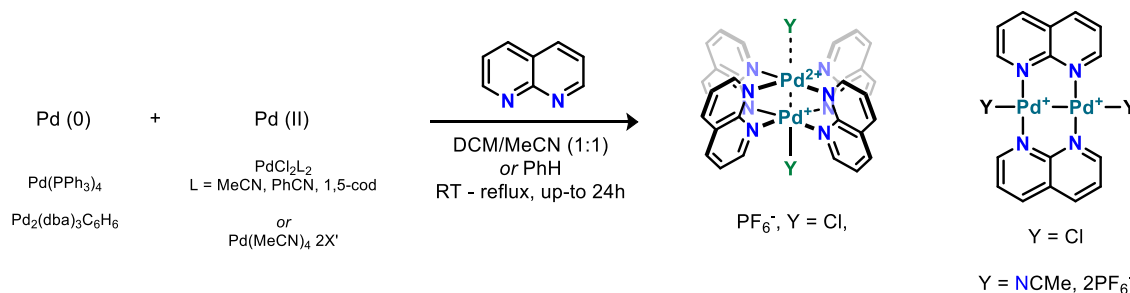
Our interpretation of the redox events can be understood from two different redox processes, either adequately accounting for the observed events in **Figure 8**: 1) a stepwise heterolytic reduction of each Pd (II) center ( $\text{Pd}^0\text{Pd}^{\text{II}}$ ,  $\text{Pd}^0\text{Pd}^0$ ), or 2) a stepwise homolytic reduction  $\text{Pd}^{\text{I}}\text{Pd}^{\text{I}}$ ,  $\text{Pd}^0\text{Pd}^0$ . However, we cannot discern between the two based of the presented electrochemical data alone, and we therefore sought to investigate the fate of this species following reactivity studies, and most likely relate to reduction of two isolated Pd (II) ions.

*1-4X' as a synthon for Pd-Pd bonded complexes.* To corroborate our electrochemical findings, we initially sought to oxidize **1.2** with various outer and inner-sphere oxidations, as outlined in **Scheme 2**. Compound **1.2** was chosen, as  $\text{BF}_4$ -counterions are more susceptible to engage in reactivity, than  $\text{PF}_6$ , with highly electrophilic metal centers. While the reaction between **1.2** and Ce (IV) ( $\text{Ce}(\text{SO}_4)_2$  with and without  $\text{BaCl}_2$ ) in MeCN or (water and MeCN) yields a bright yellow powder of ill-defined composition; CAN ( $(\text{NH}_4)_2\text{Ce}(\text{NO}_3)_6$ ) oxidations similarly leads to unproductive decomposition reactions. Exposing complex **1.2** to  $\text{NOPF}_6$  also failed to furnish any metal-based oxidation. Finally, we sought to employ hypervalent iodane sources, analogous to Cotton's preparation of  $\text{Pd}_2^{6+}$ -complex<sup>19</sup>, and in preparation of diplatinum(III) lantern complexes<sup>31</sup>. Discouragingly, we were able to recover >90% of **1.2** from the reaction mixture along other Pd (II) salts. Following these results, we then sought to obtain structural insight on any low-valent Pd entity consistent with reduction waves observed in the CV of **1.2**. We tested two different single-electron reductants ( $\text{Cp}^*\text{Fe}$ ,  $\text{Cp}^*\text{Co}$ ) and a two-electron reductant (Zn); we were unable to isolate any  $\text{Pd}^{\text{I}}\text{Pd}^{\text{I}}$  or mixed-valent ( $\text{Pd}^{\text{I}}\text{Pd}^{\text{II}}$  or  $\text{Pd}^0\text{Pd}^{\text{II}}$ ) compounds, instead, recovering materials predominantly consisting of unreacted **1.2** (>85%),  $[\text{Pd}(\text{MeCN})_4] 2\text{X}'$ , or ill-defined mixtures, with a noticeable deposition of a Pd-mirror when reducing with  $\text{Cp}^*\text{Co}$ .



**Scheme 2.** Synthetic outline for chemical oxidation of the paddlewheel complex. A range of single- and two-electron oxidants were attempted for the preparation of a  $\text{Pd}_2^{6+}$ -core.  $\text{X}' = \text{BF}_4, \text{PF}_6$ ;  $\text{Y} = \text{OAc}, \text{Cl}$ , or solvent molecules. All attempts failed in our hands.

We then sought to explore comproportionation between different  $\text{Pd}(0)$  and  $\text{Pd}(\text{II})$  sources in presence of napy, as outlined in **Scheme 3**. The coordination geometry of  $\text{Pd}$  in such dipalladium(I) complexes is different from  $\text{Pd}(\text{II})$ , in that the  $\text{Pd}-\text{Pd}$  bond is oriented along one of the coordinate axes; a consequence manifesting in the variety of complexes bearing (un)supported  $\text{Pd}-\text{Pd}$  bonds, such as  $[\text{Pd}_2(\text{MeCN})_6] 2\text{BF}_4^{32}$ ,  $[(^t\text{Bu}_3\text{P})\text{Pd}(\mu-\text{X})]_2$  ( $\text{X} = \text{Br}, \text{I}$ )<sup>33</sup>, and  $\text{Pd}_2\text{Cl}_2(\mu\text{-dppm})_2^{34}$ , respectively. However, the mixed-valent  $[\text{Ni}^{\text{I}}\text{Ni}^{\text{II}}(\mu\text{-napy})_4\text{Br}_2] \text{BPh}_4$  complex instead share two square-pyramidal  $\text{Ni}^{1.5}$ -centers, coordinated in the basal plane by the napy. As such, if possible, we may isolate a similar complex, or a dipalladium (I) complex bearing napy in varying numbers *e.g.*  $[\text{Pd}_2((\mu\text{-})\text{napy})_n] 2\text{X}'$  ( $n = 2, 4, 6$ ).



**Scheme 3.** Synthetic outline for comproportionation reactions. Suggested outcome owing to the formation of either a mixed-valent or dipalladium(I) both having bridging napy ligands.

Various combinations of  $\text{Pd}$ -precursors, solvents, reaction time, order of addition, as well as the rate of addition, were all unfruitful. These reactions either led to the deposition of a significant amount of  $\text{Pd}$  in form of a  $\text{Pd}$ -mirror or precipitation of  $\text{Pd}$ -black or showed no reactivity at all.

Moreover, a yellow/orange filtrate was collected from the reaction utilizing exogeneous or Pd-precursors bearing PPh<sub>3</sub>, from which we were able to crystallize small amounts of PdCl<sub>2</sub>PPh<sub>3</sub>(κ-N-napy), shown in **Figure 2.9**, demonstrating napy in a monodentate coordination mode to Pd.

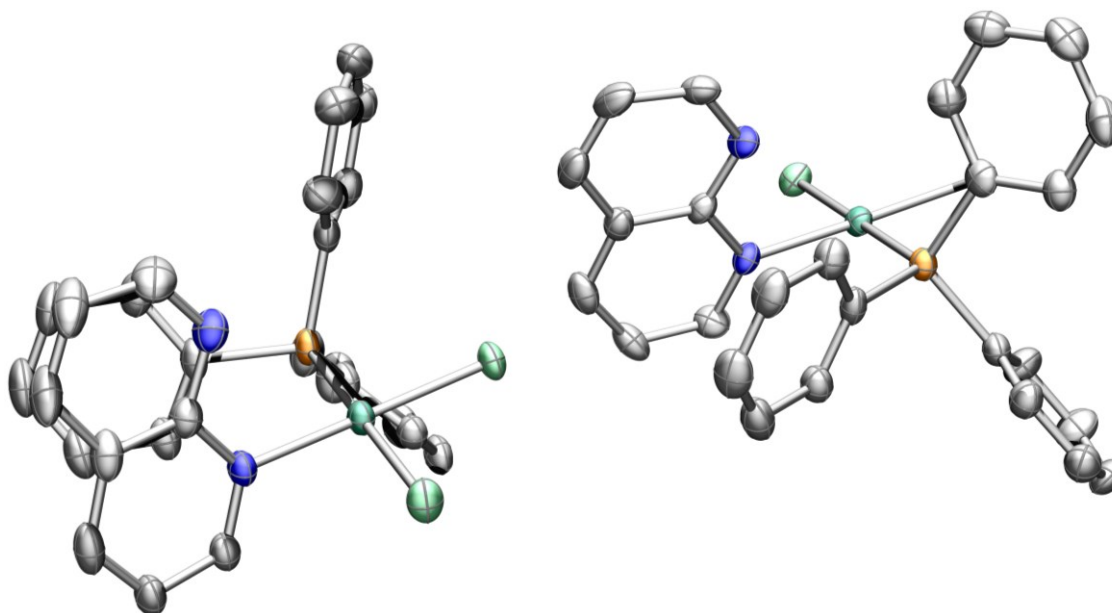


**Figure 9.** Single-crystal X-ray structure of a phosphine-napy-Pd (II) complex, complex 3. The solid-state structure of crystals found from comproportionation reactions, with thermal ellipsoids at 50% probability level. H-atoms and co-crystallized DCM molecules are omitted for clarity. Color coding: C grey, N blue, Cl green, P yellow, Pd sea green.

To corroborate these findings, we sought to understand napy's interaction with the “naked” dipalladium(I) source [Pd<sub>2</sub>(MeCN)<sub>6</sub>] 2BF<sub>4</sub>; starting from [Pd<sub>2</sub>(MeCN)<sub>6</sub>] 2BF<sub>4</sub> and adding in (increasing equivalents of) napy (one to six equivalents) in different solvents (DMF, MeCN, DCM/MeCN (1:1)) quickly led to the precipitation of Pd-black (or deposition of Pd-mirror). The addition of the Pd<sub>2</sub><sup>2+</sup>-precursor to varying equivalents of napy similarly resulted in a rapid formation of Pd-black. The (electronic) nature of the coordinating ligand seems to greatly affect the stability of the dipalladium(I) complex. Although [Pd<sub>2</sub>(MeCN)<sub>6</sub>] 2BF<sub>4</sub> is an isolatable species, we observed slow decomposition in solution. In their study of this complex, Murahashi and Kurosawa were able to coordinate various ligands with retention of the Pd-Pd bond<sup>32</sup>; two equivalents of 1,10-phenanthroline (phen) and a *N,N*-ethylenebis(benzaldimine), whereas,

addition of >2 equivalents of PPh<sub>3</sub> resulted in unidentified species. Related, Walther reported the synthesis and structure of a low-valent [Pd<sub>2</sub>(1,5-cod)<sub>2</sub>Cl<sub>2</sub>], that is thermally unstable at temperatures T > -20°C<sup>35</sup>. A tentative explanation for the observed decomposition products relates to how napy inadequately stabilizes the electron-rich Pd(I)-centers, which is different from aromatic phosphines, e.g. dppm, and PPh<sub>3</sub>, and even from heteroaromatics viz. phen. While a putative [Pd<sub>2</sub>(napy)<sub>n</sub>] 2X' (n = 2, 4, 6) may form, it is likely subject to quick thermal decomposition; thus rendering [Pd<sub>2</sub>(MeCN)<sub>6</sub>] 2BF<sub>4</sub> the better option in context of exploring ligand substitution of a synthon bearing an unsupported Pd-Pd bond as well as labile ligands.

## Conclusion

In closing, we present evidence that supports the notion that napy tether two metals closely together giving rise to distinctive electrochemical redox properties. Spectroscopic and computational analysis suggests that the close Pd-Pd distance is metalphilic in nature but does not constitute a formal bond, following full population of bonding and antibonding metal-metal molecular orbitals. Optical absorption spectroscopy combined with TD-DFT provide insight into the observed excitations. Electrochemical analysis indicates two reversible metal-centered redox events, a consequence of the ligand and the Pd-Pd proximity. From our reactivity studies, it became evident that **1-4X'** does not work as a framework for the formation of neither a Pd<sub>2</sub><sup>6+</sup> nor a Pd<sub>2</sub><sup>2+</sup>-core, despite **1-4X'** demonstrating distinctive redox properties from other paddlewheel complexes. Rather, the reduction of **1-4X'** seem to center on two two distinctive Pd (II) centers that each undergo two-electron reduction (Pd<sup>II/0</sup>), contrasting the formation of a Pd-Pd bond (Pd<sub>2</sub><sup>2+</sup>-core)

324 ASSOCIATED CONTENT

325 (Word Style “TE\_Supporting\_Information”). **Supporting Information.** A listing of the contents  
326 of each file supplied as Supporting Information should be included. For instructions on what  
327 should be included in the Supporting Information as well as how to prepare this material for  
328 publications, refer to the journal’s Instructions for Authors.

329 The following files are available free of charge.

330 brief description (file type, i.e., PDF)

331 brief description (file type, i.e., PDF)

332 AUTHOR INFORMATION

333 **Corresponding Author**

334 **Present Addresses**

335 †If an author’s address is different than the one given in the affiliation line, this information may  
336 be included here.

337 **Author Contributions**

338 The manuscript was written through contributions of all authors. All authors have given approval  
339 to the final version of the manuscript.

340 **Funding Sources**

341 **Notes**

342 ACKNOWLEDGMENT

343 ABBREVIATIONS

344 REFERENCES

- 345 (1) *Multiple Bonds Between Metal Atoms*; Cotton, F. A., Murillo, C. A., Walton, R. A., Eds.;  
346 Springer-Verlag: New York, 2005.
- 347 (2) Lewis, N. S.; Mann, K. R.; Gordon, J. G.; Gray, H. B. *J. Am. Chem. Soc.* **1976**, *98*, 7461–  
348 7463.
- 349 (3) Munakata, M.; Maekawa, M.; Kitagawa, S.; Adachi, M.; Masuda, H. *Inorganica Chim. Acta*  
350 **1990**, *167*, 181–188.
- 351 (4) Griffith, W. P.; Tse Yuen Koh; White, A. J. P.; Williams, D. J. *Polyhedron* **1995**, *14*, 2019–  
352 2025.
- 353 (5) Maekawa, M.; Munakata, M.; Kitagawa, S.; Kuroda-Sowa, T.; Suenaga, Y.; Yamamoto, M.  
354 *Inorganica Chim. Acta* **1998**, *271*, 129–136.
- 355 (6) Koizumi, T.; Tanaka, K. *Inorganica Chim. Acta* **2004**, *357*, 3666–3672.
- 356 (7) Basato, M.; Biffis, A.; Martinati, G.; Tubaro, C.; Graiff, C.; Tiripicchio, A.; Aronica, L. A.;  
357 Caporusso, A. M. *J. Organomet. Chem.* **2006**, *691*, 3464–3471.
- 358 (8) Tubaro, C.; Greggio, G.; Antonello, S.; Graiff, C.; Biffis, A. *Inorganica Chim. Acta* **2017**,  
359 *466*, 578–583.
- 360 (9) Gatteschi, D.; Mealli, C.; Sacconi, L. *J. Am. Chem. Soc.* **1973**, *95*, 2736–2738.
- 361 (10) Mealli, C.; Zanobini, F. *J. Chem. Soc., Chem. Commun.* **1982**, No. 2, 97–98.
- 362 (11) Tiripicchio, A.; Camellini, M. T.; Usón, R.; Oro, L. A.; Ciriano, M. A.; Viguri, F. *J. Chem.*  
363 *Soc., Dalt. Trans.* **1984**, No. 2, 125–131.
- 364 (12) Boelrijk, A. E. M.; van Velzen, M. M.; Neenan, T. X.; Reedijk, J.; Kooijman, H.; Spek, A.  
365 L. *J. Chem. Soc. Chem. Commun.* **1995**, No. 23, 2465.
- 366 (13) Døssing, A.; Larsen, S.; Van Lelieveld, A.; Bruun, R. M. *Acta Chem. Scand.* **1999**, *53*, 230–  
367 234.



- 368 (14) Bencini, A.; Berti, E.; Caneschi, A.; Gatteschi, D.; Giannasi, E.; Invernizzi, I. *Chem. - A*  
369 *Eur. J.* **2002**, 8, 3660.
- 370 (15) Aguirre, J. D.; Lutterman, D. A.; Angeles-Boza, A. M.; Dunbar, K. R.; Turro, C. *Inorg.*  
371 *Chem.* **2007**, 46, 7494–7502.
- 372 (16) Casas, J. M.; Diosdado, B. E.; Forniés, J.; Martín, A.; Rueda, A. J.; Orpen, A. G. *Inorg.*  
373 *Chem.* **2008**, 47, 8767–8775.
- 374 (17) Singh, P.; Clearfield, A.; Bernal, I. *J. Coord. Chem.* **1971**, 1, 29–37.
- 375 (18) Bercaw, J. E.; Durrell, A. C.; Gray, H. B.; Green, J. C.; Hazari, N.; Labinger, J. A.; Winkler,  
376 J. R. *Inorg. Chem.* **2010**, 49, 1801–1810.
- 377 (19) Cotton, F. A.; Gu, J.; Murillo, C. A.; Timmons, D. J. *J. Am. Chem. Soc.* **1998**, 120, 13280–  
378 13281.
- 379 (20) Cotton, F. A.; Matusz, M.; Poli, R.; Feng, X. *J. Am. Chem. Soc.* **1988**, 110, 1144–1154.
- 380 (21) Berry, J. F.; Bill, E.; Bothe, E.; Cotton, F. A.; Dalal, N. S.; Ibragimov, S. A.; Kaur, N.; Liu,  
381 C. Y.; Murillo, C. A.; Nellutla, S.; North, J. M.; Villagrán, D. *J. Am. Chem. Soc.* **2007**, 129,  
382 1393–1401.
- 383 (22) Carrano, J. T.; Wait, S. C. *J. Mol. Spectrosc.* **1973**, 46, 401–418.
- 384 (23) Griffith, W. P.; Koh, T. Y. *J. Raman Spectrosc.* **1995**, 26, 1067–1070.
- 385 (24) Durig, J. R.; Mitchell, B. R.; Sink, D. W.; Willis, J. N.; Wilson, A. S. *Spectrochim. Acta*  
386 *Part A Mol. Spectrosc.* **1967**, 23, 1121–1135.
- 387 (25) Morzyk-Ociepa, B.; Dysz, K.; Turowska-Tyrk, I.; Michalska, D. *J. Mol. Struct.* **2016**, 1103,  
388 202–211.
- 389 (26) Cotton, F. A.; Matusz, M.; Poli, R. *Inorg. Chem.* **1987**, 26, 1472–1474.
- 390 (27) Yao, C. L.; He, L. P.; Korp, J. D.; Bear, J. L. *Inorg. Chem.* **1988**, 27, 4389–4395.

- 391 (28) Dudkina, Y. B.; Kholin, K. V.; Gryaznova, T. V.; Islamov, D. R.; Kataeva, O. N.; Rizvanov,  
392 I. K.; Levitskaya, A. I.; Fominykh, O. D.; Balakina, M. Y.; Sinyashin, O. G.; Budnikova,  
393 Y. H. *Dalt. Trans.* **2017**, *46*, 165–177.
- 394 (29) Cotton, F. A.; Daniels, L. M.; Murillo, C. A.; Timmons, D. J.; Wilkinson, C. C. *J. Am.*  
395 *Chem. Soc.* **2002**, *124*, 9249–9256.
- 396 (30) Budnikova, Y.; Dudkina, Y.; Khrizanforov, M. *Inorganics* **2017**, *5*, 70.
- 397 (31) Wilson, J. J.; Lippard, S. J. *Inorg. Chem.* **2012**, *51*, 9852–9864.
- 398 (32) Murahashi, T.; Nagai, T.; Okuno, T.; Matsutani, T.; Kurosawa, H. *Chem. Commun.* **2000**,  
399 No. 17, 1689–1690.
- 400 (33) Vilar, R.; Mingos, D. M. P.; Cardin, C. J. *J. Chem. Soc. Dalt. Trans.* **1996**, No. 23, 4313–  
401 4314.
- 402 (34) Pringle, P. G.; Shaw, B. L. *J. Chem. Soc., Chem. Commun.* **1982**, No. 1, 81–82.
- 403 (35) Schwalbe, M.; Walther, D.; Schreer, H.; Langer, J.; Görls, H. *J. Organomet. Chem.* **2006**,  
404 *691*, 4868–4873.

# Exploration of an unsymmetric coordination environment in a macrocyclic tetra NHC complex

*Mathias T. Nielsen and Martin Nielsen\**

Department of Chemistry, Technical University of Denmark, 2800 Kgs. Lyngby, Denmark

## KEYWORDS

## ABSTRACT

### Synopsis

### Introduction

Since Hahn's metal-templated synthesis of a divalent platinum complex bearing a macrocyclic tetra *N*-heterocyclic carbene (NHC) ligand<sup>1</sup>, several new structures have emerged, most demonstrating metal coordination resembling that of *N*-porphyrins<sup>2–10</sup>. However, the strongly electron-donating NHC ligands engender an electronic environment distinctive from the *N*-porphyrin congeners<sup>11,12</sup>, apt at stabilizing high-valent metal centers and further supports the formation of multiple metal-ligand bonds, such as Fe (IV) oxo<sup>13</sup> and Fe (IV) imido<sup>14</sup>. The relatively planar structure shared amongst these complexes, lacking any elements inducing steric encumbrance, combined with the reactive metal adducts, often results in the isolation of dimerization adducts, such as  $\mu$ -oxo<sup>15,16</sup> and  $\mu$ -peroxo complexes<sup>17</sup> or negatively affects group-transfer catalysis<sup>18</sup>. Contrariwise, too flexible linkers separating the coordinating ylidine-moieties may yield metal complexes bearing the macrocyclic tetra NHC framework<sup>19</sup>, however,

simultaneously engulfs the metal to an extent that any observed transformation(s) instead is mediated by the ligand<sup>20</sup>.

To leverage the interesting coordination chemistry resulting from complexes bearing macrocyclic tetra NHC ligands, we envisioned a naphthalene-based macrocyclic tetra imidazolium proligand, which when metaled, would induce an unsymmetric coordination environment, following the preclusion of one coordination site. In this paper we present the synthesis of such a proligand, the corresponding Pd (II) metal complex, and additionally, we present our tentative data on the connectivity of the Ag (I) adduct. The hexa silver (I) adduct, mirrors that of related macrocyclic poly imidazole-2-ylidine complexes, and similarly furnish transmetalation to the macrocyclic tetra NHC complex, isolated in significantly higher yields than the direct metalation of the free carbene. Finally, we also report the synthesis and structure of a bischelate analogue, to help us extract properties originating from the macrocyclic ligand.

## Results and discussion

### Synthesis and structural analysis.

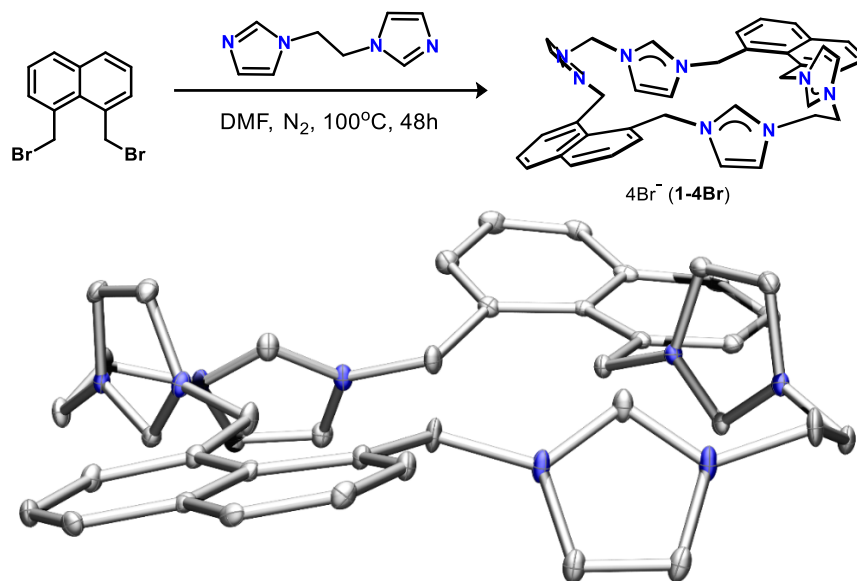


**Figure 1.** Synthesis and solid-state structure of **1-4Br**. Hydrogen atoms and bromide counterions are omitted for clarity. Thermal ellipsoids are set at a 50% probability level. Atom color-coding: N blue, and C grey.

We found that the desired macrocyclic tetra imidazolium proligand, <sup>Naph,Et</sup>LH<sub>4</sub>-4Br, **1-4Br**, is isolable as a white powder in low yields (in up to 10%) following an S<sub>N</sub>2-substitution reaction between 1,8-bis(bromomethyl)naphthalene and 1,2-bisimidazoleethane<sup>21</sup> in a 1:1 mixture in DMF, as shown in the scheme of **Figure 1**. A concentrated methanolic solution of this compound was left for slow solvent evaporation at rt, from which single-crystals suitable for single-crystal X-ray diffraction were collected after a couple of days, corroborating the desired connectivity, as shown in the lower part of **Figure 1**. We attempted other reaction conditions to increase the yield of **1-4Br**, including changing the compound bearing the electrophile and nucleophile, including reacting the stronger electrophile 1,2-triflateoethane<sup>22</sup> with imidazole-functionalized naphthalene, however, found that the initial conditions generally worked the better. The <sup>1</sup>H Nuclear Magnetic Resonance (NMR) spectrum of **1-4Br** (in DMSO-*d*<sub>6</sub>), **Figure S.I.X**, reflects the symmetrical

nature of the compound, and feature a characteristic downfield-shifted signal, which couples to  
 two aromatic signals, consistent with the protons owing to the C<sub>2</sub>, C<sub>4</sub>, and C<sub>5</sub> positions of the  
 imidazolium moiety, respectively. Moreover, the presence of just three aromatic signals, with  
 multiplicities of two doublets and a triplet, is consistent with a symmetrical di-substitution of the  
 naphthalene framework. Finally, two singlets reflect the protons owing to the benzylic and  
 aliphatic linker. These elements taken together, supports that the entity in solution is consistent  
 with the isolated structure. **1-4Br** is water-soluble and readily undergoes salt metathesis in H<sub>2</sub>O  
 with NaPF<sub>6</sub>, precipitating out the corresponding **1-4PF<sub>6</sub>** salt in nearly quantitative yields. Spectral  
 difference between **1-4Br** and **1-PF<sub>6</sub>** is only observed in the <sup>1</sup>H NMR spectrum, centers on the  
 imidazolium C<sub>2</sub> proton, which demonstrates an upfield shift from 9.32 ppm (**1-4Br**) to 8.93 ppm  
 (**1-4PF<sub>6</sub>**).

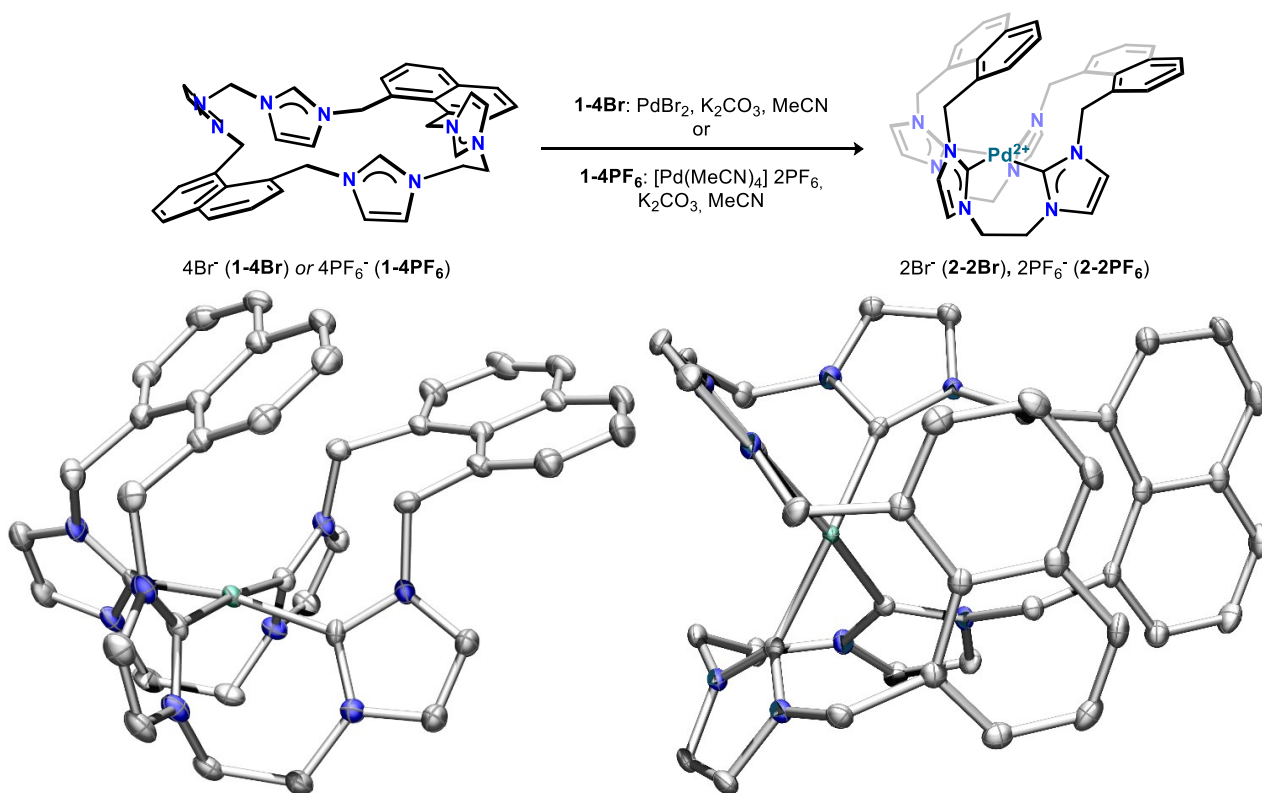


**Figure 2.** *Synthesis and solid-state structure of 2-2Br.* Hydrogen atoms, co-crystallized MeCN, and bromide counterions are omitted for clarity. Thermal ellipsoids are set at a 50% probability level. Atom color-coding: N blue, C grey, and Pd sea green.

Metalation of **1-4Br** and **1-4PF<sub>6</sub>** under mild conditions is readily effected using K<sub>2</sub>CO<sub>3</sub> as a base in presence of PdBr<sub>2</sub> and [Pd(MeCN)<sub>4</sub>] 2PF<sub>6</sub> as shown in the scheme of **Figure 2**, respectively, leading to the isolation of the respective Pd (II) complexes in yields of around 30 - 40%. We successfully characterized the resulting complex as a tetradentate NHC palladium (II) bromide salt <sup>E</sup>LPd-2Br, (**2-2Br**), shown in the lower part of **Figure 2**. The coordination of Pd in **2-2Br** differs from an expected square-planar coordination geometry: considering a mean plane of coordination spanned by the four imidazole-2-ylidines coordinating Pd, the ion resides 0.141 Å above this plane, and each of the four crystallographic different C atoms vary in their Pd-C bond length from 2.026(3) to 2.055(3) Å, which each angle (θ) out of this plane by approximately 4.00°.

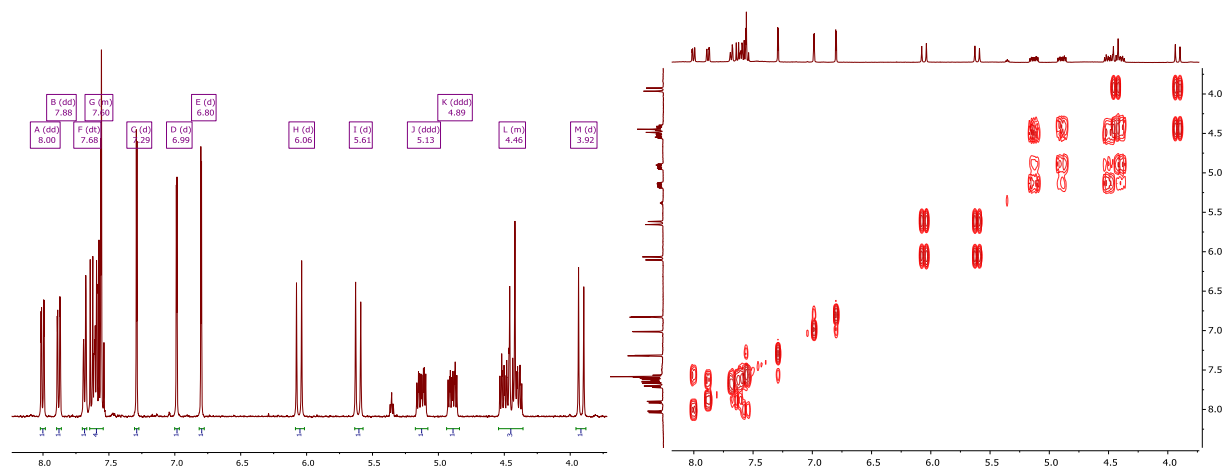


**Figure 4.** <sup>1</sup>H NMR (left) and {<sup>1</sup>H-<sup>1</sup>H} COSY (right) spectra of **2-2PF<sub>6</sub>** (CD<sub>3</sub>CN) featuring resonances and splitting patterns consistent with the solid-state structure presented in **Figure 2**.

The <sup>1</sup>H NMR spectrum of complex **2** is better resolved in MeCN-*d*<sub>3</sub> bearing the PF<sub>6</sub>-counterion, a selected range is shown in **Figure 4**, and may at first glance appear as a mixture, however, {<sup>1</sup>H-<sup>1</sup>H} COSY, shown on the right-hand side of **Figure 4**, establishes a connectivity between the four ddd signals labeled J, K, and L, consistent with two distinctive methylene groups, each proton

experiencing geminal and vicinal couplings. From this observation, we suggest that the solid-state structure shown in **Figure 2**, persists in solution, and the  $^1\text{H}$  NMR spectrum of complex **2-2PF<sub>6</sub>** may be interpreted as the same set of signals appearing in pairs of two, of which one pair is upfield shifted because of the vicinal  $\pi$ -system: the more upfield-shifted protons originate from the “center”, in contrast to the more downfield-shifted signals reflecting the protons at the periphery. To gauge whether the complex demonstrate any fluxional properties in solution, we sought to understand how easily conformational changes are thermally induced, as conceptually illustrated in the scheme in **Figure 5**: does the naphthalene moiety at the “periphery” flip between an endo and exo orientation, resulting in a “breathing” motion rendering any would-be axial coordination available?

To this end, we obtained  $^1\text{H}$  NMR spectra of complex **2-2PF<sub>6</sub>** over a temperature range, varying from -30°C to 70°C, at 20°C interval, the individual spectra stacked and presented in **Figure 5**. Minor changes appear to take place as complex **2-2PF<sub>6</sub>** is heated: transitioning from 243 to 343K, the overlapping aromatic signals appear to split into three discernable signals, the second-most upfield-shifted benzylic proton appear to experience a strong downfield-shift, and all the ethylene signals appear to largely remain unperturbed. The presence of two broad signals at 243K suggests to us, that while the predominant isomer observed is consistent with the solid-state structure, in the sense that the ethylene linkers appear to block one face, the naphthalene units may rapidly “breathe”.



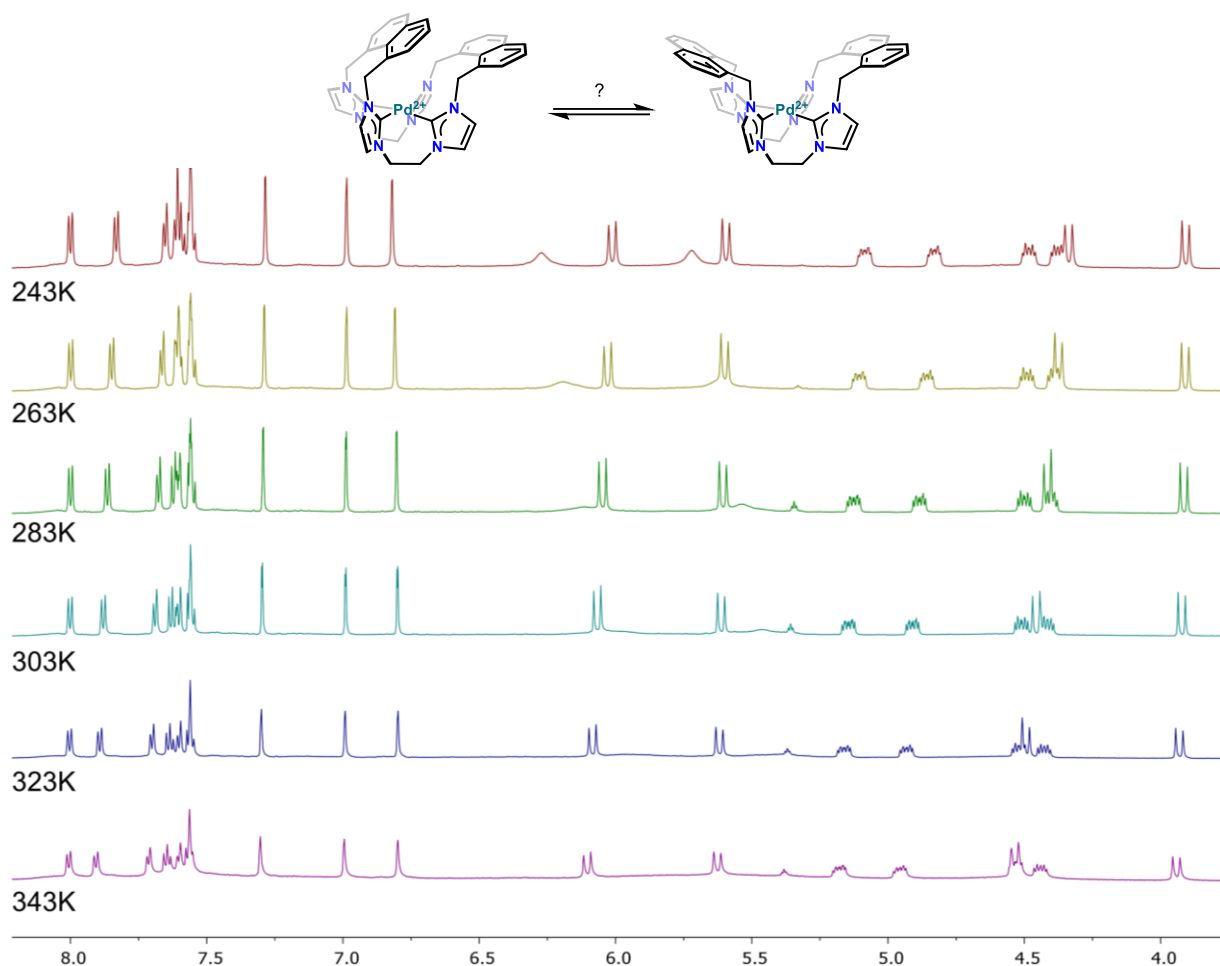
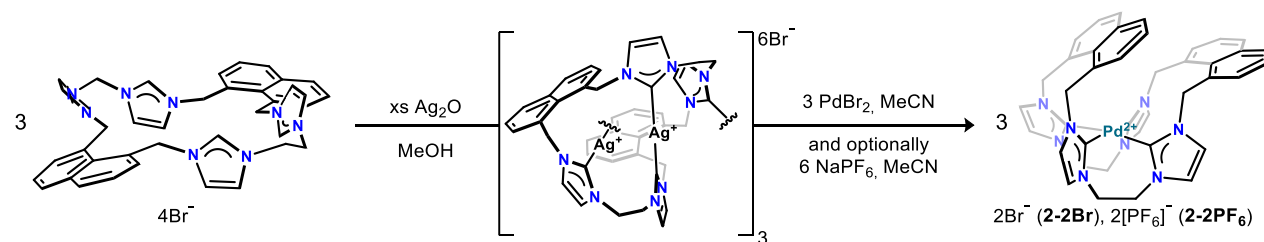


**Figure 5.** Stacked  $^1\text{H}$  NMR spectra (in  $\text{CD}_3\text{CN}$ ) of complex **2-2PF<sub>6</sub>** at selected temperatures. Variable-temperature (VT) NMR may suggest that the endo/exo isomerization is an energetically low-barrier process.

*Transmetalation from Ag-NHC carbene-transfer reagent.*



**Scheme 1.** Transmetalation strategy; intermediary hexasilver (I) complex effects isolation of Pd (II) complex in high yield.

To improve the yield of complexes **2-2Br** and **2-2PF<sub>6</sub>**, we sought to explore transmetalation of parent Ag-NHC carbene-transfer reagents as outlined in **Scheme 1**. Reacting **1-4Br** with a

minimum of 3 equivalents of Ag<sub>2</sub>O furnish the formation of a new, isolable, and quite light-sensitive colorless salt, which effect transmetalation into either **2-2Br** or **2-2PF<sub>6</sub>** in up to ~80% isolated yield. Despite that the <sup>1</sup>H and <sup>13</sup>C NMR spectra are telling of two distinctive chemical environments from the occurrence of the same signals in pair of two viz. the signals attributable to the naphthalene-moiety, of which one pair is upfield-shifted in the <sup>1</sup>H spectrum, in conjunction with the presence of four downfield-shifted resonances ( $\delta > 160$  ppm), in support of silver complexation<sup>23–25</sup>[The spectrum will be re-recorded at 201MHz, prior to submission], NMR is inadequate in discerning a potential dimer from a polymers. We were able to isolate a few crystals suitable for X-ray diffraction, rendering us able to corroborate that the connectivity of the intermediate is a trimer, as suggested in the center-most structure in **Scheme 1**; an ORTEP drawing is included in the supporting information, **Figure S.I.X**. However, we experience morphological changes during diffraction, likely from expulsion of co-crystallized solvent and/or reduction of Ag (turning grey) during diffraction, precluding meaningful discussion on bonding metrics following an incomplete dataset as of now. The bonding motif resembles that reported by the Jenkins group, where each macrocycle features a silver (I) ion tethering the macrocycle to itself<sup>26</sup>.

*Synthesis and analysis of a chelate-analogue.* In parallel, we sought to prepare an appropriate bischelate analog to the macrocyclic complex, [<sup>Et</sup>L<sub>2</sub>Pd] 2PF<sub>6</sub>, **3**, as outlined in in the scheme of **Figure 6**, to compare structural and (electro)chemical properties with complex **2**. Reacting 1,2-bisimidazolethane with benzyl bromide in MeCN effects precipitation of a dibromide-salt, which added NaPF<sub>6</sub> in water precipitates out the corresponding PF<sub>6</sub>-salt in quantitative yields. This PF<sub>6</sub>-salt, readily metalates with Ag<sub>2</sub>O in MeCN, yielding a light-sensitive compound, which transmetalates into the bischelating palladium (II) complex of **3**. Leaving a saturated solution of complex **3** in MeCN for slow solvent evaporation at rt, leaves colorless crystals suitable for X-ray

diffraction after a couple of days, the structure shown in the lower insert of **Figure 6**. The two symmetry-related chelating ligands coordinate Pd (II) in a square-planar fashion, with no bond-angle deviation from the mean plane of coordination, otherwise seen in **2** ( $\theta = 0^\circ$ ). The bond lengths of **3** are quite different, at 2.019(2) and 2.056(2) Å, respectively, however, are comparable to that of **2**. The solid-state structure of **3**, matches the entity found in solution from a diastereotopic splitting of the protons owing just to the aliphatic linker, from a vicinal and geminal coupling pattern, suggesting that parts of the molecule is rigid at rt. Another difference between **2** and **3** relates to the relative orientation of the aliphatic linker; whereas **2** features a parallel downwards orientation, the opposite is found in **3**.

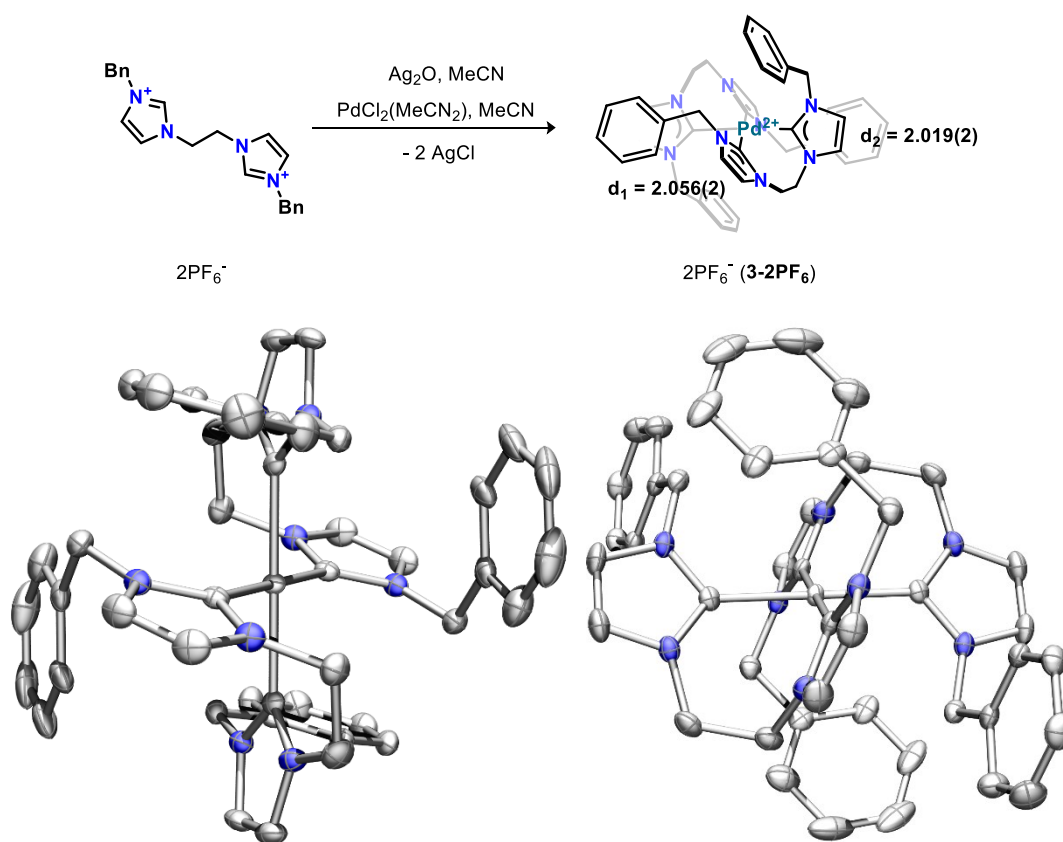


**Figure 3.** *Synthesis and solid-state structure of 3.* Hydrogen atoms, co-crystallized MeCN, and  $\text{PF}_6^-$ -counterions are omitted for clarity. Thermal ellipsoids are set at a 50% probability level. Atom color-coding: Pd sea green, N blue, and C grey.

*Electrochemical properties.* [This part is still missing, however, emphasizes on the electrochemical properties of each complex and their differences. CV will be obtained in MeCN and 1,2-difluorobenzene. Further, initial preliminary stoichiometric studies suggests that complex 2 support oxidation by hypervalent iodanes (PhICl<sub>2</sub>), however, the complex quickly decompose, destroying the complex in the process].

## **Conclusion**

In closing, we have demonstrated the synthesis of a novel naphthalene-based macrocyclic tetra imidazolium proligand effected from an S<sub>N</sub>2-substitution reaction between readily prepared precursors, 1,8-bis(bromomethyl)naphthalene and 1,2-bisimidazoleethane. This proligand readily metalates under mild conditions into a monometallic complex bearing a macrocyclic tetra NHC ligand, when bearing a Pd (II) ion deviates from the expected square-planar coordination. A higher yield of up to 80% was isolated when transmetalating *via* an intermediary Ag (I) adduct, which we found comprise of a hexasilver(I) adduct adjoining three macrocycles. The structure of the Pd (II) complex is quite interesting as VT NMR studies suggest that the ligand induce an unsymmetric binding pocket, as the ethyl-moieties separating the ylidines are fixed in place, whereas the naphthalene moieties rapidly isomerize between endo and exo positions. [The electrochemical properties of the complex are different from a bischelating analogue, suggesting that X and Y.] We are currently exploring coordination chemistry of other metal complexes bearing this peculiar ligand system.

## **ASSOCIATED CONTENT**

**Supporting Information.** A listing of the contents of each file supplied as Supporting Information should be included. For instructions on what should be included in the Supporting

174 Information as well as how to prepare this material for publications, refer to the journal's

175 Instructions for Authors.

176 The following files are available free of charge.

177 brief description (file type, i.e., PDF)

178 brief description (file type, i.e., PDF)

179 **AUTHOR INFORMATION**

180 **Corresponding Author**

181 **Present Addresses**

182 **Author Contributions**

183 The manuscript was written through contributions of both authors. Both authors have given

184 approval to the final version of the manuscript.

185 **Funding Sources**

186 **Notes**

187 **ACKNOWLEDGMENT**

188 M.T.N and M.N would like to thank PhD K. Enemark-Rasmussen for help acquiring VT NMR

189 data. M.T.N. gratefully acknowledges the Taumose Instrumentation Scholarship for partial

190 funding towards the acquisition of a WaveDriver ® 100 Potentiostat/Galvanostat from Pine

191 Research.

192 **ABBREVIATIONS**

193 NHC, N-heterocyclic carbene; NMR, Nuclear Magnetic Resonance.

## 194 REFERENCES

- 195 (1) Hahn, F. E.; Langenhahn, V.; Lügger, T.; Pape, T.; Le Van, D. *Angew. Chemie Int. Ed.*  
196 **2005**, *44*, 3759–3763.
- 197 (2) Cramer, S. A.; Jenkins, D. M. *J. Am. Chem. Soc.* **2011**, *133*, 19342–19345.
- 198 (3) Bass, H. M.; Cramer, S. A.; McCullough, A. S.; Bernstein, K. J.; Murdock, C. R.; Jenkins,  
199 D. M. *Organometallics* **2013**, *32*, 2160–2167.
- 200 (4) Schulte to Brinke, C.; Ekkehardt Hahn, F. *Dalt. Trans.* **2015**, *44*, 14315–14322.
- 201 (5) Anneser, M. R.; Haslinger, S.; Pöthig, A.; Cokoja, M.; Basset, J.-M.; Kühn, F. E. *Inorg.*  
202 *Chem.* **2015**, *54*, 3797–3804.
- 203 (6) Fei, F.; Lu, T.; Chen, X.-T.; Xue, Z.-L. *New J. Chem.* **2017**, *41*, 13442–13453.
- 204 (7) Mageed, A. H.; Skelton, B. W.; Baker, M. V. *Dalt. Trans.* **2017**, *46*, 7844–7856.
- 205 (8) Li, Z.; Wiratpruk, N.; Barnard, P. J. *Front. Chem.* **2019**, *7*.
- 206 (9) DeJesus, J. F.; Jenkins, D. M. *Chem. - A Eur. J.* **2020**, *26*, 1429–1435.
- 207 (10) Blatchford, K. M.; Mize, C. J.; Roy, S.; Jenkins, D. M. *Dalt. Trans.* **2022**, *51*, 6153–6156.
- 208 (11) Ye, S.; Kupper, C.; Meyer, S.; Andris, E.; Navrátil, R.; Krahe, O.; Mondal, B.; Atanasov,  
209 M.; Bill, E.; Roithová, J.; Meyer, F.; Neese, F. *J. Am. Chem. Soc.* **2016**.
- 210 (12) Kupper, C.; Mondal, B.; Serrano-Plana, J.; Klawitter, I.; Neese, F.; Costas, M.; Ye, S.;  
211 Meyer, F. *J. Am. Chem. Soc.* **2017**.
- 212 (13) Meyer, S.; Klawitter, I.; Demeshko, S.; Bill, E.; Meyer, F. *Angew. Chemie Int. Ed.* **2013**,  
213 *52*, 901–905.
- 214 (14) Anneser, M. R.; Elpitiya, G. R.; Townsend, J.; Johnson, E. J.; Powers, X. B.; DeJesus, J. F.;  
215 Vogiatzis, K. D.; Jenkins, D. M. *Angew. Chemie Int. Ed.* **2019**, *58*, 8115–8118.
- 216 (15) Anneser, M. R.; Haslinger, S.; Pöthig, A.; Cokoja, M.; D’Elia, V.; Högerl, M. P.; Basset,  
217 J.-M.; Kühn, F. E. *Dalt. Trans.* **2016**, *45*, 6449–6455.
- 218 (16) Schlachta, T. P.; Anneser, M. R.; Schlagintweit, J. F.; Jakob, C. H. G.; Hintermeier, C.;  
219 Böth, A. D.; Haslinger, S.; Reich, R. M.; Kühn, F. E. *Chem. Commun.* **2021**, *57*, 6644–  
220 6647.
- 221 (17) Schlagintweit, J. F.; Altmann, P. J.; Böth, A. D.; Hofmann, B. J.; Jandl, C.; Kaußler, C.;  
222 Nguyen, L.; Reich, R. M.; Pöthig, A.; Kühn, F. E. *Chem. – A Eur. J.* **2021**, *27*, 1311–1315.
- 223 (18) Cramer, S. A.; Hernández Sánchez, R.; Brakhage, D. F.; Jenkins, D. M. *Chem. Commun.*  
224 **2014**, *50*, 13967–13970.

- 225 (19) McKie, R.; Murphy, J. A.; Park, S. R.; Spicer, M. D.; Zhou, S. *Angew. Chemie Int. Ed.*  
226 **2007**, *46*, 6525–6528.
- 227 (20) Findlay, N. J.; Park, S. R.; Schoenebeck, F.; Cahard, E.; Zhou, S.; Berlouis, L. E. A.; Spicer,  
228 M. D.; Tuttle, T.; Murphy, J. A. *J. Am. Chem. Soc.* **2010**, *132*, 15462–15464.
- 229 (21) Ortiz, A.; Gómez-Sal, P.; Flores, J. C.; de Jesús, E. *Organometallics* **2018**, *37*, 3598–3610.
- 230 (22) Kuroboshi, M.; Kondo, T.; Tanaka, H. *Heterocycles* **2015**, *90*, 723–729.
- 231 (23) Arduengo, A. J.; Dias, H. V. R.; Calabrese, J. C.; Davidson, F. *Organometallics* **1993**, *12*,  
232 3405–3409.
- 233 (24) Caballero, A.; Díez-Barra, E.; Jalón, F. A.; Merino, S.; Tejeda, J. *J. Organomet. Chem.*  
234 **2001**, *617–618*, 395–398.
- 235 (25) Wanniarachchi, Y. A.; Khan, M. A.; Slaughter, L. M. *Organometallics* **2004**, *23*, 5881–  
236 5884.
- 237 (26) Lu, Z.; Cramer, S. A.; Jenkins, D. M. *Chem. Sci.* **2012**, *3*, 3081–3087.
- 238 sss

1 A surprisingly stable organometallic Ni(III) complex  
2 bearing a macrocyclic tetra *N*-heterocyclic ligand

3 *Mathias T. Nielsen<sup>1</sup>, Mike S. B. Jørgensen<sup>1</sup>, Nick Litak<sup>2</sup>, Shao-Liang Zheng<sup>2</sup>, Susanne L.*  
4 *Mossin<sup>1</sup>, and Martin Nielsen<sup>1\*</sup>*

5 **AUTHOR ADDRESS**

6 1: Department of Chemistry, Technical University of Denmark, 2800 Kgs. Lyngby, Denmark

7 2: Department of Chemistry and Chemical Biology, Harvard University, 12 Oxford St.,  
8 Cambridge, MA 02138 (USA)

9 **KEYWORDS**

10 **ABSTRACT.**

11 **Synopsis**

12



## Introduction

Organometallic complexes featuring low-valent Ni centers (oxidation states 0, I, and II) are ubiquitous, and commonly encountered as (pre) catalysts for C-X bond formation reactions, *e.g.* Negishi, Stille, and Suzuki-Miyaura couplings. Since the isolation of the first organometallic Ni<sup>III</sup> complex by Koten and co-workers<sup>1</sup>, the interest towards the higher oxidation states *viz.* Ni<sup>III</sup> and Ni<sup>IV</sup> has increased, as such complexes may also mediate the (catalytical) formation of new C-X bonds<sup>2-7</sup>. Additionally, Ni<sup>II</sup> complexes bearing inverted *N*-porphyrin ligands similarly render the characterization of *bona fide* Ni<sup>III</sup> complexes tractable, as demonstrated by Latos-Grazynski and co-worker<sup>8</sup>, Dolphin and co-workers<sup>9</sup>, as well as by Ke, Jiang, and Osuka co-workers<sup>10</sup>. Macrocyclic *N*-heterocyclic carbenes (NHCs) share a similar ligand architecture to (inverted) *N*-porphyrins, and are well-known as aptly stabilizing high-valent metal adducts, such as Fe (IV) oxo<sup>11</sup> and Fe (IV) imido<sup>12</sup>, and even Cu attributed a formal 3+ oxidation state<sup>13,14</sup>. Despite several reported Ni<sup>II</sup> complexes bearing macrocyclic tetra NHC ligands<sup>15-19</sup> studies on their high-valent adducts remain undisclosed.

In this paper, we outline the synthesis and characterization of a novel naphthalene-based tetraimidazolium proligand, the corresponding Ni<sup>II</sup> adduct, as well as the unusual oxidation of this Ni<sup>II</sup> complex with Br<sub>2</sub> resulting in a surprisingly air and water stable Ni<sup>III</sup> complex bearing formally neutral ligands, its characterization and ligand substitution reactions.

## Results and discussion

*Synthesis and solid-state structure of Ni(II).* The desired macrocyclic-proligand is isolable as the tetraazolium salt (LH<sub>4</sub>-4Br, **1-4Br**) in moderate yields of approximately 15%, effected from the *n*Bu<sub>4</sub>NBr template-assisted self-assembly reaction between 1,1'-diimidazole methane and 1,8-dibromomethylnaphtalene in DMF over 48 hours, as shown in the scheme of **Figure 1**.

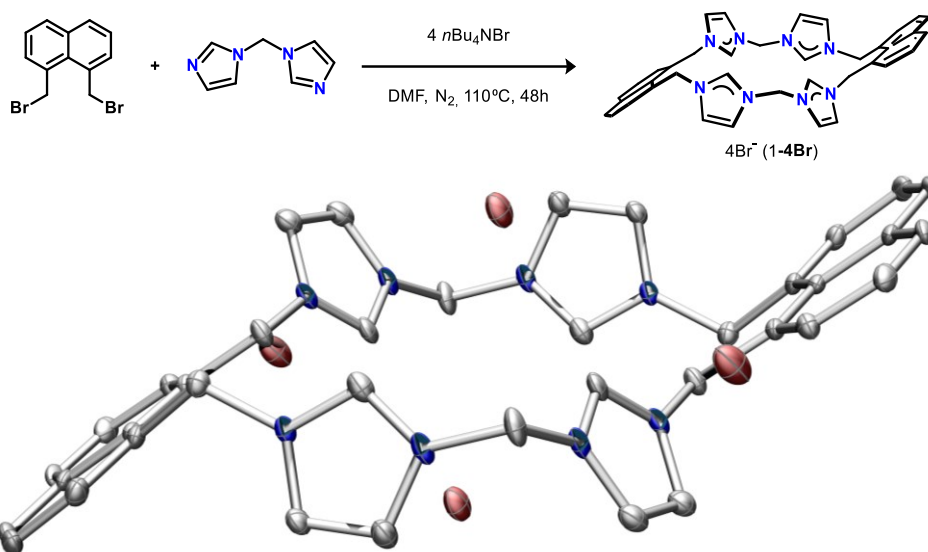


**Figure 1.** *Synthesis and solid-state structure of 1-4Br.* Hydrogen atoms and bromide counterions are omitted for clarity. Thermal ellipsoids are set at a 50% probability level. Atom color-coding: N blue, and C grey.

A concentrated methanolic solution of this compound was left for slow solvent evaporation at rt, from which single-crystals suitable for single-crystal X-ray diffraction were collected after a couple of days, corroborating the desired connectivity, as shown in the lower part of **Figure 1**. The <sup>1</sup>H Nuclear Magnetic Resonance (NMR) spectrum of **1-4Br** (in DMSO-*d*<sub>6</sub>), **Figure S.I.X**, reflects the symmetrical nature of the compound, and feature three broad signals characteristic for the protons owing to the C<sub>2</sub>, C<sub>4</sub>, and C<sub>5</sub> positions of the imidazolium moiety, respectively. Additionally, the aromatic region contains just three signals featuring multiplicities of two doublets and a triplet, which is consistent with a symmetrical di-substitution of the naphthalene moiety.

Finally, two singlets reflect the protons owing to the benzylic and aliphatic linker. These elements taken together, supports that the entity in solution is consistent with the isolated structure. Salt metathesis is readily effected by adding *e.g.* NaPF<sub>6</sub> to an aqueous solution of **1-4Br**, precipitating out the corresponding **1-4PF<sub>6</sub>** salt in quantitative yields. Treating **1-4PF<sub>6</sub>** to a mild base such as K<sub>2</sub>CO<sub>3</sub> in presence of NiCl<sub>2</sub>(glyme) in MeCN effects the transformation of **1-4PF<sub>6</sub>** into the Ni (II) complex bearing a macrocyclic tetra NHC ligand, LNi-2PF<sub>6</sub> **2-2PF<sub>6</sub>**, isolable as a colorless powder in decent yield of ~40%. Amongst the different metalation pathways relevant to NHC complexes, we found that transmetalation results in the highest yield of complex **2-2PF<sub>6</sub>**, as outlined in the scheme of **Figure 2**. Leaving a concentrated fraction of this reaction mixture for slow solvent evaporation at rt, left single-crystals suitable for X-ray diffraction after a couple of days, authenticating the connectivity of the Ni (II) complex, as shown in the lower part of **Figure 2**.

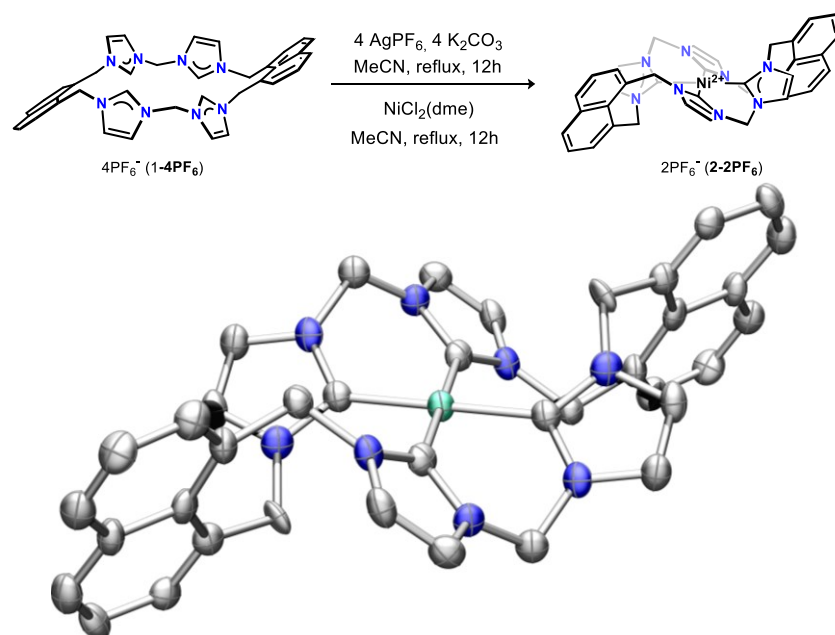


**Figure 2.** *Synthesis and solid-state of complex 2-2PF<sub>6</sub>*. One of the two crystallographic distinctive macrocycles, co-crystallized MeCN, hydrogen atoms, and PF<sub>6</sub>-counterions are omitted for clarity. Thermal ellipsoids are set at a 50% probability level. Atom color-coding: Ni aquamarine, N blue, and C grey.

As evident from **Figure 2**, complex **2-2PF<sub>6</sub>** feature a Ni (II) ion coordinated in a square-planar fashion by the macrocyclic tetra NHC ligand, demonstrating Ni-C bond lengths between 1.907(7) to 1.928(9) Å. These bond lengths compare well with similar structures reported by the groups of Murphy and Spicer<sup>15</sup>, Jenkins<sup>16,17</sup>, Hahn<sup>18</sup>, and Kühn<sup>19</sup>, varying from 1.851Å to 1.938Å. Other reports encompassing base metal complexes bearing macrocyclic tetra NHC ligands have been shown to support high-valent metal adducts, and accordingly, we wanted to explore whether our framework would render the isolation high-valent Ni-adducts possible. Based on cyclic voltammetry, **Figure S.I.X**, two oxidation waves >1V vs. Fc<sup>+0</sup>, are discernable, supporting this idea. It was then rather curious, that as a solution of **2-2PF<sub>6</sub>** was treated with 0.5 equivalents of Br<sub>2</sub>, as shown in the scheme of **Figure 3**, the resonance of the <sup>1</sup>H NMR spectrum became broad and featureless indicative of a paramagnetic species; addition of excess Br<sub>2</sub> (0.5, 1, 2 ... 5) neither transforms this entity into a diamagnetic entity nor facilitate decomposition, see **Figure S.I.X**. This transformation proceeds under strictly inert conditions, however, more interestingly, also possible under ambient conditions in wet reagents. Encouragingly, we were able to authenticate the paramagnetic species as a Ni (III) complex, **3**, as shown in the lower part of **Figure 3**. From **Figure 3**, complex **3** features Ni in a distorted octahedral coordination environment consistent with a tetragonal distortion from the slight a elongation of the ligand bond lengths along the basal plane (Ni-C), and a much larger elongation along the axial direction. Such a distortion is consistent with a low-spin *d*<sup>7</sup> electronic configuration where the SOMO comprise a Ni-centered *d*(*z*<sup>2</sup>)-atomic orbital<sup>20</sup>. Surprisingly, solvent occupy the axial coordination sites, and the Ni<sup>3+</sup> complex is surrounded by three outer sphere Br<sub>3</sub>-counterions.

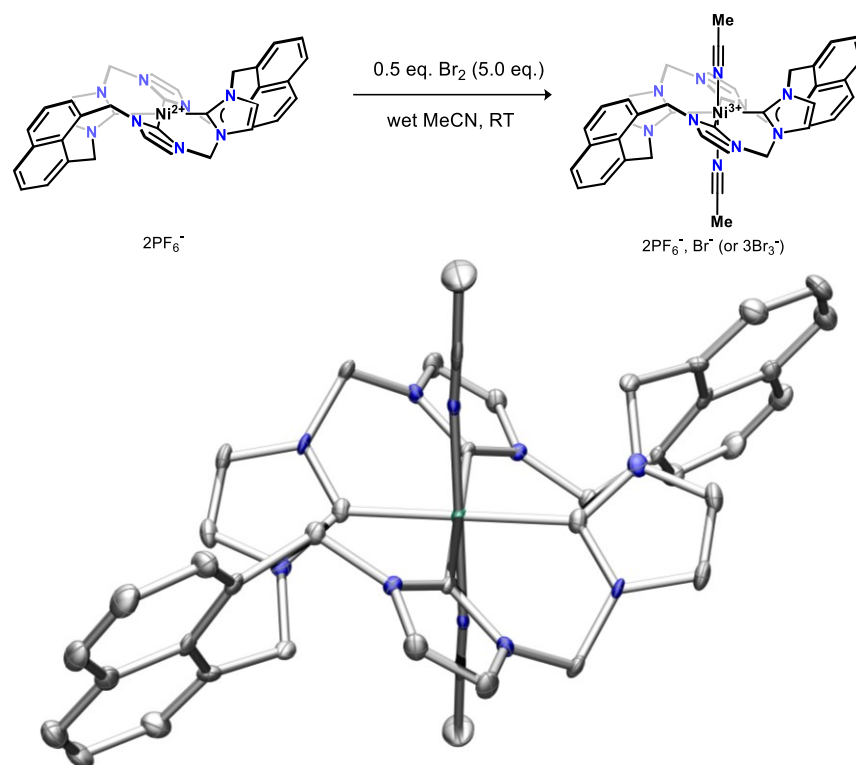


**Figure 3.** *Synthesis and solid-state structure of complex 3.* Hydrogen atoms, co-crystallized MeCN, and Br<sub>3</sub>-counterions are omitted for clarity. Thermal ellipsoids are set at a 50% probability level. Atom color-coding: N blue, C grey, and Ni aquamarine.

To address whether Br<sub>2</sub> act as a one-electron outer sphere oxidant and additionally, to obtain further insights into its electronic properties of the complex, we analyzed **3** through quantitative EPR spectroscopy. To this end, in air, using wet reagents, complex **2-2PF<sub>6</sub>** was dissolved in MeCN, and added 1.1 equiv. Br<sub>2</sub>, lightly shaken, and then quickly frozen in liquid N<sub>2</sub> (within 10 seconds) before its EPR spectrum was measured, shown on the left-hand side of **Figure 4**. Complex **2-2PF<sub>6</sub>** features no EPR signals, and quantification of the measured EPR signal, works to establish, that 100% of complex **2-2PF<sub>6</sub>** is converted into **3**.

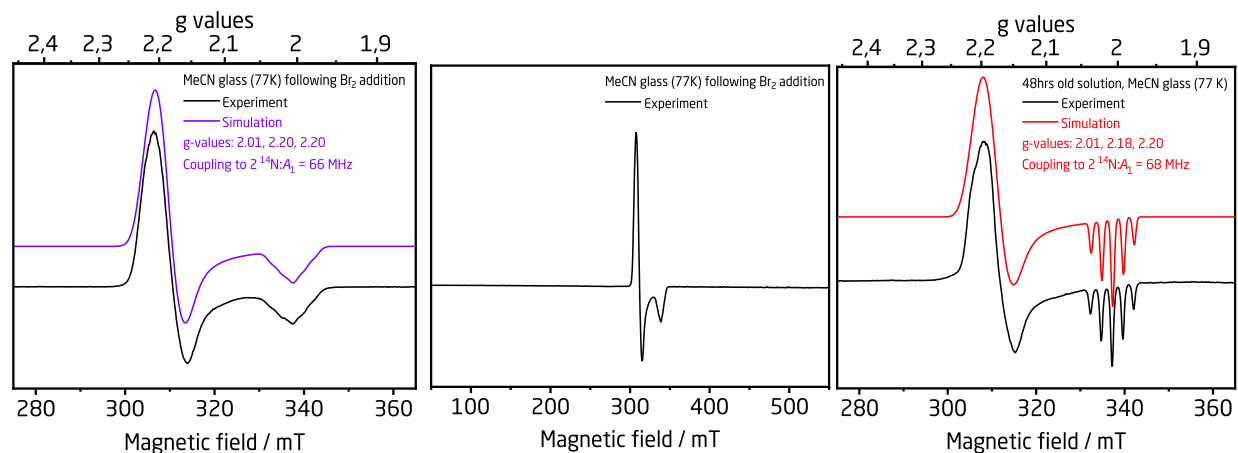


**Figure 4.** EPR spectra of complex 3. Left-hand spectrum: immediately following addition of excess Br<sub>2</sub>; center: broad field scan; right-hand: the same solution after 48hr at rt.

As evident from **Figure 4**, complex 3 features a metal-centered radical, as the g-factor values deviate from 2.00, consistent with a ground state doublet term ( $S = 1/2$ ,  $S_{\text{mult}} = 2$ ) demonstrating axial anisotropy ( $g_{\perp} > g_{\parallel}$ ). The absence of any half-field signals at g-values of approximately 4.4 (center spectrum of **Figure 4**), further substantiates that the strongly binding NHC ligands induce a low-spin electronic configuration. The left-hand spectrum of **Figure 4**, albeit poorly resolved, demonstrates a super hyperfine coupling to two <sup>14</sup>N ( $I = 1$ ) atoms, owing to MeCN, manifesting in a pentet, readily modelled with EasySpin<sup>21,22</sup>. This super hyperfine coupling corroborates that any bromide ions are outer sphere. This solution was left for 48 hours under ambient conditions, before the solution was frozen and an EPR spectrum was re-recorded, right-hand spectrum of **Figure 4**. This spectrum features the same spectral properties as the “fresh” solution, however, the super hyperfine coupling to <sup>14</sup>N is much better resolved. Still, this spectrum lacks splitting owing to hyperfine coupling to <sup>61</sup>Ni ( $I = 3/2$ ), and splitting owing to any super hyperfine coupling to <sup>13</sup>C ( $I = 1/2$ ), a consequence of their low abundance of ~1%. We sought to probe whether we could effect ligand substitution of MeCN by adding pyridine and KCN. Curiously, the MeCN molecules appear quite strongly bound as evident from the spectrum of **Figure 5**, as no change happen upon addition of pyridine nor KCN. While pyridine may not spatially fit, however, the <sup>-</sup>CN ion would. It is likely

that the MeCN molecules impart sufficient stability to the complex, which would also provide an explanation as to why Br<sub>2</sub> is able to oxidize the complex having such a low oxidation potential in MeCN<sup>23</sup>.

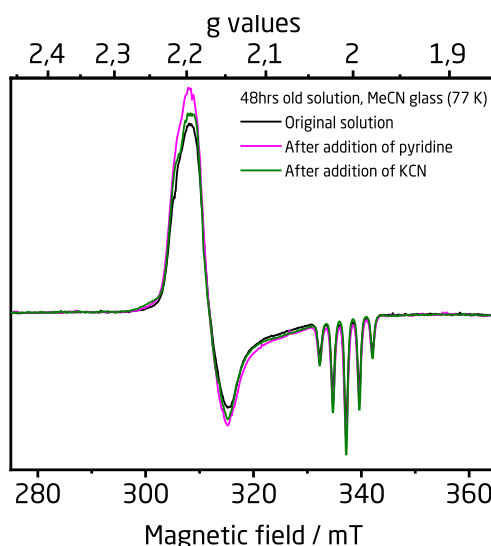


**Figure 5.** Substitution reactions of complex **3** with various nucleophiles. No change in super hyperfine coupling is observed upon addition of excess KCN, suggesting that MeCN are strongly bound.

We were computationally able to reproduce a Ni-centered radical corroborating that **3** genuinely feature a “naked” Ni<sup>3+</sup>-ion coordinated by formally neutral ligands, as none of the spin reside on neither the NHC, as evident from **Figure 6**, showing the symmetry of the SOMO matching the expected Ni-centered *d*(*z*<sup>2</sup>)-atomic orbital, which is further reflected from the spin-density plot.

Stable organometallic Ni (III) complexes are well-described in the literature, however, the reactivity of complex **3** is quite different to these. Complex **3** is surprisingly stable towards moisture, as no noticeable decomposition was observed when refluxing the complex in wet acetonitrile for an extended period of time (> 1hr).

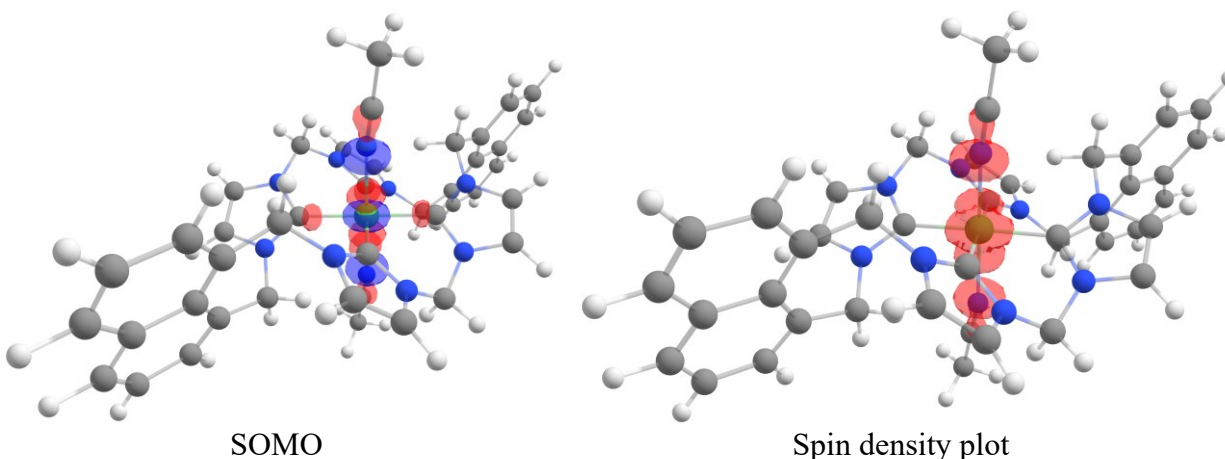
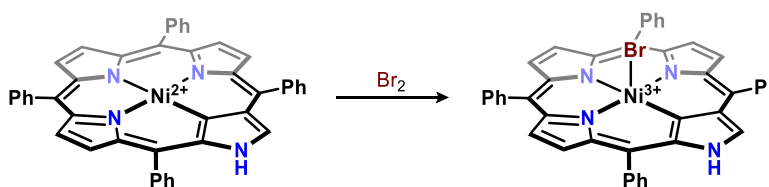


**Figure 6.** DFT-calculated SOMO and spin-density plot. The SOMO symmetry is consistent with a low-spin d7 configuration, which feature the majority spin-density at the Ni-center.

Second, while Br<sub>2</sub> oxidizes **3**, this transformation appears to happen through a one-electron outer-sphere differently from the oxidation of related Ni (II) complexes bearing “inverted” *N*-porphyrins. Latos-Grazynski used EPR to characterize the *in situ* generated Ni (III) adducts following single-electron oxidation by Br<sub>2</sub>, as in **Scheme 1**, and CAN, and subsequent ligand substitution reactions<sup>8</sup>. In each reaction, the Ni (III) adduct is bound by the respective ligand of interest, *e.g.* Br, CN, NO<sub>3</sub>, OH, H<sub>2</sub>O.



**Scheme 1.** Oxidation of Ni (II) bearing an inverted *N*-porphyrin. Complexes were only characterized *in situ*, as such the connectivity of is only suggestive of the actual structure.

Similarly, two other well-characterized Ni (III) complexes bearing this ligand architecture are known by Dolphin<sup>9</sup>, as well as by Ke, Jiang, and Osuka<sup>10</sup>, which both demonstrate stabilization of the resulting Ni (III) complex through coordination of formally anionic ligands. The reactivity of these related complexes, when juxtaposed to that of **3** really emphasize the complex’ rather odd



149 reactivity. All taken together, the results corroborates that the oxidation of complex **2-2PF<sub>6</sub>** with  
150 Br<sub>2</sub> yields a complex bearing a “naked” Ni (III) ion, a rather curious result.

## 151 **Conclusion**

152 In closing, we have presented the synthesis of a novel naphthalene-based macrocyclic  
153 tetraimidazolium salt, which readily undergoes metalation with Ni (II) in varying yields, of which  
154 transmetalation through an in-situ generated Ag (I) adduct renders the isolation of complex **2-2PF<sub>6</sub>**  
155 possible in good yield ~80%. Treating this complex to Br<sub>2</sub> instantaneously oxidizes complex **2** into  
156 the corresponding Ni<sup>3+</sup>-complex, through a putative single-electron, outer-sphere mechanism. The  
157 Ni (III) compound was characterized by a myriad of different techniques all corroborating a  
158 “naked” Ni (III) complex insofar as that all charge is centered on the Ni-ion; the MeCN ligands  
159 appear to strongly bind, as we were unable in substituting them with stronger ligands, *e.g.* <sup>-</sup>CN.  
160 Further studies pertaining to this complex are in preparation as of the writing of this manuscript,  
161 including the connectivity of the silver intermediate, ligand substitution of complex **3**, and the  
162 isolation of Ni<sup>IV</sup>-adducts.

164    **Experimental section**

165    *Methods and materials.*

166    *X-ray Crystallographic Analysis*

167    *Density-functional theory*

168    *Attenuated-Total-Reflection Fourier Transform Infrared Spectroscopy*

169    *Electrochemical studies.*

170    ASSOCIATED CONTENT

171    **Supporting Information.**

172    The following files are available free of charge. brief description (file type, i.e., PDF) brief  
173    description (file type, i.e., PDF)

174    AUTHOR INFORMATION

175    **Corresponding Author**

176    Give contact information for the author(s) to whom correspondence should be addressed.

177    **Present Addresses**

178    †If an author's address is different than the one given in the affiliation line, this information may  
179    be included here.

180    **Author Contributions**

181    The manuscript was written through contributions of all authors. All authors have given approval  
182    to the final version of the manuscript.

183   **Funding Sources**

184   **Notes**

185   Any additional relevant notes should be placed here.

186   **ACKNOWLEDGMENT**

187   **ABBREVIATIONS**

188   NHC, *N*-heterocyclic carbene; NMR, Nuclear Magnetic Resonance.

189   **REFERENCES**

- 190   (1)   Grove, D. M.; Van Koten, G.; Zoet, R.; Murrall, N. W.; Welch, A. J. *J. Am. Chem. Soc.*  
191       **1983**, *105*, 1379–1380.
- 192   (2)   Bour, J. R.; Camasso, N. M.; Meucci, E. A.; Kampf, J. W.; Canty, A. J.; Sanford, M. S. *J.*  
193       *Am. Chem. Soc.* **2016**, *138*, 16105–16111.
- 194   (3)   Schultz, J. W.; Fuchigami, K.; Zheng, B.; Rath, N. P.; Mirica, L. M. *J. Am. Chem. Soc.*  
195       **2016**, *138*, 12928–12934.
- 196   (4)   Corona, T.; Draksharapu, A.; Padamati, S. K.; Gamba, I.; Martin-Diaconescu, V.; Acuña-  
197       Parés, F.; Browne, W. R.; Company, A. *J. Am. Chem. Soc.* **2016**, *138*, 12987–12996.
- 198   (5)   Diccianni, J. B.; Hu, C.; Diao, T. *Angew. Chemie Int. Ed.* **2017**, *56*, 3635–3639.
- 199   (6)   Smith, S. M.; Planas, O.; Gómez, L.; Rath, N. P.; Ribas, X.; Mirica, L. M. *Chem. Sci.* **2019**,  
200       *10*, 10366–10372.
- 201   (7)   Roberts, C. C.; Camasso, N. M.; Bowes, E. G.; Sanford, M. S. *Angew. Chemie Int. Ed.* **2019**,  
202       *58*, 9104–9108.
- 203   (8)   Chmielewski, P. J.; Latos-Grażyński, L. *Inorg. Chem.* **1997**, *36*, 840–845.
- 204   (9)   Xiao, Z.; Patrick, B. O.; Dolphin, D. *Inorg. Chem.* **2003**, *42*, 8125–8127.

- 205 (10) He, H.; Ye, Z.; Shimizu, D.; Sumra, I.; Zhang, Y.; Liang, Z.; Zeng, Y.; Xu, L.; Osuka, A.;  
206 Ke, Z.; Jiang, H.-W. *Chem. – A Eur. J.* **2022**, *28*, e202103272.
- 207 (11) Meyer, S.; Klawitter, I.; Demeshko, S.; Bill, E.; Meyer, F. *Angew. Chemie Int. Ed.* **2013**,  
208 *52*, 901–905.
- 209 (12) Anneser, M. R.; Elpitiya, G. R.; Townsend, J.; Johnson, E. J.; Powers, X. B.; DeJesus, J. F.;  
210 Vogiatzis, K. D.; Jenkins, D. M. *Angew. Chemie Int. Ed.* **2019**, *58*, 8115–8118.
- 211 (13) Ghavami, Z. S.; Anneser, M. R.; Kaiser, F.; Altmann, P. J.; Hofmann, B. J.; Schlagintweit,  
212 J. F.; Grivani, G.; Kühn, F. E. *Chem. Sci.* **2018**, *9*, 8307–8314.
- 213 (14) Geoghegan, B. L.; Liu, Y.; Peredkov, S.; Dechert, S.; Meyer, F.; DeBeer, S.; Cutsail, G. E.  
214 *J. Am. Chem. Soc.* **2022**, *144*, 2520–2534.
- 215 (15) Findlay, N. J.; Park, S. R.; Schoenebeck, F.; Cahard, E.; Zhou, S.; Berlouis, L. E. A.; Spicer,  
216 M. D.; Tuttle, T.; Murphy, J. A. *J. Am. Chem. Soc.* **2010**, *132*, 15462–15464.
- 217 (16) Lu, Z.; Cramer, S. A.; Jenkins, D. M. *Chem. Sci.* **2012**, *3*, 3081–3087.
- 218 (17) Bass, H. M.; Cramer, S. A.; McCullough, A. S.; Bernstein, K. J.; Murdock, C. R.; Jenkins,  
219 D. M. *Organometallics* **2013**, *32*, 2160–2167.
- 220 (18) Schulte to Brinke, C.; Ekkehardt Hahn, F. *Dalt. Trans.* **2015**, *44*, 14315–14322.
- 221 (19) Anneser, M. R.; Haslinger, S.; Pöthig, A.; Cokoja, M.; D’Elia, V.; Högerl, M. P.; Basset,  
222 J.-M.; Kühn, F. E. *Dalt. Trans.* **2016**, *45*, 6449–6455.
- 223 (20) Grove, D. M.; Van Koten, G.; Mul, P.; Van der Zeijden, A. A. H.; Terheijden, J.; Zoutberg,  
224 M. C.; Stam, C. H. *Organometallics* **1986**, *5*, 322–326.
- 225 (21) Stoll, S.; Britt, R. D. *Phys. Chem. Chem. Phys.* **2009**, *11*, 6614.
- 226 (22) Stoll, S.; Schweiger, A. *J. Magn. Reson.* **2006**, *178*, 42–55.
- 227 (23) Connelly, N. G.; Geiger, W. E. *Chem. Rev.* **1996**, *96*, 877–910.